STRATEGIES FOR THE MECHANICALLY TRIGGERED RELEASE OF SMALL MOLECULES

Thesis by

Corey Christopher Husic

In Partial Fulfillment of the Requirements for
the Degree of
Doctor of Philosophy

CALIFORNIA INSTITUTE OF TECHNOLOGY
Pasadena, California

2023
(Defended 21 April 2023)

Corey Christopher Husic
ORCID: 0000-0003-0248-7484

To mountains and music, which kept me going

ACKNOWLEDGEMENTS

Over the past several years, Caltech has served as the grounds for my growth as a human and as a scientist. I will be forever grateful for the friends and acquaintances I have made here. First, I would like to thank my advisor Prof. Maxwell Robb. I joined his lab with uncertain scientific interests, and he provided a space for me to explore and continue to be curious. I am especially grateful for the opportunity he provided for me to branch out from the synthetic focus of the lab to explore computational projects in addition to my experimental work. I would also like to thank my thesis committee members Prof. Sarah Reisman, Prof. Rustem Ismagilov, and Prof. Hosea Nelson for their guidance, support, and keen scientific insights during my time at Caltech.

Before arriving at Caltech, I was fortunate enough to have excellent scientific mentors. Prof. Karin Öberg was my first research mentor at Harvard. I knew nothing about the field of astrochemistry, but she welcomed me into her lab and always made time to teach and help in any way that she could. Little did I know that the coding skills she pushed me to learn would make an impact in graduate school, where my focus occasionally took a computational detour. I also owe immense thanks to Prof. George Whitesides for the opportunity to work in his laboratory at Harvard. It was this experience that solidified my intent on pursuing chemistry as a career. George's unique way of approaching science and thinking about the world left a significant impact on me. I would also like to thank Dr. Lewis Kraft for his excellent scientific mentorship and for his tendency to give unsolicited bad life advice that I still chuckle about to this day. Discussing my time at Harvard would not be complete without mentioning Dr. Ryan Spoering and Prof. Tobias Ritter who ignited my interest in organic chemistry. These two instructors remain some of the best teachers I have ever had, and I am so thankful for having been introduced to organic chemistry in this manner.

Here at Caltech, I have been surrounded by an incredible group of friends. The entire Robb Group has been a wonderful crew to spend the last few years with. I am especially grateful for my Crellin 360 office pals: Anna Overholts, Brooke Versaw, May Zeng, Dr. Peng Liu, Debbie Tseng, and Jolly Patro. These labmates have regularly made me laugh to the point of ending up on the office floor. They have made graduate school bearable. Thank you especially to Anna who has been my best friend and confidant, without whom I may not have pushed through. I would also like to thank Dr. Xiaoran Hu for his mentorship in my early years in the Robb Group. Xiaoran and May were amazing collaborators for much of my work during grad school. Beyond this lab, I am thankful for a host of other Caltech friends who made my time here brighter. Even while speeding her way through her own PhD, Sadie Dutton managed to lift me up from my darkest of places. Isabel Klein and Bryce Hickam always left their door open when I needed some company. Chloe Williams and Sepand Nistanaki downstairs in the Nelson Lab never seemed to mind a mid-afternoon interruption to chat or vent. I am thankful to so many others who I haven't listed here.

Without a tremendous support staff, the chemistry department would not function and my work would have taken significantly longer. I would like to thank Annette Luymes for her work to keep the Robb Group organized, for helping us with the impossible task of scheduling, and for her fountain of campus gossip. Thank you to Joe Drew for keeping the buildings from falling down and always responding promptly to the leaks that plagued Church 320. Scott Virgil has an impossible job of keeping an endless library of instruments running, yet he managed to find time to teach me a ton about his beloved Agilent stacks.

Thank you to Dave Vander Velde without whom the NMR room (and my email inbox) would be a very different place. I am certainly not alone in feeling grateful for Alison Ross who has kept this program running. Seeing Alison at sunrise at a trailhead in the Eastern Sierra was a happy surprise I won't soon forget.

I am thankful for the beautiful campus here at Caltech, a nice reprieve from the sometimes-overwhelming urban environment. Thanks to Bryan Vejar for keeping the trees healthy and beautiful. Thank you to the turtles that probably run this campus. Hardly a day goes by that I don't walk past the turtle pond—and it always makes me smile. Thanks especially to that one adorable softshell turtle.

Beyond Caltech, so many other people have supported me in one way or another. I am immensely thankful to Solveig Millett for her support and compassion; thank you for all the music. Thank you to Éowyn Lucas for introducing me to the Sierra and igniting my love for that corner of California. I would like to thank Elyssa Collins for her friendship and companionship in the mountains. My birding/nature friends, especially Luke Tiller, Catherine Hamilton, Landy Figueroa, Dave Bell, and Jonathan Feenstra were always down for an evening hang when I needed to stop thinking about chemistry. Thank you to Ally Frickman for pushing me to act and think beyond my comfort zone and for always being willing to jump into a frigid alpine lake with me. Thanks to Ruby Drake for being a wonderful friend and for giving me a glimpse into Hollywood. Amalia Mathewson and her sweet pup Greta have been amazing friends, even though we've only known each other for a brief moment. That is the sort of friendship that will last. I also have incredible friends who have supported me from afar; I am so thankful for the texts, phone calls, and letters from Lindsey

Terrell, Kimberly Rivers, Allison Black, and others that have never failed to brighten my day.

Music is an immeasurably important part of my life, and I am grateful for the old-time music community. Here in LA, the 1842 jam crew has felt like a family to me. I am especially grateful for my friendships with Jeff McLeod, Jonathan Shifflett, Kelly Martin, and Joe Wack. The whole Echo Mountain band has made my time in LA incredibly fun. I'll never think of corn muffins in the same way. Thank you to David Bunn for opening his home at Deep End Ranch and providing a space for incredible music and memories.

I would like to thank my parents Dave and Diane Husic for their never-ending support. They are my biggest inspirations. They always allowed me to be curious and gave me room to explore, which let me become the person I am today. I thank my mom for teaching me how to be a leader and how to make a difference in the world. She taught me how to bake a pie and grow a garden. I couldn't ask for a better hiking, birding, or travel partner. My dad taught me how to love and play the fiddle. He showed me how to be gentle and thoughtful. There is no one I am more comfortable with on this planet than my dad. I am grateful for my brother who, in his own unique way, has always been there for me. Sometimes that means comforting me while I cry on the phone, other times discussing surface integrals at 3 am.

Finally, I would like to thank my tabby, Melvin. I adopted him on February 1st, 2020, and he soon became the greatest roommate I could ask for. He is always up for a conversation or some cuddles. There are few things in my life that compare to the feeling of waking up on a sunny weekend morning to find Melvin stretched out and pressed against me. I am not sure how I would've survived the pandemic lockdown without his companionship.

I haven’t always loved living in Los Angeles, but I will certainly miss this place. The friendships I have made here are some of the deepest connections I have ever felt, and I don’t intend to let those connections fade away. Perhaps more than anything, though, I will miss these mountains. The San Gabriels were my second home, an escape when life began to feel unbearable. The Eastern Sierra quickly became a true love, and I savored every chance I had to be there. These are places I won’t soon forget—the sorts of places that I won’t be able to stay away from.

ABSTRACT

The development of force-responsive molecules called mechanophores is a central component of the field of polymer mechanochemistry. Mechanophores enable the design and fabrication of polymers for a variety of applications ranging from sensing to self-healing materials. Nevertheless, an insufficient understanding of structure–activity relationships limits experimental development, and thus computation is necessary to guide structural design. Herein, we use the constrained geometries simulate external force (CoGEF) method to evaluate a library of covalent mechanophores using density functional theory (DFT). We use these results to identify key parameters that accurately predict experimentally determined mechanochemical reactivity.

Polymers that release small molecules upon external stimulation are promising for a wide range of applications, including sensing, catalysis, and drug delivery. Mechanophores are uniquely suited to enable molecular release with excellent selectivity and control. We have designed a general platform for mechanically gated small molecule release that leverages a latent 2-furylcarbinol species masked as a mechanically labile Diels–Alder adduct. Here, we describe the computationally guided design of metastable 2-furylcarbinol derivatives through the prediction of activation energy values and construction of structure–activity relationships. These results enable a molecular release platform suitable for a wide scope of cargo molecules across a broad range of chemical environments.

PUBLISHED CONTENT AND CONTRIBUTIONS

Portions of the work described herein were disclosed in the following publications:

1. Hu, X.; Zeng, T.; **Husic, C. C.**; Robb, M. J. *J. Am. Chem. Soc.* **2019**, *141*, 15018. DOI: https://doi.org/10.1021/jacs.9b08663.

C. C. H. contributed to the computational work, synthesis, data acquisition and analysis, and manuscript preparation.

2. Klein, I. M.;[†] **Husic, C. C.**;[†] Kovács, D. P.; Choquette, N. J.; Robb, M. J. *J. Am. Chem. Soc.* **2020**, *142*, 16364. DOI: https://doi.org/10.1021/jacs.0c06868. [†]authors contributed equally

C. C. H. contributed to the computational work, data preparation and analysis, and manuscript preparation.

3. Hu, X.; Zeng, T.; **Husic, C. C.**; Robb, M. J. *ACS Cent. Sci.* **2021**, *7*, 1216. DOI: https://doi.org/10.1021/acscentsci.1c00460.

C. C. H. contributed to the project conception, computational work, synthesis, data acquisition and analysis, and manuscript preparation.

4. **Husic, C. C.**; Hu, X.; Robb, M. J. *ACS Macro Lett.* **2022**, *11*, 948. DOI: https://doi.org/10.1021/acsmacrolett.2c00344.

C. C. H. contributed to the project conception, computational work, synthesis, data acquisition analysis, and manuscript preparation.

TABLE OF CONTENTS

LIST OF ABBREVIATIONS

+	diffuse function
*	(d)
**	(d,p)
‡	transition state
±	racemic
Å	angstrom(s)
ABq	AB quartet
Ac	acetyl
AFM	atomic force microscopy
AISMD	*ab initio* steered molecular dynamics
aq.	aqueous
Ar	aryl
ATRP	atom transfer radical polymerization
Bn	benzyl
BPA	bisphenol A
br	broad
Bu	butyl
°C	degree(s) Celsius
calc’d	calculated
cm^{-1}	wavenumber(s)

CoGEF	constrained geometries simulate external force
δ	chemical shift in ppm
Δ	heat or difference
Đ	polydispersity
d	day(s) or doublet
d	deutero
dd	doublet of doublets
DBU	1,8-diazabicyclo[5.4.0]undec-7-ene
DCM	dichloromethane
DIC	*N,N'*-diisopropylcarbodiimde
DFT	density functional theory
DMAP	4-dimethylaminopyridine
DMF	*N,N'*-dimethylformamide
DMPU	*N,N'*-dimethylpropyleneurea
DMSO	dimethylsulfoxide
DPTS	4-(dimethylamino)pyridinium 4-toluenesulfonate
ε	dielectric constant
E	energy
E_{max}	maximum energy
Et	ethyl
equiv.	equivalent(s)
ESI	electrospray ionization
F	force

F_{max}	maximum force
FMPES	force-modified potential energy surface
G	Gibbs free energy
$G^{\ddagger}$	Gibbs free energy of transition states
$\Delta G^{\ddagger}$	activation energy
g	gram
g	gem
*g*DCC	*gem*-dichlorocyclopropane
GPC	gel permeation chromatography
h	hour(s)
HF	Hartree–Fock
HFIP	hexafluoroisopropanol
HMPA	hexamethylphosphoramide
HRMS	high resolution mass spectrometry
IS	internal standard
J	joule
J	*J*-coupling
K	Kelvin
k_{B}	Boltzmann constant
kcal	kilocalorie(s)
kDa	kilodalton(s)
kHz	kilohertz
kJ	kilojoule

LCMS	liquid chromatography–mass spectrometry
LDA	lithium diisopropylamide
LiHMDS	lithium bis(trimethylsilyl)amide
M	molar
m	meter or multiplet
m	*meta*
M_n	number-average molecular weight
MALS	multiangle light scattering
*m*CBPA	*meta*-chloroperoxybenxoic acid
Me	methyl
Me_6TREN	tris[2-(dimethylamino)ethyl]amine
MHz	megahertz
min	minute(s)
mL	milliliter(s)
mM	millimolar
mmol	millimole(s)
mol	mole(s)
m/z	mass-to-charge ratio
N	newton(s)
n	*normal* (e.g., *n*-BuLi)
nm	nanometer(s)
NMR	nuclear magnetic resonance
nN	nanonewton(s)

Nuc	nucleophile
o	*ortho*
[O]	oxidation
φ	dihedral angle
p	*para*
Ph	phenyl
PMA	poly(methyl acrylate)
ppm	part(s) per million
PPTS	pyridinium *para*-toluenesulfonate
q	quartet
quant.	quantitative
R	generic group
R_f	retention factor
ROMP	ring-opening metathesis polymerization
RRF	relative response factor
rt	room temperature
s	second(s) or singlet
sat.	saturated
SET-LRP	single-electron transfer living radical polymerization
SMFS	single molecule force spectroscopy
T	temperature
t	*tert*
$\mathrm{t}_{1/2}$	half-life

TBAF	tetra-*n*-butylammonium fluoride
TBDPS	*tert*-butyldiphenylsilyl
TBS	*tert*-butyldimethylsilyl
Tf	trifloromethanesulfonyl
THF	tetrahydrofuran
THP	tetrahydropyranyl
TIPS	triisopropylsilyl
TLC	thin-layer chromatography
Ts	toluenesulfonyl (tosyl)
μL	microliter
μM	micromolar
μmol	micromole(s)
UV	ultraviolet
Vis	visible
v/v	volume concentration
W	watt(s)
X	halide or leaving group

Chapter 1

VALIDATION OF THE CoGEF METHOD AS A PREDICTIVE TOOL FOR POLYMER MECHANOCHEMISTRY

1.1 Introduction

The nascent field of polymer mechanochemistry aims to harness mechanical energy to activate chemical transformations.[1,2] Force is transmitted to stress-responsive molecules called mechanophores through covalently linked polymer chains, leading to productive chemical changes via mechanically selective bond scission.[3] Mechanophores have been designed to undergo a wide variety of mechanochemical reactions including those that produce a change in color or luminescence,[4–7] release small molecules,[8–10] generate reactive functional groups,[11–14] switch electrical conductivity,[15] and reveal catalytic activity.[16,17] In turn, mechanophores engender polymeric materials with advantageous properties such as the ability to strengthen under typically destructive forces[13] and autonomously report on critical stress and strain through easily detected visible signals.[4] The development of new mechanophores is crucial for both advancing fundamental insight into mechanochemical reactivity and expanding the repertoire of mechanochemically responsive materials. Nevertheless, an underdeveloped knowledge of structure–function relationships along with the time and resource requirements of synthesis and evaluation in the laboratory limit experimental pursuits. A simple, rapid, and reliable computational method for screening the mechanochemical activity of molecules prior to experimental investigation is necessary for accelerating mechanophore discovery.

Computational chemistry has had a significant impact on the advancement and fundamental understanding of mechanochemical reactivity. Theoretical studies have revealed that the unique reactivity of mechanophores originates from a distortion of the potential energy surface under large forces, altering the trajectories of chemical reactions.[18–20] Several quantum chemical methods have been leveraged over the past two decades to investigate the effects of force and mechanical deformation on molecular reactivity. *Ab initio* steered molecular dynamics (AISMD) simulations approximate the action of external force on a molecule by applying constant pulling velocities to terminal atoms and following the dynamics of the system over a few picoseconds.[21] Computational methods that consider force explicitly under isotensional stretching have also been introduced, including the force-modified potential energy surface (FMPES),[22] external force is explicitly included (EFEI),[18] and enforced geometry optimization (EGO)[23] models. While these specialized approaches provide detailed information on the energetics and mechanisms of mechanochemical transformations, they are less suited as screening tools for the experimental development of new mechanophores.

The constrained geometries simulate external force (CoGEF) method,[24] on the other hand, is both computationally inexpensive and simple to implement, providing a highly accessible quantum chemistry platform for testing proposed mechanophores *in silico*. The CoGEF method was developed by Beyer in 2000 and simulates the effect of molecular elongation through constrained geometry optimizations. In a typical CoGEF calculation, the distance between two terminal atoms that represent polymer attachment positions is constrained and the geometry of the truncated molecule is optimized. Increasing the end-to-end distance incrementally and optimizing the constrained geometry at each step simulates isometric stretching and enables prediction of the chemical changes that accompany mechanical distortion of the molecule along the reaction coordinate. The CoGEF technique can be implemented in every major commercial software package using any quantum chemistry method that allows constrained geometry optimizations and the mechanochemical reactivity of moderately sized molecules can be evaluated relatively quickly on a desktop computer. Due to its ease of implementation and accessibility, the CoGEF method has been employed to corroborate experimental observations and has become an important component in the workflow for the development of new mechanophores.[3] However, despite the ubiquity of this method in polymer mechanochemistry, CoGEF has yet to be systematically validated.

Here we provide a comprehensive investigation and validation of the CoGEF method applied consistently to every covalent mechanophore structure reported in the literature to date. Mechanochemical reactions involving activation of organometallic compounds,[16,17,25–28] rotaxanes,[29,30] and ionic species[31] have been previously described; however, only mechanophores that undergo covalent bond transformations are considered in this study. We identify over 100 mechanophores and compare the results of CoGEF simulations with their experimentally determined mechanochemical reactivity. In addition, the consistency between CoGEF calculations and the experimentally determined behavior of molecules previously demonstrated to exhibit unproductive reactivity via non-specific bond scission under mechanical force are evaluated as negative controls. Excellent agreement is observed between CoGEF calculations and experimental data at the commonly employed B3LYP/6-31G* level of density functional theory (DFT). Furthermore, the maximum force associated with bond rupture obtained from CoGEF calculations is compared to single molecule force spectroscopy (SMFS) measurements across several classes of mechanophores and demonstrated to be a reliable indicator of mechanochemical activity. This comprehensive evaluation, applied broadly to the experimental literature, reveals that the CoGEF method is a powerful predictive tool for polymer mechanochemistry.

1.2 Methods

CoGEF calculations were performed for each reported structure at the B3LYP/6-31G* level of theory, which has been nearly universally employed in the polymer mechanochemistry literature and provides an appropriate compromise between accuracy and computational cost.[32,33] The results of each CoGEF simulation were then compared to experimental data from the literature to determine the accuracy of the calculation. Chemical structures were truncated to include tethers that accurately reflect the polymer connectivity in the reported experimental studies. The CoGEF calculation was determined to be successful if the predicted products were consistent with the products of the mechanochemical reaction determined from experiments. To assess the ability of CoGEF to predict features beyond qualitative reactivity, calculated forces were also compared to rupture forces determined experimentally from SMFS measurements and other quantitative metrics reported in the literature.

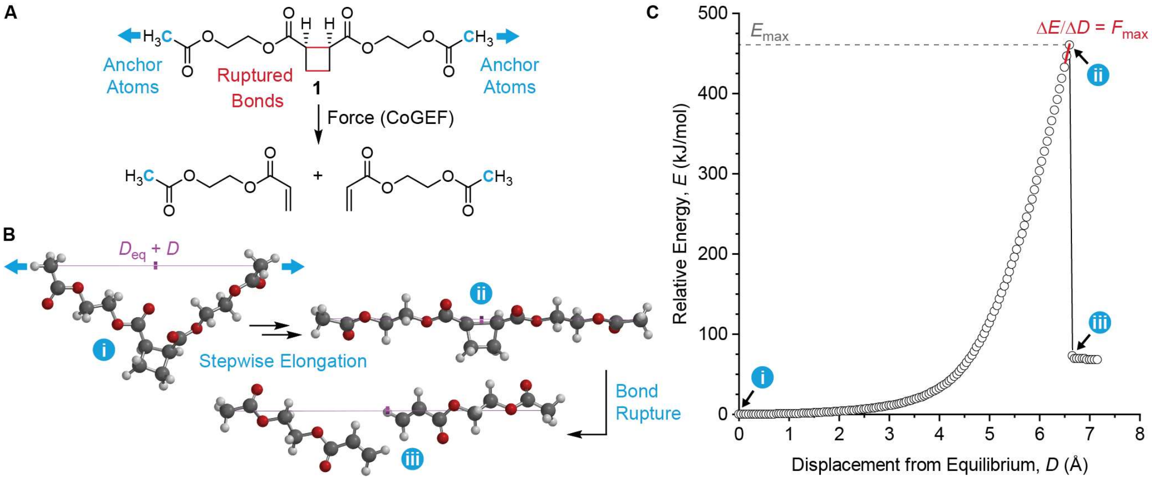

Figure 1.1 Illustration of the CoGEF method applied to representative cyclobutane mechanophore **1**. (A) Structures of the truncated mechanophore and products resulting from a formal retro-[2+2] cycloaddition reaction upon stepwise mechanical elongation predicted at the B3LYP/6-31G* level of theory. Blue carbon atoms designate the anchor points defining the distance constraint. Bonds that are broken in the calculation are colored red. (B) Computed structures at critical points in the CoGEF calculation: (i) the force-free equilibrium geometry, (ii) the constrained geometry immediately prior to bond rupture, and (iii) the predicted product(s). The corresponding points in the CoGEF curve are indicated in part C. (C) Relative energy, E, plotted as a function of displacement from equilibrium, D. E_{max} is the bond dissociation energy associated with the covalent transformation and F_{max} is the maximum force, calculated from the slope of the curve immediately prior to bond rupture.

As a demonstration of the method, a representative CoGEF calculation is illustrated for the mechanochemical formal retro-[2+2] cycloaddition reaction of cyclobutane mechanophore **1** (Figure 1.1A). The equilibrium geometry of the unconstrained model structure is first computed at the B3LYP/6-31G* level of DFT. Subsequently, the distance between terminal atoms (colored blue), which serve as anchor points, is constrained (D_{eq}). The displacement between anchor points, D, relative to the equilibrium geometry is then increased in increments of 0.05 Å, and a constrained geometry optimization is carried out after each step (Figure 1.1B). This process is repeated until a chemical transformation is predicted to occur, as evidenced by the rupture and reorganization of one or more covalent bonds. In addition to qualitatively identifying the structure of the predicted mechanochemical reaction product(s), the energy of the system relative to the energy of the unconstrained, force-free equilibrium geometry, E, is plotted as a function of displacement to generate the CoGEF potential (Figure 1.1C).[24] Two important metrics are obtained from this CoGEF curve. First, the bond dissociation energy is defined as the maximum relative energy immediately prior to bond rupture (E_{max}). Second, the slope of the CoGEF curve ($\Delta E/\Delta D$) at any point along the reaction coordinate reflects the force experienced by the molecule during the simulated isometric stretching. The maximum force, F_{max}, along the CoGEF curve represents the force associated with the mechanochemical transformation (see Appendix A for details). As a static quantum chemical method, rupture forces calculated with CoGEF are typically overestimated compared to experiments because thermal effects are neglected.[19] Nevertheless, they provide a useful metric for evaluating the relative mechanochemical activity of mechanophores as demonstrated below.

The structures of each molecule investigated are presented in Charts 1–8 and the results of each CoGEF calculation are provided in corresponding Tables 1–8, along with references to the primary literature describing the experimentally investigated mechanochemical reactivity of each compound. Mechanophores are classified based on reaction mechanism, although we note that the actual mechanochemical reaction mechanisms have not been determined for most mechanophores and in such cases compounds are categorized based on their formal reactivity. The bonds that are predicted to break in the CoGEF calculations are colored red. The overall reaction predicted by each CoGEF calculation is identified as being either consistent (✓) or inconsistent (✗) with the reported experimental mechanochemical reactivity. We discuss that in some cases in which the calculation is inconsistent with the reported reactivity, the available experimental data is either insufficient or suggest that a structural revision may be necessary. Calculated values of F_{max} and E_{max} are summarized in the tabulated data for each structure. Complete computational data for each structure are included in Appendix A.

1.3 Results and Discussion

1.3.1 Retro-[2+2] Cycloaddition Reactions

The mechanochemical reactivity of molecules containing four-membered rings has been extensively studied. Moore and coworkers reported the mechanochemical generation of cyanoacrylate functional groups resulting from the formal retro-[2+2] cycloaddition reaction of cyano-substituted cyclobutanes in 2010.[34] Subsequently, a number of other cyclobutane mechanophores have been identified as well as mechanochemically active heterocyclic 1,2-dioxetane,[5] beta-lactam,[14] and 1,2-diazetidinone[35] compounds (Chart 1.1). CoGEF calculations successfully predict the anticipated mechanochemical reaction for 32 of the 34 structures in this category (Table 1.1).

In a seminal paper published in 2011,[36] Kryger *et al.* reported a systematic study of the relative reactivity of substituted cyclobutane mechanophores, comparing the results of ultrasound-induced mechanochemical activation experiments to predictions from CoGEF calculations. A threshold molecular weight was determined for each chain-centered cyclobutane derivative and used as a proxy for mechanochemical activity, with a lower molecular weight threshold indicating a more reactive substrate. The trends in experimental reactivity were generally found to be consistent with the results of CoGEF calculations. In our hands, CoGEF calculations performed on analogous cyclobutane compounds **1**–**6**

Chart 1.1 Structures Associated with Formal Retro-[2+2] Cycloaddition Reactions

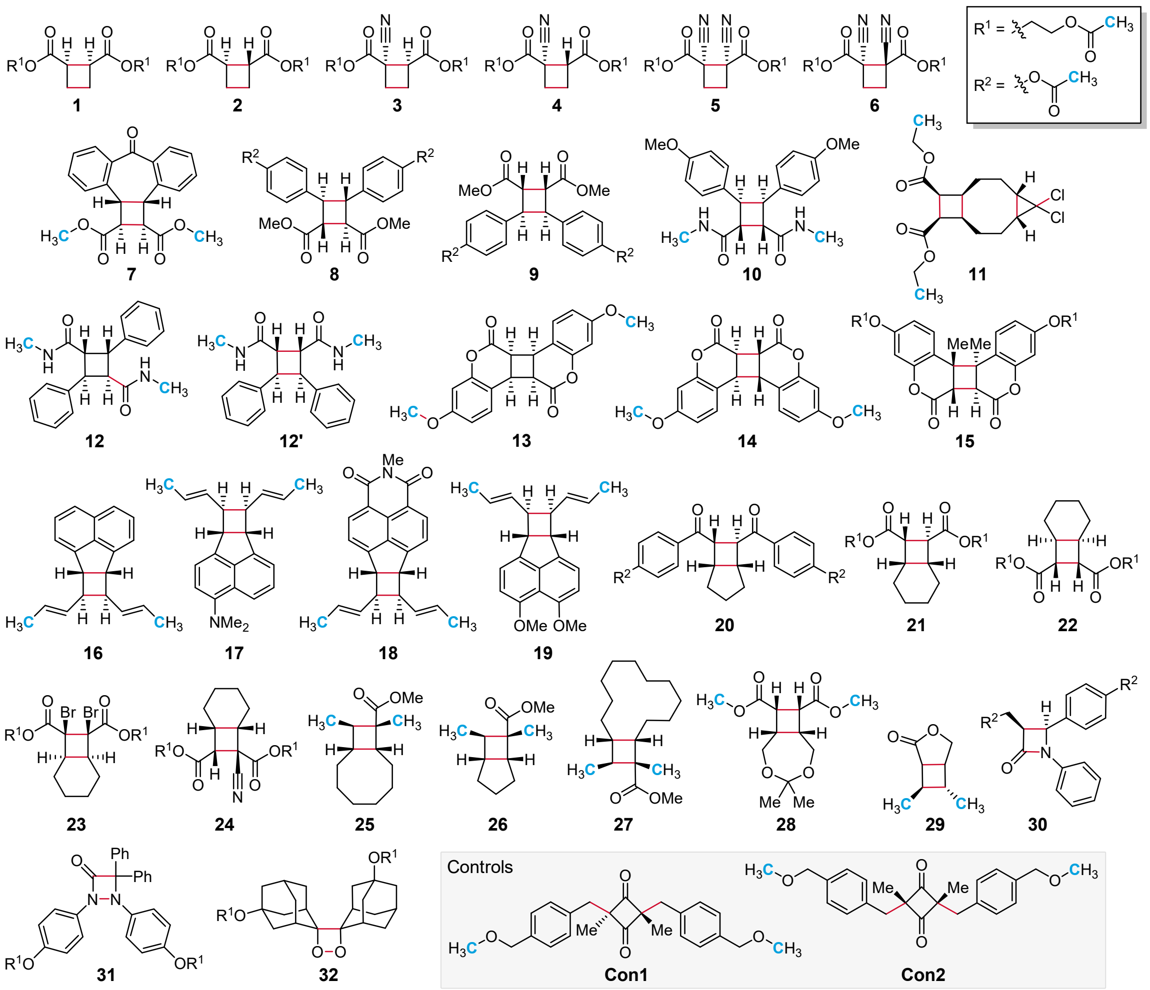

produce similar results; however, subtle variation in the truncation of the computed structures compared to those investigated by Kryger *et al.* reveals an important consideration. Here, cyclobutane mechanophores **1**–**6** include longer tethers compared to the structures computed by Kryger *et al.*, which contained terminal methyl ester groups directly attached to the cyclobutane cores. Despite the differences in truncation, our calculated values of F_{max} closely match those reported previously; however, the calculated values of E_{max} are highly variable, differing by more than 350 kJ/mol for cyclobutane **2**, for instance. This case study typifies a general observation that F_{max} is a robust quantitative

Table 1.1 CoGEF Results for Formal Retro-[2+2] Cycloaddition Reactions§

Structure	Result[a]	F_{max} (nN)	E_{max} (kJ/mol)	Ref.
1	✓	4.6	460	36
2	✓	5.9	746	36
3	✓	4.0	335	36
4	✓	4.8	426	36
5	✓	3.4	285	34,36
6	✓	5.0	444	34,36
7	✓	4.5	413	37
8	✓	5.0	417	38
9	✓	2.5	253	38
10	✓	4.4	364	39
11	✓	4.7, 3.8[b]	395, 291[b]	40
12	×	5.9	498	41,42
12′	✓[c]	4.4	359	-
13	×	6.3	658	43
14	✓	5.6	633	43
15	✓	5.9	1017	44
16	✓	3.3	244	45
17	✓	3.3	241	45
18	✓	3.3	244	45
19	✓	3.3	236	45
20	✓	5.5	692	46
21	✓	5.2	562	47
22	✓	4.6	469	47
23	✓	3.6	332	47
24	✓	4.0	313	47
25	✓	3.8	302	48
26	✓	3.5	278	48
27	✓	3.7	306	48
28	✓	4.4	345	49
29	✓	5.4	331	50
30	✓	3.5	284	14
31	✓	3.6	260	35
32	✓	4.4	495	5
Con1	✓	6.3	947	51
Con2	✓	6.4	959	51

§B3LYP/6-31G* level of DFT. [a]Consistency between CoGEF prediction and reported experimental reactivity. [b]Computed values associated with reaction of the *g*DCC subunit. [c]Structural revision results in CoGEF prediction matching expected reactivity.

metric obtained from CoGEF calculations and a better descriptor of relative mechanochemical activity than E_{max}. We therefore focus on the calculated values of F_{max} in the discussion of quantitative mechanochemical relationships for illustrative examples within each class of mechanochemical reactions and return to a more general discussion of quantitative aspects of CoGEF toward the end of the article.

The influence of both stereochemistry and regiochemistry at the polymer attachment positions is evident in the CoGEF results for this class of mechanophores. Another consistent feature that emerges from the data is the impact of *cis* versus *trans* stereochemistry at the pulling positions. In particular, cyclobutanes containing a *cis* pulling geometry are predicted to have lower values of $F_{\max}$ compared to the corresponding *trans* isomer, which is again consistent with previous observations of Kryger *et al.* for cyclobutanes **1**–**6**.[36] Furthermore, we note that the reactions predicted for different mechanophores often proceed with a range of synchronicity. In many cases, the reaction occurs in a single elongational step, while asynchronous or stepwise fragmentation of other mechanophores is observed that occurs over multiple steps of the CoGEF profile to ultimately furnish the expected products. These variations potentially reflect differences in mechanism, such as diradicaloid character in an asynchronous reaction,[36] although mechanistic interpretations should be treated carefully due to the constraints imposed on the system and the level of theory employed. Nevertheless, the results presented herein suggest that many mechanistic features are accurately captured using the CoGEF method.

Compound **11** is unique among this class of mechanophores, as it possesses two distinct mechanochemically active subunits. Wang *et al.* demonstrated that each subunit is activated in sequence upon mechanical elongation, illustrating the concept of mechanical gating whereby the ring-opening reaction of the *gem*-dichlorocyclopropane unit is contingent upon the cycloelimination reaction of the cyclobutane motif.[40] CoGEF simulations are consistent with this result, predicting initial fragmentation of the cyclobutane group via a formal retro-[2+2] cycloaddition reaction with an F_{max} value of 4.7 nN followed by further molecular extension that ultimately leads to ring-opening of the more reactive *gem*-dichlorocyclopropane at a lower F_{max} value of 3.8 nN. The concept of gating has led to a number of developments in polymer mechanochemistry recently being applied to mechanically gated photoswitching,[52] photochemically gated chain scission,[53] mechanically triggered molecular release,[10] and mechanically gated polymer degradation.[49,50]

For cyclobutane compound **12**, the CoGEF calculation predicts C–C bond cleavage at a location peripheral to the four-membered ring that is inconsistent with the reported reactivity. Each of the four-membered-ring mechanophores for which CoGEF correctly predicts a formal cycloelimination reaction exhibits a 1,2-disubstitution pattern for the positions of polymer attachment. In contrast, cinnamamide dimer **12** was reported to have a 1,3-disubstitution geometry on the cyclobutane ring.[41,42] The available experimental data are insufficient to confirm the structure of the dimer in question, but the photodimerization of cinnamic acid and related derivatives has been shown to produce the head-to-head dimer corresponding to the 1,2-disubstituted cyclobutane.[54,55] CoGEF calculations performed on alternative head-to-head dimer **12′** predict a formal cycloelimination reaction upon mechanical elongation, in agreement with the computational results for other 1,2-disubstituted cyclobutane mechanophores. Based on this evaluation, we speculate that the fluorogenic mechanochemical activity previously observed for the cinnamamide dimer mechanophore may originate from reaction of the 1,2-disubstituted compound **12′**. Additionally, the CoGEF calculation performed on head-to-tail coumarin dimer **13** predicts scission of the C–O bond adjacent to the pulling position, rather than the experimentally observed retro-[2+2] cycloaddition reaction. Compared to head-to-head coumarin dimer **14**, the head-to-tail dimer was demonstrated to be significantly less reactive.[43]

Although the number of compounds that have been reported in the literature to exhibit non-productive reactivity under mechanical force is relatively limited, the ability to accurately identify this type of behavior in negative controls is critical to validate the CoGEF method as a reliable predictive tool. Two such examples are available in this class of mechanochemical reactions. The mechanochemical reactivity of *cis* and *trans* disubstituted 1,3-cyclobutanedione molecules **Con1** and **Con2** was investigated by Sijbesma and coworkers and both molecules were found to undergo non-specific bond scission under ultrasound-induced mechanical force rather than formal cycloelimination.[51] Consistent with these experimental observations, CoGEF calculations predict C–C bond scission peripheral to the cyclobutanedione core. Intriguingly, both benzylic C–C bonds cleave simultaneously in the CoGEF calculations to form a product consistent with the structure of 1,3-dimethylbicyclo[1.1.0]butane-2,4-dione for both the *cis* and *trans* cyclobutanedione stereoisomers. These results further reinforce the apparent regiochemical constraints for mechanochemical activation of four-membered-ring compounds and point to the privileged mechanochemical reactivity derived from 1,2-disubstitution.

1.3.2 Retro-[4+2] Cycloaddition Reactions

Mechanically activated formal retro-[4+2] cycloaddition reactions have also been demonstrated for a variety of mechanophores (Chart 1.2). Within this category, retro-Diels–Alder reactions are prominent transformations that have garnered significant attention for applications including stress sensing[52,56,57] and triggered small molecule release.[9,10] CoGEF calculations successfully reproduce the reported experimental mechanochemical reactivity for 13 of the 18 structures in this category (Table 1.2).

CoGEF calculations performed on mechanophores **33**–**37** result in C–C, C–O, or C–S bond rupture that is inconsistent with the reported cycloelimination reactions. The mechanochemical reaction of oxanorbornadiene mechanophore **33** was achieved under compression in crosslinked elastomers resulting in the release of a small molecule furan derivative.[9] Mechanical activation of **33** was hypothesized to proceed via a unique "flex activation" mechanism whereby force-induced bond-bending motions promote the desired retro-[4+2] cycloaddition reaction. Other computational studies have suggested that this reaction manifold is less sensitive to external mechanical perturbation and that a significant thermal component is still required for activation under relatively large forces.[20] Poor orientational alignment between the scissile bonds and the direction of applied force along the reaction coordinate results in weak mechanochemical coupling in these systems, and mechanical force alone is insufficient for activation. The formal retro-Diels–Alder reaction

Chart 1.2 Structures Associated with Formal Retro-[4+2] Cycloaddition Reactions

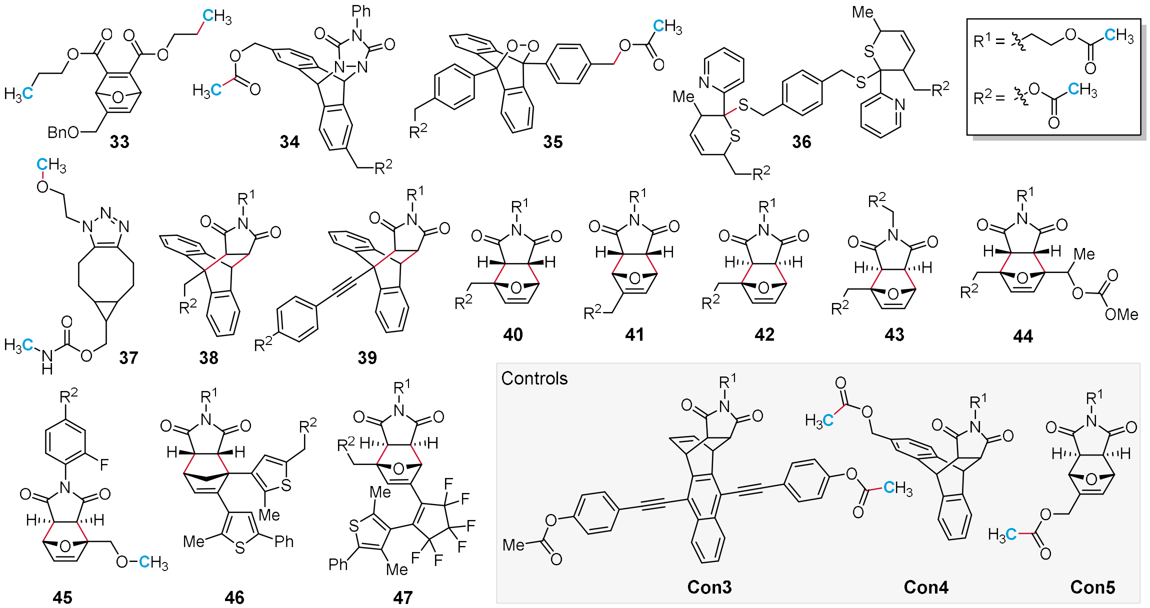

Table 1.2 CoGEF Results for Formal Retro-[4+2] Cycloaddition Reactions[§]

Structure	Result[a]	$F_{\max}$ (nN)	$E_{\max}$ (kJ/mol)	Ref.
33	×	6.2	676	9,58
34	×	6.0	693	59
35	×	5.8	736	60
36	×	2.9	295	61
37	×	6.5	772	62
38	✓	4.1	306	63,64
39	✓	4.0	372	56
40	✓	3.9	230	65
41	✓	4.8	504	65
42	✓	4.1	285	65,66
43	✓	4.0	264	67
44	✓	4.0	245	10
45	✓	3.8	284	68
46	✓	4.6	396	52
47	✓	3.9	243	53
Con3	✓	6.0	843	56
Con4	✓	6.0	832	63
Con5	✓	6.0	650	65

[§]B3LYP/6-31G* level of DFT. [a]Consistency between CoGEF prediction and reported experimental reactivity.

of phenyltriazolinedione–anthracene adduct **34** was also investigated experimentally in crosslinked elastomers under tension where mechanical activation is expected to proceed via force-induced planarization.[59] In addition to mechanical strain, simultaneous heating was required to achieve activation on the order of ~1% at 125 °C, indicating a relatively low level of mechanochemical reactivity. The reaction of **35** was recently reported to produce singlet oxygen under mechanical stress via a similar planarization process,[60] although it is important to note that control experiments to rule out thermal activation were not presented. For these flex-activated mechanophores, proper consideration of the thermal energy is critical in order to accurately model their reactivity. CoGEF calculations performed on compound **36** predict C–S bond scission instead of a retro-[4+2] cycloaddition reaction. Characterization data suggest that the bis-hetero-Diels–Alder adduct investigated was symmetric,[69] although the reported structure of **36** differs in the configuration of each adduct.[61] Nevertheless, CoGEF calculations performed on simple models of individual hetero-Diels–Alder adducts comprising all of the different possible regio- and stereoisomers result in the same C–S bond scission (Figure 1.2). We cautiously

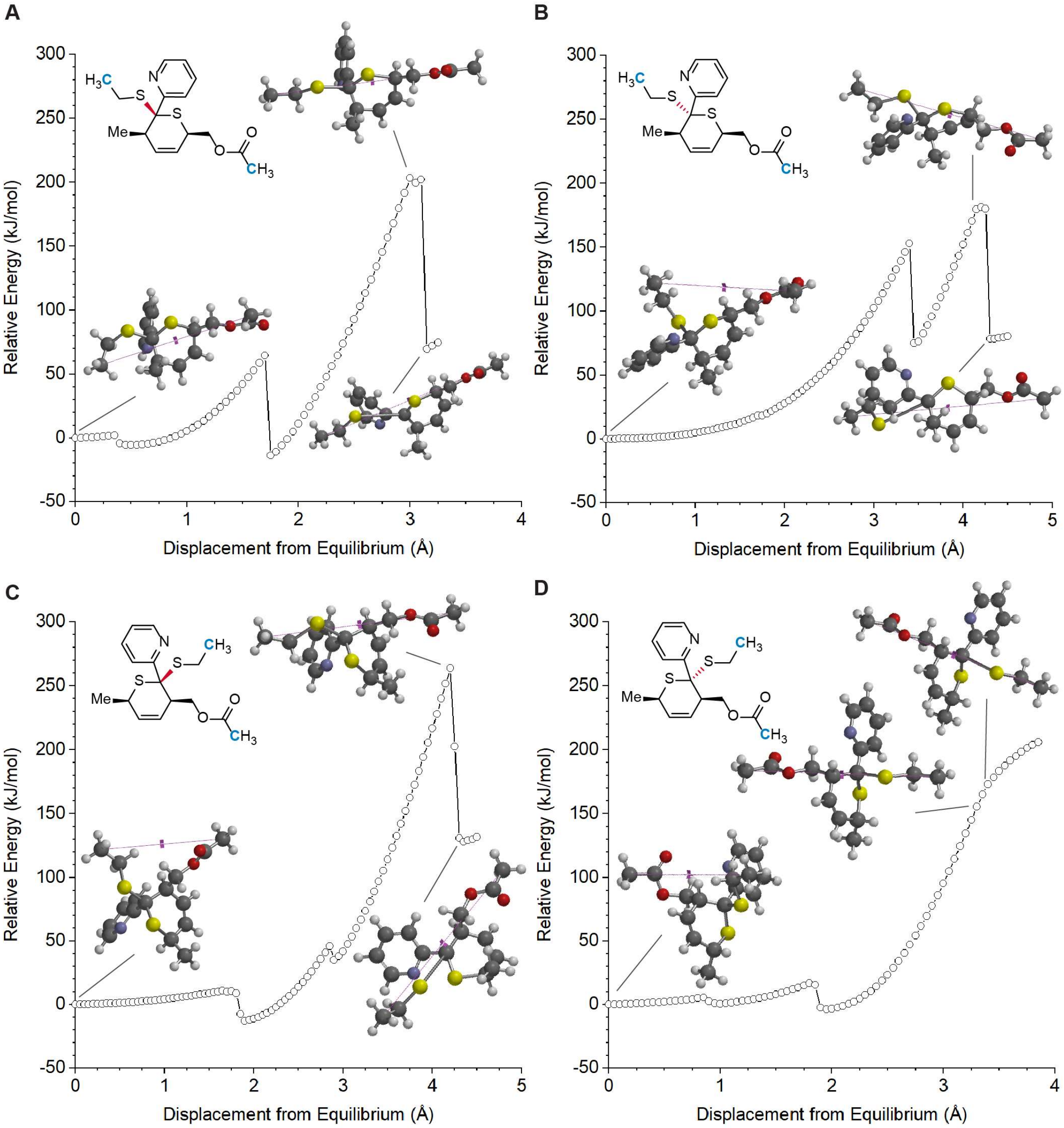

Figure 1.2 CoGEF results for four possible isomers of a hetero-Diels–Alder adduct corresponding to the reactive subunits of reported mechanophore **36**. All isomers are predicted to undergo C–S bond scission rather than the formal retro-[4+2] cycloaddition reaction.

note that additional experimental investigation is warranted to confirm the mechanochemical reactivity of the hetero-Diels–Alder adduct(s) represented by compound **36**, as well as compound **35**.

The mechanochemical cycloreversion of 1,2,3-triazoles has been the subject of debate in the mechanochemistry literature.[19,70] This transformation has piqued interest due to the ubiquitous use of azide–alkyne cycloaddition "click" chemistry.[71] Blank and coworkers previously demonstrated that the CoGEF method predicts a retro-[4+2] cycloaddition reaction for some 1,2,3-triazoles, although the reactivity is highly sensitive to pulling geometry.[33] For triazoles derived from terminal alkynes, the cycloreversion reaction is only predicted for the 1,5-regioisomer, whereas non-specific bond scission adjacent to the triazole ring is expected for the 1,4-regioisomer accessed through the popular copper-catalyzed[72,73] cycloaddition reaction. Stauch and Dreuw further demonstrated that even for 1,5-substitued 1,2,3-triazoles, cycloreversion competes with rupture of the C–N bond at the location of polymer attachment on the triazole ring because the forces associated with both processes are similar.[74] Experimentally, the cycloreversion reaction of a 1,5-disubstituted 1,2,3-triazole was investigated using atomic force microscopy (AFM) methods leading to inconclusive results.[75] In another AFM study, the mechanochemical cycloreversion reaction of the strain-promoted azide–alkyne cycloaddition product **37** was probed, which suggested that cycloreversion of the triazole was achieved at the single molecule level as deduced through a series of subsequent labeling experiments.[62] Nevertheless, the methods employed in the study did not permit conclusive chemical analysis of the reaction products. The CoGEF calculation for compound **37** predicts C–O bond scission in the tether and not the cycloreversion reaction, similar to the results of previous computational studies on this scaffold.[33]

Three molecules have been studied experimentally that serve as negative controls for this category of formal retro-[4+2] cycloaddition reactions. In contrast to mechanophores **38** and **39** that reveal fluorescent anthracene derivatives upon mechanochemical activation, anthracene–maleimide Diels–Alder adducts **Con3** and **Con4** with distal pulling geometries do not undergo a retro-[4+2] cycloaddition reaction under force.[56,63] CoGEF calculations are consistent with these experimental results, predicting C–C bond scission at a terminal position in the tether groups instead of cycloelimination. In addition, Stevenson and De Bo elegantly illustrated the impact of both regiochemistry and stereochemistry on the mechanochemical reactivity of furan–maleimide adducts.[65] Compound **Con5** with *exo* stereochemistry and a distal pulling position relative to the furan–maleimide junction was demonstrated to be mechanically inert under ultrasound-induced elongational force due to poor alignment of the scissile bonds with the force vector. This behavior is accurately captured by the CoGEF calculation for this substrate, which predicts C–C bond rupture adjacent to the terminal pulling position rather than the retro-[4+2] cycloaddition reaction observed in the CoGEF calculations for experimentally verified mechanophores **40**–**42**. In addition, the calculated values of F_{max} for these three furan–maleimide mechanophores are also consistent with their experimentally determined reactivity. For example, *proximal–endo* isomer **40** exhibited the lowest threshold molecular weight while *distal–endo* isomer **41** had the highest threshold molecular weight of the mechanochemically active adducts. The calculated values of F_{max} for mechanophores **40** and **41** are 3.9 nN and 4.8 nN, respectively.

1.3.3 Retro-[4+4] Cycloaddition Reactions

Anthracene dimers **48** and **49** have been reported to undergo a formal retro-[4+4] cycloaddition reaction under mechanical compression in polymeric materials to generate fluorescent anthracene moieties (Chart 1.3).[76,77] CoGEF calculations do not predict the anticipated cycloelimination reaction for either compound, instead suggesting unproductive C–C or C–N bond scission near the pulling point (Table 1.3). However,

Chart 1.3 Structures Associated with Formal Retro-[4+4] Cycloaddition Reactions

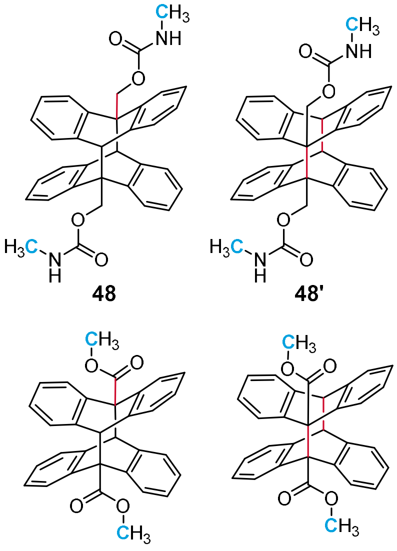

48 **48'**

49 **49'**

Table 1.3 CoGEF Results for Formal Retro-[4+4] Cycloaddition Reactions[§]

Structure	Result[a]	$F_{\max}$ (nN)	$E_{\max}$ (kJ/mol)	Ref.
48	×	6.9	844	76
48′	✓[b]	2.3	140	-
49	×	5.8	557	77
49′	✓[b]	2.2	167	-

[§]B3LYP/6-31G* level of DFT. [a]Consistency between CoGEF prediction and reported experimental reactivity. [b]Structural revision results in CoGEF prediction matching expected reactivity.

unlike the bond elongation process typically operative in the activation of other mechanophores, we envisioned that the structure of these adducts may be uniquely susceptible to mechanical activation through compression-induced planarization. Modified CoGEF calculations were performed on **48** and **49** in which two carbon atoms in opposing phenyl rings were brought closer together in a typical series of constrained geometry calculations at the B3LYP/6-31G* level of theory. For both compounds, this alternative CoGEF model does indeed predict the formal retro-[4+4] cycloaddition reaction to generate a pair of anthracene products (Figure 1.3). These results may suggest that typical CoGEF calculations do not properly reflect the mode of mechanical activation for anthracene dimer mechanophores. However, it is important to note that the unconventional constrained geometry calculations were designed specifically to emulate the geometric distortions that are anticipated to occur for the anthracene dimers under compressive stress. We caution against applying these alternative methods broadly because they do not represent a realistic mode of mechanical activation for most mechanophores.

Based on the regiochemical effects observed for other classes of mechanophores, we were also curious to investigate the impact of regiochemistry on the predicted mechanochemical reactivity of the anthracene dimer. The photodimerization of anthracene derivatives typically produces the head-to-tail isomer selectively; however, the head-to-head configuration is also accessible under certain conditions.[78,79] The typical CoGEF operation performed on alternative head-to-head dimers **48′** and **49′** predicts the desired cycloelimination reactions. Although mechanistic interpretations should again be treated with caution, the CoGEF simulations performed on the anthracene dimer indicate that the

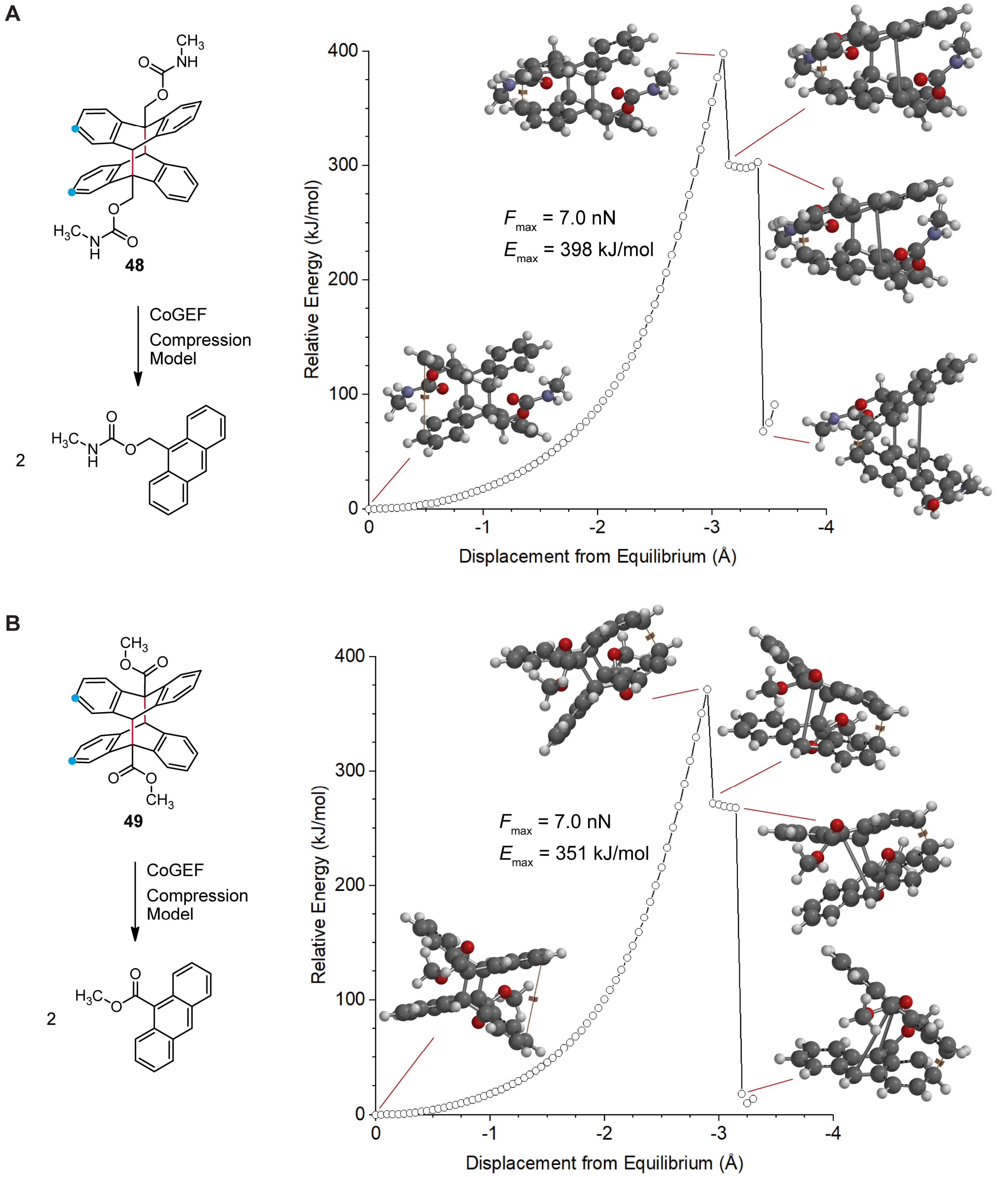

Figure 1.3 CoGEF calculations performed in an alternative compression mode for head-to-tail anthracene dimer mechanophores (A) **48** and (B) **49**. The distance between carbon atoms labeled with a blue dot was decreased incrementally starting from the force-free equilibrium geometry. At each step, the geometry was optimized at the B3LYP/6-31G* level of DFT. Both molecules are predicted to undergo a formal retro-[4+4] cycloaddition reaction upon simulated compression. The transformation proceeds through an apparent stepwise pathway suggesting an intermediate with diradical character.

cycloelimination reaction does not proceed via a concerted retro-[4+4] cycloaddition reaction. Instead, the calculations suggest a stepwise reaction involving sequential, discrete bond-breaking events before ultimately generating the two anthracene products. This behavior is observed for both the head-to-tail and head-to-head dimers regardless of the simulated mode of mechanical activation.

1.3.4 2π Electrocyclic Ring-Opening Reactions

Since first reported by Craig and coworkers in 2009,[12] the mechanochemical 2π electrocyclic ring-opening reaction of *gem*-dihalocyclopropane (gDHC) mechanophores to generate 2,3-dihaloalkenes has been studied extensively. In addition to cyclopropanes, the mechanochemical reactivity of three-membered heterocycles including epoxides[80,81] and aziridines[82] has also been explored (Chart 1.4). Unlike most of the mechanophores presented above that undergo cycloelimination reactions, mechanophores that undergo electrocyclic ring-opening reactions are non-scissile, allowing for the incorporation of many reactive units per polymer chain, thus enabling a greater degree of activation per stretching event.[83] CoGEF calculations successfully predict a 2π electrocyclic ring-opening

Chart 1.4 Structures Associated with Formal 2π Electrocyclic Ring-Opening Reactions

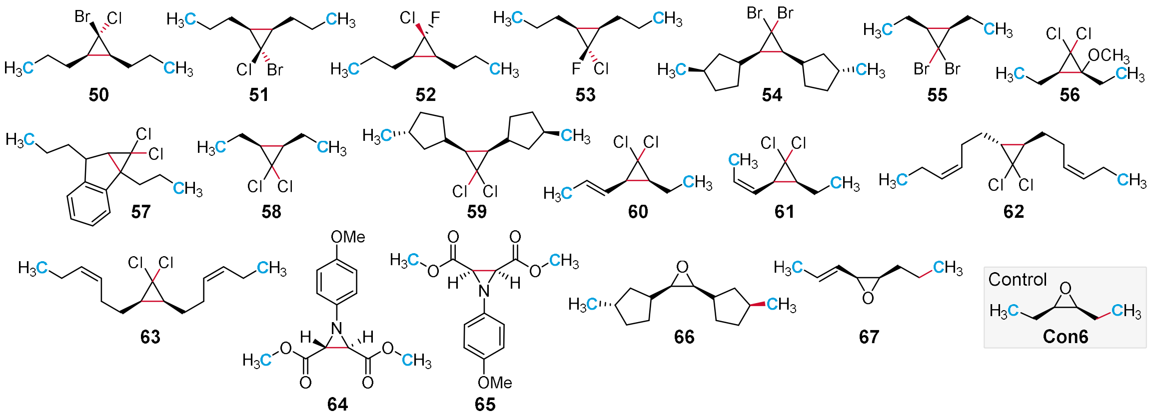

reaction that is consistent with the determined experimental behavior for 16 of the 19 structures in this category (Table 1.4).

Table 1.4 CoGEF Results for Formal 2π Electrocyclic Ring-Opening Reactions§

Structure	Result[a]	F_{max} (nN)	E_{max} (kJ/mol)	Ref.
50	✓	3.6	216	84,85
51	✓	3.3	184	84,85
52	✓	3.5	262	86
53	✓	3.2	183	86
54	✓	3.3	164	87
55	✓	3.7	180	13,84,85,88
56	✓	3.6	166	89
57	✓	5.7	448	8
58	✓	3.8	205	12,84,87
59	✓	3.4	190	87
60	✓	3.2	148	90
61	✓	3.7	202	90
62	×	5.2	557	12,91
63	✓	3.8	340	12,91
64	✓	5.4	300	82
65	✓	5.6	416	82
66	×	6.4	729	80
67	×	6.2	549	81
Con6	✓	6.2	607	80

§B3LYP/6-31G* level of DFT. [a]Consistency between CoGEF prediction and reported experimental reactivity.

CoGEF calculations correctly predict the C–C bond cleavage and concerted halide migration to form a 2,3-dihaloalkene product consistent with the anticipated 2π electrocyclic ring-opening reaction of *g*DHCs with only one exception, as noted below. The halide *anti* to the outwardly rotating alkyl substituents is the preferred leaving group for the thermal electrocyclic ring-opening reaction according to the Woodward–Hoffman–DePuy (WHD) rules.[92–94] For *gem*-bromochlorocyclopropanes (*g*BCC) **50** and **51**, CoGEF calculations follow the WHD predicted pathways and occur with migration of chlorine and bromine, respectively, which are *anti* to the alkyl substituents in each case. These results are consistent with experiments for the mechanical activation of a copolymer containing each *g*BCC isomer, which proceeded to form both the chlorine and bromine migration products.[85] On the other hand, CoGEF calculations predict chlorine migration for both *gem*-chlorofluorocyclopropane (gCFC) mechanophores **52** and **53**, which contradicts the WHD rules, but again is consistent with experimental findings.[86] In this case, radical trapping experiments indicate that *syn*-Cl isomer **52** reacts via a mechanism involving a transition state with considerable diradicaloid character, similar to the isomerization reaction of *gem*-difluorocyclopropane (*g*DFC) mechanophores (*vide infra*). The value of $F_{\max}$ calculated for *syn*-Cl *g*CFC **52** is approximately 0.3 nN larger than the $F_{\max}$ for *anti*-Cl *g*CFC **53**, which also agrees with the relative reactivity of the two mechanophores observed from SMFS experiments.[86] Finally, we note that CoGEF calculations performed on mechanophores **56** and **57** successfully predict the expected 2π electrocyclic ring-opening reactions accompanied by chlorine migration; however, the corresponding 2,3-dichloroalkene products in these cases are thermally unstable and undergo subsequent elimination of HCl in the laboratory,[8,89] which is not captured in the simulations, as expected.

The diversity of structural variations for the *g*DHC mechanophores provides an opportunity to compare the results of CoGEF calculations to experimentally determined structure–property relationships. For example, comparing mechanophores **58**, **59**, and **60** reveals the impact of a so-called lever-arm effect[87] that has been demonstrated to reduce the force required for ring-opening by providing more efficient force transfer to the mechanophore. SMFS experiments confirm that a polynorbornene backbone attached to the *gem*-dichlorocycloproprane (*g*DCC) mechanophore (**59**) or the addition of an *E*-alkene substituent (**60**) lowers the force required to promote the mechanochemical ring-opening reaction from approximately 1.3 nN for **58** to 0.9 and 0.8 nN for **59** and **60**, respectively.[87,90] The results of CoGEF calculations are consistent with these experimentally determined trends in reactivity. The CoGEF calculation performed on *cis*-*g*DCC mechanophore **58** with simple alkyl substituents predicts an $F_{\max}$ value of 3.8 nN. Modifying the tethers to include terminal cyclopentyl groups that mimic the structure of a polynorbornene backbone lowers the calculated value of $F_{\max}$ to 3.4 nN for **59**, while incorporation of an *E*-alkene adjacent to the *g*DCC results in a calculated $F_{\max}$ of 3.2 nN for **60**. The incorporation of a *Z*-alkene substituent is less effective than the *E*-alkene, requiring a force of approximately 1.2 nN to achieve the ring-opening reaction in SMFS experiments.[90] The relative impact of the *Z*-alkene is also accurately reflected in the CoGEF calculation with a predicted $F_{\max}$ value of 3.7 nN for **61**, just below the calculated value of $F_{\max}$ for dialkyl substituted mechanophore **58**.

The CoGEF calculation performed on *trans*-*g*DCC mechanophore **62** does not predict a 2π electrocyclic ring-opening reaction with concurrent halide migration to generate a 2,3-dichloroalkene product. Instead, the predicted transformation mirrors the CoGEF results for the *g*DFC mechanophores described below, indicating cleavage of the central C–C bond to form a product consistent with a transient diradical species. Although the mechanochemical reaction of *cis* and *trans* *g*DCC isomers was previously demonstrated to occur with nearly equal probability under ultrasonication conditions,[12] SMFS measurements revealed substantially different plateau forces of 1.3 nN and 2.3 nN for *cis*-*g*DCC and *trans*-*g*DCC, respectively.[91] Despite the different reaction pathways predicted by CoGEF, the calculated values of $F_{\max}$ reflect the impact of *cis* and *trans* stereochemistry on the *g*DCC mechanophore observed in SMFS experiments. The value of F_{max} calculated for the electrocyclic ring-opening reaction of *cis*-*g*DCC mechanophore **63** is 3.8 nN, while the F_{max} value predicted for the reaction of *trans*-*g*DCC analog **62** is 5.2 nN. The significantly larger force measured for the reaction of the *trans*-*g*DCC mechanophore is consistent with an electrocyclic ring-opening reaction that proceeds via a formally symmetry-forbidden conrotatory pathway.[91] Alternatively, the CoGEF results for **62** suggest another intriguing mechanistic possibility, in analogy to the reactivity observed for *g*DFC mechanophores.[95] That is, isomerization of the *trans*-*g*DCC into the *cis* isomer via a transient mechanical force and subsequent reaction via the expected electrocyclic ring-opening pathway would ultimately furnish the 2,3-dichloroalkene product. To the best of our knowledge, this hypothesis has not been tested experimentally.

The mechanochemical ring-opening reaction of epoxides to generate carbonyl ylide intermediates has been demonstrated for mechanophores **66** and **67**, although the reactivity is low.[80,81] SMFS measurements have revealed that the rate of ring-opening for even the most mechanochemically reactive allylic epoxide **67** is very slow under significantly large forces of approximately 2.5 nN,[81] suggesting that ring-opening likely competes with non-specific bond scission in the polymer backbone. CoGEF calculations performed on these epoxide mechanophores fail to reproduce the ring-opening behavior and instead predict C–C bond scission adjacent to the pulling point. The mechanochemical ring-opening reaction of epoxidized polybutadiene has also been characterized by SMFS measurements, which did not reveal any evidence for epoxide ring-opening at forces up to 2.5 nN.[80] Again, the cyclopentyl groups of structure **66** reflect a polynorbornene backbone, which has been suggested to provide more efficient force transduction compared to polybutadiene.[87]

Similar to the other epoxides, the CoGEF calculation performed on **Con6** does not predict a ring-opening reaction, which in this case is consistent with the experimental observation that epoxidized polybutadiene is mechanochemically inactive.

1.3.5 4π Electrocyclic Ring-Opening Reactions

In 2007, Moore and coworkers described the mechanochemical 4π electrocyclic ring-opening reaction of benzocyclobutene.[11] Remarkably, both the *cis* and *trans* 1,2-disubstituted benzocyclobutenes were demonstrated to undergo formal disrotatory and conrotatory electrocyclic ring-opening reactions, respectively, to generate identical *E*,*E*-*ortho*-quinodimethide intermediates. For the formally symmetry-forbidden disrotatory electrocyclic ring-opening reaction of the *cis*-isomer, FMPES calculations suggest that mechanical force reduces the activation barrier of the concerted pathway, which becomes barrierless at sufficiently high forces.[22] Six benzocyclobutene congeners have been investigated experimentally that differ in the substitution and stereochemistry at the positions of polymer attachment (Chart 1.5). CoGEF calculations predict a formal 4π electrocyclic ring-opening reaction for all six benzocyclobutene compounds reported in the literature (Table 1.5).

Chart 1.5 Structures Associated with Formal 4π Electrocyclic Ring-Opening Reactions

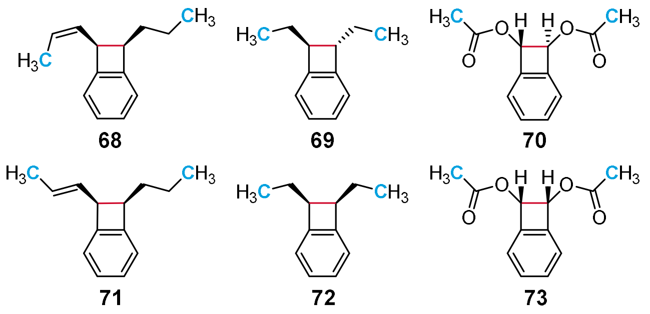

Table 1.5 CoGEF Results for Formal 4π Electrocyclic Ring-Opening Reactions§

Structure	Result[a]	F_{max} (nN)	E_{max} (kJ/mol)	Ref.
68	✓	3.7	282	96
69	✓	4.1	186	91
70	✓	4.1	211	11,97
71	✓	3.1	244	96
72	✓	3.7	367	91
73	✓	3.0	310	11,97

§B3LYP/6-31G* level of DFT. [a]Consistency between CoGEF prediction and reported experimental reactivity.

The CoGEF calculations performed on *cis* and *trans* 1,2-disubstitued benzocyclobutenes result in the formation of the same *ortho*-quinodimethide products, consistent with experimental measurements. The simulated ring-opening reactions of **68**–**71** are consistent with a synchronous transformation in which the breaking and reformation of bonds occurs over a single elongation step in the CoGEF profile. On the other hand, the CoGEF calculations performed on mechanophores **72** and **73** appear to proceed through a highly asynchronous ring-opening process, which could suggest the formation of significant diradicaloid character prior to formation of the *ortho*-quinodimethide product. This behavior is not consistent with orbital symmetry arguments as the predicted ring-opening reaction of other *cis*-disubstituted benzocyclobutenes **68** and **71** occurs synchronously, so the origin of these qualitative differences in the CoGEF profiles is unclear.

The impact of *cis* and *trans* stereochemistry of the pulling positions on the four-membered-ring follows the same trends as the cyclobutane and *gem*-dichlorocyclopropane mechanophores presented above. The predicted F_{max} is lower for *cis*-isomer **72** compared to the corresponding *trans*-isomer **69**, with calculated values of 3.7 and 4.1 nN, respectively. This trend is also consistent with the relative forces measured experimentally using SMFS.[91] Similar to the lever arm effect observed for *gem*-dichlorocyclopropanes,[90] the *E*-alkene substituent of *cis*-disubstituted benzocyclobutene **71** results in a lower calculated F_{max} value of 3.1 nN compared to *cis*-dialkyl substituted analog **72** with a calculated F_{max} of 3.7 nN, which is again consistent with the relative forces measured by SMFS.[96]

1.3.6 6π Electrocyclic Ring-Opening Reactions

Spiropyran[97] and naphthopyran[98] undergo a 6π electrocyclic ring-opening reaction under mechanical force to generate colored merocyanine dyes (Chart 1.6). The mechanochromic behavior of these mechanophores makes them particularly useful as molecular force probes for visual stress sensing applications. The mechanochemical reactivity of a variety of spiropyran and naphthopyran structures has been studied experimentally, providing insight into structure–mechanochemical activity relationships.

Chart 1.6 Structures Associated with Formal 6π Electrocyclic Ring-Opening Reactions

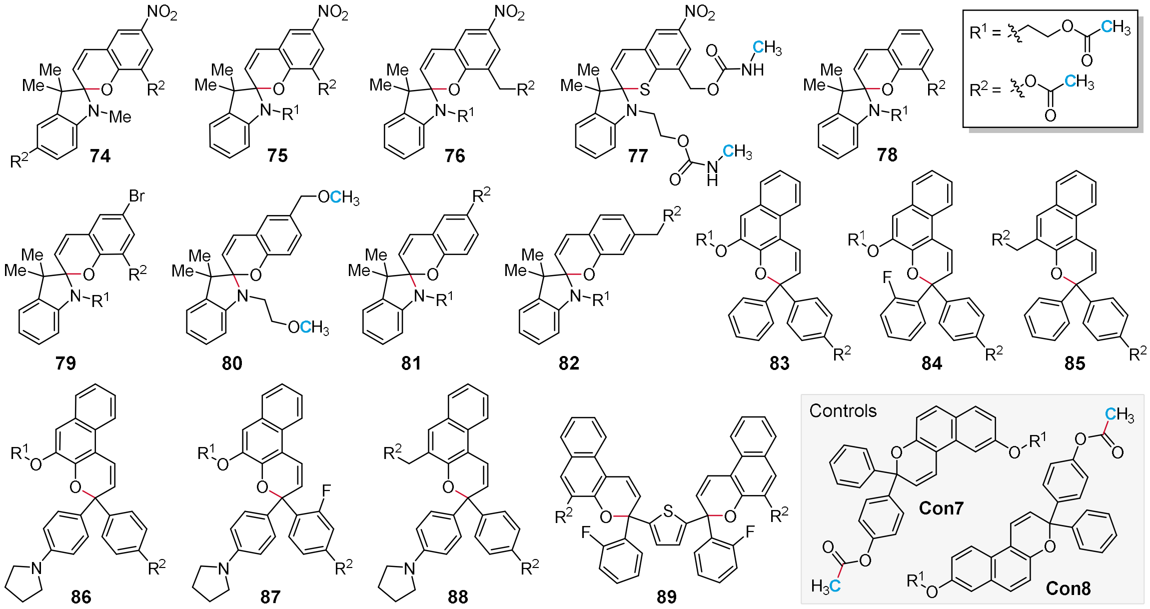

CoGEF calculations successfully predict the expected 6π electrocyclic ring-opening reaction for 16 out of 18 reported structures in this class (Table 1.6).

Table 1.6 CoGEF Results for Formal 6π Electrocyclic Ring-Opening Reactions[§]

Structure	Result[a]	F_{max} (nN)	E_{max} (kJ/mol)	Ref.
74	✓	4.4	381	4,97,99,100
75	✓	2.7	165	59,99–101
76	✓	2.6	150	102
77	✓	2.0	74	103
78	✓	3.5	271	101,104
79	✓	3.2	248	101
80	×	5.9	536	105
81	×	5.7	567	104
82	✓	4.8	386	104
83	✓	4.3	418	98
84	✓	4.4	483	106
85	✓	4.1	370	106
86	✓	3.7	348	106
87	✓	3.7	334	106
88	✓	3.9	332	106
89	✓	4.1, 4.6	652, 740	7
Con7	✓	6.0	716	98
Con8	✓	6.0	650	98

[§]B3LYP/6-31G* level of DFT. [a]Consistency between CoGEF prediction and reported experimental reactivity.

Spiropyran is one of the most widely studied mechanophores in the literature. Similar to the *g*DHC mechanophores, the mechanochemical reactivity of a number of different spiropyran mechanophores with varying connectivity and substitution has been investigated using different experimental techniques enabling the elucidation of important structure–activity relationships. The two most commonly employed spiropyran mechanophores, **74** and **75**, vary in the position of polymer attachment on the indoline portion of the molecule resulting in different mechanochemical activity in SMFS experiments.[99] Attachment at the indoline nitrogen for mechanophore **75** leads to a greater mechanical advantage compared to **74**, which is manifested in different plateau forces of 0.24 and 0.26 nN, respectively. The F_{max} values calculated from CoGEF are qualitatively consistent with this trend in reactivity; however, as discussed in greater detail below, the

F_{max} value of 4.4 nN calculated for mechanophore **74** is unexpectedly large compared to the F_{max} value of 2.7 nN calculated for spiropyran **75**. Notably, spirothiopyran **77** is predicted to have one of the lowest predicted values of F_{max} (2.0 nN) of any mechanophore studied, although the force required for this ring-opening reaction has not been measured experimentally.

The effect of electronic substitution on the mechanochemical reactivity of spiropyran has also been recently studied using SMFS.[101] The force required for ring opening was shown to vary depending on the nature of the substituent *para* to the oxygen on the benzopyran portion of the molecule following a classic Hammett relationship. The plateau forces measured for the ring-opening reaction of mechanophores **78**, **79**, and **75** were 0.41, 0.36, and 0.24 nN, respectively, indicating enhanced stabilization of negative charge in the transition state as the electron withdrawing power of the substituent increases going from hydrogen to bromine to a nitro group. The values of F_{max} calculated for **78** (R = H), **79** (R = Br), and **75** (R = NO_2) are 3.5, 3.2, and 2.7 nN, respectively, which are in agreement with the trend in reactivity determined from SMFS experiments.

Spiropyran mechanophores **80** and **81** with pulling positions *para* to the pyran oxygen on the benzopyran fragment of the molecule are both predicted to undergo cleavage of the spiro C–N bond instead of the expected C–O bond. The C–N bond scission appears to be heterolytic in nature and occurs with predicted F_{max} values of 5.9 nN (**80**) and 5.7 nN (**81**), which are significantly higher than values of F_{max} computed for the ring-opening reaction of other spiropyran mechanophores. A prior investigation of the effects of regiochemistry on the mechanochemical activation of spiropyran in bulk materials revealed that *para*-substituted mechanophore **81** is significantly less sensitive to mechanical force than analogous mechanophores with polymer attachment at the *ortho* and *meta* positions (**78** and **82**, respectively).[104] Interestingly, CoGEF calculations predict the expected C–O bond cleavage reaction leading to merocyanine formation for structure **81** when the pulling point is changed to a hydrogen atom at either the *meta* or *ortho* position on the benzopyran portion of the molecule, indicating that the computed reactivity is affected strongly by the pulling geometry and not purely electronic factors (Figure 1.4). We further note that the computed visible absorption spectrum of the product resulting from C–N bond cleavage of spiropyran **81** is similar to that of the merocyanine species resulting from the expected 6π electrocyclic ring-opening reaction, possibly confounding the interpretation of colorimetric analyses if this competing reaction pathway is indeed experimentally accessible.

Similar to the regiochemical effects discussed above for spiropyran and other classes of mechanophores, the mechanochemical activity of naphthopyran is highly dependent upon the positions of polymer attachment. While naphthopyrans **83–88** are mechanochemically active, regioisomers **Con7** and **Con8** do not undergo electrocyclic ring-opening reactions in polymeric materials under tension.[98] This behavior is accurately

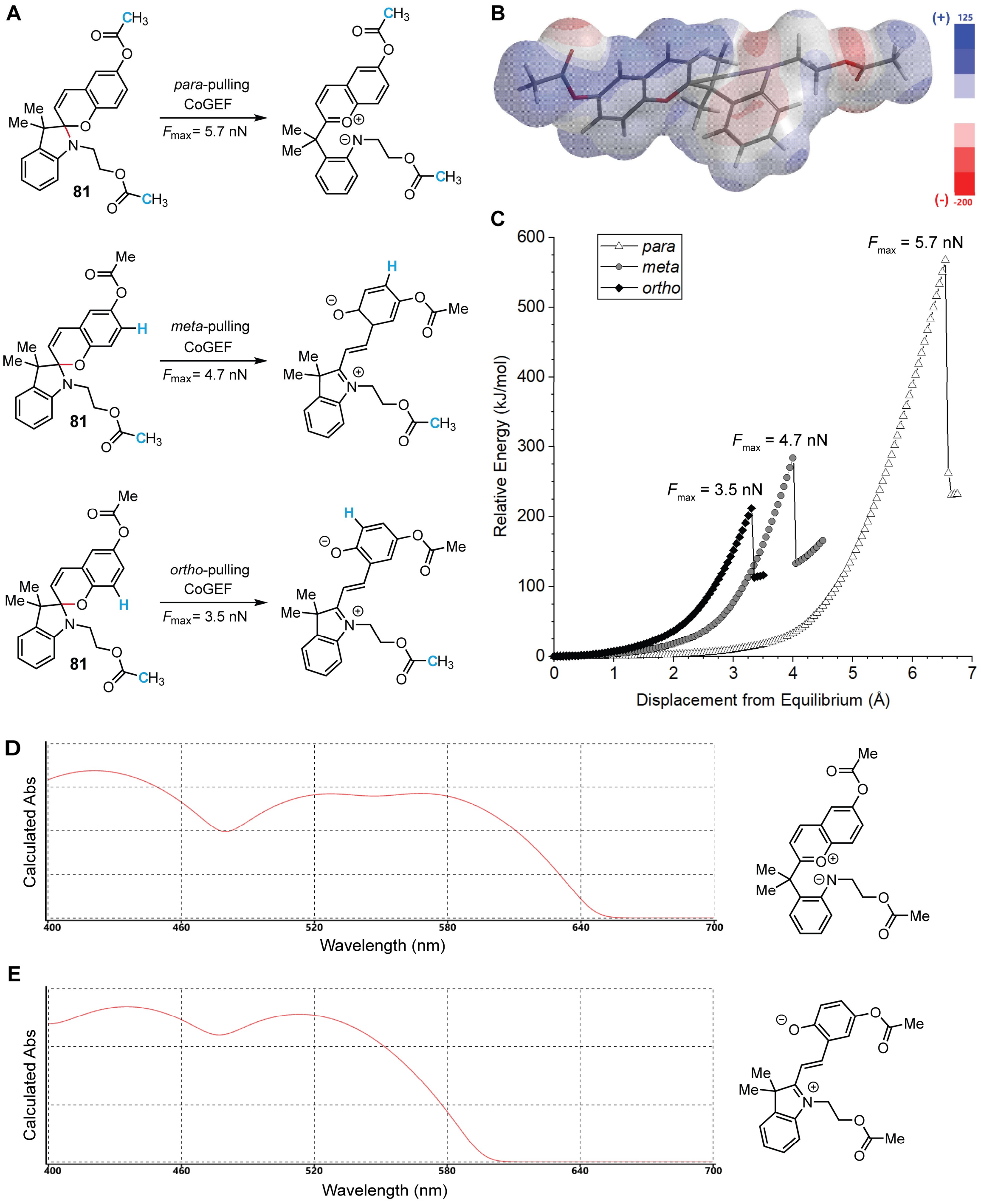

Figure 1.4 Investigation of regiochemical effects on the predicted mechanochemical reactivity of spiropyran **81**. (A) Changing the pulling position results in the anticipated scission of the C–O pyran bond leading to formation of the merocyanine. (B) Electrostatic potential map of the product predicted by CoGEF (*para*-pulling) indicating heterolytic fragmentation of the C–N bond. (C) CoGEF profiles associated with the schemes in panel A. (D, E) Visible absorption spectra calculated at the B3LYP/6-31G* level of TD-DFT for the product resulting from C–N bond scission, and the expected merocyanine species.

reproduced in the CoGEF calculations, which predict C–C bond scission adjacent to the pulling point for both control molecules. The regioisomer-specific mechanochemical reactivity of naphthopyran **83** was previously attributed to better alignment between the labile C–O pyran bond and the direction of the applied force, which was quantified by a specific angle denoted here as the force–bond angle.[98] The angle between the C–O pyran bond and the external force vector at maximum extension was calculated from molecular models to be relatively narrow for mechanophore **83**, whereas the angle is substantially wider for the two unreactive naphthopyran regioisomers **Con7** and **Con8**. While proper orientation between the external force vector and the labile bond in a mechanophore is a critical parameter that influences mechanochemical coupling, in general we find no correlation between force–bond angle and mechanochemical activity when analyzed broadly across the entire library of mechanophores and control structures (Figure 1.5).

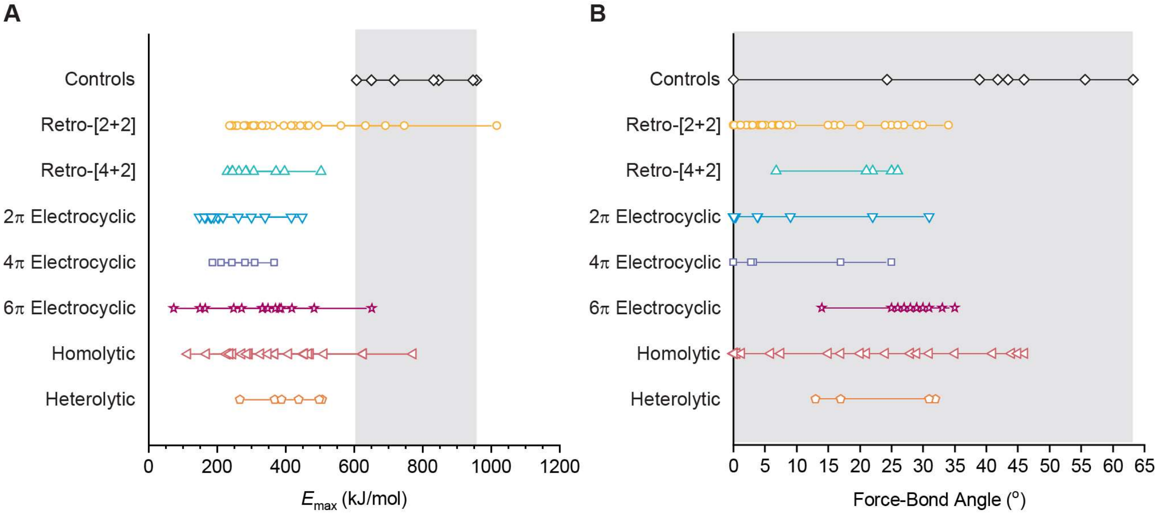

Figure 1.5 Summary of (A) E_{max} values and (B) force–bond angles determined using the CoGEF method for each mechanochemical reaction class. The CoGEF results for control structures are universally indistinguishable from the mechanophores when quantitative metrics E_{max} and force–bond angle are compared, indicating that these metrics are poor predictors of mechanochemical reactivity. Data from calculations that are inconsistent with experimentally determined reactivity are excluded.

Another notable example in this reaction class is bis-naphthopyran mechanophore **89**, which contains two separate reactive sites and exhibits force-dependent changes in visible absorption due to distinctly colored merocyanine products resulting from the ring-opening reaction of either one or both pyrans.[7] While the CoGEF calculation performed on bis-naphthopyran **89** predicts that both pyrans successfully undergo the anticipated ring-opening reactions under force, the geometry constraints imposed by the CoGEF method necessitate a sequential ring-opening process upon molecular extension. Experiments indicate, however, that both rings open in tandem under ultrasound-induced mechanical elongation. Multiple chain scission reactions have been observed for cyclic polymers during a single high-strain-rate extensional event that suggest potentially important dynamic effects under ultrasonication conditions,[107] which are not accurately captured by the CoGEF method.

1.3.7 Homolytic Reactions

In a seminal report by Moore and coworkers in 2005, the mechanochemical site-specific chain scission of polymers containing mechanophore **90** with a mechanically weak azo group near the chain midpoint was demonstrated to occur through the putative homolytic expulsion of nitrogen.[108] A number of diverse mechanophores have since been developed that react via radical pathways (Chart 1.7). For example, this category includes mechanochromic mechanophores **94–97** that generate colored stable free radicals under mechanical force,[6,109–111] and ladderenes **98** and **99** that unzip to generate semiconducting polyacetylene.[15,112] CoGEF calculations successfully predict the expected homolytic bond

Chart 1.7 Structures Associated with Homolytic Reactions

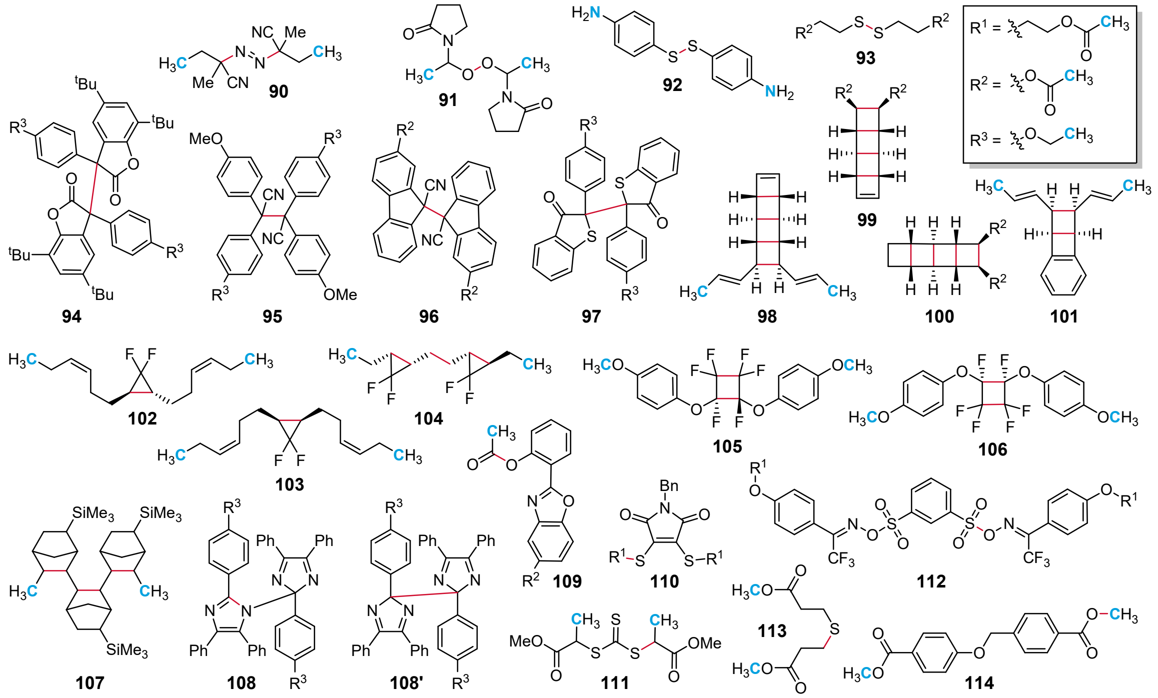

scission reactions for 23 out of 25 experimentally studied mechanophores in this class (Table 1.7).

In addition to transformations involving simple homolytic bond scission, CoGEF calculations also successfully capture the mechanochemical behavior of more complex, multistep reactions. In many cases, CoGEF calculations accurately reproduce computations performed using more sophisticated approaches. According to FMPES calculations, the unzipping reaction of ladderene and ladderane mechanophores **98–100** proceeds via a mechanism that involves two transient diradical transition states.[15,112] The complex stepwise unzipping reaction of these mechanophores is successfully captured by CoGEF calculations. While the mechanochemical reaction mechanism of benzoladderene **101** has not been confirmed experimentally, we include it in this category in the context of other ladderene structures.[113] Notably, the CoGEF calculation performed on

Table 1.7 CoGEF Results for Homolytic Reactions§

Structure	Result[a]	F_{max} (nN)	E_{max} (kJ/mol)	Ref.
90	✓	3.7	366	108,114
91	✓	5.2	230	115
92	✓	2.0	114	116
93	✓	3.6	271	117
94	✓	3.5	169	6,118
95	✓	4.5	294	109
96	✓	4.3	326	110
97	✓	4.4	287	111
98	✓	3.2, 3.9	236, 239	15,112
99	✓	4.2, 4.0	451, 346	112
100	✓	4.2, 3.9	511, 326	112
101	✓	3.3	245	113
102	✓	4.8	466	91,95,119
103	✓	3.4	292	91,95,119,120
104	✓	4.9	771	119
105	✓	4.2	455	121
106	✓	3.4	409	121
107	✓	3.5, 2.6, 3.5	348, 521, 617	122
108	✗	5.1	536	123
108′	✓[b]	4.3	258	-
109	✓	4.7	369	124
110	✓	4.3	472	125
111	✓	4.3	227	126
112	✓	4.3	625	127
113	✓	4.6	626	[114]
114	✗	6.1	611	[114]

§B3LYP/6-31G* level of DFT. [a]Consistency between CoGEF prediction and reported experimental reactivity. [b]Structural revision results in CoGEF prediction matching expected reactivity.

benzoladderene **101** predicts that the ring-opening reaction occurs through a stepwise mechanism similar to the other ladderene mechanophores. In contrast to the electrocyclic ring-opening reactions of other *g*DHCs described above, *gem*-difluorocyclopropane (*g*DFC) mechanophores **102** and **103** undergo homolytic bond scission leading to a transient diradical intermediate under force.[95] As an interesting example, the CoGEF calculation performed on a representative dimer structure **104** predicts sequential ring-opening reactions of the *cis* followed by the *trans* disubstituted *g*DFC groups to generate an apparent tetraradical species, which subsequently disproportionates to form two identical 3,3-difluoroalkene radicals. This reactivity predicted by CoGEF is consistent with experimental characterization of reaction products by ^{1}H and ^{19}F NMR spectroscopy following ultrasound-induced mechanochemical activation and reproduces the results from AISMD simulations.[119] Similarly, the mechanochemical reaction of perfluorocyclobutane mechanophores **105** and **106** has been demonstrated to proceed via a stepwise mechanism with a diradical intermediate,[121] which is accurately reflected in the CoGEF calculations performed on these two structures. In another interesting example, the ring-opening reaction of vinyl-addition polynorbornene surrogate **107** is predicted to occur in a stepwise fashion to produce the ROMP-type polynorbornene repeat unit structure observed experimentally.[122]

The CoGEF calculation performed on triphenylimidazole dimer **108** predicts bond scission that differs from the anticipated reaction. Compound **108** was reported to undergo homolytic cleavage of the central C–N bond to generate a pair of stable triphenylimidazolyl radicals under force.[123] Instead, CoGEF calculations predict fragmentation of a C–N bond in one of the imidazole rings. While the imidazole dimer containing a central C–N linkage is expected to be the major product of oxidative coupling, this species exists in equilibrium with other isomers.[123] Performing the CoGEF calculation on isomer **108′** comprising a structure in which the imidazole rings are coupled via a central C–C bond results in the expected homolytic cleavage producing two identical triphenylimidazolyl radicals consistent with the experimentally observed behavior. The CoGEF calculations performed on compounds **109–113** predict homolytic bond scission that is consistent with the reported reactivity of these compounds, although we note that the products of these mechanochemical transformations have not been fully characterized. The CoGEF calculation performed on **114**, however, predicts scission of the C–O bond in a terminal ester group, rather than the anticipated C–O bond of the benzyl ether moiety. In fact, the reactivity of benzyl phenyl ether **114** was found to be surprisingly low.[114] Poor mechanochemical coupling was attributed to contraction of the molecule as the benzyl carbon atom rehybridizes from sp^3 to sp^2 upon formation of the benzyl radical. In that scenario, the CoGEF process may bias the reaction along a trajectory that does not correspond to the global minimum energy force-coupled pathway.

1.3.8 Heterolytic Reactions

Mechanochemical reactions that involve heterolytic fragmentation of covalent bonds to generate charged species are less common.[128–132] Nevertheless, several mechanophores have been reported in the literature to undergo heterolytic covalent bond cleavage under mechanical force (Chart 1.8). The CoGEF calculations performed on models of all such structures successfully reproduce the experimentally demonstrated reactivity (Table 1.8). Notably, a series of N-heterocyclic carbene precursors (**115–117**)

Chart 1.8 Structures Associated with Heterolytic Reactions

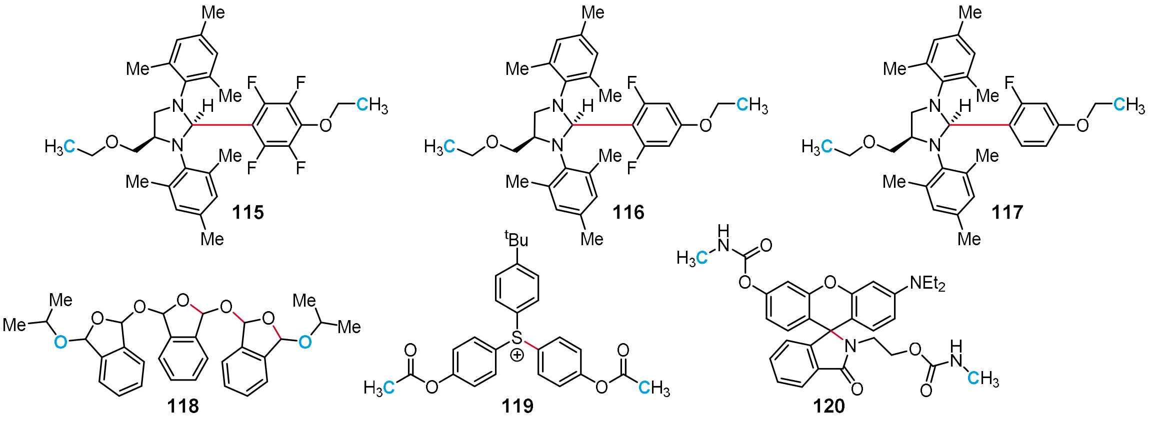

was recently discovered that undergoes selective C–C bond scission under mechanical force via three concomitant dissociation pathways.[132] CoGEF calculations predict the heterolytic fragmentation of all three compounds; however, experiments demonstrated that the proportion of heterolytic fragmentation diminishes with decreasing fluorination of the aryl group, favoring a concerted mechanism for mechanophores **116** and **117** with a less polarized scissile bond.

Table 1.8 CoGEF Results for Heterolytic Reactions[§]

Structure	Result[a]	F_{max} (nN)	E_{max} (kJ/mol)	Ref.
115	✓	5.2	388	132
116	✓	5.5	438	132
117	✓	5.8	499	132
118	✓	5.6	507	128,129
119	✓	3.7	266	130
120	✓	4.6	368	131,133

[§]B3LYP/6-31G* level of DFT. [a]Consistency between CoGEF prediction and reported experimental reactivity.

Poly(*o*-phthalaldehyde) undergoes a mechanically triggered unzipping reaction above its ceiling temperature to generate *o*-phthalaldehyde monomers.[128,129] The proposed mechanism, which is supported by AISMD simulations, involves mechanochemical chain cleavage via an initial heterolytic bond scission event followed by a depolymerization cascade.[128] The CoGEF calculation performed on model structure **118**, which represents a short repeating unit segment of poly(*o*-phthalaldehyde), predicts the simultaneous cleavage of three C–O bonds along the oligomer backbone including one central linking bond and two internal bonds on adjacent monomer units. The chemical transformation predicted by the CoGEF method is consistent with heterolytic fragmentation and two concurrent ring-opening reactions to generate two new aldehyde functional groups, with an oxocarbenium ion and an oxyanion localized on the separate portions. These results are in excellent agreement with the prior mechanistic findings for mechanically initiated depolymerization of poly(*o*-phthalaldehyde).

Triarylsulfonium compound **119** was reported to undergo heterolytic scission of the central polarized C–S bond to afford a phenyl cation, which was demonstrated experimentally through trapping experiments.[130] The CoGEF calculation performed on mechanophore **119** predicts the rupture of the anticipated C–S bond that is consistent with the reported mechanochemical behavior. In addition, rhodamine mechanophore **120** undergoes a force-induced ring-opening reaction that leads to a change in color and fluorescence in polymeric materials.[131,133] Although the mechanism has not been studied in detail, the C–N bond is presumed to cleave heterolytically, possibly with assistance from the diethylamine substituent *para* to the developing carbocation. The CoGEF calculation performed on mechanophore **120** predicts the selective scission of the anticipated central C–N bond. However, in the absence of a polarizable continuum model to simulate a polar solvent environment, a [1,3]-sigmatropic rearrangement is predicted to occur, resulting in the formation of a new oxygen-containing five-membered ring bearing an exocyclic C–N double bond. When the CoGEF calculation is repeated with a polar solvent model, heterolytic cleavage of the central C–N bond is observed without any rearrangement (see Appendix A for details).

1.3.9 F_{max} as a reliable descriptor of mechanochemical reactivity

Calculated values of F_{max} are reliable and consistent indicators of the relative mechanochemical reactivity of mechanophores, as demonstrated above for various reactions within each formal mechanistic category. The value of F_{max} from each successful CoGEF calculation across every reaction class is illustrated in Figure 1.6. For mechanophores where the predicted reactivity from the CoGEF calculation agrees with experimental results, the values of F_{max} range from the lowest of 2.0 nN for spirothiopyran **77** and diaryldisulfide **92** to the highest of 5.9 nN for *trans*-cyclobutane **2**. Notably, there is a clear distinction between the values of F_{max} calculated for each mechanophore and the values of F_{max} associated with bond scission in the negative controls, which in every case are ≥ 6.0 nN. In contrast, the CoGEF results for control structures are universally

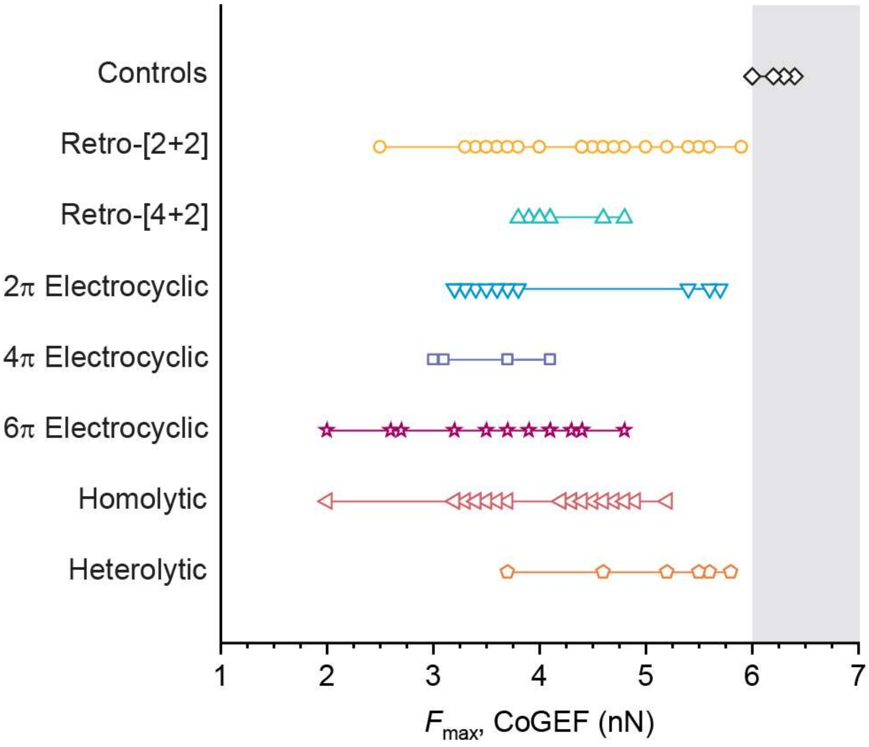

Figure 1.6 Summary of F_{max} values calculated by the CoGEF method across all mechanistic categories. Data from calculations that are inconsistent with reported experimental reactivity are excluded.

indistinguishable from the mechanophores when alternative quantitative metrics E_{max} and force–bond angle are compared (Figure 1.5). While the values of E_{max} generally exhibit a positive correlation with F_{max}, there is no such correlation with force–bond angle (Figure 1.7). It is worth reiterating, however, that the magnitude of E_{max} values from CoGEF calculations is highly variable, whereas F_{max} is a more robust predictor of mechanochemical activity. We mention in passing that the use of unrestricted calculations (Figure 1.8) and dispersion corrections (Figure 1.9) appears to have minimal influence on the results of CoGEF calculations.

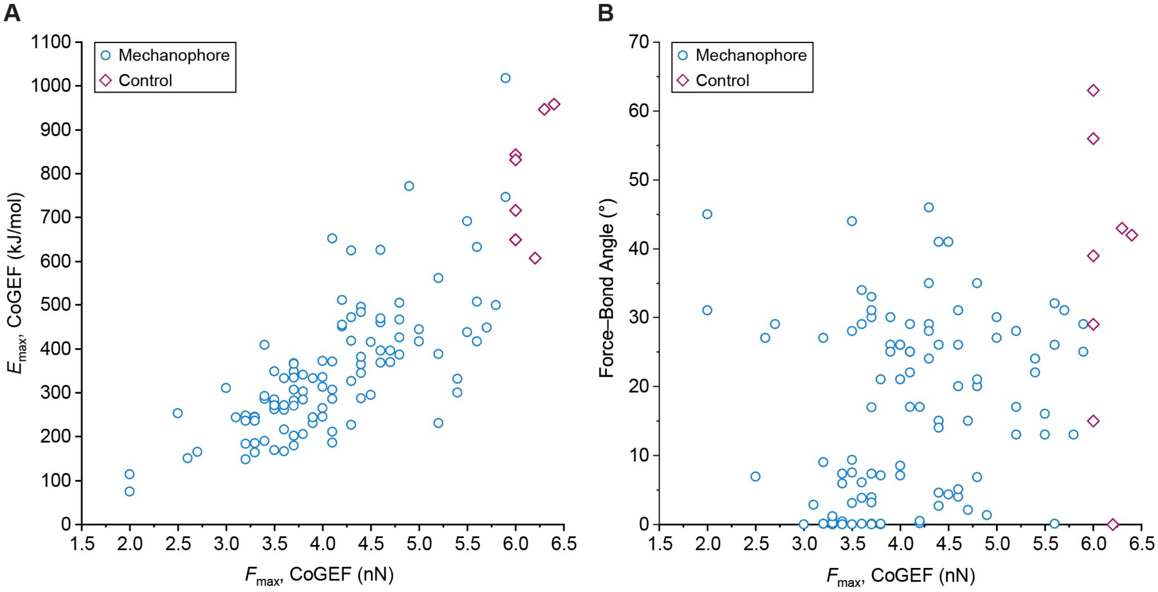

Figure 1.7 Relationship between calculated values of (A) E_{max} and (B) force–bond angle with the calculated values of F_{max} determined with the CoGEF method at the B3LYP/6-31G* level of DFT. There is a positive correlation between the values of E_{max} and F_{max}, while there is no apparent correlation between force–bond angle and values of F_{max}.

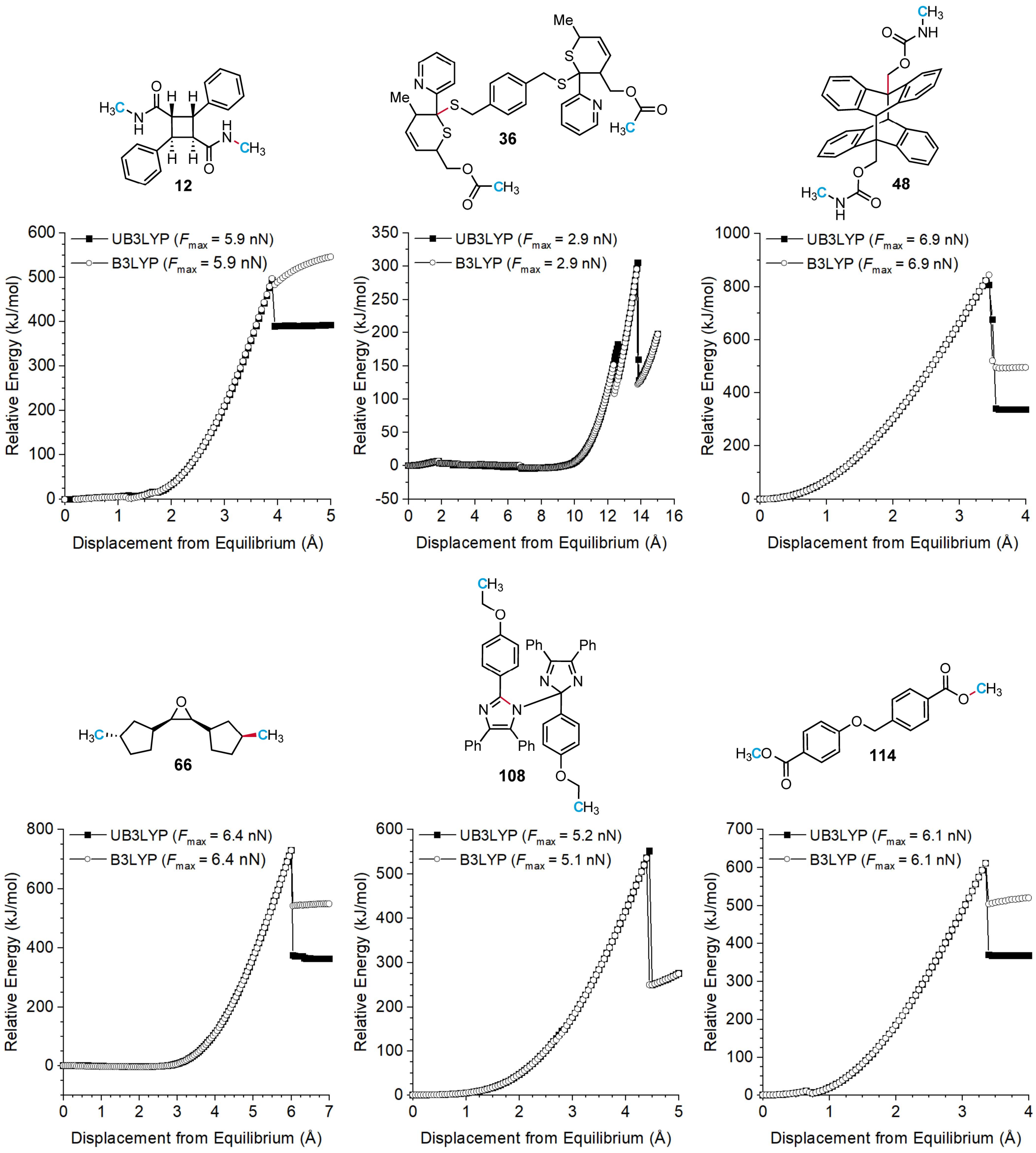

Figure 1.8 CoGEF calculations performed using unrestricted DFT (UB3LYP/6-31G*) on representative mechanophores for which CoGEF calculations at the B3LYP/6-31G* level of DFT predict reactions that are inconsistent with the reported experimental behavior. Use of the UB3LYP functional has minimal influence on the results of the CoGEF simulations. The same chemical transformations are predicted in each case.

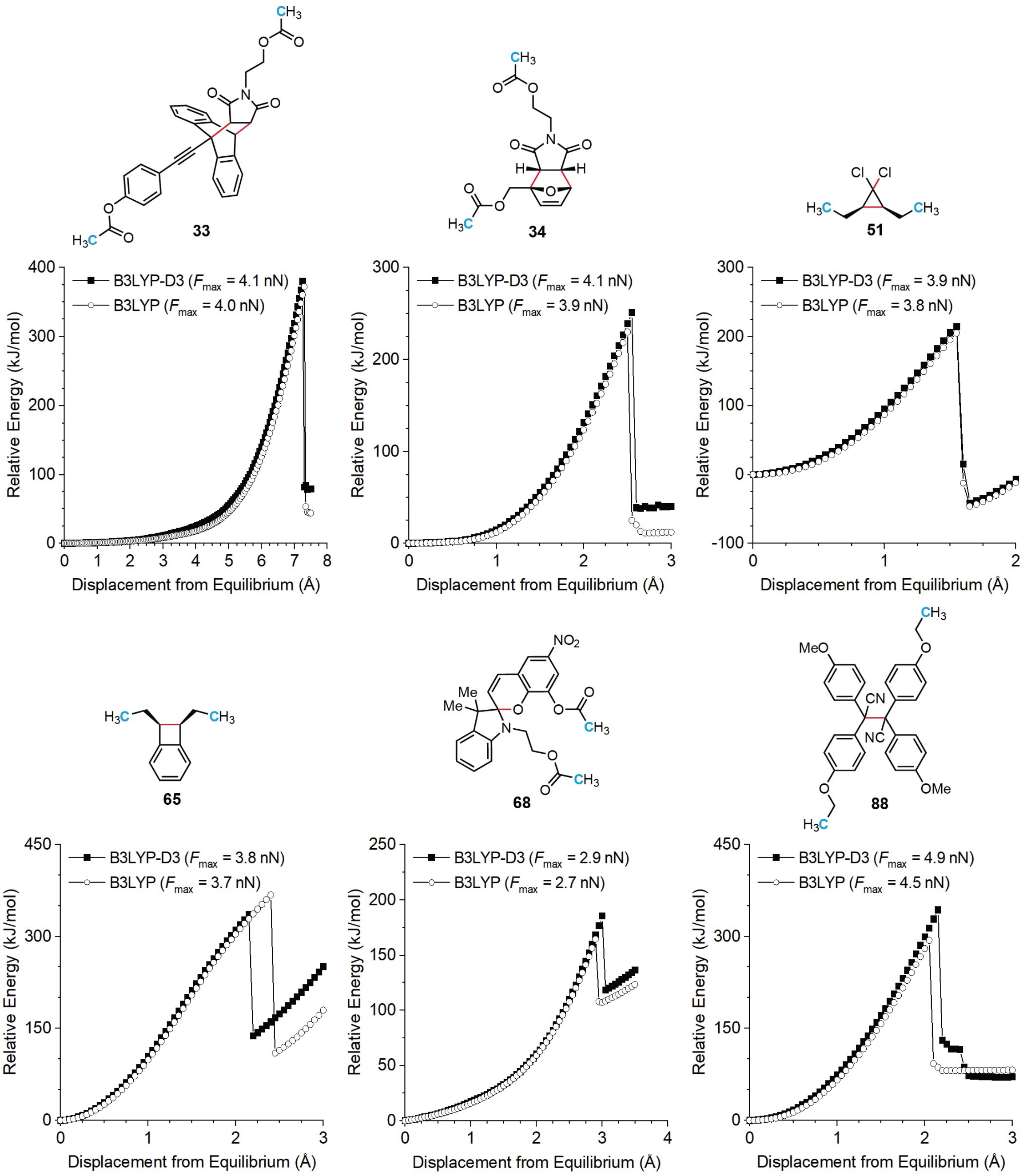

Figure 1.9 Comparison of CoGEF calculations performed on representative mechanophores at the B3LYP/6-31G* level of DFT and using a dispersion-corrected functional (B3LYP-D3/6-31G*). Use of the dispersion-corrected B3LYP-D3 functional has minimal influence on the results of the CoGEF simulations. The same chemical transformations are predicted in each case.

Calculated values of $F_{\max}$ obtained from CoGEF calculations also correlate well with the mechanochemical reactivity of different mechanophores determined experimentally (Figure 1.10). While systematic studies of structure–reactivity relationships using threshold molecular weight as a quantitative metric are limited to substituted cyclobutanes[36] and furan–maleimide Diels–Alder adducts,[65] there is a positive correlation between the calculated values of $F_{\max}$ and the experimentally measured threshold molecular weight for these mechanophores (Figure 1.10A). Mechanochemical reactivity is more accurately quantified using SMFS, which has been performed consistently on a relatively large number of mechanophores including spiropyrans,[99,101] benzocyclobutenes,[91,96] and cyclopropanes.[86,87,90,91] Again, there is a positive correlation between the values of $F_{\max}$ calculated using CoGEF and the forces measured experimentally using SMFS (Figure 1.10B). As mentioned previously, spiropyran mechanophore **74** is a notable exception to this trend with an anomalously high calculated

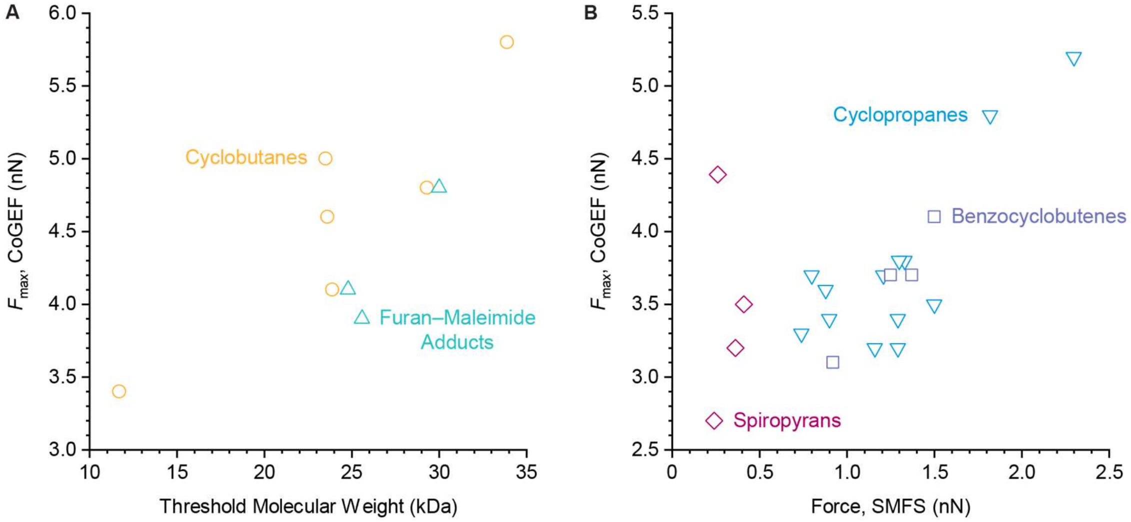

Figure 1.10 Values of $F_{\max}$ from CoGEF calculations compared to experimentally determined values of (A) threshold molecular weight obtained from rates of ultra-sound induced mechanochemical activation, and (B) forces determined from single molecule force spectroscopy (SMFS) measurements.

F_{max} value of 4.4 nN compared to the exceptionally low measured force of 0.26 nN.[99] The rupture forces calculated with the CoGEF method are consistently greater than forces determined from experiments, in part because thermal effects are neglected.[19] In addition, the forces measured using SMFS are dependent upon the loading velocity, with all of the forces considered here measured with a loading velocity of 300 nm/s. Nevertheless, the relationship between calculated values of F_{max} and experimentally determined forces demonstrates that the CoGEF method is able to reliably predict the relative mechanochemical activity of mechanophores, further reinforcing the qualitative trends in reactivity highlighted above.

1.4 Conclusions

The constrained geometries simulate external force (CoGEF) method is an operationally simple and highly accessible quantum chemistry technique that enables prediction of mechanochemical reactivity. In this study, we apply the CoGEF method systematically to every covalent mechanophore reported in the literature and compare the predicted reactivity against the experimentally determined behavior. CoGEF calculations are also performed on molecules that have been determined to be mechanochemically inactive as negative controls. Out of the 128 structures investigated with reactions that span eight distinct mechanistic categories, CoGEF calculations performed at the B3LYP/6-31G* level of DFT predict mechanochemical transformations that are consistent with the reported experimental reactivity for 112 molecules, including every negative control. In total, this corresponds to a success rate of 88%; however, analysis suggests that the accuracy of the CoGEF method is likely even higher. In some cases, for example, computational results combined with experimental characterization data indicate that revision of prior structural assignments may be merited or that additional experiments are needed to substantiate the reported reactivity.

The utility of the CoGEF method is revealed not only in its general ability to accurately predict covalent bond transformations, but also in quantitative comparisons of mechanochemical reactivity. We demonstrate that the maximum force predicted for bond rupture in CoGEF calculations is correlated with forces measured using single molecule force spectroscopy, suggesting that the CoGEF method is a reliable predictor of the relative activity of mechanophores. On the other hand, some notable limitations of the CoGEF method are revealed. The inability to account for thermal effects as a static quantum chemistry method manifests in limitations for calculating the mechanochemical reactivity of “flex activated” mechanophores, for instance, where proper consideration of the contribution from thermal energy to the overall activation is essential. Additionally, the inherent geometric constraints imposed by CoGEF can obscure dynamic effects, such as those that may be involved in some specific reactions under high strain rate conditions, or possibly bias reactions by stretching molecules along trajectories that do not correspond to global minimum energy force-coupled pathways. Nevertheless, the ability of the CoGEF method to reproduce more sophisticated computations as well as accurately predict remarkable transformations, like those that formally violate classical orbital-symmetry rules or proceed in a complex stepwise process, suggest that the technique is capable of providing important insight into mechanochemical reactions beyond identifying scissile bonds. Our results demonstrate that despite its simplicity, which is an enabling feature for practitioners of experimental polymer mechanochemistry, the CoGEF method is a powerful tool for predicting and understanding mechanochemical reactivity.

1.5 Experimental Details

1.5.1 General methods

CoGEF calculations were performed using Spartan ′18 Parallel Suite according to previously reported methods.[24,36] A guide to running CoGEF calculations in Spartan can be found in Appendix B. Chemical structures were composed in ChemDraw, saved as .mol files, and then imported into Spartan. Structures were truncated to include tethers that accurately reflect the structure of the molecules used in the experimental studies. Ground state energies were calculated using DFT at the B3LYP/6-31G* level of theory in vacuum, unless specified otherwise. For the three mechanophores in the heterolytic category, CoGEF calculations were also performed using a polarizable continuum model (dielectric constant of 37) to simulate a polar solvent. Starting from the equilibrium geometry of the unconstrained molecule (relative energy = 0 kJ/mol), the distance between the terminal anchor atoms of the truncated structure was increased in increments of 0.05 Å and the energy was minimized at each step. This operation was carried out automatically using the Energy Profile calculation in Spartan. Calculations were run until a chemical transformation was predicted to occur, as evidenced by the rupture and reorganization of one or more covalent bonds. In some cases, an initial equilibrium conformer calculation was performed using Molecular Mechanics (MMFF) before performing the steps outlined above. The maximum number of geometry optimization cycles was increased beyond the default value using the GEOMETRYCYCLE option to ensure convergence at each step in the CoGEF profile.

1.5.2 Determination of F_{max}

The maximum force predicted for each mechanochemical transformation was calculated from the slope between contiguous points in the energy–displacement curve. In most cases, F_{max} coincides with the displacement immediately prior to a discontinuity in the relative energy profile. The value of F_{max} is thus calculated from the slope between the two data points preceding the abrupt attenuation in energy. More rarely, a continuous change in energy is observed that approaches an apparent plateau value at long displacements. In these cases, F_{max} occurs at the inflection point in the CoGEF curve. The value of the slope is divided by the Avogadro constant and adjusted to provide force in units of nJ/m (nN).

1.5.3 Determination of E_{max}

The maximum energy relative to the energy of the unconstrained molecule at equilibrium is reported as E_{max}. The value of E_{max} is determined from the CoGEF curve at the displacement corresponding to F_{max}. Typically, this means that E_{max} represents the highest relative energy on the CoGEF curve; however, for instances in which the CoGEF profile exhibits a sigmoidal shape and/or a discontinuity is absent, E_{max} corresponds to the relative energy at the inflection point.

1.5.4 Determination of Force–Bond Angle

Force–bond angles were calculated according to the previously described method using structural models from CoGEF calculations at the displacement corresponding to F_{max}.[98] The external force vector was approximated using the coordinates of the two terminal atoms that define the distance constraint in the CoGEF calculation.

1.6 References

(1) Beyer, M. K.; Clausen-Schaumann, H. Mechanochemistry: The mechanical activation of covalent bonds. *Chem. Rev.* **2005**, *105*, 2921–2948.

(2) Caruso, M. M.; Davis, D. A.; Shen, Q.; Odom, S. A.; Sottos, N. R.; White, S. R.; Moore, J. S. Mechanically-Induced Chemical Changes in Polymeric Materials. *Chem. Rev.* **2009**, *109*, 5755–5798.

(3) Li, J.; Nagamani, C.; Moore, J. S. Polymer Mechanochemistry: From Destructive to Productive. *Acc. Chem. Res.* **2015**, *48*, 2181–2190.

(4) Davis, D. A.; Hamilton, A.; Yang, J. L.; Cremar, L. D.; Van Gough, D.; Potisek, S. L.; Ong, M. T.; Braun, P. V.; Martinez, T. J.; White, S. R.; Moore, J. S.; Sottos, N. R. Force-induced activation of covalent bonds in mechanoresponsive polymeric materials. *Nature* **2009**, *459*, 68–72.

(5) Chen, Y. L.; Spiering, A. J. H.; Karthikeyan, S.; Peters, G. W. M.; Meijer, E. W.; Sijbesma, R. P. Mechanically induced chemiluminescence from polymers incorporating a 1,2-dioxetane unit in the main chain. *Nat. Chem.* **2012**, *4*, 559–562.

(6) Imato, K.; Irie, A.; Kosuge, T.; Ohishi, T.; Nishihara, M.; Takahara, A.; Otsuka, H. Mechanophores with a Reversible Radical System and Freezing-Induced Mechanochemistry in Polymer Solutions and Gels. *Angew. Chem. Int. Ed.* **2015**, *54*, 6168–6172.

(7) McFadden, M. E.; Robb, M. J. Force-Dependent Multicolor Mechanochromism from a Single Mechanophore. *J. Am. Chem. Soc.* **2019**, *141*, 11388–11392.

(8) Diesendruck, C. E.; Steinberg, B. D.; Sugai, N.; Silberstein, M. N.; Sottos, N. R.; White, S. R.; Braun, P. V.; Moore, J. S. Proton-Coupled Mechanochemical Transduction: A Mechanogenerated Add. *J. Am. Chem. Soc.* **2012**, *134*, 12446–12449.

(9) Larsen, M. B.; Boydston, A. J. "Flex-Activated" Mechanophores: Using Polymer Mechanochemistry To Direct Bond Bending Activation. *J. Am. Chem. Soc.* **2013**, *135*, 8189–8192.

(10) Hu, X.; Zeng, T.; Husic, C. C.; Robb, M. J. Mechanically Triggered Small Molecule Release from a Masked Furfuryl Carbonate. *J. Am. Chem. Soc.* **2019**, *141*, 15018–15023.

(11) Hickenboth, C. R.; Moore, J. S.; White, S. R.; Sottos, N. R.; Baudry, J.; Wilson, S. R. Biasing reaction pathways with mechanical force. *Nature* **2007**, *446*, 423–427.

(12) Lenhardt, J. M.; Black, A. L.; Craig, S. L. gem-Dichlorocyclopropanes as Abundant and Efficient Mechanophores in Polybutadiene Copolymers under Mechanical Stress. *J. Am. Chem. Soc.* **2009**, *131*, 10818–10819.

(13) Ramirez, A. L. B.; Kean, Z. S.; Orlicki, J. A.; Champhekar, M.; Elsakr, S. M.; Krause, W. E.; Craig, S. L. Mechanochemical strengthening of a synthetic polymer in response to typically destructive shear forces. *Nat. Chem.* **2013**, *5*, 757–761.

(14) Robb, M. J.; Moore, J. S. A Retro-Staudinger Cycloaddition: Mechanochemical Cycloelimination of a beta-Lactam Mechanophore. *J. Am. Chem. Soc.* **2015**, *137*, 10946–10949.

(15) Chen, Z. X.; Mercer, J. A. M.; Zhu, X. L.; Romaniuk, J. A. H.; Pfattner, R.; Cegelski, L.; Martinez, T. J.; Burns, N. Z.; Xia, Y. Mechanochemical unzipping of

insulating polyladderene to semiconducting polyacetylene. *Science* **2017**, *357*, 475–478.

(16) Piermattei, A.; Karthikeyan, S.; Sijbesma, R. P. Activating catalysts with mechanical force. *Nat. Chem.* **2009**, *1*, 133–137.

(17) Michael, P.; Binder, W. H. A Mechanochemically Triggered "Click" Catalyst. *Angew. Chem. Int. Ed.* **2015**, *54*, 13918–13922.

(18) Ribas-Arino, J.; Shiga, M.; Marx, D. Understanding Covalent Mechanochemistry. *Angew. Chem. Int. Ed.* **2009**, *48*, 4190–4193.

(19) Stauch, T.; Dreuw, A. Advances in Quantum Mechanochemistry: Electronic Structure Methods and Force Analysis. *Chem. Rev.* **2016**, *116*, 14137–14180.

(20) Roessler, A. G.; Zimmerman, P. M. Examining the Ways to Bend and Break Reaction Pathways Using Mechanochemistry. *J. Phys. Chem. C* **2018**, *122*, 6996–7004.

(21) Ribas-Arino, J.; Marx, D. Covalent Mechanochemistry: Theoretical Concepts and Computational Tools with Applications to Molecular Nanomechanics. *Chem. Rev.* **2012**, *112*, 5412–5487.

(22) Ong, M. T.; Leiding, J.; Tao, H. L.; Virshup, A. M.; Martinez, T. J. First Principles Dynamics and Minimum Energy Pathways for Mechanochemical Ring Opening of Cyclobutene. *J. Am. Chem. Soc.* **2009**, *131*, 6377–6379.

(23) Wolinski, K.; Baker, J. Theoretical predictions of enforced structural changes in molecules. *Mol. Phys.* **2009**, *107*, 2403–2417.

(24) Beyer, M. K. The mechanical strength of a covalent bond calculated by density functional theory. *J. Chem. Phys.* **2000**, *112*, 7307–7312.

(25) Kersey, F. R.; Yount, W. C.; Craig, S. L. Single-Molecule Force Spectroscopy of Bimolecular Reactions: System Homology in the Mechanical Activation of Ligand Substitution Reactions. *J. Am. Chem. Soc.* **2006**, *128*, 3886–3887.

(26) Paulusse, J. M. J.; Sijbesma, R. P. Selectivity of mechanochemical chain scission in mixed palladium(II) and platinum(II) coordination polymers. *Chem. Commun.* **2008**, *2008*, 4416–4418.

(27) Di Giannantonio, M.; Ayer, M. A.; Verde-Sesto, E.; Lattuada, M.; Weder, C.; Fromm, K. M. Triggered Metal Ion Release and Oxidation: Ferrocene as a Mechanophore in Polymers. *Angew. Chem. Int. Ed.* **2018**, *57*, 11445–11450.

(28) Sha, Y.; Zhang, Y. D.; Xu, E. H.; Wang, Z.; Zhu, T. Y.; Craig, S. L.; Tang, C. B. Quantitative and Mechanistic Mechanochemistry in Ferrocene Dissociation. *ACS Macro Lett.* **2018**, *7*, 1174–1179.

(29) Sagara, Y.; Karman, M.; Verde-Sesto, E.; Matsuo, K.; Kim, Y.; Tamaoki, N.; Weder, C. Rotaxanes as Mechanochromic Fluorescent Force Transducers in Polymers. *J. Am. Chem. Soc.* **2018**, *140*, 1584–1587.

(30) Sagara, Y.; Karman, M.; Seki, A.; Pannipara, M.; Tamaoki, N.; Weder, C. Rotaxane-Based Mechanophores Enable Polymers with Mechanically Switchable White Photoluminescence. *ACS Cent. Sci.* **2019**, *5*, 874–881.

(31) Li, Z. A.; Toivola, R.; Ding, F. Z.; Yang, J.; Lai, P. N.; Howie, T.; Georgeson, G.; Jang, S. H.; Li, X. S.; Flinn, B. D.; Jen, A. K. Y. Highly Sensitive Built-In Strain Sensors for Polymer Composites: Fluorescence Turn-On Response through Mechanochemical Activation. *Adv. Mater.* **2016**, *28*, 6592–6597.

(32) Iozzi, M. F.; Helgaker, T.; Uggerud, E. Assessment of theoretical methods for the determination of the mechanochemical strength of covalent bonds. *Mol. Phys.* **2009**, *107*, 2537–2546.

(33) Jacobs, M. J.; Schneider, G.; Blank, K. G. Mechanical Reversibility of Strain-Promoted Azide–Alkyne Cycloaddition Reactions. *Angew. Chem. Int. Ed.* **2016**, *55*, 2899–2902.

(34) Kryger, M. J.; Ong, M. T.; Odom, S. A.; Sottos, N. R.; White, S. R.; Martinez, T. J.; Moore, J. S. Masked Cyanoacrylates Unveiled by Mechanical Force. *J. Am. Chem. Soc.* **2010**, *132*, 4558–4559.

(35) Lin, Y.; Chang, C.-C.; Craig, S. L. Mechanical generation of isocyanate by mechanically induced retro [2 + 2] cycloaddition of a 1,2-diazetidinone mechanophore. *Org. Chem. Front.* **2019**, *6*, 1052–1057.

(36) Kryger, M. J.; Munaretto, A. M.; Moore, J. S. Structure-Mechanochemical Activity Relationships for Cyclobutane Mechanophores. *J. Am. Chem. Soc.* **2011**, *133*, 18992–18998.

(37) Li, M.; Zhang, H.; Gao, F.; Tang, Z.; Zeng, D.; Pan, Y.; Su, P.; Ruan, Y.; Xu, Y.; Weng, W. A cyclic cinnamate dimer mechanophore for multimodal stress responsive and mechanically adaptable polymeric materials. *Polym. Chem.* **2019**, *10*, 905–910.

(38) Zhang, H.; Li, X.; Lin, Y. J.; Gao, F.; Tang, Z.; Su, P. F.; Zhang, W. K.; Xu, Y. Z.; Weng, W. G.; Boulatov, R. Multi-modal mechanophores based on cinnamate dimers. *Nat Commun* **2017**, *8*, 1174.

(39) Pill, M. F.; Holz, K.; Preusske, N.; Berger, F.; Clausen-Schaumann, H.; Luning, U.; Beyer, M. K. Mechanochemical Cycloreversion of Cyclobutane Observed at the Single Molecule Level. *Chem-Eur J* **2016**, *22*, 12034–12039.

(40) Wang, J. P.; Kouznetsova, T. B.; Boulatov, R.; Craig, S. L. Mechanical gating of a mechanochemical reaction cascade. *Nat. Commun.* **2016**, *7*, 13433.

(41) Nofen, E. M.; Zimmer, N.; Dasgupta, A.; Gunckel, R.; Koo, B.; Chattopadhyay, A.; Dai, L. Stress-Sensing Thermoset Polymer Network via Grafted Cinnamoyl/Cyclobutane Mechanophore Units in Epoxy. *Polym. Chem.* **2016**, *7*, 7249–7259.

(42) Gunckel, R.; Koo, B.; Xu, Y.; Pauley, B.; Hall, A.; Chattopadhyay, A.; Dai, L. L. Grafted Cinnamoyl-based Mechanophores for Self-Sensing and Photochemical Healing Capabilities in Epoxy. *ACS Appl. Polym. Mater.* **2020**, DOI: 10.1021/acsapm.0c00599.

(43) Zhang, Y.; Lund, E.; Gossweiler, G. R.; Lee, B.; Niu, Z.; Khripin, C.; Munch, E.; Couty, M.; Craig, S. L. Molecular Damage Detection in an Elastomer Nanocomposite with a Coumarin Dimer Mechanophore. *Macromol. Rapid Commun.* **2020**, DOI: 10.1002/marc.202000359.

(44) Kean, Z. S.; Gossweiler, G. R.; Kouznetsova, T. B.; Hewage, G. B.; Craig, S. L. A coumarin dimer probe of mechanochemical scission efficiency in the sonochemical activation of chain-centered mechanophore polymers. *Chem. Commun.* **2015**, *51*, 9157–9160.

(45) Yang, J.; Horst, M.; Werby, S. H.; Cegelski, L.; Burns, N. Z.; Xia, Y. Bicyclohexene-peri-naphthalenes: Scalable Synthesis, Diverse Functionalization,

Efficient Polymerization, and Facile Mechanoactivation of Their Polymers. *J. Am. Chem. Soc.* **2020**, DOI: 10.1021/jacs.0c06454.

(46) Kean, Z. S.; Ramirez, A. L. B.; Yan, Y. F.; Craig, S. L. Bicyclo[3.2.0]heptane Mechanophores for the Non-scissile and Photochemically Reversible Generation of Reactive Bis-enones. *J. Am. Chem. Soc.* **2012**, *134*, 12939–12942.

(47) Kean, Z. S.; Niu, Z. B.; Hewage, G. B.; Rheingold, A. L.; Craig, S. L. Stress-Responsive Polymers Containing Cyclobutane Core Mechanophores: Reactivity and Mechanistic Insights. *J. Am. Chem. Soc.* **2013**, *135*, 13598–13604.

(48) Bowser, B. H.; Ho, C.-H.; Craig, S. L. High Mechanophore Content, Stress-Relieving Copolymers Synthesized via RAFT Polymerization. *Macromolecules* **2019**, *52*, 9032–9038.

(49) Lin, Y.; Kouznetsova, T. B.; Craig, S. L. Mechanically Gated Degradable Polymers. *J. Am. Chem. Soc.* **2020**, *142*, 2105–2109.

(50) Hsu, T.-G.; Zhou, J.; Su, H.-W.; Schrage, B. R.; Ziegler, C. J.; Wang, J. A Polymer with "Locked" Degradability: Superior Backbone Stability and Accessible Degradability Enabled by Mechanophore Installation. *J. Am. Chem. Soc.* **2020**, *142*, 2100–2104.

(51) Groote, R.; Szyja, B. M.; Leibfarth, F. A.; Hawker, C. J.; Doltsinis, N. L.; Sijbesma, R. P. Strain-Induced Strengthening of the Weakest Link: The Importance of Intermediate Geometry for the Outcome of Mechanochemical Reactions. *Macromolecules* **2014**, *47*, 1187–1192.

(52) Hu, X. R.; McFadden, M. E.; Barber, R. W.; Robb, M. J. Mechanochemical Regulation of a Photochemical Reaction. *J. Am. Chem. Soc.* **2018**, *140*, 14073–14077.

(53) Kida, J.; Imato, K.; Goseki, R.; Aoki, D.; Morimoto, M.; Otsuka, H. The photoregulation of a mechanochemical polymer scission. *Nat. Commun.* **2018**, *9*, 3504.

(54) Bernstein, H. I.; Quimby, W. C. The Photochemical Dimerization of trans-Cinnamic Acid. *J. Am. Chem. Soc.* **1943**, *65*, 1845–1846.

(55) Ishigami, T.; Murata, T.; Endo, T. The Solution Photodimerization of (E)-p-Nitrocinnamates. *Bull. Chem. Soc. Jpn.* **1976**, *49*, 3578–3583.

(56) Gostl, R.; Sijbesma, R. P. pi-extended anthracenes as sensitive probes for mechanical stress. *Chem. Sci.* **2016**, *7*, 370–375.

(57) P. Kabb, C.; S. O’Bryan, C.; D. Morley, C.; E. Angelini, T.; S. Sumerlin, B. Anthracene-based mechanophores for compression-activated fluorescence in polymeric networks. *Chem. Sci.* **2019**, *10*, 7702–7708.

(58) Larsen, M. B.; Boydston, A. J. Successive Mechanochemical Activation and Small Molecule Release in an Elastomeric Material. *J. Am. Chem. Soc.* **2014**, *136*, 1276–1279.

(59) Gossweiler, G. R.; Hewage, G. B.; Soriano, G.; Wang, Q. M.; Welshofer, G. W.; Zhao, X. H.; Craig, S. L. Mechanochemical Activation of Covalent Bonds in Polymers with Full and Repeatable Macroscopic Shape Recovery. *ACS Macro Lett.* **2014**, *3*, 216–219.

(60) Turksoy, A.; Yildiz, D.; Aydonat, S.; Beduk, T.; Canyurt, M.; Baytekin, B.; U. Akkaya, E. Mechanochemical generation of singlet oxygen. *RSC Adv.* **2020**, *10*, 9182–9186.

(61) Wang, Z.; Ma, Z.; Zhang, Z.; Wu, F.; Jiang, H.; Jia, X. Mechanical activation of a dithioester derivative-based retro RAFT-HDA reaction. *Polym. Chem.* **2014**, *5*, 6893–6897.

(62) Khanal, A.; Long, F.; Cao, B.; Shahbazian-Yassar, R.; Fang, S. Y. Evidence of Splitting 1,2,3-Triazole into an Alkyne and Azide by Low Mechanical Force in the Presence of Other Covalent Bonds. *Chem. Eur. J.* **2016**, *22*, 9760–9767.

(63) Konda, S. S. M.; Brantley, J. N.; Varghese, B. T.; Wiggins, K. M.; Bielawski, C. W.; Makarov, D. E. Molecular Catch Bonds and the Anti-Hammond Effect in Polymer Mechanochemistry. *J. Am. Chem. Soc.* **2013**, *135*, 12722–12729.

(64) Li, J.; Shiraki, T.; Hu, B.; Wright, R. A. E.; Zhao, B.; Moore, J. S. Mechanophore Activation at Heterointerfaces. *J. Am. Chem. Soc.* **2014**, *136*, 15925–15928.

(65) Stevenson, R.; De Bo, G. Controlling Reactivity by Geometry in Retro-Diels-Alder Reactions under Tension. *J. Am. Chem. Soc.* **2017**, *139*, 16768–16771.

(66) Zhang, M.; De Bo, G. Impact of a Mechanical Bond on the Activation of a Mechanophore. *J. Am. Chem. Soc.* **2018**, *140*, 12724–12727.

(67) Duan, H. Y.; Wang, Y. X.; Wang, L. J.; Min, Y. Q.; Zhang, X. H.; Du, B. Y. An Investigation of the Selective Chain Scission at Centered Diels-Alder Mechanophore under Ultrasonication. *Macromolecules* **2017**, *50*, 1353–1361.

(68) Lyu, B.; Cha, W.; Mao, T.; Wu, Y.; Qian, H.; Zhou, Y.; Chen, X.; Zhang, S.; Liu, L.; Yang, G.; Lu, Z.; Zhu, Q.; Ma, H. Surface Confined Retro Diels–Alder

Reaction Driven by the Swelling of Weak Polyelectrolytes. *ACS Appl. Mater. Interfaces* **2015**, *7*, 6254–6259.

(69) Inglis, A. J.; Sinnwell, S.; Stenzel, M. H.; Barner-Kowollik, C. Ultrafast Click Conjugation of Macromolecular Building Blocks at Ambient Temperature. *Angew. Chem. Int. Ed.* **2009**, *48*, 2411–2414.

(70) Krupicka, M.; Dopieralski, P.; Marx, D. Unclicking the Click: Metal-Assisted Mechanochemical Cycloreversion of Triazoles Is Possible. *Angew. Chem. Int. Ed.* **2017**, *56*, 7745–7749.

(71) Kolb, H. C.; Finn, M. G.; Sharpless, K. B. Click Chemistry: Diverse Chemical Function from a Few Good Reactions. *Angew. Chem. Int. Ed.* **2001**, *40*, 2004–2021.

(72) Rostovtsev, V. V.; Green, L. G.; Fokin, V. V.; Sharpless, K. B. A Stepwise Huisgen Cycloaddition Process: Copper(I)-Catalyzed Regioselective "Ligation" of Azides and Terminal Alkynes. *Angew. Chem. Int. Ed.* **2002**, *41*, 2596–2599.

(73) Tornoe, C. W.; Christensen, C.; Meldal, M. Peptidotriazoles on Solid Phase: [1,2,3]-Triazoles by Regiospecific Copper(I)-Catalyzed 1,3-Dipolar Cycloadditions of Terminal Alkynes to Azides. *J. Org. Chem.* **2002**, *67*, 3057–3064.

(74) Stauch, T.; Dreuw, A. Force-induced retro-click reaction of triazoles competes with adjacent single-bond rupture. *Chem. Sci.* **2017**, *8*, 5567–5575.

(75) Schütze, D.; Holz, K.; Müller, J.; Beyer, M. K.; Lüning, U.; Hartke, B. Pinpointing Mechanochemical Bond Rupture by Embedding the Mechanophore into a Macrocycle. *Angew. Chem. Int. Ed.* **2015**, *54*, 2556–2559.

(76) Kan, L.; Cheng, H.; Li, B.; Zhang, X.; Wang, Q.; Wei, H.; Ma, N. Anthracene dimer crosslinked polyurethanes as mechanoluminescent polymeric materials. *New J. Chem.* **2019**, *43*, 2658–2664.

(77) Song, Y.-K.; Lee, K.-H.; Hong, W.-S.; Cho, S.-Y.; Yu, H.-C.; Chung, C.-M. Fluorescence sensing of microcracks based on cycloreversion of a dimeric anthracene moiety. *J. Mater. Chem.* **2011**, *22*, 1380–1386.

(78) Wu, D.-Y.; Zhang, L.-P.; Wu, L.-Z.; Wang, B.; Tung, C.-H. Water-in-oil microemulsions as microreactors to control the regioselectivity in the photocycloaddition of 9-substituted anthracenes. *Tetrahedron Lett.* **2002**, *43*, 1281–1283.

(79) Becker, H. Dieter. Unimolecular photochemistry of anthracenes. *Chem. Rev.* **1993**, *93*, 145–172.

(80) Klukovich, H. M.; Kean, Z. S.; Ramirez, A. L. B.; Lenhardt, J. M.; Lin, J. X.; Hu, X. Q.; Craig, S. L. Tension Trapping of Carbonyl Ylides Facilitated by a Change in Polymer Backbone. *J. Am. Chem. Soc.* **2012**, *134*, 9577–9580.

(81) Barbee, M. H.; Wang, J.; Kouznetsova, T.; Lu, M.; Craig, S. L. Mechanochemical Ring-Opening of Allylic Epoxides. *Macromolecules* **2019**, *52*, 6234–6240.

(82) Jung, S.; Yoon, H. J. Mechanical Force Induces Ylide-Free Cycloaddition of Nonscissible Aziridines. *Angew. Chem. Int. Ed.* **2020**, *59*, 4883–4887.

(83) Bowser, B.; L Craig, S. Empowering mechanochemistry with multi-mechanophore polymer architectures. *Polym. Chem.* **2018**, *9*, 3583–3593.

(84) Lenhardt, J. M.; Black, A. L.; Beiermann, B. A.; Steinberg, B. D.; Rahman, F.; Samborski, T.; Elsakr, J.; Moore, J. S.; Sottos, N. R.; Craig, S. L. Characterizing

the mechanochemically active domains in gem-dihalocyclopropanated polybutadiene under compression and tension. *J. Mater. Chem.* **2011**, *21*, 8454–8459.

(85) Black, A. L.; Orlicki, J. A.; Craig, S. L. Mechanochemically triggered bond formation in solid-state polymers. *J. Mater. Chem.* **2011**, *21*, 8460–8465.

(86) Wang, J. P.; Kouznetsova, T. B.; Craig, S. L. Reactivity and Mechanism of a Mechanically Activated anti-Woodward-Hoffmann-DePuy Reaction. *J. Am. Chem. Soc.* **2015**, *137*, 11554–11557.

(87) Klukovich, H. M.; Kouznetsova, T. B.; Kean, Z. S.; Lenhardt, J. M.; Craig, S. L. A backbone lever-arm effect enhances polymer mechanochemistry. *Nat. Chem.* **2013**, *5*, 110–114.

(88) Wu, D.; Lenhardt, J. M.; Black, A. L.; Akhremitchev, B. B.; Craig, S. L. Molecular Stress Relief through a Force-Induced Irreversible Extension in Polymer Contour Length. *J. Am. Chem. Soc.* **2010**, *132*, 15936–15938.

(89) Lin, Y.; Kouznetsova, T. B.; Craig, S. L. A Latent Mechanoacid for Time-Stamped Mechanochromism and Chemical Signaling in Polymeric Materials. *J. Am. Chem. Soc.* **2020**, *142*, 99–103.

(90) Wang, J. P.; Kouznetsova, T. B.; Kean, Z. S.; Fan, L.; Mar, B. D.; Martinez, T. J.; Craig, S. L. A Remote Stereochemical Lever Arm Effect in Polymer Mechanochemistry. *J. Am. Chem. Soc.* **2014**, *136*, 15162–15165.

(91) Wang, J. P.; Kouznetsova, T. B.; Niu, Z. B.; Ong, M. T.; Klukovich, H.; Rheingold, A. L.; Martinez, T. J.; Craig, S. L. Inducing and quantifying forbidden

reactivity with single-molecule polymer mechanochemistry. *Nat. Chem.* **2015**, *7*, 323–327.

(92) Woodward, R. B.; Hoffmann, R. Stereochemistry of Electrocyclic Reactions. *J. Am. Chem. Soc.* **1965**, *87*, 395–397.

(93) DePuy, C. H.; Schnack, L. G.; Hausser, J. W.; Wiedemann, W. Chemistry of Cyclopropanols. III. The Mechanism of the Solvolysis of Cyclopropyl Tosylates. *J. Am. Chem. Soc.* **1965**, *87*, 4006–4006.

(94) DePuy, C. H.; Schnack, L. G.; Hausser, J. W. Chemistry of Cyclopropanols. IV. The Solvolysis of Cycopropyl Tosylates1,2. *J. Am. Chem. Soc.* **1966**, *88*, 3343–3346.

(95) Lenhardt, J. M.; Ong, M. T.; Choe, R.; Evenhuis, C. R.; Martinez, T. J.; Craig, S. L. Trapping a Diradical Transition State by Mechanochemical Polymer Extension. *Science* **2010**, *329*, 1057–1060.

(96) Wang, J. P.; Kouznetsova, T. B.; Niu, Z. B.; Rheingold, A. L.; Craig, S. L. Accelerating a Mechanically Driven anti-Woodward-Hoffmann Ring Opening with a Polymer Lever Arm Effect. *J. Org. Chem.* **2015**, *80*, 11895–11898.

(97) Potisek, S. L.; Davis, D. A.; Sottos, N. R.; White, S. R.; Moore, J. S. Mechanophore-Linked Addition Polymers. *J. Am. Chem. Soc.* **2007**, *129*, 13808–13809.

(98) Robb, M. J.; Kim, T. A.; Halmes, A. J.; White, S. R.; Sottos, N. R.; Moore, J. S. Regioisomer-Specific Mechanochromism of Naphthopyran in Polymeric Materials. *J. Am. Chem. Soc.* **2016**, *138*, 12328–12331.

(99) Gossweiler, G. R.; Kouznetsova, T. B.; Craig, S. L. Force-Rate Characterization of Two Spiropyran-Based Molecular Force Probes. *J. Am. Chem. Soc.* **2015**, *137*, 6148–6151.

(100) Kim, T. A.; Robb, M. J.; Moore, J. S.; White, S. R.; Sottos, N. R. Mechanical Reactivity of Two Different Spiropyran Mechanophores in Polydimethylsiloxane. *Macromolecules* **2018**.

(101) Barbee, M. H.; Kouznetsova, T. B.; Barrett, S. L.; Gossweiler, G. R.; Lin, Y.; Rastogi, S. K.; Brittain, W. J.; Craig, S. L. Substituent effects and mechanism in a mechanochemical reaction. *J. Am. Chem. Soc.* **2018**, *140*, 12746–12750.

(102) O'Bryan, G.; Wong, B. M.; McElhanon, J. R. Stress Sensing in Polycaprolactone Films via an Embedded Photochromic Compound. *ACS Appl. Mater. Interfaces* **2010**, *2*, 1594–1600.

(103) Zhang, H.; Gao, F.; Cao, X. D.; Li, Y. Q.; Xu, Y. Z.; Weng, W. G.; Boulatov, R. Mechanochromism and Mechanical-Force-Triggered Cross-Linking from a Single Reactive Moiety Incorporated into Polymer Chains. *Angew. Chem. Int. Ed.* **2016**, *55*, 3040–3044.

(104) Lin, Y. J.; Barbee, M. H.; Chang, C. C.; Craig, S. L. Regiochemical Effects on Mechanophore Activation in Bulk Materials. *J. Am. Chem. Soc.* **2018**, *140*, 15969–15975.

(105) Peterson, G. I.; Larsen, M. B.; Ganter, M. A.; Storti, D. W.; Boydston, A. J. 3D Printed Mechanochromic Materials. *ACS Appl. Mater. Interfaces* **2015**, *7*, 577–583.

(106) Versaw, B. A.; McFadden, M. E.; Husic, C. C.; Robb, M. J. Designing Naphthopyran Mechanophores with Tunable Mechanochromic Behavior. *Chem. Sci.* **2020**, *11*, 4525–4530.

(107) Lin, Y.; Zhang, Y.; Wang, Z.; Craig, S. L. Dynamic Memory Effects in the Mechanochemistry of Cyclic Polymers. *J. Am. Chem. Soc.* **2019**, *141*, 10943–10947.

(108) Berkowski, K. L.; Potisek, S. L.; Hickenboth, C. R.; Moore, J. S. Ultrasound-induced site-specific cleavage of azo-functionalized poly(ethylene glycol). *Macromolecules* **2005**, *38*, 8975–8978.

(109) Sumi, T.; Goseki, R.; Otsuka, H. Tetraarylsuccinonitriles as mechanochromophores to generate highly stable luminescent carbon-centered radicals. *Chem. Commun.* **2017**, *53*, 11885–11888.

(110) Sakai, H.; Sumi, T.; Aoki, D.; Goseki, R.; Otsuka, H. Thermally Stable Radical-Type Mechanochromic Polymers Based on Difluorenylsuccinonitrile. *ACS Macro Lett.* **2018**, *7*, 1359–1363.

(111) Ishizuki, K.; Oka, H.; Aoki, D.; Goseki, R.; Otsuka, H. Mechanochromic Polymers That Turn Green Upon the Dissociation of Diarylbibenzothiophenonyl: The Missing Piece toward Rainbow Mechanochromism. *Chem. Eur. J.* **2018**, *24*, 3170–3173.

(112) Chen, Z.; Zhu, X.; Yang, J.; Mercer, J. A. M.; Burns, N. Z.; Martinez, T. J.; Xia, Y. The cascade unzipping of ladderane reveals dynamic effects in mechanochemistry. *Nat. Chem.* **2020**, *12*, 302–309.

(113) Yang, J. H.; Horst, M.; Romaniuk, J. A. H.; Jin, Z. X.; Cegelski, L.; Xia, Y. Benzoladderene Mechanophores: Synthesis, Polymerization, and Mechanochemical Transformation. *J. Am. Chem. Soc.* **2019**, *141*, 6479–6483.

(114) Lee, B.; Niu, Z. B.; Wang, J. P.; Slebodnick, C.; Craig, S. L. Relative Mechanical Strengths of Weak Bonds in Sonochemical Polymer Mechanochemistry. *J. Am. Chem. Soc.* **2015**, *137*, 10826–10832.

(115) Encina, M. V.; Lissi, E.; Sarasúa, M.; Gargallo, L.; Radic, D. Ultrasonic degradation of polyvinylpyrrolidone: Effect of peroxide linkages. *J. Polym. Sci. B Polym. Lett. Ed.* **1980**, *18*, 757–760.

(116) Luzuriaga, A. R. de; Matxain, J. M.; Ruipérez, F.; Martin, R.; Asua, J. M.; Cabanero, G.; Odriozola, I. Transient mechanochromism in epoxy vitrimer composites containing aromatic disulfide crosslinks. *J. Mater. Chem. C* **2016**, *4*, 6220–6223.

(117) Li, Y. C.; Nese, A.; Matyjaszewski, K.; Sheiko, S. S. Molecular Tensile Machines: Anti-Arrhenius Cleavage of Disulfide Bonds. *Macromolecules* **2013**, *46*, 7196–7201.

(118) Imato, K.; Kanehara, T.; Ohishi, T.; Nishihara, M.; Yajima, H.; Ito, M.; Takahara, A.; Otsuka, H. Mechanochromic Dynamic Covalent Elastomers: Quantitative Stress Evaluation and Autonomous Recovery. *ACS Macro Lett.* **2015**, *4*, 1307–1311.

(119) Lenhardt, J. M.; Ogle, J. W.; Ong, M. T.; Choe, R.; Martinez, T. J.; Craig, S. L. Reactive Cross-Talk between Adjacent Tension-Trapped Transition States. *J. Am. Chem. Soc.* **2011**, *133*, 3222–3225.

(120) Wang, J.; Kouznetsova, T. B.; Craig, S. L. Single-molecule Observation of a Mechanically Activated Cis-to-Trans Cyclopropane Isomerization. *J. Am. Chem. Soc.* **2016**, *138*, 10410–10412.

(121) Klukovich, H. M.; Kean, Z. S.; Iacono, S. T.; Craig, S. L. Mechanically Induced Scission and Subsequent Thermal Remending of Perfluorocyclobutane Polymers. *J. Am. Chem. Soc.* **2011**, *133*, 17882–17888.

(122) Lee, D. C.; Kensy, V. K.; Maroon, C. R.; Long, B. K.; Boydston, A. J. The Intrinsic Mechanochemical Reactivity of Vinyl-Addition Polynorbornene. *Angew. Chem. Int. Ed.* **2019**, *58*, 5639–5642.

(123) Verstraeten, F.; Gostl, R.; Sijbesma, R. P. Stress-induced colouration and crosslinking of polymeric materials by mechanochemical formation of triphenylimidazolyl radicals. *Chem. Commun.* **2016**, *52*, 8608–8611.

(124) Karman, M.; Verde-Sesto, E.; Weder, C. Mechanochemical Activation of Polymer-Embedded Photoluminescent Benzoxazole Moieties. *ACS Macro Lett.* **2018**, *7*, 1028–1033.

(125) Karman, M.; Verde-Sesto, E.; Weder, C.; Simon, Y. C. Mechanochemical Fluorescence Switching in Polymers Containing Dithiomaleimide Moieties. *ACS Macro Lett.* **2018**, *7*, 1099–1104.

(126) Gordon, M. B.; Wang, S.; Knappe, G. A.; Wagner, N. J.; Epps, T. H.; Kloxin, C. J. Force-induced cleavage of a labile bond for enhanced mechanochemical crosslinking. *Polym. Chem.* **2017**, *8*, 6485–6489.

(127) Nagamani, C.; Liu, H. Y.; Moore, J. S. Mechanogeneration of Acid from Oxime Sulfonates. *J. Am. Chem. Soc.* **2016**, *138*, 2540–2543.

(128) Diesendruck, C. E.; Peterson, G. I.; Kulik, H. J.; Kaitz, J. A.; Mar, B. D.; May, P. A.; White, S. R.; Martinez, T. J.; Boydston, A. J.; Moore, J. S. Mechanically triggered heterolytic unzipping of a low-ceiling-temperature polymer. *Nat. Chem.* **2014**, *6*, 624–629.

(129) Peterson, G. I.; Boydston, A. J. Kinetic Analysis of Mechanochemical Chain Scission of Linear Poly(phthalaldehyde). *Macromol. Rapid Commun.* **2014**, *35*, 1611–1164.

(130) Shiraki, T.; Diesendruck, C. E.; Moore, J. S. The mechanochemical production of phenyl cations through heterolytic bond scission. *Faraday Discuss* **2014**, *170*, 385–394.

(131) Wang, Z.; Ma, Z.; Wang, Y.; Xu, Z.; Luo, Y.; Wei, Y.; Jia, X. A Novel Mechanochromic and Photochromic Polymer Film: When Rhodamine Joins Polyurethane. *Adv. Mater.* **2015**, *27*, 6469–6474.

(132) Nixon, R.; De Bo, G. Three concomitant C–C dissociation pathways during the mechanical activation of an N-heterocyclic carbene precursor. *Nat. Chem.* **2020**, DOI: 10.1038/s41557-020-0509-1.

(133) Wang, T.; Zhang, N.; Dai, J.; Li, Z.; Bai, W.; Bai, R. Novel Reversible Mechanochromic Elastomer with High Sensitivity: Bond Scission and Bending-Induced Multicolor Switching. *ACS Appl. Mater. Interfaces* **2017**, *9*, 11874–11881.

Chapter 2

COMPUTATIONAL INVESTIGATION OF STRUCTURE–ACTIVITY RELATIONSHIPS OF 2-FURYLCARBINOL DERIVATIVES FOR MOLECULAR RELEASE

2.1 Introduction

2.1.1 Mechanically triggered molecular release

Polymers that release functional molecules in response to mechanical force are desirable for a range of applications, including catalysis, sensing, self-healing, and drug delivery.[1–3] To this end, various approaches have been reported, including physically entrapped payloads in a polymeric matrix,[4] dissociation of supramolecular assemblies,[5,6] and the use of fluid-filled microcapsules[7] or vascular networks[8] that release a payload after being ruptured. Recently, the use of mechanical force as an external stimulus to promote covalent chemical transformations has emerged as an attractive strategy for molecular release.[9] Through this approach, force is transduced via polymer chains to mechanically sensitive molecules known as mechanophores, which respond in a chemoselective manner to promote a productive chemical reaction.[10,11] Moore and Craig have reported *gem*-dichlorocyclopropane mechanophores that undergo mechanochemical rearrangements that result in the release of HCl.[12,13] Boydston has developed an oxanorbornadiene mechanophore to release a benzyl furfuryl ether via a mechanically induced cycloreversion reaction.[14] Göstl and Herrmann developed a release platform that relies on the mechanochemical cleavage of a disulfide moiety and subsequent 5-*exo-trig* cyclization to release an alcohol attached via a β-carbonate linker.[15] Recently, several groups have reported the mechanically triggered release of gases, including CO[16,17] and singlet O_2.[18]

2.1.2 Mechanically triggered release from a latent furylcarbinol derivative

Working to develop a general platform capable of releasing a wide range of cargo molecules from a single mechanophore core, we took inspiration from Gillies and coworkers, who reported the development of a thermal trigger for the depolymerization of self-immolative polymers (Scheme 2.1), whereby the thermal cycloreversion reaction of a furan–maleimide adduct reveals an unstable furfuryl carbonate.[19] The decomposition of this furfuryl carbonate motif initiates the depolymerization of a covalently linked polymer chain.

Scheme 2.1 Thermally triggered depolymerization via a latent furfuryl carbonate developed by Gillies and coworkers

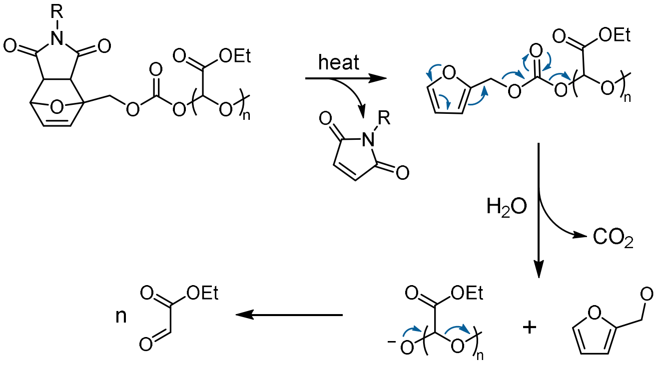

Our strategy relied on a mechanically triggered cascade reaction in which a mechanochemical retro-cycloaddition reaction unveils an unstable furylcarbinol derivative that subsequently decomposes under mild conditions to release its molecular payload (Scheme 2.2).[20] This modular approach to molecular release facilitates the use of a wide range of functional cargo molecules and enables independent modulation of the mechanochemical retro-cycloaddition reaction and the thermal decomposition release reaction.

Scheme 2.2 Mechanically triggered small molecule release based on a latent furfuryl carbonate

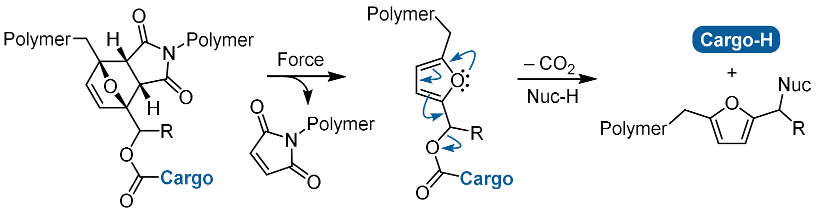

The proposed mechanism for molecular release involves the formation of a furfuryl cation intermediately upon decomposition of the metastable furfurylcarbinol derivative (Scheme 2.3 **Thermal decomposition/release reaction from a furfuryl carbonate via a furfuryl cation intermediate**). We hypothesized that the stability of this furfuryl cation species could be turned through electronic properties of the furan.

Scheme 2.3 Thermal decomposition/release reaction from a furfuryl carbonate via a furfuryl cation intermediate

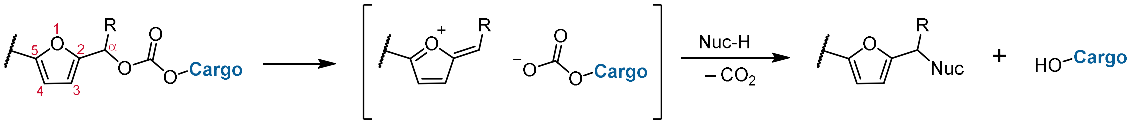

The work presented here focuses on the kinetics of this thermal decomposition reaction, which we probe using computational methods to develop key structure–activity relationships for this class of molecules. While these relationships could be developed through synthesis and experimentation, a computational investigation enables predictions of reactivity without expending laboratory resources and time. Additionally, the highly reactive substrates proposed to achieve rapid molecular release are not expected to be easily isolable. This makes unambiguous characterization of their experimental reactivity more difficult. Here, we describe a method for estimating transition state energies for the thermal decomposition reaction of furfuryl carbonates and related compounds. Using this method, we develop initial structure–activity relationships for this class of compounds.

2.2 Methods

The primary intent of this work was to develop a workflow to accurately estimate the relative activation barriers ($\Delta G^{\ddagger}$) for the thermal decomposition of a range of furfuryl carbonates and related compounds using density functional theory (DFT). Additionally, we aimed to create a relatively simple and intuitive method that could be implemented by chemists who do not have substantial computational background. Finally, we used computational techniques that enabled the use of a desktop computer without the need for high performance computing. All calculations presented here were run on a desktop computer using Spartan'18/Spartan'20 Parallel Suite software.[21] The calculated geometries for all compounds presented in this chapter can be found in Appendix C. A step-by-step guide for conducting a simple transition state calculation in the Spartan software can be found in Appendix D.

For the initial work, we chose to focus on a simple furfuryl carbonate structure, although other payloads are examined later. For most compounds, our model structures included a simplified leaving group (e.g., methyl carbonate) for the sake of computational expediency. Similarly, we did not consider the effect of a protic solvent environment. Although these simplifications may reduce the accuracy of absolute activation energy values, we anticipate that relative reactivity trends will hold.

2.2.1 Initial transition state guess

Transition state geometry optimization methods require a starting geometry that is close to the actual transition state. To provide an initial transition state guess for subsequent transition state optimization calculations, we chose to employ a relaxed scan across the proposed reaction coordinate for the fragmentation. In our system, we expected this coordinate to involve the stretching of the C–O bond linking the carbonate oxygen to the α-position of the furan (Scheme 2.4).

Scheme 2.4 An unsubstituted furfuryl carbonate showing the bond-breaking mode of interest

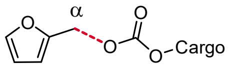

We extended the length of this C–O bond in a stepwise fashion, calculating the equilibrium geometry of the molecule at each step. Starting from the equilibrium geometry of the furfuryl carbonate, we extended the relaxed scan to 1.5 Å beyond the equilibrium C–O bond length. As shown in Figure 2.1, we tested a range of functionals and basis sets for these relaxed scan calculations.

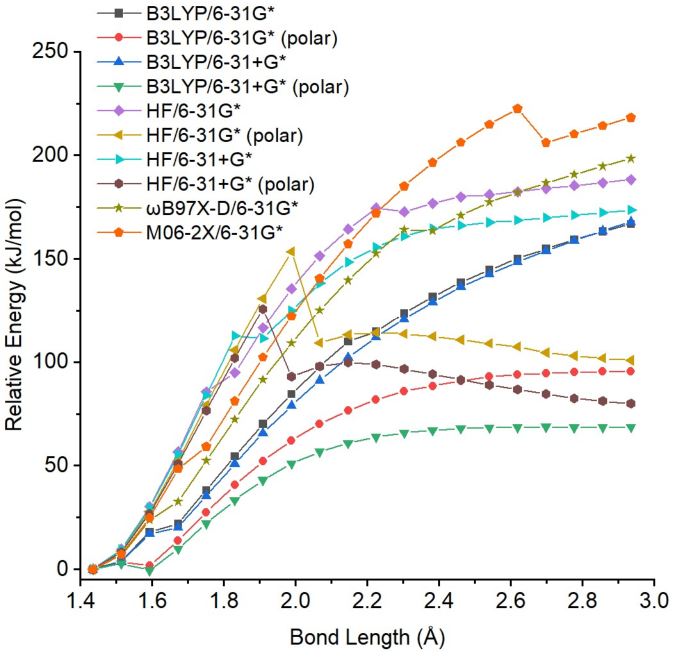

Figure 2.1 Relaxed scans across several levels of theory for a simple furfuryl carbonate, elongating the C–O bond that is expected to break in the decomposition/release reaction. Most methods show an increasing trend with no clear energy maximum. However, HF methods in a polar dielectric constant continuum produce a clear energy maximum at ~2.2 Å. Note that the sharp energy drop-offs below 2 Å for the HF methods correspond to conformational changes.

In a relaxed scan across a reaction coordinate, we expect to find an energy maximum corresponding to an approximate transition state structure. With the widely used B3LYP functional across a range of small basis sets, we do not observe a maximum in the energy profile. Instead, we see continuously increasing profiles that do not suggest a transition state along this coordinate. Other DFT functionals including ωB97X-D and M06-2X show similar increasing energy trends (the sharp energy drop-offs in some of these profiles correspond to conformational changes in the molecule, not transition states). Moving away from DFT functionals, we tested Hartree–Fock (HF) methods. Both 6-31G* and 6-31+G* basis sets yielded similar energy profiles to the DFT methods. However, implementation of a polarizable continuum model to simulate a polar solvent ($\varepsilon = 37.22$) resulted in reaction coordinate profiles with an obvious energy maximum. The incorporation of this uniform dielectric did not improve the performance of the B3LYP functional. Based on these results, we chose to implement HF/6-31+G* (polar) for our initial calculations.

2.2.2 Transition state geometry optimization

To further refine our transition state structure, we used the transition state geometry optimization method within Spartan'18 to calculate an optimized transition state geometry for our molecule of interest. The maximum energy geometry from the relaxed scan calculations served as our starting transition state guess. We again employed the HF/6-31+G* level of theory for these calculations. We found that the results of these calculations result in a structure with a C–O bond length typically less than 0.03 Å different from the result of our initial relaxed scan.

2.2.3 Transition state energy calculation using constrained geometry optimization

A transition state exists at a first-order saddle point on the potential energy surface such that it is a maximum along only one reaction coordinate and a minimum for all others. In transition state calculations, this is identified by finding the point where a single eigenvector (reaction coordinate) has a negative eigenvalue in the Hessian matrix of the potential energy surface. When evaluating a transition state calculation, we expect a valid transition state to exhibit a single negative vibrational frequency corresponding to the bond breaking/bond forming coordinate of interest. In our system, we found that molecular geometries calculated from the transition state search at the HF/6-31+G* level of theory exhibited several small negative vibrational frequencies ($> -50\ \mathrm{cm}^{-1}$) in addition to the primary C–O bond breaking mode ($< -250\ \mathrm{cm}^{-1}$).

To further refine the structure and eliminate these unwanted vibrational modes, we implemented a constrained equilibrium geometry calculation as the final step in the transition state search. We constrained the elongated C–O bond length from the initial transition state optimization and relaxed the remainder of the molecule. Hoping to achieve accurate predictions for the transition state energy, we moved away from HF methods. We opted for the M06-2X functional, which is well suited for this application and is widely used to derive kinetic parameters.[22] Other widely used functionals like B3LYP have been shown to yield inaccurate results for kinetics applications, especially those involving diffuse electron systems.[23] A larger basis set was chosen to enable more accurate transition state energy calculations. The 6-311+G(d,p) basis set (also represented as 6-311+G**) was selected for its expanded orbital representation and incorporation of diffuse functions, as we are probing a developing anion and non-equilibrium, long-range electronic interactions. Calculations at this level of theory were performed with a (99,590) Lebedev integration grid for higher precision with the M06-2X functional. The difference in Gibbs free energy between the optimized transition state geometry ($G^{\ddagger}$) and the equilibrium geometry of the starting material (G_0) was used to calculate the activation energy ($\Delta G^{\ddagger}$).

2.3 Results and discussion

2.3.1 Effects of substitution at the 5- and α-positions of a furfuryl carbonate

We began our computational investigation with a series of furfuryl carbonates based on the thermal depolymerization trigger reported by Gillies (Figure 2.2).[19] The simplest furfuryl carbonate **1** consists of a methyl carbonate linked to the 2-position of an otherwise unsubstituted furan by a methylene group. We found the activation energy at room temperature for the decomposition of this compound to be 29.4 kcal/mol. The Eyring equation (eq. 1) tells us that the corresponding half-life of decomposition for this molecule is predicted to be >10 years at room temperature, much too slow for our intended applications.

$$k = \frac{\kappa k_B T}{h} e^{-\frac{\Delta G^{\ddagger}}{RT}} \qquad (1)$$

We next incorporated a methyl substituent at the 5-position of the furan to model the effect of the polymer tether point that we anticipated for our polymer-bound platform. This methyl group in furfuryl carbonate **2** lowers the activation energy to 25.8 kcal/mol. Hoping to achieve an even lower activation barrier to achieve rapid release at room temperature, we proposed the addition of an additional methyl substituent at the α-position of the furan (furfuryl carbonate **3**), which we expected to stabilize the developing carbocation at this atom. This substituent results in a pronounced decrease in activation energy to 22.0 kcal/mol, corresponding to a half-life of <1 h at room temperature.

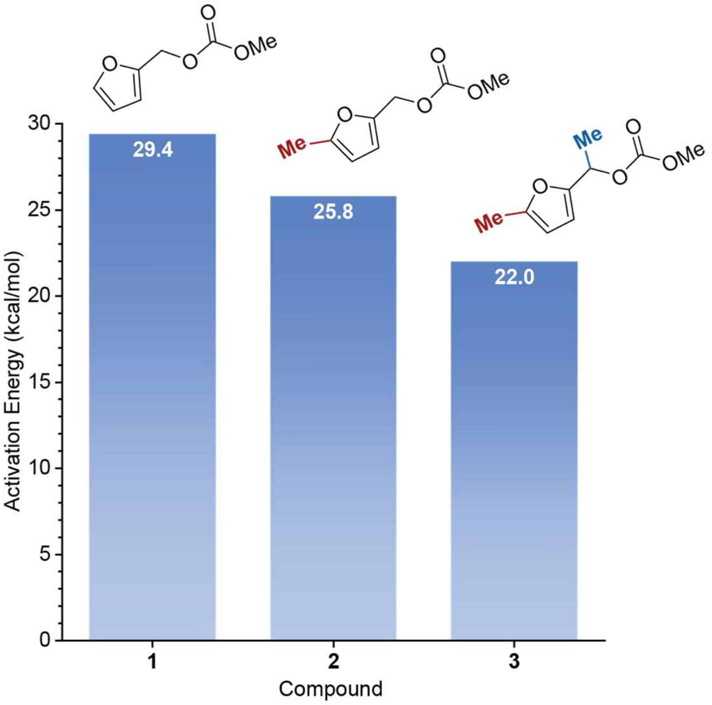

Figure 2.2 Calculated activation energy values (M06-2X/6-311+G**) for the decomposition of furfuryl carbonates **1–3**. The addition of methyl substituents at the 5- and α-positions of the furan result in a reduced activation barrier.

2.3.2 Role of the payload identity in transition state calculations

For the sake of computation expediency, we chose a simple payload motif by using a methyl carbonate leaving group. If we instead use phenyl carbonate **4** to stimulate the release of a phenol, we calculate an activation energy of 19.3 kcal/mol (Chart 2.1

Comparison of the activation barrier for release of an alkyl alcohol and a phenol). Although a simplified cargo molecule may reduce the accuracy of the absolute activation energy values, we anticipate the predicted reactivity trends to hold. Additionally, we found that the use of the larger phenolic cargo led to significantly longer computation times (DFT typically scales as ~N^3 for N atoms in the molecule) and identifying a transition state became more difficult due to the inclusion of additional possible vibrational modes. As a result, we chose to continue with the simplified payload motif.

Chart 2.1 Comparison of the activation barrier for release of an alkyl alcohol and a phenol

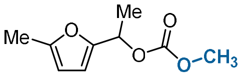

3

$\Delta G^‡$ = 22.0 kcal/mol

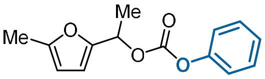

4

$\Delta G^‡$ = 19.3 kcal/mol

2.3.3 *Experimental validation of predicted furfuryl carbonate decomposition kinetics*

Our computational results suggest that an unsubstituted 2-furfuryl carbonate will exhibit high stability at room temperature, while the addition of substitution at the 2- and α-positions greatly increases the reactivity. To evaluate this experimentally, we synthesized model compound **M1** and **M3** corresponding to structures **1** and **3** shown above, respectively (Chart 2.2). A hydroxycoumarin (7-hydroxy-4-methylcoumarin) cargo was used for these model compounds. Both compounds were incubated in 3:1 (v/v) acetonitrile-d_3:MeOH at room temperature and monitored by ^{1}H NMR to measure the half-life of hydroxycoumarin release. Compound **M1** exhibits a very slow half-life of 17 days, while furfuryl carbonate **M3** reacts with a significantly shorter half-life of 79 min.

Chart 2.2 Experimentally determined half-lives of hydroxycoumarin release for two furfuryl carbonates

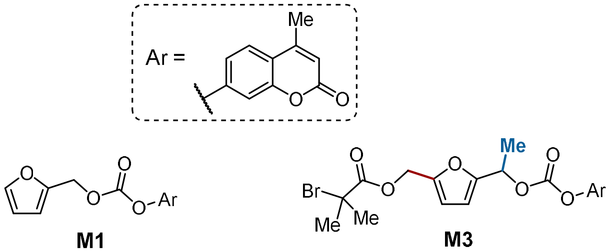

M1

$t_{1/2}$ = 17 d

M3

$t_{1/2}$ = 79 min

Although the absolute activation energies do not perfectly match the computed values, we note that the trend in reactivity is consistent. Sonication experiments investigating the mechanically triggered release of hydroxycoumarin (measured by fluorescence spectroscopy) exhibited a thermal release half-life of 46 min from polymer-bound furfuryl carbonate **P3** (Chart 2.3).

Chart 2.3 Experimental half-life of polymer-tethered furfuryl carbonate with an α-methyl group

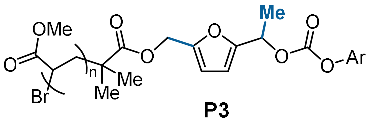

P3

$t_{1/2}$ = 46 min

2.3.4 *Release of an aniline cargo from a simple furfuryl carbamate*

We found that methyl substitution at both the 2- and α-positions of the furan motif of a furfuryl carbonate enabled efficient release of an alcohol cargo, with experimental results supporting the computational conclusions. However, when this platform was used to release an amine (Scheme 2.5), the experimental rate of release was extremely slow, occurring with a half-life of 240 days.[24] Consistent with this long half-life, transition state calculations predict a high activation energy for furfuryl carbamate **5** of 28.9 kcal/mol, nearly 7 kcal/mol higher than for analogous furfuryl carbonate **3**.

Scheme 2.5 Release of an amine cargo molecule from a furfuryl carbamate

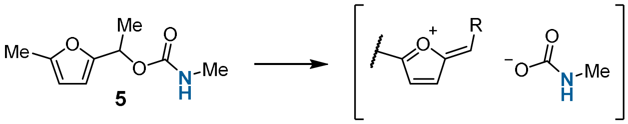

2.3.5 *Modulating the rate of release through additional furan substitution*

Given that the first-generation release platform did not enable efficient release of non-phenolic cargo molecules, we sought to improve the kinetics of the furfuryl carbonate decomposition reaction. Noting that stabilization of the developing furfuryl cation through the addition of an α-methyl substituent led to a substantial decrease in the activation energy, we proposed further stabilization of the furfuryl cation through the addition of electron donating substituents to the 3-position of the furan. We envisioned an electron-rich furan could better stabilize the cation forming during the transition state, thus lowering the activation barrier of release. To achieve the greatest improvement in activation energy, we coupled these proposed substituents with the 2-methyl and α-methyl substituents previously described. Our transition state calculations predict that all four proposed electron-donating substituents result in a reduced activation energy relative to furfuryl carbonate **3** (Figure 2.3). The addition of a 3-methyl substituent (compound **6**) lowered the activation energy to 20.3 kcal/mol, while a 3-phenyl group (compound **7**) further reduced this value to 19.0 kcal/mol. The more strongly electron donating 3-phenoxy group in furfuryl carbonate **8** dropped the activation energy to 18.3 kcal/mol, and the 3-methoxy substituent (compound **9**) exhibited the lowest activation barrier at 16.1 kcal/mol. These results suggest that the incorporation of an electron-donating substituent at the 3-position of a furfuryl carbonate can significantly attenuate the activation barrier for decomposition, enabling more rapid payload release.

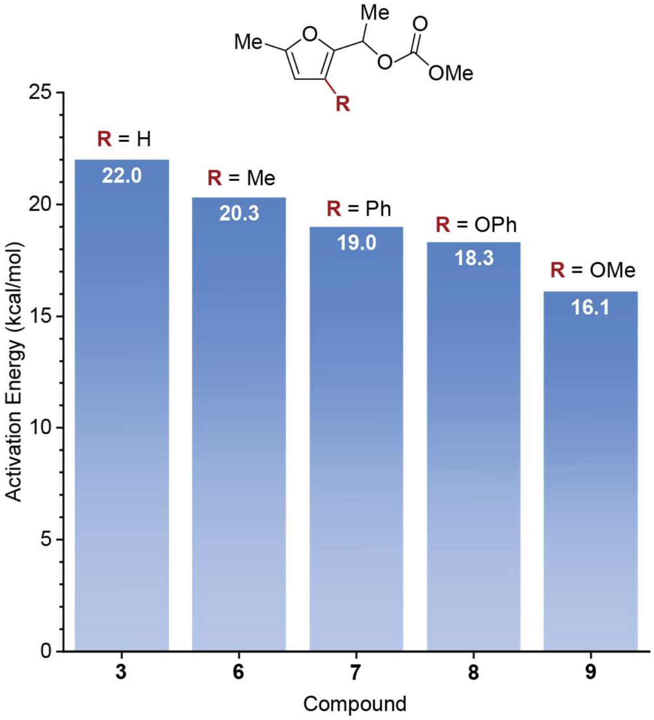

Figure 2.3 Calculated activation energy values (M06-2X/6-311+G**) for the decomposition of furfuryl carbonates with varying substitution at the 3-position of the furan. Increasingly electron donating substituents at this position result in a decreasing trend in activation energy.

Although the 3-methoxyfurfuryl carbonate was shown to exhibit the highest reactivity, we chose to pursue 3-phenoxyfurfuryl carbonate **8** for its more facile synthesis. Before conducting laboratory experiments, we dove deeper into the structure–activity relationships of these substituted furfuryl carbonates to better understand the tunability of the release rate through varied furfuryl carbonate substitution. We investigated a series of furfuryl carbonates with varied substitution at the 3- and α-positions of the furan (Figure 2.4). This series demonstrated that modulating only these two substituents enabled tunable activation energies ranging from 18.3 kcal/mol to 25.8 kcal/mol for the release an alcoholic cargo. Furfuryl carbonate **3** with only an α-methyl substitution and compound **10** with only the 3-phenoxy group are predicted to have similar activation barriers (22.0 and 21.5 kcal/mol, respectively) as determined computationally. Experimentally, we observe that the 3-phenoxy/α-H furfuryl carbonate (corresponding the compound **10**) decomposes much faster.[24] With a furfuryl carbonate with 3-phenoxy and α-methyl groups (corresponding to compound **8**), we observed instantaneous release of hydroxycoumarin at room temperature in laboratory experiments.

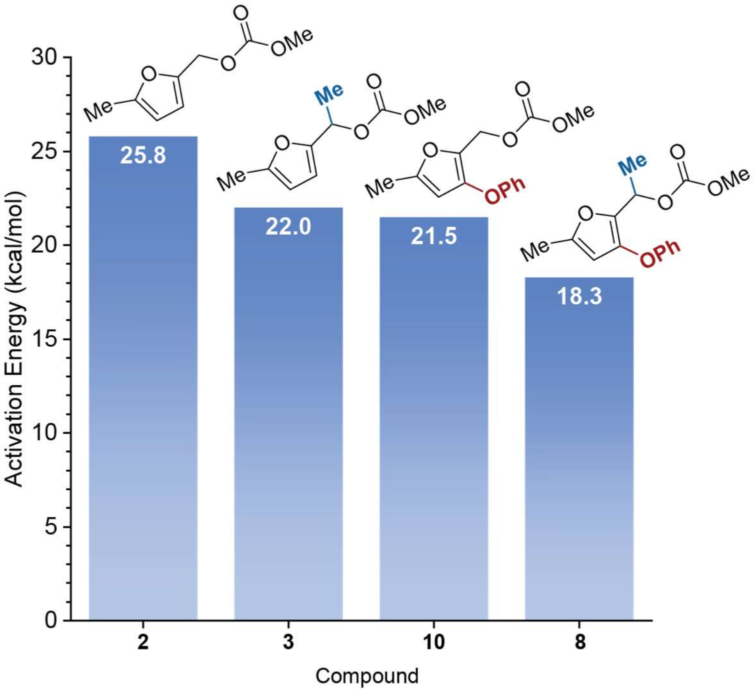

Figure 2.4 Calculated activation energy values (M06-2X/6-311+G**) for the decomposition of a series of furfuryl carbonates with varied substitution at the 3- and α-positions of the furan. An α-methyl group and a 3-phenoxy substituent both lead to reductions in the predicted activation barrier.

2.3.6 Improved release of an amine cargo with a 3-phenoxy furfuryl carbonate

Analogous to our exploration of the alcoholic cargo, we next investigated the impact of a 3-phenoxy substituent and an α-methyl group on the release of an amine using our transition state method (Figure 2.5). Without either substitution as illustrated in furfuryl carbamate **11**, these calculations predict a high activation barrier of 33.4 kcal/mol. Addition of the α-methyl substituent in furfuryl carbamate **5** lowers the transition state energy to 28.9 kcal/mol. Experimentally, an analogous furfuryl carbamate with an aminocoumarin cargo exhibited a release half-life of 240 days.[24] The presence of a 3-phenoxy group without the α-methyl group present (compound **12**) results in an activation energy of 28.2 kcal/mol. Although our calculations predict a minimal decrease in the energy barrier, we observe a substantial reduction in the experimental half-life of cargo release to 6.5 days.[24] (This is consistent with the unexpected experimental results of the 3-phenoxy/α-methyl furfuryl carbonate described in Section 2.3.5. We are uncertain of the origin of this discrepancy between computational and experimental results.) Finally, compound **13** with both substituents is predicted to have an activation barrier of 23.8 kcal/mol. Consistent with this predicted reduction in the activation energy, the experimental half-life of amine release from an analogous furfuryl carbamate is shown to be 41 min.

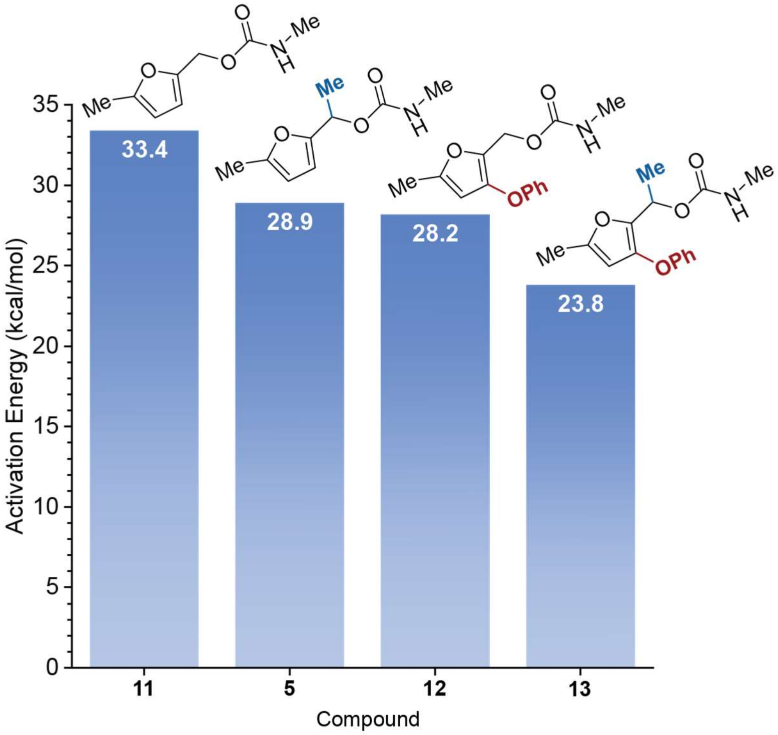

Figure 2.5 Calculated activation energy values (M06-2X/6-311+G**) for the decomposition of a series of furfuryl carbamates with varied substitution at the 3- and α-positions of the furan. An α-methyl group and a 3-phenoxy substituent both lead to reductions in the predicted activation barrier.

2.3.7 Release of additional functional cargo molecules

With the development of the efficient 3-phenoxy/α-methyl furylcarbinol platform, we sought to investigate the release of a range of additional cargo molecules. We first looked at the release of a carboxylic acid from a furfuryl ester (Chart 2.4). We predicted the activation barrier for release of this cargo to be higher than that for alcohol release, as the ester substrate no longer has the added anion delocalization afforded by the carbonate. With only the α-methyl substitution, our transition state calculations predict a high activation energy of 27.4 kcal/mol for furfuryl ester **14**. The addition of the 3-phenoxy group in compound **15** lowers this value to 22.5 kcal/mol, within the range of rapid release at room temperature.

Chart 2.4 Activation energies of release for two furfuryl esters capable of carboxylic acid release

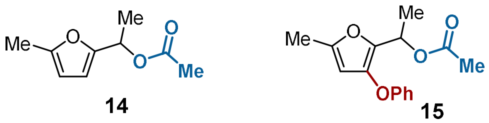

14 $\Delta G^{\ddagger}$ = 27.4 kcal/mol

15 $\Delta G^{\ddagger}$ = 22.5 kcal/mol

Experimentally, the release of a carboxylic acid was shown to occur with a half-life of 28 h. We did not exhaustively evaluate a wide scope of molecular payloads using our computational methods, but we experimentally demonstrated that the 3-phenoxy/α-methyl furylcarbinol platform achieves rapid molecular release rates for a wide range of cargo molecules (Chart 2.5).

Chart 2.5 Experimental half-lives of release for a broad range of cargo molecules from a 3-phenoxy substituted furfurylcarbinol derivative

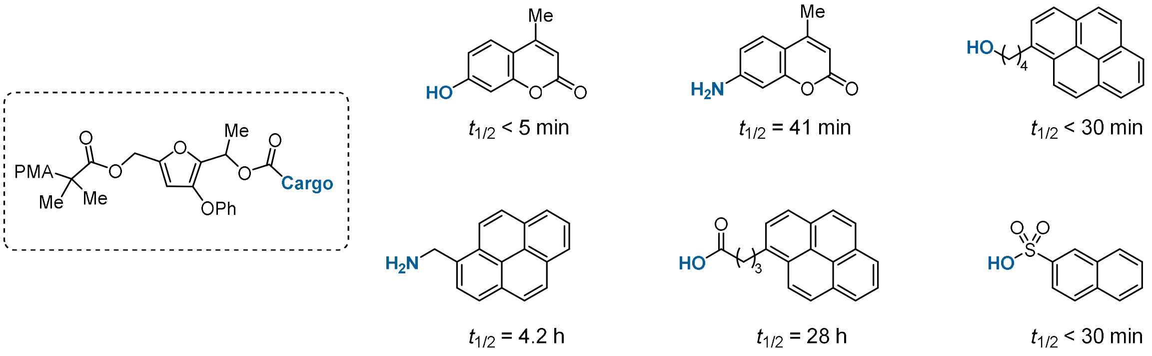

Although not studied experimentally, we evaluated the release of a thiol from this platform (Chart 2.6). Furfuryl thiocarbonate **16** is predicted to have an extremely low activation energy of 14.9 kcal/mol.

Chart 2.6 Activation energy of thiol release from a 3-phenoxy substituted furfuryl thiocarbonate

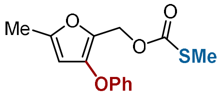

16

$\Delta G^{\ddagger}$ = 14.9 kcal/mol

2.3.8 Geometry considerations for the improved release rate from the 3-phenoxy furylcarbinol platform

We designed the 3-phenoxy substituted furfuryl carbonate with the intent of stabilizing the resulting furfuryl cation through greater electron density afforded by an electron-donating substituent. This effect likely plays a substantial role in lowering the activation energy relative to an unsubstituted furfuryl carbonate, but we note that the equilibrium conformation of these substrates may also contribute to the reduced activation barrier. In furfuryl carbonates **2** and **3** with no substitution at the 3-position of the furan, we see that the furan and carbonate are planar (Figure 2.6). We found that the dihedral angle (*φ*) between these two elements is 0.0° for compound **2** and 2.6° for compound **3** with an α-methyl substituent. This planarity likely allows for stabilization of the furfuryl carbonate through conjugation of these two portions of the molecule. However, when a 3-phenoxy substituent is added to the furan, the furfuryl carbonate adopts a conformation that places the carbonate group out of the plane of the furan. For furfuryl carbonate **10**, we calculate a dihedral angle of –116.4° and for furfuryl carbonate **8** with both 3-phenoxy and α-methyl substituents, we see a dihedral angle of 111.1°. We propose that the lack of planarity observed for the 3-phenoxy substituted furfuryl carbonates plays a role in reducing the activation barrier for decomposition through destabilization of the starting material relative to the unsubstituted analogs.

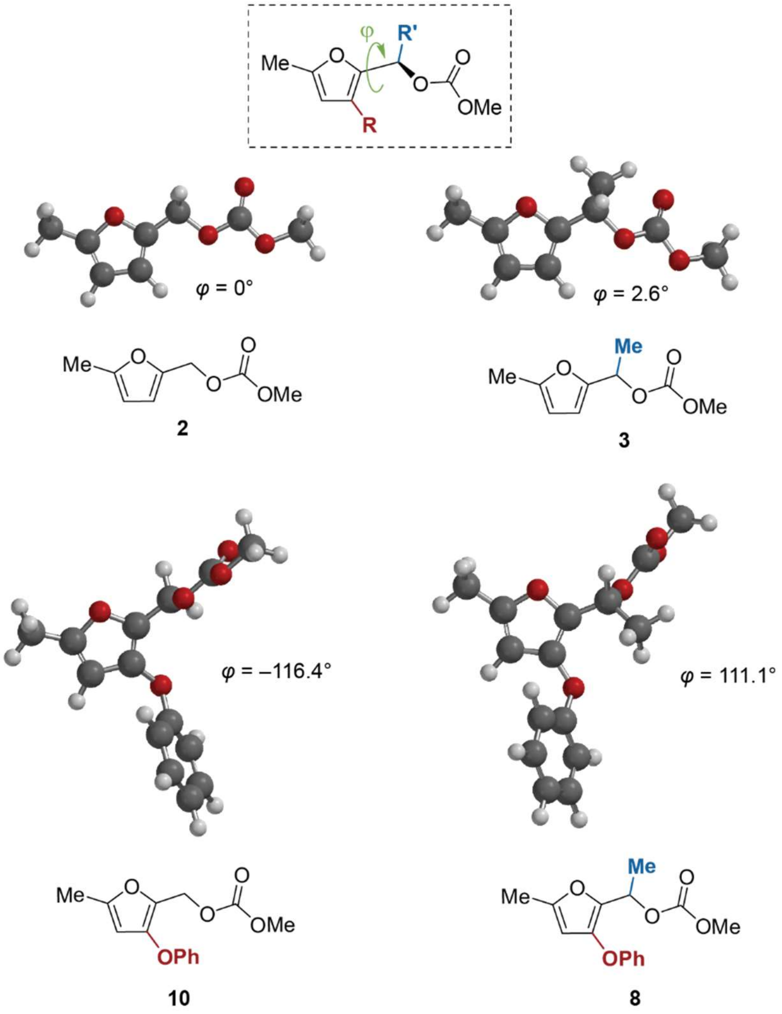

Figure 2.6 Computed structures and dihedral angles (*φ*) for a series of furfuryl carbonates with varied substitution at the 3- and α-positions of the furan. The presence of a 3-phenoxy group breaks the planarity between the furan and the carbonate, which likely disrupts electron delocalization, leading to lower stability of the 3-phenoxy substrates.

2.3.9 Effect of electron-withdrawing substituents on the furan

Through the addition of electron donating positions at the 3-position on the furan component of a furfuryl carbonate, we were able to achieve rapid cargo release at room temperature. To further explore the structure–activity relationships of this class of compounds, we chose to investigate two modified furfuryl carbonates that incorporate electron withdrawing substituents at the 3-position of the furan motif (Chart 2.7). We anticipated these substitutions would lead to higher activation barriers, and thus slower cargo release. This effect might be desirable to control the decomposition of highly reactive species (e.g., furfuryl thiocarbonates, see Section 2.3.7) or in highly polar, protic environments (e.g., aqueous solutions).

3-bromofurfuryl carbonate **17** is predicted to have an activation barrier of 25.0 kcal/mol, which is 3 kcal/mol higher than furfuryl carbonate **3** with no substitution at this position. A 3-cyano group (compound **18**) results in a very high activation barrier of 32.6 kcal/mol.

Chart 2.7 Activation energies of release for furfuryl carbonates with electron-withdrawing substituents

17 $\Delta G^{\ddagger}$ = 25.0 kcal/mol

18 $\Delta G^{\ddagger}$ = 32.6 kcal/mol

Thus, we have shown that it is possible to generate furfuryl carbonates that are inert, highly reactive, or anywhere in between through judicious substitutions to the 3- and α-positions

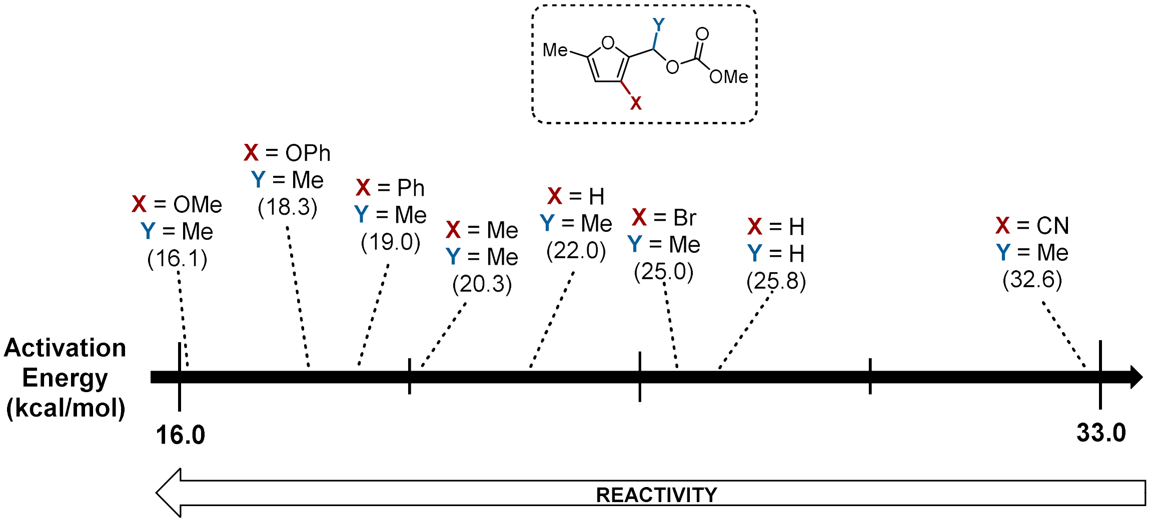

Figure 2.7 Comparison of computationally derived activation energy values and reactivities for a series of furfuryl carbonates with varied substitution at the 3- and α-positions.

of the furan (Figure 2.7). We anticipate this will enable the development of highly tunable molecular release platforms for a wide range of cargo molecules and environments.

2.3.10 Effect of an α-tethered alcohol

Through laboratory experiments, we found that a protic solvent environment is necessary to achieve efficient, clean cargo release from furfuryl carbonates. Functionality of this platform in aprotic environments would enable its utility for a wider range of applications, including in bulk polymeric materials. To overcome this limitation, we proposed the incorporation of a tethered alcohol directly onto the furfuryl carbonate to provide a local polar, protic environment.[25] This work is described in detail in Chapter 3. When a primary alcohol is tethered to the α-position of the furfuryl carbonate, we observed a marked reduction in the activation barrier of release. Our calculations suggest that furfuryl carbonate **19** will have an activation energy of 18.1 kcal/mol, a significant reduction compared to compound **3** containing an α-methyl substitution ($\Delta G^{\ddagger} = 22.0$ kcal/mol).

As described in Chapter 3, our DFT calculations suggest that this effect is facilitated by an intramolecular hydrogen bonding interaction between the tethered alcohol and the carbonate leaving group. To further probe the effect of the proposed hydrogen bonding stabilization of the carbonate leaving group, we investigated two additional furfuryl carbonates with tethered groups unable to participate in hydrogen bonding (Figure 2.8). We first looked at a butyl chain at the α-position (compound **20**). The decomposition of this compound is predicted to have an activation energy of 23.5 kcal/mol. The increase in this transition state energy compared to the α-methyl substituted substrate **3** may be due to the destabilization of the highly polar transition state in the presence of the added non-polar alkyl chain. We also calculated the activation energy for release from furfuryl carbonate **21** with a tethered methyl ether, which is predicted to be 23.4 kcal/mol. This suggests that the presence of a tethered oxygen atom alone is insufficient to stabilize the release reaction, and that the hydrogen bond enabled by the alcohol moiety is necessary to achieve the reduction in activation energy.

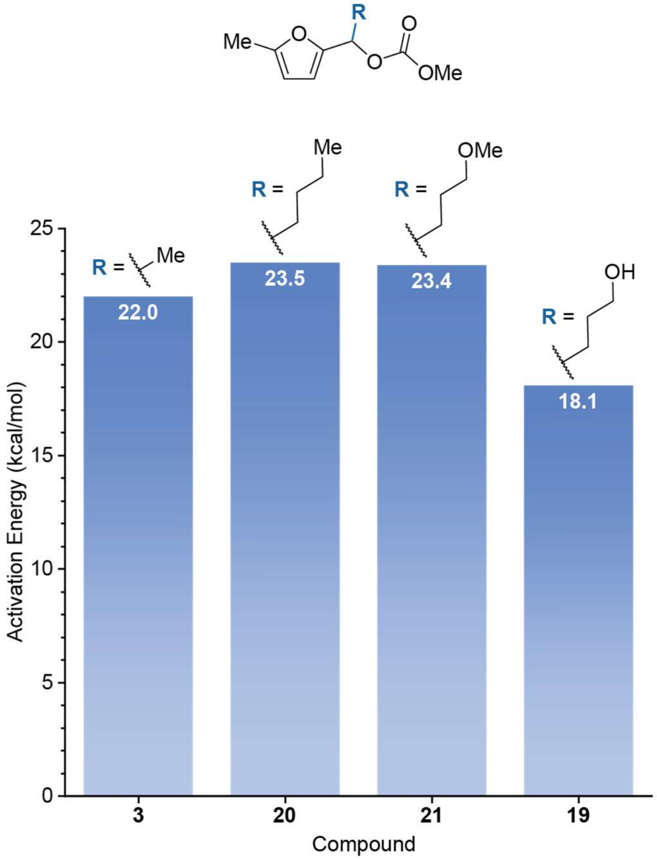

Figure 2.8 Calculated activation energy values (M06-2X/6-311+G**) for the decomposition of a series of furfuryl carbonates with varied substitution at the α-positions of the furan. A tethered primary alcohol at this position leads to a significant reduction in the activation barrier.

2.3.11 Release from pyrrole-linked carbonates

The primary focus of our work is on molecular release from furfuryl carbonates due to the well-studied nature of the furan–maleimide Diels–Alder adduct used for the development of a mechanophore platform. However, we envisioned that a similar release platform could be derived from an alternative heterocyclic diene. We turned our attention to pyrrole compounds, which we expected to exhibit improved release over furfuryl carbonates due to the greater electron donation from the pyrrole nitrogen compared to the furan oxygen. Additionally, the ability functionalize the pyrrole nitrogen would enable the synthesis of a unique Diels–Alder adduct mechanophore with a symmetric pulling position.

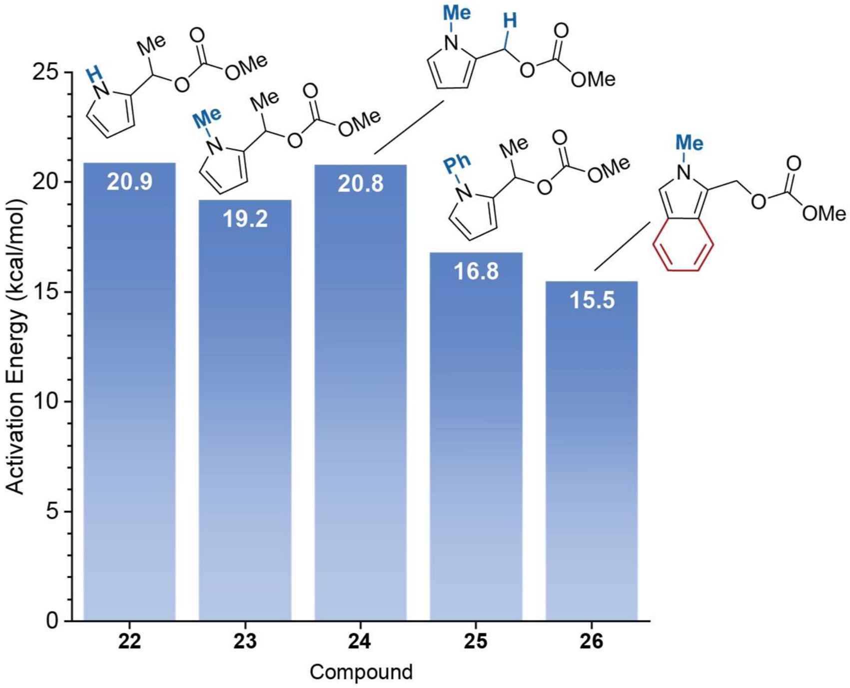

Figure 2.9 Calculated activation energy values (M06-2X/6-311+G**) for the decomposition of a series of pyrrolyl carbonates with varied substitution. *N*-functionalization leads to a reduction in the activation barrier. Isoindole **27** exhibits an extremely low barrier to decomposition.

We first calculated transition state energies for release from a series of pyrrolyl carbonates to evaluate the reactivity of this class of compounds (Figure 2.9). Pyrrolyl carbonate **22** with no substitution on the nitrogen (N–H) is expected to have an activation energy of 20.9 kcal/mol. Adding a methyl substituent to the nitrogen (N–Me) as in compound **23** lowers this barrier to 19.2 kcal/mol. An *N*-methyl pyrrole without an α-methyl group (compound **24**) is predicted to have an activation energy of 20.8 kcal/mol. If the N–Me group is substituted for an N–Ph substitution (compound **25**), we see that the addition of this aromatic group lowers the activation energy of 16.8 kcal/mol.

While the activation energy values for this class of molecules are promising, forming Diels–Alder adducts with pyrrolic compounds can be difficult.[26] However, the use isoindoles as dienes in Diels–Alder reactions has been reported.[27] We found the predicted activation energy for release from *N*-methyl isoindole **26** to be 15.5 kcal/mol. Unfortunately, we were unable to identify a transition state for an *N*-aryl isoindole carbonate.

2.3.12 Release from a 5-aryloxyfurfuryl carbonate

In 2021, our group reported a modified furfuryl carbonate-based release platform that employs a 5-aryloxy substituent that simultaneously serves as a polymer tether point on the furan as well as providing electron donation to facilitate the desired release reaction (Chart 2.8 A 5-aryloxy furfuryl carbonate).[28] It was shown that the synthesis of this modified release platform was significantly more efficient than the 3-phenoxy platform described in detail above. However, attempts to calculate the transition state energy for the decomposition of furfuryl carbonate **27** were unsuccessful.

Chart 2.8 A 5-aryloxy furfuryl carbonate

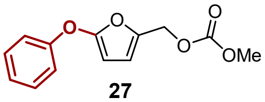

27

Working under the assumption that the release mechanism for the 5-aryloxy system is similar to that proposed for other furfuryl carbonates, we were unable to identify a transition state corresponding to the simple bond breaking mode of the α C–O bond. This result may indicate a distinct mode of reactivity for the 5-aryloxy system, which is consistent with unexpected reaction products observed experimentally.[28] The mechanism of this decomposition reaction was not elucidated computationally or experimentally.

2.4 Conclusions

Through the development of a simple workflow for predicting the activation energy associated with the decomposition of 2-furylcarbinol derivatives, we have begun to elucidate key structure–activity relationships for this class of compounds. These relationships will enable tunable platforms for thermally and mechanically triggered small molecule release that rely on this thermal decomposition reaction. Using this method, we identified a library of 2-furylcarbinol derivatives that exhibit activation energy values spanning from 15.5 kcal/mol to 29.4 kcal/mol for the release of an alcohol cargo molecule. These values correspond to release half-lives ranging from near-instantaneous to over a decade. In addition to identifying electronic factors that effect the rate of molecular release, we also demonstrated how molecular configuration as dictated by steric repulsion can modulate the predicted molecular release behavior. We hope that these results and this computational method further the development of predictable and highly tunable platforms for molecular release across a wide range of applications.

2.5 References

(1) Swager, T. M. Sensor Technologies Empowered by Materials and Molecular Innovations. *Angew. Chem. Int. Ed.* **2018**, *57*, 4248–4257.

(2) Roth, M. E.; Green, O.; Gnaim, S.; Shabat, D. Dendritic, Oligomeric, and Polymeric Self-Immolative Molecular Amplification. *Chem. Rev.* **2016**, *116*, 1309–1352.

(3) Patrick, J. F.; Robb, M. J.; Sottos, N. R.; Moore, J. S.; White, S. R. Polymers with autonomous life-cycle control. *Nature* **2016**, *540*, 363–370.

(4) Lee, K. Y.; Peters, M. C.; Mooney, D. J. Controlled Drug Delivery from Polymers by Mechanical Signals. *Advanced Materials* **2001**, *13*, 837–839.

(5) Huo, S.; Zhao, P.; Shi, Z.; Zou, M.; Yang, X.; Warszawik, E.; Loznik, M.; Göstl, R.; Herrmann, A. Mechanochemical bond scission for the activation of drugs. *Nat. Chem.* **2021**, *13*, 131–139.

(6) Küng, R.; Pausch, T.; Rasch, D.; Göstl, R.; Schmidt, B. M. Mechanochemical Release of Non-Covalently Bound Guests from a Polymer-Decorated Supramolecular Cage. *Angewandte Chemie International Edition* **2021**, *60*, 13626–13630.

(7) White, S. R.; Sottos, N. R.; Geubelle, P. H.; Moore, J. S.; Kessler, M. R.; Sriram, S. R.; Brown, E. N.; Viswanathan, S. Autonomic healing of polymer composites. *Nature* **2001**, *409*, 794–797.

(8) Toohey, K. S.; Sottos, N. R.; Lewis, J. A.; Moore, J. S.; White, S. R. Self-healing materials with microvascular networks. *Nature Mater* **2007**, *6*, 581–585.

(9) Versaw, B. A.; Zeng, T.; Hu, X.; Robb, M. J. Harnessing the Power of Force: Development of Mechanophores for Molecular Release. *J. Am. Chem. Soc.* **2021**, *143*, 21461–21473.

(10) Beyer, M. K.; Clausen-Schaumann, H. Mechanochemistry: The Mechanical Activation of Covalent Bonds. *Chem. Rev.* **2005**, *105*, 2921–2948.

(11) Caruso, M. M.; Davis, D. A.; Shen, Q.; Odom, S. A.; Sottos, N. R.; White, S. R.; Moore, J. S. Mechanically-Induced Chemical Changes in Polymeric Materials. *Chem. Rev.* **2009**, *109*, 5755–5798.

(12) Lin, Y.; Kouznetsova, T. B.; Craig, S. L. A Latent Mechanoacid for Time-Stamped Mechanochromism and Chemical Signaling in Polymeric Materials. *J. Am. Chem. Soc.* **2020**, *142*, 99–103.

(13) Diesendruck, C. E.; Steinberg, B. D.; Sugai, N.; Silberstein, M. N.; Sottos, N. R.; White, S. R.; Braun, P. V.; Moore, J. S. Proton-Coupled Mechanochemical Transduction: A Mechanogenerated Acid. *J. Am. Chem. Soc.* **2012**, *134*, 12446–12449.

(14) Larsen, M. B.; Boydston, A. J. “Flex-Activated” Mechanophores: Using Polymer Mechanochemistry To Direct Bond Bending Activation. *J. Am. Chem. Soc.* **2013**, *135*, 8189–8192.

(15) Shi, Z.; Song, Q.; Göstl, R.; Herrmann, A. Mechanochemical activation of disulfide-based multifunctional polymers for theranostic drug release. *Chem. Sci.* **2021**, *12*, 1668–1674.

(16) Sun, Y.; Neary, W. J.; Burke, Z. P.; Qian, H.; Zhu, L.; Moore, J. S. Mechanically Triggered Carbon Monoxide Release with Turn-On Aggregation-Induced Emission. *J. Am. Chem. Soc.* **2022**, *144*, 1125–1129.

(17) Nijem, S.; Song, Y.; Schwarz, R.; E. Diesendruck, C. Flex-activated CO mechanochemical production for mechanical damage detection. *Polymer Chemistry* **2022**, *13*, 3986–3990.

(18) Turksoy, A.; Yildiz, D.; Aydonat, S.; Beduk, T.; Canyurt, M.; Baytekin, B.; U. Akkaya, E. Mechanochemical generation of singlet oxygen. *RSC Adv.* **2020**, *10*, 9182–9186.

(19) Fan, B.; Trant, J. F.; Hemery, G.; Sandre, O.; Gillies, E. R. Thermo-responsive self-immolative nanoassemblies: direct and indirect triggering. *Chem. Commun.* **2017**, *53*, 12068–12071.

(20) Hu, X.; Zeng, T.; Husic, C. C.; Robb, M. J. Mechanically Triggered Small Molecule Release from a Masked Furfuryl Carbonate. *J. Am. Chem. Soc.* **2019**, *141*, 15018–15023.

(21) Shao, Y.; Molnar, L. F.; Jung, Y.; Kussmann, J.; Ochsenfeld, C.; Brown, S. T.; Gilbert, A. T. B.; Slipchenko, L. V.; Levchenko, S. V.; O'Neill, D. P.; Jr, R. A. D.; Lochan, R. C.; Wang, T.; Beran, G. J. O.; Besley, N. A.; Herbert, J. M.; Lin, C. Y.; Voorhis, T. V.; Chien, S. H.; Sodt, A.; Steele, R. P.; Rassolov, V. A.; Maslen, P. E.; Korambath, P. P.; et al. Advances in methods and algorithms in a modern quantum chemistry program package. *Phys. Chem. Chem. Phys.* **2006**, *8*, 3172–3191.

(22) Walker, M.; Harvey, A. J. A.; Sen, A.; Dessent, C. E. H. Performance of M06, M06-2X, and M06-HF Density Functionals for Conformationally Flexible Anionic

Clusters: M06 Functionals Perform Better than B3LYP for a Model System with Dispersion and Ionic Hydrogen-Bonding Interactions. *J. Phys. Chem. A* **2013**, *117*, 12590–12600.

(23) Goerigk, L.; Grimme, S. A thorough benchmark of density functional methods for general main group thermochemistry, kinetics, and noncovalent interactions. *Phys Chem Chem Phys* **2011**, *13*, 6670–6688.

(24) Hu, X.; Zeng, T.; Husic, C. C.; Robb, M. J. Mechanically Triggered Release of Functionally Diverse Molecular Payloads from Masked 2-Furylcarbinol Derivatives. *ACS Cent. Sci.* **2021**, *7*, 1216–1224.

(25) Husic, C. C.; Hu, X.; Robb, M. J. Incorporation of a Tethered Alcohol Enables Efficient Mechanically Triggered Release in Aprotic Environments. *ACS Macro Lett.* **2022**, *11*, 948–953.

(26) Kamimura, A.; Nakano, T. Use of the Diels−Alder Adduct of Pyrrole in Organic Synthesis. Formal Racemic Synthesis of Tamiflu. *J. Org. Chem.* **2010**, *75*, 3133–3136.

(27) Lin, C.; Zhen, L.; Cheng, Y.; Du, H.-J.; Zhao, H.; Wen, X.; Kong, L.-Y.; Xu, Q.-L.; Sun, H. Visible-Light Induced Isoindoles Formation To Trigger Intermolecular Diels–Alder Reactions in the Presence of Air. *Org. Lett.* **2015**, *17*, 2684–2687.

(28) Zeng, T.; Hu, X.; Robb, M. J. 5-Aryloxy substitution enables efficient mechanically triggered release from a synthetically accessible masked 2-furylcarbinol mechanophore. *Chem. Commun.* **2021**, *57*, 11173–11176.

Chapter 3

INCORPORATION OF A TETHERED ALCOHOL ENABLES EFFICIENT MECHANICALLY TRIGGERED RELEASE IN APROTIC ENVIRONMENTS

3.1 Introduction

Polymers that release functional small molecules upon external stimulation are desirable for a range of applications including sensing, catalysis, and drug delivery.[1,2] Mechanical force is an appealing stimulus that can be applied with spatial and temporal control and benefits from a variety of activation methods including tension, compression, and shear in solid materials;[3] high intensity focused ultrasound;[4,5] and solution-phase ultrasonication.[6] In polymer mechanochemistry, stress-responsive molecules known as mechanophores are designed to undergo specific and productive chemical transformations in response to mechanical force, which is transduced by covalently bound polymer chains.[7–9] A growing number of mechanophore platforms have been developed in recent years for mechanically triggered release.[10] For example, Moore and Craig have developed *gem*-dichlorocyclopropane mechanophores that generate HCl upon mechanochemical activation.[11,12] Moore and coworkers also recently reported a novel fluorogenic norborn-2-en-7-one mechanophore that releases carbon monoxide gas.[13] Flex-activation strategies have been used by Boydston and coworkers to enable the release of a furan small molecule from an oxanorbornadiene mechanophore[14] and to generate *N*-heterocyclic carbenes from a carbodiimide motif.[15] This concept was also extended recently by Diesendruck and coworkers for CO release.[16] In a more modular design, Herrmann and Göstl have developed a mechanophore platform that relies on the mechanochemical cleavage of a disulfide unit that initiates an intramolecular cyclization reaction to release a cargo molecule bound through a carbonate linkage.[17–19]

In 2019, our group introduced a platform for mechanically triggered molecular release based on an unstable furfuryl carbonate masked as a mechanochemically active Diels–Alder adduct (Scheme 3.1a).[20] This general design strategy relies on the decomposition of a latent 2-furylcarbinol derivative,[21,22] which is gated by a mechanochemical retro-Diels–Alder reaction. Decoupling the mechanochemical activation step from 2-furylcarbinol decomposition provides for a highly modular system that we have further developed to enable the mechanically triggered release of functionally diverse molecular payloads including alcohols, amines, carboxylic acids, and sulfonic acids.[23,24] Notably, a polar protic environment is typically required for clean and efficient fragmentation of the latent 2-furylcarbinol derivative, which decomposes via a putative furfuryl cation intermediate. While this constraint does not pose a challenge for potential

Scheme 3.1 A Tethered Alcohol Facilitates Mechanically Triggered Release in Aprotic Environments

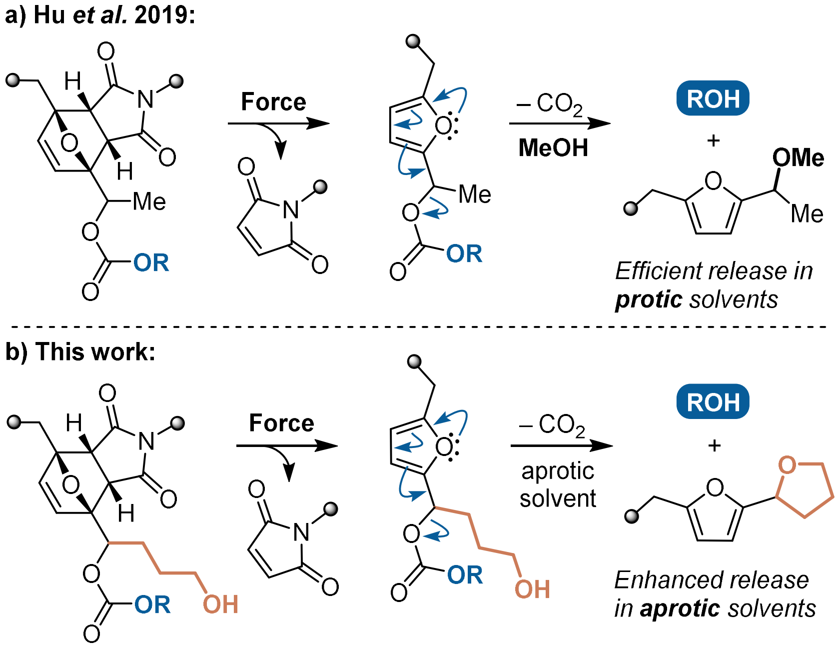

biological applications in aqueous media, for instance, it limits the applicability of the mechanophore in a broader range of environments.

Here we describe the design of a unique mechanophore scaffold that incorporates a tethered primary alcohol on the masked furfuryl carbonate to facilitate the efficient mechanically triggered release of small molecules in an aprotic environment (Scheme 3.1b). We hypothesized that the tethered alcohol would supplant the role of the protic additive – either methanol or water – in our previous studies by both stabilizing the polar transition state and serving as a nucleophile to intercept the furfuryl cation intermediate. We describe the computationally supported design and reactivity of this tethered furfuryl carbonate and demonstrate significantly enhanced molecular release upon ultrasound-induced mechanochemical activation of the mechanophore under aprotic conditions in comparison to the original mechanophore design.

3.2 Results and Discussion

3.2.1 Computational investigation of the tethered alcohol substrate

We first investigated the influence of the tethered alcohol on the decomposition reaction of the furfuryl carbonate scaffold using density functional theory (DFT). Activation energies for carbonate fragmentation were calculated for models **FC1** and **FC2** at the M06-2X/6-311+G** level of theory using a polarizable continuum model to simulate a polar solvent environment (Figure 3.1, see Section 3.4.5 for details). The reaction barrier is reduced by 3.9 kcal/mol for furfuryl carbonate **FC2** incorporating the tethered alcohol motif in comparison to α-methyl derivative **FC1**, suggesting an increased rate of fragmentation leading to cargo release. The calculated geometry of transition state structure

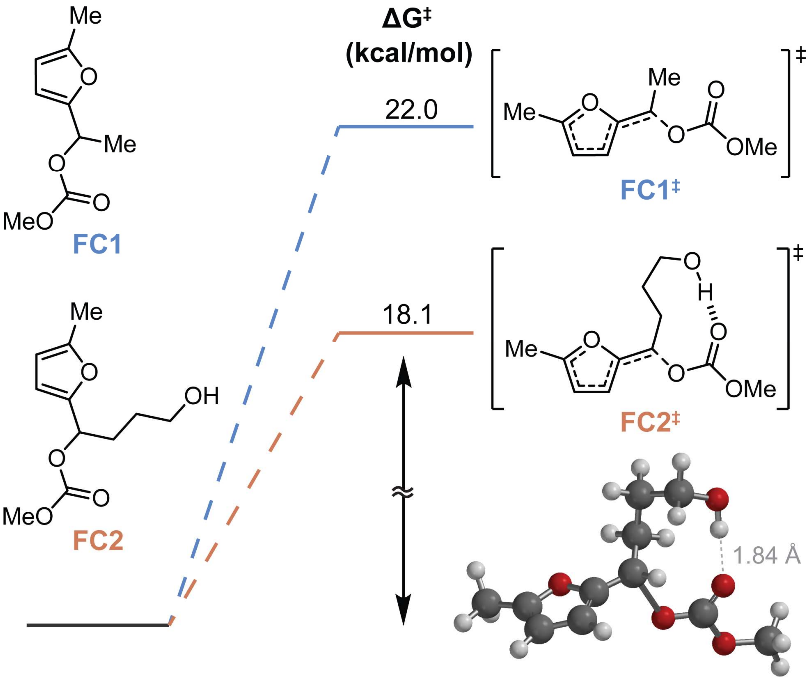

Figure 3.1 Density functional theory (DFT) calculations performed on furfuryl carbonate models **FC1** and **FC2** at the M06-2X/6-311+G** level of theory using a polarizable continuum model to simulate a polar solvent environment. These results demonstrate a significantly reduced activation energy for **FC2** incorporating a tethered primary alcohol. The computed structure of **FC2**‡ exhibits an apparent hydrogen bonding interaction suggesting stabilization of the transition state leading to carbonate fragmentation.

FC2‡ indicates an intramolecular hydrogen bond between the tethered primary alcohol and the carbonyl oxygen of the carbonate, which is proposed to stabilize the developing negative charge on the carbonate leaving group. Read de Alaniz and coworkers have previously demonstrated that Brønsted acid facilitates the thermal decomposition of more stable furfuryl carbamates.[25] The prior role of the protic additive in the decomposition of similar 2-furylcarbinol derivatives has not been explicitly studied, but based on these computational results, it may be reasonable to assume a similar activation manifold. Additional calculations using the constrained geometries simulate external force (CoGEF) method[26,27] predict that mechanical activation of a furan–maleimide Diels–Alder adduct corresponding to **FC2** generates the expected furfuryl carbonate via a formal retro-[4+2] cycloaddition reaction at a force of 4.2 nN (Figure 3.2), which is comparable to rupture forces determined for other experimentally validated furan–maleimide mechanophores.[27,28]

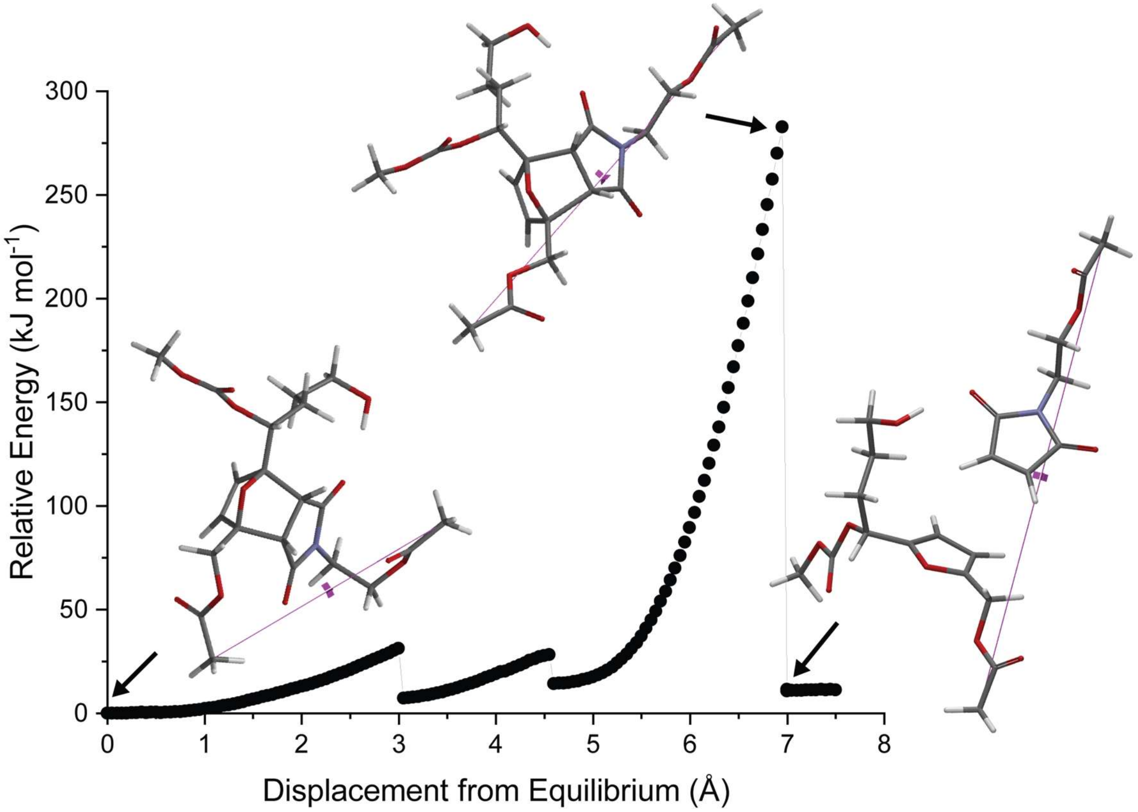

Figure 3.2 DFT calculations performed on a truncated Diels–Alder adduct using the constrained geometries simulate external force (CoGEF) method at the B3LYP/6-31G* level of theory. The rupture force (F_{max}) is calculated to be 4.2 nN, and the calculations predict the formation of the expected furan and maleimide products via a formal retro-Diels–Alder reaction upon elongation.

3.2.2 Mechanophore synthesis

Encouraged by the computational predictions, we set out to synthesize a small molecule Diels–Alder adduct incorporating a masked furfuryl carbonate endowed with a tethered primary alcohol (Scheme 3.2). Two-fold lithiation of furfuryl alcohol followed by the addition of TBS-protected 4-hydroxybutanal generated diol **1** containing a TBS-protected tethered alcohol and a secondary alcohol for cargo attachment. Following esterification of the primary alcohol with *α*-bromoisobutyryl bromide, furan **2** was subjected to a [4+2] cycloaddition reaction with 2-hydroxyethylmaleimide to produce an isomeric mixture of Diels–Alder adducts from which *endo* diastereomer (±)-**3** was isolated

Scheme 3.2 Synthesis of a Masked Furfuryl Carbonate with a Tethered Primary Alcohol and a Hydroxycoumarin Payload

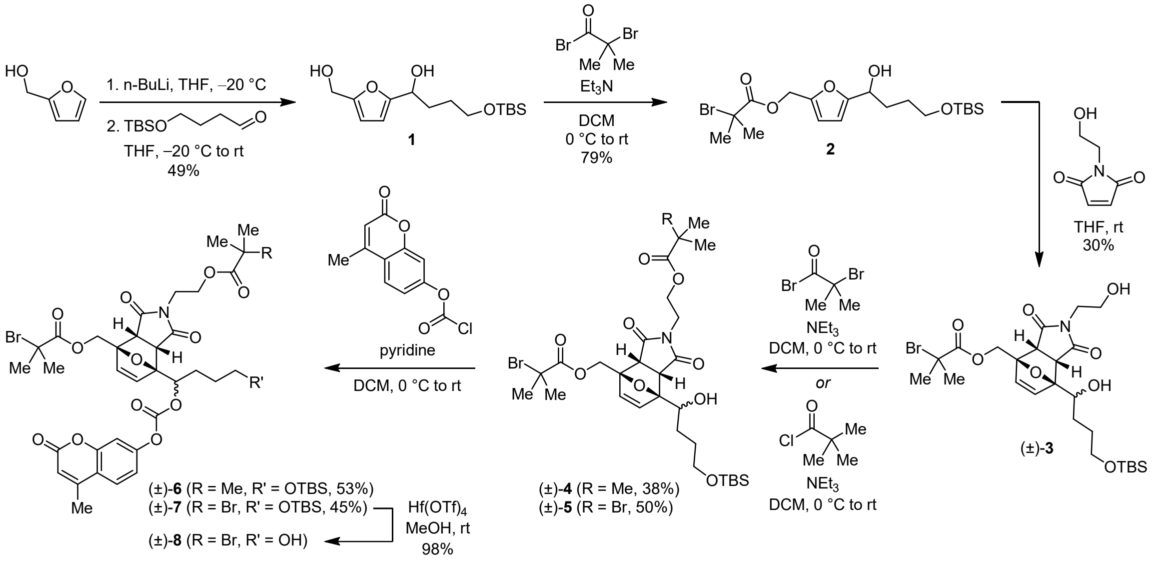

by reverse phase chromatography. Selective esterification of the primary alcohol with α-bromoisobutyryl bromide afforded adduct (±)-**5** followed by installation of a hydroxycoumarin payload via reaction with the chloroformate to give carbonate (±)-**7**. Deprotection of the tethered alcohol was accomplished using catalytic $Hf(OTf)_4$[29] to provide bis-initiator (±)-**8**. We note that typical conditions employing tetrabutylammonium fluoride to remove the TBS group resulted in some undesired release of hydroxycoumarin.

3.2.3 Small molecule decompisition model experiment

We next investigated the thermal reactivity of small molecule Diels–Alder adduct (±)-**8** in pure acetonitrile to experimentally evaluate the impact of the tethered alcohol on the decomposition reaction of the latent furfuryl carbonate in the absence of any protic additive. A solution of (±)-**8** in anhydrous acetonitrile-d_3 was heated at 50 °C to promote the thermal retro-[4+2] cycloaddition reaction and the resulting mixture was analyzed by

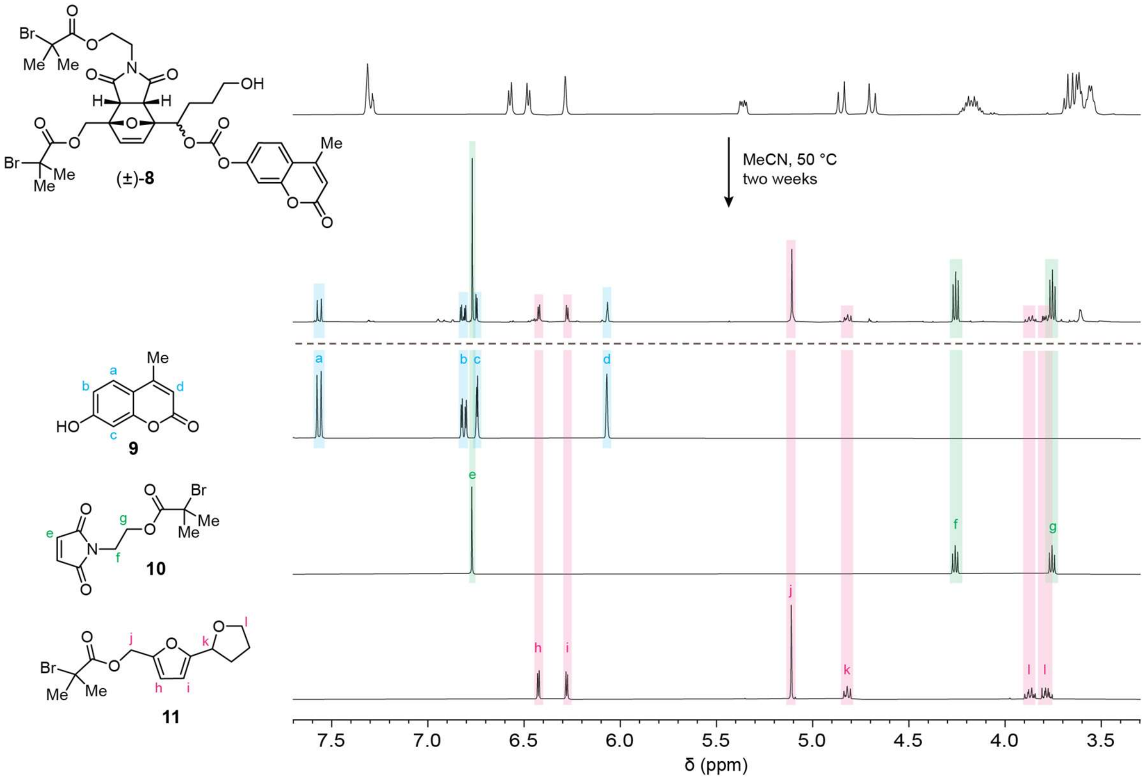

Figure 3.3 Characterization of the reactivity of small molecule (±)-**8** in acetonitrile (4.4 mM) at 50 °C. The thermally induced retro-Diels–Alder/decarboxylation reaction cascade is anticipated to proceed via a furfuryl cation intermediate, which is intercepted through intramolecular ether formation by the tethered alcohol. ^{1}H NMR spectra (acetonitrile-d_3, 400 MHz) demonstrate clean conversion of (±)-**8** to the hydroxycoumarin, maleimide, and cyclic ether products.

^{1}H NMR spectroscopy and LCMS (Figure 3.3 and Figure 3.4). Upon full conversion of (±)-**8** after 14 days, the major ^{1}H NMR resonances in the crude reaction mixture match the spectra of hydroxycoumarin **9**, maleimide ester **10**, and cyclic ether **11**. Formation of cyclic ether **11** is consistent with the expected decomposition pathway for the latent furfuryl carbonate in which the tethered alcohol undergoes an intramolecular cyclization reaction with the furfuryl cation intermediate.

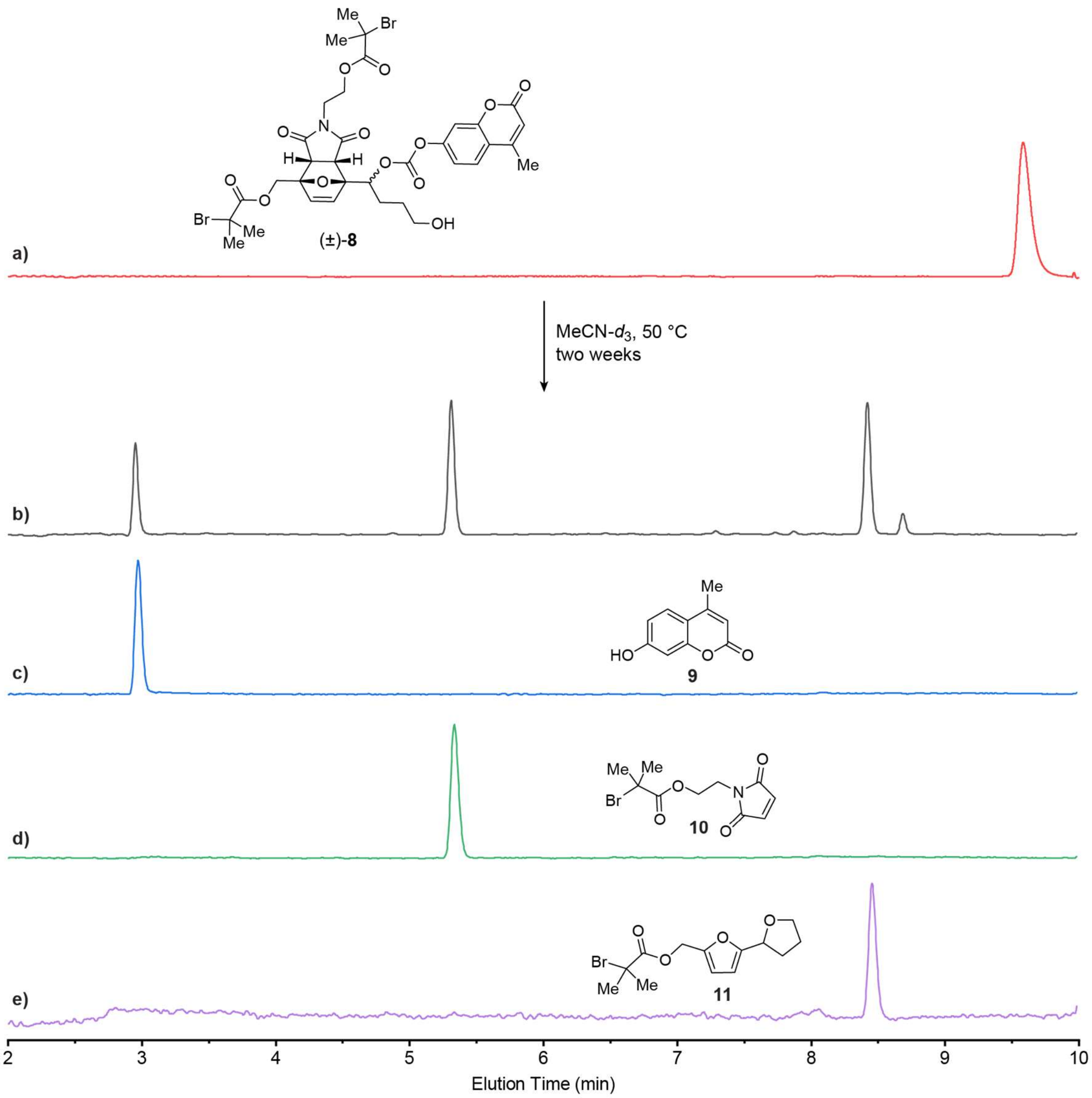

Figure 3.4 Characterization of the thermal decomposition reaction of small molecule model (±)-**8** in acetonitrile-d_3 at 50 °C using HPLC with a UV detector (λ = 230 nm). HPLC chromatograms of (a) starting material (±)-**8**, and (b) the crude reaction mixture after 14 days in comparison to the HPLC chromatograms of analytical samples of (c) hydroxycoumarin **9**, (d) maleimide **10**, and (e) cyclic ether **11**. The identity of the compound producing the small peak at ~8.7 min was not determined.

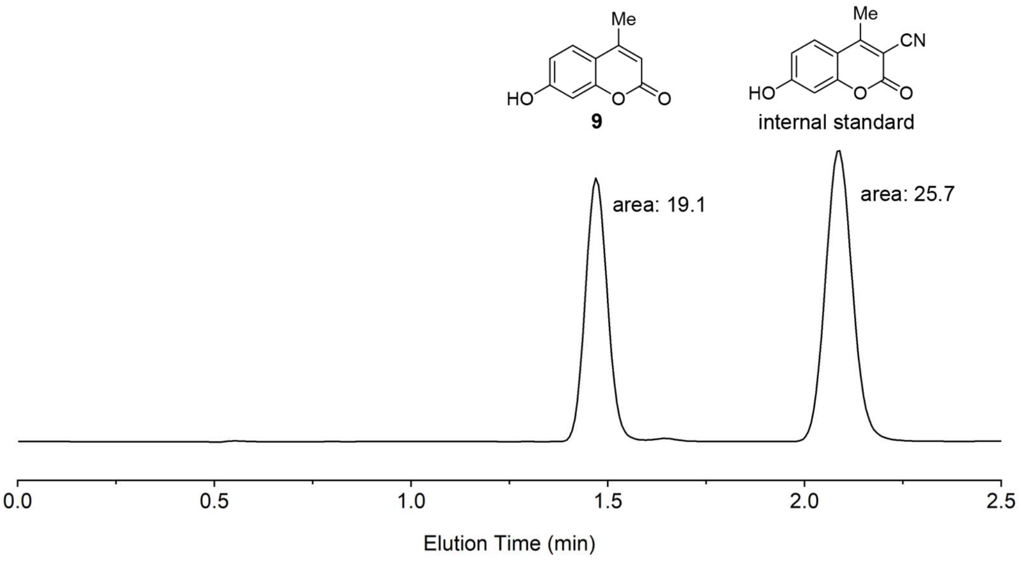

Figure 3.5 Characterization of the release of hydroxycoumarin **9** from the thermal decomposition reaction of (±)-**8** in acetonitrile-d_3 at 50 °C for 14 d using HPLC with a UV detector (λ = 320 nm). A 75% yield of hydroxycoumarin release was determined using an internal standard of 3-cyano-7-hydroxy-4-methylcoumarin (3.73 mM).

Both ^{1}H NMR and LCMS results indicate relatively clean conversion of (±)-**8** to these three anticipated products, releasing the hydroxycoumarin cargo in 75% yield as determined by HPLC measurements (Figure 3.5). In direct contrast, treatment of the analogous Diels–Alder adduct **12** derived from the α-methyl substituted furfuryl carbonate[20] under similar conditions results in a complex mixture of products with hydroxycoumarin **9** ultimately being generated in a significantly lower yield of 37% (Figure 3.6–Figure 3.8). While the decomposition pathway for the α-methyl furfuryl carbonate under these conditions is not known, we speculate that adventitious water or another protic source may play a role in hydroxycoumarin formation.

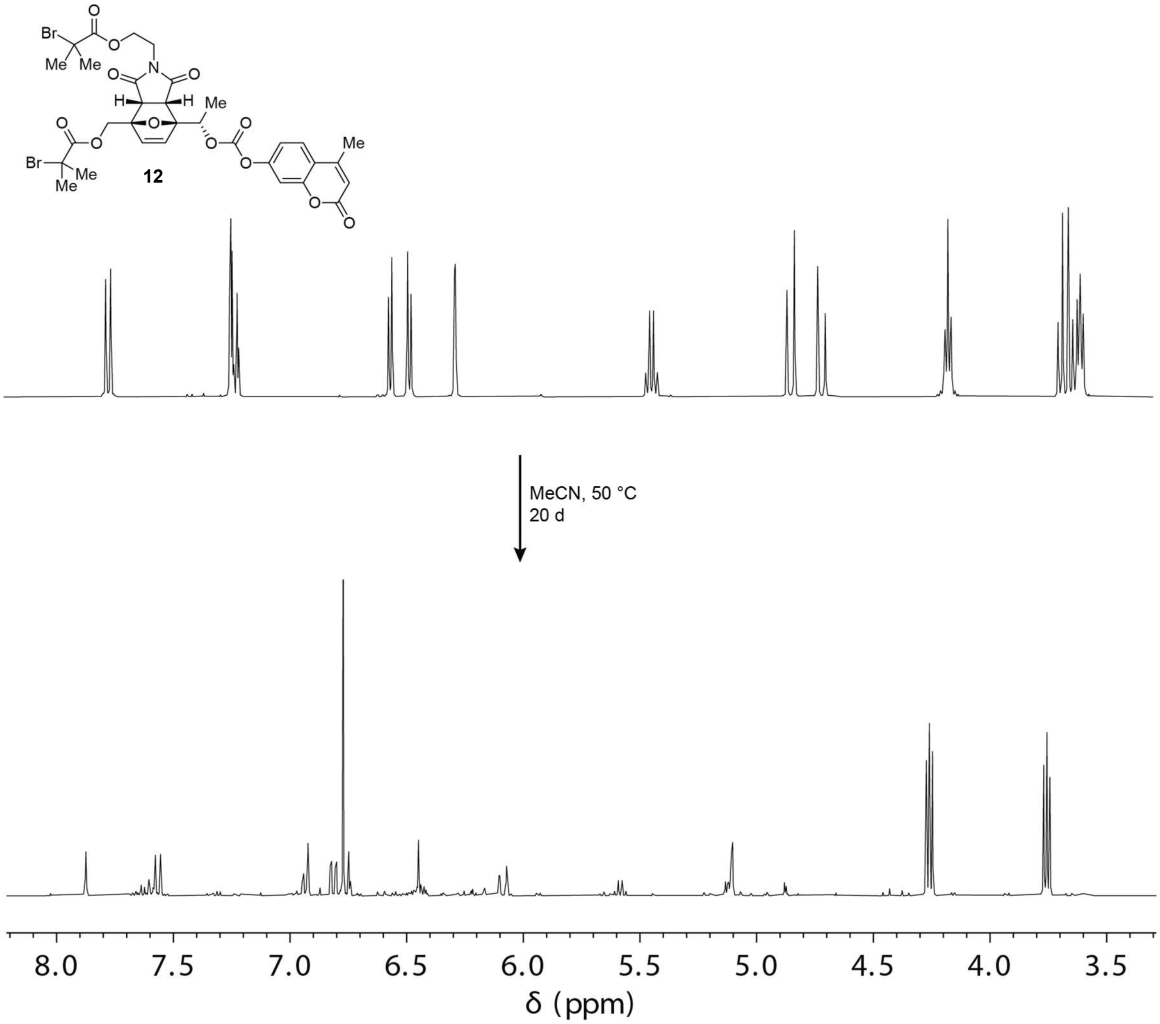

Figure 3.6 ^{1}H NMR spectra (acetonitrile-d_3, 400 MHz) before and after heating the indicated Diels–Alder adduct **12**[20] at 50 °C for 20 days. Initial concentration of substrate was 5.9 mM. Compound **12** was used as the bis-initiator to synthesize **PMA-Me**.

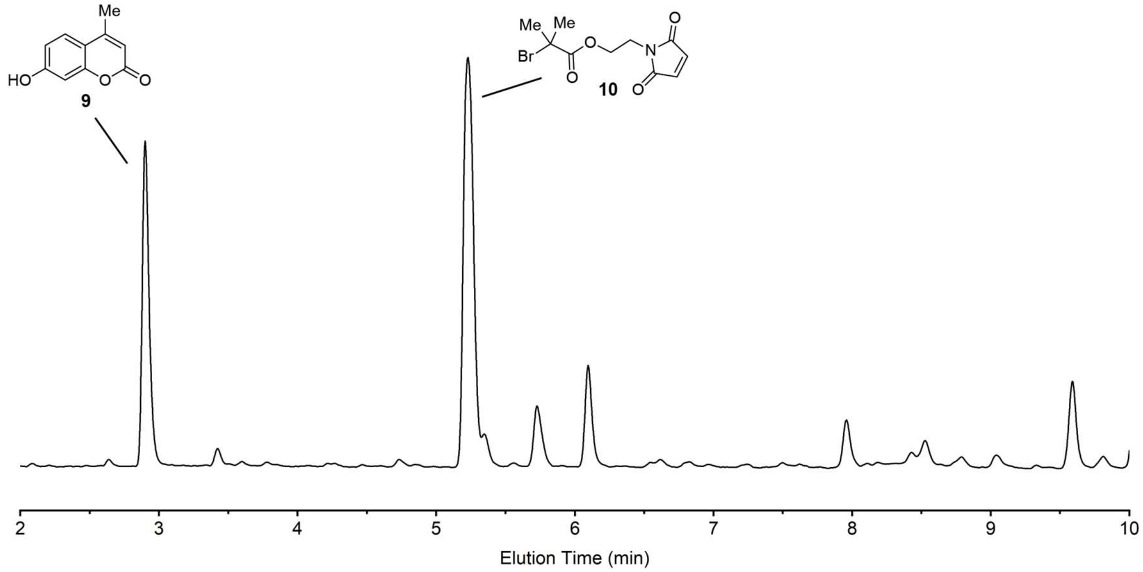

Figure 3.7 Characterization of the thermal decomposition reaction (acetonitrile-d_3, 50 °C, 20 d) of the bis-initiator Diels–Alder adduct **12** containing an α-methyl carbonate. The HPLC chromatogram (λ=230 nm) of the crude reaction mixture shows formation of hydroxycoumarin **9** and maleimide ester **10**, in addition to a number of unidentified products.

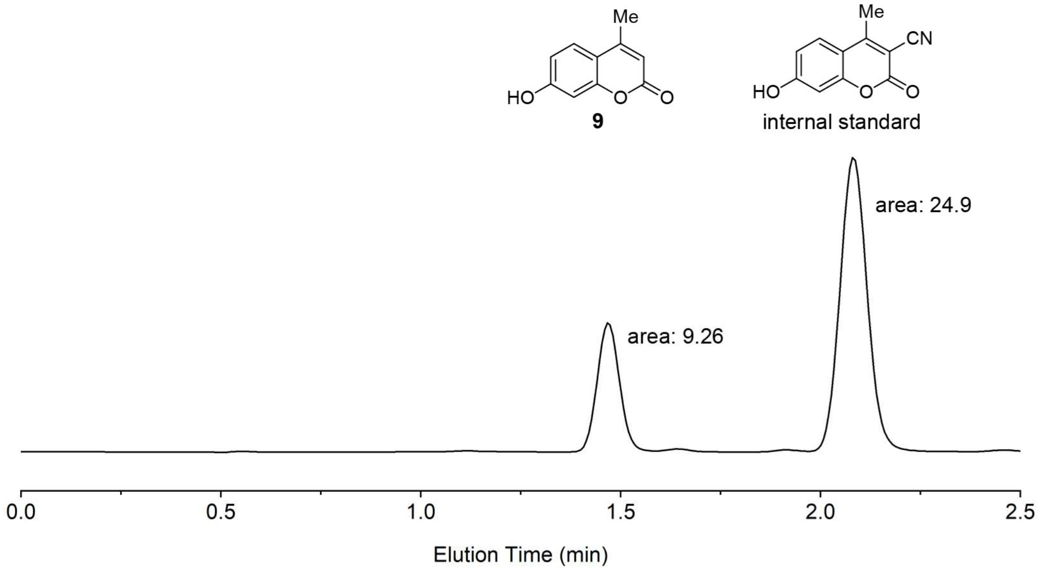

Figure 3.8 Characterization of the release of hydroxycoumarin **9** from the thermal decomposition reaction (acetonitrile-d_3, 50 °C, 20 d)) of the bis-initiator Diels–Alder adduct **12** containing an α-methyl carbonate, using HPLC with a UV detector (λ = 320 nm). A 37% yield of hydroxycoumarin release was determined using an internal standard of 3-cyano-7-hydroxy-4-methylcoumarin (3.73 mM).

Diels–Alder adduct (±)-**8** exhibits similar thermal stability as our original α-methyl analogue,[23] undergoing ~4% retro-Diels–Alder reaction after 14 days at room temperature in acetonitrile as anticipated for simple *endo* furan–maleimide adducts (Figure 3.9). These results confirm the predicted reactivity of the furfuryl carbonate scaffold incorporating a tethered alcohol and highlight the substantially improved release performance in aprotic environments.

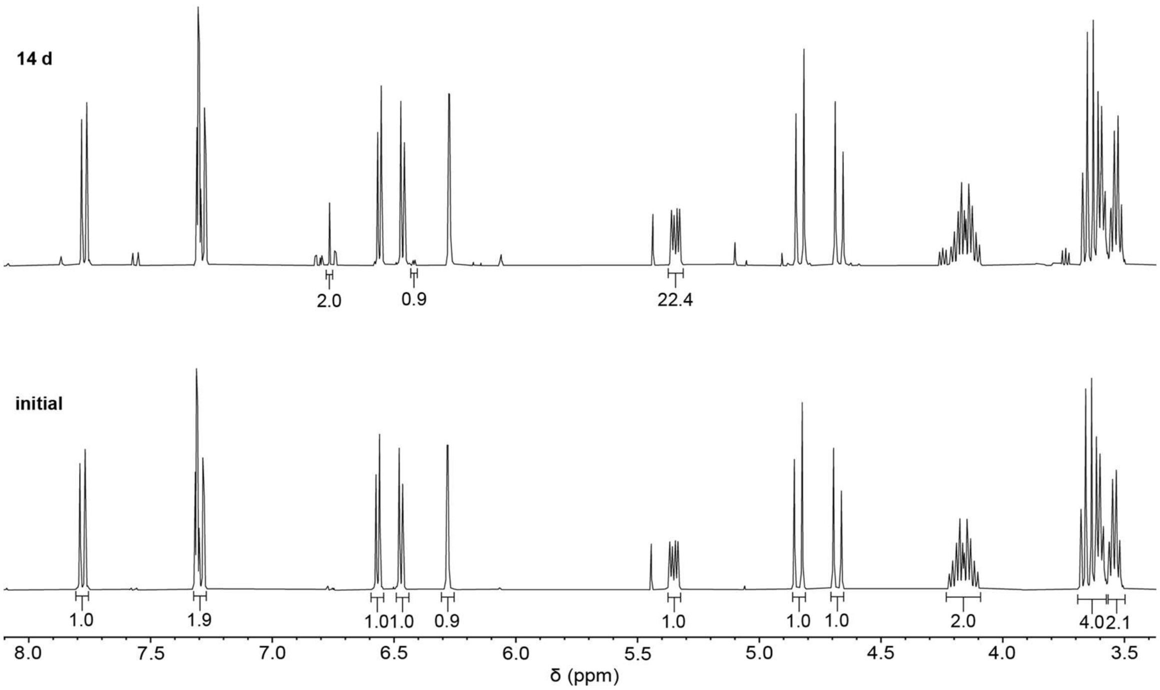

Figure 3.9 ^{1}H NMR spectra (acetonitrile-d_3, 400 MHz) of model compound (±)-**8** acquired after 13 days in solution at room temperature. Approximately 4% retro-[4+2] cycloaddition is observed based on the integrated signals corresponding to starting material (±)-**8** (5.35 ppm), maleimide **10** (6.76 ppm), and furfuryl ether **11** (6.42 ppm).

3.2.4 Mechanophore incorporation into poly(methyl acrylate) polymers

We next synthesized a series of poly(methyl acrylate) (PMA) polymers containing the furan–maleimide Diels–Alder adducts for solution-phase ultrasonication experiments to evaluate their mechanochemical reactivity. Solvodynamic shear generated with ultrasonication results in rapid chain elongation with mechanical force maximized near the center of the polymer.[30] Therefore, polymers containing chain-centered Diels–Alder adducts incorporating the masked furfuryl carbonate with a tethered alcohol (**PMA-OH**) and the α-methyl derivative (**PMA-Me**) were prepared along with a chain-end control polymer (**PMA-Control**) derived from the adduct with a tethered alcohol (Chart 3.1).

Chart 3.1 Poly(methyl acrylate) (PMA) Polymers Containing a Masked Furfuryl Carbonate Mechanophore with a Hydroxycoumarin Payload

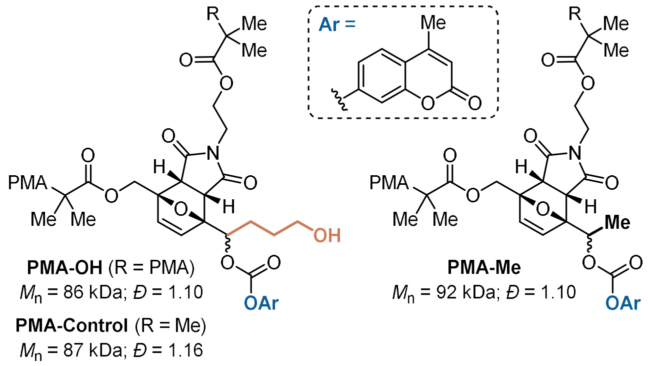

Polymers were synthesized via controlled radical polymerization using Cu wire/Me_6TREN in dimethyl sulfoxide from the corresponding Diels–Alder initiators bearing α-bromoester functional groups.[20,31] Bis-initiator (±)-**8** with a tethered primary alcohol was initially employed in the synthesis of **PMA-OH**; however, some undesired release of the hydroxycoumarin cargo occurred during polymerization in the presence of the Me_6TREN ligand, likely through activation of the alcohol toward intramolecular carbonate substitution. Instead, polymerization from TBS-protected bis-initiator (±)-**7** followed by removal of the TBS protecting group using an ion exchange resin (Amberlyst 15)[32] afforded **PMA-OH** (M_n = 86 kDa, Đ = 1.10) (Figure 3.10 and Figure 3.11, see Section 3.4.2 for details). A similar polymerization procedure[20] was used to prepare **PMA-Me** (M_n = 92 kDa, Đ = 1.10) allowing for the direct comparison of mechanochemical behavior and the influence of the tethered alcohol as well as **PMA-Control** (M_n = 87 kDa, $Đ$ = 1.16) to confirm the mechanical origin of reactivity.

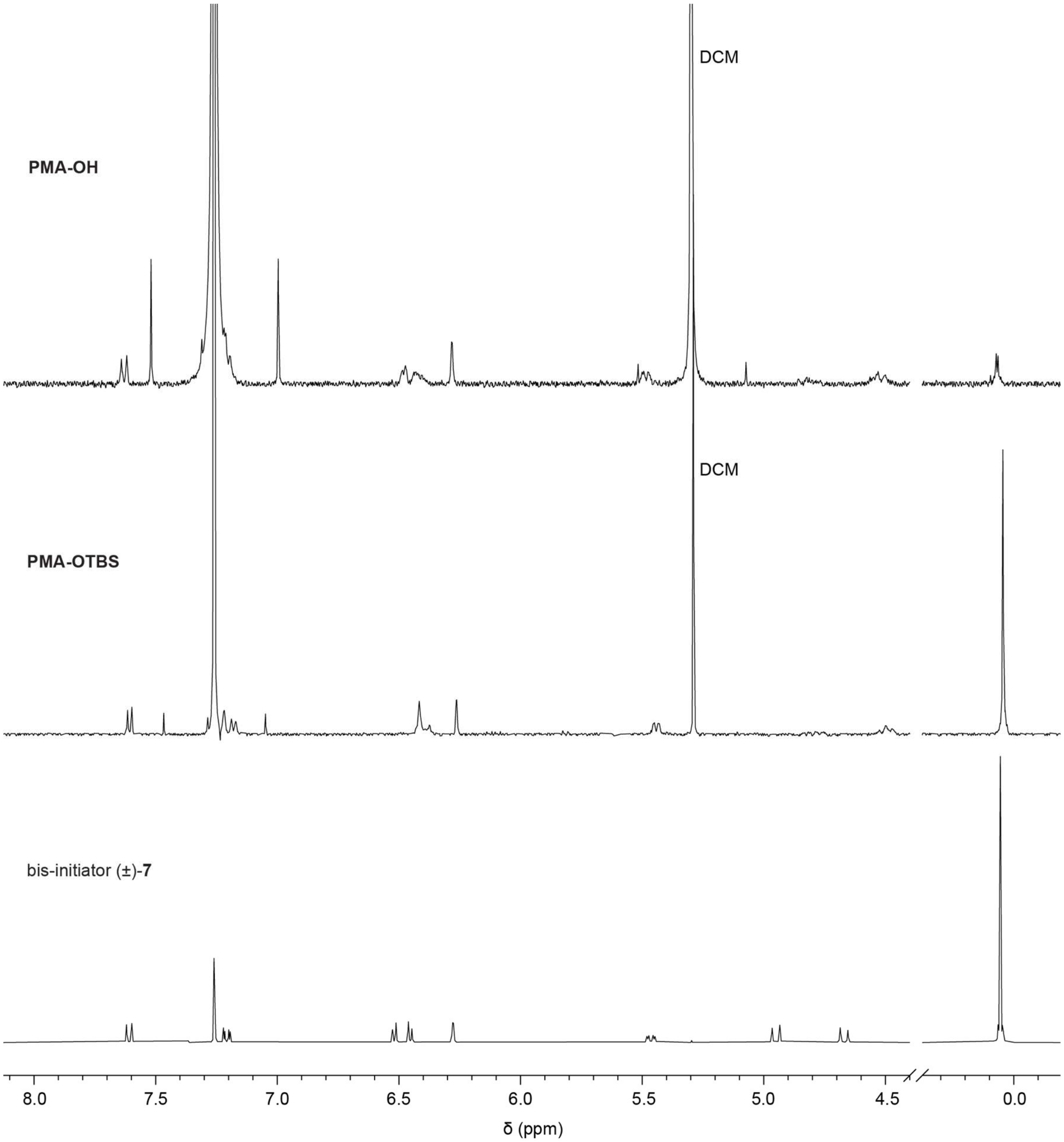

Figure 3.10 ^{1}H NMR spectra ($CDCl_3$, 400 MHz) of bis-initiator (±)-**7**, **PMA-OTBS**, and **PMA-OH** showing successful removal of the TBS protecting group, as suggested by the nearly complete disappearance of the singlet at 0.05 ppm. Downfield signals corresponding to the chain-centered mechanophore remain intact after the deprotection reaction and no signals for release hydroxycoumarin are present.

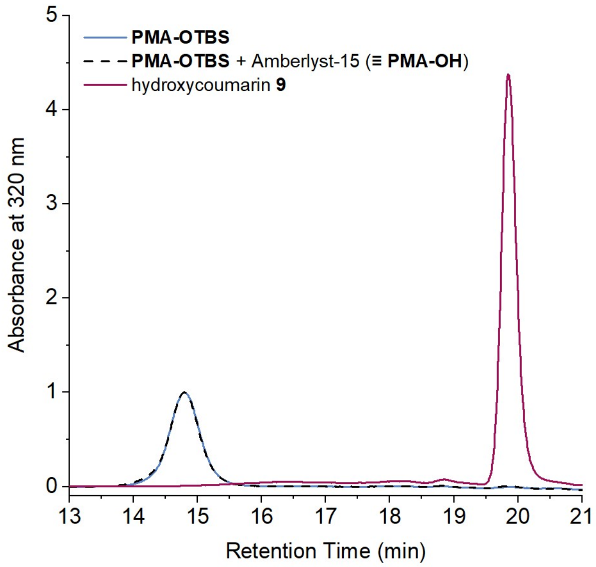

Figure 3.11 Characterization of the crude deprotection reaction of **PMA-OTBS** using analytical gel permeation chromatography monitored with a UV detector (λ=320 nm). No small molecule peak corresponding to hydroxycoumarin **9** is observed in the crude deprotection reaction, indicating survival of the carbonate motif. The polymer peaks for **PMA-OTBS** and **PMA-OH** are nearly identical, indicating the polymer backbone is unaffected by the deprotection conditions.

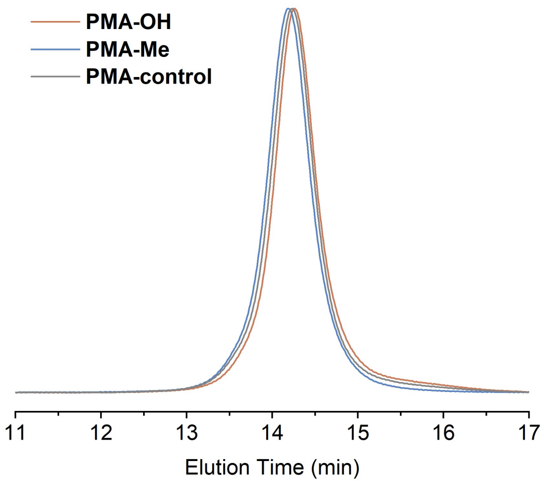

Figure 3.12 GPC traces (refractive index response) for the three polymers used in this study: **PMA-OH** (M_n = 86 kDa, Đ = 1.10), **PMA-Me** (M_n = 92 kDa, Đ = 1.10), and **PMA-control** (M_n = 87 kDa, Đ = 1.16).

3.2.5 Characterization of mechanochemical reactivity

The mechanically triggered release of hydroxycoumarin **9** from dilute solutions of **PMA-OH** and **PMA-Me** in pure acetonitrile was evaluated using pulsed ultrasonication (1 s on/2 s off, 6–9 °C, 20 kHz, 15.5W/cm^2). Aliquots were removed from solution over the course of the experiment and the generation of hydroxycoumarin **9** was monitored using HPLC equipped with a UV detector. Samples from sonicated solutions of **PMA-OH** and **PMA-Me** were incubated at room temperature for 72 h and 120 h, respectively, to allow for nearly complete decomposition of the unmasked furfuryl carbonate prior to quantifying the release of hydroxycoumarin using an internal standard (see Section 3.4.4 for details). As illustrated in Figure 3.13a, release of hydroxycoumarin is much more efficient from **PMA-OH** compared to **PMA-Me** under these conditions in the absence of any protic additive.

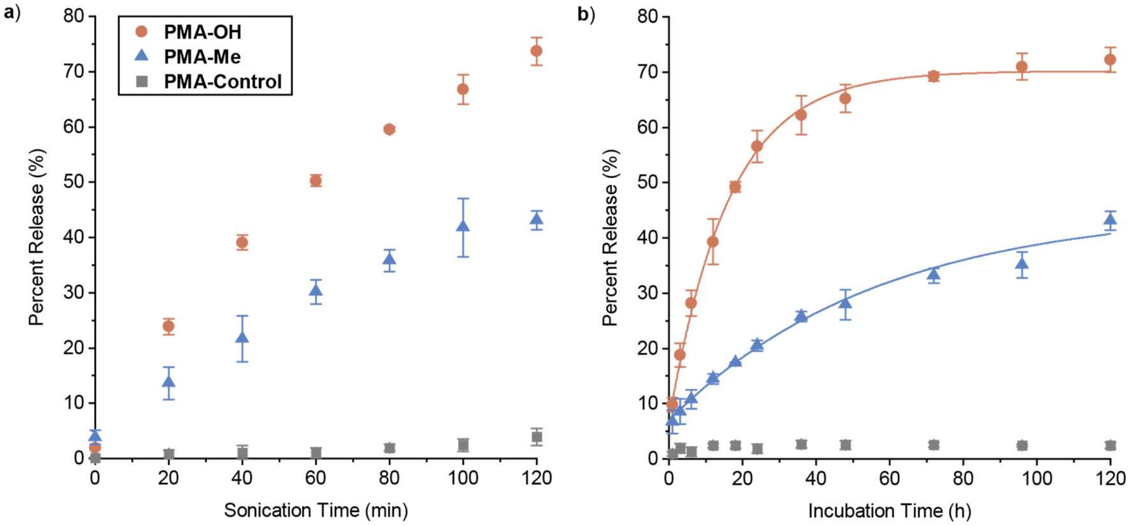

Figure 3.13 Characterization of mechanically triggered release in acetonitrile. (a) Release of hydroxycoumarin **9** from polymers (2 mg/mL in acetonitrile) subjected to ultrasound-induced mechanochemical activation for various durations of sonication. Samples were subsequently incubated at rt for 72 h (**PMA-OH**) or 120 h (**PMA-Me**) and release was quantified using HPLC. (b) Time-dependent generation of hydroxycoumarin **9** from the unmasked furfuryl carbonate during incubation at rt as monitored by HPLC immediately following 120 min of ultrasonication. Error bars represent standard deviation from three replicate experiments.

Consistent with the small molecule reactivity described above, fitting the sonication time-dependent release data to a first-order rate expression highlights the improved release efficiency attributed to the tethered alcohol. The extent of release is projected to plateau at 85% from **PMA-OH**, while the release of hydroxycoumarin from **PMA-Me** under these conditions is only projected to reach ~53% at full conversion (Figure 3.14 and**Figure 3.15**). Negligible release was observed upon ultrasonication of chain-end functionalized control polymer **PMA-control** under the same conditions, confirming that the release of hydroxycoumarin occurs from the unmasked furfuryl carbonate only upon mechanochemical activation of the furan–maleimide mechanophore.

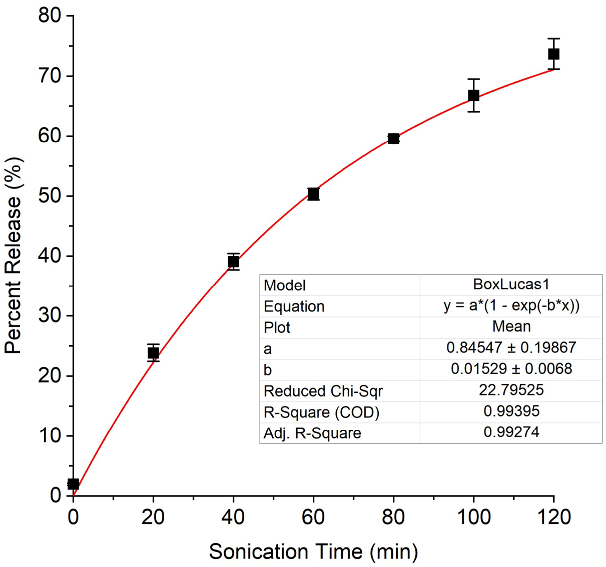

Model	BoxLucas1
Equation	y = a*(1 - exp(-b*x))
Plot	Mean
a	0.84547 ± 0.19867
b	0.01529 ± 0.0068
Reduced Chi-Sqr	22.79525
R-Square (COD)	0.99395
Adj. R-Square	0.99274

Figure 3.14 Release of hydroxycoumarin **9** from **PMA-OH** as a function of sonication time (2 mg/mL polymer in MeCN) as quantified by HPLC analysis. Aliquots were removed from the sonicated solution and incubated at room temperature for 72 h prior to measurement. Error bars represent standard deviation from three replicate experiments. Fitting the data to a first-order rate expression gives a projected maximum release of ~85%.

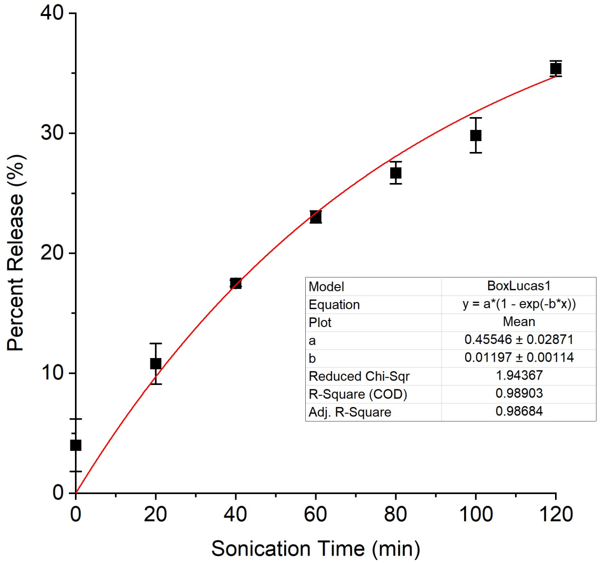

Figure 3.15 Release of hydroxycoumarin **9** from **PMA-Me** as a function of sonication time (2 mg/mL polymer in MeCN) monitored using HPLC. Aliquots were removed from the sonicated solution and incubated at room temperature for 120 h prior to measurement. Error bars represent standard deviation from three replicate experiments. Fitting the data to a first-order rate expression gives a projected maximum release of ~53%.

To more clearly elucidate the difference in cargo release kinetics enabled by the tethered alcohol as predicted by the computational study, an aliquot from each polymer solution was characterized by HPLC at regular time intervals starting immediately after 120 min of ultrasonication (Figure 3.13b). These data were fitted to a first-order rate expression to determine relative release kinetics in pure acetonitrile from **PMA-OH** and **PMA-Me**. The similar size of each polymer is expected to result in comparable mechanophore conversion upon exposure to ultrasonication for the same amount of time. Therefore, differences in hydroxycoumarin release result nearly exclusively from differences in the decomposition reactions of each mechanically revealed furfuryl carbonate species. As anticipated, release of hydroxycoumarin from **PMA-OH** is significantly faster ($t_{1/2}$ = 11 h) compared to **PMA-Me** ($t_{1/2}$ = 39 h), suggesting that the tethered alcohol facilitates furfuryl carbonate decomposition under these aprotic solvent conditions (Figure 3.16 and Figure 3.17). The release of hydroxycoumarin from **PMA-OH** plateaus at 70% of full release following 120 min of ultrasonication. In contrast, the release of hydroxycoumarin from **PMA-Me** is projected to plateau at only 45% of the theoretical maximum value, emphasizing the environmental limitations of molecular release from that system. These results demonstrate the enhanced payload release in aprotic environments enabled by a tethered alcohol motif on the masked furfuryl carbonate, fostering opportunities for mechanically triggered molecular release in diverse environments.

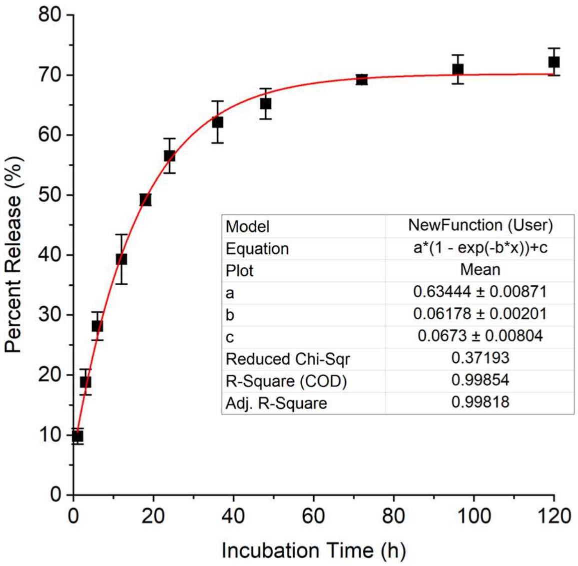

Model	NewFunction (User)
Equation	a*(1 - exp(-b*x))+c
Plot	Mean
a	0.63444 ± 0.00871
b	0.06178 ± 0.00201
c	0.0673 ± 0.00804
Reduced Chi-Sqr	0.37193
R-Square (COD)	0.99854
Adj. R-Square	0.99818

Figure 3.16 Release of hydroxycoumarin **9** from **PMA-OH** as a function of incubation time at room temperature following 120 min ultrasonication (2 mg/mL in MeCN) monitored using HPLC. Error bars represent standard deviation from three replicate experiments. Fitting the data to a first-order rate expression provides a reaction half-life of ~11 h.

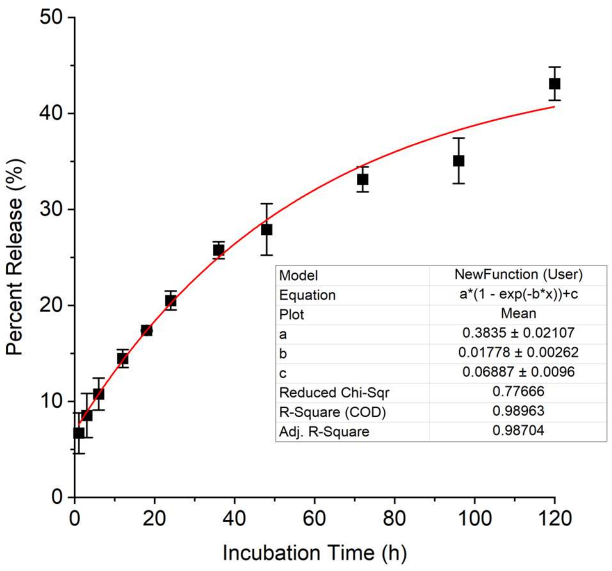

Figure 3.17 Release of hydroxycoumarin **9** from **PMA-Me** as a function of incubation time at room temperature following 120 min ultrasonication (2 mg/mL in MeCN) monitored using HPLC. Error bars represent standard deviation from three replicate experiments. Fitting the data to a first-order rate expression provides a reaction half-life of ~39 h.

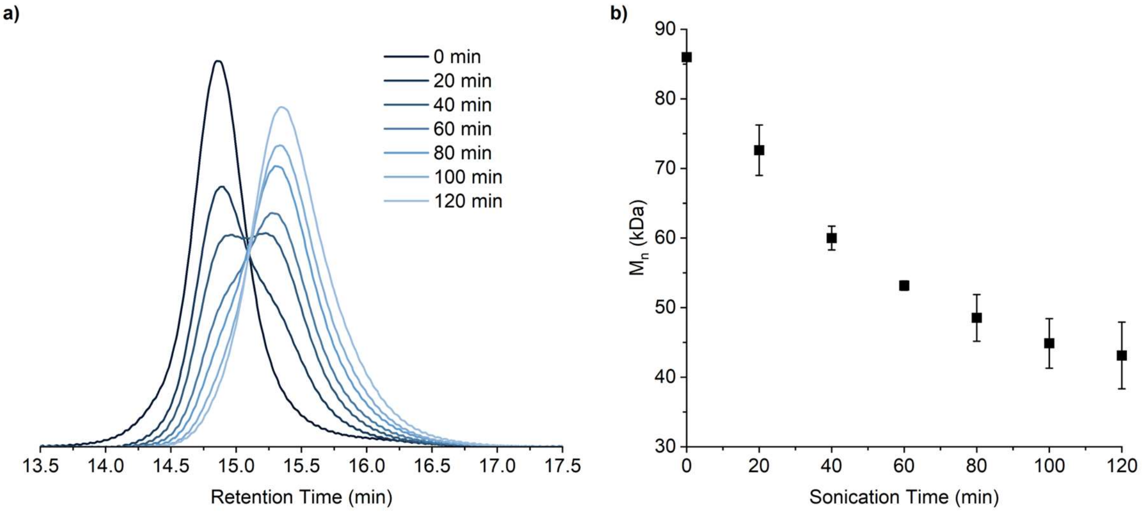

Figure 3.18 Characterization of **PMA-OH** by gel permeation chromatography (GPC) during the course of 120 min ultrasonication. (a) GPC traces as a function of ultrasonication time monitored with a refractive index (RI) detector. (b) M_n as a function of ultrasonication time showing a steady decrease in molecular weight as a result of ultrasound-induced mechanochemical activation.

3.3 Conclusion

In summary, we have designed a masked furfuryl carbonate mechanophore endowed with a tethered alcohol motif that significantly enhances mechanically triggered molecular release in aprotic environments, overcoming a limitation of previous systems. Experiments demonstrate that a tethered primary alcohol incorporated onto a secondary furfuryl carbonate promotes clean decomposition in pure acetonitrile. Ultrasound-induced mechanochemical activation of the furan–maleimide mechanophore results in the release of a hydroxycoumarin cargo molecule with improved efficiency and faster release kinetics compared to the original α-methyl derivative. Density functional calculations suggest a favorable intramolecular hydrogen bonding interaction between the tethered alcohol and the carbonyl oxygen of the carbonate that reduces the activation barrier for furfuryl carbonate decomposition leading to cargo release. This study broadens the scope of mechanically triggered release from masked 2-furylcarbinol mechanophores, which will be useful for the implementation of this strategy in a wider range of environments including bulk polymeric materials.

3.4 Experimental

3.4.1 General experimental details and methods

Reagents from commercial sources were used without further purification unless otherwise stated. Methyl acrylate was passed through a short plug of basic alumina to remove inhibitor immediately prior to use. Copper wire was cleaned prior to use by soaking in 1 M HCl for 5 min, and rinsed consecutively with deionized water, acetone, and DCM and then dried. Dry THF, DCM, and MeCN were obtained from a Pure Process Technology solvent purification system. All reactions were performed under a N_2 atmosphere unless specified otherwise. Silica column chromatography was performed on a Biotage Isolera system using SiliCycle SiliaSep HP flash cartridges. Preparatory reverse phase chromatography was performed with an Agilent 1100 Series high-performance liquid chromatography (HPLC) system using an Agilent Eclipse C18 column (990967-202).

NMR spectra were recorded using a 400 MHz Bruker Avance III HD with Prodigy Cryoprobe, a 400 MHz Bruker Avance Neo, or Varian Inova 500 MHz spectrometers. All ^{1}H NMR spectra are reported in parts per million (ppm) and were measured relative to the signals for residual chloroform (7.26 ppm), dichloromethane (5.32 ppm), or acetonitrile (1.94 ppm) in deuterated solvent. All ^{13}C NMR spectra were measured in deuterated solvents and are reported in ppm relative to the signals for $CDCl_3$ (77.16 ppm), CD_2Cl_2 (53.84 ppm), or acetonitrile-d_3 (1.32 ppm). Multiplicity and qualifier abbreviations are as follows: s = singlet, d = doublet, t = triplet, q = quartet, dd = doublet of doublets, td = triplet of doublets, ABq = AB quartet, m = multiplet, br = broad.

High resolution mass spectra (HRMS) were obtained from an Agilent 6230 series time-of-flight mass spectrometer equipped with an Agilent G1958 Jet Stream Electrospray Ionization Source.

Analytical gel permeation chromatography (GPC) was performed using an Agilent 1260 series pump equipped with two Agilent PLgel MIXED-B columns (7.5 x 300 mm), an Agilent 1200 series diode array detector, a Wyatt 18-angle DAWN HELEOS light scattering detector, and an Optilab rEX differential refractive index detector. The mobile phase was THF at a flow rate of 1 mL/min. Molecular weights and molecular weight distributions were calculated by light scattering using a dn/dc value of 0.062 mL/g (25 °C) for poly(methyl acrylate).

Analytical high-performance liquid chromatography (HPLC) measurements were performed with an Agilent Eclipse Plus C18 column (959961-902) using a single-wavelength UV-vis detector.

Ultrasound experiments were performed in a sound abating enclosure using a 500-watt Vibra Cell 505 liquid processor (20 kHz) equipped with a 0.5-inch diameter solid probe (part #630-0217), sonochemical adapter (part #830-00014), and a Suslick reaction vessel made by the Caltech glass shop (analogous to vessel #830-00014 from Sonics and Materials).

3.4.2 Synthetic details

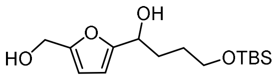

1

4-((tert-butyldimethylsilyl)oxy)-1-(5-(hydroxymethyl)furan-2-yl)butan-1-ol (1). A flame-dried 500 mL two-neck flask equipped with a stir bar was charged with furfuryl alcohol (1.43 mL, 16.5 mmol) and THF (120 mL). The solution was cooled to −20 °C with an ice/brine bath before adding n-butyllithium (2.5 M in hexanes, 13.9 mL, 34.7 mmol) dropwise via an addition funnel. The reaction mixture was allowed to stir at −20 °C for 1 h before adding 4-((*tert*-butyldimethylsilyl)oxy)butanal[33] (7.35 g, 36.3 mmol) dropwise. The reaction was allowed to slowly warm to room temperature overnight. The reaction was quenched by the slow addition of sat. $NaHCO_3$ (100 mL). The mixture was then extracted with EtOAc (3x150 mL), and the combined organic extracts were washed consecutively with water (200 mL) and brine (200 mL). The organic layer was dried over Na_2SO_4, filtered, and concentrated under reduced pressure. The crude product was purified by column chromatography (25–50% EtOAc/hexanes) to provide the title compound as an orange oil (2.45 g, 49%). R_f= 0.35 (50% EtOAc/hexanes).

<u>HRMS (ESI, *m/z*):</u> calcd for $[C_{15}H_{28}O_4SiNa]^+$ $(M+Na)^+$, 323.1649; found, 323.1654.

<u>^{1}H NMR (500 MHz, MeCN) δ:</u> 6.18 (d, *J* = 3.1 Hz, 1H), 6.14 (d, *J* = 3.1 Hz, 1H), 4.56 (dd, *J* = 7.7, 5.9 Hz, 2H), 3.54 (t, *J* = 6.3 Hz, 2H), 1.80 (m, 2H), 1.53 (m, 2H), 0.89 (s, 9H), 0.05 (s, 6H) ppm.

<u>^{13}C{^{1}H} NMR (101 MHz, MeCN) δ:</u> 158.4, 155.1, 108.6, 107.0, 67.7, 63.7, 57.2, 33.1, 29.8, 26.3, 18.9, −5.1 ppm.

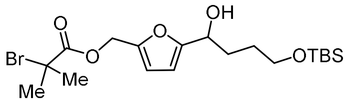

2

(5-(4-((tert-butyldimethylsilyl)oxy)-1-hydroxybutyl)furan-2-yl)methyl 2-bromo-2-methylpropanoate (2). A flame-dried 50 mL two-neck flask equipped with a stir bar was charged with compound **1** (0.650 g, 2.16 mmol) and DCM (17 mL). The solution was cooled to 0 °C, and triethylamine (0.603 mL, 4.33 mmol) was added to the reaction flask. A solution of α-bromoisobutyryl bromide (0.267 mL, 2.16 mmol) in DCM (12 mL) was added slowly via an addition funnel. The reaction was stirred at 0 °C for 2 h, and quenched with the addition of water (10 mL). The mixture was extracted with DCM (3 x 30 mL), and then dried with Na_2SO_4, filtered, and concentrated under reduced pressure. The crude product was purified by column chromatography (10–30% EtOAc/hexanes) to yield the title compound as a pale yellow oil (0.766 g, 79%). R_f = 0.80 (50% EtOAc/hexanes).

HRMS (ESI, *m/z*): calcd for $[C_{19}H_{33}BrO_5SiNa]^+$ $(M+Na)^+$, 471.1173; found, 471.1189.

^1H NMR (400 MHz, $CDCl_3$) δ: 6.38 (d, *J* = 3.2 Hz, 1H), 6.22 (d, *J* = 3.3 Hz, 1H), 5.12 (s, 2H), 4.71 (dd, *J* = 7.9, 4.8 Hz, 1H), 3.69 (m, 2H), 3.30 (br, 1H, -OH), 1.96 (m, 2H), 1.92 (s, 6H), 1.66 (m, 2H), 0.90 (s, 9H), 0.08 (s, 6H) ppm.

$^{13}C\{^1H\}$ NMR (101 MHz, $CDCl_3$) δ: 171.5, 158.3, 148.0, 111.8, 106.7, 67.9, 63.5, 59.8, 55.8, 33.5, 30.9, 29.0, 26.1, 18.5, −5.2 ppm.

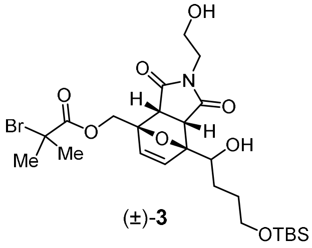

(±)-**3**

(7-(4-((tert-butyldimethylsilyl)oxy)-1-hydroxybutyl)-2-(2-hydroxyethyl)-1,3-dioxo-1,2,3,3a,7,7a-hexahydro-4H-4,7-epoxyisoindol-4-yl)methyl 2-bromo-2-methylpropanoate ((±)-3). A 25 mL round-bottom flask equipped with a stir bar was charged with furan **2** (2.00 g, 4.45 mmol), *N*-(2-hydroxyethyl)maleimide[34] (1.26 g, 8.90 mmol), and THF (7 mL). The reaction was stirred at room temperature for 7 days, and then concentrated under reduced pressure. The crude reaction mixture was separated by column chromatography (60–100% EtOAc/hexanes). The four diastereomeric products of the Diels–Alder reaction were separated by reverse phase chromatography (85% MeCN/H_2O) to yield the desired *endo* isomer as a foamy white solid (0.788 g, 30%). R_f= 0.18 (50% EtOAc/hexanes).

HRMS (ESI, *m/z*): calcd for $[C_{25}H_{40}BrO_8SiH]^+$ $(M+H)^+$, 590.1780; found, 590.1806.

^{1}H NMR (500 MHz, MeCN) δ: 6.35 (s, 2H), 4.90 (d, *J* = 12.5 Hz, 1H), 4.67 (d, *J* = 12.5 Hz, 1H), 4.22 (dd, *J* = 10.3, 2.4 Hz, 1H), 3.91 (d, *J* = 7.7 Hz, 1H), 3.72 (m, 2H), 3.66 (m, 2H), 3.55 (m, 3H), 3.44 (s, 1H, -OH), 1.94 (m, 6H), 1.89 (m, 1H), 1.78 (m, 2H), 1.63 (m, 1H), 0.90 (s, 9H), 0.08 (m, 6H) ppm.

$^{13}C\{^1H\}$ NMR (101 MHz, MeCN) δ: 175.9, 175.2, 171.3, 136.2, 134.7, 94.9, 89.4, 69.5, 63.5, 60.7, 55.6, 49.4, 47.5, 41.5, 30.8, 30.8, 30.5, 29.5, 26.1, 18.4, −5.2, −5.3 ppm.

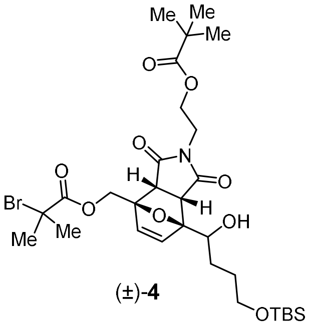

(±)-**4**

2-((3aS,4S,7R,7aR)-4-(((2-bromo-2-methylpropanoyl)oxy)methyl)-7-(4-((tert-butyldimethylsilyl)oxy)-1-hydroxybutyl)-1,3-dioxo-1,3,3a,4,7,7a-hexahydro-2H-4,7-epoxyisoindol-2-yl)ethyl pivalate ((±)-4). A flame-dried 10 mL two-neck flask was charged with Diels–Alder adduct (±)-**3** (70.0 mg, 0.119 mmol), triethylamine (63.0 µL, 0.462 mmol), DMAP (1.00 mg, 0.008 mmol), and DCM (5 mL). The solution was cooled to 0 °C, and pivaloyl chloride (16.0 μL, 0.130 mmol) was added dropwise. The reaction was allowed to warm to room temperature. After 26 h, the reaction was diluted with DCM (20 mL), and washed with sat. NH_4Cl (10 mL), water (10 mL), and brine (10 mL). The organic layer was dried over Na_2SO_4, filtered, and concentrated under reduced pressure. The crude reaction mixture was purified by column chromatography (20–50% EtOAc/hexanes) to yield the title compound as a colorless oil (40.3 mg, 50%). R_f = 0. 72 (50% EtOAc/hexanes).

HRMS (ESI, *m/z*): calcd for $[C_{30}H_{48}BrNO_9SiH]^+$ $(M+H)^+$, 674.2355; found, 674.2348.

^{1}H NMR (400 MHz, $CDCl_3$) δ: 6.34 (s, 2H), 4.90 (d, *J* = 12.5 Hz, 1H), 4.65 (d, *J* = 12.5 Hz, 1H), 4.21 (dd, *J* = 10.3, 2.5 Hz, 1H), 4.09 (m, 2H), 3.87 (d, *J* = 7.8 Hz, 1H), 3.72 (m, 2H), 3.59 (m, 2H), 3.50 (d, *J* = 7.8 Hz, 1H), 1.94 (m, 6H), 1.90 (m, 1H), 1.77 (m, 2H), 1.62 (m, 1H), 1.16 (s, 9H), 0.90 (s, 9H), 0.07 (m, 6H) ppm.

^{13}C{^{1}H} NMR (101 MHz, $CDCl_3$) δ: 178.3, 174.8, 174.2, 171.2, 136.2, 134.7, 94.7, 89.3, 69.5, 63.5, 63.5, 61.0, 55.6, 49.4, 47.5, 38.8, 37.9, 30.8, 30.8, 30.5, 29.5, 27.3, 26.1, 18.4, −5.2 ppm.

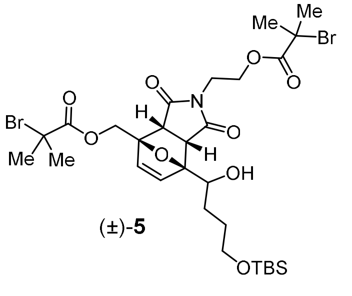

(±)-**5**

((3aS,4S,7R,7aR)-2-(2-((2-bromo-2-methylpropanoyl)oxy)ethyl)-7-(4-((tert-butyldimethylsilyl)oxy)-1-hydroxybutyl)-1,3-dioxo-1,2,3,3a,7,7a-hexahydro-4H-4,7-

epoxyisoindol-4-yl)methyl 2-bromo-2-methylpropanoate ((±)-5). A flame-dried 25 mL two-neck flask was charged with compound (±)-**3** (0.150 g, 0.254 mmol) and DCM (10 mL). The reaction mixture was then cooled to 0 °C, followed by the sequential dropwise addition of triethylamine (42.5 µL, 0.305 mmol) and then α-bromoisobutyryl bromide (34.5 µL, 0.279 mmol) via microsyringe. After 18 h, the crude reaction mixture was diluted with DCM (50 mL) and then washed consecutively with sat. NH_4Cl (20 mL) and brine (20 mL). The organic layer was then dried with Na_2SO_4, filtered, and concentrated under reduced pressure. The crude product was purified by column chromatography (20–40% EtOAc/hexanes) to yield the title compound as a viscous colorless oil (0.144 g, 38%). R_f = 0.81 (50% EtOAc/hexanes).

HRMS (ESI, *m/z*): calcd for $[C_{29}H_{45}Br_2NO_9SiH]^+$ $(M+H)^+$, 738.1304; found, 738.1324.

^{1}H NMR (400 MHz, CD_2Cl_2) δ: 6.38 (ABq, J_{AB} = 5.7 Hz, 2H), 4.87 (d, *J* = 12.6 Hz, 1H), 4.66 (d, *J* = 12.4 Hz, 1H), 4.19 (m, 2H), 4.15 (m, 1H), 3.83 (d, *J* = 7.7 Hz, 1H), 3.70 (m, 2H), 3.64 (m, 2H), 3.52 (d, *J* = 7.7 Hz, 1H), 3.16 (d, *J* = 6.0 Hz, 1H), 1.94 (s, 6H), 1.91 (m, 1H), 1.89 (s, 6H), 1.76 (m, 2H), 1.61 (m, 1H), 0.90 (s, 9H), 0.08 (m, 6H) ppm.

^{13}C{^{1}H} NMR (101 MHz, $CDCl_3$) δ: 175.0, 174.5, 171.7, 171.4, 136.7, 134.9, 95.1, 89.6, 69.9, 63.7, 62.9, 56.3, 56.2, 49.5, 47.8, 37.7, 30.9, 30.9, 30.6, 30.1, 29.8, 26.1, 18.6, −5.3 ppm.

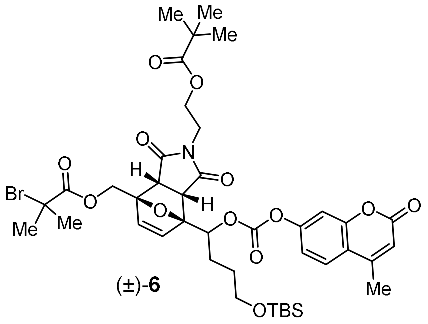

(±)-**6**

2-((3aS,4S,7R,7aR)-4-(((2-bromo-2-methylpropanoyl)oxy)methyl)-7-(4-((tert-butyldimethylsilyl)oxy)-1-((((4-methyl-2-oxo-2H-chromen-7-yl)oxy)carbonyl)oxy)butyl)-1,3-dioxo-1,3,3a,4,7,7a-hexahydro-2H-4,7-epoxyisoindol-2-yl)ethyl pivalate ((±)-6). A flame-dried 8 mL septum-capped vial was charged with compound (±)-**4** (25.8 mg, .0382 mmol), pyridine (12.0 µL, 0.145 mmol), and DCM (0.5 mL). A solution of coumarin chloroformate[20] (36.0 mg, 0.153 mmol) in DCM (1 mL) was added dropwise to the reaction mixture. The reaction was monitored by TLC, and after 19 h the crude mixture was filtered through a short plug of Celite to remove the insoluble bisarylcarbonate. The crude product was purified by column chromatography (30–60% EtOAc/hexanes) to yield the title compound as sticky white solid (17.7 mg, 53% yield). R_f = 0.57 (50% EtOAc/hexanes).

HRMS (ESI, *m/z*): calcd for $[C_{41}H_{54}BrNO_{13}SiH]^+$ $(M+H)^+$, 876.2621; found, 876.2647.

^{1}H NMR (400 MHz, $CDCl_3$) δ: 7.61 (d, *J* = 8.7 Hz, 1H), 7.25 (m, 1H), 7.21 (dd, *J* = 8.7, 2.3 Hz, 1H), 6.47 (d, *J* = 5.8 Hz, 1H), 6.41 (d, *J* = 5.7 Hz, 1H), 6.28 (q, *J* = 1.3 Hz, 1H), 5.46 (dd, *J* = 10.0, 3.1 Hz, 1H), 4.95 (d, *J* = 12.6 Hz, 1H), 4.67 (d, *J* = 12.6 Hz, 1H), 4.12 (t, *J* = 5.2 Hz, 2H), 3.70 (m, 2H), 3.59 (m, 4H), 2.44 (d, *J* = 1.3 Hz, 3H), 2.24 (m, 1H), 1.94 (m, 6H), 1.88 (m, 1H), 1.73 (m, 2H), 1.16 (s, 9H), 0.89 (s, 9H), 0.06 (s, 6H) ppm.

<u>$^{13}C\{^1H\}$ NMR (101 MHz, CDCl$_3$) δ:</u> 178.4, 173.5, 173.4, 171.2, 160.5, 154.3, 153.4, 152.7, 151.9, 135.6, 135.1, 125.6, 118.2, 117.5, 114.9, 110.0, 92.6, 89.3, 63.2, 62.4, 61.0, 55.4, 49.2, 48.7, 38.8, 38.2, 30.8, 30.8, 28.7, 27.3, 26.8, 26.1, 18.9, 18.5, −5.2 ppm.

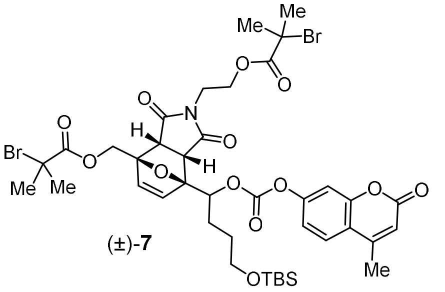

(±)-**7**

((3aS,4S,7R,7aR)-2-(2-((2-bromo-2-methylpropanoyl)oxy)ethyl)-7-(4-((tert-butyldimethylsilyl)oxy)-1-((((4-methyl-2-oxo-2H-chromen-7-yl)oxy)carbonyl)oxy)butyl)-1,3-dioxo-1,2,3,3a,7,7a-hexahydro-4H-4,7-epoxyisoindol-4-yl)methyl 2-bromo-2-methylpropanoate ((±)-7). An oven-dried 8 mL vial equipped with a stir bar and septum cap was charged with (±)-**5** (0.141 g, 0.191 mmol), pyridine (95.3 µL, 1.163 mmol), and DCM (0.5 mL). The reaction mixture was cooled to 0 °C and a solution of coumarin chloroformate[20] (0.270 g, 1.144 mmol) in DCM (5 mL) was added dropwise. The reaction was allowed to slowly warm to room temperature and stir for 2 days. The reaction mixture was then diluted with DCM (50 mL) and washed consecutively with water (20 mL) and brine (20 mL). The organic layer was dried over Na_2SO_4, filtered, and concentrated under reduced pressure. The crude mixture was taken up in EtOAc (5 mL) and filtered through a short plug of Celite to remove the insoluble bisarylcarbonate byproduct. The crude product was purified by column chromatography

(25–50% EtOAc/hexanes) to yield the title compound as a colorless oil (81.6 mg, 45%). R*f* = 0.75 (50% EtOAc/hexanes).

HRMS (ESI, *m/z*): calcd for $[C_{40}H_{51}Br_2NO_{13}SiH]^+$ $(M+H)^+$, 940.1570; found, 940.1586.

^{1}H NMR (400 MHz, $CDCl_3$) δ: 7.61 (d, *J* = 8.7 Hz, 1H), 7.26 (m, 1H), 7.21 (dd, *J* = 8.7, 2.4 Hz, 1H), 6.52 (d, *J* = 5.7 Hz, 1H), 6.45 (d, *J* = 5.7 Hz, 1H), 6.28 (d, *J* = 1.3 Hz, 1H), 5.46 (dd, *J* = 10.0, 3.2 Hz, 1H), 4.95 (d, *J* = 12.6 Hz, 1H), 4.67 (d, *J* = 12.5 Hz, 1H), 4.23 (t, *J* = 5.2 Hz, 2H), 3.71 (m, 4H), 3.59 (m, 2H), 2.44 (d, *J* = 1.3 Hz, 3H), 2.23 (m, 1H), 1.94 (d, *J* = 1.8 Hz, 6H), 1.90 (s, 6H), 1.85 (m, 1 H), 1.73 (m, 2H), 0.89 (s, 9H), 0.06 (s, 6H) ppm.

$^{13}C\{^1H\}$ NMR (101 MHz, $CDCl_3$) δ: 173.5, 173.4, 171.5, 171.2, 160.5, 154.3, 153.4, 152.7, 151.9, 135.8, 135.2, 125.6, 118.2, 117.5, 114.8, 110.0, 92.6, 89.4, 68.1, 63.1, 62.5, 62.4, 55.7, 55.4, 49.2, 48.8, 37.7, 30.8, 28.7, 26.8, 26.1, 18.9, 18.5, −5.2 ppm.

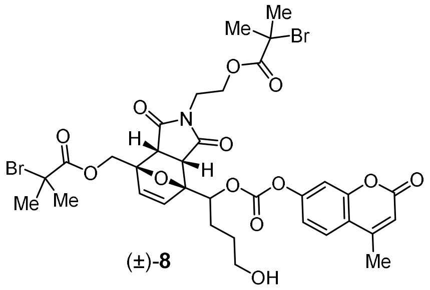

(±)-**8**

((3aS,4S,7R,7aR)-2-(2-((2-bromo-2-methylpropanoyl)oxy)ethyl)-7-(4-hydroxy-1-((((4-methyl-2-oxo-2H-chromen-7-yl)oxy)carbonyl)oxy)butyl)-1,3-dioxo-1,2,3,3a,7,7a-hexahydro-4H-4,7-epoxyisoindol-4-yl)methyl 2-bromo-2-methylpropanoate ((±)-8). Compound (±)-**7** (0.020 g, 0.0212 mmol) was suspended in MeOH (1.5 mL) in an oven-dried vial equipped with a stir bar and septum cap. A solution of $Hf(OTf)_4$ (0.8 mg, 0.0011 mmol) in MeOH (150 μL) was then added to the mixture. After stirring for 11 h, the reaction mixture became clear indicating full conversion of starting material, at which point the mixture was concentrated under reduced pressure. The crude product was purified by reverse phase chromatography (95% $MeCN/H_2O$) to provide the title compound as a foamy white solid (17.0 mg, 98%). R_f= 0.36 (50% EtOAc/hexanes).

HRMS (ESI, *m/z*): calcd for $[C_{34}H_{37}Br_2NO_{13}H]^+$ $(M+H)^+$, 826.0705; found, 826.0721.

^1H NMR (400 MHz, $CDCl_3$) δ: 7.63 (d, *J* = 8.7 Hz, 1H), 7.37 (d, *J* = 2.3 Hz, 1H), 7.29 (dd, *J* = 8.7, 2.3 Hz, 1H), 6.60 (d, *J* = 5.8 Hz, 1H), 6.46 (d, *J* = 5.8 Hz, 1H), 6.28 (d, *J* = 1.3 Hz, 1H), 5.38 (dd, *J* = 9.7, 3.4 Hz, 1H), 4.89 (d, *J* = 12.7 Hz, 1H), 4.72 (d, *J* = 12.7 Hz, 1H), 4.23 (m, 2H), 3.68 (m, 6H), 2.45 (d, *J* = 1.3 Hz, 3H), 1.96 (s, 6H), 1.83 (m, 4H), 1.80 (m, 6H).

$^{13}C\{^1H\}$ NMR (101 MHz, $CDCl_3$) δ: 173.6, 173.6, 171.5, 171.2, 160.6, 154.3, 153.6, 153.4, 152.0, 135.5, 134.8, 125.6, 118.3, 117.9, 114.8, 110.5, 91.7, 89.7, 63.0, 62.6, 62.3, 55.7, 55.5, 50.8, 49.1, 37.8, 30.8, 30.8, 30.8, 28.4, 27.5, 18.9 ppm.

Maleimide **10** was prepared according to the literature.[35]

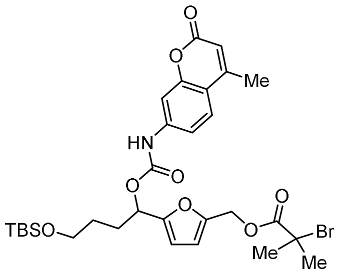

S1

(5-(4-((tert-butyldimethylsilyl)oxy)-1-(((4-methyl-2-oxo-2H-chromen-7-yl)carbamoyl)oxy)butyl)furan-2-yl)methyl 2-bromo-2-methylpropanoate (S1). A flame-dried 25 mL two-necked flask was charged with compound **2** (0.150 g, 0334 mmol), coumarin isocyanate[23] (0.134 g, 0.667 mmol), and DCM (10 mL). The mixture was then cooled to 0 °C, and DMAP (4.0 mg, 0.033 mmol) was added and the reaction was allowed to warm slowly to rt. After stirring for 18 h, the reaction mixture was diluted with DCM (50 mL) and washed consecutively with water (2 x 30 mL) and brine (30 mL). The organic layer was dried over Na_2SO_4, filtered, and concentrated under reduced pressure. The crude product was purified by column chromatography (20–60% EtOAc/hexanes) to provide the title compound as a foamy white solid (0.167 g, 77% yield) R_f= 0.79 (50% EtOAc/hexanes).

HRMS (ESI, *m/z*): calcd for $[C_{30}H_{40}BrNO_8SiNa]^+$ $(M+Na)^+$, 672.1599; found, 672.1610.

^{1}H NMR (400 MHz, $CDCl_3$) δ: 7.51 (d, *J* = 8.7 Hz, 1H), 7.41 (d, *J* = 2.2 Hz, 1H), 7.34 (dd, *J* = 8.7, 2.2 Hz, 1H), 6.86 (s, 1H), 6.40 (d, *J* = 3.3 Hz, 1H), 6.37 (d, *J* = 3.2 Hz, 1H), 6.19 (d, *J* = 1.3 Hz, 1H), 5.85 (t, *J* = 7.2 Hz, 1H), 5.14 (ABq, J_{AB} = 13.2 Hz, 2H), 3.64, (td, *J* = 6.3, 1.4 Hz, 2H), 2.40 (d, *J* = 1.3 Hz, 3H), 2.07 (q, *J* = 7.6 Hz, 2H), 1.92 (d, *J* = 2.0 Hz, 6H), 1.56 (m, 2H), 1.56 (s, 3H), 0.89 (s, 9H), 0.04 (s, 6H) ppm.

<u>$^{13}C\{^{1}H\}$ NMR (101 MHz, $CDCl_3$) δ:</u> 171.4, 161.1, 154.6, 153.2, 152.3, 152.2, 149.1, 141.4, 125.5, 115.7, 114.4, 113.4, 111.7, 110.0, 106.0, 70.3, 62.6, 59.7, 55.7, 30.8, 29.3, 28.7, 25.4, 18.7, 18.5, −5.2 ppm.

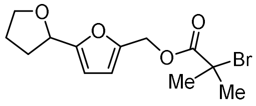

11

(5-(tetrahydrofuran-2-yl)furan-2-yl)methyl 2-bromo-2-methylpropanoate (11). Compound **S1** (0.010 g, 0.0153 mmol) was dissolved in MeCN (1 mL) in a small vial. A solution of $Hf(OTf)_4$ (0.5 mg, 0.6 μmol) in MeCN (250 μL) was added dropwise. After 5 h, the reaction mixture was concentrated under reduced pressure. The reaction mixture was purified by column chromatography (10–50% EtOAc/hexanes) to provide the title compound as a colorless oil (1.4 mg, 29% yield). R_f = 0.52 (20% EtOAc/hexanes).

<u>HRMS (ESI, *m/z*):</u> calcd for $[C_{13}H_{17}BrO_4Na]^+$ $(M+Na)^+$, 339.0203; found, 339.0206.

<u>^{1}H NMR (400 MHz, $CDCl_3$) δ:</u> 6.37 (d, *J* = 3.2 Hz, 1H), 6.25 (d, *J* = 3.1 Hz, 1H), 5.13 (s, 2H), 4.90 (t, *J* = 6.7 Hz, 1H), 3.99 (m, 1H), 3.88 (m, 1H), 2.20 (m, 1H), 2.08 (m, 2H), 1.98 (m, 1H), 1.93 (s, 6H) ppm.

<u>$^{13}C\{^{1}H\}$ NMR (101 MHz, $CDCl_3$) δ:</u> 171.5, 156.3, 148.6, 111.7, 107.7, 74.0, 68.5, 59.9, 55.8, 33.5, 30.9, 30.5, 26.0 ppm.

Synthesis of poly(methyl acrylate) containing a chain-centered mechanophore with a TBS-protected tethered alcohol (PMA-OTBS). A 10 mL Schlenk flask with a stir bar was charged with bis-initiator (±)-**7** (10.6 mg, 11.3 μmol), DMSO (1.51 mL), copper wire (1 cm length, 20 gauge), and methyl acrylate (1.51 mL, 17 mmol). The flask was sealed, the solution was deoxygenated with five freeze-pump-thaw cycles, and then backfilled with nitrogen. The flask was warmed to rt, and Me_6TREN (6.0 μL, 23 μmol) was then added via microsyringe. After stirring at rt for 87 min, the flask was opened to air and the solution was diluted with DCM. The polymer solution as precipitated into cold methanol (x3) and the isolated material was dried under vacuum to yield 0.839 g of polymer. M_n = 88 kDa, $Đ$ = 1.10.

Synthesis of poly(methyl acrylate) containing a chain-centered mechanophore with a tethered primary alcohol (PMA-OH). An oven-dried 8 mL vial was charged with **PMA-OTBS** (0.316 g) and MeCN (20 mL). Amberlyst-15 resin beads (0.275 g) were added, and the reaction was allowed to proceed under air at rt for 17 h. The mixture was filtered to recover the resin beads and the polymer solution was concentrated under reduced pressure. The polymer was then dissolved into DCM, precipitated into hexanes, and centrifuged to recover the polymer as a pellet. The polymer was then dried under vacuum to provide **PMA-OH** (0.255 g, 81%). M_n = 86 kDa, $Đ$ = 1.10.

Synthesis of poly(methyl acrylate) control polymer containing a mechanophore with a TBS-protected tethered alcohol at the chain end (PMA-control-OTBS). A 10 mL Schlenk flask with a stir bar was charged with bis-initiator (±)-**6** (8.9 mg, 10.1 μmol), DMSO (1.36 mL), copper wire (1 cm length, 20 gauge), and methyl acrylate (1.36 mL, 15 mmol). The flask was sealed, the solution was deoxygenated with five freeze-pump-thaw cycles, and then backfilled with nitrogen. The flask was warmed to rt, and Me_6TREN (5.0 μL, 19.5 μmol) was then added via microsyringe. After stirring at rt for 79 min, the flask was opened to air and the solution was diluted with DCM. The polymer solution was precipitated into cold methanol (x3) and the isolated material was dried under vacuum to yield 0.683 g of polymer. M_n = 85 kDa, $Đ$ = 1.17.

Synthesis of poly(methyl acrylate) control polymer containing a mechanophore with a tethered primary alcohol at the chain end (PMA-control). An oven-dried 8 mL septum-capped vial was charged with **PMA-control-OTBS** (0.200 g) and MeCN (15 mL). Amberlyst-15 resin beads (0.150 g) were added, and the reaction was allowed to proceed under air at rt for 10 h. The mixture was filtered to recover the resin beads and the polymer solution was concentrated under reduced pressure. The polymer was then dissolved into DCM, precipitated into hexanes, and centrifuged to recover the polymer as a pellet. The polymer was then dried under vacuum to provide **PMA-control** (0.171 g, 86%). M_n = 87 kDa, $Đ$ = 1.16.

Synthesis of poly(methyl acrylate) containing a chain-centered mechanophore with an α-methyl carbonate (PMA-Me). Polymer **PMA-Me** was synthesized according to the previously reported procedure.[20] M_n = 92 kDa, $Đ$ = 1.10.

3.4.3 General procedure for ultrasonication experiments

An oven-dried sonication vessel was fitted with rubber septa, placed onto the sonication probe, and allowed to cool under a stream of dry argon. The vessel was charged with a solution of the polymer in anhydrous acetonitrile (2.0 mg/mL, 15 mL) and submerged in an ice bath. The solution was sparged with argon for 20 min prior to sonication and for the duration of the sonication experiment. Pulsed ultrasound (1 s on/2 s off, 30% amplitude, 20 kHz, 15.5 W/cm^2) was then applied to the system. Aliquots (1 mL) were removed at 0, 20, 40, 60, 80, 100, and 120 min (sonication "on" time) and 14 μL of a 0.50 mM solution of 3-cyano-7-hydroxy-4-methylcoumarin internal standard in anhydrous MeCN was added. Samples were filtered through a 0.45 μm syringe filter prior to analysis by GPC and HPLC. Ultrasonic intensity was calibrated using the method described by Berkowski *et al.*[6]

3.4.4 Characterization of molecular release by HPLC

Calculation of Relative Response Factors (RRF). A standard solution with known concentrations of the internal standard (IS) molecule (3-cyano-7-hydroxy-4-methylcoumarin) and the small molecule analyte (7-hydroxy-4-methylcoumarin **9**) was prepared and analyzed by HPLC equipped with a UV detector (λ = 320 nm). The RRF is calculated from the HPLC results of the standard solution using eq 1 and was determined to be 1.41.

$$\mathrm{RRF} = \frac{\text{response factor of the analyte}}{\text{response factor of the IS}} = \left(\frac{\text{peak area of analyte}}{\text{concentration of analyte}}\right) / \left(\frac{\text{peak area of IS}}{\text{concentration of IS}}\right) \tag{1}$$

Determination of the concentration of released hydroxycoumarin cargo from polymers after ultrasound-induced mechanical activation. Aliquots were removed during ultrasonication experiments and 3-cyano-7-hydroxy-4-methylcoumarin (7.0 μM) was added as the internal standard. The solution was then kept at room temperature and analyzed by HPLC at various time intervals (HPLC conditions: 30:70 MeCN/water + 0.1% AcOH, 2 mL/min, λ = 320 nm). The concentration of hydroxycoumarin (analyte) in the solution was calculated using eq 2:

$$\text{concentration of analyte} = \frac{\text{peak area of analyte}}{\text{peak area of IS}} * \frac{1}{\text{RRF}} * \text{concentration of IS} \qquad (2)$$

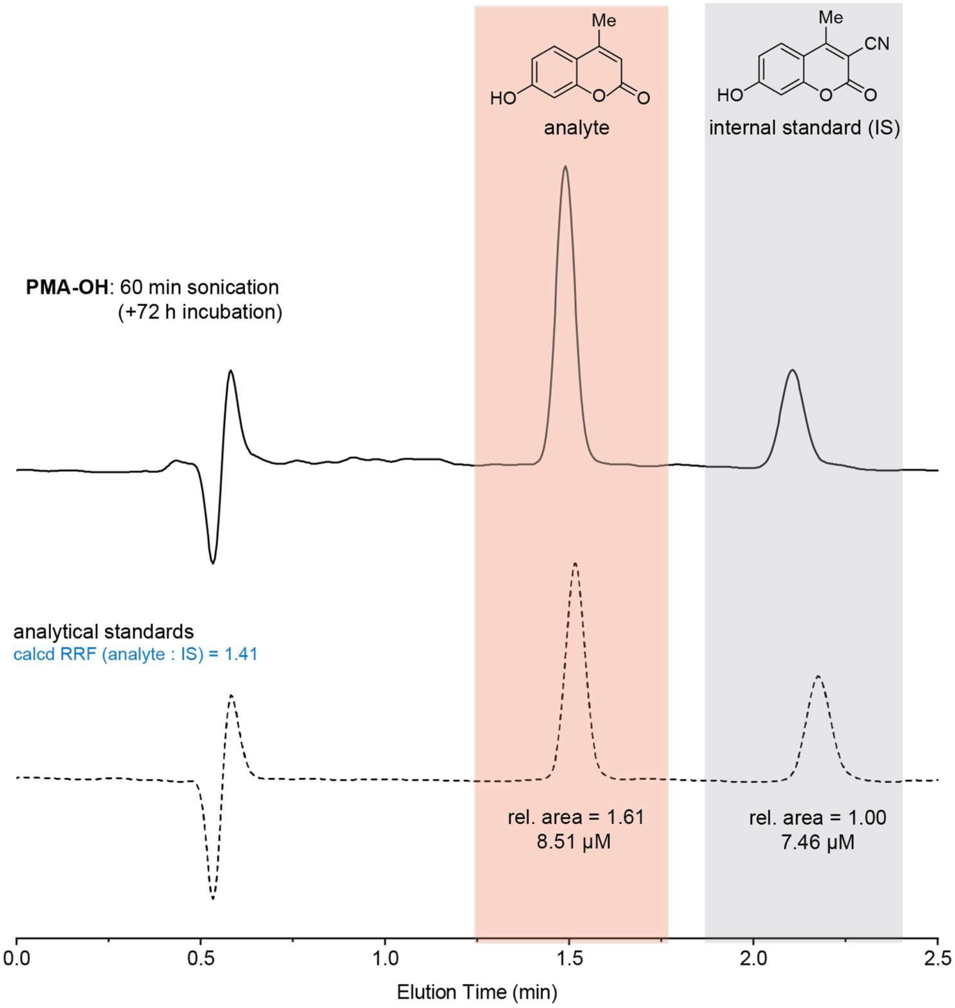

Figure 3.19 Representative HPLC chromatograms for the analysis of mechanically triggered release of hydroxycoumarin **9** from **PMA-OH** containing a chain-centered mechanophore with a tethered alcohol. HPLC conditions: 30:70 MeCN/water + 0.1% AcOH, isocratic, 2 mL/min, λ = 320 nm.

Table 3.1 Release of hydroxycoumarin payload from PMA-OH monitored by HPLC[a]

	Trial 1			**Trial 2**			**Trial 3**		
Sonication time (min)	Payload peak area	IS peak area	Released payload, calcd (μM)	Payload peak area	IS peak area	Released payload, calcd (μM)	Payload peak area	IS peak area	Released payload, calcd (μM)
0	1.1	10.8	0.503	1.0	11.3	0.437	1.0	11.7	0.422
20	11.1	9.3	5.89	10.6	10.0	5.23	11.3	10.1	5.52
40	18.0	9.4	9.45	17.1	9.5	8.88	21.0	11.6	8.93
60	22.4	9.3	11.9	22.5	9.7	11.4	24.3	10.2	11.8
80	26.6	9.4	14.0	26.8	9.6	13.8	28.3	10.1	13.8
100	29.8	9.6	15.3	30.6	9.3	16.2	32.3	10.6	15.0
120	31.9	9.3	16.9	32.1	8.9	17.8	38.2	11.3	16.7

[a] Each sample incubated at rt for 72 h prior to characterization

Table 3.2 Release of hydroxycoumarin payload from PMA-Me monitored by HPLC[a]

	Trial 1			Trial 2			Trial 3		
Sonication time (min)	Payload peak area	IS peak area	Released payload, calcd (µM)	Payload peak area	IS peak area	Released payload, calcd (µM)	Payload peak area	IS peak area	Released payload, calcd (µM)
0	2.3	9.8	1.16	1.3	10	0.642	1.5	10.6	0.698
20	5.7	7.7	3.65	5.0	10.3	2.40	5.4	9.4	2.83
40	9.1	8.1	5.54	7.7	7.9	4.81	8.0	10.5	3.76
60	11.2	7.8	7.09	10.3	8.0	6.35	10.2	8.1	6.21
80	12.9	7.9	8.06	12.8	7.9	8.00	13.0	8.8	7.29
100	14.6	7.3	9.87	15.0	7.7	9.61	13.7	8.7	7.77
120	17.1	8.7	9.70	20.5	10.7	9.45	18.7	10.3	8.96

[a]Each sample incubated at rt for 120 h prior to characterization

Table 3.3 Release of hydroxycoumarin payload from PMA-control monitored by HPLC[a]

	Trial 1			Trial 2			Trial 3		
Sonication time (min)	Payload peak area	IS peak area	Released payload, calcd (µM)	Payload peak area	IS peak area	Released payload, calcd (µM)	Payload peak area	IS peak area	Released payload, calcd (µM)
0	0	8.93	0	0	9.00	0	0.113	10.8	0.051
20	2.49	9.27	0.133	0.677	9.72	0.344	0.123	9.07	0.067
40	8.59	7.90	0.536	0	10.1	0	0.367	9.58	0.189
60	2.08	9.01	0.114	1.69	9.10	0.092	0.764	7.98	0.473
80	4.68	7.76	0.298	1.08	9.37	0.566	0.710	8.07	0.434
100	4.66	9.13	0.252	1.25	8.72	0.708	1.15	8.53	0.666
120	2.19	8.52	1.27	1.45	9.65	0.740	1.10	8.93	0.606

[a]Each sample incubated at rt for 72 h prior to characterization

Table 3.4 Release of hydroxycoumarin payload from PMA-OH after 120 min ultrasonication monitored by HPLC

	Trial 1			Trial 2			Trial 3		
Time post-sonication (h)	Payload peak area	IS peak area	Released payload, calcd (µM)	Payload peak area	IS peak area	Released payload, calcd (µM)	Payload peak area	IS peak area	Released payload, calcd (µM)
1	5.3	12.1	2.16	5.0	12.0	2.06	6.6	12.4	2.63
3	9.6	11.9	3.98	9.9	11.6	4.21	11.6	11.6	4.93
6	14.6	12.1	5.95	15.5	11.5	6.65	16.7	11.7	7.04
12	21.7	11.5	9.31	22.0	13.4	8.10	22.9	11.3	10.0
18	28.0	12.3	11.2	26.9	11.6	11.4	26.7	11.3	11.7
24	30.5	11.7	12.9	31.3	11.1	13.9	28.5	11.1	12.7
36	34.0	11.6	14.5	32.8	10.6	15.3	44.5	16.1	13.6
48	33.3	10.9	15.1	31.7	9.9	15.8	33.2	11.2	14.6
72	33.8	10.5	15.9	33.2	10.1	16.2	46.6	14.2	16.2
96	34.7	10.6	16.2	35.8	10.9	16.2	34.4	9.9	17.1
120	34.4	10.2	16.6	34.8	10.5	16.4	34.5	9.8	17.4

Table 3.5 Release of hydroxycoumarin payload from PMA-Me after 120 min ultrasonication monitored by HPLC

	Trial 1			Trial 2			Trial 3		
Time post-sonication (h)	Payload peak area	IS peak area	Released payload, calcd (μM)	Payload peak area	IS peak area	Released payload, calcd (μM)	Payload peak area	IS peak area	Released payload, calcd (μM)
1	4.6	12.3	1.85	2.4	12.5	0.947	3.5	11	1.57
3	6	13.2	2.24	3.3	12.6	1.29	4.5	10.9	2.04
6	6.3	11.7	2.66	5	12.7	1.94	5.5	11.2	2.42
12	10.4	15.3	3.35	7	11.7	2.95	7.1	11.2	3.13
18	8.7	11.3	3.80	5.2	6.8	3.77	8.4	11.0	3.77
24	9.8	11.1	4.36	9.1	10.4	4.31	10.2	10.7	4.70
36	11.7	10.3	5.61	12.2	10.4	5.79	11.5	10.5	5.40
48	13.3	9.9	6.63	13.4	12.1	5.46	14.1	11.4	6.10
72	16	10.5	7.52	14	9.9	6.98	18.0	12.5	7.11
96	17.3	10.4	8.21	15	10.2	7.26	15.6	10.4	7.40
120	17.1	8.70	9.70	20.5	10.7	9.45	18.7	10.3	8.96

Table 3.6 Release of hydroxycoumarin payload from PMA-control after 120 min ultrasonication monitored by HPLC

	Trial 1			Trial 2			Trial 3		
Time post-sonication (h)	Payload peak area	IS peak area	Released payload, calcd (μM)	Payload peak area	IS peak area	Released payload, calcd (μM)	Payload peak area	IS peak area	Released payload, calcd (μM)
1	0.523	12.1	0.213	0.278	11.4	0.121	0.682	11.8	0.285
3	1.40	11.5	0.597	0.511	11.2	0.225	1.06	11.3	0.463
6	0.246	9.80	0.124	0.601	11.8	0.251	1.13	11.3	0.491
12	1.53	11.8	0.639	0.973	10.4	0.463	1.06	10.3	0.507
18	1.04	10.7	0.480	1.022	10.5	0.479	1.47	10.7	0.677
24	0.468	10.0	0.231	1.24	10.6	0.578	0.886	10.1	0.432
36	0.886	9.95	0.439	1.23	9.42	0.642	1.38	9.40	0.724
48	0.821	9.52	0.425	1.08	10.5	0.506	1.53	10.1	0.748
72	1.32	9.49	0.686	1.18	10.8	0.540	1.10	10.8	0.503
96	1.37	12.0	0.561	1.40	11.5	0.600	1.04	10.1	0.508
120	1.07	11.5	0.459	1.35	10.6	0.630	1.85	9.39	0.972

3.4.5 DFT calculations

CoGEF calculations. CoGEF calculations were performed using Spartan ′18 Parallel Suite according to previously reported methods.[36,37] Ground state energies were calculated using DFT at the B3LYP/6-31G* level of theory. Starting from the equilibrium geometry of the unconstrained molecule (relative energy = 0 kJ/mol), the distance between the terminal methyl groups of the truncated structure was increased in increments of 0.05 Å and the energy was minimized at each step. The maximum force associated with the retro-Diels–Alder reaction was calculated from the slope of the curve immediately prior to bond cleavage.

Calculation of Activation Energies. Activation energies for model furfuryl carbonate compounds were calculated using Spartan ′18 Parallel Suite following our previous methods.[20] All calculations were run with a solvent dielectric constant of 37.22. Equilibrium geometries and corresponding energies of each furfuryl carbonate or carbamate reactant were calculated at the M06-2X/6-311+G** level of theory with a fine integration grid (99,590). Transition state geometries were approximated using an initial energy profile at the HF/6-31+G* level of theory by lengthening the C–O bond involved in the desired fragmentation reaction. The energy maximum from each profile was then chosen as the starting point for a transition state geometry optimization, which was conducted at the same level of theory. Subsequent geometry optimizations were performed at the M06-2X/6-311+G** level of theory and the optimized structures were subjected to a final energy and frequency calculation at the M06-2X/6-311+G** level of theory using a fine integration grid (99,590). Each structure returned a single imaginary vibrational frequency corresponding to the expected bond-breaking mode.

Optimized geometry coordinates determined for reactants:

FC1

C	0.625870	0.060233	-3.079388
C	-0.637531	-0.421937	-2.982456
C	-0.958334	-0.466695	-1.578856
C	0.141027	-0.011012	-0.934275
O	1.112139	0.314046	-1.827252
C	0.489080	0.196547	0.504506
O	-0.676679	-0.235035	1.232016
C	-0.838989	0.275808	2.450477
O	-1.929208	-0.255985	2.982270
O	-0.120637	1.085376	2.979217
C	-2.251437	0.195065	4.308507
C	1.709154	-0.601630	0.937563
C	1.534882	0.347566	-4.218350
H	-1.267337	-0.711777	-3.809040
H	-1.876857	-0.792916	-1.118582
H	0.643752	1.260760	0.698978
H	-3.160018	-0.334074	4.579274
H	-2.420655	1.270945	4.304919
H	-1.442508	-0.055861	4.993306
H	1.532383	-1.666656	0.776346
H	1.923473	-0.420230	1.991323
H	2.572651	-0.292093	0.347233
H	1.031381	0.101527	-5.152617
H	1.814767	1.403443	-4.238781
H	2.449632	-0.245416	-4.146337

Gibbs free energy: -650.852643 hartrees

FC2

C	0.681912	-3.279260	-0.070842
C	1.118496	-3.184708	1.210410
C	0.924384	-1.817554	1.614734
C	0.377291	-1.189522	0.547284
O	0.221891	-2.062461	-0.484780

C	0.608892	-4.390273	-1.053715
C	-0.029486	0.218496	0.267593
C	1.104177	1.076656	-0.302322
O	-0.473257	0.774845	1.523858
C	-1.262991	1.839184	1.422291
O	-1.578488	2.254522	2.634313
O	-1.635465	2.342564	0.387201
C	-2.434362	3.409968	2.692085
C	1.366160	0.813688	-1.786496
C	0.140190	1.070049	-2.664280
O	-0.463559	2.334608	-2.411545
H	1.527026	-3.991515	1.798614
H	1.155431	-1.369413	2.568268
H	0.998837	-5.300606	-0.599623
H	1.199438	-4.162190	-1.944182
H	-0.422764	-4.568195	-1.365977
H	-0.886162	0.198319	-0.409409
H	0.841351	2.129363	-0.170949
H	2.007171	0.892345	0.283948
H	-2.584174	3.602204	3.750043
H	-3.382537	3.193465	2.202326
H	-1.945968	4.256857	2.212272
H	1.696554	-0.218009	-1.944162
H	2.181588	1.467104	-2.107192
H	0.438287	1.076220	-3.713499
H	-0.598927	0.270531	-2.542321
H	-0.890937	2.312718	-1.543947

Gibbs free energy: -804.621845 hartrees

Optimized geometry coordinates determined for transition states:

FC1‡

C	0.073604	-0.834324	-2.979311
C	-0.869568	-1.766528	-2.596366
C	-1.385115	-1.320899	-1.370519
C	-0.737277	-0.135217	-1.071603
O	0.160097	0.143795	-2.074375
C	-0.847487	0.729874	0.015097
O	0.581266	-0.098879	1.385189
C	0.270574	0.178566	2.584081
O	1.183177	-0.316826	3.475021
O	-0.706692	0.808274	2.988891
C	0.929207	-0.050229	4.853305
C	0.953177	-0.744765	-4.165913

C	-0.295783	2.103570	-0.005012
H	-1.136816	-2.651513	-3.151222
H	-2.143208	-1.784077	-0.755986
H	-1.637803	0.502012	0.720133
H	0.920061	1.023505	5.044726
H	1.743875	-0.518718	5.401374
H	-0.023924	-0.480650	5.162460
H	0.772576	-1.593836	-4.822418
H	0.756368	0.182168	-4.709369
H	2.000866	-0.742062	-3.856617
H	0.661026	2.146153	-0.523101
H	-0.210336	2.493176	1.006863
H	-1.011866	2.727429	-0.555329

Gibbs free energy: -650.817542 hartrees

FC2‡

C	1.119523	-3.362485	0.226211
C	-0.202107	-3.685325	0.457523
C	-0.926940	-2.492753	0.314258
C	-0.012958	-1.504728	-0.005767
O	1.242541	-2.061892	-0.051461
C	2.355076	-4.177092	0.231569
C	-0.178387	-0.138613	-0.242889
C	0.858802	0.679563	-0.931535
O	-0.061072	0.689892	1.673383
C	-0.656860	1.808986	1.713124
O	-0.673044	2.341800	2.962015
O	-1.191153	2.416344	0.777551
C	-1.313211	3.612103	3.102388
C	0.498253	0.853330	-2.421835
C	-0.807079	1.616522	-2.641026
O	-0.823774	2.869974	-1.975381
H	-0.574442	-4.668386	0.696753
H	-1.990818	-2.340475	0.421184
H	2.113460	-5.210479	0.472375
H	3.057405	-3.787195	0.971805
H	2.836125	-4.136221	-0.748268
H	-1.209925	0.190370	-0.293890
H	0.901775	1.666073	-0.470351
H	1.837352	0.211029	-0.831800
H	-1.222959	3.872516	4.154407
H	-2.364373	3.546177	2.821080
H	-0.817155	4.362235	2.486153
H	0.429613	-0.120639	-2.915540

H	1.319464	1.402455	-2.889259
H	-0.923703	1.820781	-3.706725
H	-1.667688	1.012168	-2.331623
H	-0.951741	2.713963	-1.024427

Gibbs free energy: -804.592990 hartrees

3.5 References

(1) Ghanem, M. A.; Basu, A.; Behrou, R.; Boechler, N.; Boydston, A. J.; Craig, S. L.; Lin, Y.; Lynde, B. E.; Nelson, A.; Shen, H.; Storti, D. W. The role of polymer mechanochemistry in responsive materials and additive manufacturing. *Nat Rev Mater* **2021**, *6*, 84–98.

(2) Zhang, Y.; Yu, J.; Bomba, H. N.; Zhu, Y.; Gu, Z. Mechanical Force-Triggered Drug Delivery. *Chem. Rev.* **2016**, *116*, 12536–12563.

(3) Davis, D. A.; Hamilton, A.; Yang, J.; Cremar, L. D.; Van Gough, D.; Potisek, S. L.; Ong, M. T.; Braun, P. V.; Martínez, T. J.; White, S. R.; Moore, J. S.; Sottos, N. R. Force-induced activation of covalent bonds in mechanoresponsive polymeric materials. *Nature* **2009**, *459*, 68–72.

(4) Kim, G.; Lau, V. M.; Halmes, A. J.; Oelze, M. L.; Moore, J. S.; Li, K. C. High-intensity focused ultrasound-induced mechanochemical transduction in synthetic elastomers. *Proc. Natl. Acad. Sci. USA* **2019**, *116*, 10214–10222.

(5) Kim, G.; Wu, Q.; Chu, J. L.; Smith, E. J.; Oelze, M. L.; Moore, J. S.; Li, K. C. Ultrasound controlled mechanophore activation in hydrogels for cancer therapy. *Proc. Natl. Acad. Sci. U.S.A.* **2022**, *119*, e2109791119.

(6) Berkowski, K. L.; Potisek, S. L.; Hickenboth, C. R.; Moore, J. S. Ultrasound-Induced Site-Specific Cleavage of Azo-Functionalized Poly(ethylene glycol). *Macromolecules* **2005**, *38*, 8975–8978.

(7) Beyer, M. K.; Clausen-Schaumann, H. Mechanochemistry: The Mechanical Activation of Covalent Bonds. *Chem. Rev.* **2005**, *105*, 2921–2948.

(8) Caruso, M. M.; Davis, D. A.; Shen, Q.; Odom, S. A.; Sottos, N. R.; White, S. R.; Moore, J. S. Mechanically-Induced Chemical Changes in Polymeric Materials. *Chem. Rev.* **2009**, *109*, 5755–5798.

(9) Li, J.; Nagamani, C.; Moore, J. S. Polymer Mechanochemistry: From Destructive to Productive. *Acc. Chem. Res.* **2015**, *48*, 2181–2190.

(10) Versaw, B. A.; Zeng, T.; Hu, X.; Robb, M. J. Harnessing the Power of Force: Development of Mechanophores for Molecular Release. *J. Am. Chem. Soc.* **2021**, *143*, 21461–21473.

(11) Lin, Y.; Kouznetsova, T. B.; Craig, S. L. A Latent Mechanoacid for Time-Stamped Mechanochromism and Chemical Signaling in Polymeric Materials. *J. Am. Chem. Soc.* **2020**, *142*, 99–103.

(12) Diesendruck, C. E.; Steinberg, B. D.; Sugai, N.; Silberstein, M. N.; Sottos, N. R.; White, S. R.; Braun, P. V.; Moore, J. S. Proton-Coupled Mechanochemical Transduction: A Mechanogenerated Acid. *J. Am. Chem. Soc.* **2012**, *134*, 12446–12449.

(13) Sun, Y.; Neary, W. J.; Burke, Z. P.; Qian, H.; Zhu, L.; Moore, J. S. Mechanically Triggered Carbon Monoxide Release with Turn-On Aggregation-Induced Emission. *J. Am. Chem. Soc.* **2022**, *144*, 1125–1129.

(14) Larsen, M. B.; Boydston, A. J. “Flex-Activated” Mechanophores: Using Polymer Mechanochemistry To Direct Bond Bending Activation. *J. Am. Chem. Soc.* **2013**, *135*, 8189–8192.

(15) Shen, H.; Larsen, M. B.; Roessler, A.; Zimmerman, P.; Boydston, A. J. Mechanochemical Release of N-heterocyclic Carbenes from Flex-Activated Mechanophores. *Angew. Chem. Int. Ed.* **2021**, *60*, 13559–13563.

(16) Nijem, S.; Song, Y.; Schwarz, R.; Diesendruck, C. E. Flex-activated CO Mechanochemical Production for Mechanical Damage Detection. *Polym. Chem.* **2022**, DOI: 10.1039/D2PY00503D.

(17) Huo, S.; Zhao, P.; Shi, Z.; Zou, M.; Yang, X.; Warszawik, E.; Loznik, M.; Göstl, R.; Herrmann, A. Mechanochemical bond scission for the activation of drugs. *Nat. Chem.* **2021**, *13*, 131–139.

(18) Shi, Z.; Song, Q.; Göstl, R.; Herrmann, A. Mechanochemical activation of disulfide-based multifunctional polymers for theranostic drug release. *Chem. Sci.* **2021**, *12*, 1668–1674.

(19) Shi, Z.; Song, Q.; G, östl R.; Herrmann, A. The Mechanochemical Release of Naphthalimide Fluorophores from β-Carbonate and β-Carbamate Disulfide-Centered Polymers. *CCS Chemistry* **2021**, *3*, 2333–2344.

(20) Hu, X.; Zeng, T.; Husic, C. C.; Robb, M. J. Mechanically Triggered Small Molecule Release from a Masked Furfuryl Carbonate. *J. Am. Chem. Soc.* **2019**, *141*, 15018–15023.

(21) Fan, B.; Trant, J. F.; Hemery, G.; Sandre, O.; Gillies, E. R. Thermo-responsive self-immolative nanoassemblies: direct and indirect triggering. *Chem. Commun.* **2017**, *53*, 12068–12071.

(22) Taimoory, S. M.; Sadraei, S. I.; Fayoumi, R. A.; Nasri, S.; Revington, M.; Trant, J. F. Preparation and Characterization of a Small Library of Thermally-Labile End-Caps for Variable-Temperature Triggering of Self-Immolative Polymers. *J. Org. Chem.* **2018**, *83*, 4427–4440.

(23) Hu, X.; Zeng, T.; Husic, C. C.; Robb, M. J. Mechanically Triggered Release of Functionally Diverse Molecular Payloads from Masked 2-Furylcarbinol Derivatives. *ACS Cent. Sci.* **2021**, *7*, 1216–1224.

(24) Zeng, T.; Hu, X.; Robb, M. J. 5-Aryloxy substitution enables efficient mechanically triggered release from a synthetically accessible masked 2-furylcarbinol mechanophore. *Chem. Commun.* **2021**, *57*, 11173–11176.

(25) Nichol, M. F.; Clark, K. D.; Dolinski, N. D.; Alaniz, J. R. de. Multi-stimuli responsive trigger for temporally controlled depolymerization of self-immolative polymers. *Polym. Chem.* **2019**, *10*, 4914–4919.

(26) Beyer, M. K. The mechanical strength of a covalent bond calculated by density functional theory. *J. Chem. Phys.* **2000**, *112*, 7307–7312.

(27) Klein, I. M.; Husic, C. C.; Kovács, D. P.; Choquette, N. J.; Robb, M. J. Validation of the CoGEF Method as a Predictive Tool for Polymer Mechanochemistry. *J. Am. Chem. Soc.* **2020**, *142*, 16364–16381.

(28) Stevenson, R.; De Bo, G. Controlling Reactivity by Geometry in Retro-Diels–Alder Reactions under Tension. *J. Am. Chem. Soc.* **2017**, *139*, 16768–16771.

(29) Zheng, X.-A.; Kong, R.; Huang, H.-S.; Wei, J.-Y.; Chen, J.-Z.; Gong, S.-S.; Sun, Q. Hafnium Triflate as a Highly Potent Catalyst for Regio- and Chemoselective-Deprotection of Silyl Ethers. *Synthesis* **2019**, *51*, 944–952.

(30) May, P. A.; Moore, J. S. Polymer mechanochemistry: techniques to generate molecular force via elongational flows. *Chem. Soc. Rev.* **2013**, *42*, 7497–7506.

(31) Nguyen, N. H.; Rosen, B. M.; Lligadas, G.; Percec, V. Surface-Dependent Kinetics of Cu(0)-Wire-Catalyzed Single-Electron Transfer Living Radical Polymerization of Methyl Acrylate in DMSO at 25 °C. *Macromolecules* **2009**, *42*, 2379–2386.

(32) Bunce, R. A.; Hertzler, D. V. A selective method for oxygen deprotection in bistrimethylsilylated terminal alkynols. *J. Org. Chem.* **1986**, *51*, 3451–3453.

(33) Asano, K.; Matsubara, S. Asymmetric Catalytic Cycloetherification Mediated by Bifunctional Organocatalysts. *J. Am. Chem. Soc.* **2011**, *133*, 16711–16713.

(34) Heo, Y.; Sodano, H. A. Self-Healing Polyurethanes with Shape Recovery. *Advanced Functional Materials* **2014**, *24*, 5261–5268.

(35) Deng, G.; Chen, Y. A Novel Way To Synthesize Star Polymers in One Pot by ATRP of *N* -[2-(2-Bromoisobutyryloxy)ethyl]maleimide and Styrene. *Macromolecules* **2004**, *37*, 18–26.

(36) Beyer, M. K. The mechanical strength of a covalent bond calculated by density functional theory. *J. Chem. Phys.* **2000**, *112*, 7307–7312.

(37) Klein, I. M.; Husic, C. C.; Kovács, D. P.; Choquette, N. J.; Robb, M. J. Validation of the CoGEF Method as a Predictive Tool for Polymer Mechanochemistry. *J. Am. Chem. Soc.* **2020**, *142*, 16364–16381.

Appendix A

SUMMARIES OF INDIVIDUAL CoGEF CALCULATIONS PRESENTED IN CHAPTER 1

A summary of the results of each individual CoGEF calculation from Chapter 1 is presented on the pages below. All calculations were performed using DFT at the B3LYP/6-31G* level of theory in vacuum, unless specified otherwise. A reaction scheme depicts the structure of the truncated molecule and the product(s) predicted from the CoGEF calculation. Atoms colored blue indicate the anchor positions (i.e., pulling points) for defining the distance constraint and bonds that are predicted to cleave are colored red. Representative images of computed structures at critical points in the CoGEF profile are included that depict the force-free equilibrium geometry as well as the structure(s) immediately before and after bond cleavage events. The length of the distance constraint is included below each computed structure and the corresponding positions on the CoGEF curve are denoted. Electrostatic potential maps are included for the products predicted by CoGEF calculations in the heterolytic category. The calculated values of F_{max}, E_{max}, and force–bond angle are tabulated for each calculation. Note that the former bonds persist as artifacts in Spartan after a reaction is predicted to occur. For references to the primary literature describing the experimental reactivity of each compound, refer to the tables in Chapter 1.

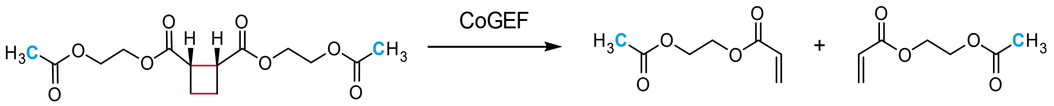

1

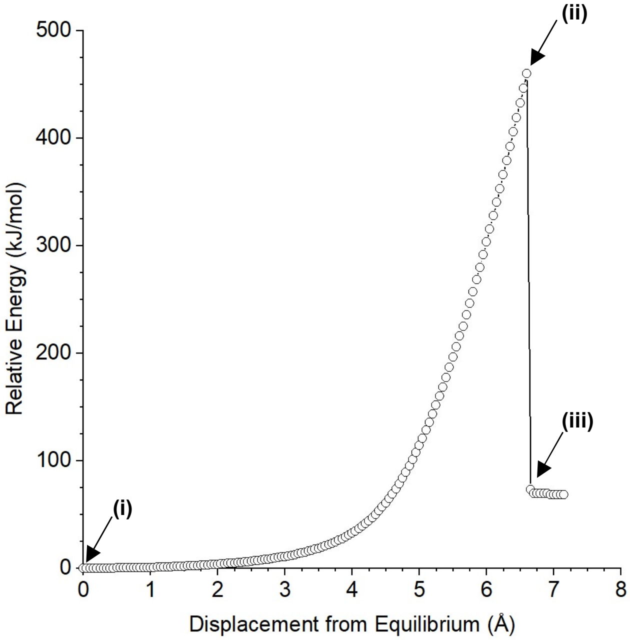

(i) Equilibrium Geometry

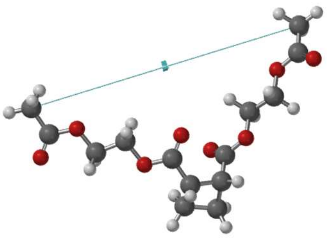

13.344 Å

(ii) Immediately Prior to Bond Cleavage

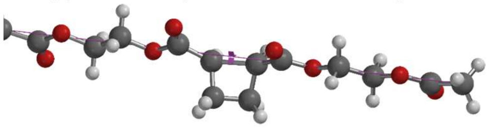

20.294 Å

(iii) Immediately After Bond Cleavage

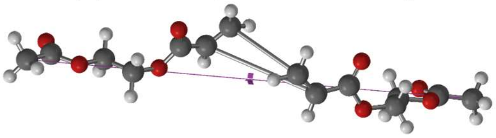

20.344 Å

Summary of CoGEF Results	
F	

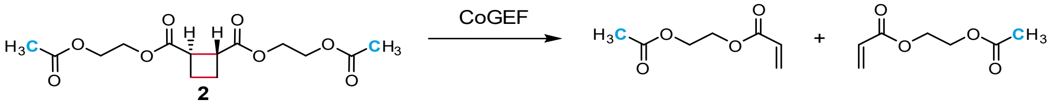

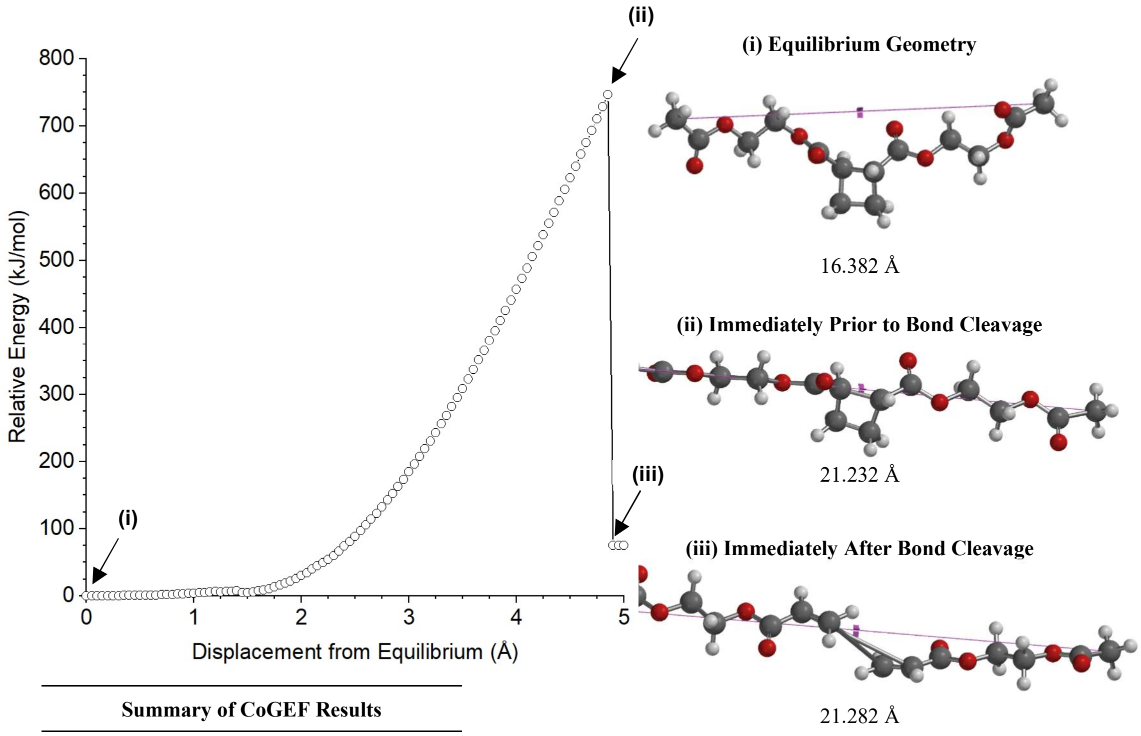

Summary of CoGEF Results	
F_{max}	5.9 nN
E_{max}	746 kJ/mol
Force-Bond Angle	25°

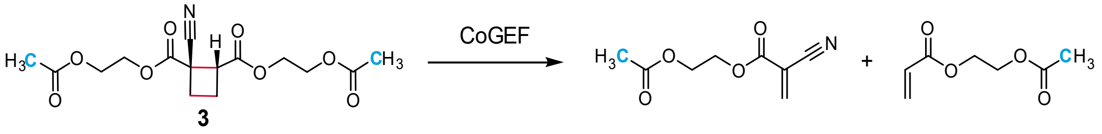

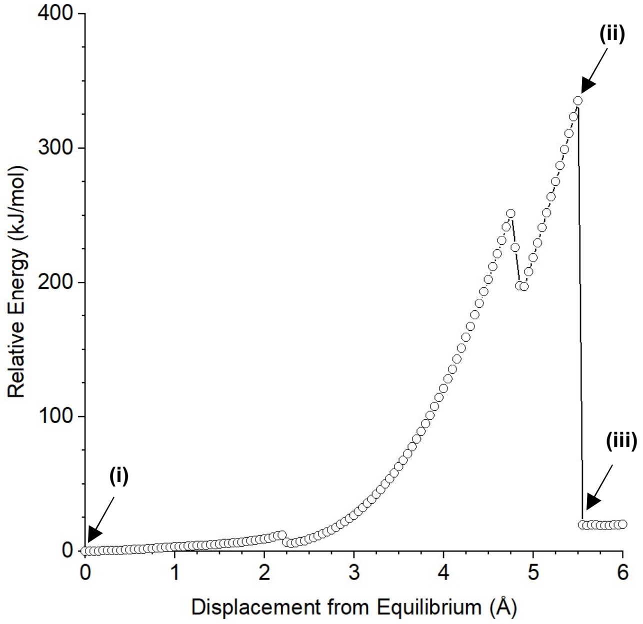

(i) Equilibrium Geometry

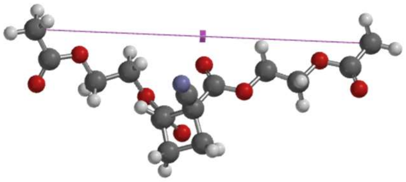

14.479 Å

(ii) Immediately Prior to Bond Cleavage

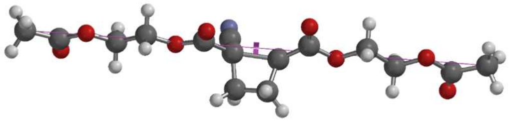

19.979 Å

(iii) Immediately After Bond Cleavage

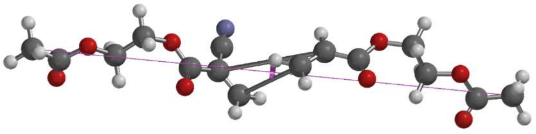

20.029 Å

Summary of CoGEF Results	
F_{max}	4.0 nN
E_{max}	335 kJ/mol
Force-Bond Angle	7.1°

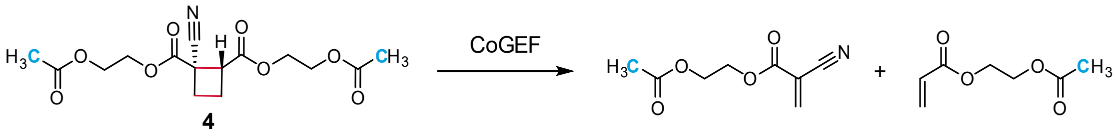

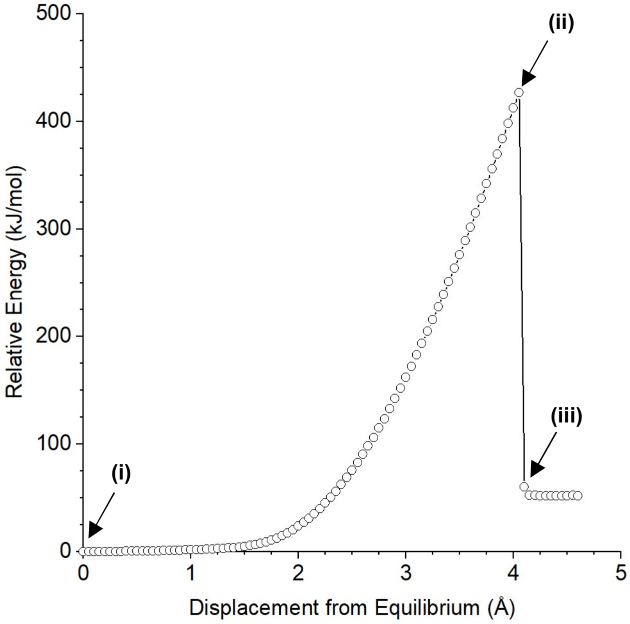

Summary of CoGEF Results

F_{max}	4.8 nN
E_{max}	426 kJ/mol
Force-Bond Angle	20°

(i) Equilibrium Geometry

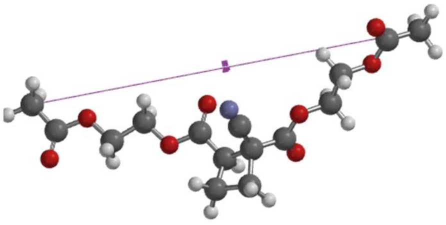

16.271 Å

(ii) Immediately Prior to Bond Cleavage

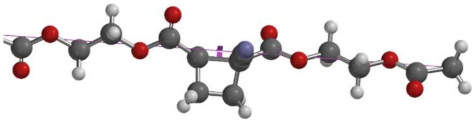

20.321 Å

(iii) Immediately After Bond Cleavage

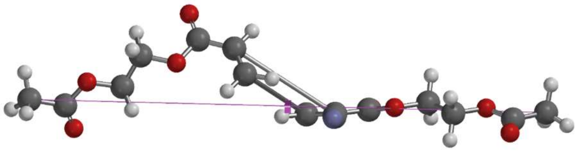

20.371 Å

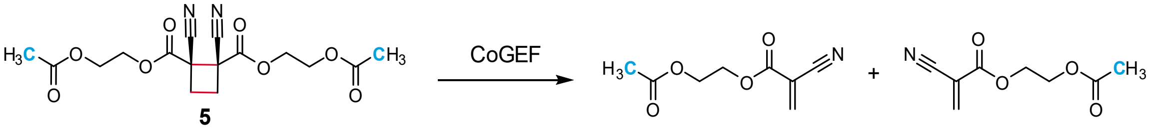

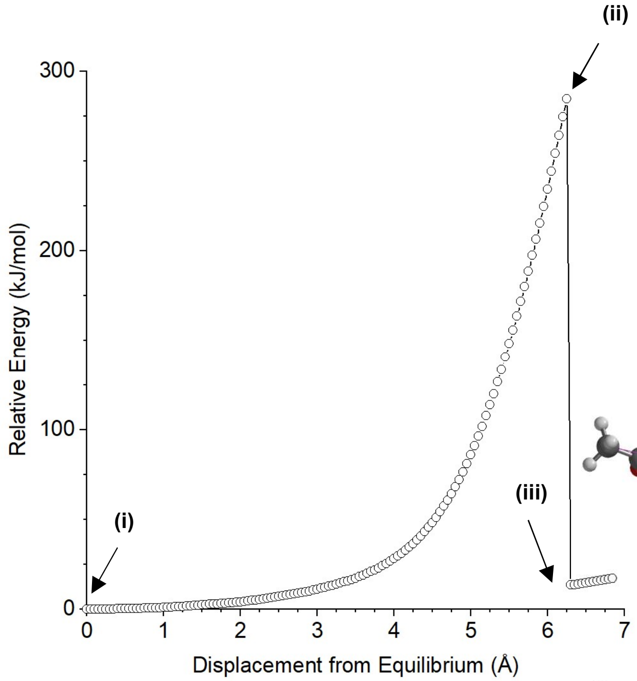

(i) Equilibrium Geometry

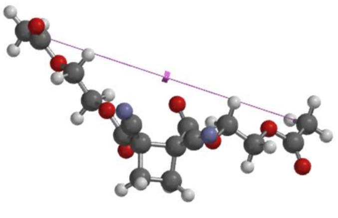

13.303 Å

(ii) Immediately Prior to Bond Cleavage

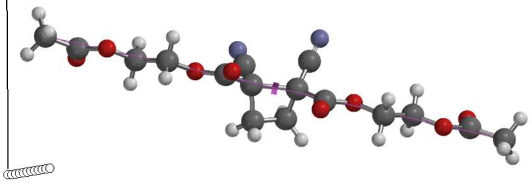

19.553 Å

(iii) Immediately After Bond Cleavage

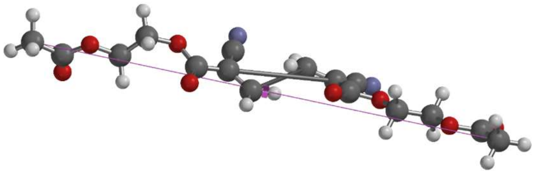

19.603 Å

Summary of CoGEF Results	
***F**$_{max}$*	3.4 nN
***E**$_{max}$*	285 kJ/mol
Force-Bond angle	7.3°

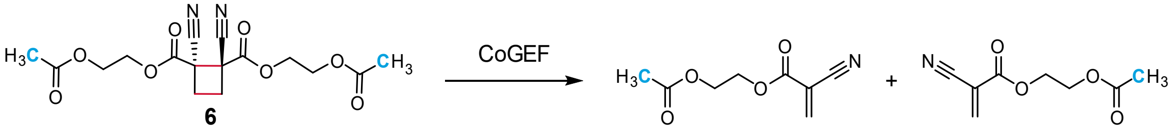

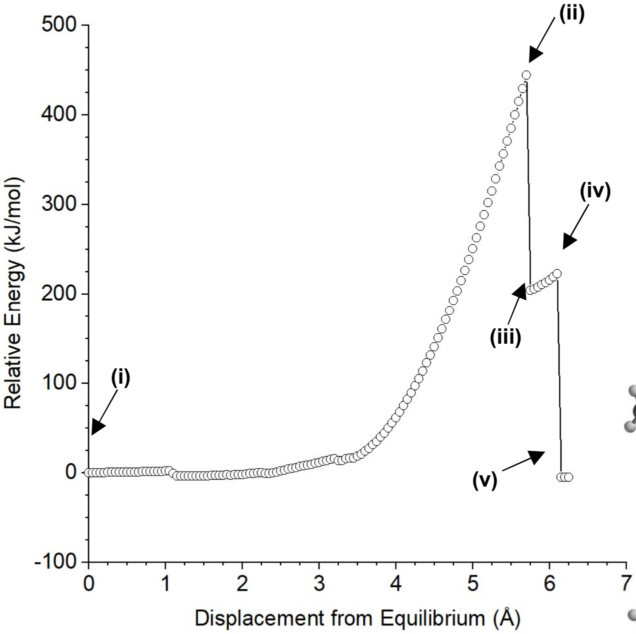

Summary of CoGEF Results	
F_{max}	5.0 nN
E_{max}	444 kJ/mol
Force-Bond Angle	27°

(i) Equilibrium Geometry

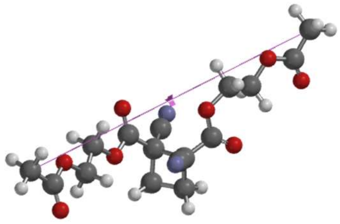

14.667 Å

(ii) Immediately Prior to First Bond Cleavage

20.417 Å

(iii) Immediately After First Bond Cleavage

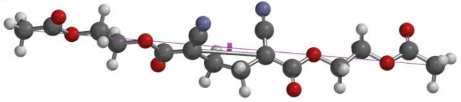

20.467 Å

(iv) Immediately Prior to Second Bond Cleavage

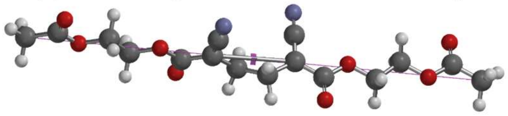

20.817

(iv) Immediately After Second Bond Cleavage

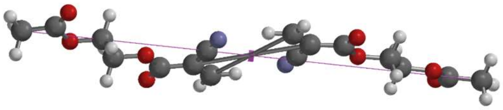

20.867 Å

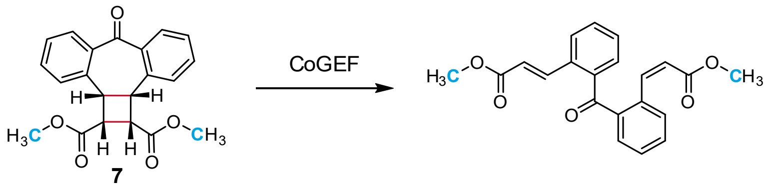

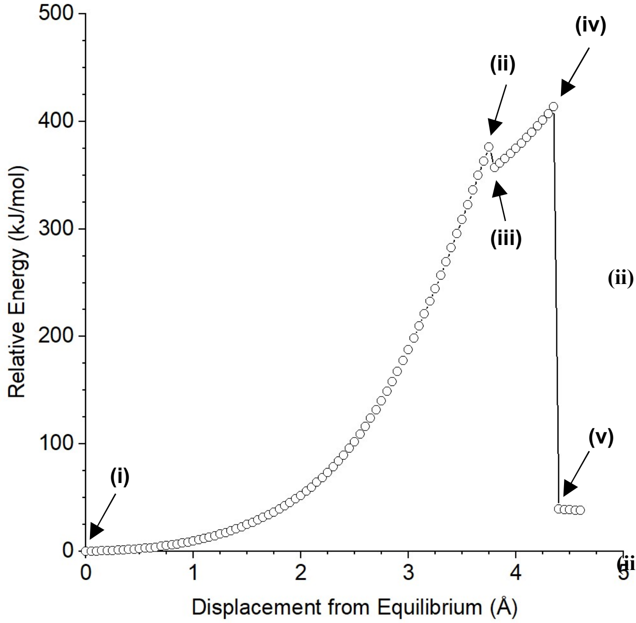

Summary of CoGEF Results	
F_{max}	4.5 nN
E_{max}	413 kJ/mol
Force-Bond Angle	4.3°

(i) Equilibrium Geometry

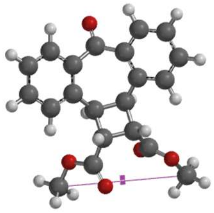

6.295 Å

(ii) Immediately Prior to First Bond Cleavage

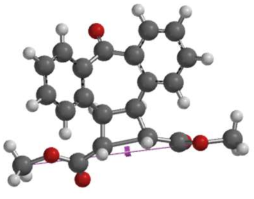

10.045 Å

(iii) Immediately After First Bond Cleavage

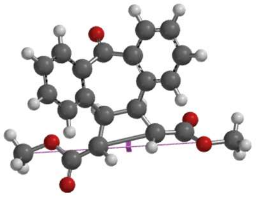

10.095 Å

(iv) Immediately Before Second Bond Cleavage

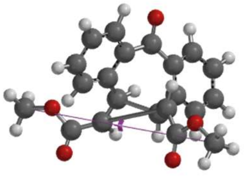

10.645 Å

(v) Immediately After Second Bond Cleavage

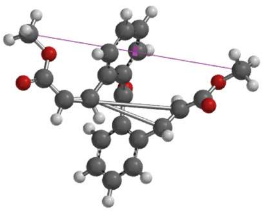

10.695 Å

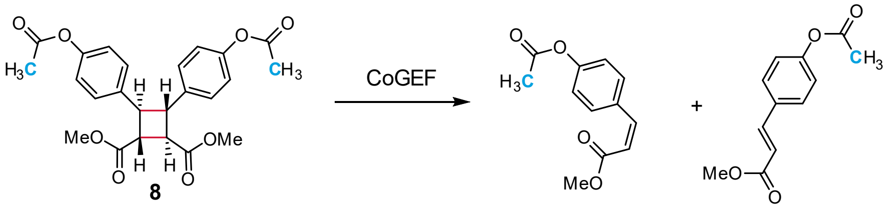

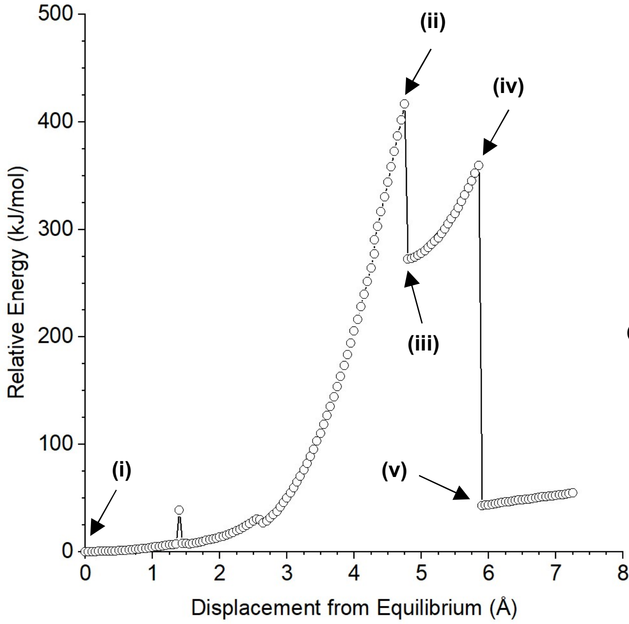

Summary of CoGEF Results

F_{max}	5.0 nN
E_{max}	417 kJ/mol
Force-Bond Angle	30°

(i) Equilibrium Geometry

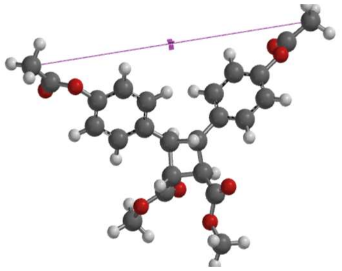

14.256 Å

(ii) Immediately Prior to First Bond Cleavage

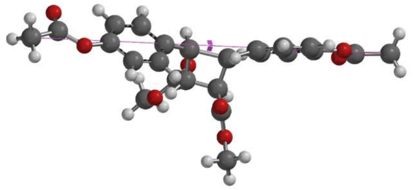

19.006 Å

(iii) Immediately After First Bond Cleavage

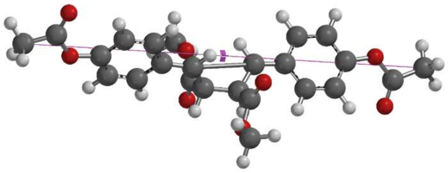

19.056 Å

(iv) Immediately Prior to Second Bond Cleavage

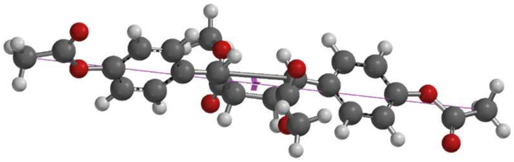

20.106

(v) Immediately After Second Bond Cleavage

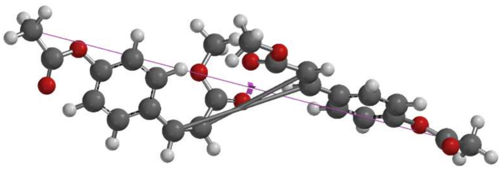

20.156 Å

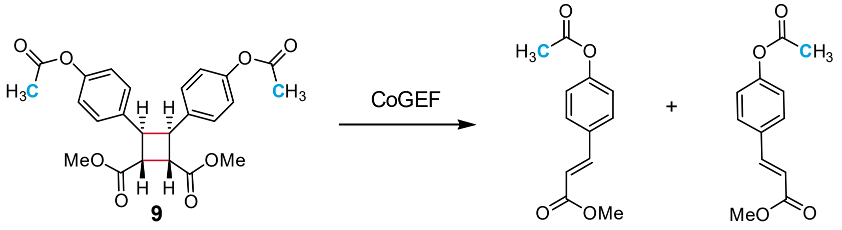

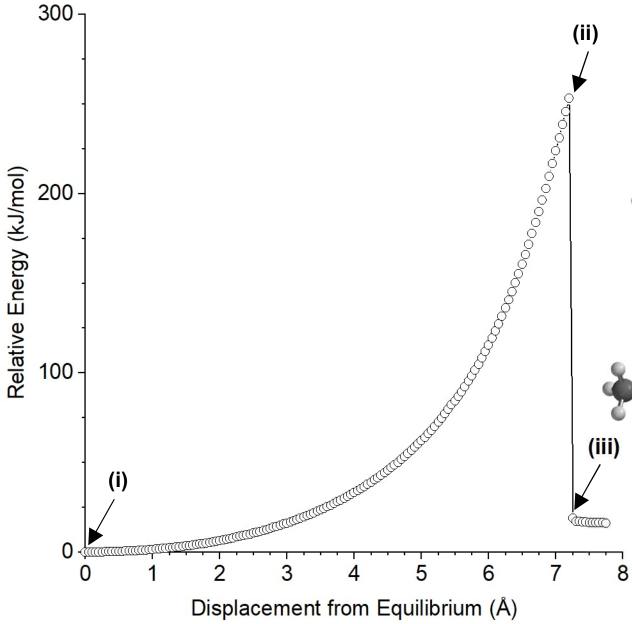

Summary of CoGEF Results

***F**$_{max}$*	2.5 nN
***E**$_{max}$*	253 kJ/mol
Force-Bond Angle	6.9°

(i) Equilibrium Geometry

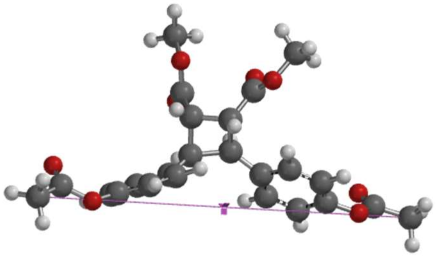

10.962 Å

(ii) Immediately Prior to First Bond Cleavage

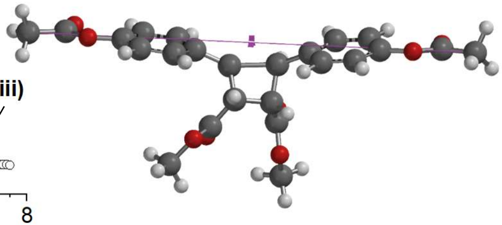

18.162 Å

(iii) Immediately After First Bond Cleavage

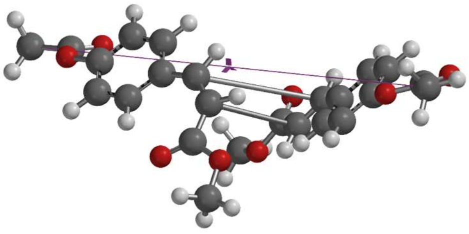

18.212 Å

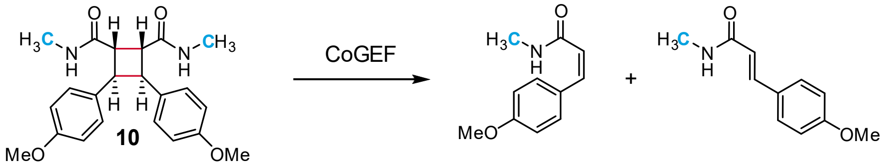

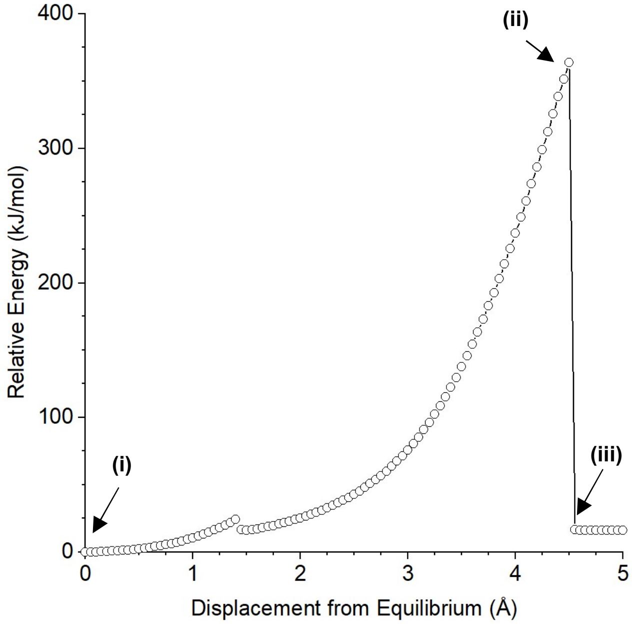

Summary of CoGEF Results

F_{max}	4.4 nN
E_{max}	364 kJ/mol
Force-Bond Angle	2.7°

(i) Equilibrium Geometry

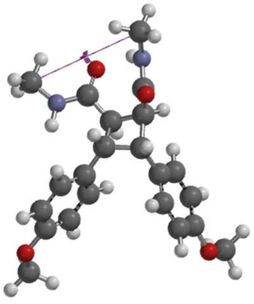

5.759 Å

(ii) Immediately Prior to First Bond Cleavage

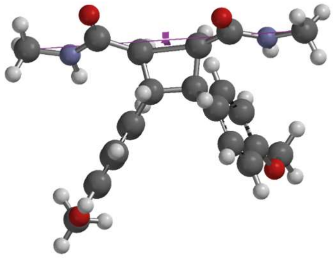

10.259 Å

(iii) Immediately After First Bond Cleavage

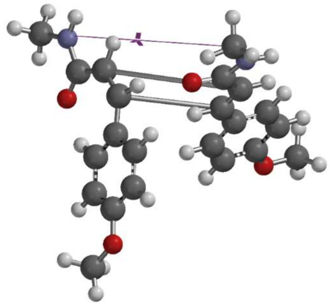

10.309 Å

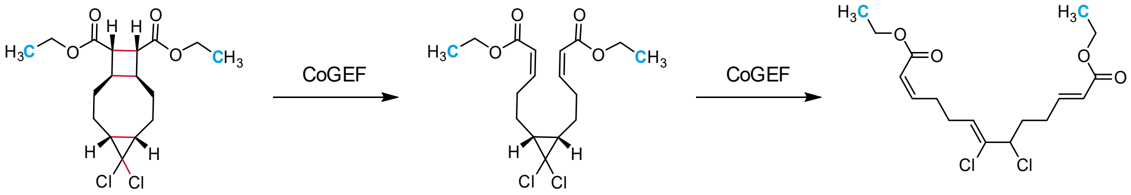

11

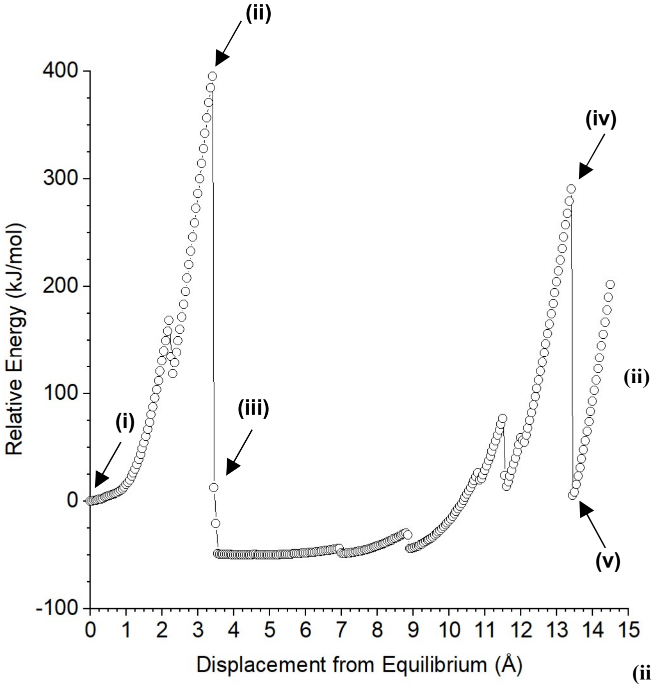

(i) Equilibrium Geometry

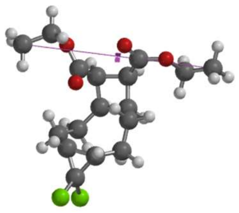

9.485 Å

(ii) Immediately Prior to First Bond Cleavage

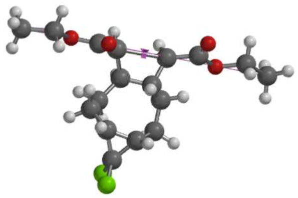

12.885 Å

(iii) Immediately After First Bond Cleavage

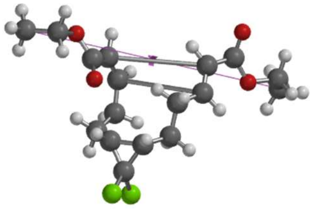

12.935 Å

(iv) Immediately Before Second Bond Cleavage

22.885 Å

(v) Immediately After Second Bond Cleavage

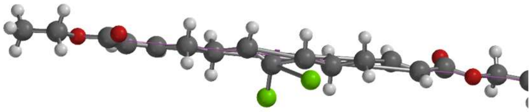

22.935 Å

Summary of CoGEF Results

	cyclobutane	*g*DCC
F_{max}	4.7 nN	3.8 nN
E_{max}	395 kJ/mol	291 kJ/mol
Force-Bond Angle	2.1°	0.4°

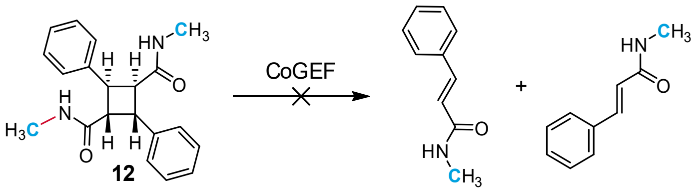

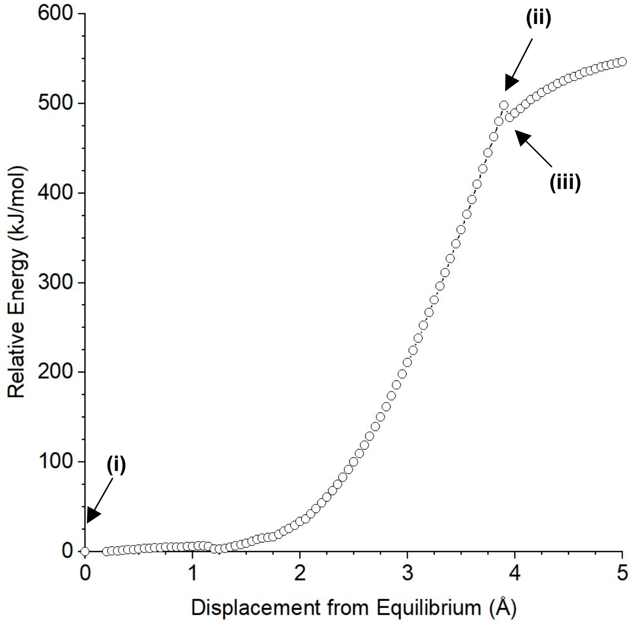

Summary of CoGEF Results

F_{max}	5.9 nN
E_{max}	498 kJ/mol
Force-Bond Angle	44°

(i) Equilibrium Geometry

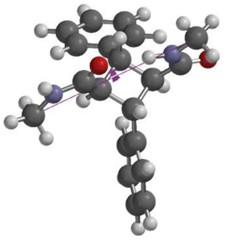

7.497 Å

(ii) Immediately Prior to Bond Cleavage

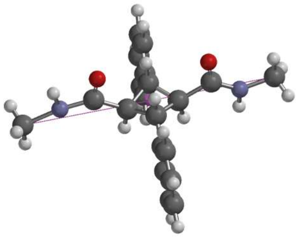

11.397 Å

(iii) Immediately After Bond Cleavage

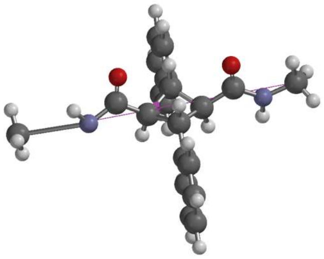

11.5447 Å

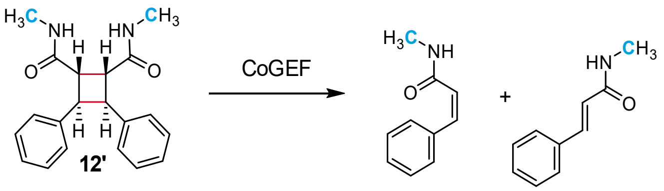

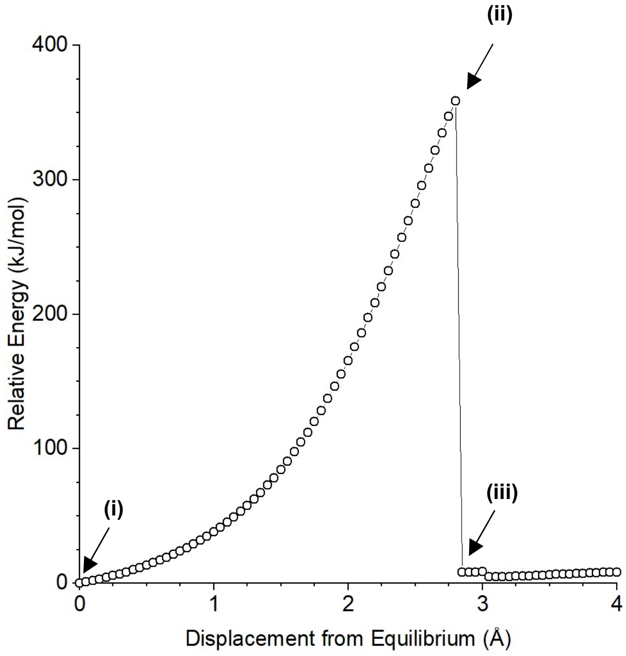

Summary of CoGEF Results	
***F**$_{max}$*	4.4 nN
***E**$_{max}$*	359 kJ/mol
Force-Bond Angle	2.2°

(i) Equilibrium Geometry

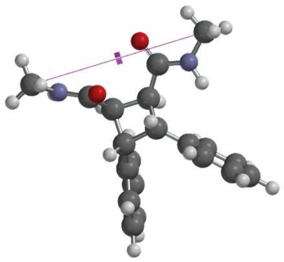

7.519 Å

(ii) Immediately Prior to Bond Cleavage

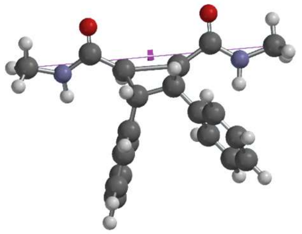

10.319 Å

(iii) Immediately After Bond Cleavage

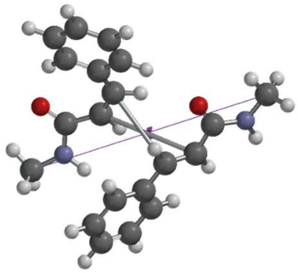

10.369 Å

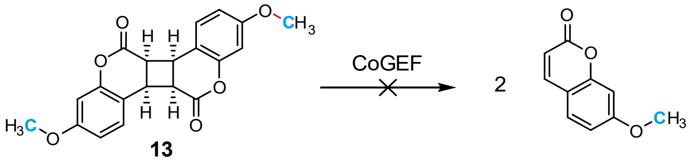

13

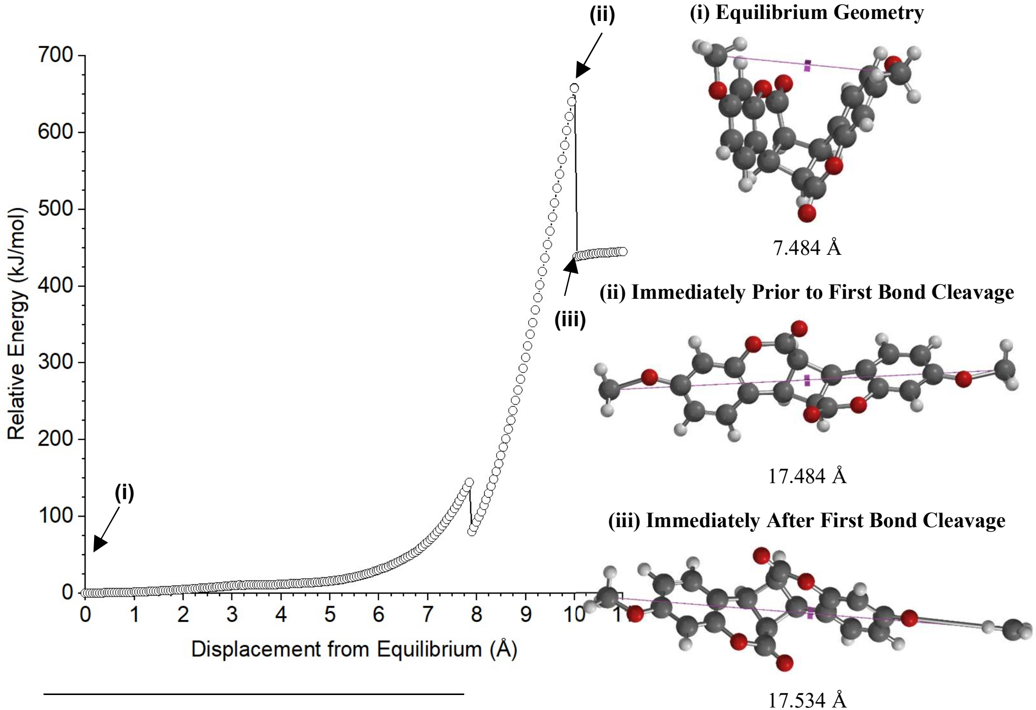

Summary of CoGEF Results	
F	

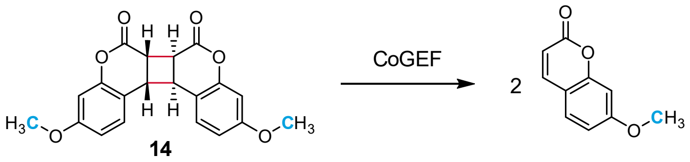

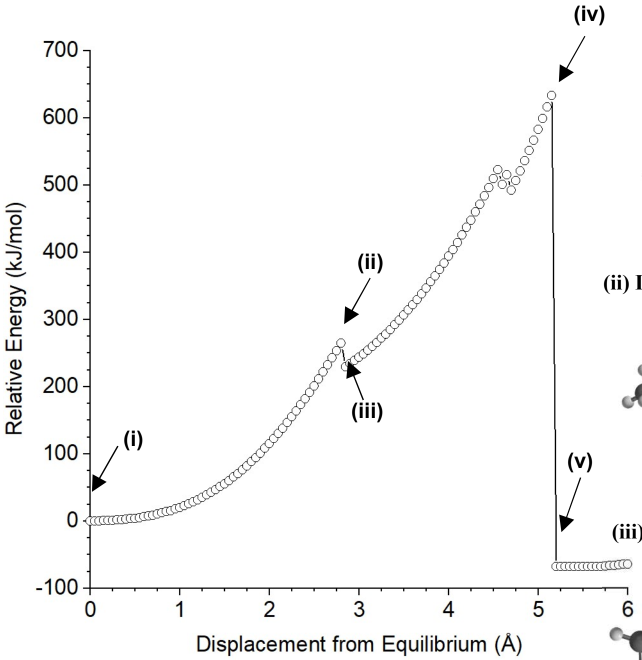

Summary of CoGEF Results	
***F**_{max}*	5.6 nN
***E**_{max}*	633 kJ/mol
Force-Bond Angle	26°

(i) Equilibrium Geometry

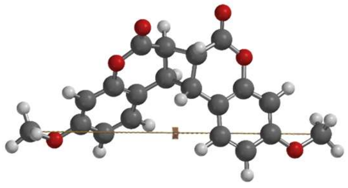

13.066 Å

(ii) Immediately Prior to First Bond Cleavage

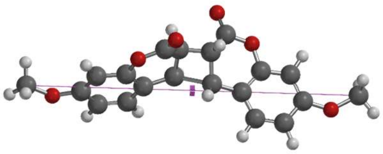

15.866 Å

(iii) Immediately After First Bond Cleavage

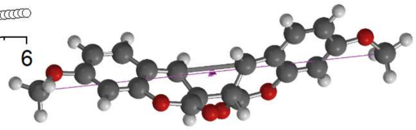

15.916 Å

(iv) Immediately Before Second Bond Cleavage

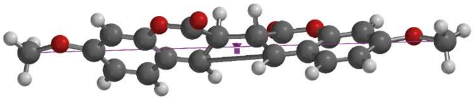

18.216 Å

(v) Immediately After Second Bond Cleavage

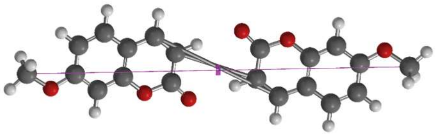

18.266 Å

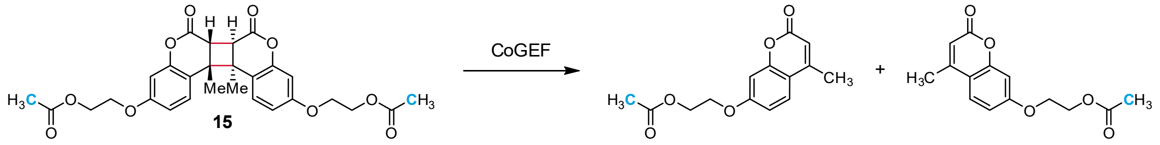

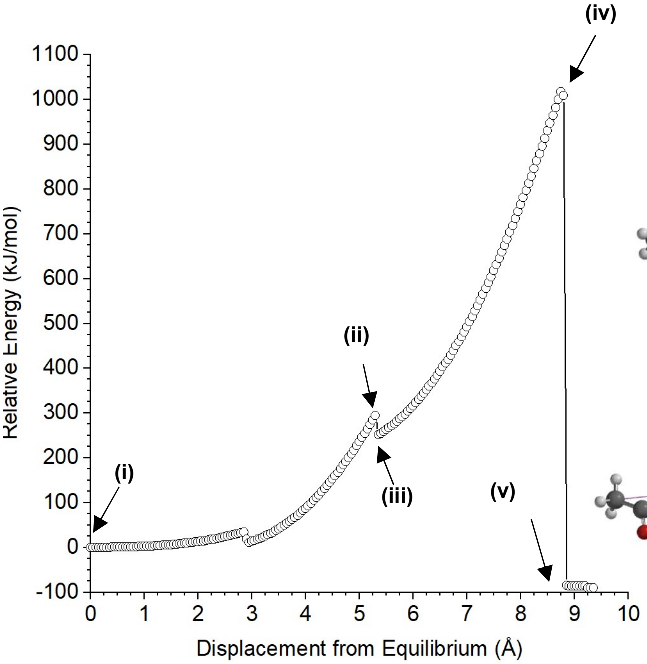

Summary of CoGEF Results	
F F_{max}	5.9 nN
E_{max}	1017 kJ/mol
Force-Bond Angle	29°

(i) Equilibrium Geometry

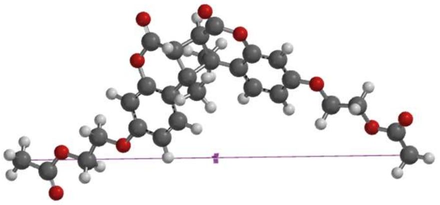

20.607 Å

(ii) Immediately Prior to First Bond Cleavage

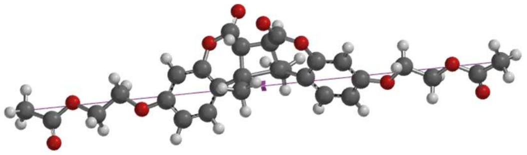

25.907 Å

(iii) Immediately After First Bond Cleavage

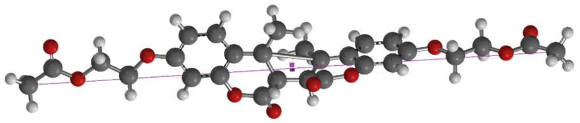

25.957 Å

(iv) Immediately Before Second Bond Cleavage

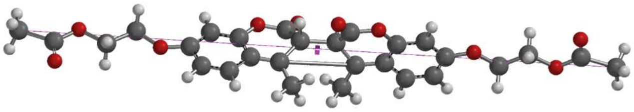

29.407 Å

(v) Immediately After Second Bond Cleavage

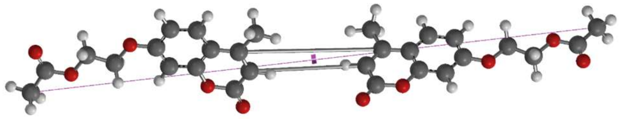

29.457 Å

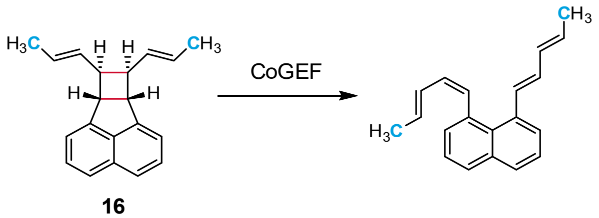

(i) Equilibrium Geometry

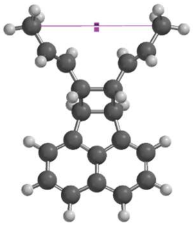

6.366 Å

(ii) Immediately Prior to First Bond Cleavage

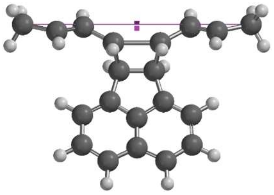

10.066 Å

(iii) Immediately After First Bond Cleavage

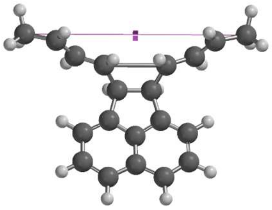

10.116 Å

(v) Immediately Prior to Second Bond Cleavage

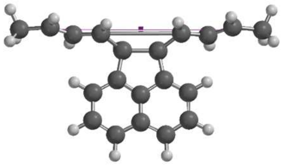

12.216 Å

(vi) Immediately After Second Bond Cleavage

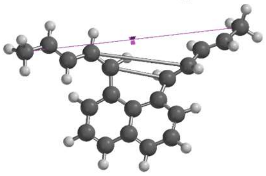

12.266 Å

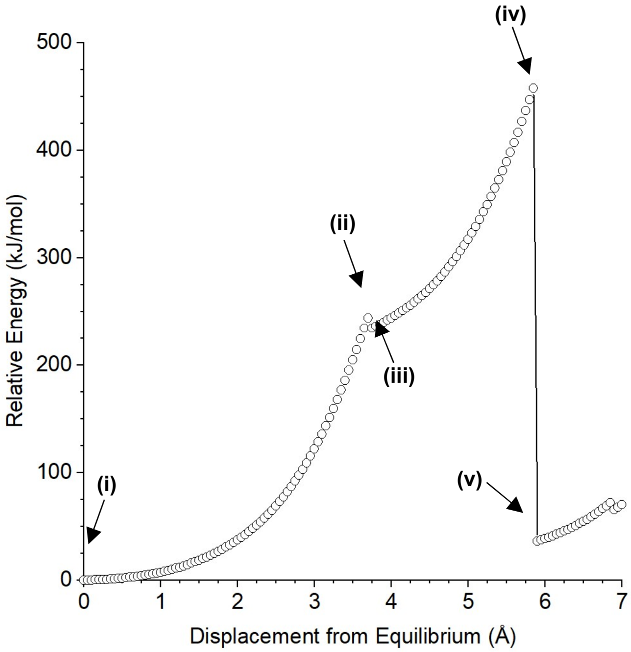

Summary of CoGEF Results	
***F**_{max}*	3.3 nN
***E**_{max}*	244 kJ/mol
Force-Bond Angle	0.0°

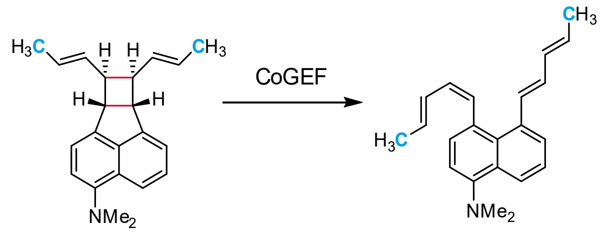

17

(i) Equilibrium Geometry

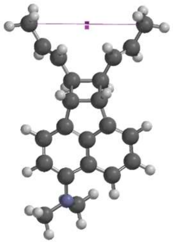

6.351 Å

(ii) Immediately Prior to First Bond Cleavage

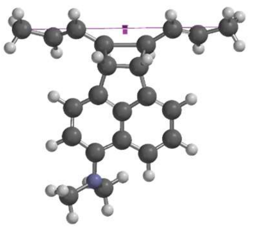

10.051 Å

(iii) Immediately After First Bond Cleavage

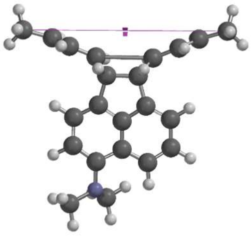

10.101 Å

(v) Immediately Prior to Second Bond Cleavage

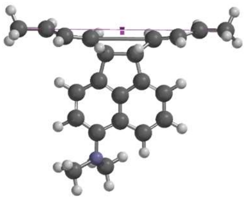

11.351 Å

(vi) Immediately After Second Bond Cleavage

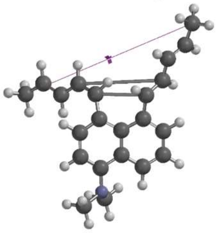

11.401 Å

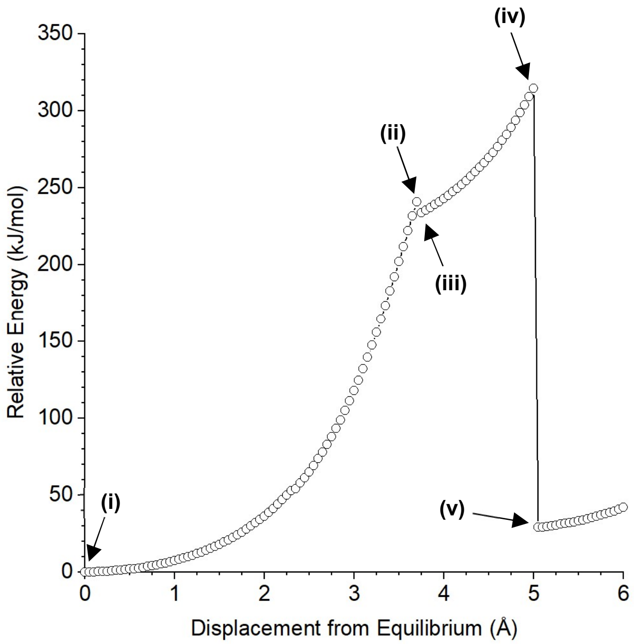

Summary of CoGEF Results	
***F**max*	3.3 nN
***E**max*	241 kJ/mol
Force-Bond Angle	1.0°

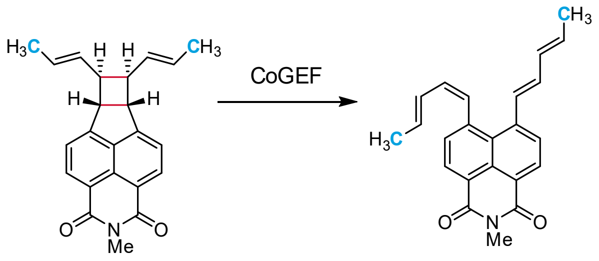

18

(i) Equilibrium Geometry

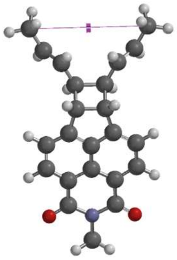

6.319 Å

(ii) Immediately Prior to First Bond Cleavage

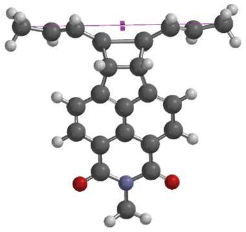

10.069 Å

(iii) Immediately After First Bond Cleavage

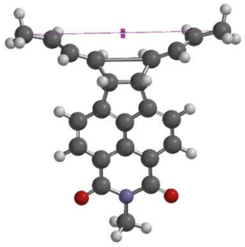

10.119 Å

(v) Immediately Prior to Second Bond Cleavage

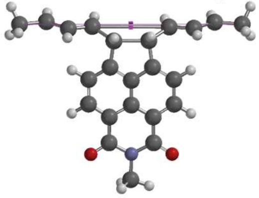

12.569 Å

(vi) Immediately After Second Bond Cleavage

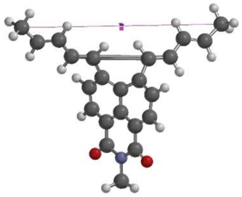

12.619 Å

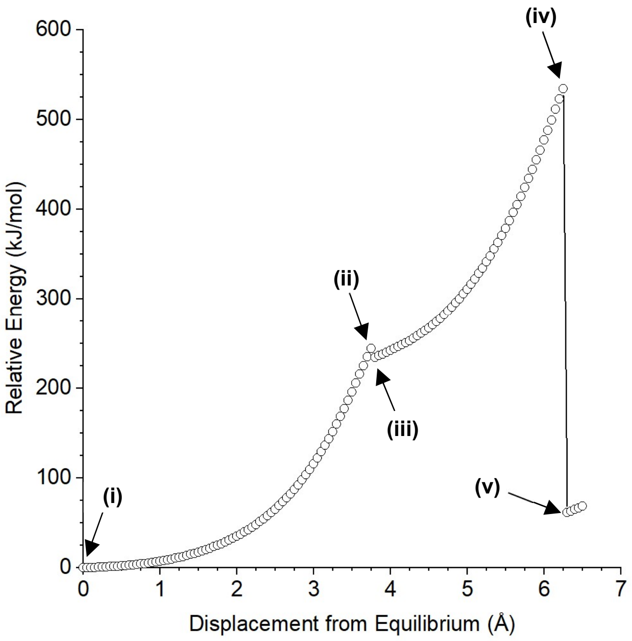

Summary of CoGEF Results	
F	

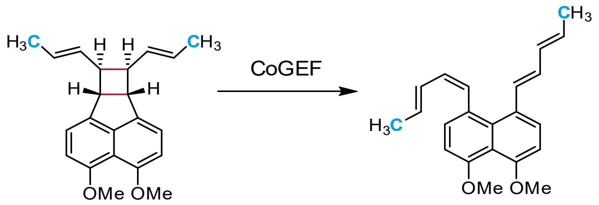

19

(i) Equilibrium Geometry

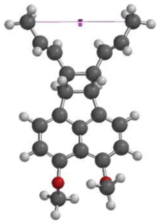

6.325 Å

(ii) Immediately Prior to First Bond Cleavage

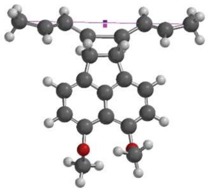

10.025 Å

(iii) Immediately After First Bond Cleavage

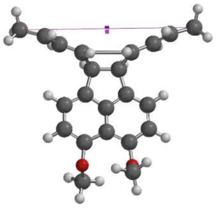

10.075 Å

(v) Immediately Prior to Second Bond Cleavage

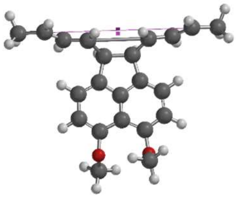

11.325 Å

(vi) Immediately After Second Bond Cleavage

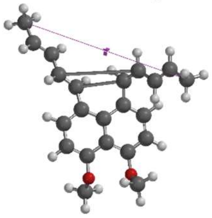

11.375 Å

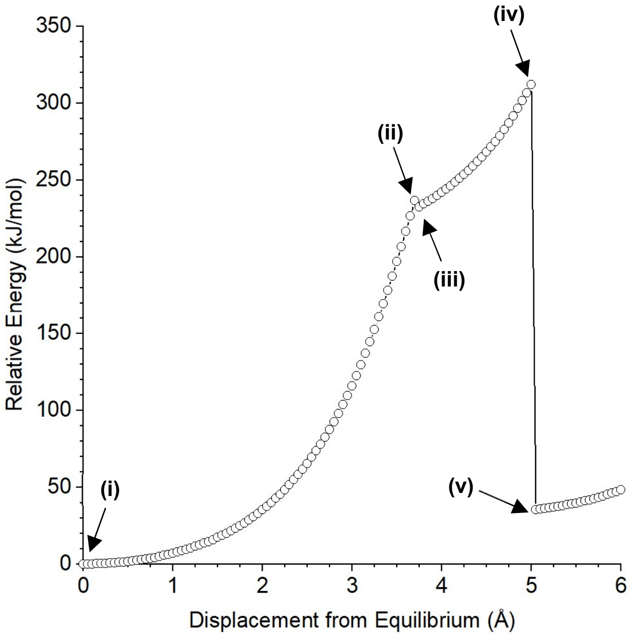

Summary of CoGEF Results

F_{max}	3.3 nN
E_{max}	236 kJ/mol
Force-Bond Angle	1.2°

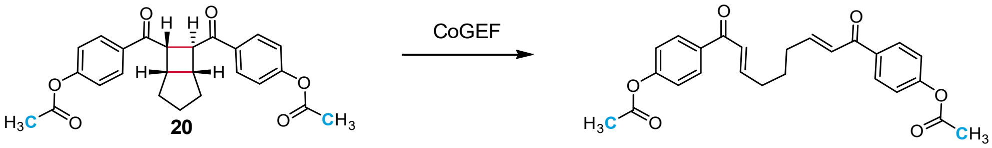

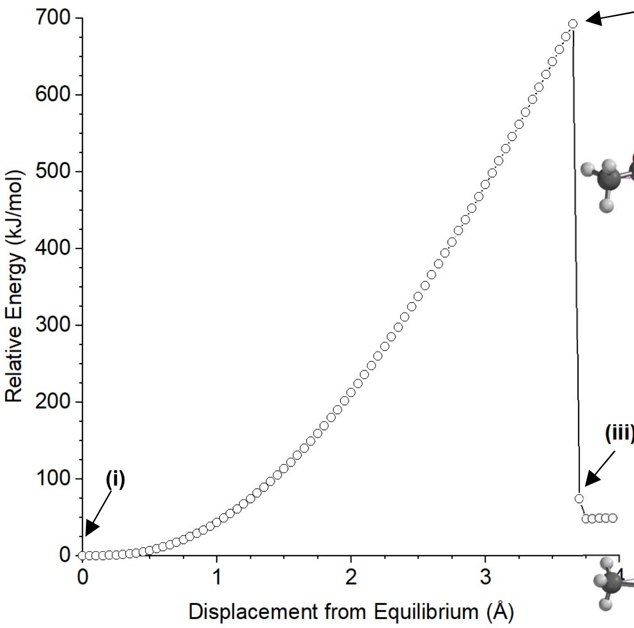

Summary of CoGEF Results	
***F**$_{max}$*	5.5 nN
***E**$_{max}$*	692 kJ/mol
Force-Bond Angle	16°

(i) Equilibrium Geometry

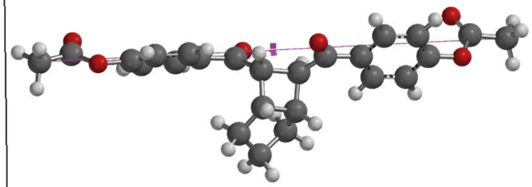

18.900 Å

(i) Immediately Prior to Bond Cleavage

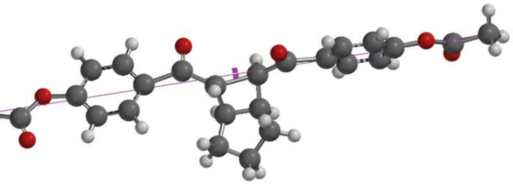

22.550 Å

(iii) Immediately After Bond Cleavage

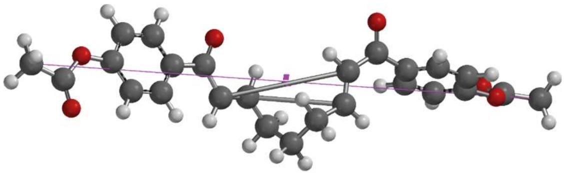

22.600 Å

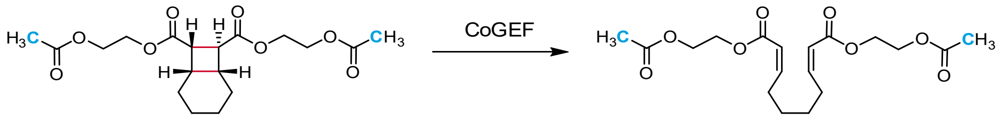

21

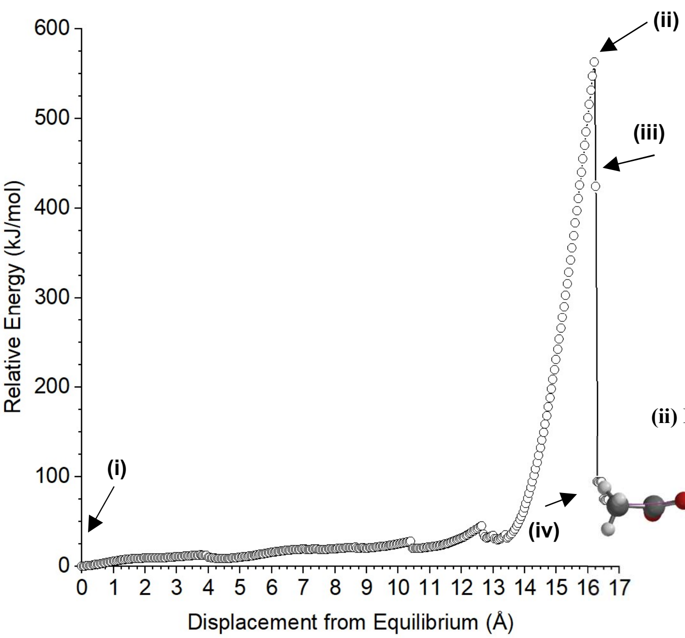

Summary of CoGEF Results	
F_{max}	5.2 nN
E_{max}	562 kJ/mol
Force-Bond Angle	17°

(i) Equilibrium Geometry

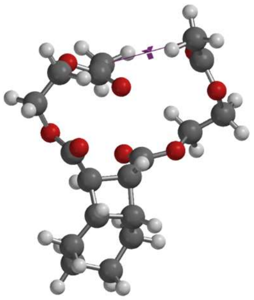

4.462 Å

(ii) Immediately Prior to First Bond Cleavage

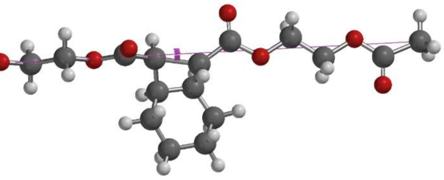

20.662 Å

(iii) Immediately After First Bond Cleavage

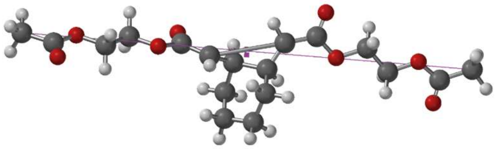

20.712 Å

(iv) Immediately After Second Bond Cleavage

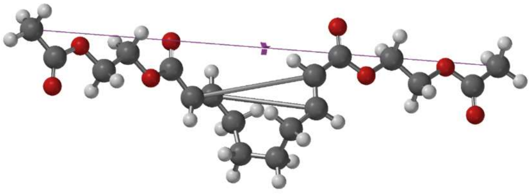

20.762 Å

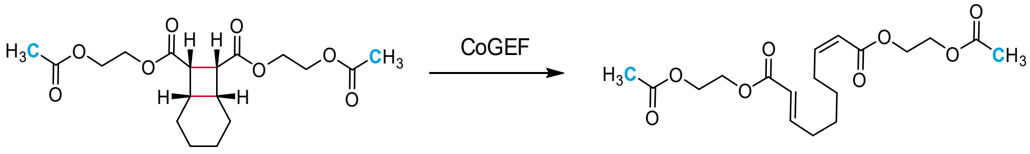

22

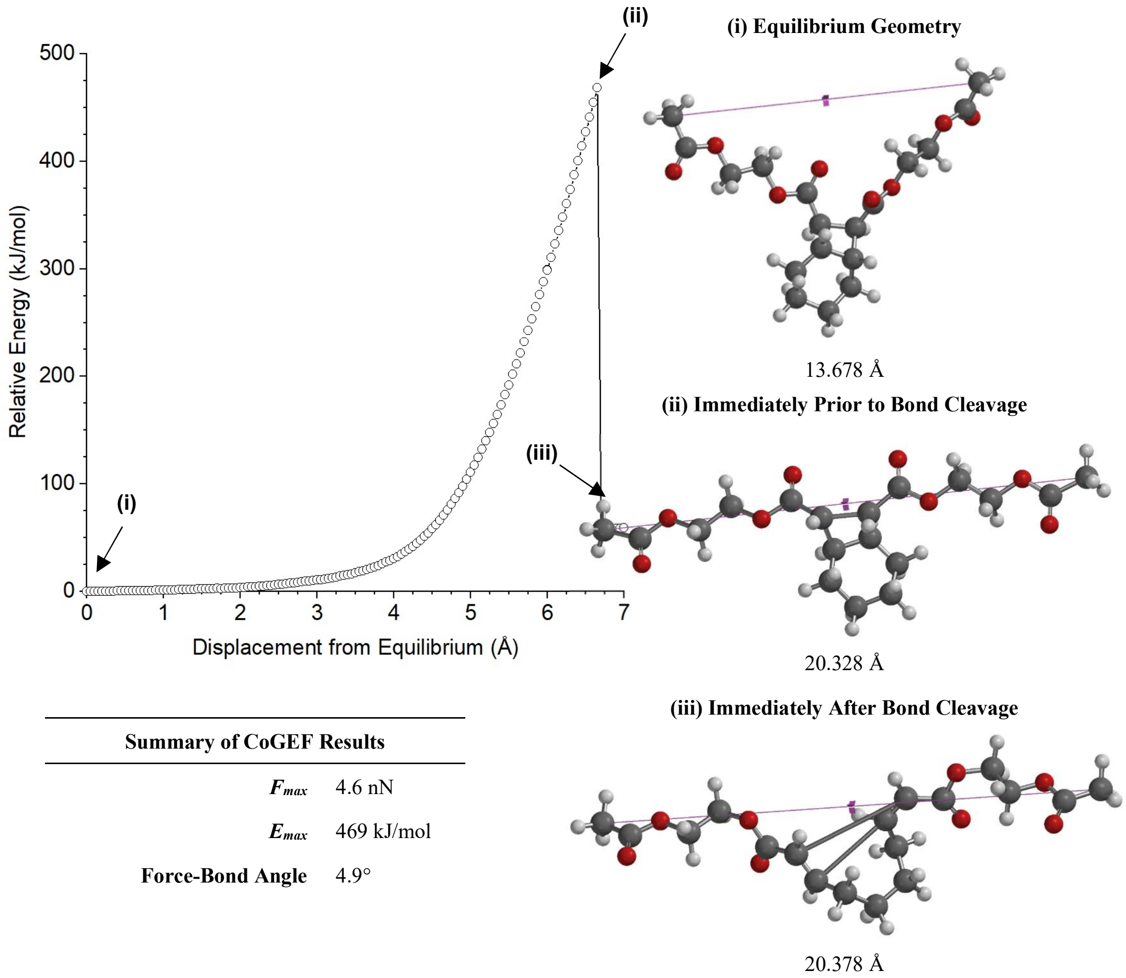

Summary of CoGEF Results	
F_{max}	4.6 nN
E_{max}	469 kJ/mol
Force-Bond Angle	4.9°

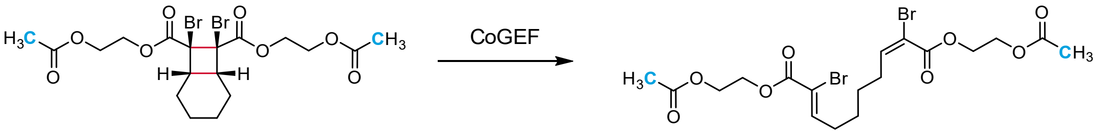

23

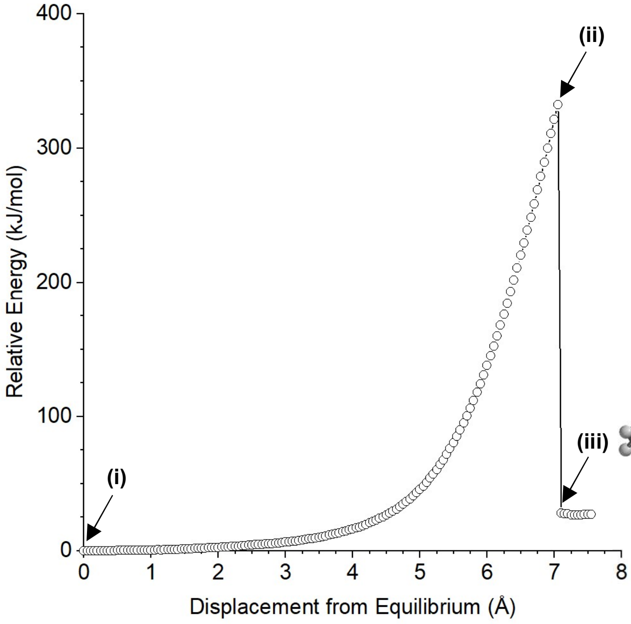

Summary of CoGEF Results	
F_{max}	3.6 nN
E_{max}	332 kJ/mol
Force-Bond Angle	6.2°

(i) Equilibrium Geometry

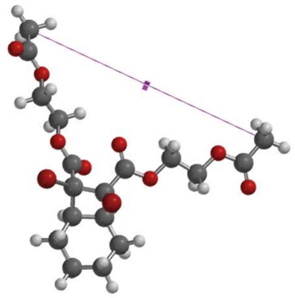

12.604 Å

(ii) Immediately Prior to First Bond Cleavage

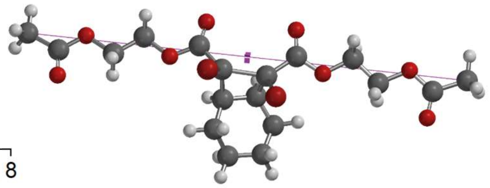

19.654 Å

(iii) Immediately After First Bond Cleavage

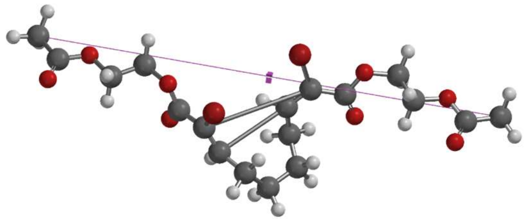

19.704 Å

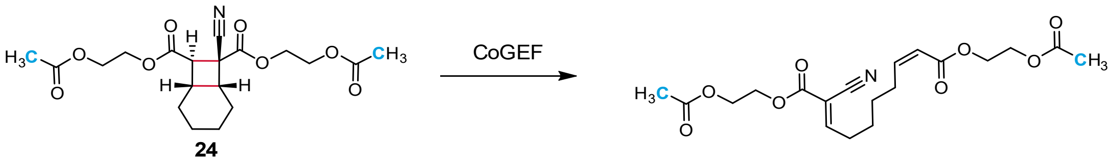

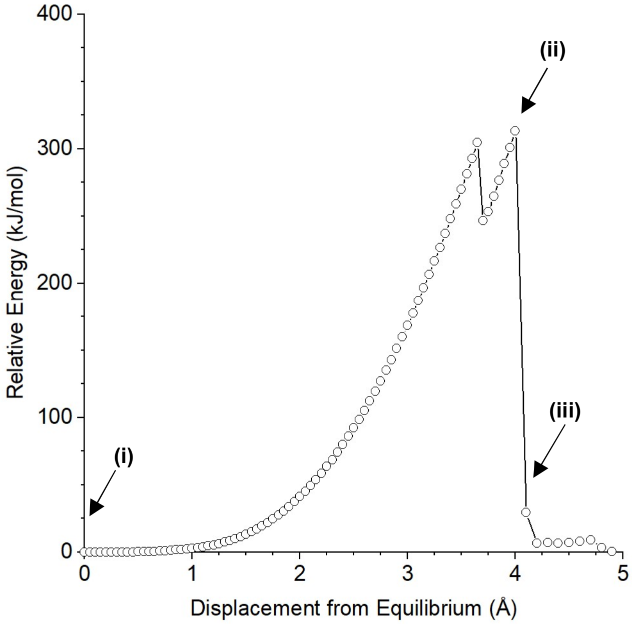

Summary of CoGEF Results	
F_{max}	4.0 nN
E_{max}	313 kJ/mol
Force-Bond Angle	8.5°

(i) Equilibrium Geometry

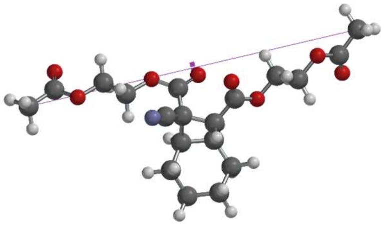

15.909 Å

(ii) Immediately Prior to Bond Cleavage

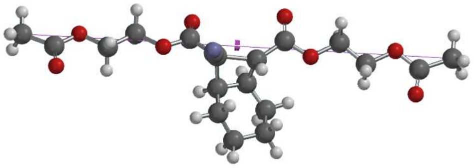

19.909 Å

(iii) Immediately After Bond Cleavage

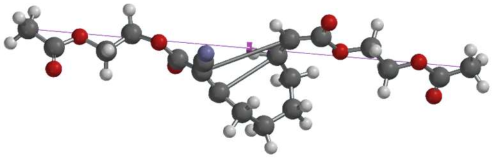

20.009 Å

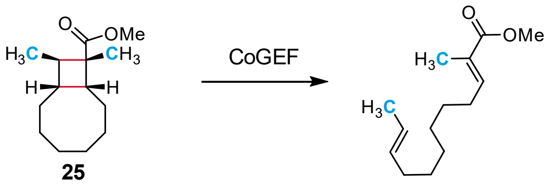

25

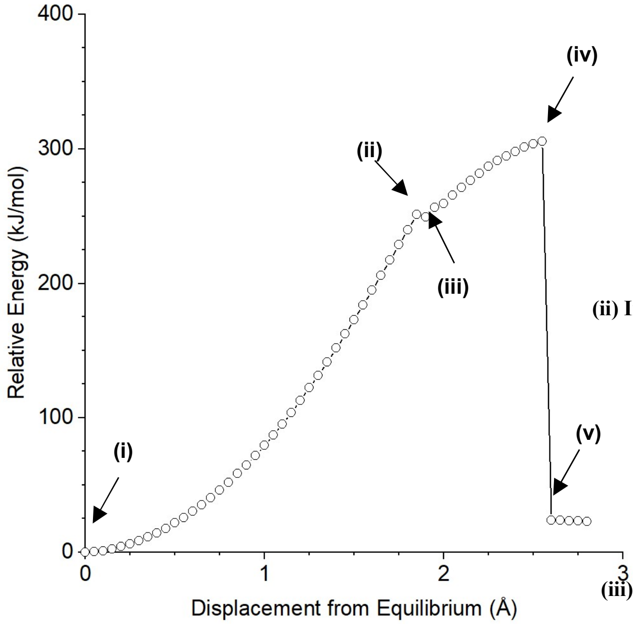

Summary of CoGEF Results	
F	

(i) Equilibrium Geometry

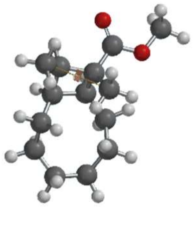

3.052 Å

(ii) Immediately Prior to First Bond Cleavage

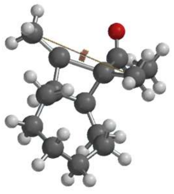

4.902 Å

(iii) Immediately After First Bond Cleavage

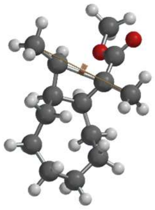

4.952 Å

(iv) Immediately Prior to Second Bond Cleavage

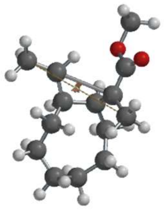

5.552 Å

(v) Immediately After Second Bond Cleavage

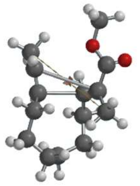

5.602 Å

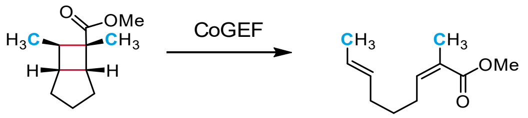

26

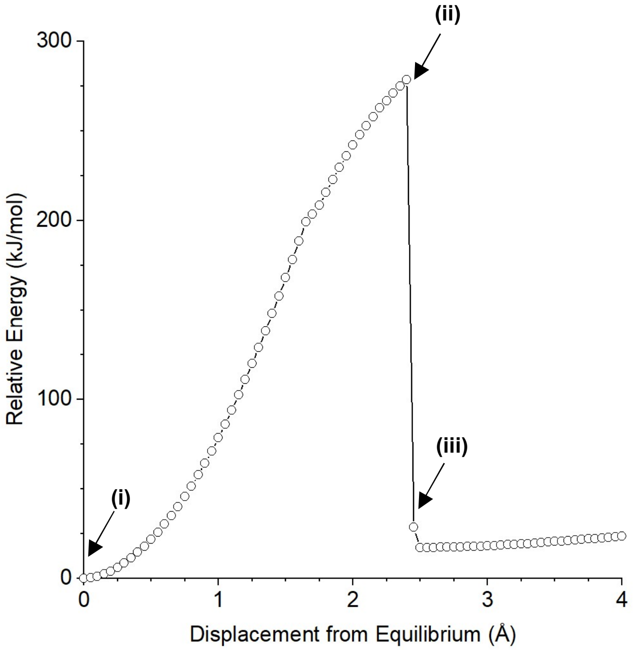

(i) Equilibrium Geometry

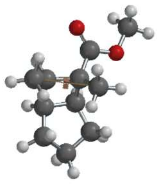

3.057 Å

(ii) Immediately Prior to Bond Cleavage

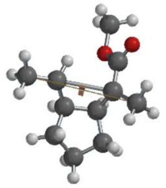

5.457 Å

(iii) Immediately After Bond Cleavage

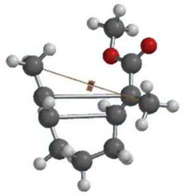

5.507 Å

Summary of CoGEF Results

***F**max*	3.5 nN
***E**max*	278 kJ/mol
Force-Bond Angle	3.1°

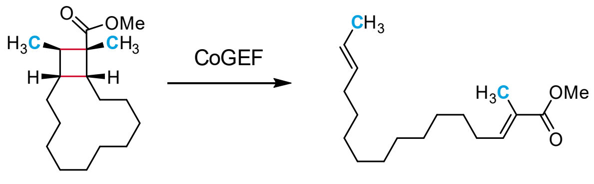

27

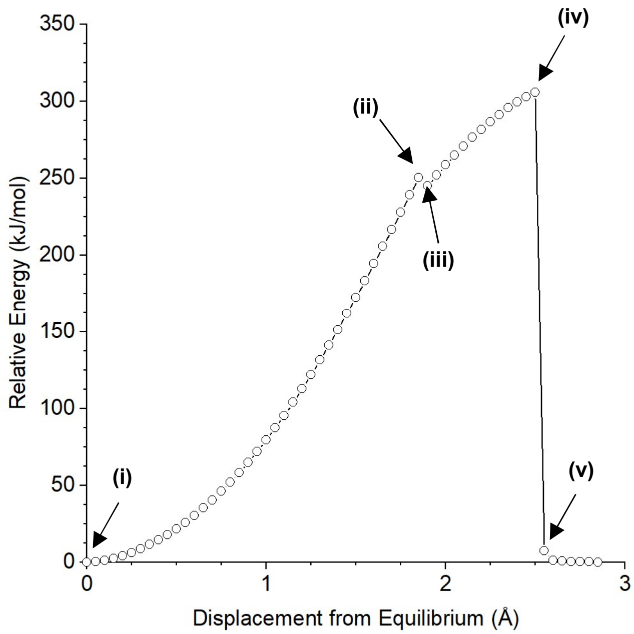

Summary of CoGEF Results	
***F**$_{max}$*	3.7 nN
***E**$_{max}$*	306 kJ/mol
Force-Bond Angle	7.3°

(i) Equilibrium Geometry

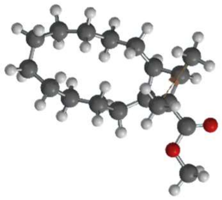

3.051 Å

(ii) Immediately Prior to First Bond Cleavage

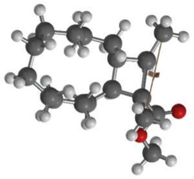

4.901 Å

(iii) Immediately After First Bond Cleavage

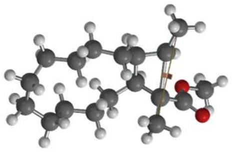

4.951 Å

(iv) Immediately Prior to Second Bond Cleavage

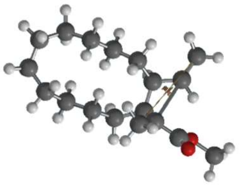

5.551 Å

(v) Immediately After Second Bond Cleavage

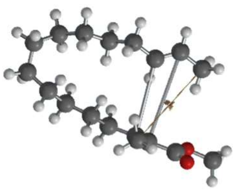

5.601 Å

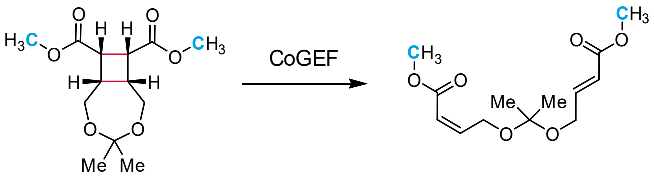

28

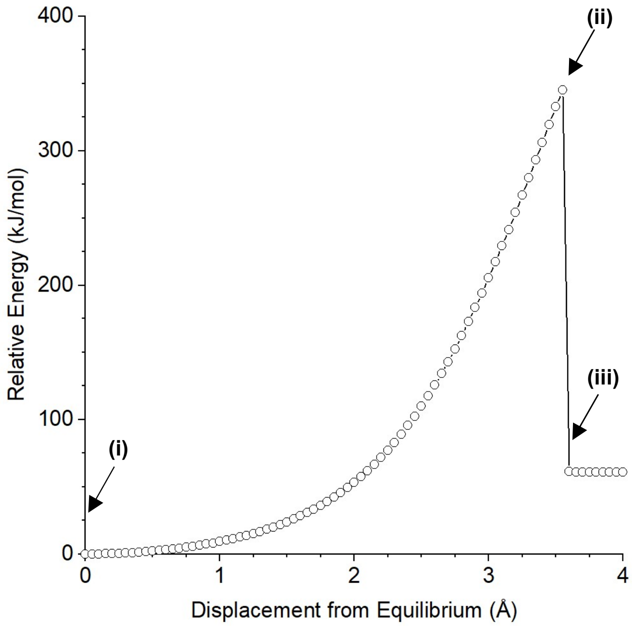

Summary of CoGEF Results	
***F**$_{max}$*	4.4 nN
***E**$_{max}$*	345 kJ/mol
Force-Bond Angle	4.6 °

(i) Equilibrium Geometry

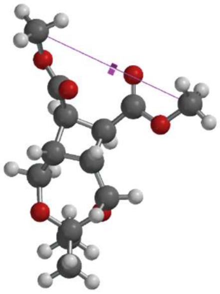

6.476 Å

(ii) Immediately Prior to Bond Cleavage

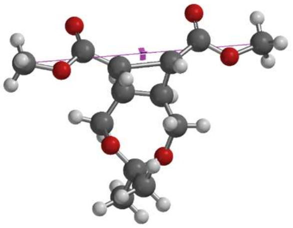

10.026 Å

(iii) Immediately After Bond Cleavage

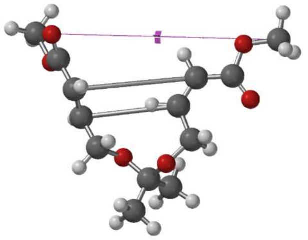

10.076 Å

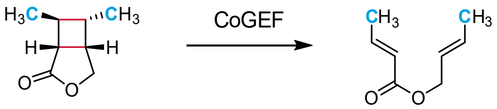

29

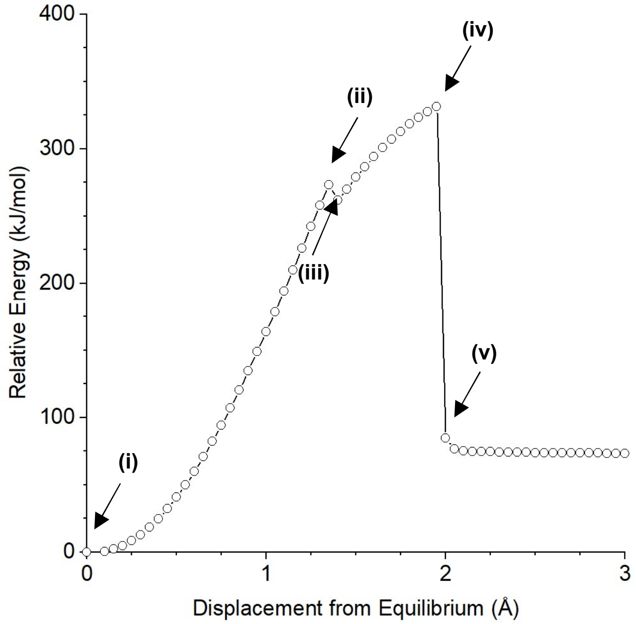

Summary of CoGEF Results	
F_{max}	5.4 nN
E_{max}	331 kJ/mol
Force-Bond Angle	24°

(i) Equilibrium Geometry

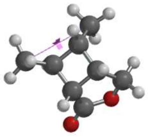

3.769 Å

(ii) Immediately Prior to First Bond Cleavage

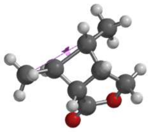

5.119 Å

(iii) Immediately After First Bond Cleavage

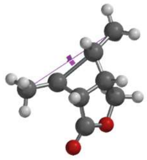

5.169 Å

(iv) Immediately Prior to Second Bond Cleavage

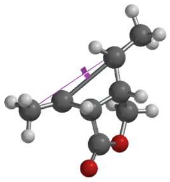

5.719 Å

(v) Immediately After Second Bond Cleavage

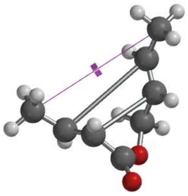

5.769 Å

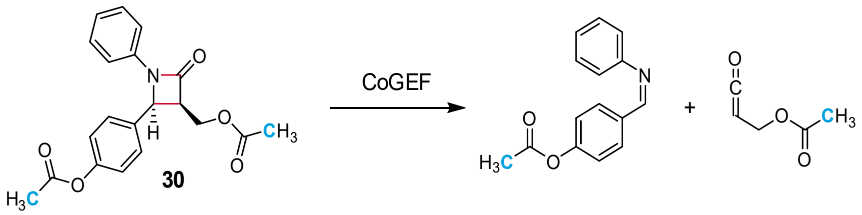

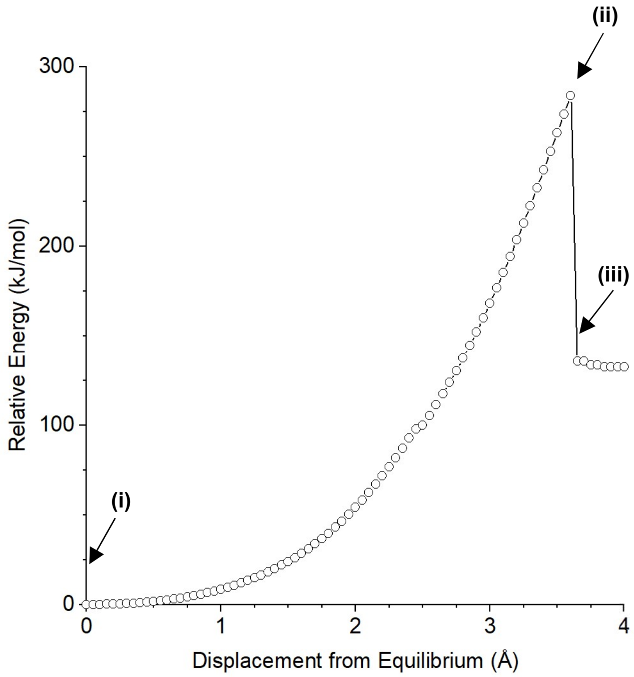

(i) Equilibrium Geometry

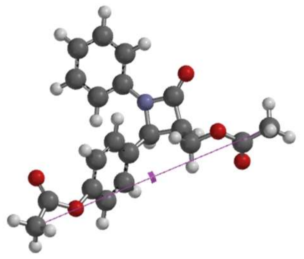

11.759 Å

(ii) Immediately Prior to Bond Cleavage

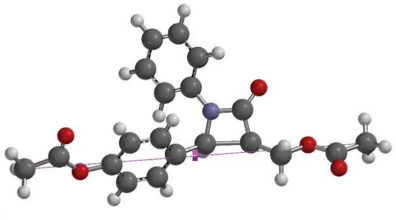

15.359 Å

(iii) Immediately After Bond Cleavage

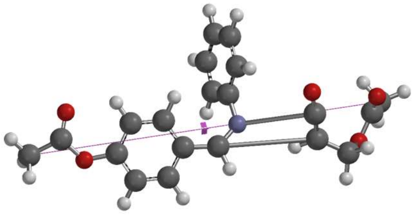

15.409 Å

Summary of CoGEF Results	
***F**$_{max}$*	3.5 nN
***E**$_{max}$*	284 kJ/mol
Force-Bond Angle	9.3°

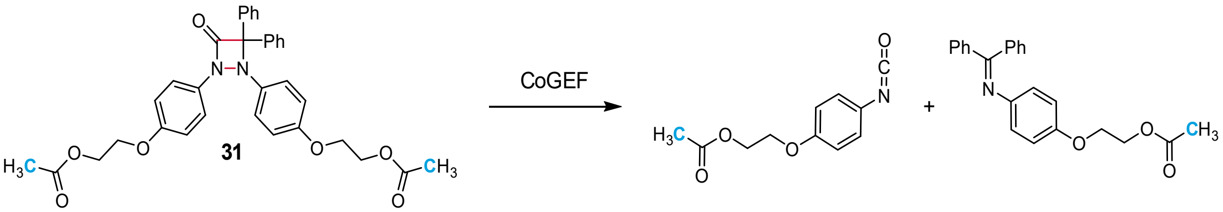

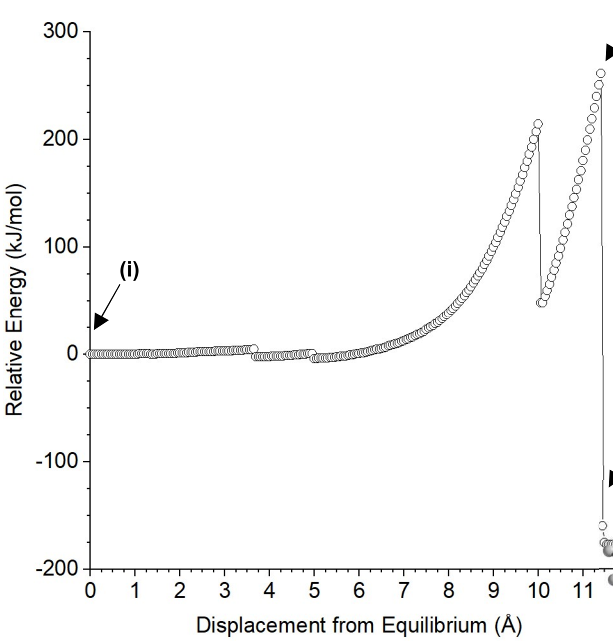

Summary of CoGEF Results

F$_{max}$	3.6 nN
E$_{max}$	260 kJ/mol
Force-Bond Angle	34°

(i) Equilibrium Geometry

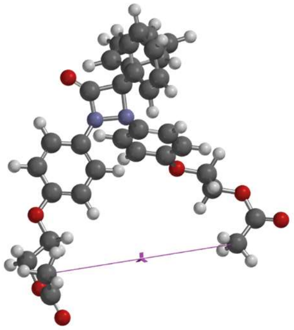

14.018 Å

(ii) Immediately Prior to Bond Cleavage

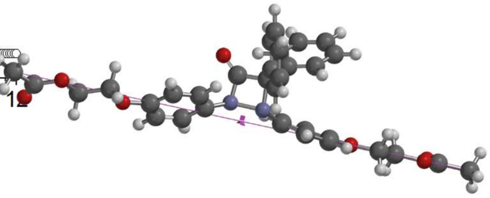

25.418 Å

(iii) Immediately After Bond Cleavage

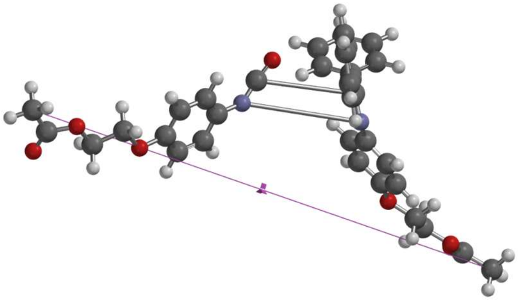

25.468 Å

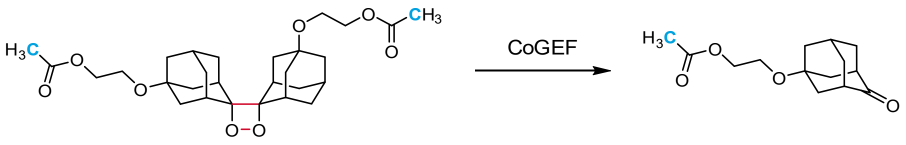

32

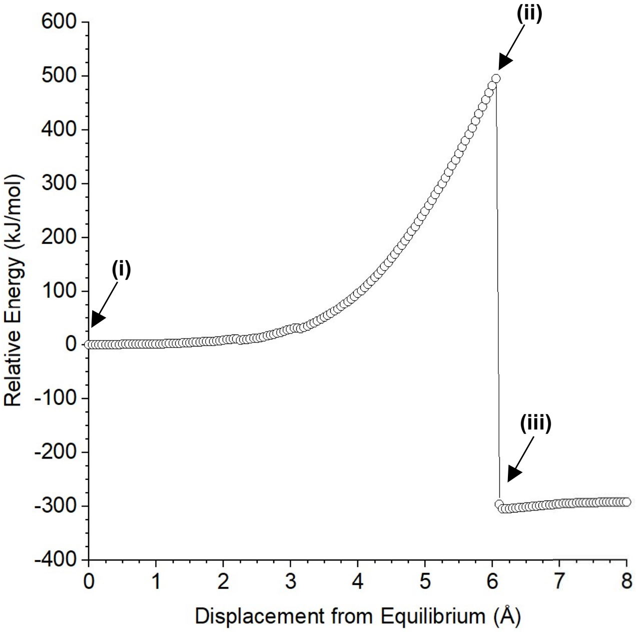

Summary of CoGEF Results	
F_{max}	4.4 nN
E_{max}	495 kJ/mol
Force-Bond Angle	15°

(i) Equilibrium Geometry

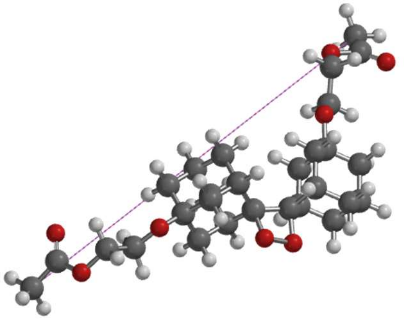

18.153 Å

(ii) Immediately Prior to Bond Cleavage

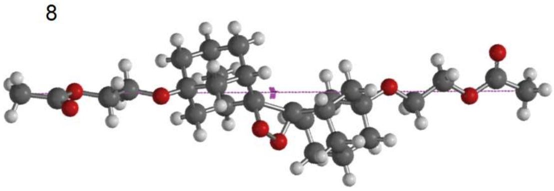

24.203 Å

(iii) Immediately After Bond Cleavage

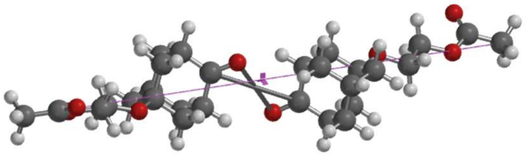

24.253 Å

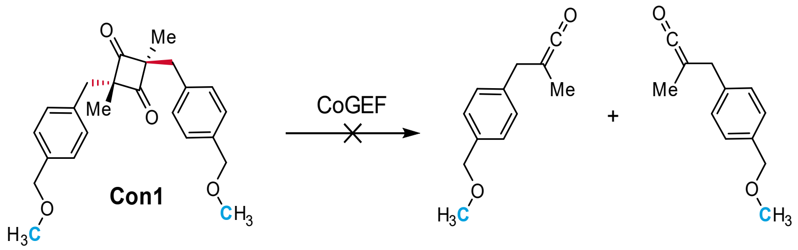

Con1

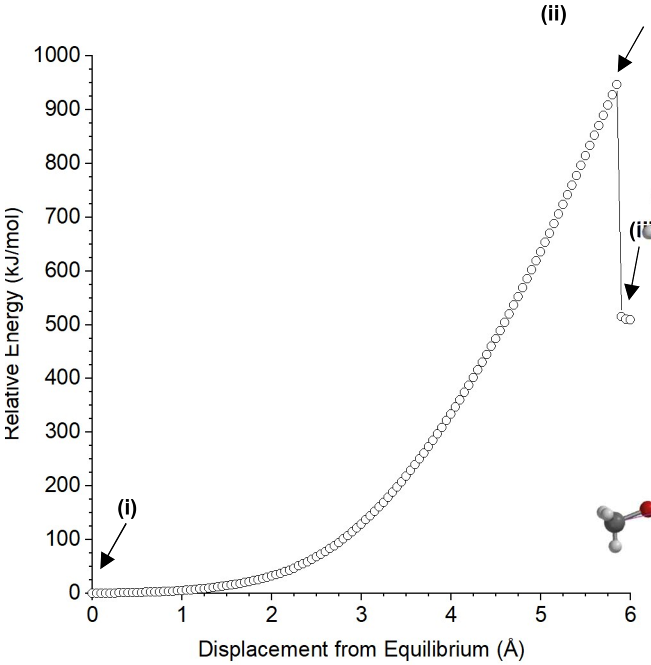

(i) Equilibrium Geometry

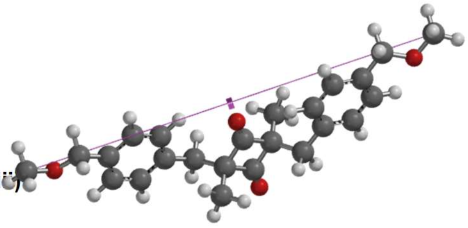

18.385 Å

(ii) Immediately Prior to Bond Cleavage

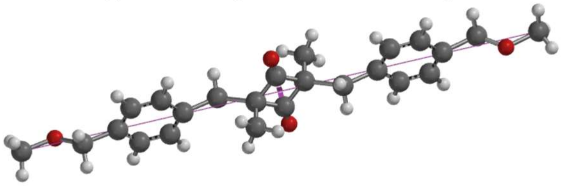

24.235 Å

(iii) Immediately After Bond Cleavage

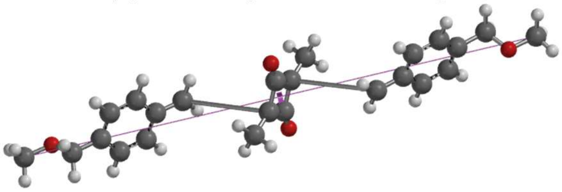

24.305 Å

Summary of CoGEF Results	
***F**$_{max}$*	6.3 nN
***E**$_{max}$*	947 kJ/mol
Force-Bond Angle	43°

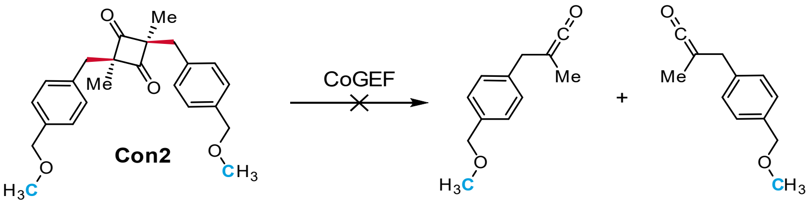

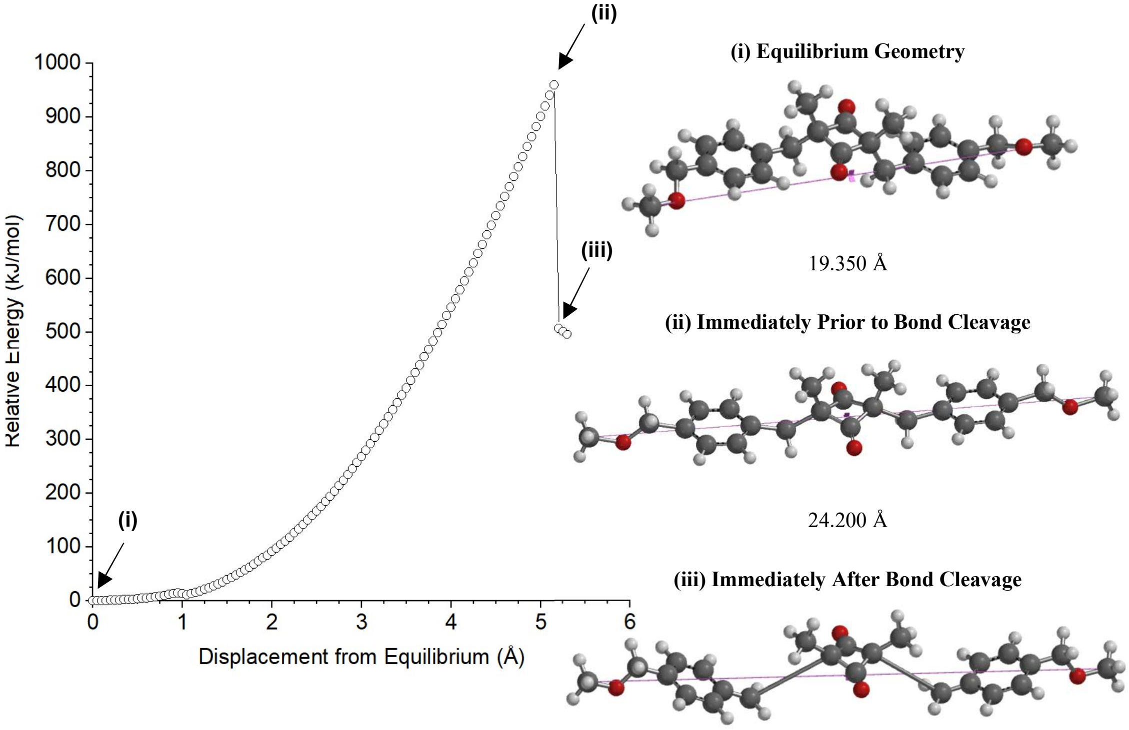

(i) Equilibrium Geometry

19.350 Å

(ii) Immediately Prior to Bond Cleavage

24.200 Å

(iii) Immediately After Bond Cleavage

24.250 Å

Summary of CoGEF Results	
FF_{max}	6.4 nN
E_{max}	959 kJ/mol
Force-Bond Angle	42°

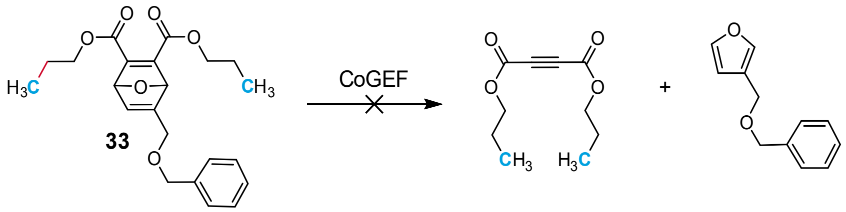

33

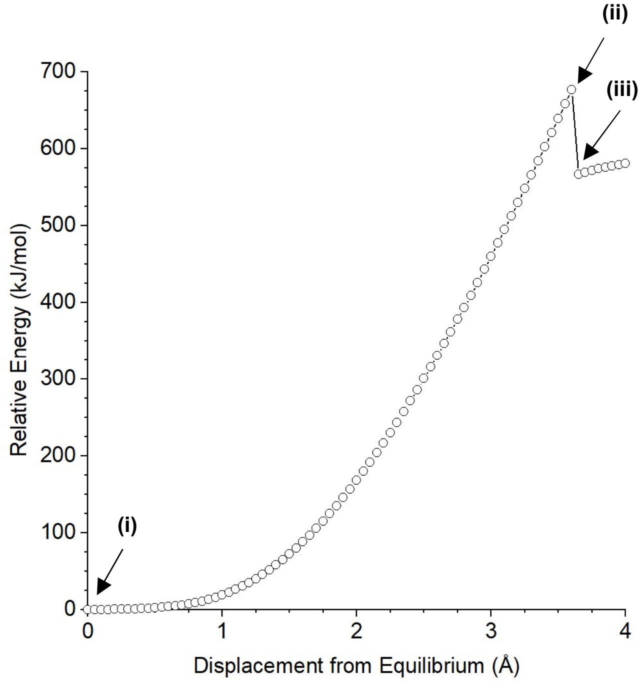

Summary of CoGEF Results	
F_{max}	6.2 nN
E_{max}	676 kJ/mol
Force-Bond Angle	78°

(i) Equilibrium Geometry

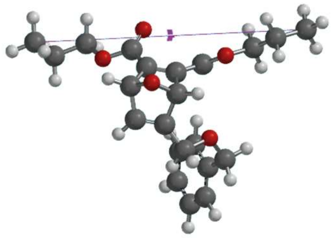

12.509 Å

(ii) Immediately Prior to Bond Cleavage

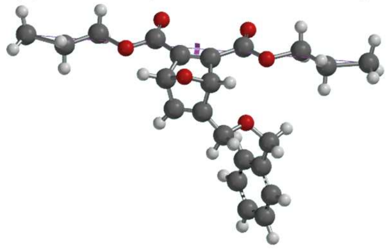

16.109 Å

(iii) Immediately After Bond Cleavage

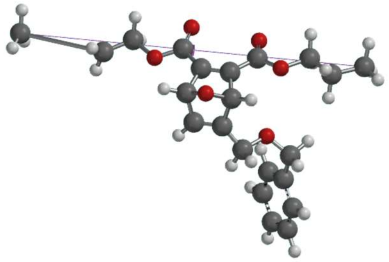

16.159 Å

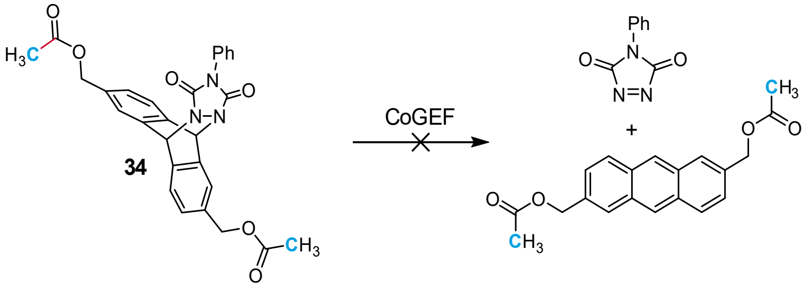

34

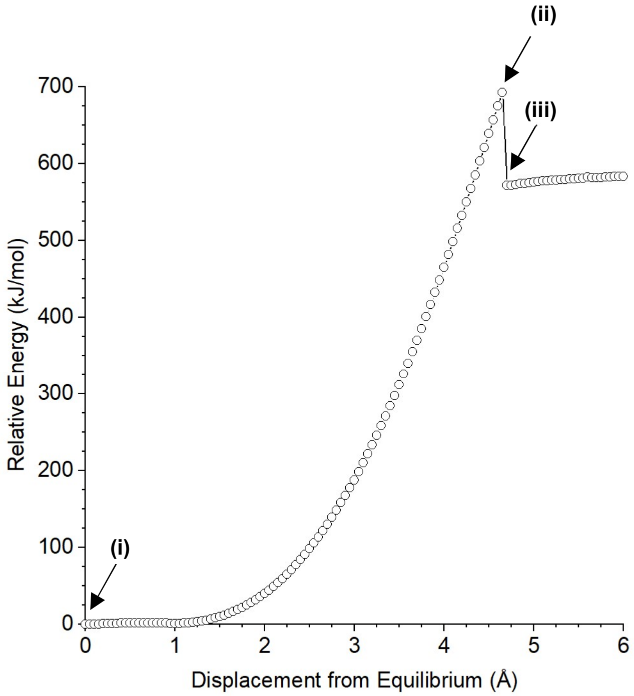

(i) Equilibrium Geometry

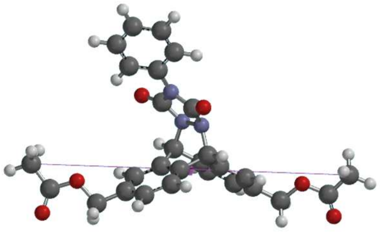

15.358 Å

(ii) Immediately Prior to Bond Cleavage

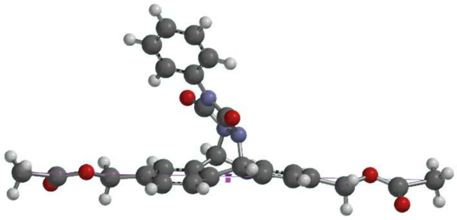

20.008 Å

(iii) Immediately After Bond Cleavage

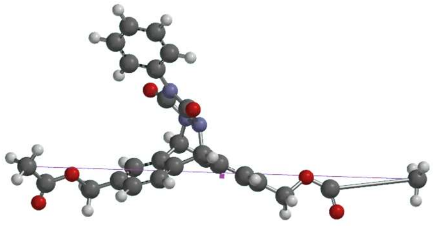

20.058 Å

Summary of CoGEF Results	
F_{max}	6.0 nN
E_{max}	693 kJ/mol
Force-Bond Angle	85°

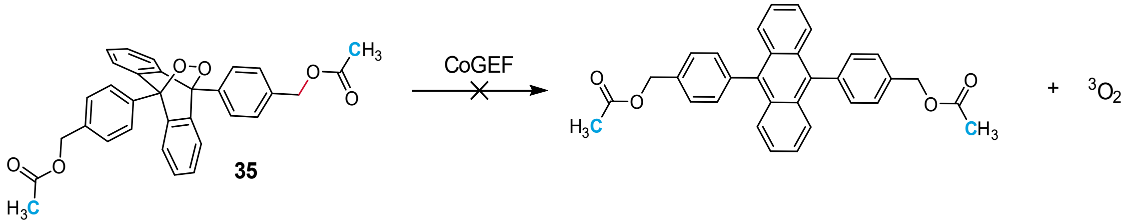

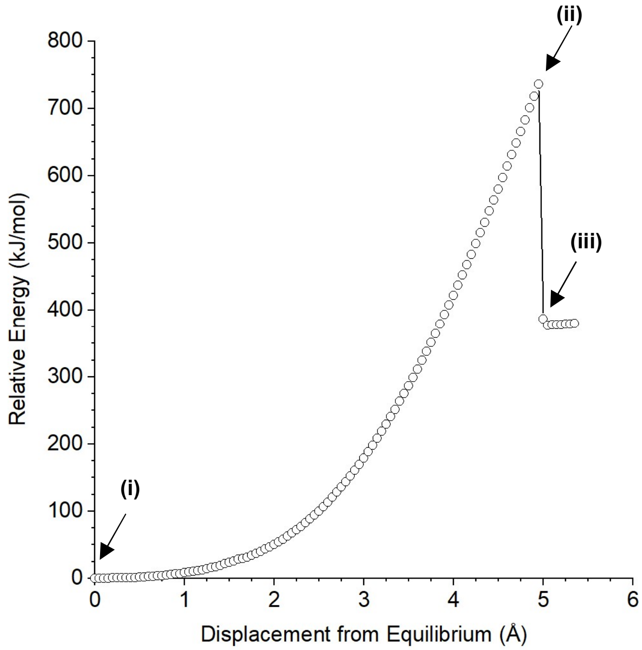

Summary of CoGEF Results

***F**_{max}*	5.8 nN
***E**_{max}*	736 kJ/mol
Force-Bond Angle	66°

(i) Equilibrium Geometry

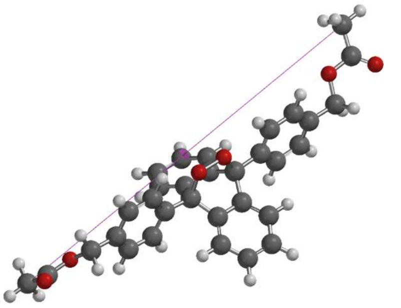

19.243 Å

(ii) Immediately Prior to Bond Cleavage

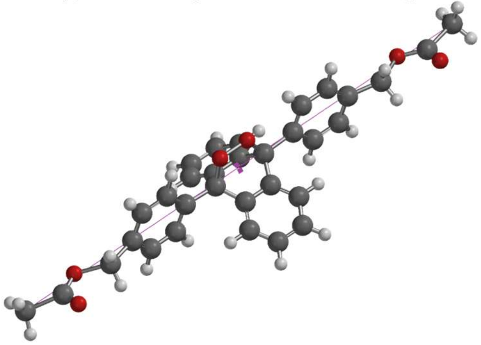

24.193 Å

(iii) Immediately After Bond Cleavage

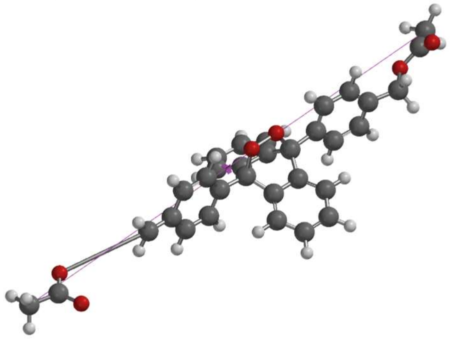

24.243 Å

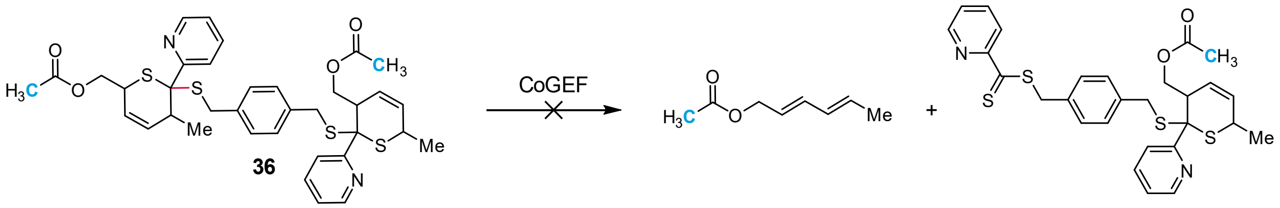

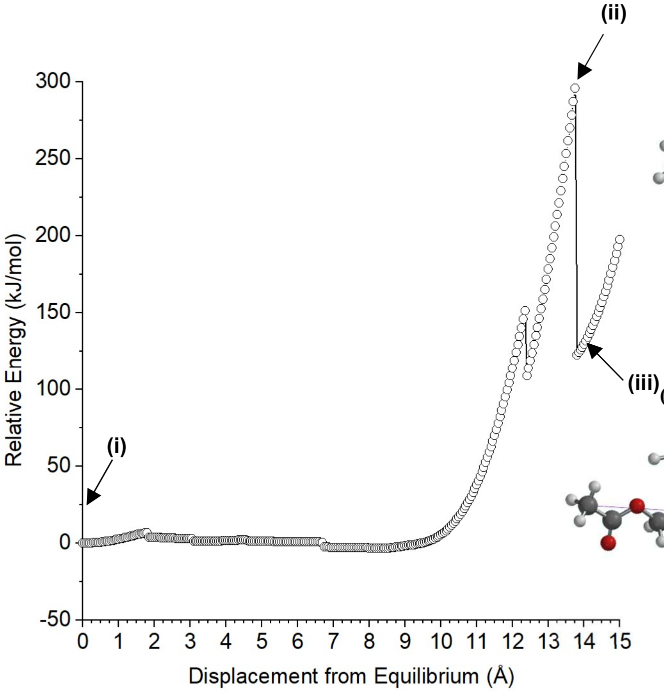

(i) Equilibrium Geometry

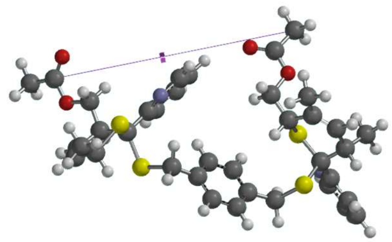

13.209 Å

(ii) Immediately Prior to Bond Cleavage

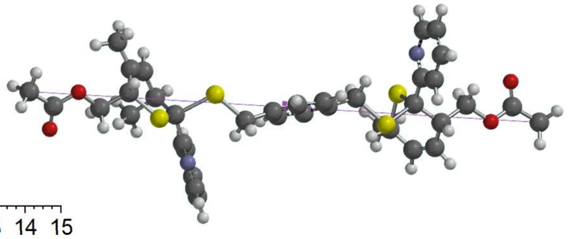

26.959 Å

(iii) Immediately After Bond Cleavage

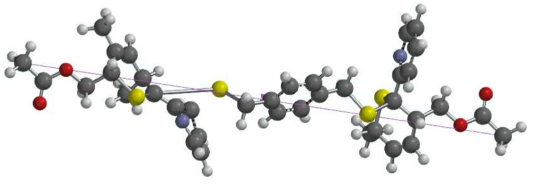

27.009 Å

Summary of CoGEF Results	
F_{max}	2.9 nN
E_{max}	295 kJ/mol
Force-Bond Angle	32°

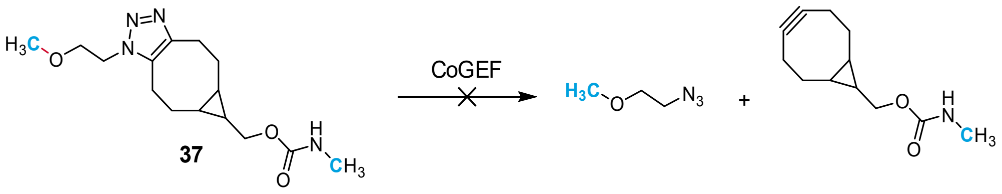

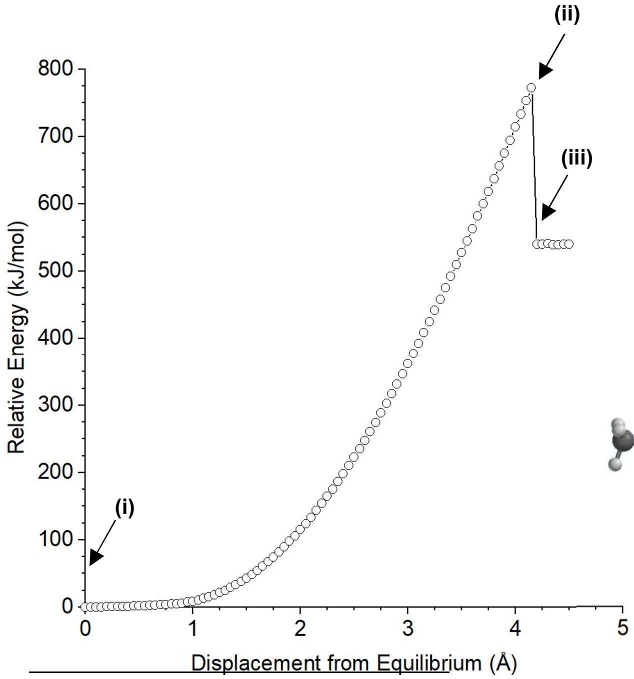

(i) Equilibrium Geometry

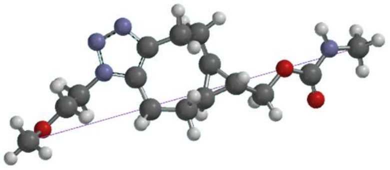

15.627 Å

(ii) Immediately Prior to Bond Cleavage

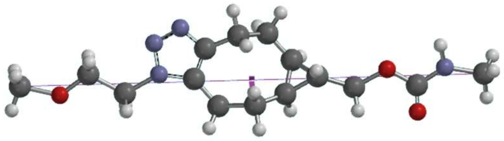

19.777 Å

(iii) Immediately After Bond Cleavage

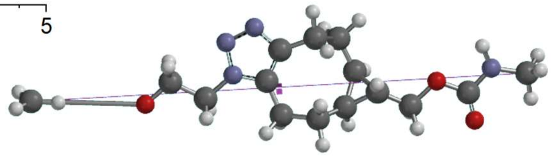

19.827 Å

Summary of CoGEF Results

F_{max}	6.5 nN
E_{max}	772 kJ/mol
Force/Bond angle	8.9°

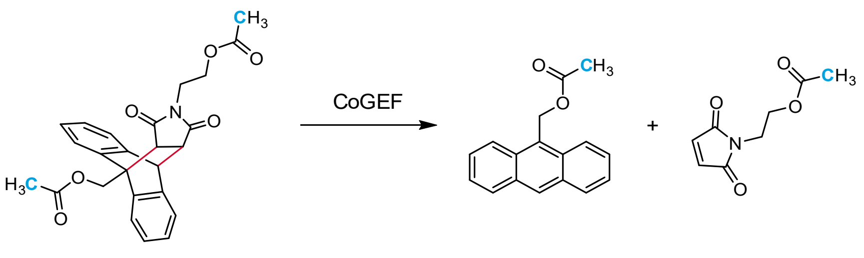

38

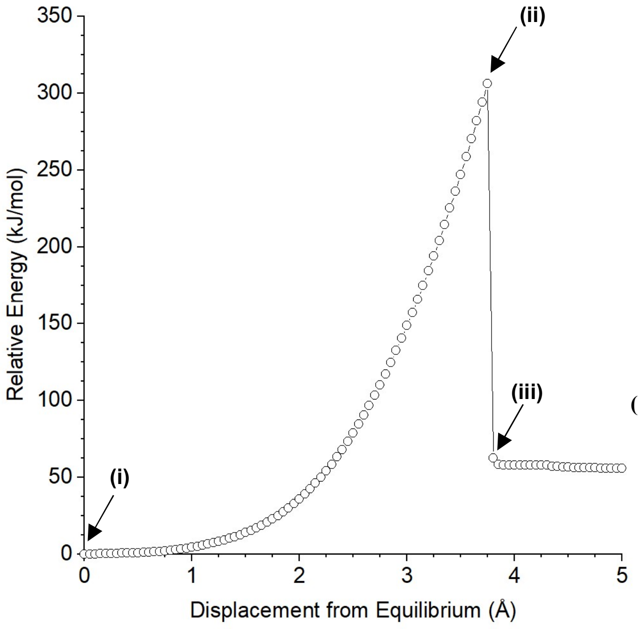

Summary of CoGEF Results	
***F**$_{max}$*	4.1 nN
***E**$_{max}$*	306 kJ/mol
Force/Bond angle	25°

(i) Equilibrium Geometry

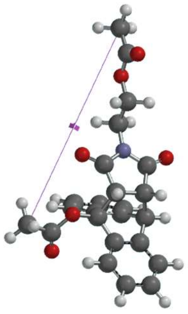

10.918 Å

(ii) Immediately Prior to Bond Cleavage

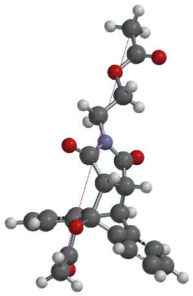

14.668Å

(iii) Immediately After Bond Cleavage

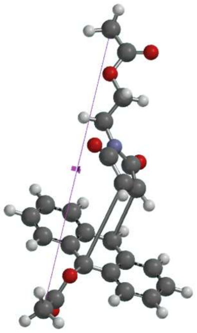

14.718 Å

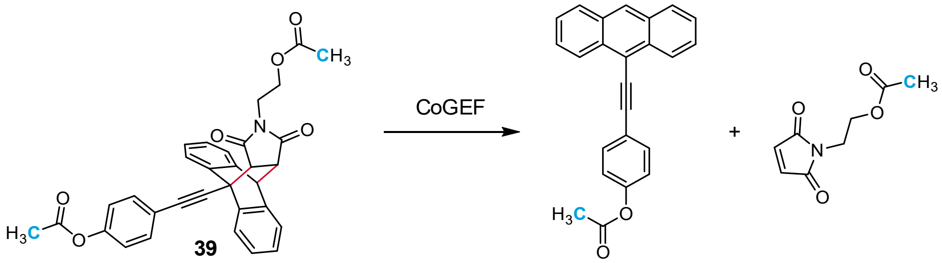

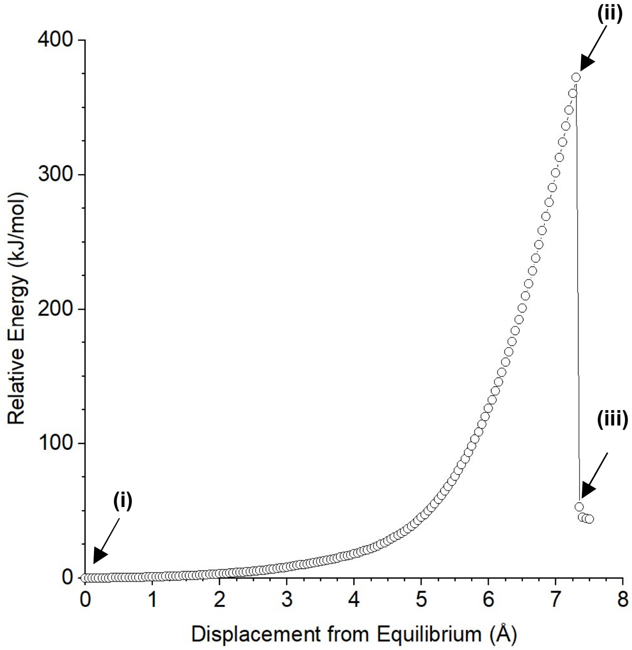

Summary of CoGEF Results	
***F**$_{max}$*	4.0 nN
***E**$_{max}$*	372 kJ/mol
Force-Bond Angle	26°

(i) Equilibrium Geometry

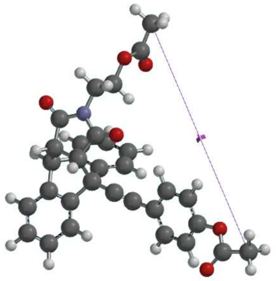

14.542 Å

(ii) Immediately Prior to Bond Cleavage

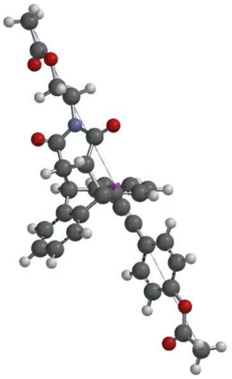

21.842 Å

(iii) Immediately After Bond Cleavage

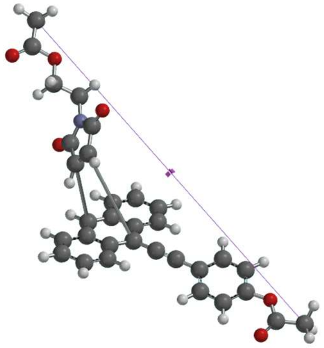

21.892 Å

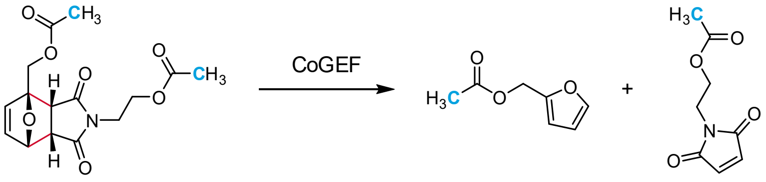

40

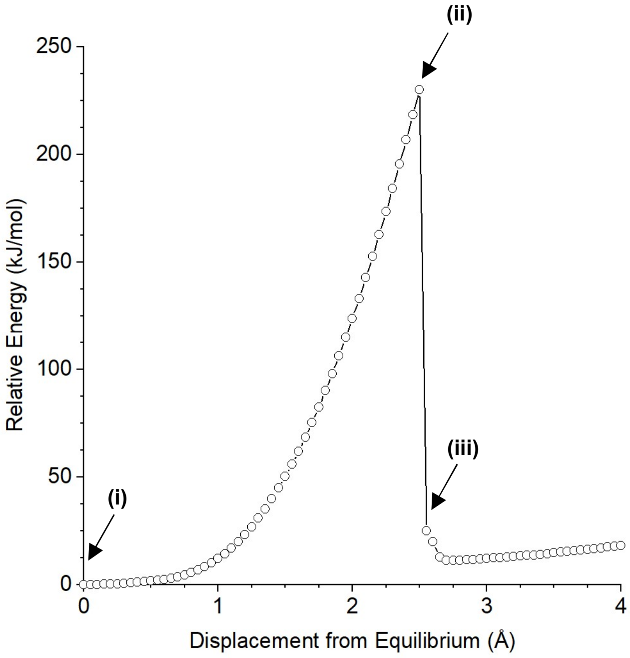

Summary of CoGEF Results	
F_{max}	3.9 nN
E_{max}	230 kJ/mol
Force-Bond Angle	26°

(i) Equilibrium Geometry

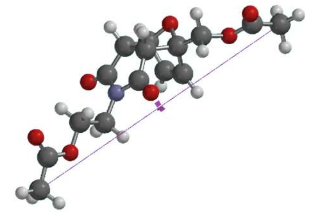

13.422 Å

(ii) Immediately Prior to Bond Cleavage

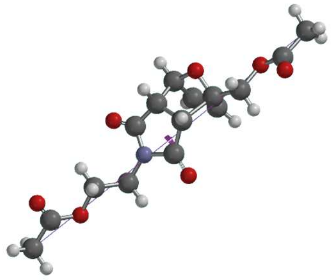

15.922 Å

(iii) Immediately After Bond Cleavage

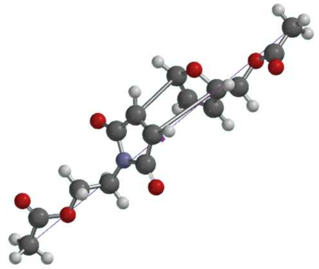

15.972 Å

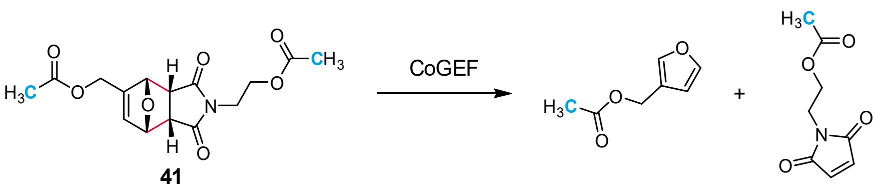

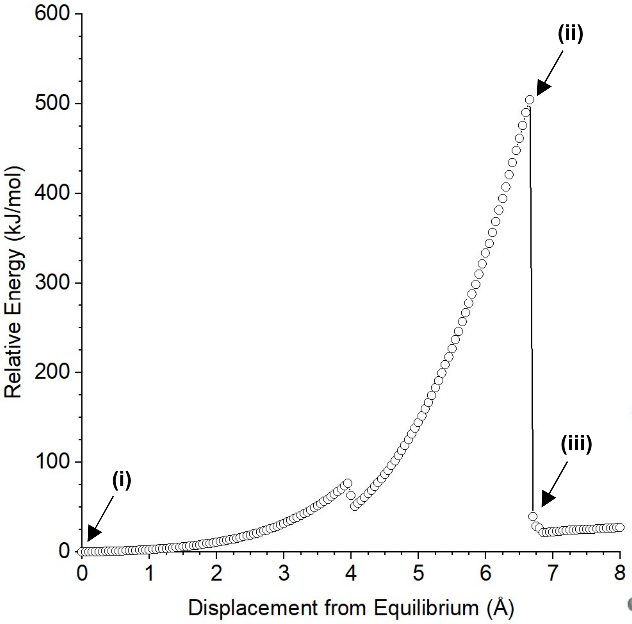

Summary of CoGEF Results	
F_{max}	4.8 nN
E_{max}	504 kJ/mol
Force-Bond Angle	6.8°

(i) Equilibrium Geometry

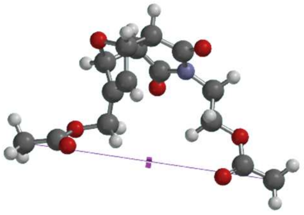

10.731 Å

(ii) Immediately Prior to Bond Cleavage

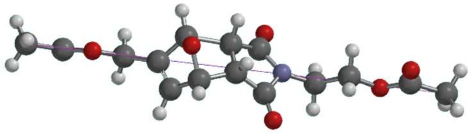

17.381 Å

(iii) Immediately After Bond Cleavage

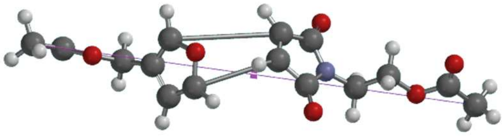

17.431 Å

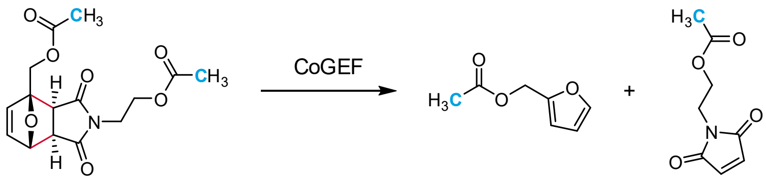

42

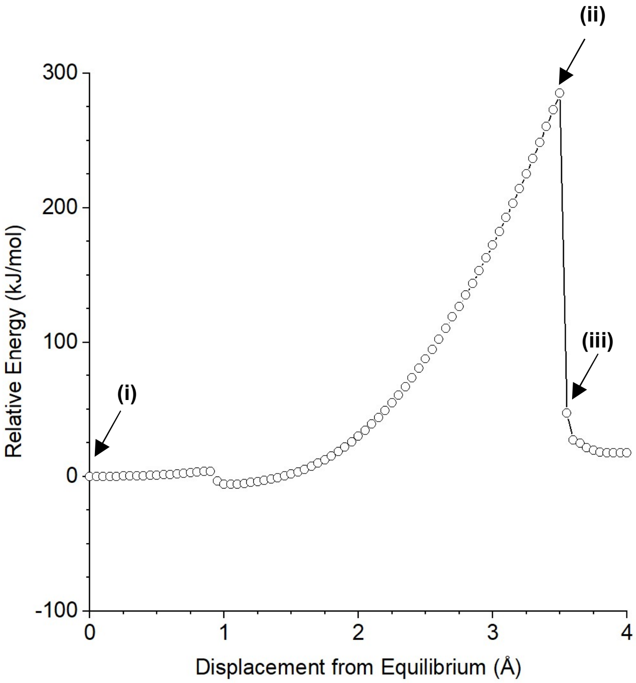

(i) Equilibrium Geometry

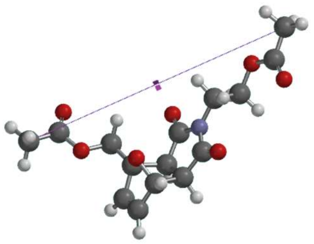

12.433 Å

(ii) Immediately Prior to Bond Cleavage

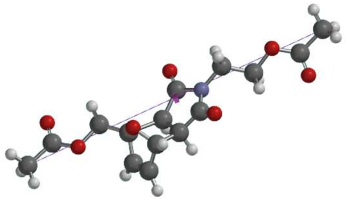

15.933Å

(iii) Immediately After Bond Cleavage

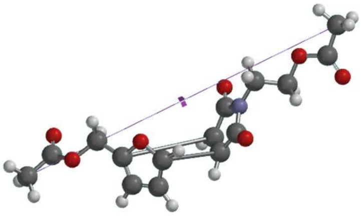

15.983 Å

Summary of CoGEF Results

***F**_{max}*	4.1 nN
***E**_{max}*	285 kJ/mol
Force-Bond Angle	22°

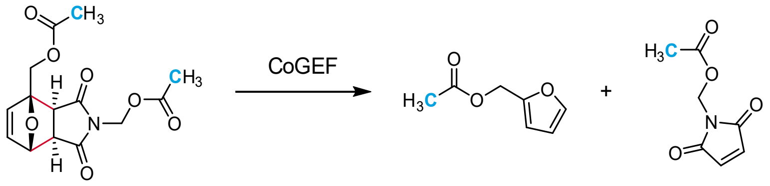

43

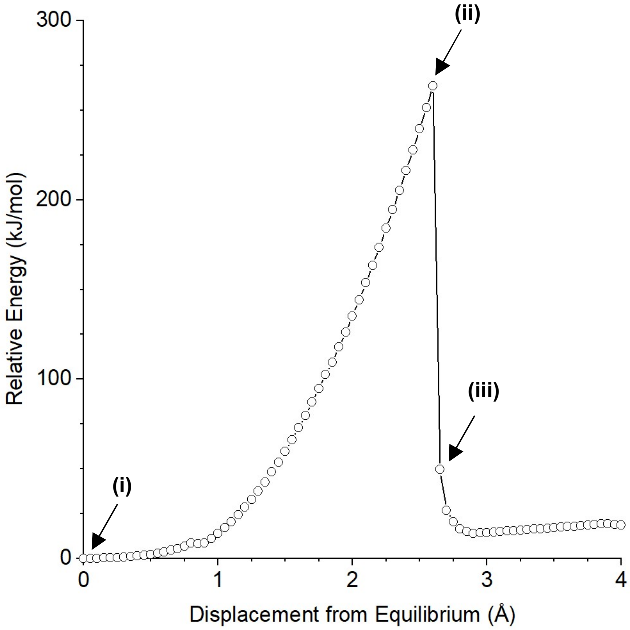

(i) Equilibrium Geometry

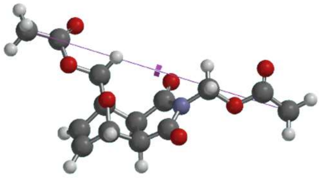

11.874 Å

(ii) Immediately Prior to Bond Cleavage

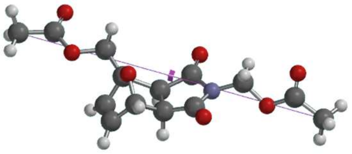

14.474 Å

(iii) Immediately After Bond Cleavage

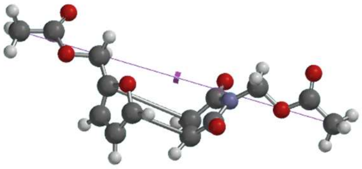

14.524 Å

Summary of CoGEF Results	
F_{max}	4.0 nN
E_{max}	264 kJ/mol
Force-Bond Angle	21°

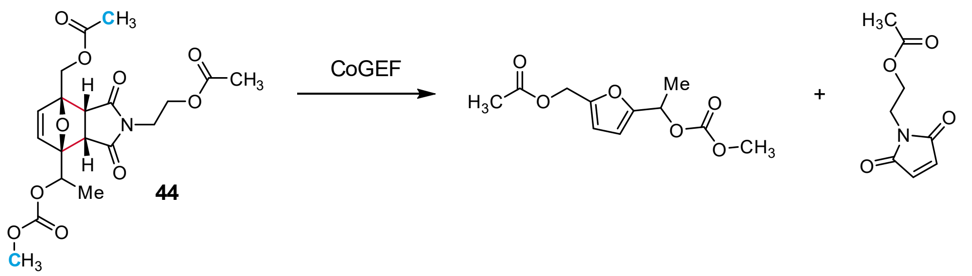

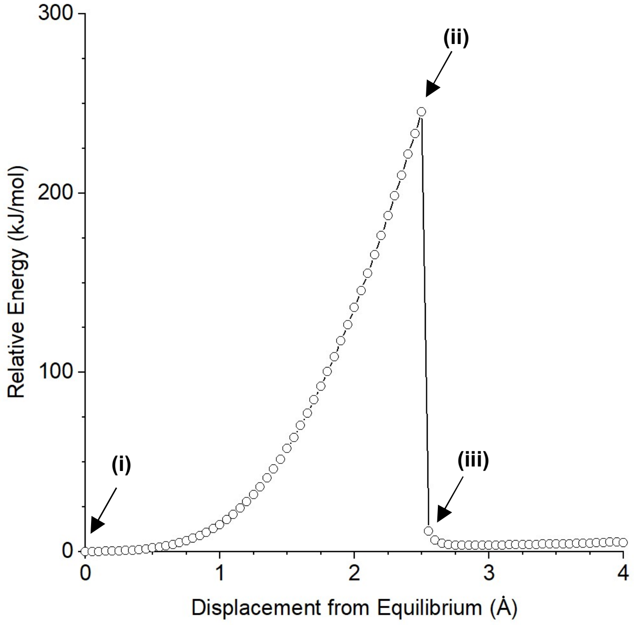

Summary of CoGEF Results

F_{max}	4.0 nN
E_{max}	245 kJ/mol
Force-Bond Angle	26°

(i) Equilibrium Geometry

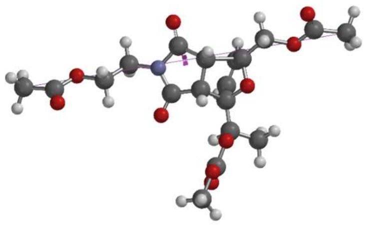

13.491 Å

(ii) Immediately Prior to Bond Cleavage

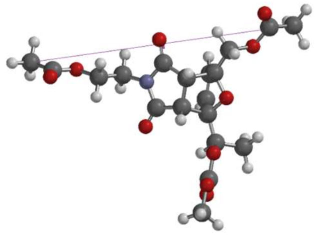

15.991 Å

(iii) Immediately After Bond Cleavage

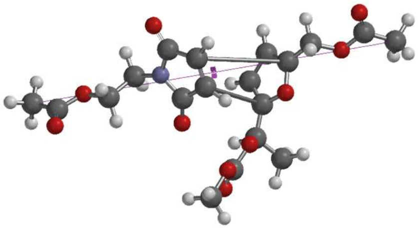

16.041 Å

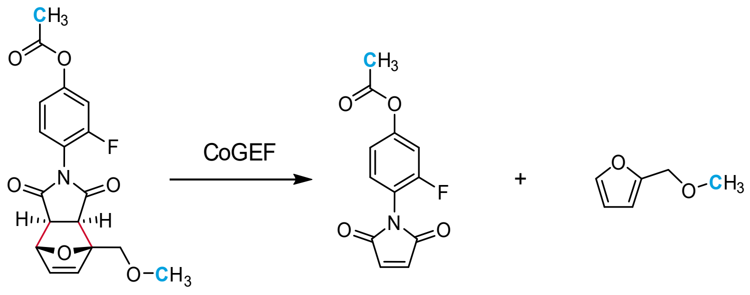

45

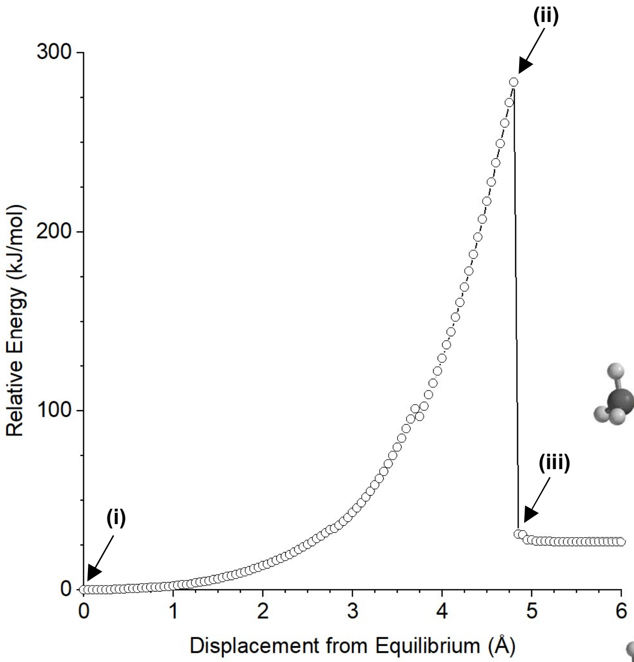

(i) Equilibrium Geometry

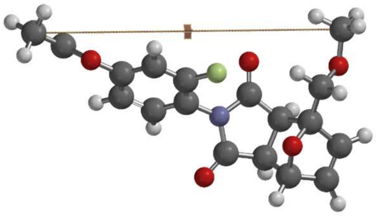

11.583 Å

(ii) Immediately Prior to Bond Cleavage

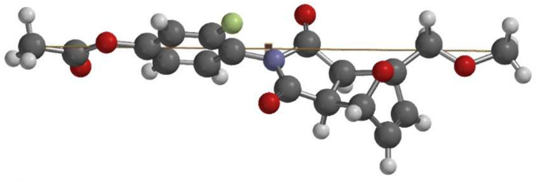

16.383 Å

(iii) Immediately After Bond Cleavage

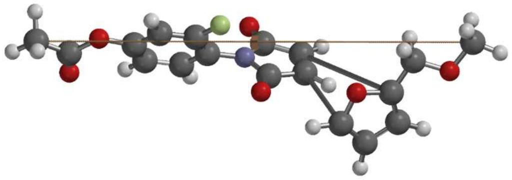

16.433 Å

Summary of CoGEF Results	
FF_{max}	3.8 nN
E_{max}	284 kJ/mol
Force-Bond Angle	21°

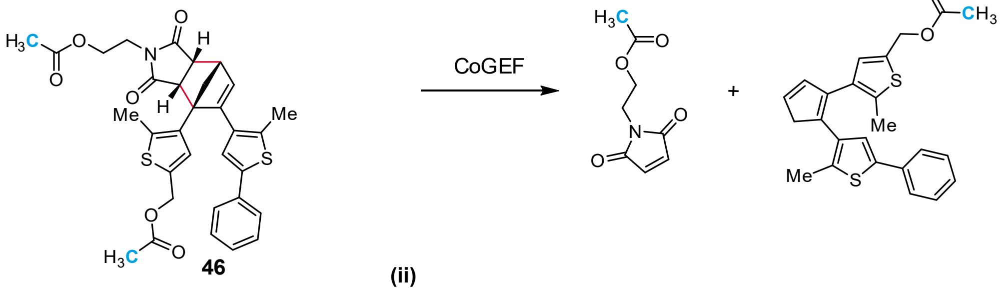

46

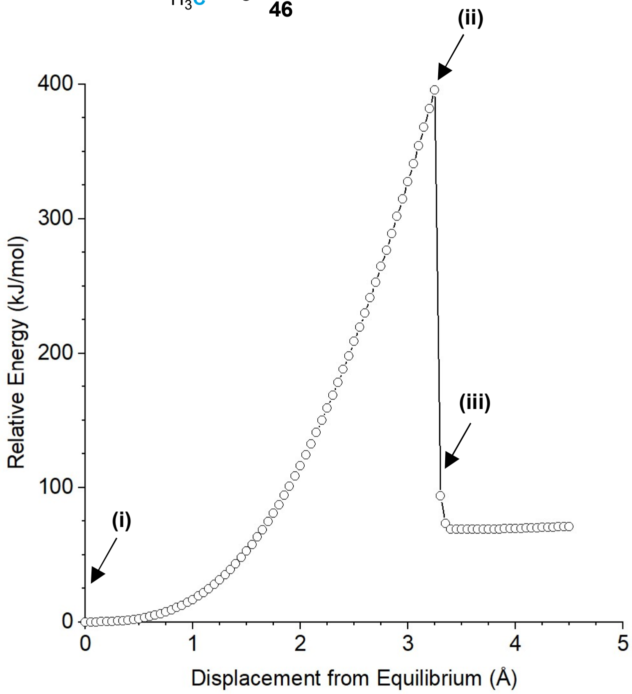

Summary of CoGEF Results

F$_{max}$	4.6 nN
E$_{max}$	396 kJ/mol
Force-Bond Angle	26°

(i) Equilibrium Geometry

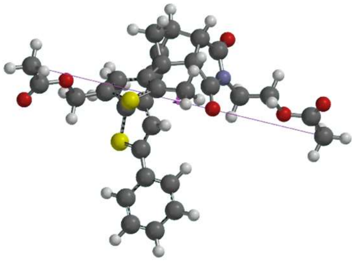

17.075 Å

(ii) Immediately Prior to Bond Cleavage

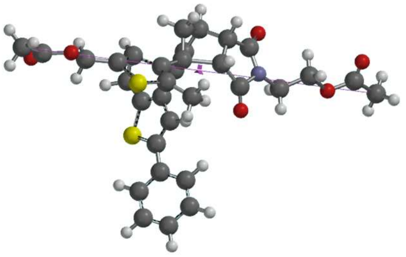

20.325 Å

(iii) Immediately After Bond Cleavage

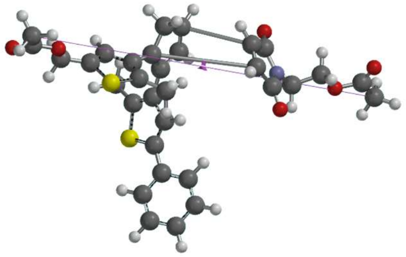

20.375 Å

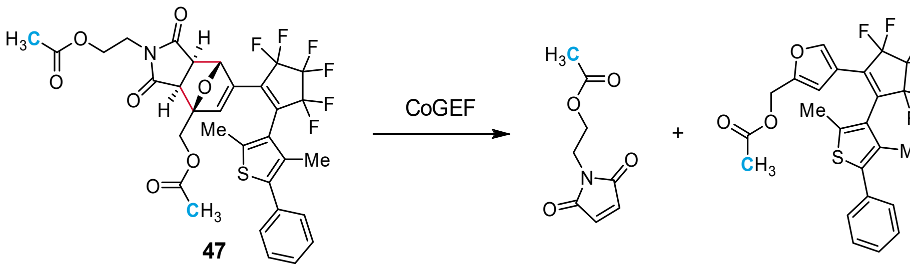

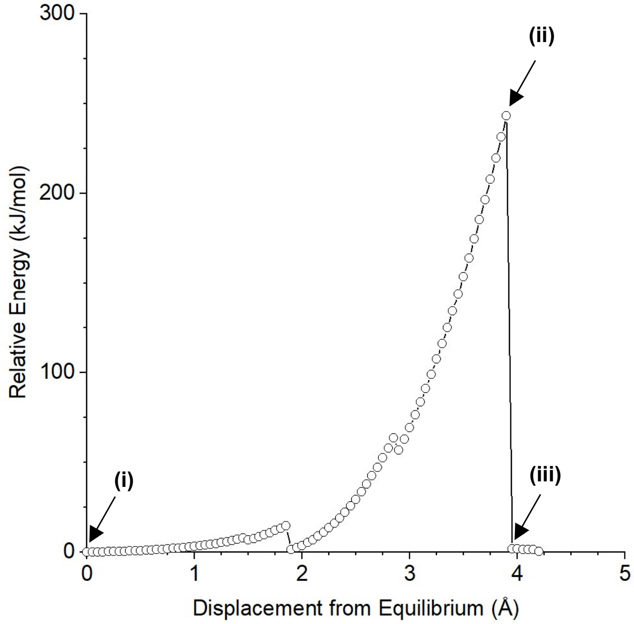

(i) Equilibrium Geometry

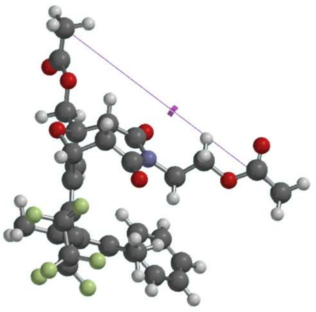

12.087 Å

(ii) Immediately Prior to Bond Cleavage

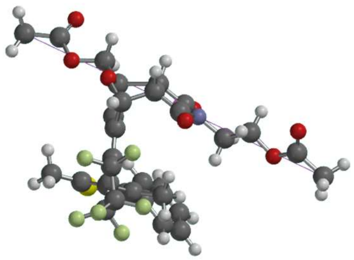

15.987 Å

(iii) Immediately After Bond Cleavage

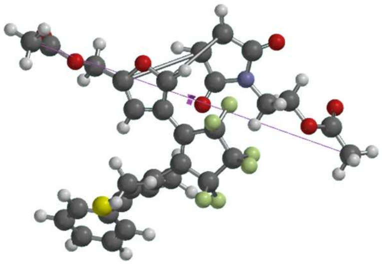

16.037 Å

Summary of CoGEF Results

F_{max}	3.9 nN
E_{max}	243 kJ/mol
Force-Bond Angle	25°

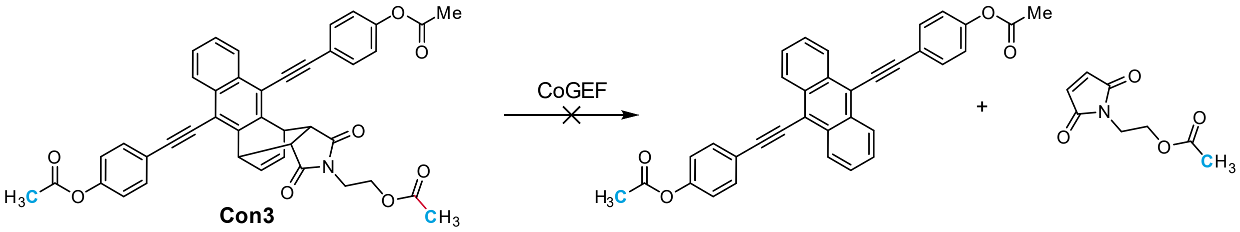

Con3

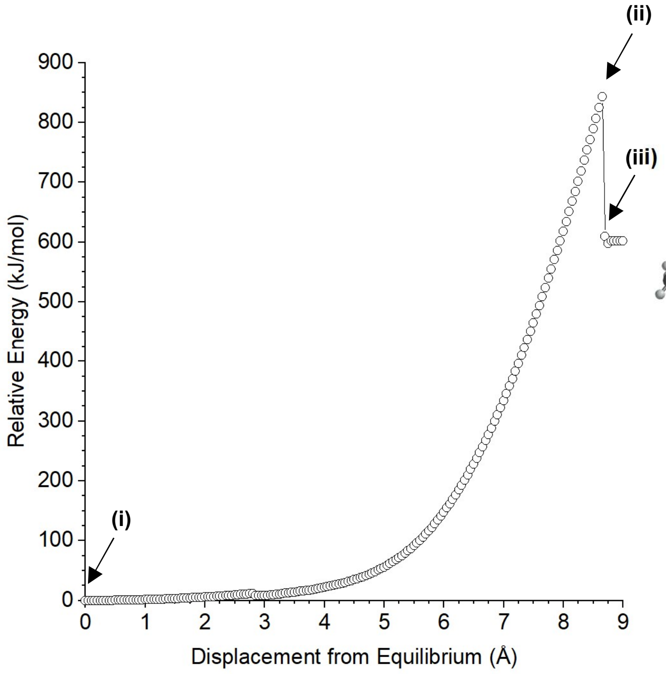

Summary of CoGEF Results	
F_{max}	6.0 nN
E_{max}	843 kJ/mol
Force-Bond Angle	29°

(i) Equilibrium Geometry

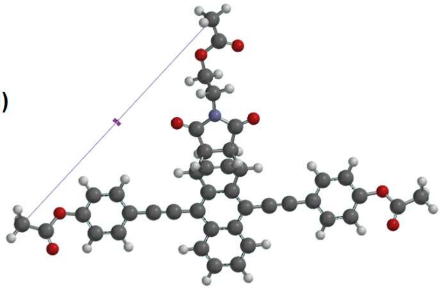

16.84 Å

(ii) Immediately Prior to Bond Cleavage

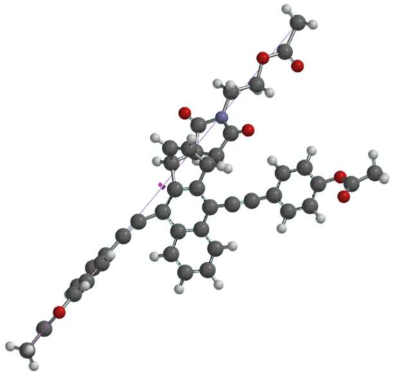

25.49 Å

(iii) Immediately After Bond Cleavage

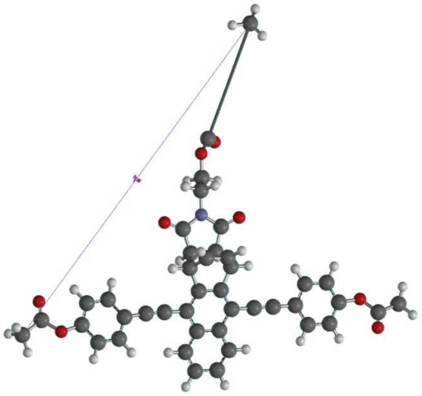

25.54 Å

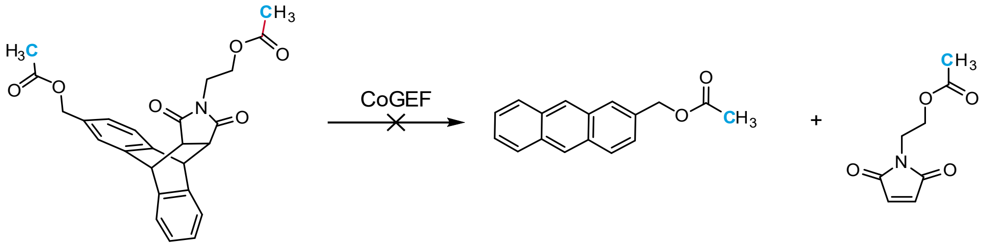

Con4

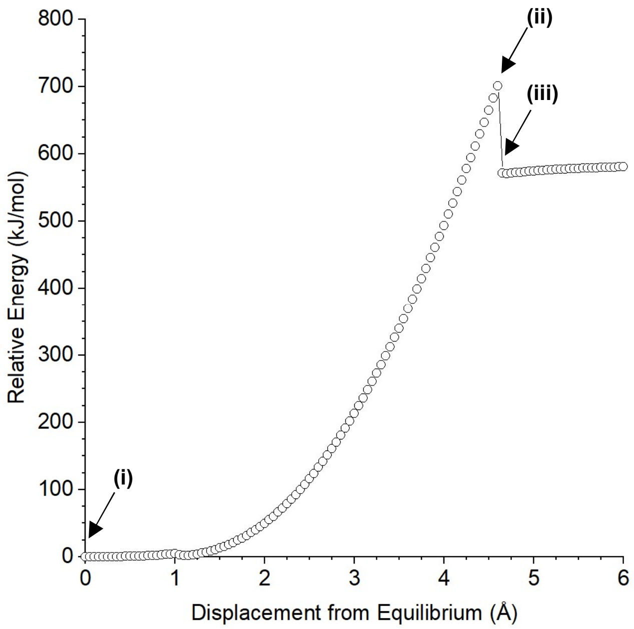

Summary of CoGEF Results

F_{max}	6.0 nN
E_{max}	832 kJ/mol
Force-Bond Angle	15°

(i) Equilibrium Geometry

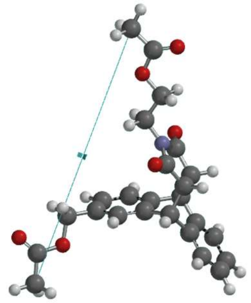

16.321 Å

(ii) Immediately Prior to Bond Cleavage

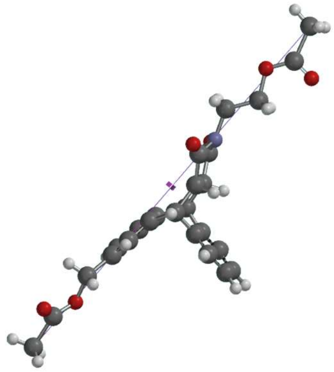

20.821 Å

(iii) Immediately After Bond Cleavage

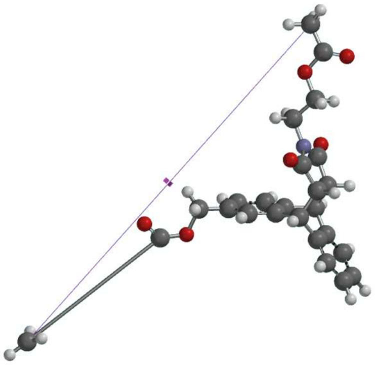

20.871 Å

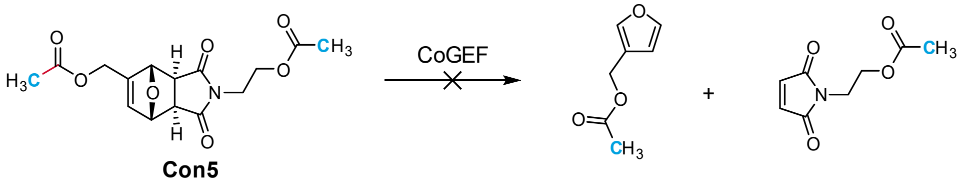

Con5

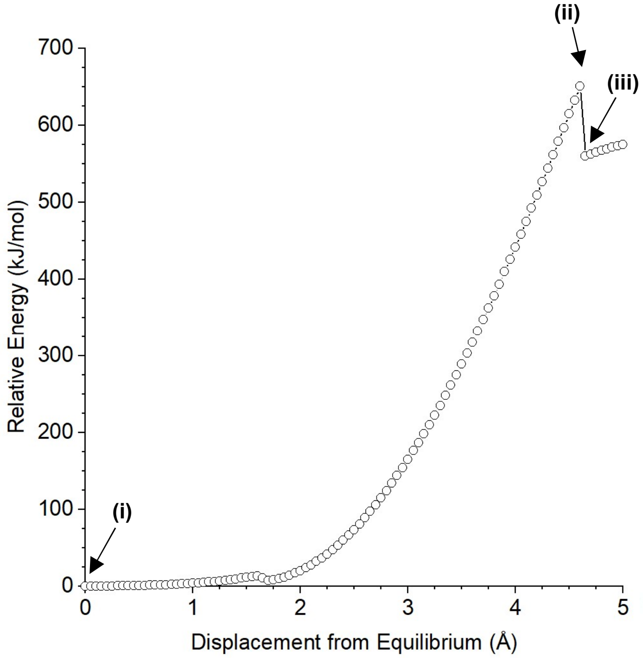

(i) Equilibrium Geometry

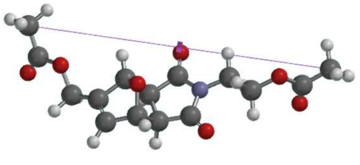

13.761 Å

(ii) Immediately Prior to Bond Cleavage

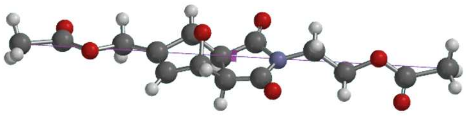

18.361 Å

(iii) Immediately After Bond Cleavage

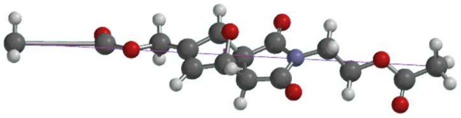

18.411 Å

Summary of CoGEF Results	
F_{max}	6.0 nN
E_{max}	650 kJ/mol
Force-Bond Angle	39°

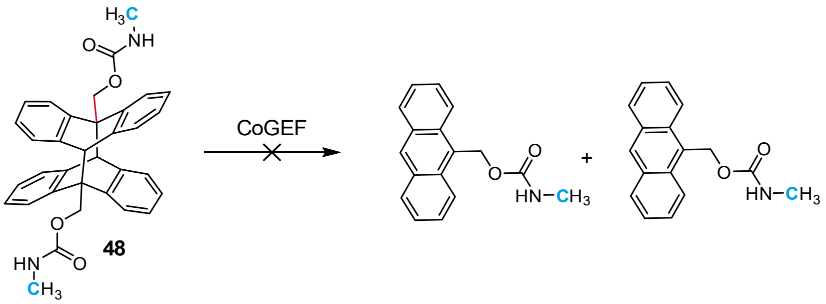

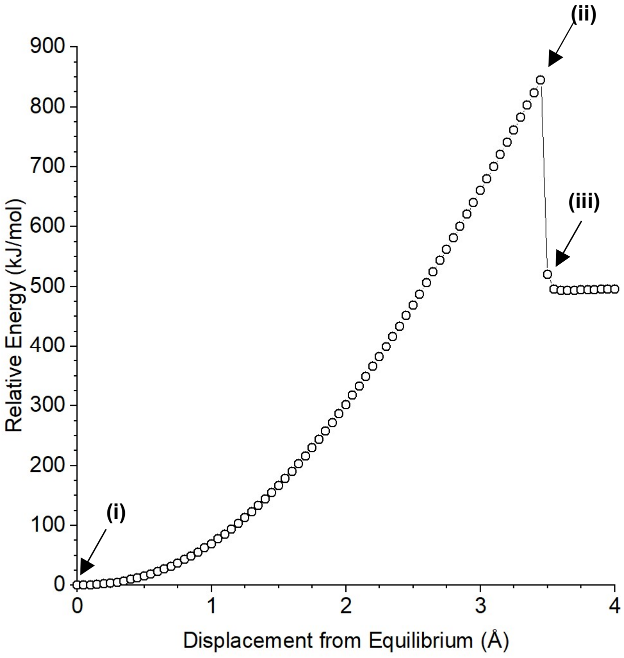

Summary of CoGEF Results	
***F**_{max}*	6.9 nN
***E**_{max}*	844 kJ/mol
Force-Bond Angle	53°

(i) Equilibrium Geometry

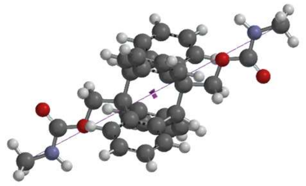

15.288 Å

(ii) Immediately Prior to Bond Cleavage

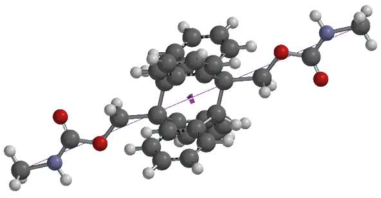

18.738 Å

(iii) Immediately After Bond Cleavage

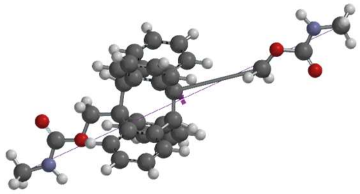

18.788 Å

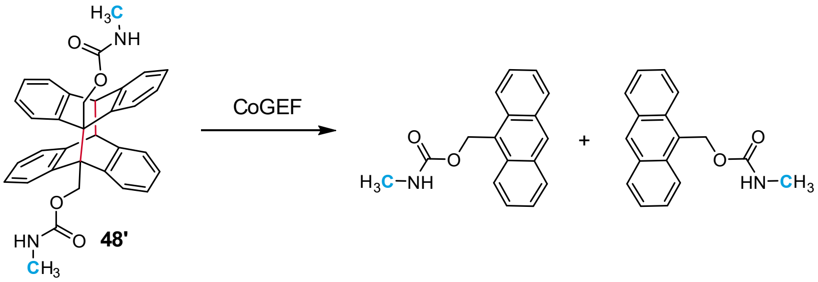

48'

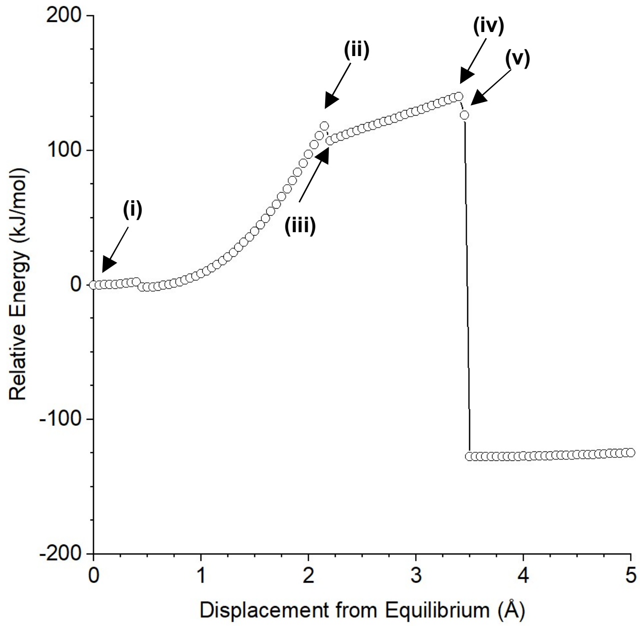

Summary of CoGEF Results

***F**_{max}*	2.3 nN
***E**_{max}*	140 kJ/mol
Force-Bond Angle	5.7°

(i) Equilibrium Geometry

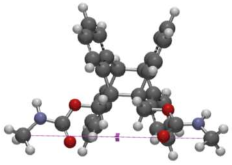

11.492 Å

(ii) Immediately Prior to First Bond Cleavage

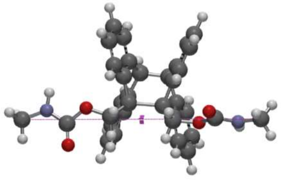

13.642 Å

(iii) Immediately After First Bond Cleavage

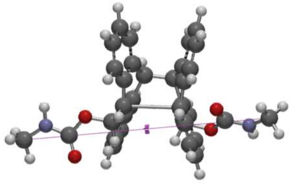

13.692 Å

(iv) Immediately Prior to Second Bond Cleavage

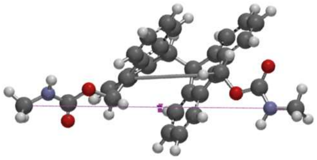

14.892 Å

(v) Immediately After Second Bond Cleavage

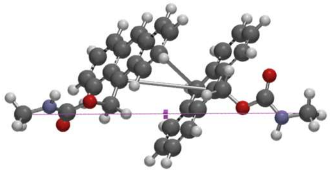

14.942 Å

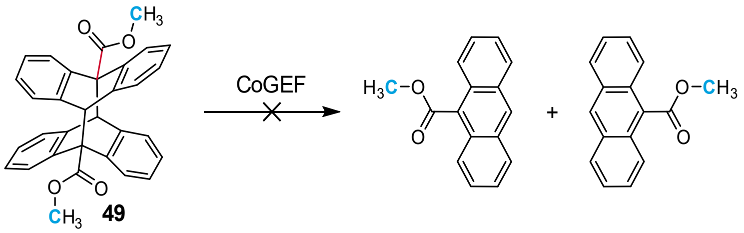

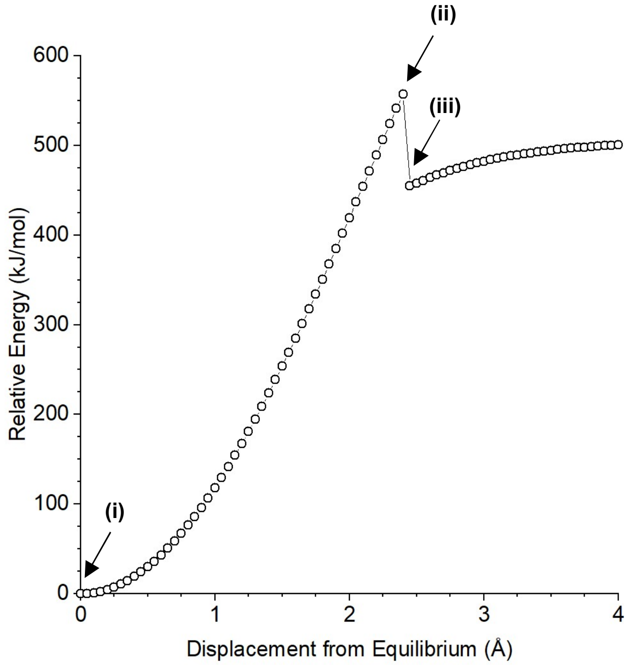

Summary of CoGEF Results	
F F_{max}	5.8 nN
E_{max}	557 kJ/mol
Force-Bond Angle	57.8°

(i) Equilibrium Geometry

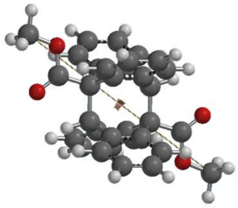

10.728 Å

(ii) Immediately Prior to Bond Cleavage

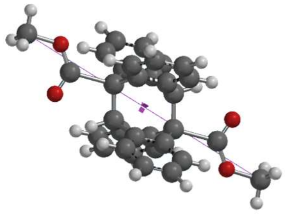

13.128 Å

(iii) Immediately After Bond Cleavage

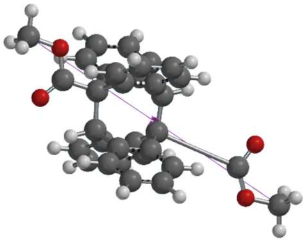

13.178 Å

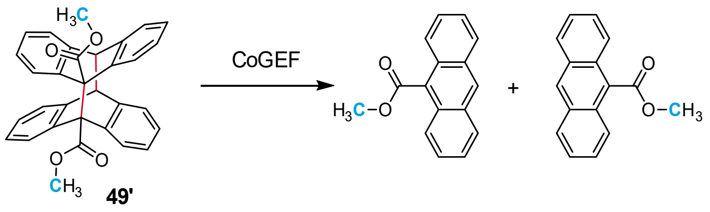

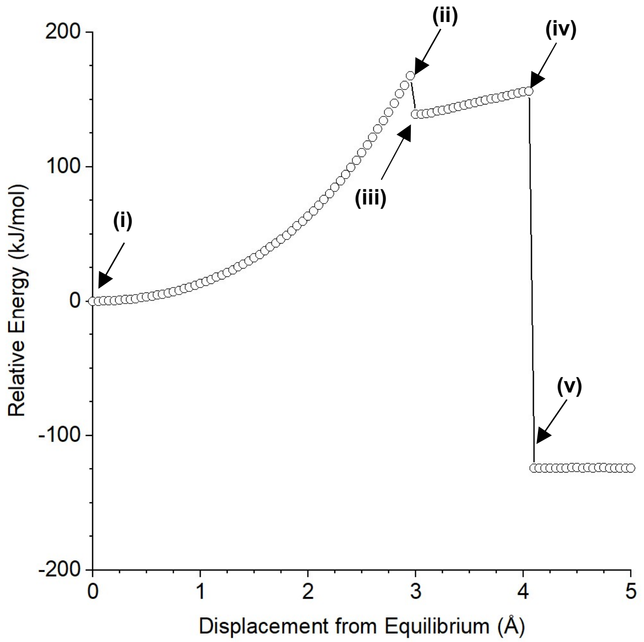

Summary of CoGEF Results	
F_{max}	2.2 nN
E_{max}	167 kJ/mol
Force-Bond Angle	0.5°

(i) Equilibrium Geometry

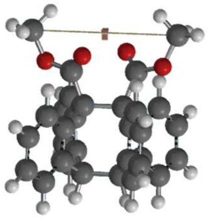

6.033 Å

(ii) Immediately Prior to First Bond Cleavage

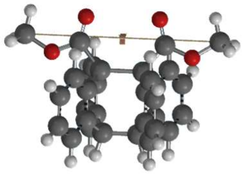

8.983 Å

(iii) Immediately After First Bond Cleavage

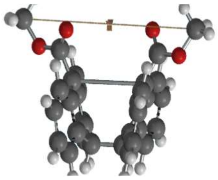

9.033 Å

(iv) Immediately Prior to Second Bond Cleavage

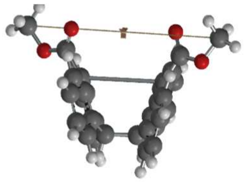

10.083 Å

(v) Immediately After Second Bond Cleavage

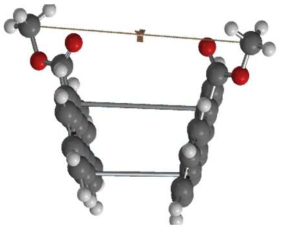

10.133 Å

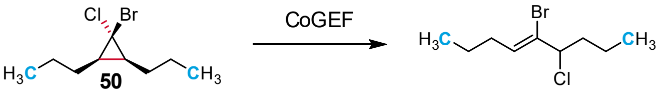

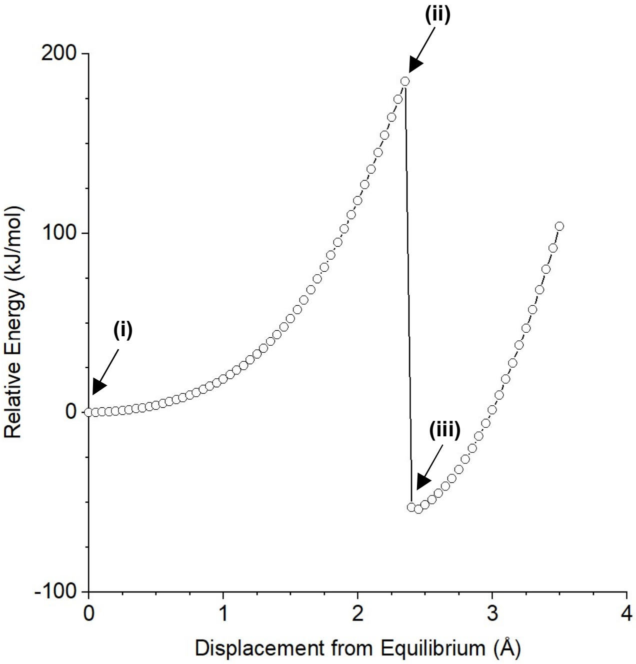

(i) Equilibrium Geometry

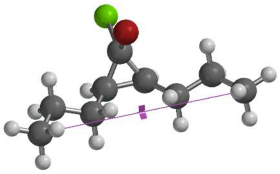

7.809 Å

(ii) Immediately Prior to Bond Cleavage

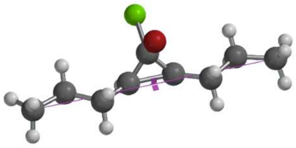

10.359 Å

(iii) Immediately After Bond Cleavage

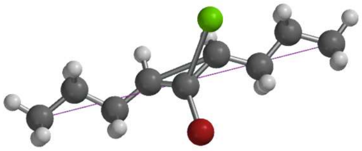

10.359 Å

Summary of CoGEF Results	
***F*$_{max}$**	3.6 nN
***E*$_{max}$**	216 kJ/mol
Force-Bond Angle	0.1°

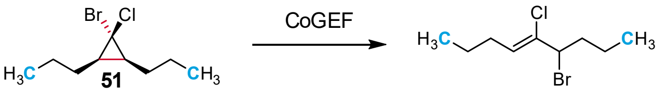

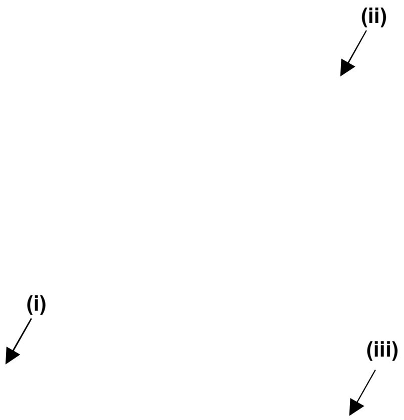

(i) Equilibrium Geometry

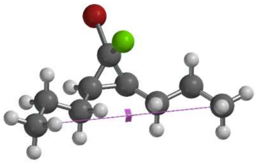

7.824 Å

(ii) Immediately Prior to Bond Cleavage

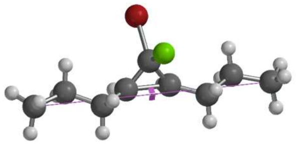

10.174 Å

(iii) Immediately After Bond Cleavage

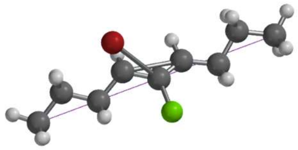

10.224 Å

Summary of CoGEF Results	
***F**$_{max}$*	3.3 nN
***E**$_{max}$*	184 kJ/mol
Force-Bond Angle	0.1°

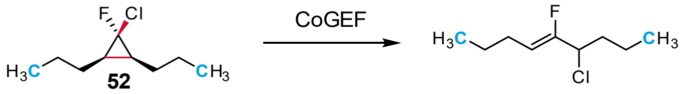

52

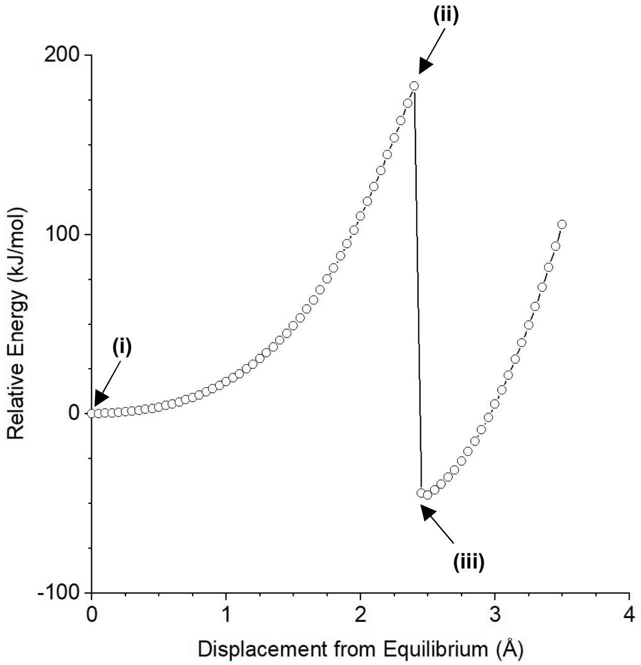

(i) Equilibrium Geometry

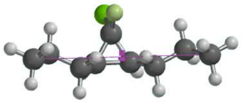

7.776 Å

(ii) Immediately Prior to Bond Cleavage

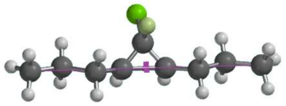

10.176 Å

(iii) Immediately After Bond Cleavage

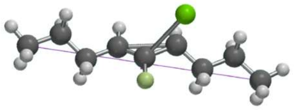

10.226 Å

Summary of CoGEF Results	
F_{max}	3.5 nN
E_{max}	262 kJ/mol
Force-Bond Angle	0.0°

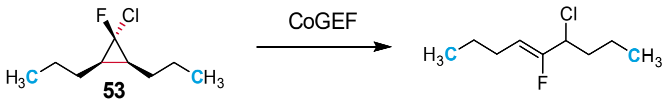

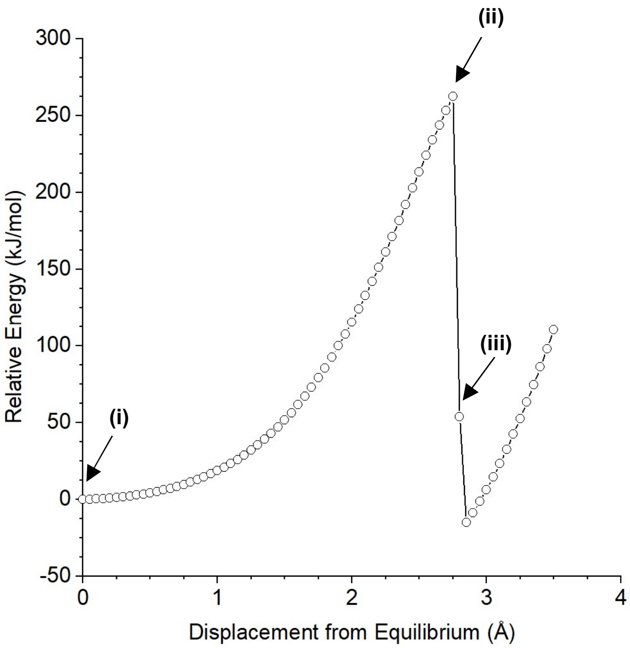

(i) Equilibrium Geometry

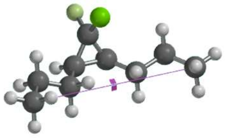

7.816Å

(ii) Immediately Prior to Bond Cleavage

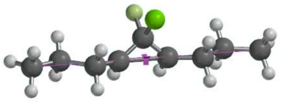

10.566 Å

(iii) Immediately After Bond Cleavage

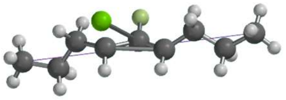

10.616Å

Summary of CoGEF Results	
***F**$_{max}$*	3.2 nN
***E**$_{max}$*	183 kJ/mol
Force-Bond Angle	0.1°

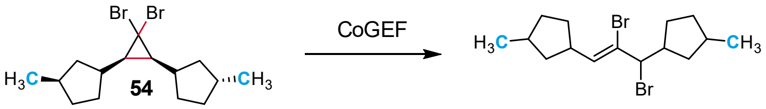

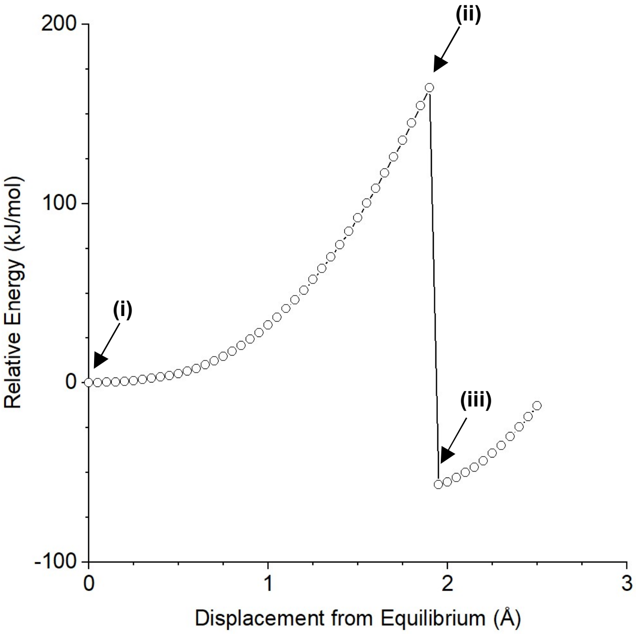

Summary of CoGEF Results	
F_{max}	3.3 nN
E_{max}	164 kJ/mol
Force-Bond Angle	0.3°

(i) Equilibrium Geometry

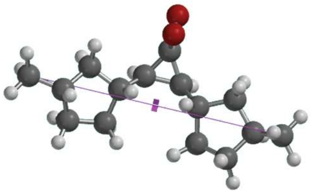

10.675 Å

(ii) Immediately Prior to Bond Cleavage

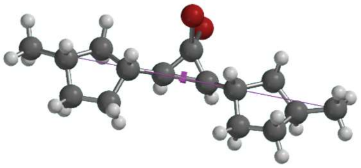

12.575 Å

(iii) Immediately After Bond Cleavage

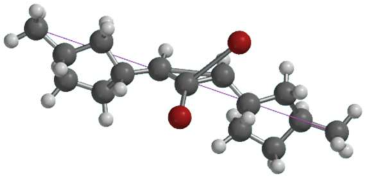

12.625 Å

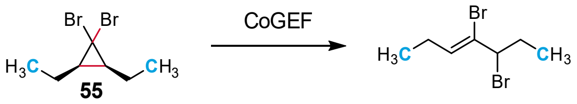

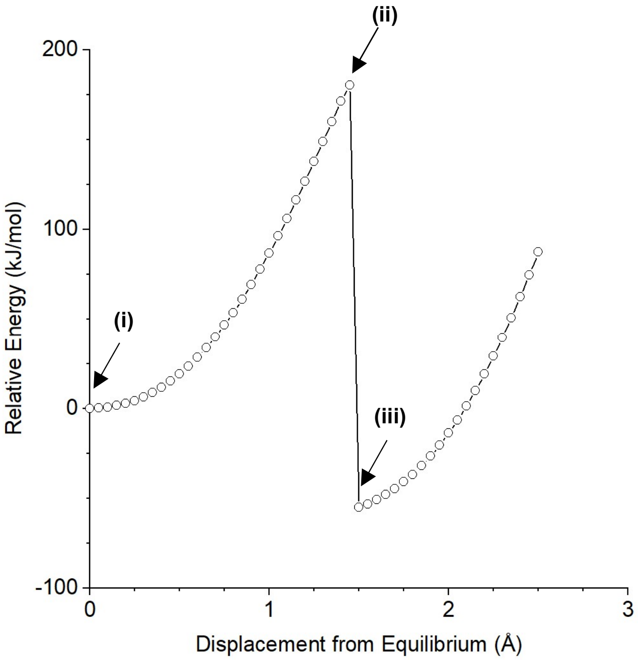

(i) Equilibrium Geometry

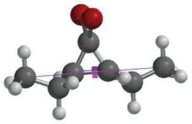

6.081 Å

(ii) Immediately Prior to Bond Cleavage

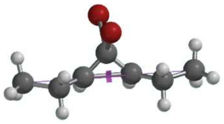

7.531 Å

(iii) Immediately After Bond Cleavage

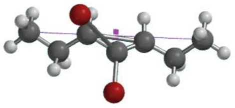

7.581 Å

Summary of CoGEF Results	
***F**max*	3.7 nN
***E**max*	180 kJ/mol
Force-Bond Angle	0.1°

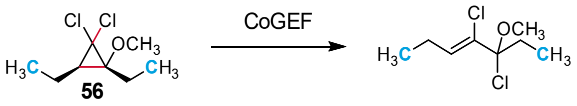

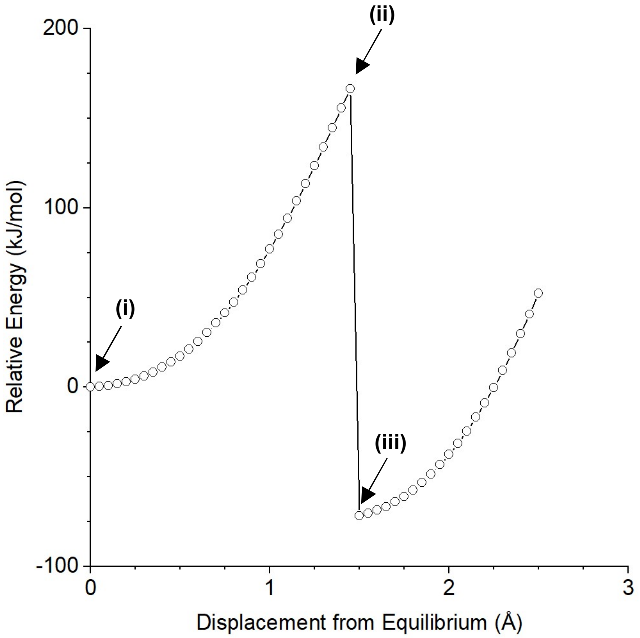

(i) Equilibrium Geometry

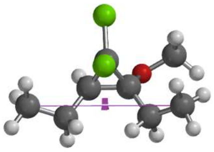

5.971 Å

(ii) Immediately Prior to Bond Cleavage

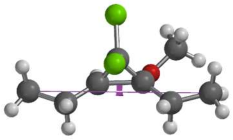

7.421 Å

(iii) Immediately After Bond Cleavage

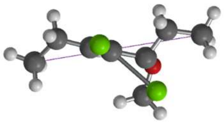

7.471 Å

Summary of CoGEF Results

***F**max*	3.6 nN
***E**max*	166 kJ/mol
Force-Bond Angle	3.8°

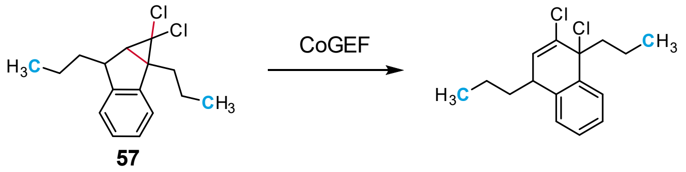

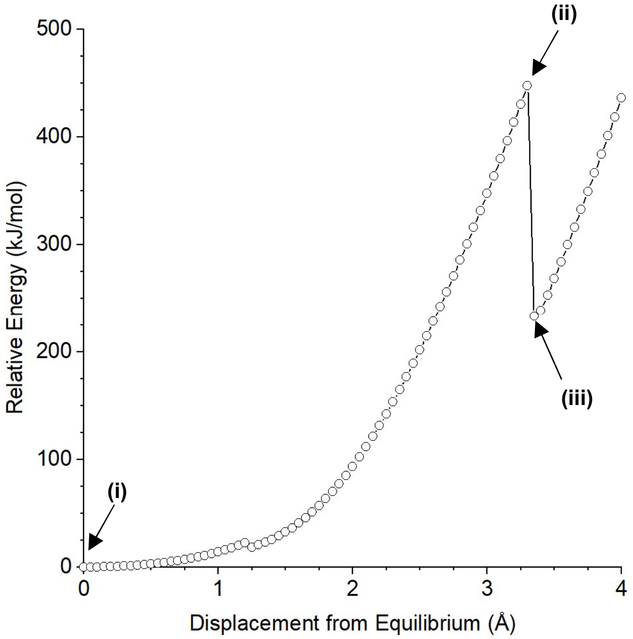

(i) Equilibrium Geometry

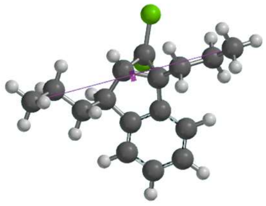

8.972 Å

(ii) Immediately Prior to Bond Cleavage

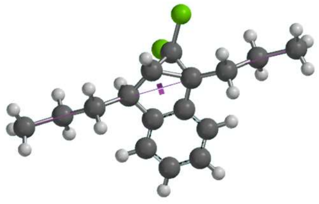

12.272 Å

(iii) Immediately After Bond Cleavage

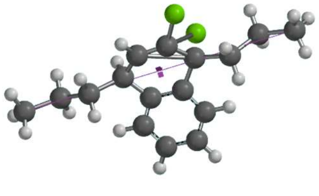

12.322 Å

Summary of CoGEF Results

F_{max}	5.7 nN
E_{max}	448 kJ/mol
Force-Bond Angle	31°

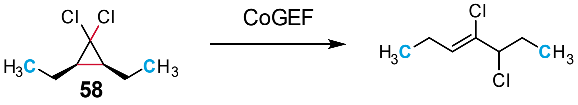

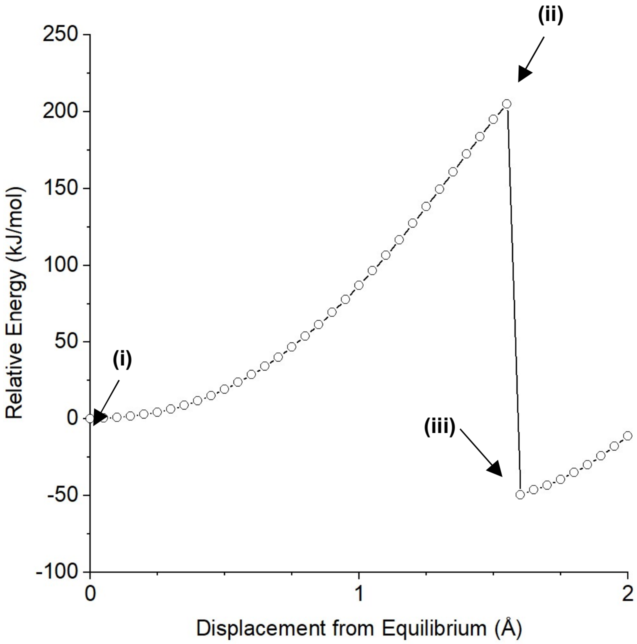

(i) Equilibrium Geometry

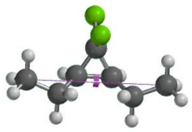

6.079 Å

(ii) Immediately Prior to Bond Cleavage

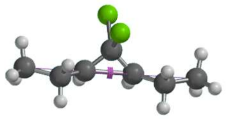

7.629 Å

(iii) Immediately After Bond Cleavage

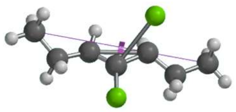

7.679 Å

Summary of CoGEF Results	
F_{max}	3.8 nN
E_{max}	205 kJ/mol
Force-Bond Angle	0.0°

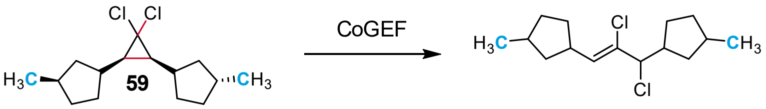

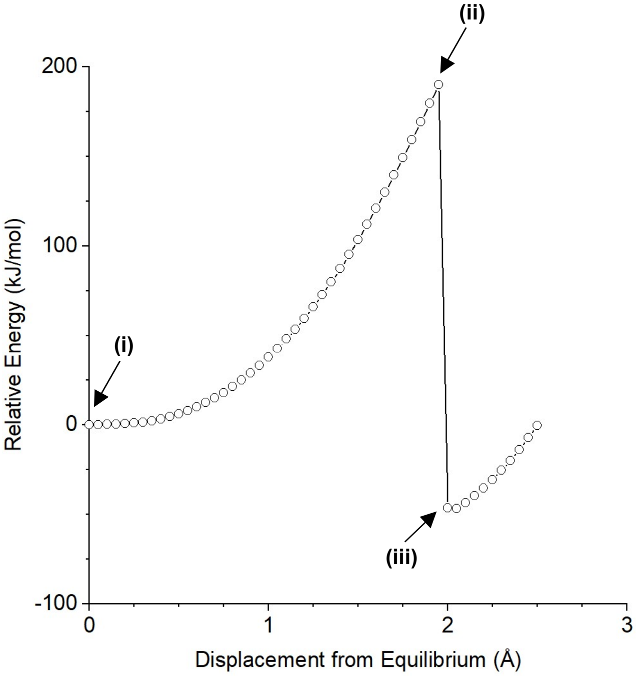

(i) Equilibrium Geometry

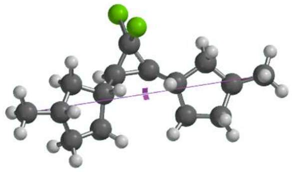

10.746 Å

(ii) Immediately Prior to Bond Cleavage

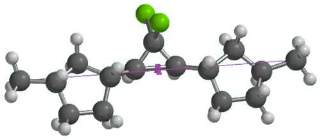

12.696 Å

(iii) Immediately After Bond Cleavage

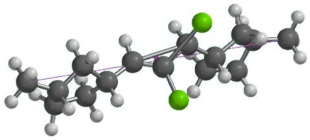

12.746 Å

Summary of CoGEF Results

F_{max}	3.4 nN
E_{max}	190 kJ/mol
Force-Bond Angle	0.4°

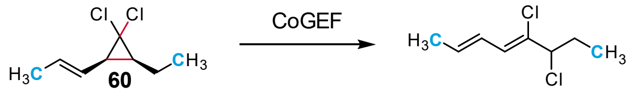

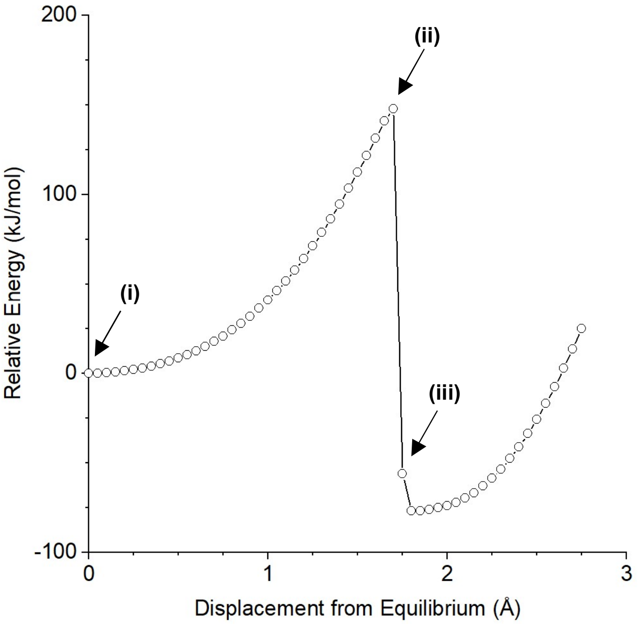

(i) Equilibrium Geometry

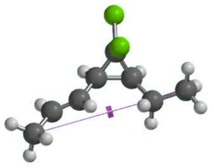

6.904 Å

(ii) Immediately Prior to Bond Cleavage

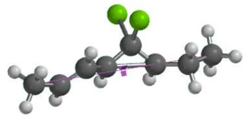

8.604 Å

(iii) Immediately After Bond Cleavage

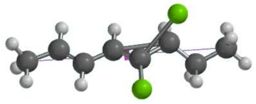

8.654 Å

Summary of CoGEF Results	
F F_{max}	3.2 nN
E_{max}	148 kJ/mol
Force-Bond Angle	9.0°

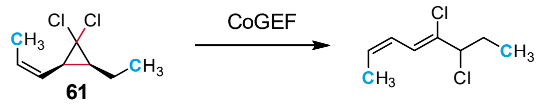

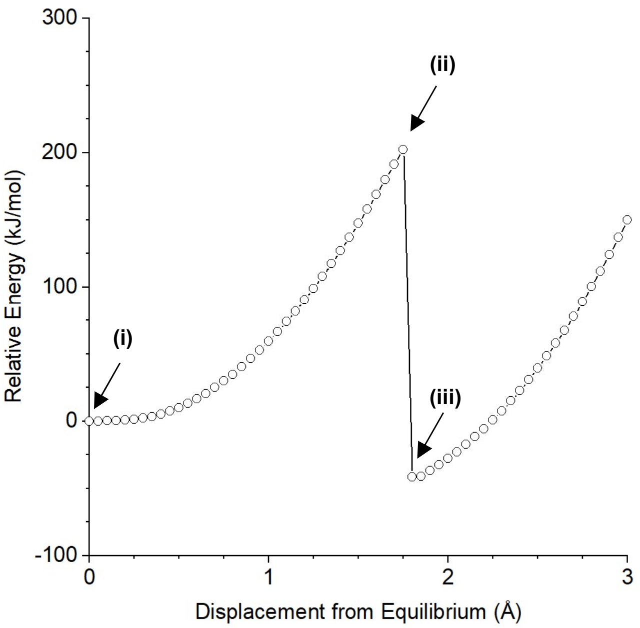

(i) Equilibrium Geometry

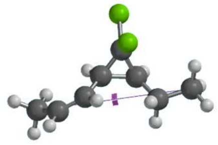

6.787 Å

(ii) Immediately Prior to Bond Cleavage

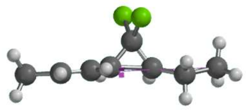

8.537 Å

(iii) Immediately After Bond Cleavage

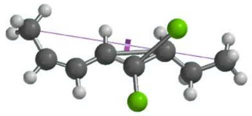

8.587 Å

Summary of CoGEF Results	
***F**$_{max}$*	3.7 nN
***E**$_{max}$*	202 kJ/mol
Force-Bond Angle	3.9°

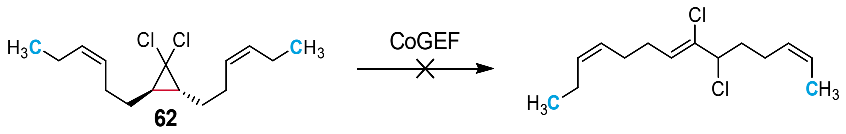

62

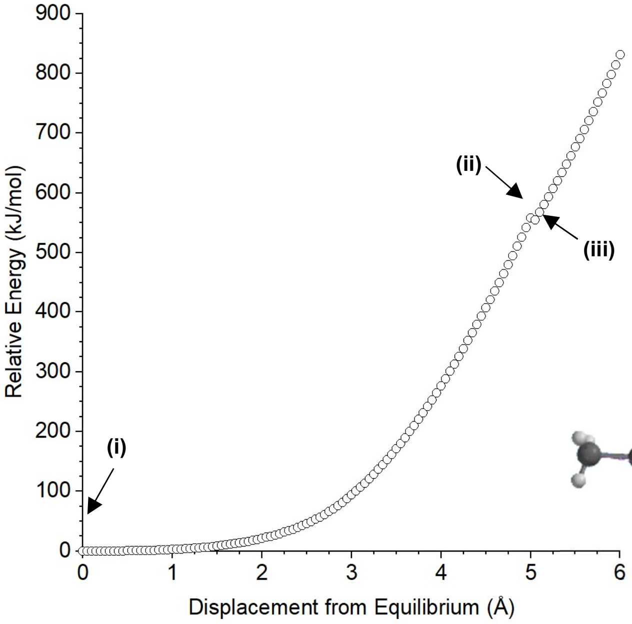

Summary of CoGEF Results	
***F**$_{max}$*	5.2 nN
***E**$_{max}$*	557 kJ/mol
Force-Bond Angle	20°

(i) Equilibrium Geometry

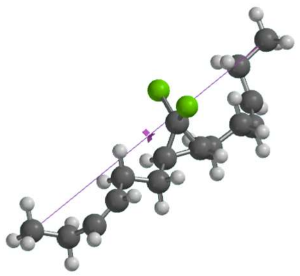

13.974 Å

(ii) Immediately Prior to Bond Cleavage

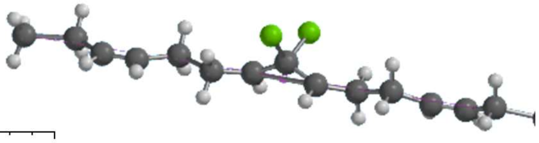

21.174 Å

(iii) Immediately After Bond Cleavage

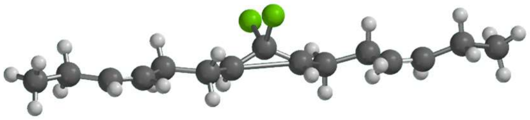

21.224 Å

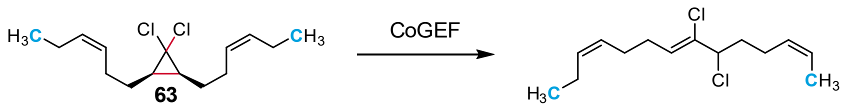

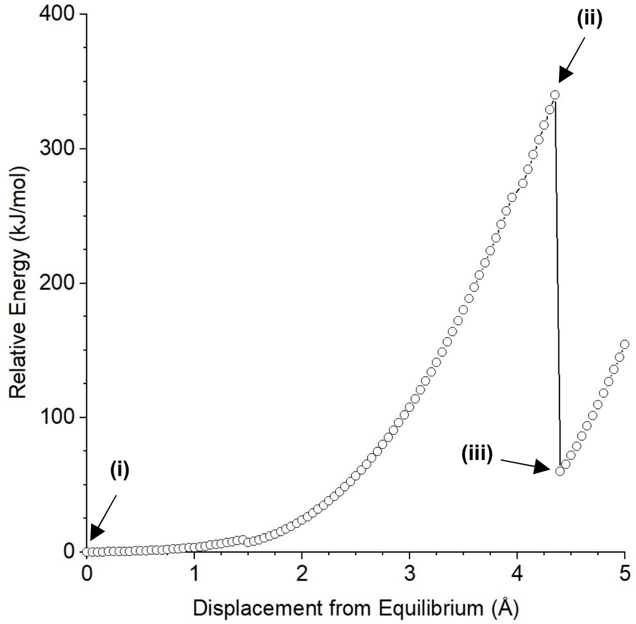

(i) Equilibrium Geometry

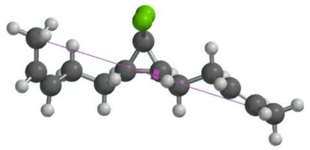

11.037 Å

(i) Immediately Prior to Bond Cleavage

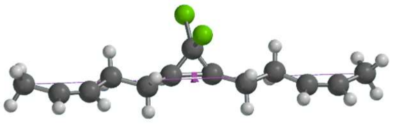

15.337 Å

(ii) Immediately After Bond Cleavage

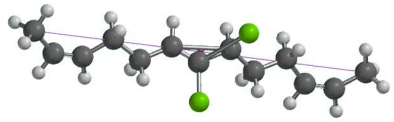

15.387 Å

Summary of CoGEF Results	
***F**_{max}*	3.8 nN
***E**_{max}*	340 kJ/mol
Force/Bond angle	0.1°

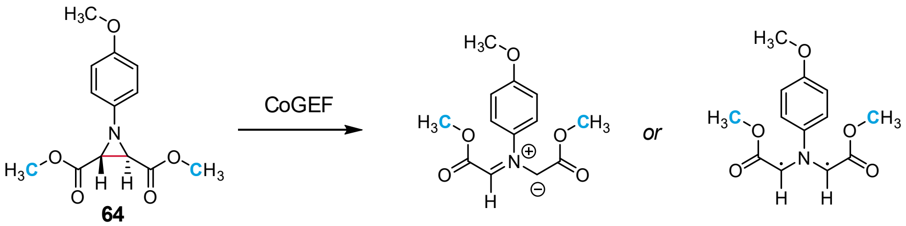

64

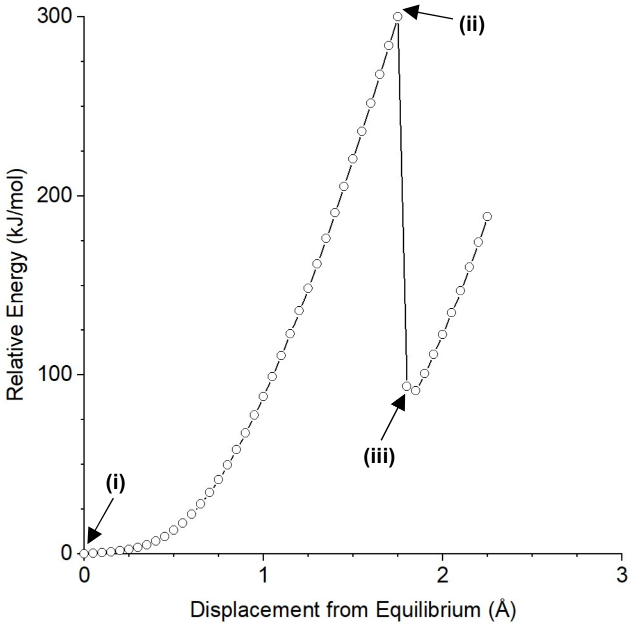

Summary of CoGEF Results	
***F**max*	5.4 nN
***E**max*	300 kJ/mol
Force-Bond Angle	22°

(i) Equilibrium Geometry

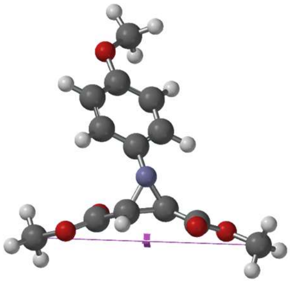

8.232 Å

(ii) Immediately Prior to Bond Cleavage

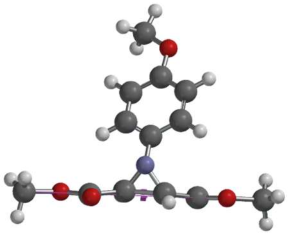

9.982 Å

(iii) Immediately After Bond Cleavage

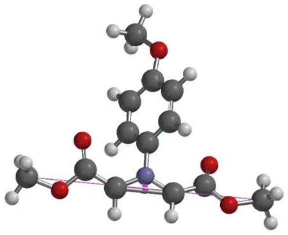

10.032 Å

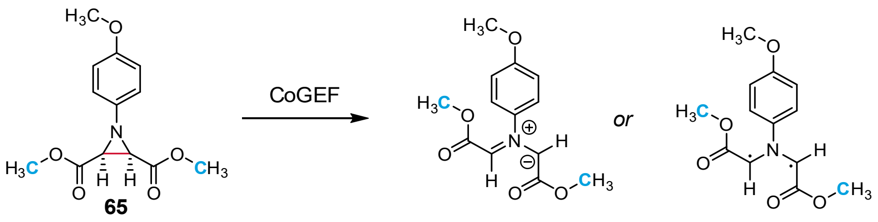

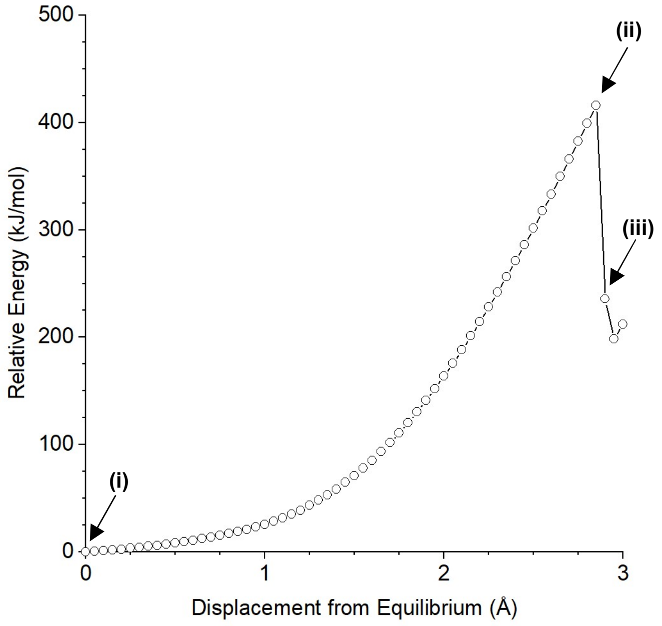

Summary of CoGEF Results	
***F**_{max}*	5.6 nN
***E**_{max}*	416 kJ/mol
Force-Bond Angle	0.1°

(i) Equilibrium Geometry

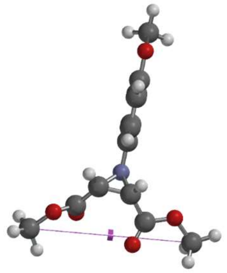

7.37 Å

(ii) Immediately Prior to Bond Cleavage

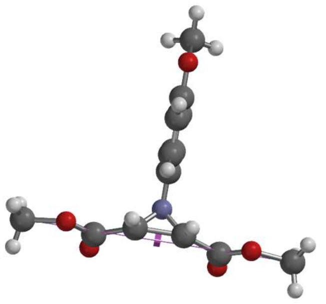

10.22 Å

(iii) Immediately After Bond Cleavage

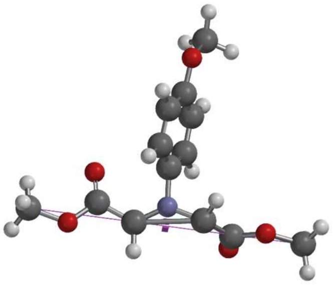

10.27 Å

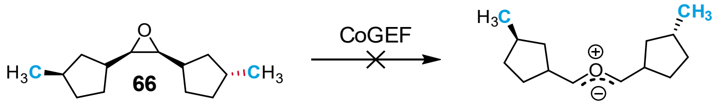

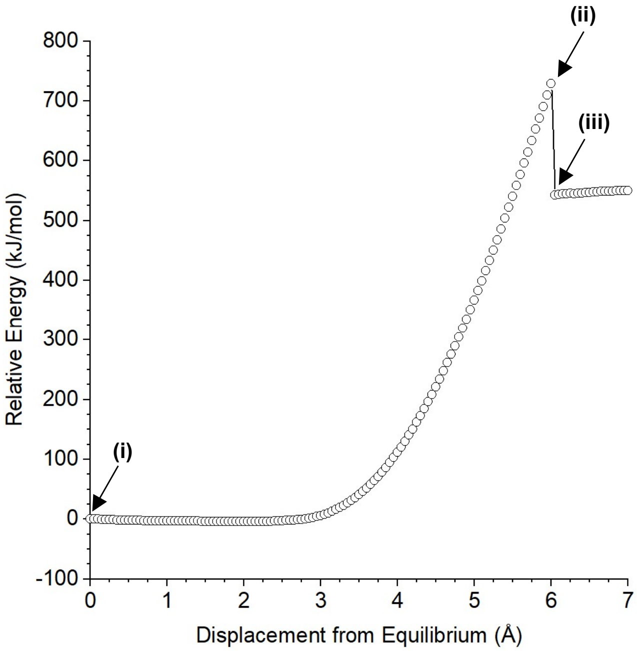

(i) Equilibrium Geometry

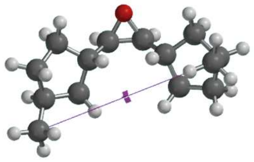

8.113 Å

(ii) Immediately Prior to Bond Cleavage

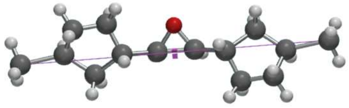

14.113 Å

(iii) Immediately After Bond Cleavage

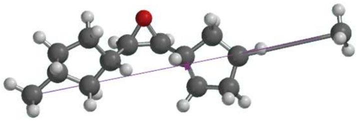

14.163 Å

Summary of CoGEF Results	
F	

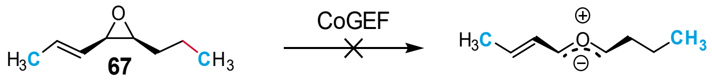

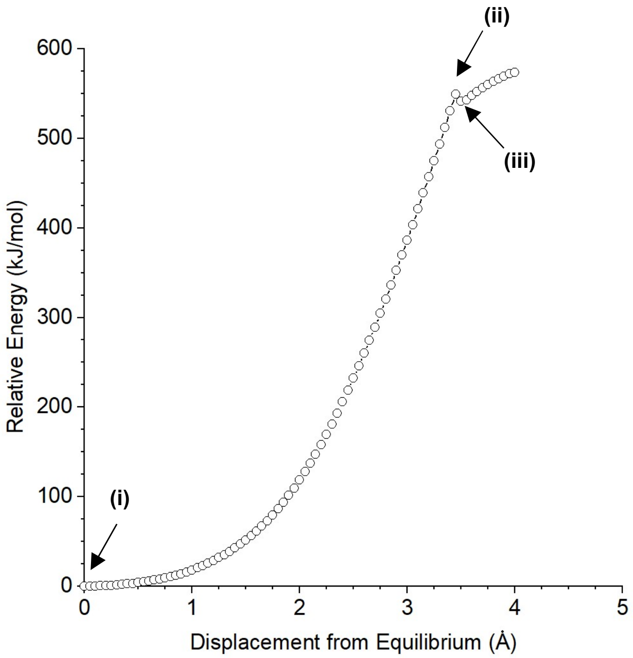

Summary of CoGEF Results	
F	

(i) Equilibrium Geometry

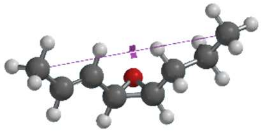

7.555 Å

(ii) Immediately Prior to Bond Cleavage

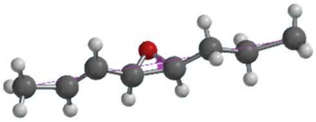

11.005 Å

(iii) Immediately After Bond Cleavage

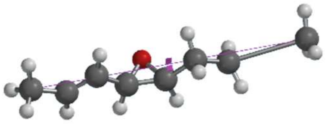

11.055 Å

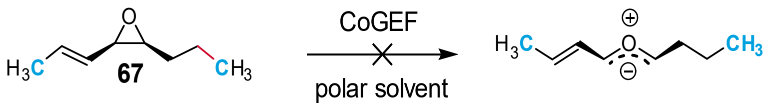

67

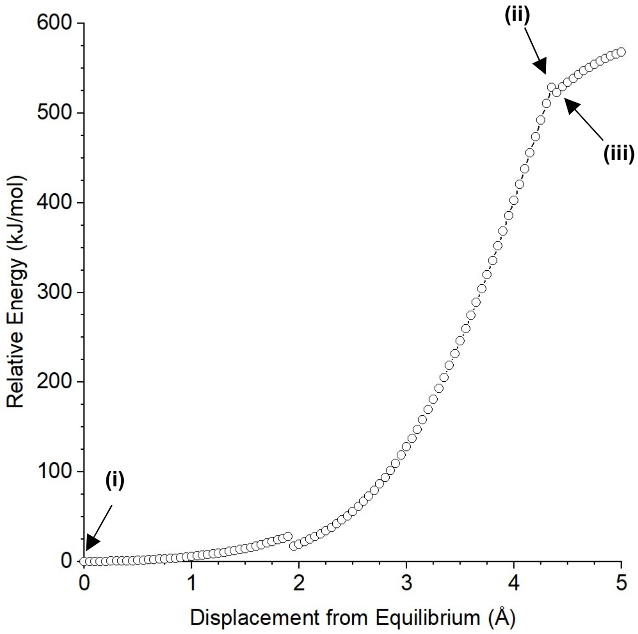

(i) Equilibrium Geometry

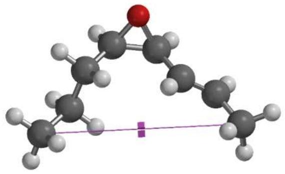

6.606 Å

(ii) Immediately Prior to Bond Cleavage

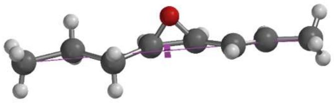

10.956 Å

(iii) Immediately After Bond Cleavage

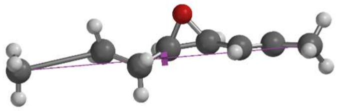

11.006 Å

Summary of CoGEF Results

***F**$_{max}$*	6.1 nN
***E**$_{max}$*	529 kJ/mol
Force-Bond Angle	1.6°

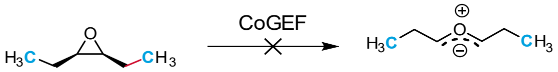

Con6

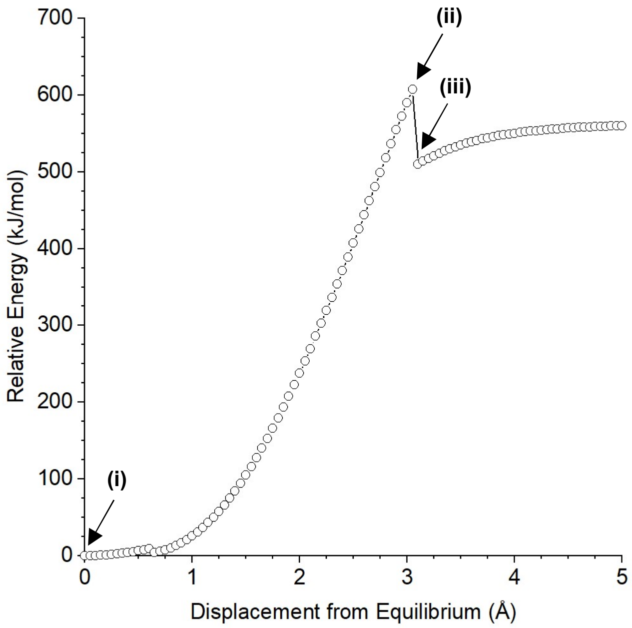

(i) Equilibrium Geometry

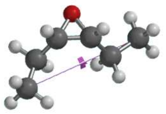

5.523 Å

(ii) Immediately Prior to Bond Cleavage

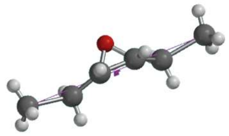

8.573 Å

(iii) Immediately After Bond Cleavage

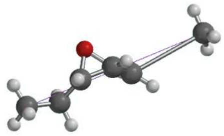

8.623 Å

Summary of CoGEF Results	
***F**$_{max}$*	6.2 nN
***E**$_{max}$*	607 kJ/mol
Force-Bond Angle	0.0°

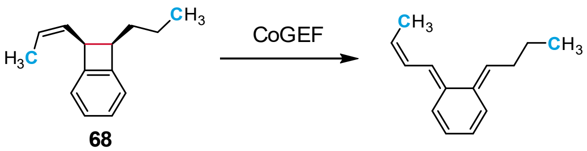

68

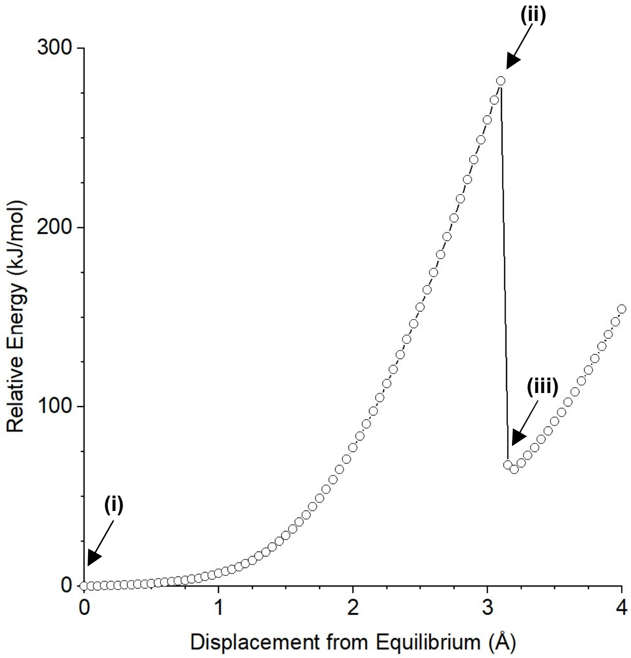

(i) Equilibrium Geometry

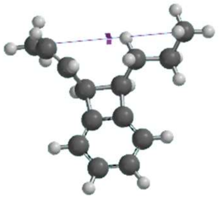

7.067 Å

(ii) Immediately Prior to Bond Cleavage

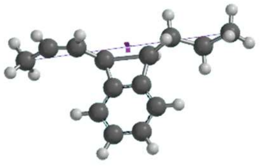

10.167 Å

(iii) Immediately After Bond Cleavage

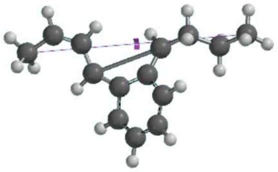

10.217 Å

Summary of CoGEF Results

F_{max}	3.7 nN
E_{max}	282 kJ/mol
Force/Bond angle	3.2°

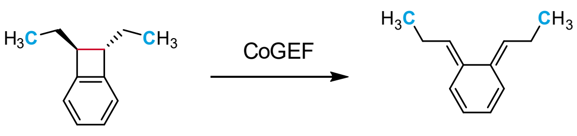

69

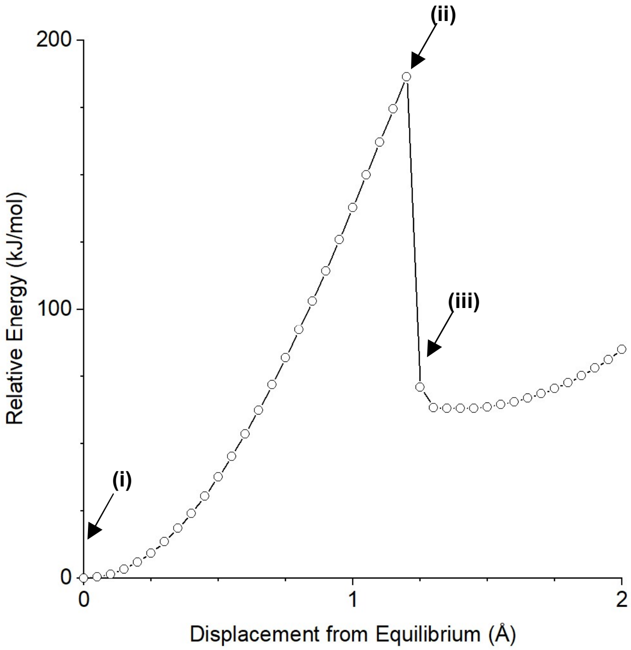

Summary of CoGEF Results	
***F**$_{max}$*	4.1 nN
***E**$_{max}$*	186 kJ/mol
Force/Bond angle	17°

(i) Equilibrium Geometry

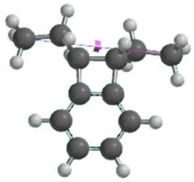

6.463 Å

(ii) Immediately Prior to Bond Cleavage

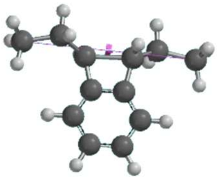

7.663 Å

(iii) Immediately After Bond Cleavage

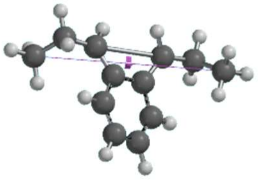

7.713 Å

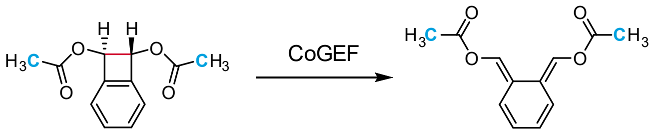

70

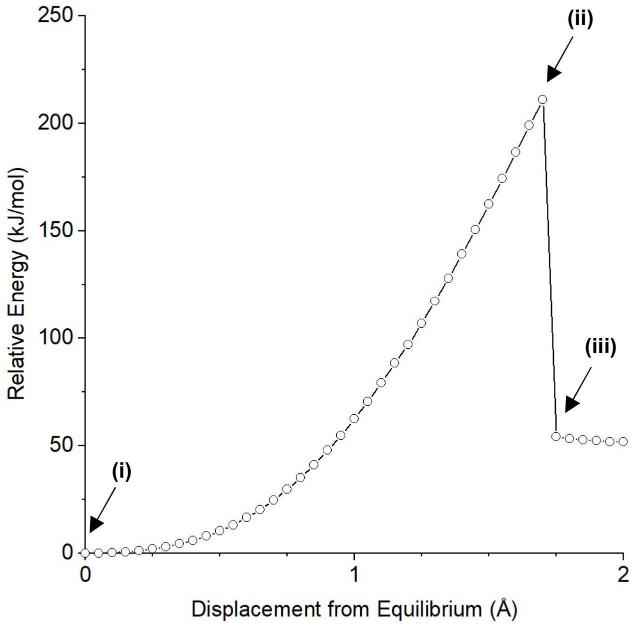

(i) Equilibrium Geometry

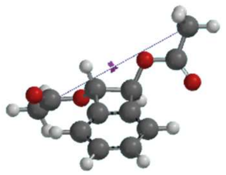

7.936 Å

(ii) Immediately Prior to Bond Cleavage

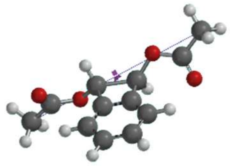

9.636 Å

(iii) Immediately After Bond Cleavage

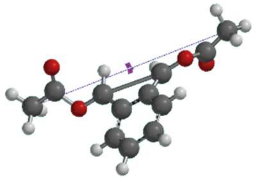

9.686 Å

Summary of CoGEF Results	
F*max*	4.1 nN
E*max*	211 kJ/mol
Force-Bond Angle	25°

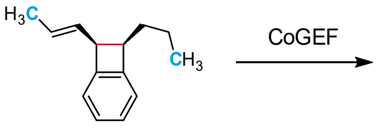

71

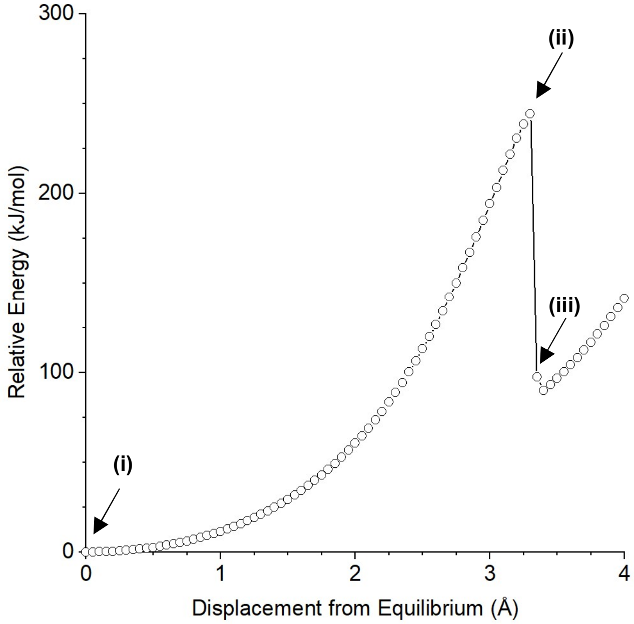

Summary of CoGEF Results	
F_{max}	3.1 nN
E_{max}	244 kJ/mol
Force-Bond Angle	2.8°

(i) Equilibrium Geometry

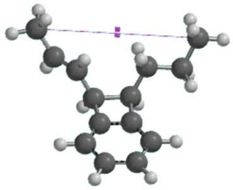

7.011 Å

(ii) Immediately Prior to Bond Cleavage

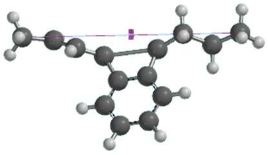

10.161 Å

(iii) Immediately After Bond Cleavage

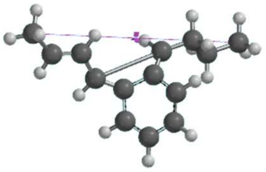

10.211 Å

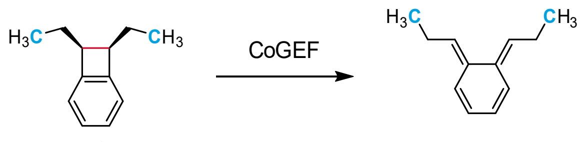

72

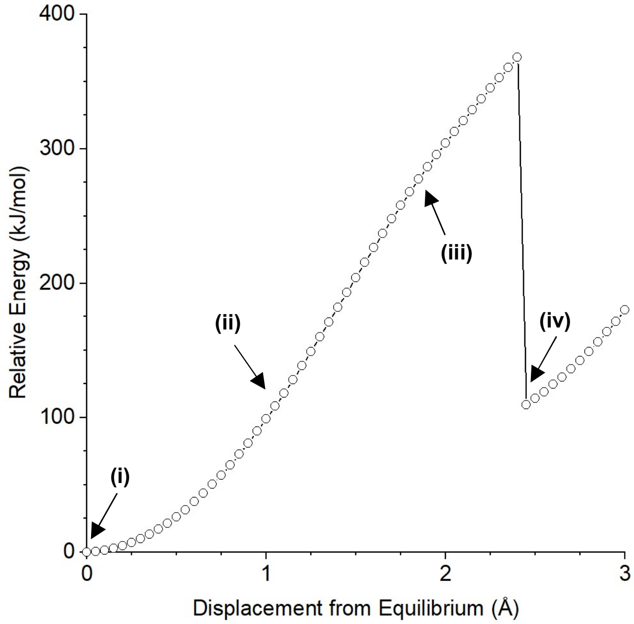

Summary of CoGEF Results

F_{max}	3.7 nN
E_{max}	367 kJ/mol
Force/Bond angle	0.0°

(i) Equilibrium Geometry

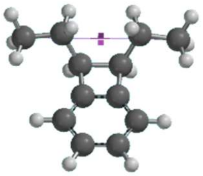

6.123 Å

(ii) Prior to Bond Cleavage

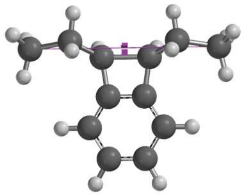

7.273 Å

(iii) After Bond Cleavage

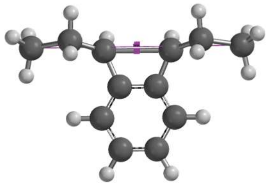

8.123

(iv) After Formation of Double Bonds

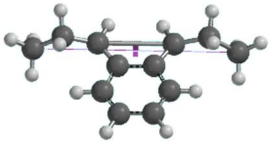

8.573 Å

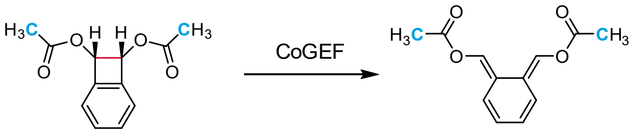

73

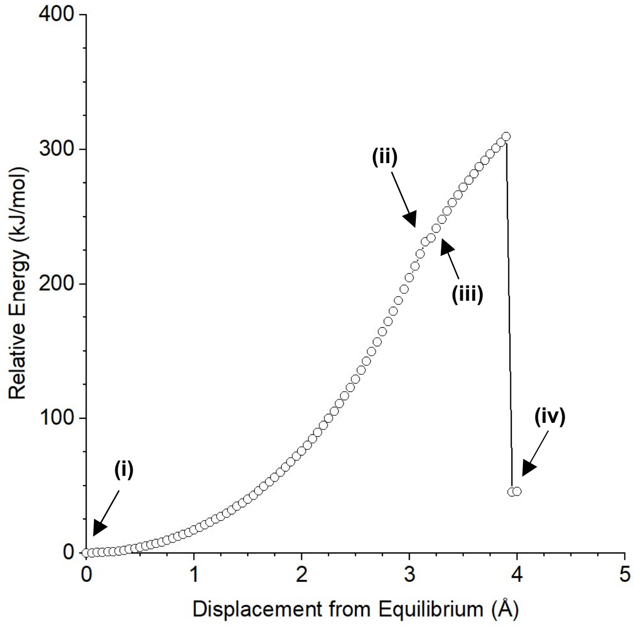

(i) Equilibrium Geometry

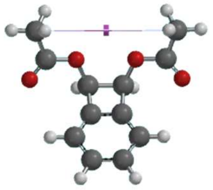

6.275 Å

(ii) Immediately Prior to Bond Cleavage

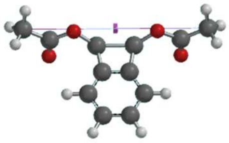

9.425 Å

(iii) Immediately After Bond Cleavage

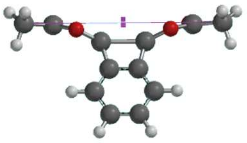

9.475 Å

(iv) After Formation of Double Bonds

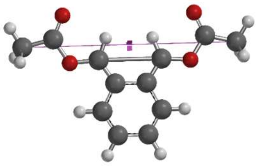

10.225 Å

Summary of CoGEF Results	
F	

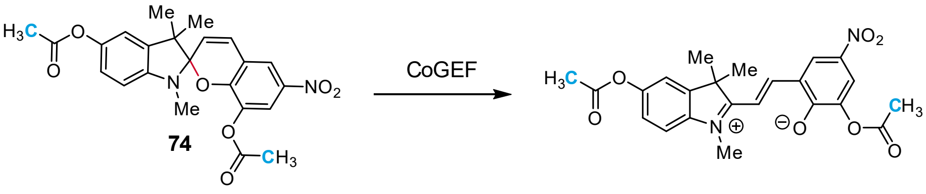

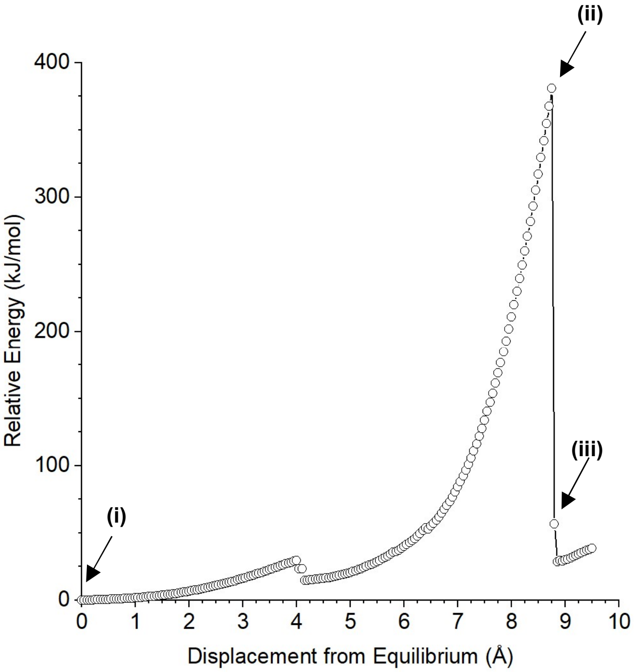

Summary of CoGEF Results	
F_{max}	4.4 nN
E_{max}	381 kJ/mol
Force-Bond Angle	14°

(i) Equilibrium Geometry

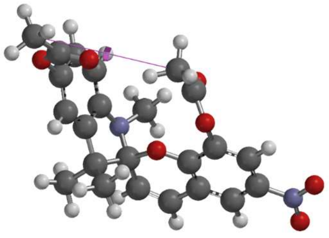

6.048 Å

(ii) Immediately Prior to Bond Cleavage

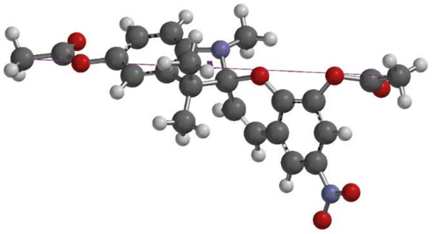

16.648 Å

(iii) Immediately After Bond Cleavage

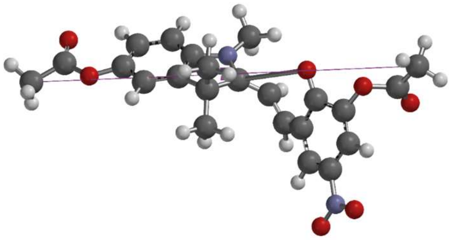

16.698 Å

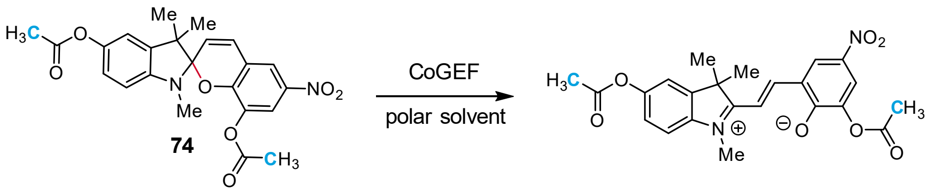

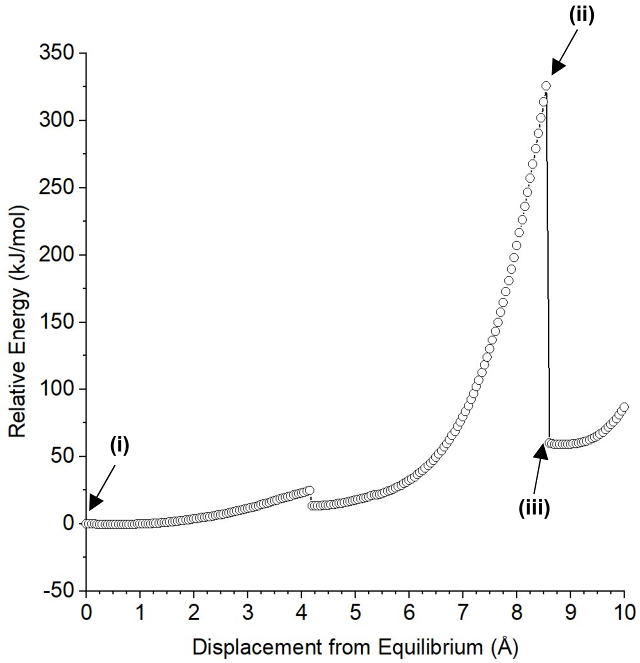

(i) Equilibrium Geometry

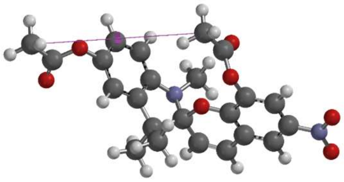

7.920 Å

(ii) Immediately Prior to Bond Cleavage

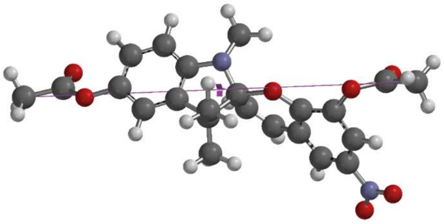

16.470 Å

(iii) Immediately After Bond Cleavage

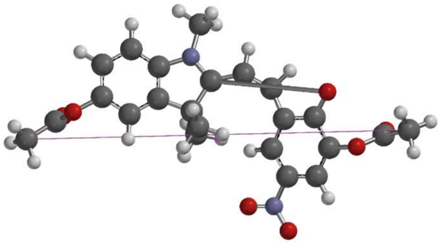

16.520 Å

Summary of CoGEF Results	
F_{max}	4.0 nN
E_{max}	325 kJ/mol
Force-Bond Angle	14°

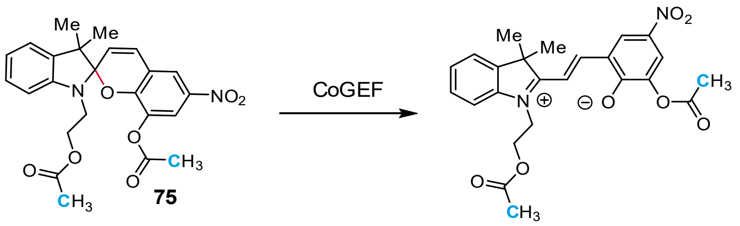

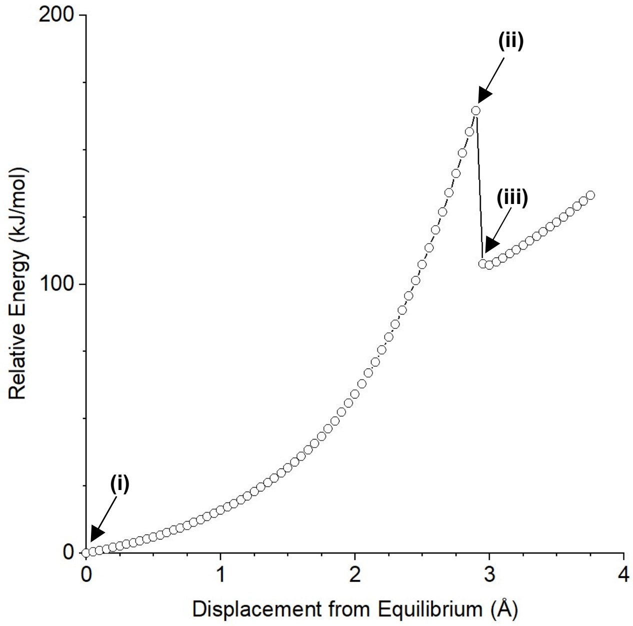

Summary of CoGEF Results	
***F**$_{max}$*	2.7 nN
***E**$_{max}$*	165 kJ/mol
Force-Bond Angle	29°

(i) Equilibrium Geometry

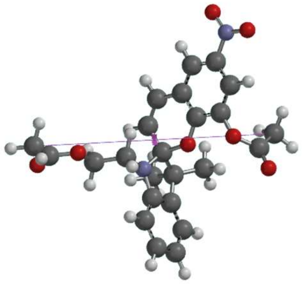

11.600 Å

(ii) Immediately Prior to Bond Cleavage

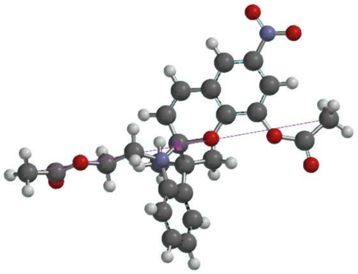

14.500 Å

(iii) Immediately After Bond Cleavage

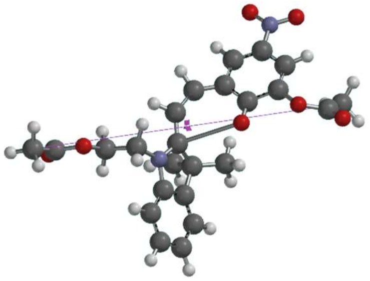

14.550 Å

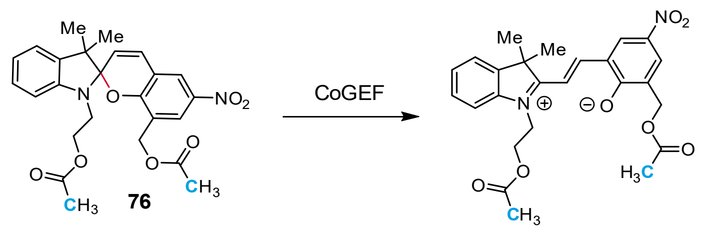

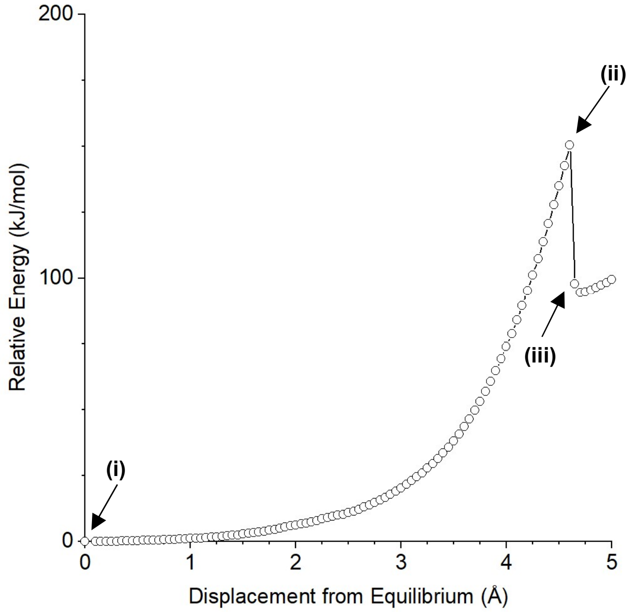

Summary of CoGEF Results	
F_{max}	2.6 nN
E_{max}	150 kJ/mol
Force-Bond Angle	27°

(i) Equilibrium Geometry

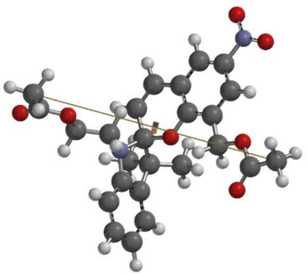

11.322 Å

(ii) Immediately Prior to Bond Cleavage

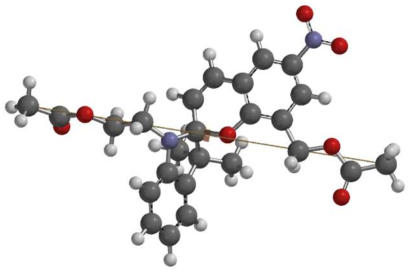

15.922 Å

(iii) Immediately After Bond Cleavage

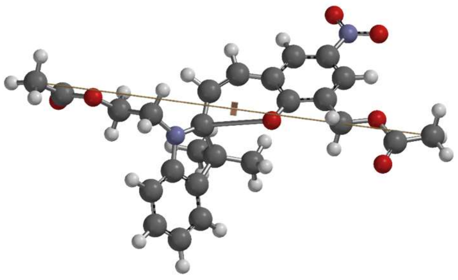

15.972 Å

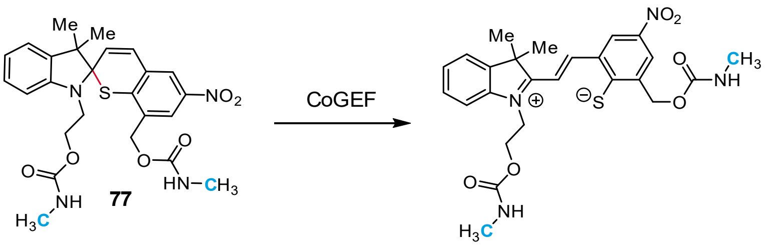

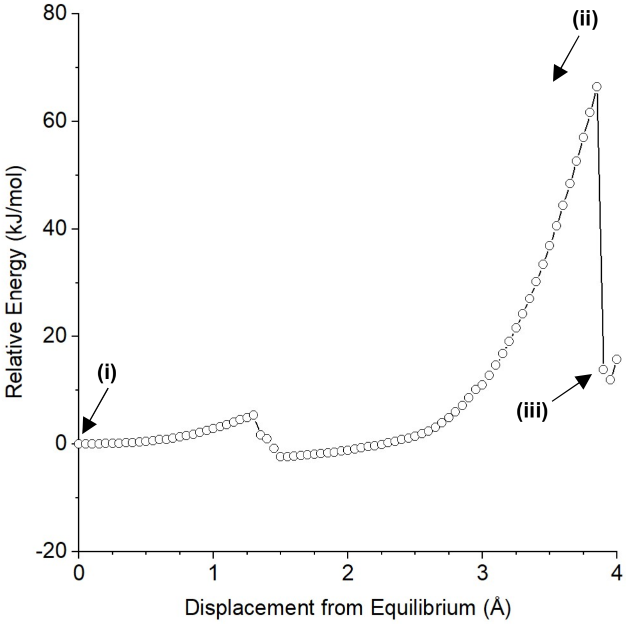

Summary of CoGEF Results

F_{max}	2.0 nN
E_{max}	74 kJ/mol
Force-Bond Angle	31°

(i) Equilibrium Geometry

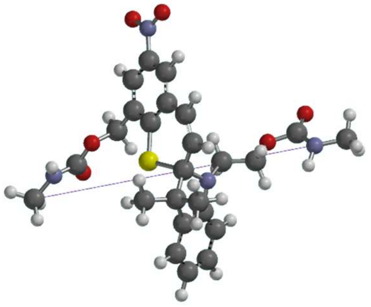

14.303 Å

(ii) Immediately Prior to Bond Cleavage

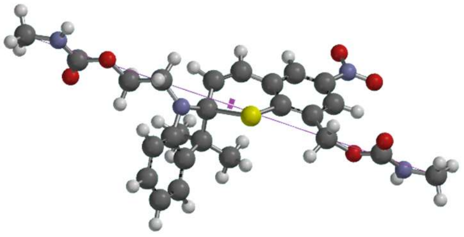

18.803 Å

(iii) Immediately After Bond Cleavage

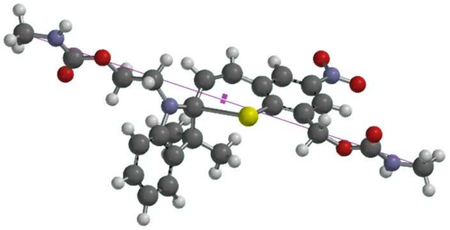

18.853 Å

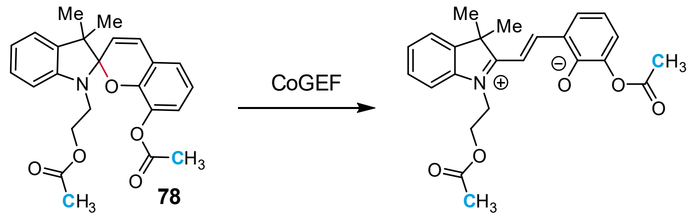

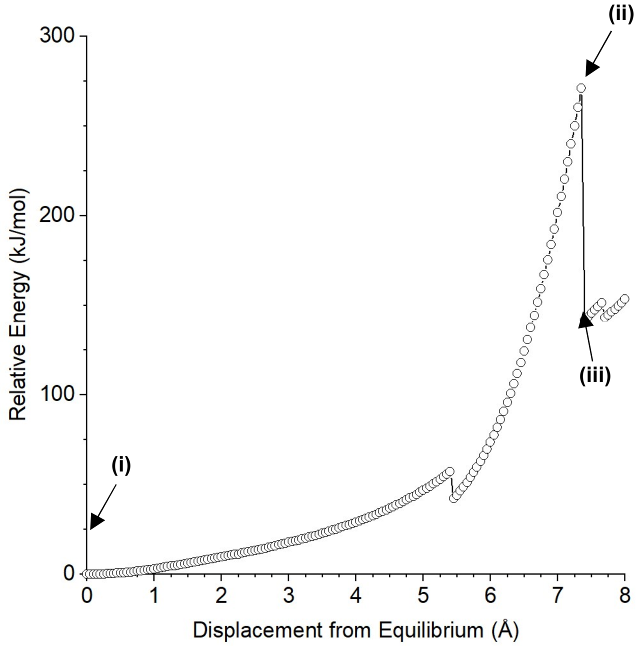

Summary of CoGEF Results	
F$_{max}$	3.5 nN
E$_{max}$	271 kJ/mol
Force-Bond Angle	28°

(i) Equilibrium Geometry

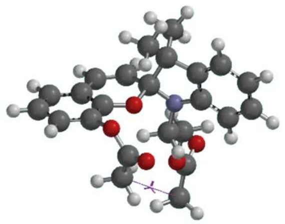

7.625 Å

(ii) Immediately Prior to Bond Cleavage

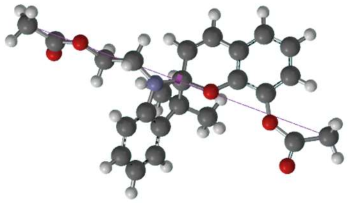

14.975 Å

(iii) Immediately After Bond Cleavage

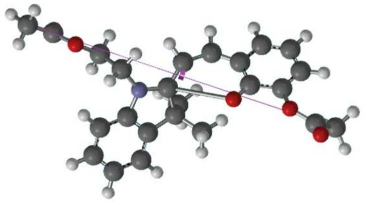

15.025 Å

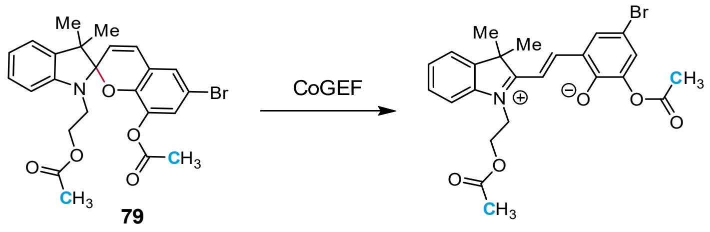

79

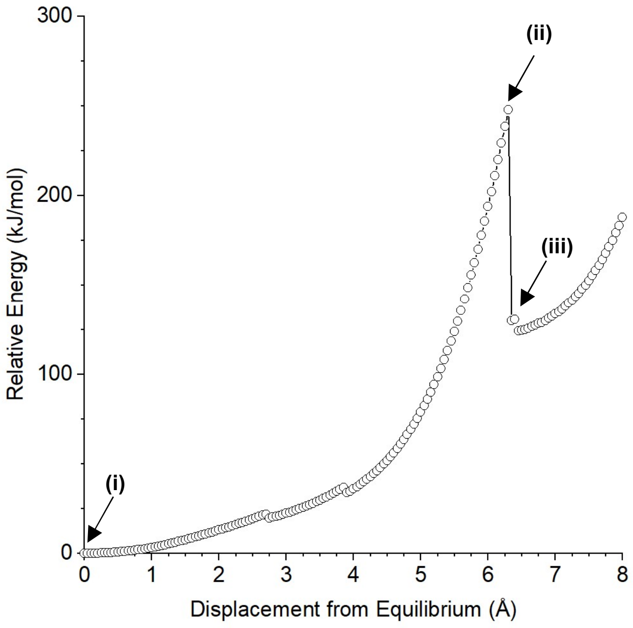

(i) Equilibrium Geometry

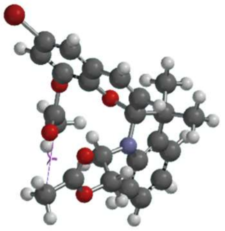

8.544 Å

(ii) Immediately Prior to Bond Cleavage

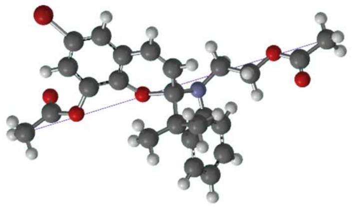

14.844 Å

(iii) Immediately After Bond Cleavage

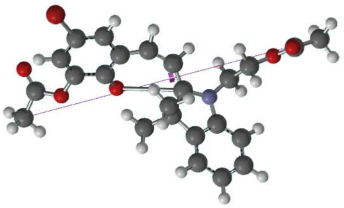

14.894 Å

Summary of CoGEF Results

F_{max}	3.2 nN
E_{max}	248 kJ/mol
Force-Bond Angle	27°

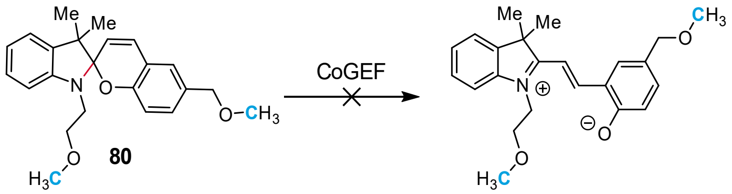

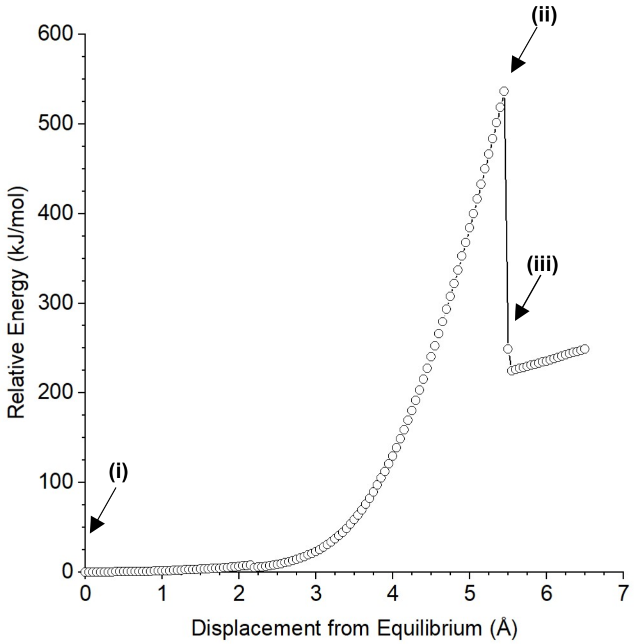

Summary of CoGEF Results	
***F*$_{max}$**	5.9 nN
***E*$_{max}$**	536 kJ/mol
Force-Bond Angle	47°

(i) Equilibrium Geometry

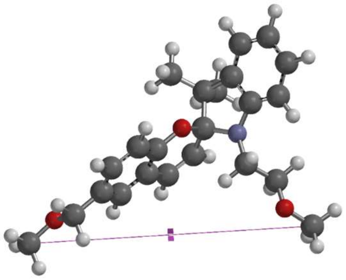

11.447 Å

(ii) Immediately Prior to Bond Cleavage

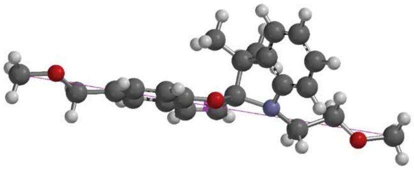

16.897 Å

(iii) Immediately After Bond Cleavage

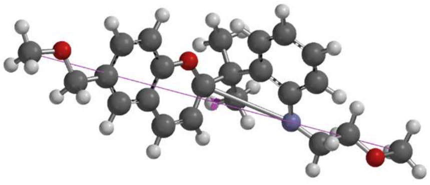

16.947 Å

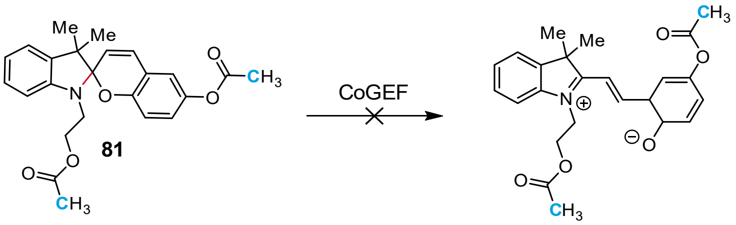

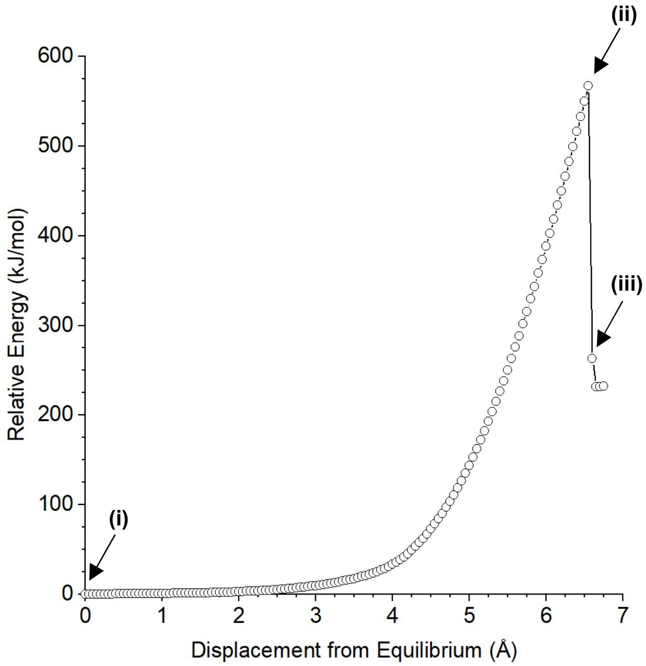

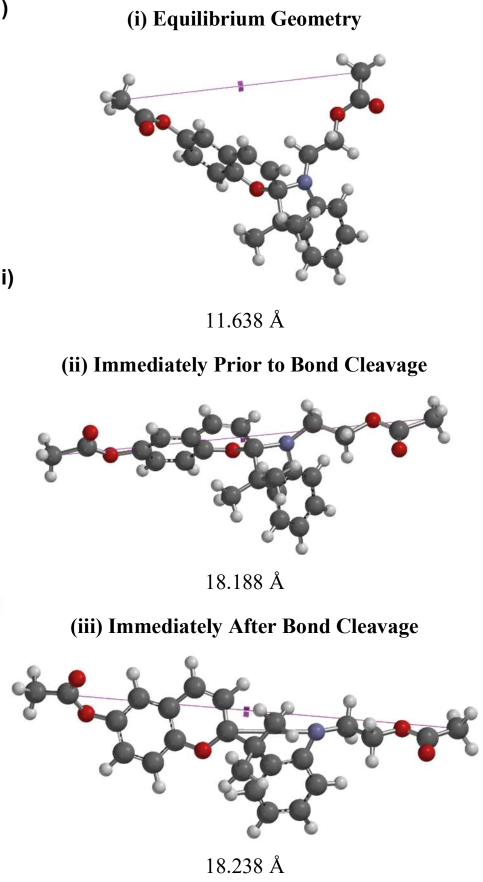
(i) Equilibrium Geometry

11.638 Å

(ii) Immediately Prior to Bond Cleavage

18.188 Å

(iii) Immediately After Bond Cleavage

18.238 Å

Summary of CoGEF Results	
***F**_{max}*	5.7 nN
***E**_{max}*	567 kJ/mol
Force-Bond Angle	49°

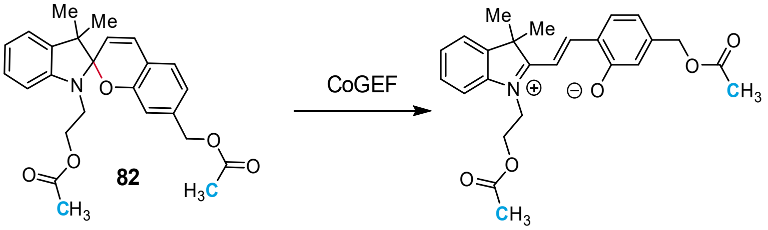

82

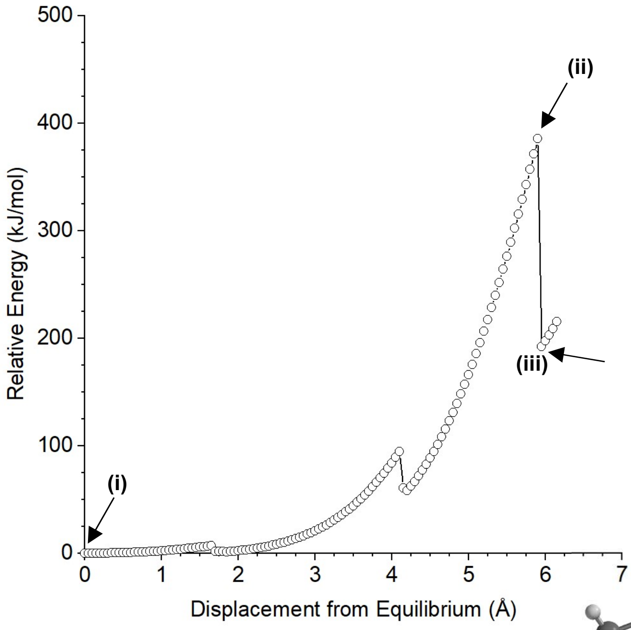

Summary of CoGEF Results	
F_{max}	4.8 nN
E_{max}	386 kJ/mol
Force-Bond Angle	35°

(i) Equilibrium Geometry

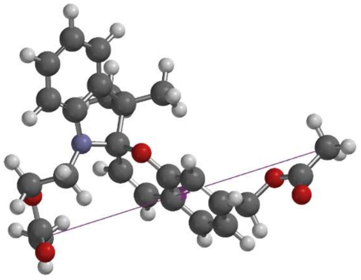

12.787 Å

(ii) Immediately Prior to Bond Cleavage

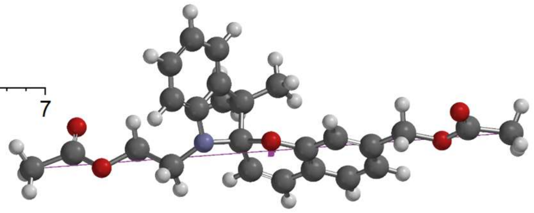

18.687 Å

(iii) Immediately After Bond Cleavage

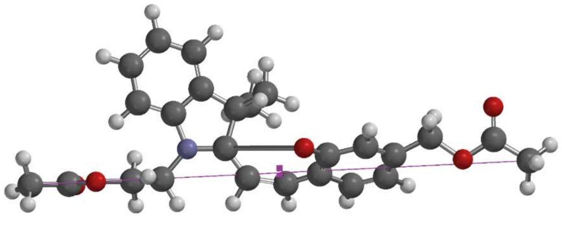

18.737 Å

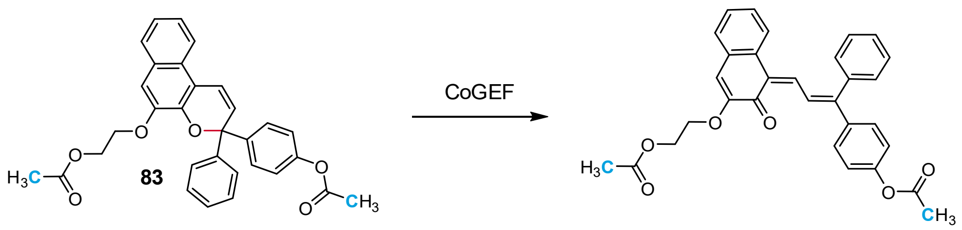

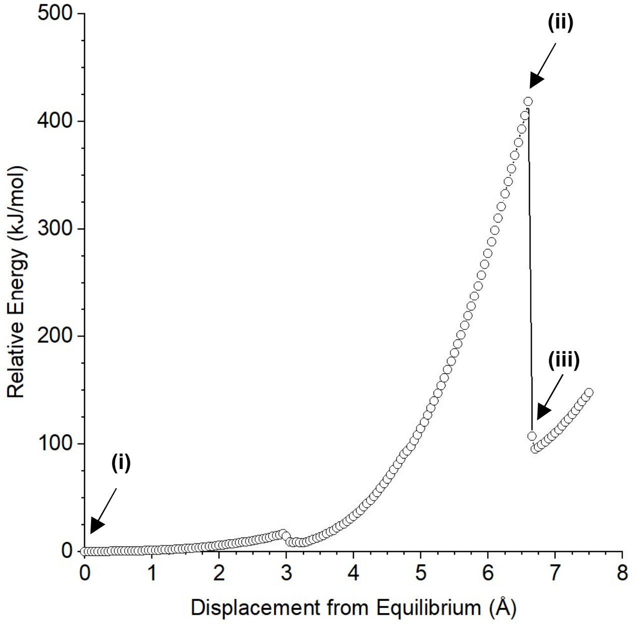

Summary of CoGEF Results

***F**_{max}*	4.3 nN
***E**_{max}*	418 kJ/mol
Force-Bond Angle	29°

(i) Equilibrium Geometry

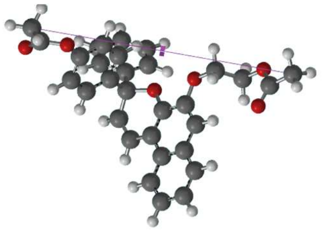

13.325 Å

(ii) Immediately Prior to Bond Cleavage

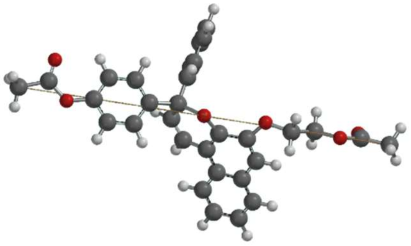

19.925 Å

(iii) Immediately After Bond Cleavage

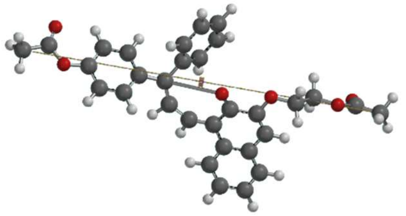

19.975 Å

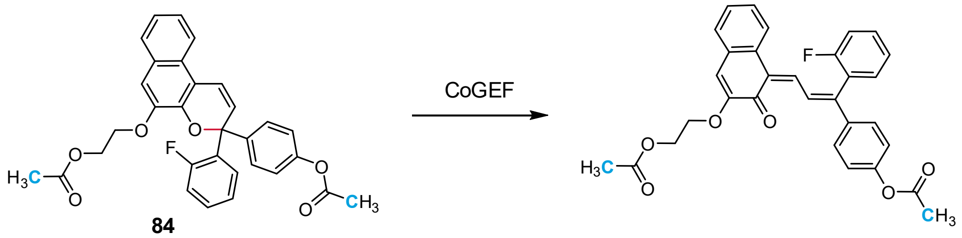

84

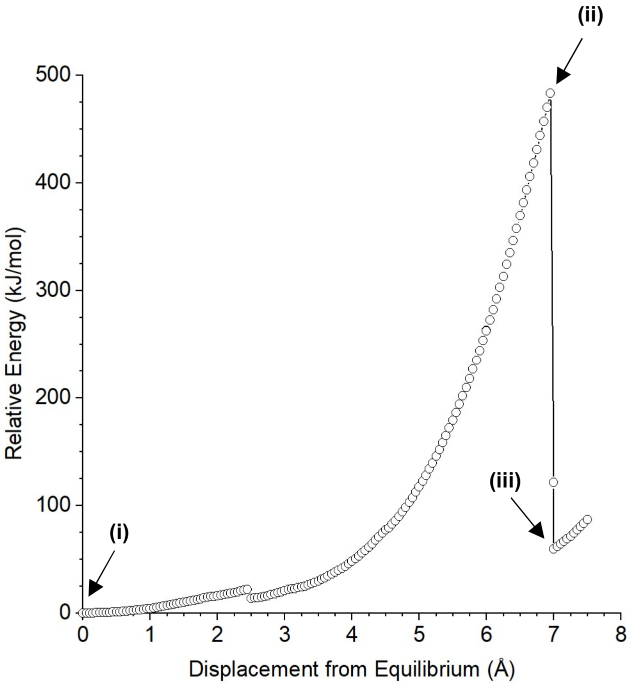

Summary of CoGEF Results	
F_{max}	4.4 nN
E_{max}	483 kJ/mol
Force-Bond Angle	26°

(i) Equilibrium Geometry

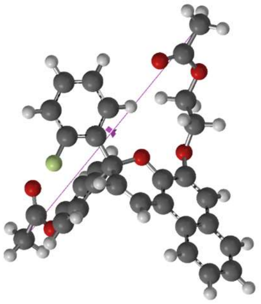

13.160 Å

(ii) Immediately Prior to Bond Cleavage

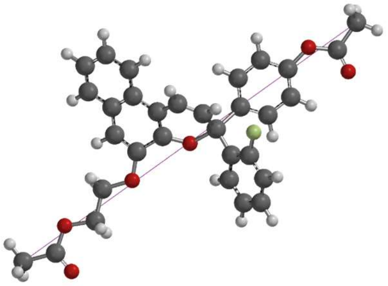

20.110 Å

(iii) Immediately After Bond Cleavage

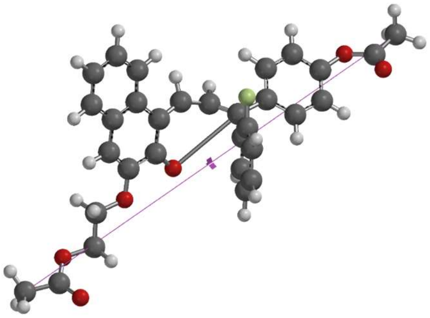

20.160 Å

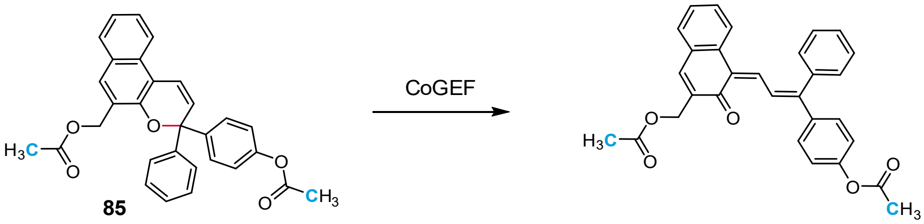

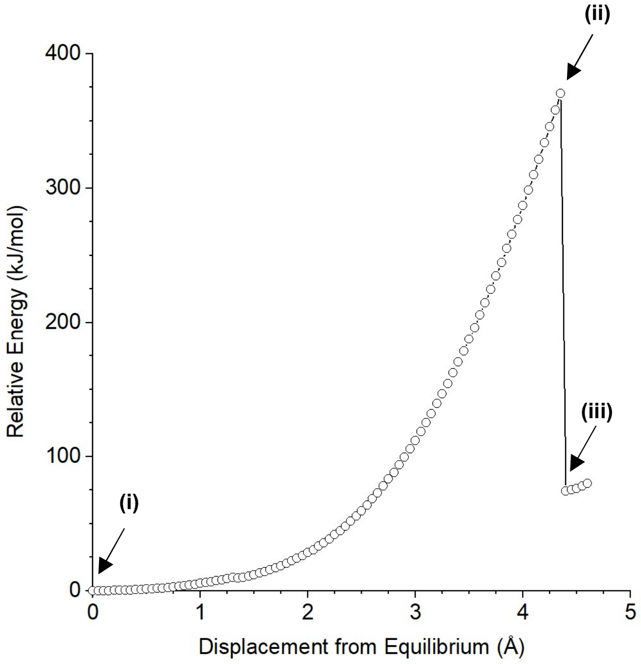

Summary of CoGEF Results	
F_{max}	4.1 nN
E_{max}	370 kJ/mol
Force-Bond Angle	29°

(i) Equilibrium Geometry

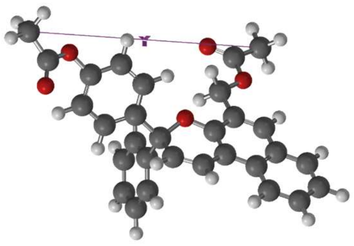

13.153 Å

(ii) Immediately Prior to Bond Cleavage

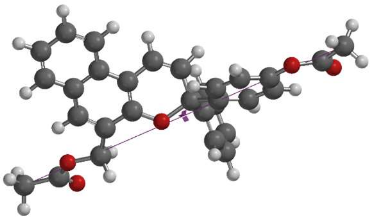

17.503 Å

(iii) Immediately After Bond Cleavage

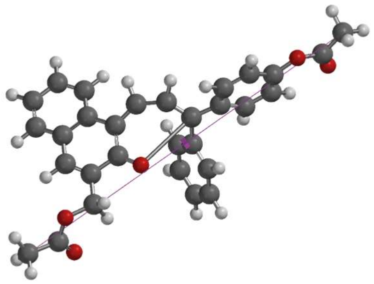

17.553 Å

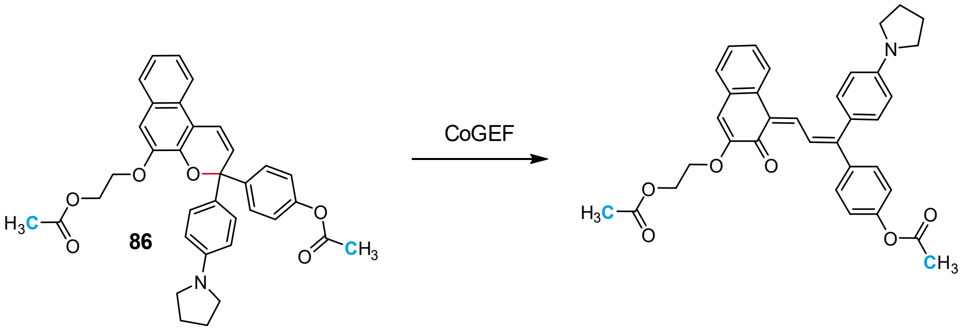

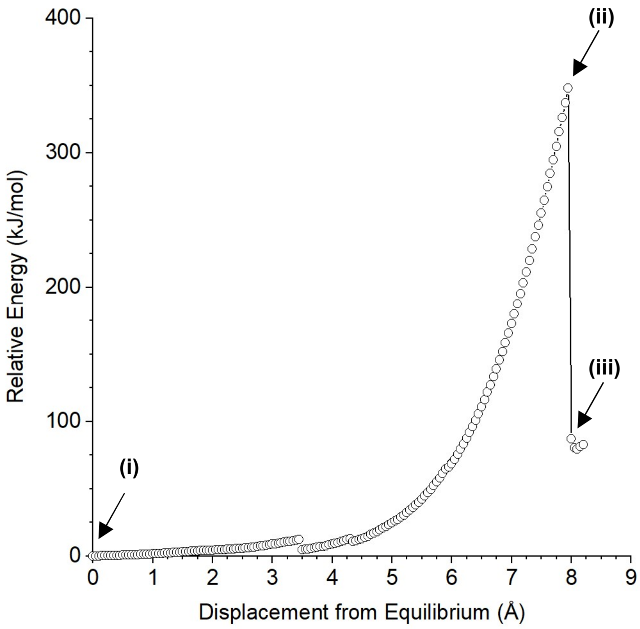

Summary of CoGEF Results	
***F*$_{max}$**	3.7 nN
***E*$_{max}$**	348 kJ/mol
Force-Bond Angle	30°

(i) Equilibrium Geometry

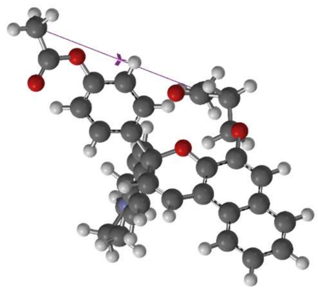

11.651 Å

(ii) Immediately Prior to Bond Cleavage

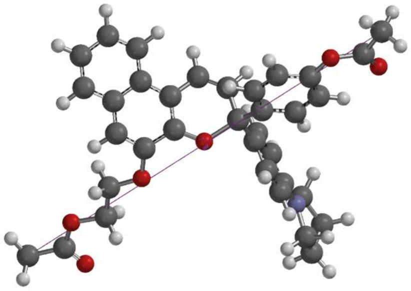

19.601 Å

(iii) Immediately After Bond Cleavage

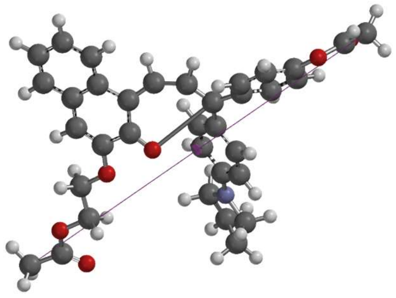

19.651 Å

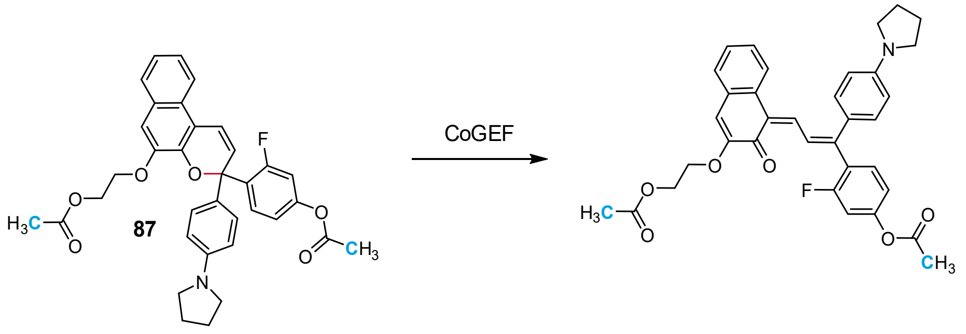

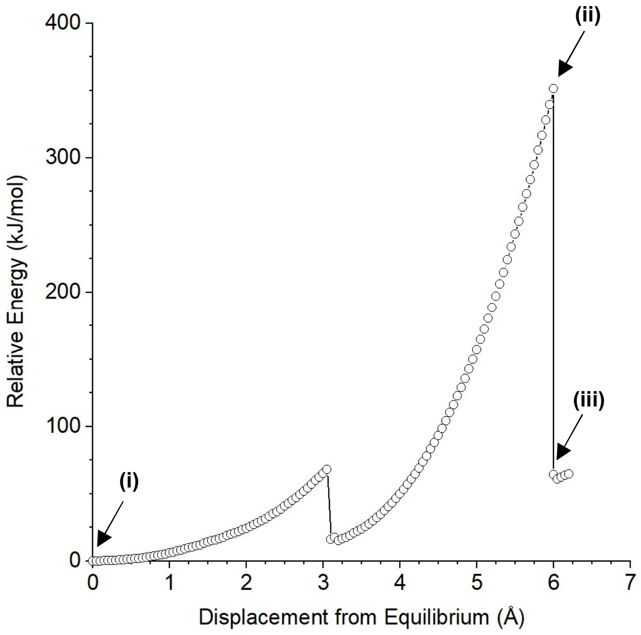

Summary of CoGEF Results	
***F**$_{max}$*	3.7 nN
***E**$_{max}$*	334 kJ/mol
Force-Bond Angle	33°

(i) Equilibrium Geometry

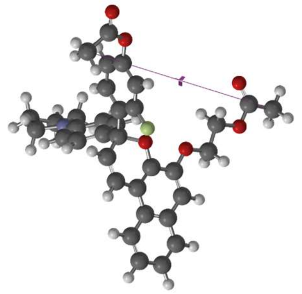

11.190 Å

(ii) Immediately Prior to Bond Cleavage

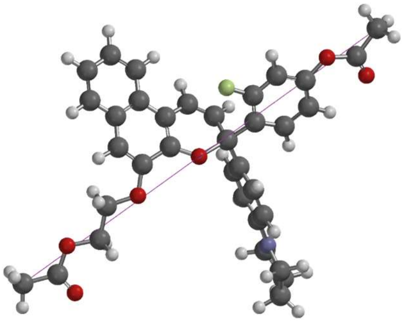

19.590 Å

(iii) Immediately After Bond Cleavage

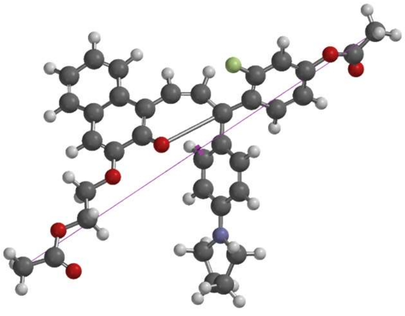

19.640 Å

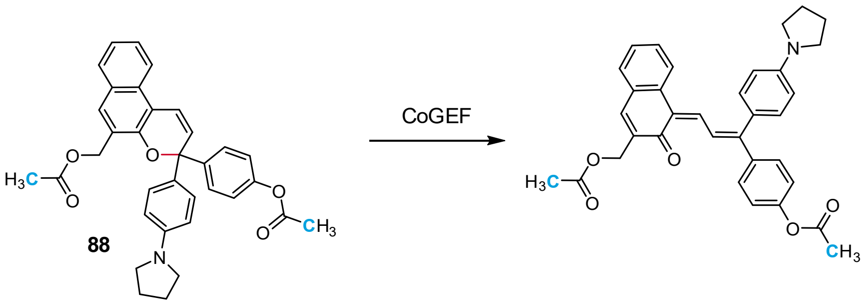

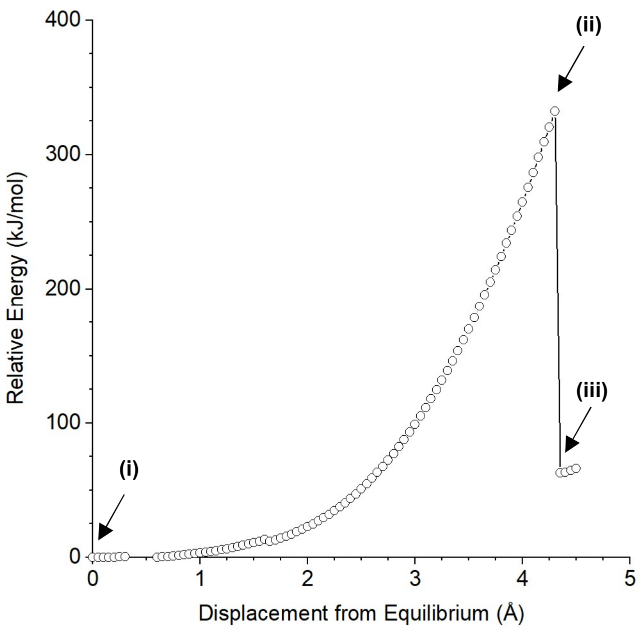

Summary of CoGEF Results	
F_{max}	3.9 nN
E_{max}	332 kJ/mol
Force-Bond Angle	30°

(i) Equilibrium Geometry

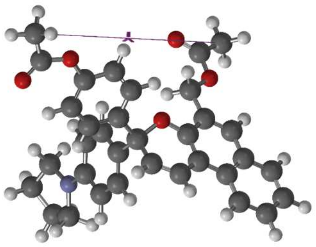

13.054 Å

(ii) Immediately Prior to Bond Cleavage

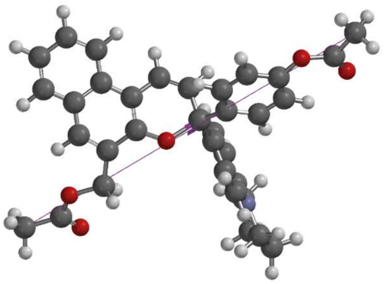

17.354 Å

(iii) Immediately After Bond Cleavage

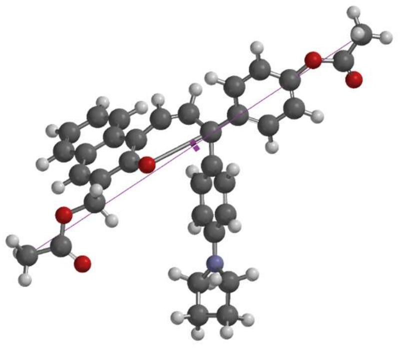

17.404 Å

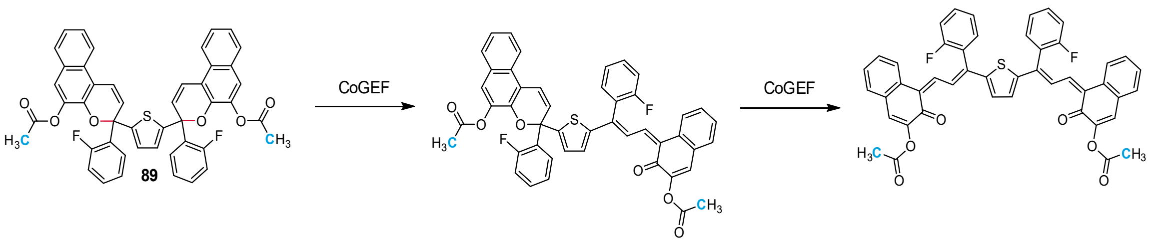

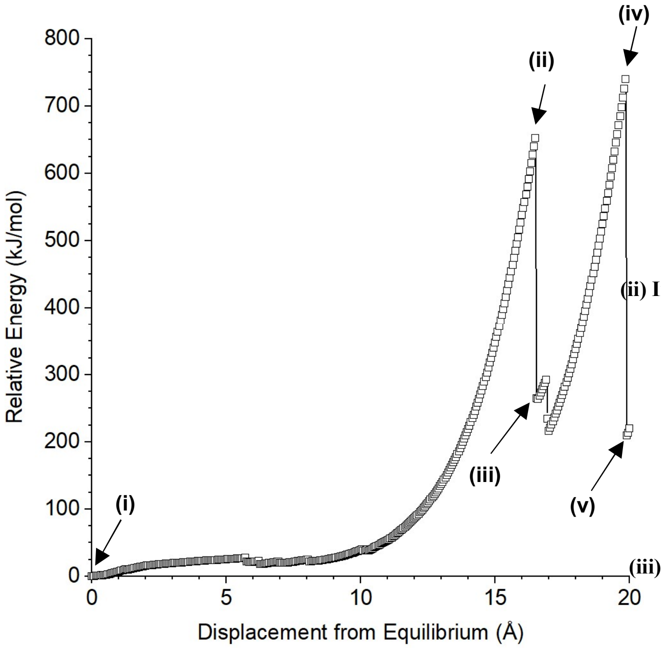

(i) Equilibrium Geometry

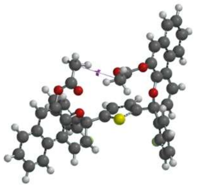

4.159 Å

(ii) Immediately Prior to First Bond Cleavage

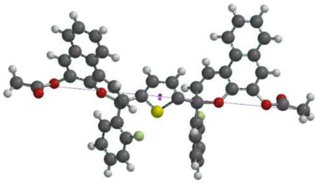

20.659 Å

(iii) Immediately After Bond First Cleavage

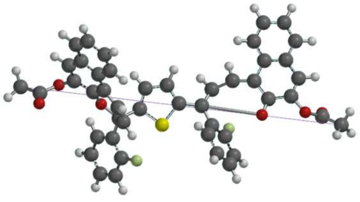

20.709 Å

(iv) Immediately Prior to Second Bond Cleavage

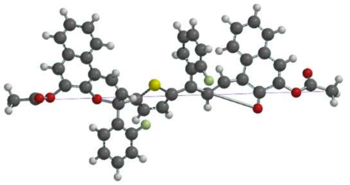

24.009 Å

(v) Immediately After Bond Second Cleavage

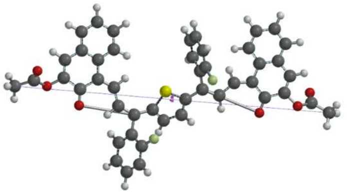

24.059 Å

Summary of CoGEF Results (S,S)

F_{max}	4.1 nN (first) 4.6 nN (second)
E_{max}	652 kJ/mol (first) 740 kJ/mol (second)
Force-Bond Angle	25° (first), 27° (second)

The results presented here correspond to the (S,S)-isomer of compound **82**. The CoGEF results for the (R,S)-isomer are similar:

Summary of CoGEF Results (R,S)

F_{max}	4.1 nN (first) 4.5 nN (second)
E_{max}	644 kJ/mol (first) 727 kJ/mol (second)
Force-Bond Angle	24° (first), 26° (second)

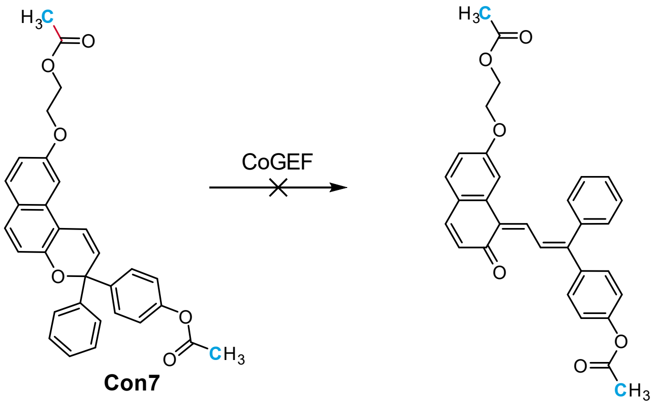

Con7

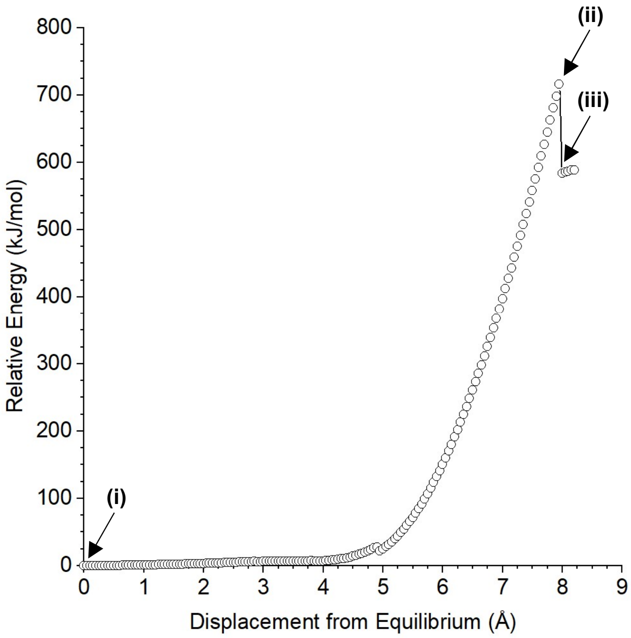

Summary of CoGEF Results

F_{max}	6.0 nN
E_{max}	716 kJ/mol
Force-Bond Angle	63°

(i) Equilibrium Geometry

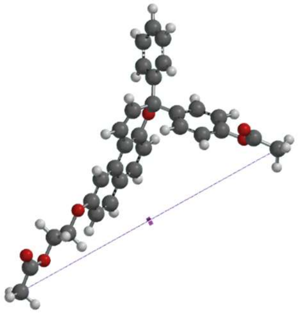

16.735 Å

(ii) Immediately Prior to Bond Cleavage

24.685 Å

(iii) Immediately After Bond Cleavage

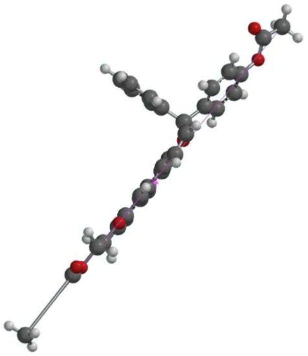

24.735 Å

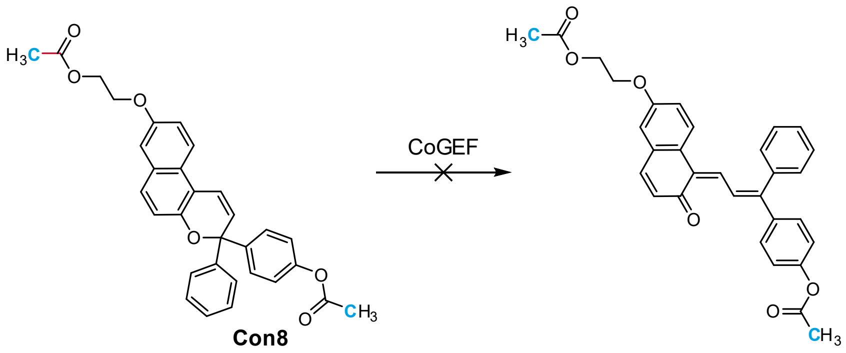

Con8

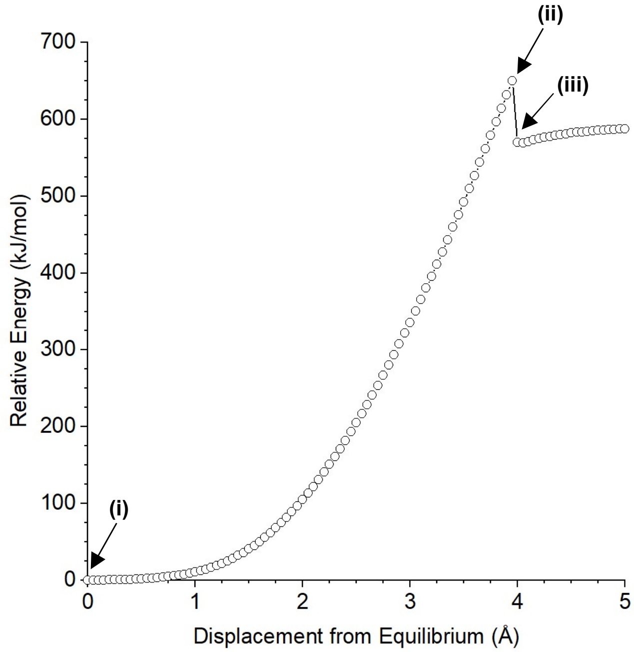

Summary of CoGEF Results	
F_{max}	6.0 nN
E_{max}	650 kJ/mol
Force-Bond Angle	56°

(i) Equilibrium Geometry

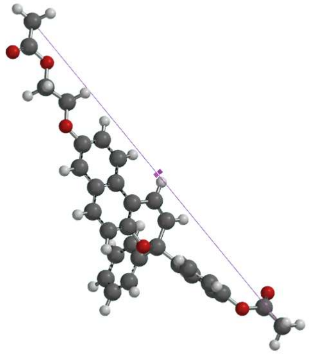

21.141 Å

(ii) Immediately Prior to Bond Cleavage

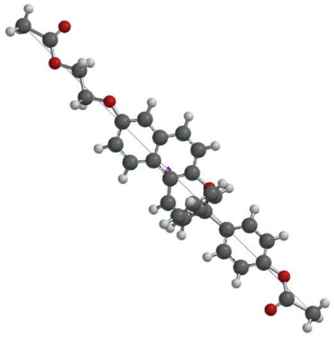

25.091 Å

(iii) Immediately After Bond Cleavage

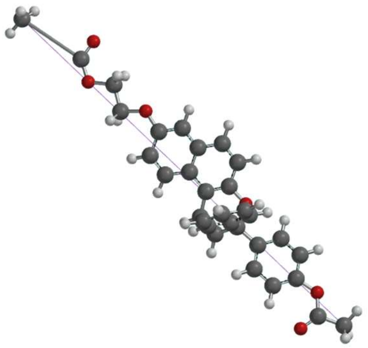

25.141 Å

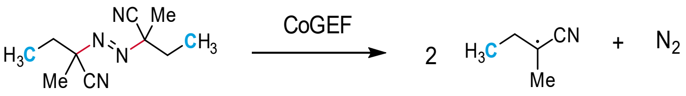

90

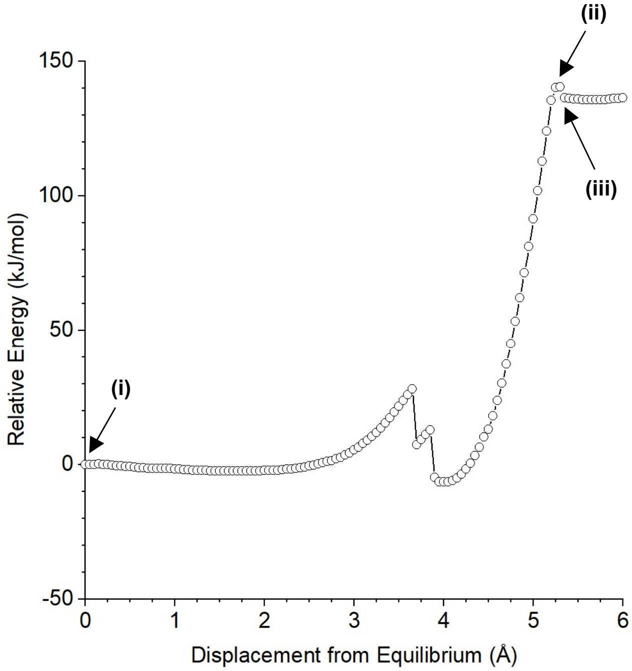

(i) Equilibrium Geometry

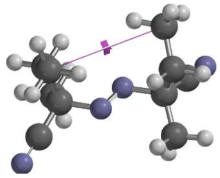

4.452 Å

(ii) Immediately Prior to Bond Cleavage

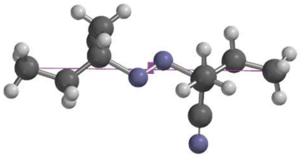

9.652 Å

(iii) Immediately After Bond Cleavage

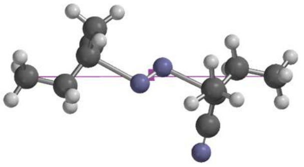

9.702 Å

Summary of CoGEF Results	
***F**max*	3.7 nN
***E**max*	140 kJ/mol
Force-Bond Angle	29°

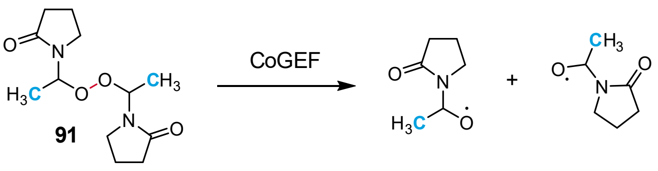

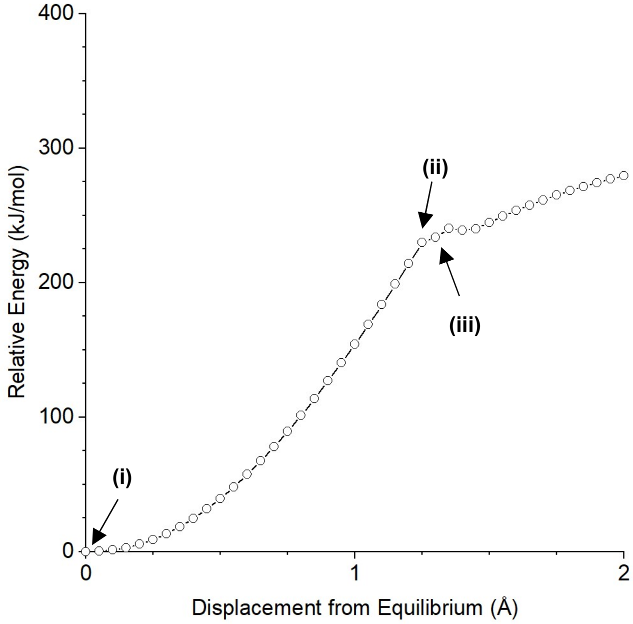

(i) Equilibrium Geometry

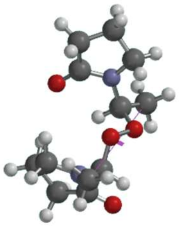

5.818 Å

(ii) Immediately Prior to Bond Cleavage

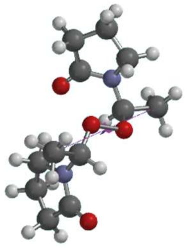

7.068 Å

(iii) Immediately After Bond Cleavage

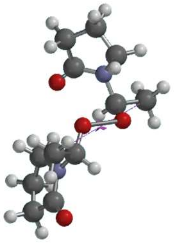

7.118 Å

Summary of CoGEF Results	
F_{max}	5.2 nN
E_{max}	230 kJ/mol
Force-Bond Angle	28°

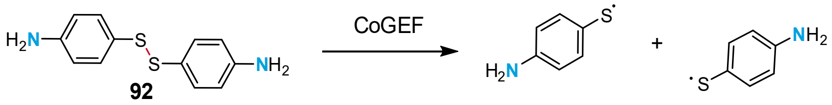

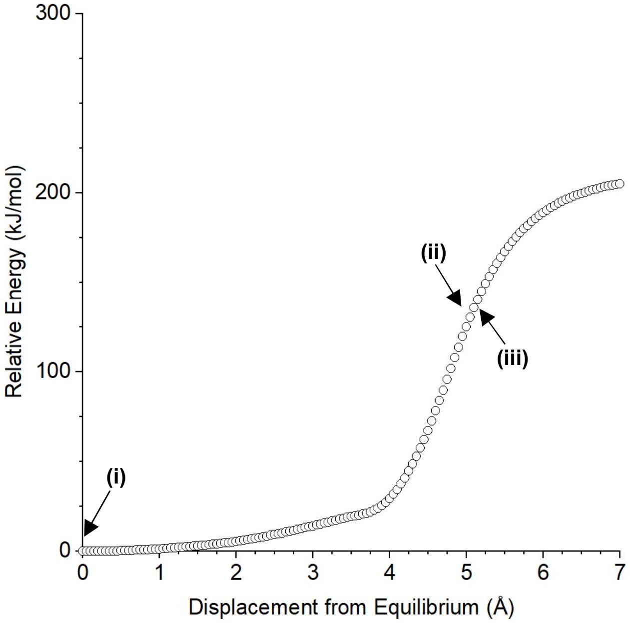

(i) Equilibrium Geometry

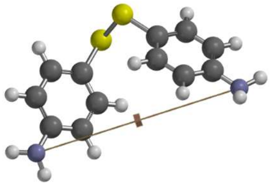

9.023 Å

(ii) Immediately Prior to Bond Cleavage

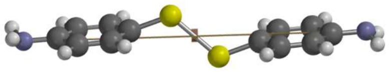

13.923 Å

(iii) Immediately After Bond Cleavage

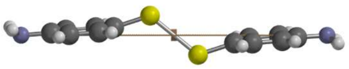

13.973 Å

Summary of CoGEF Results

***F*$_{max}$**	2.0 nN
***E*$_{max}$**	114 kJ/mol
Force-Bond Angle	45°

93

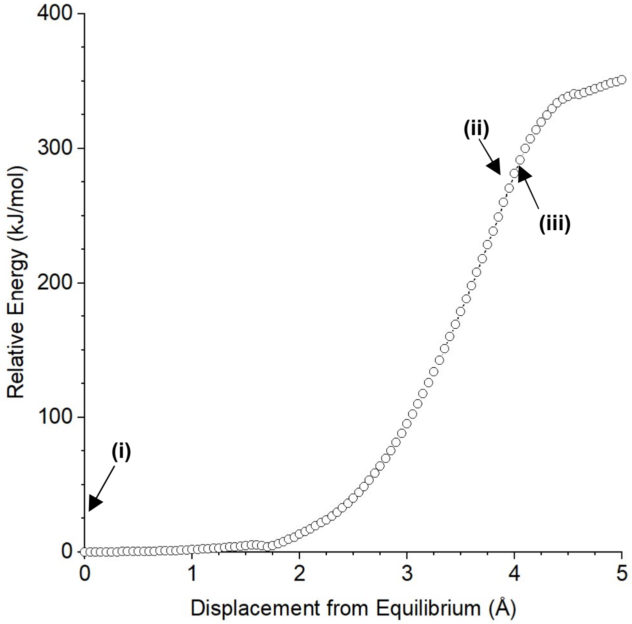

Summary of CoGEF Results	
F F_{max}	3.6 nN
E_{max}	271 kJ/mol
Force-Bond Angle	29°

(i) Equilibrium Geometry

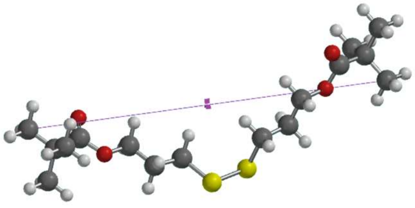

11.920 Å

(ii) Immediately Prior to Bond Cleavage

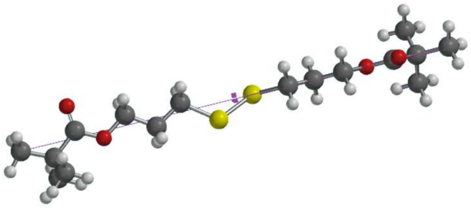

15.920 Å

(iii) Immediately After Bond Cleavage

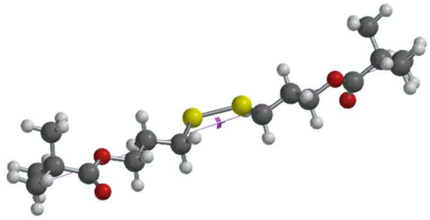

15.970 Å

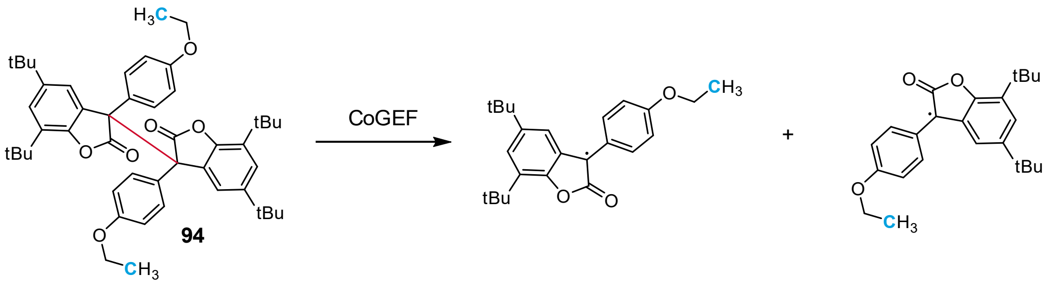

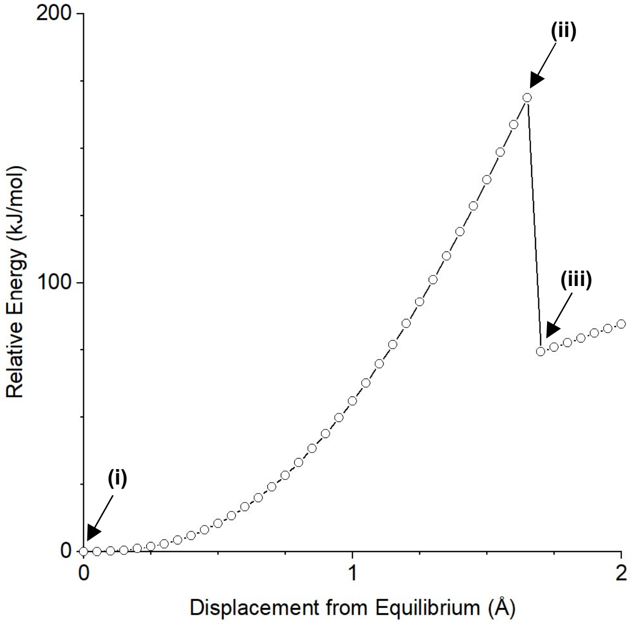

Summary of CoGEF Results	
F_{max}	3.5 nN
E_{max}	169 kJ/mol
Force-Bond Angle	44°

(i) Equilibrium Geometry

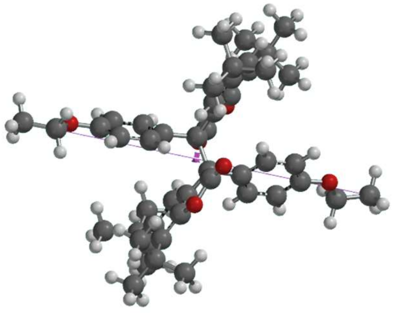

16.559 Å

(ii) Immediately Prior to Bond Cleavage

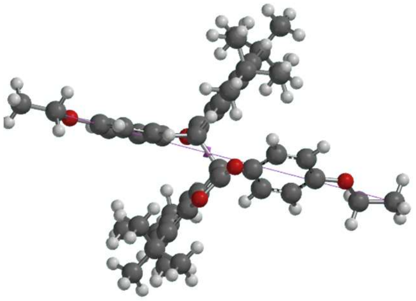

18.209 Å

(iii) Immediately After Bond Cleavage

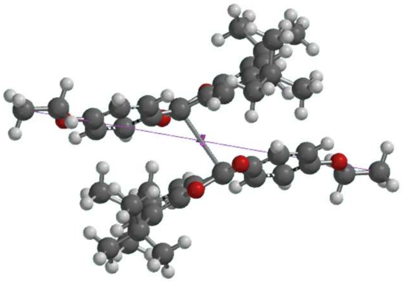

18.259 Å

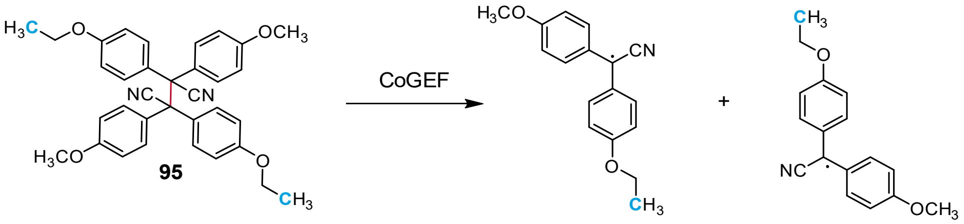

95

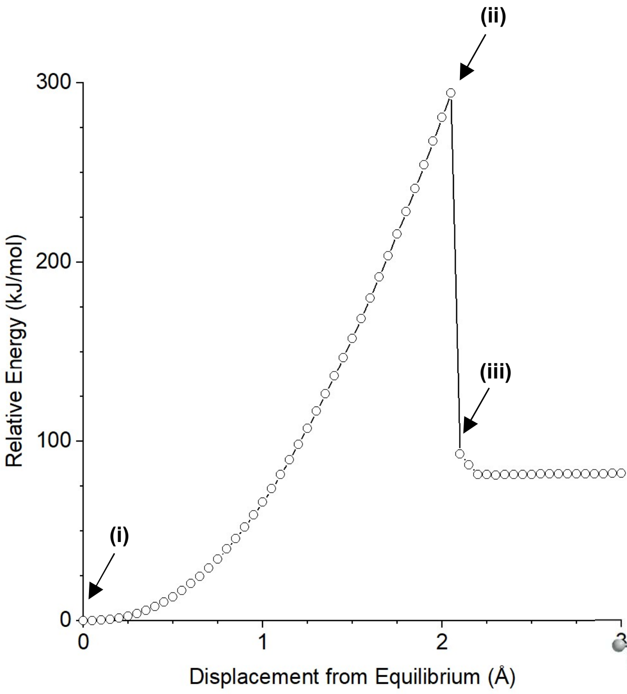

Summary of CoGEF Results	
F_{max}	4.5 nN
E_{max}	294 kJ/mol
Force-Bond Angle	41°

(i) Equilibrium Geometry

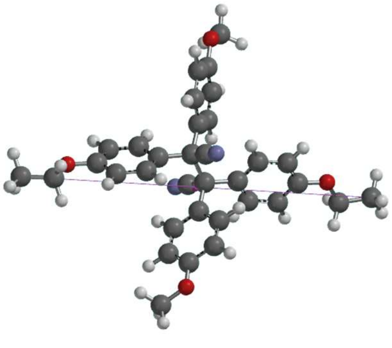

16.700 Å

(ii) Immediately Prior to Bond Cleavage

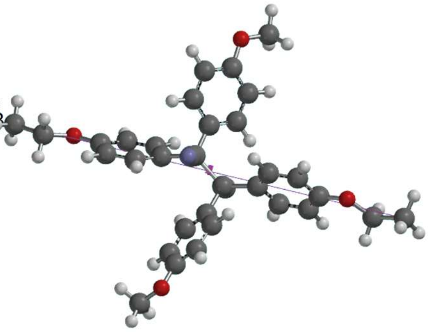

18.750 Å

(iii) Immediately After Bond Cleavage

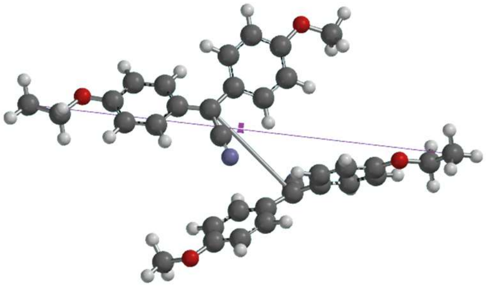

18.800Å

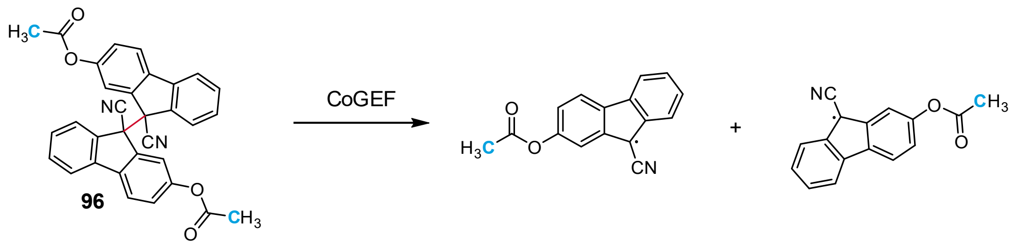

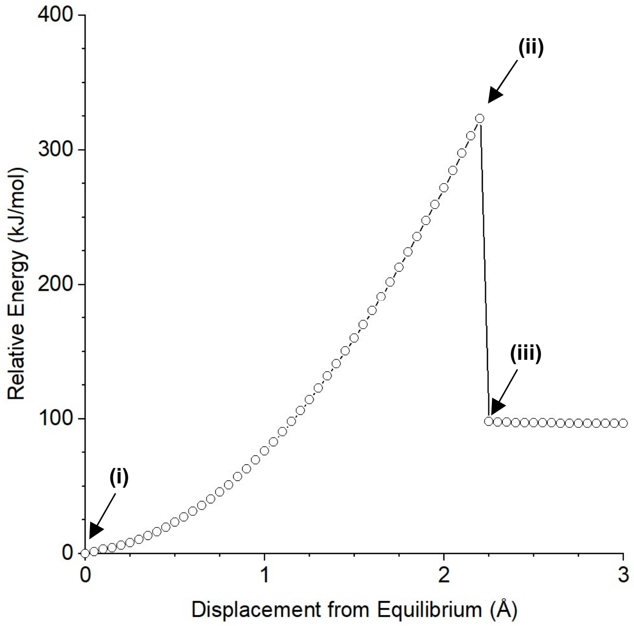

Summary of CoGEF Results

F_{max}	4.3 nN
E_{max}	326 kJ/mol
Force-Bond Angle	46°

(i) Equilibrium Geometry

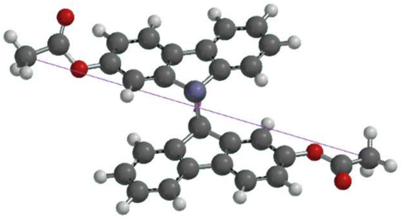

15.307 Å

(ii) Immediately Prior to Bond Cleavage

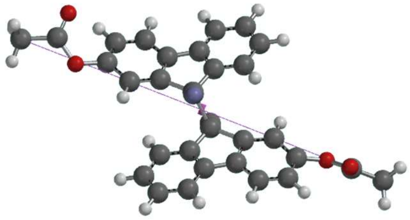

17.507 Å

(iii) Immediately After Bond Cleavage

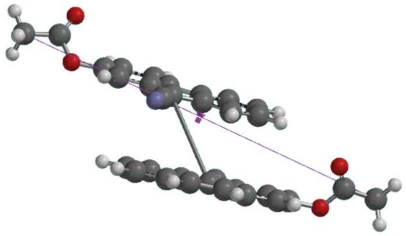

17.557 Å

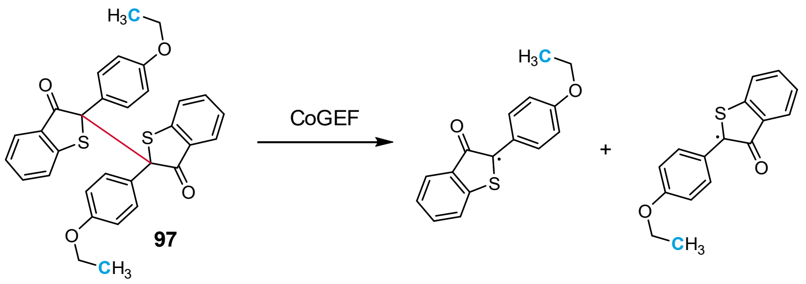

97

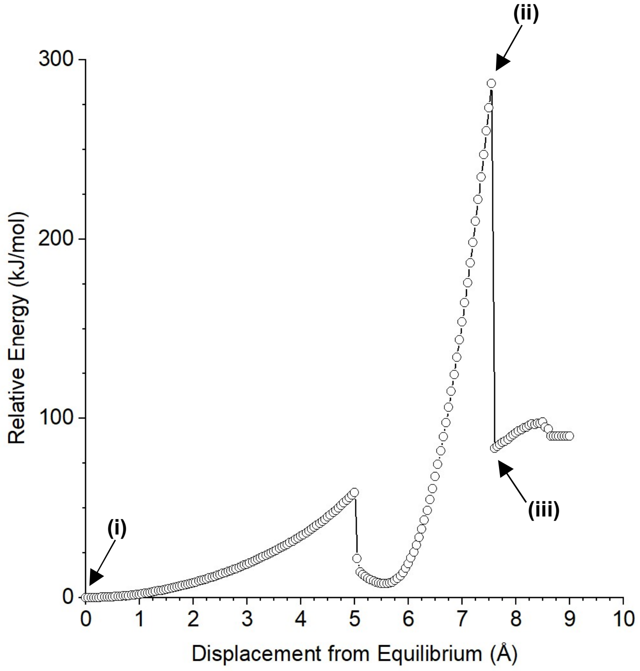

Summary of CoGEF Results	
***F**$_{max}$*	4.4 nN
***E**$_{max}$*	287 kJ/mol
Force-Bond Angle	41°

(i) Equilibrium Geometry

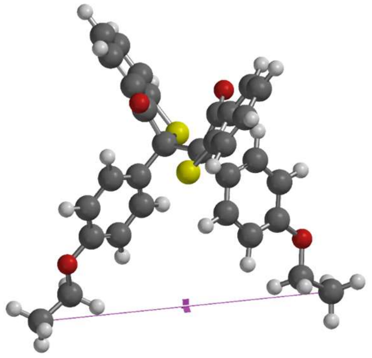

11.109 Å

(ii) Immediately Prior to Bond Cleavage

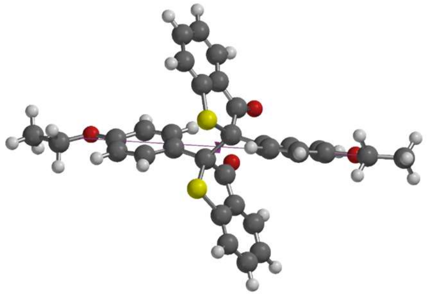

18.659 Å

(iii) Immediately After Bond Cleavage

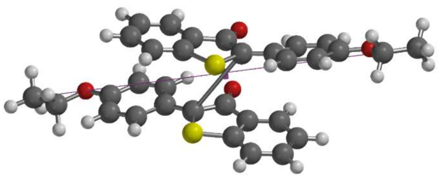

18.709 Å

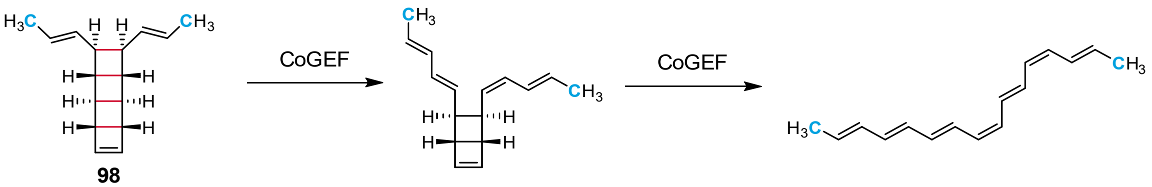

98

(i) Equilibrium Geometry

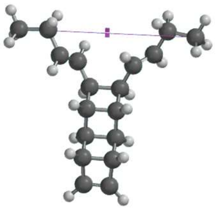

6.269 Å

(ii) Immediately Prior to First Bond Cleavage

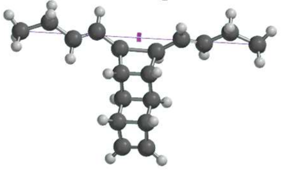

10.019 Å

(iii) Immediately After First Bond Cleavage

10.069 Å

(iv) Immediately Prior to Second Bond Cleavage

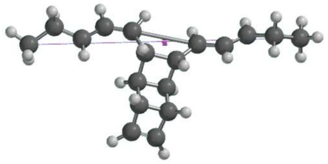

10.169 Å

(v) Immediately After Second Bond Cleavage

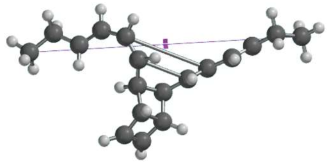

10.219 Å

(vi) Immediately Prior to Third Bond Cleavage

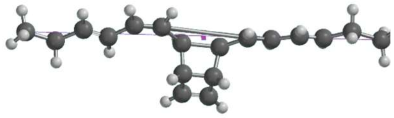

15.219 Å

(vii) Immediately After Third Bond Cleavage

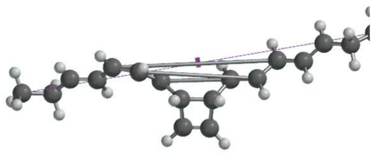

15.269 Å

(viii) Immediately After Fourth Bond Cleavage

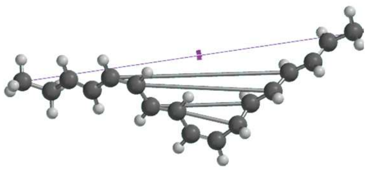

15.319 Å

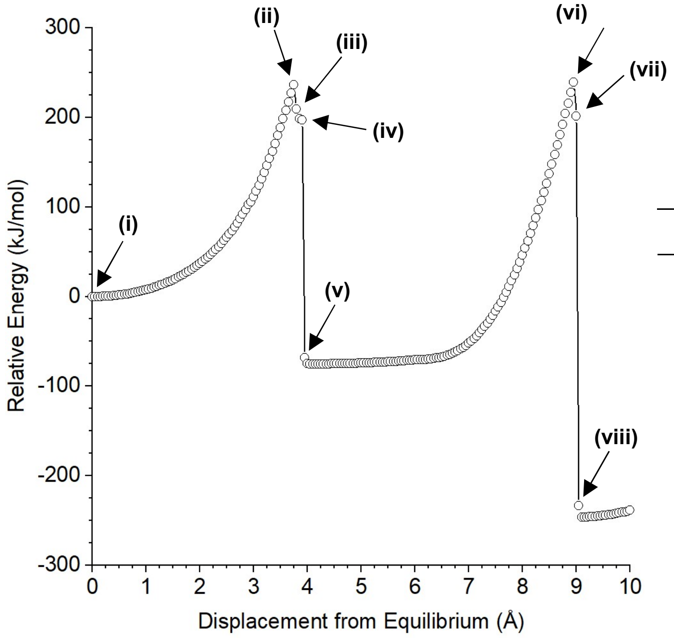

Summary of CoGEF Results	
F_{max}	3.2 nN (first) 3.9 nN (second)
E_{max}	236 kJ/mol (first) 239 kJ/mol (second)
Force-Bond Angle	0.1° (first), 4.4° (second)

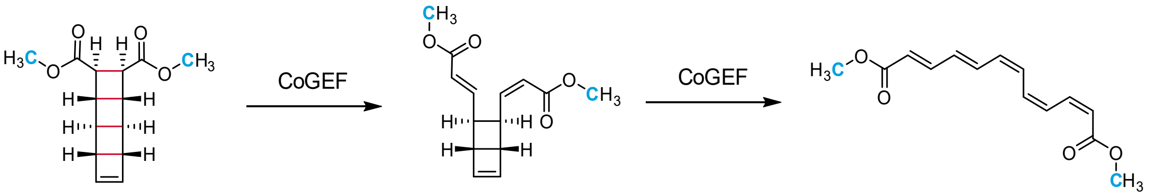

99

(i) Equilibrium Geometry

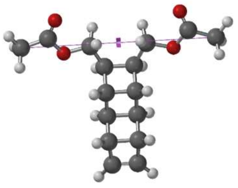

10.304 Å

(ii) Immediately Prior to First Bond Cleavage

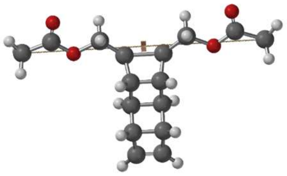

12.554 Å

(iii) Immediately After First Bond Cleavage

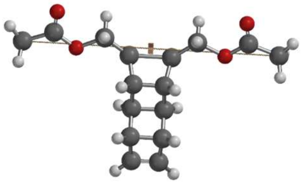

12.604 Å

(iv) Immediately Prior to Second Bond Cleavage

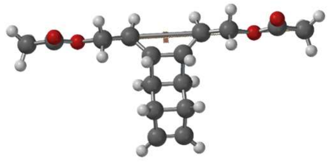

13.754 Å

(v) Immediately After Second Bond Cleavage

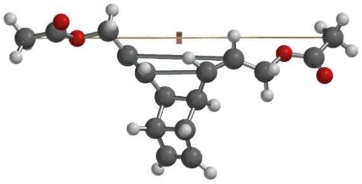

13.804 Å

(vi) Immediately Prior to Third Bond Cleavage

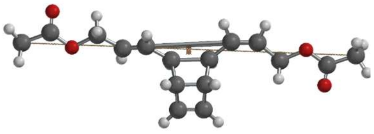

17.554 Å

(vii) Immediately After Third Bond Cleavage

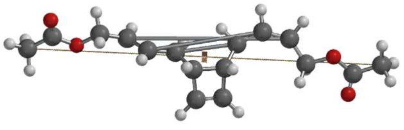

17.604 Å

(viii) Immediately After Fourth Bond Cleavage

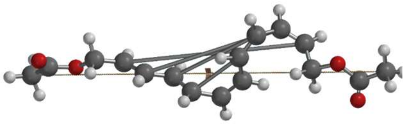

17.654 Å

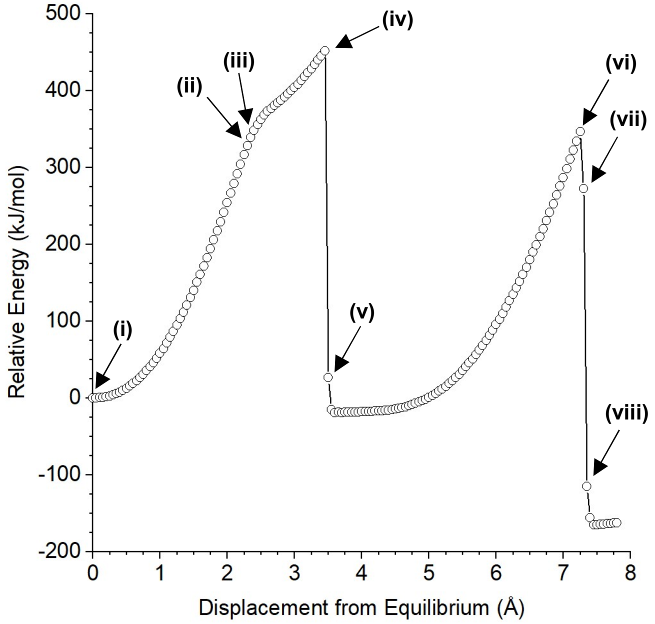

Summary of CoGEF Results

F_{max}	4.2 nN 4.0 nN
E_{max}	451 kJ/mol 346 kJ/mol
Force-Bond Angle	0.2° (first) 3.4° (second)

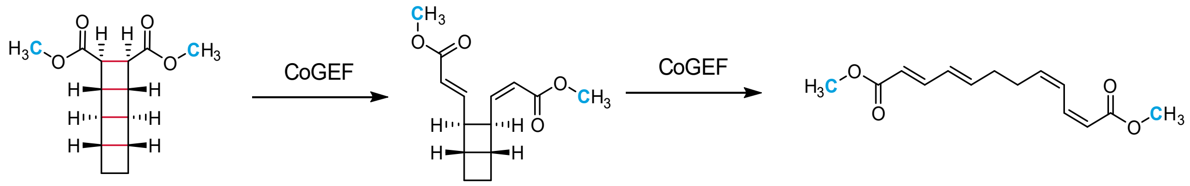

100

(i) Equilibrium Geometry

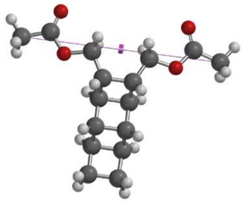

10.308 Å

(ii) Immediately Prior to First Bond Cleavage

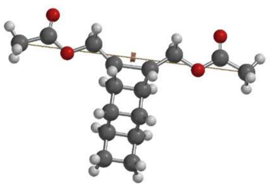

12.458 Å

(iii) Immediately After First Bond Cleavage

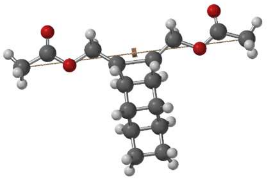

12.508 Å

(iv) Immediately Prior to Second Bond Cleavage

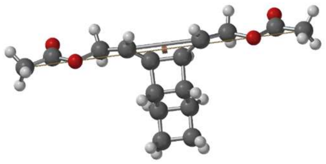

14.208 Å

(v) Immediately After Second Bond Cleavage

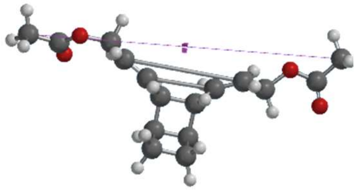

14.258 Å

(vi) Immediately Prior to Third Bond Cleavage

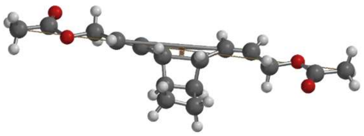

17.508 Å

(vii) Immediately After Third Bond Cleavage

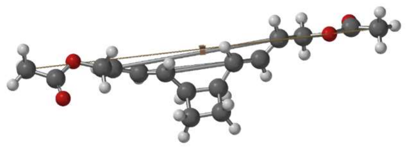

17.558 Å

(viii) Immediately After Fourth Bond Cleavage

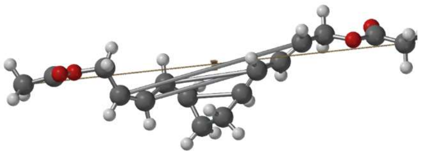

17.708 Å

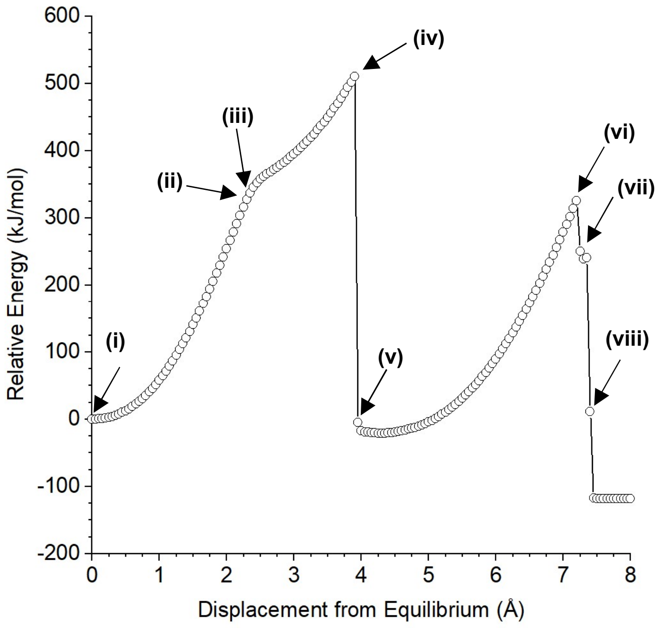

Summary of CoGEF Results	
F_{max}	4.2 nN (first) 3.9 nN (second)
E_{max}	511 kJ/mol (first) 326 kJ/mol (second)
Force-Bond Angle	0.5° (first) 4.0° (second)

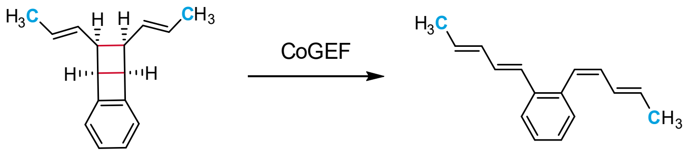

101

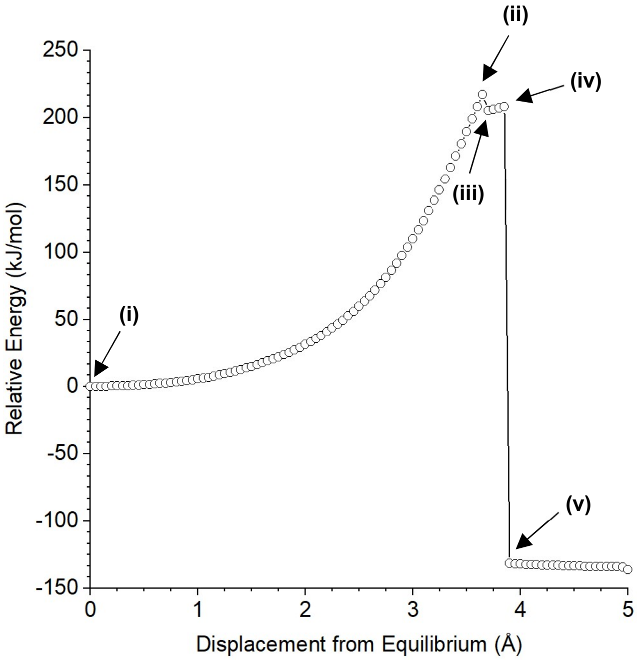

Summary of CoGEF Results	
F F_{max}	3.1 nN
E_{max}	207 kJ/mol
Force-Bond Angle	0.1°

(i) Equilibrium Geometry

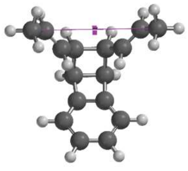

6.368 Å

) Immediately Prior to First Bond Cleavage

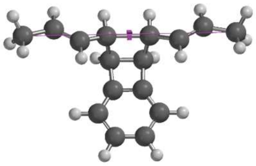

10.018 Å

ii) Immediately After First Bond Cleavage

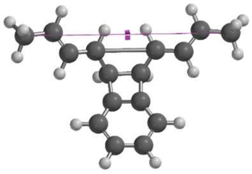

10.068 Å

(iv) Immediately Prior to Second Bond Cleavage

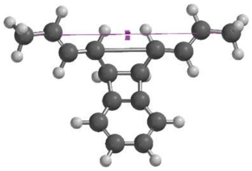

10.218 Å

(v) Immediately After Second Bond Cleavage

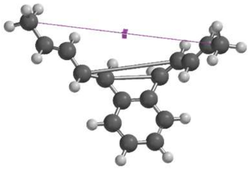

10.268 Å

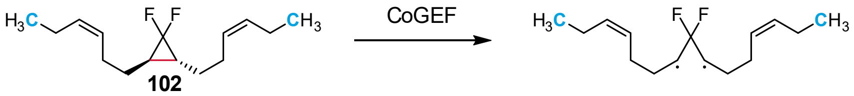

102

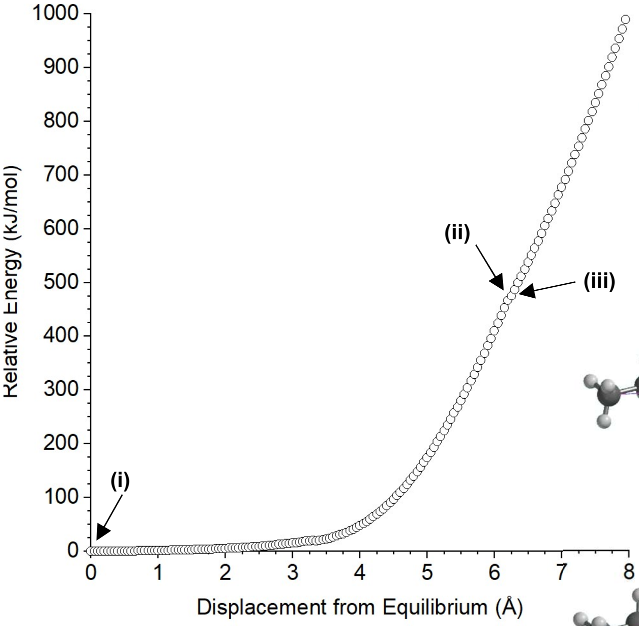

(i) Equilibrium Geometry

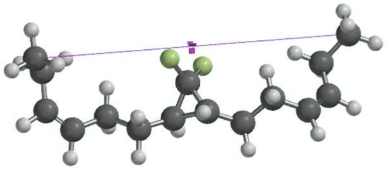

12.504 Å

(ii) Immediately Prior to Bond Cleavage

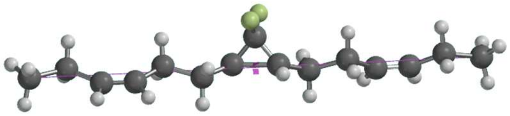

18.704 Å

(iii) Immediately After Bond Cleavage

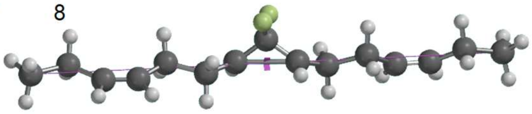

18.754 Å

Summary of CoGEF Results	
F_{max}	4.8 nN
E_{max}	466 kJ/mol
Force-Bond Angle	21°

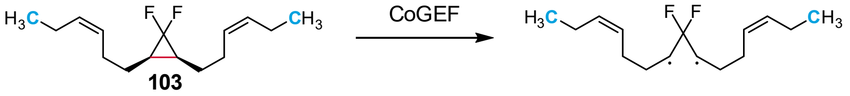

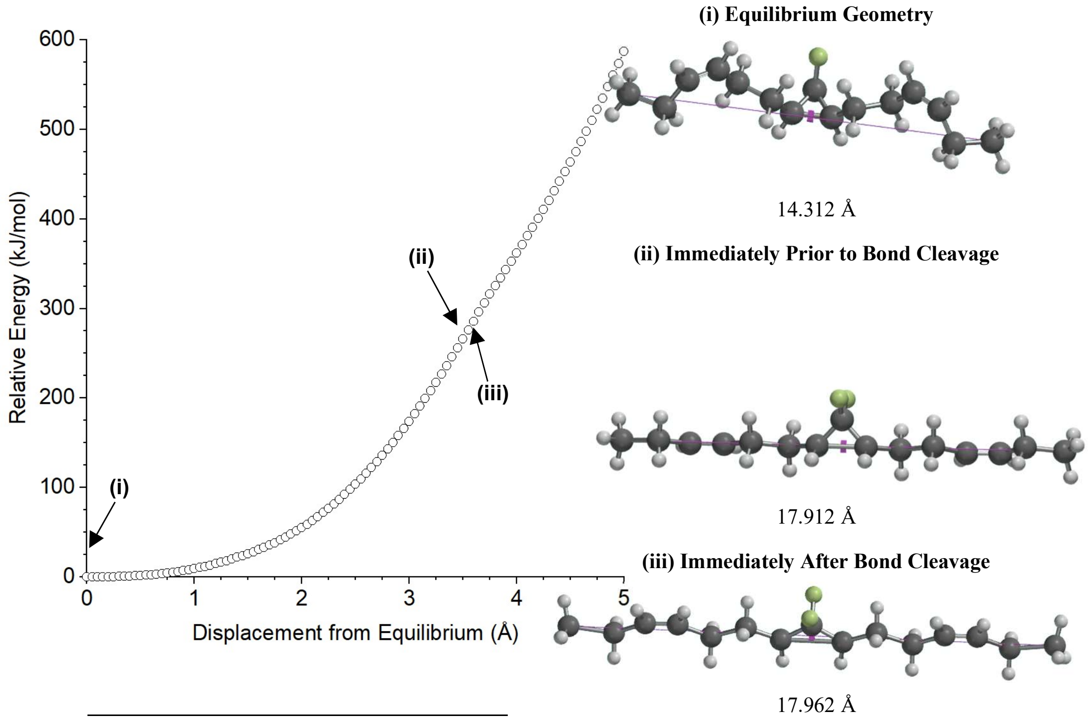

(i) Equilibrium Geometry

14.312 Å

(ii) Immediately Prior to Bond Cleavage

17.912 Å

(iii) Immediately After Bond Cleavage

17.962 Å

Summary of CoGEF Results	
F_max	3.4 nN
E_max	292 kJ/mol
Force-Bond Angle	0.0°

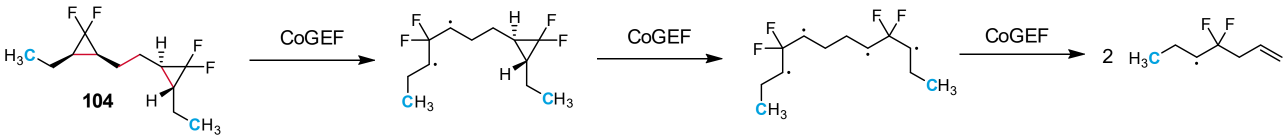

(i) Equilibrium Geometry

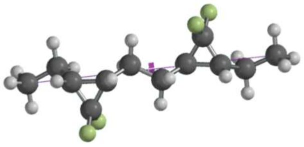

10.904 Å

(ii) Immediately Prior to First Bond Cleavage

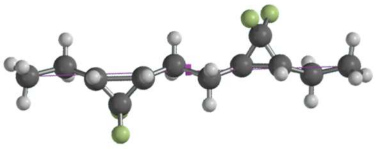

13.104 Å

(iii) Immediately After First Bond Cleavage

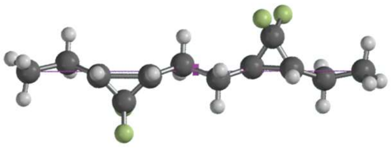

13.154 Å

(iv) Immediately Prior to Second Bond Cleavage

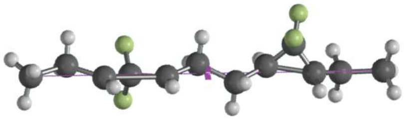

14.604 Å

(v) Immediately After Second Bond Cleavage

14.654 Å

(vi) Immediately Prior to Disproportionation

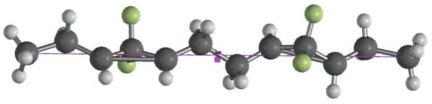

15.404 Å

(vii) Immediately After Disproportionation

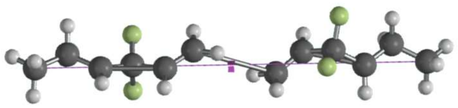

15.454 Å

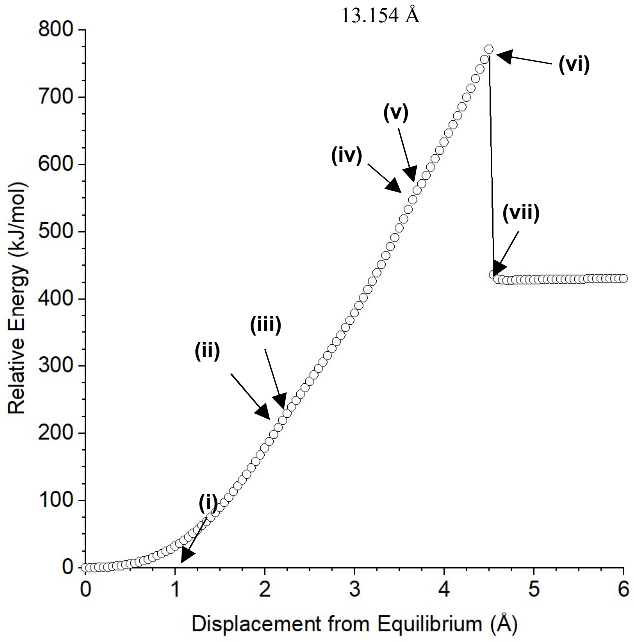

Summary of CoGEF Results	
F	

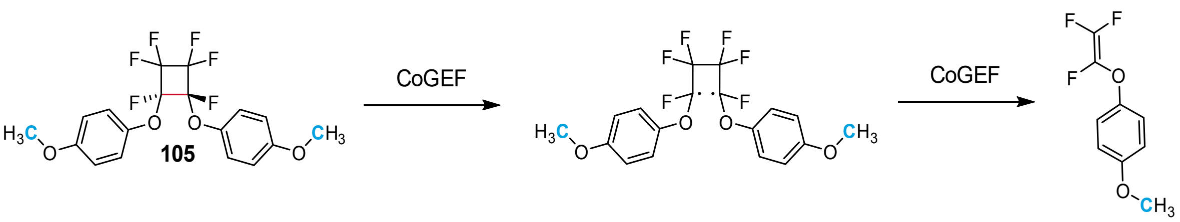

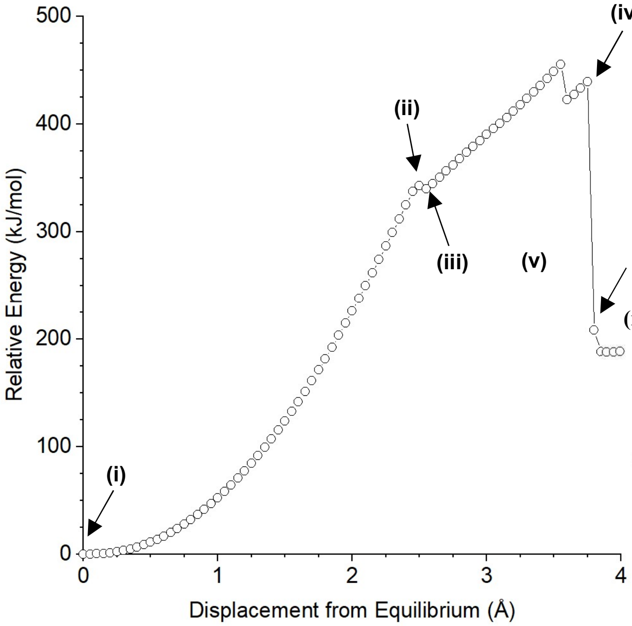

Summary of CoGEF Results	
***F*$_{max}$**	4.2 nN
***E*$_{max}$**	455 kJ/mol
Force-Bond Angle	17°

(i) Equilibrium Geometry

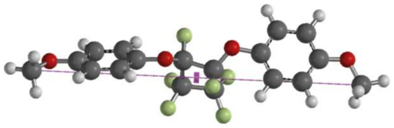

15.764 Å

(ii) Immediately Prior to First Bond Cleavage

18.214 Å

(iii) Immediately After First Bond Cleavage

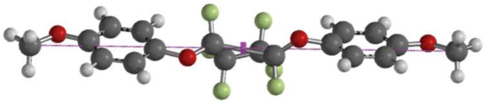

18.264 Å

(iv) Immediately Before Second Bond Cleavage

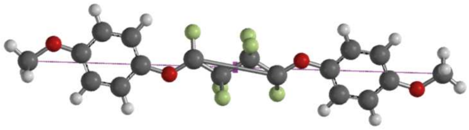

19.514 Å

(v) Immediately After Second Bond Cleavage

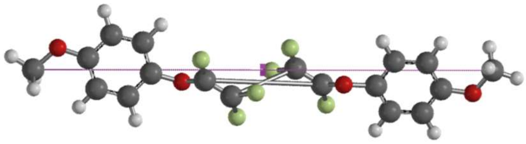

19.562 Å

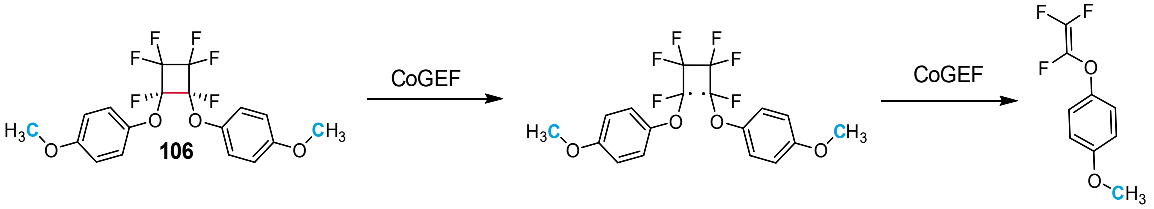

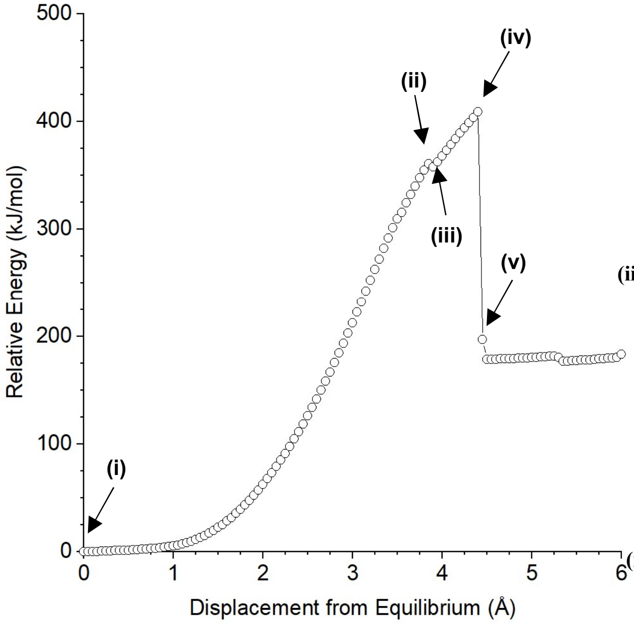

Summary of CoGEF Results	
***F**max*	3.4 nN
***E**max*	409 kJ/mol
Force-Bond Angle	5.9°

(i) Equilibrium Geometry

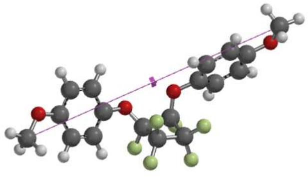

14.522 Å

(ii) Immediately Prior to First Bond Cleavage

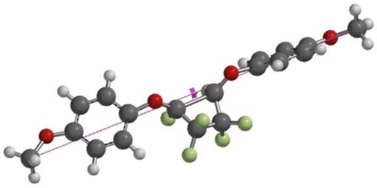

17.772 Å

(iii) Immediately After First Bond Cleavage

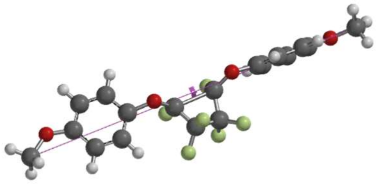

17.822 Å

(iv) Immediately Before Second Bond Cleavage

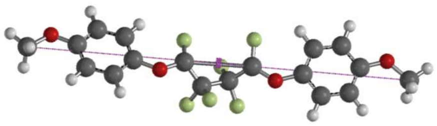

18.922 Å

(v) Immediately After Second Bond Cleavage

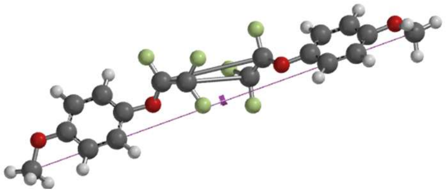

18.972 Å

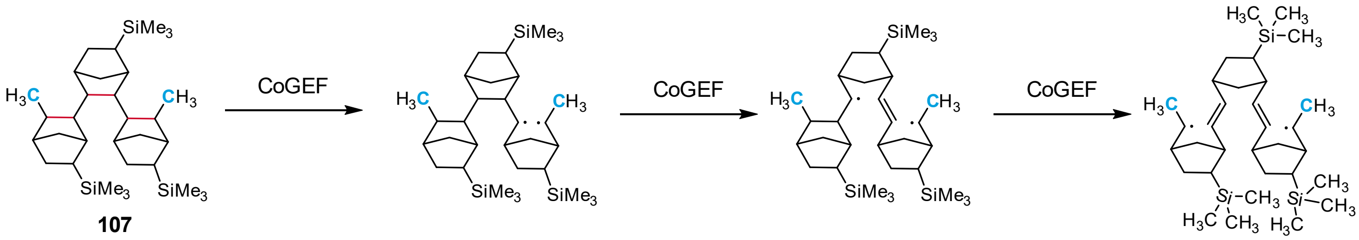

(i) Equilibrium Geometry

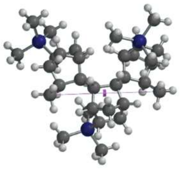

8.084 Å

(ii) Immediately Prior to First Bond Cleavage

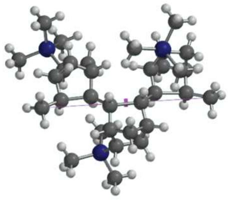

10.534 Å

(iii) Immediately After First Bond Cleavage

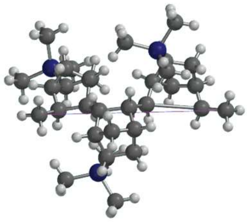

10.584 Å

(iv) Immediately Prior to Second Bond Cleavage

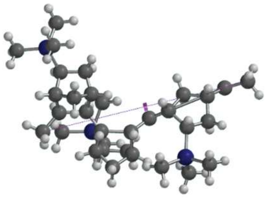

13.234 Å

(v) Immediately After Second Bond Cleavage

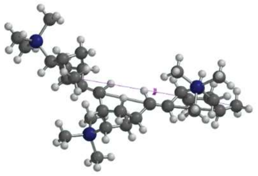

13.284 Å

(vi) Immediately Prior to Third Bond Cleavage

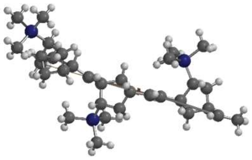

17.734 Å

(vii) Immediately After Third Bond Cleavage

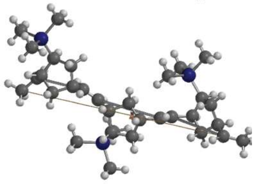

17.784 Å

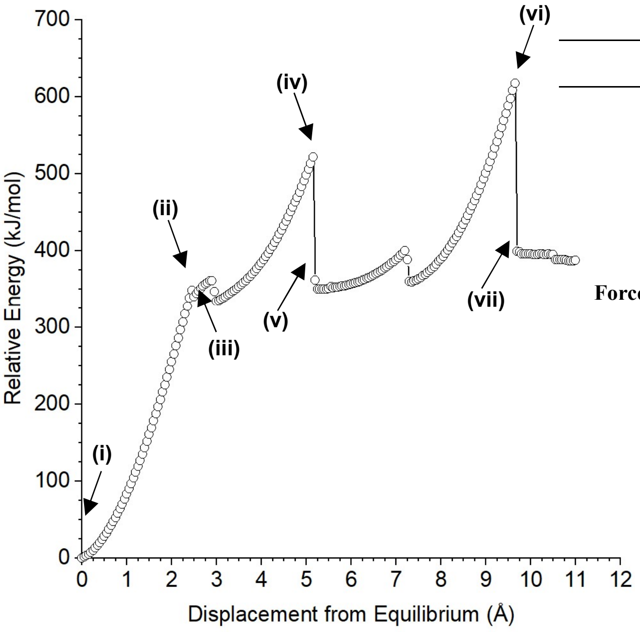

Summary of CoGEF Results	
***F**$_{max}$*	3.5 nN (first) 2.6 nN (second) 3.5 nN (third)
***E**$_{max}$*	348 kJ/mol (first) 521 kJ/mol (second) 617 kJ/mol (third)
Force-Bond Angle	7.5° (first) 16° (second) 7.0° (third)

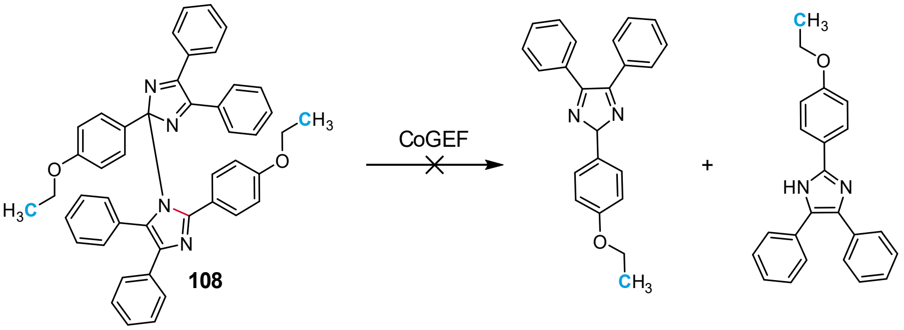

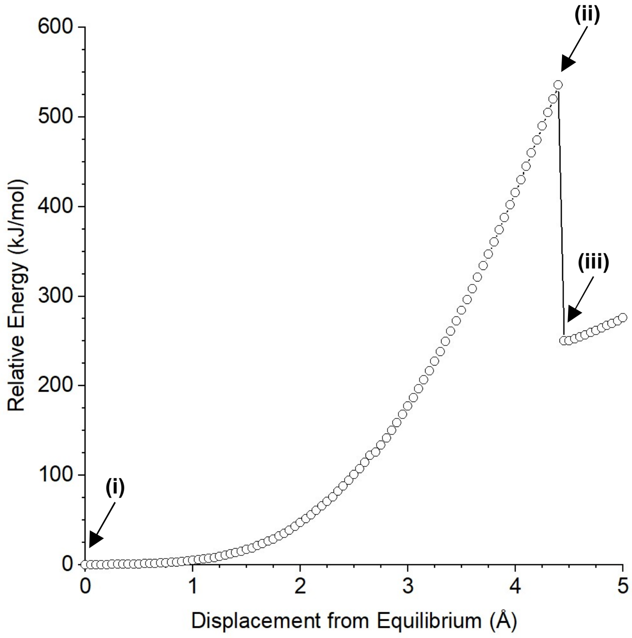

Summary of CoGEF Results

F_{max}	5.1 nN
E_{max}	536 kJ/mol
Force-Bond Angle	43°

(i) Equilibrium Geometry

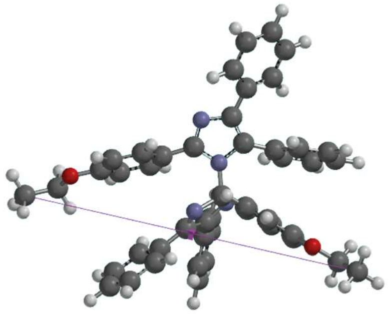

15.861 Å

(ii) Immediately Prior to Bond Cleavage

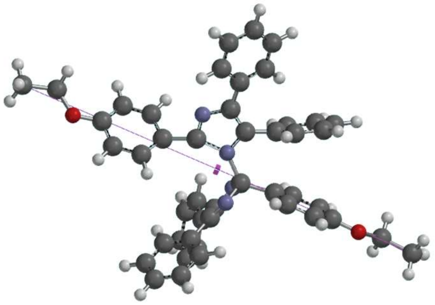

20.261 Å

(iii) Immediately After Bond Cleavage

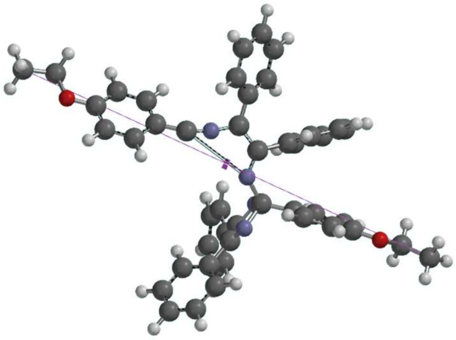

20.311 Å

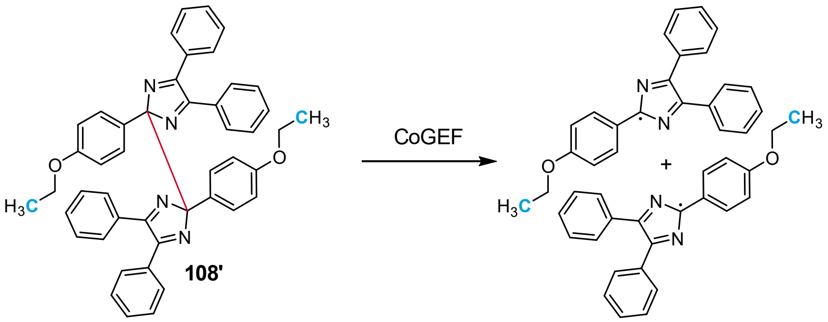

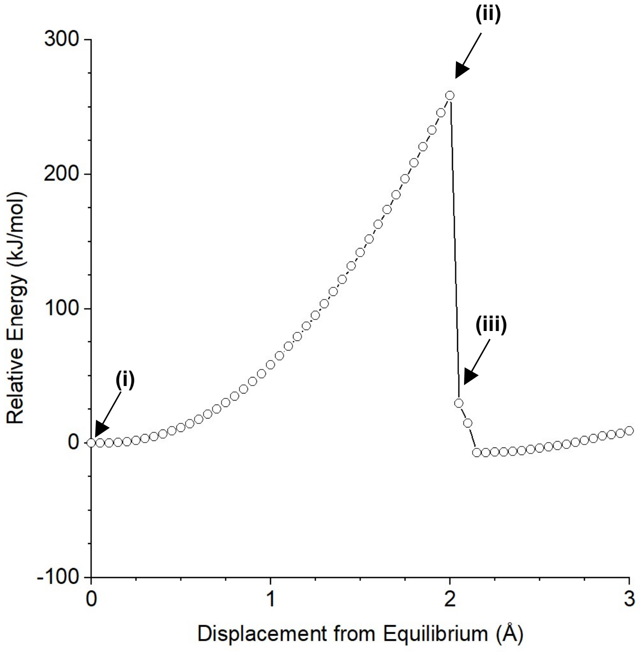

Summary of CoGEF Results	
F_{max}	4.3 nN
E_{max}	258 kJ/mol
Force-Bond Angle	40°

(i) Equilibrium Geometry

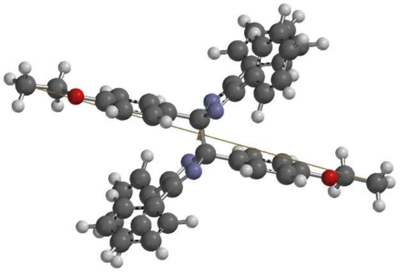

16.537 Å

(ii) Immediately Prior to Bond Cleavage

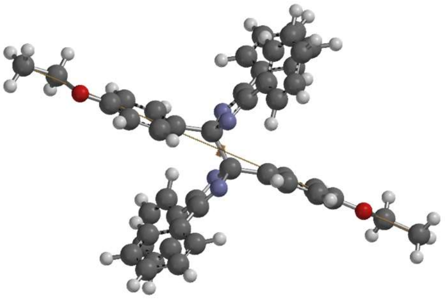

18.537 Å

(iii) Immediately After Bond Cleavage

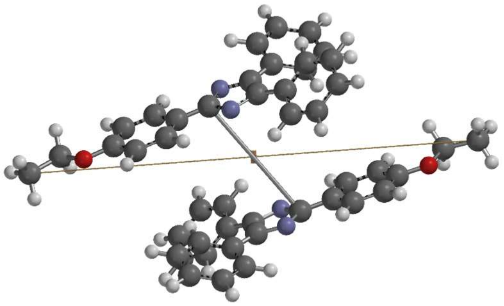

18.587 Å

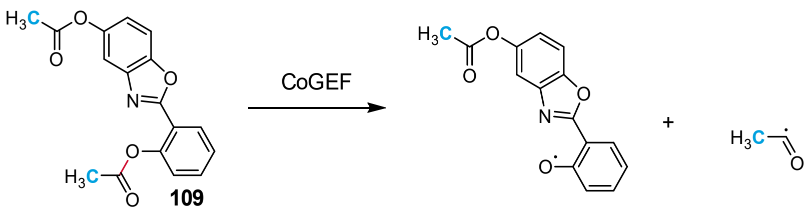

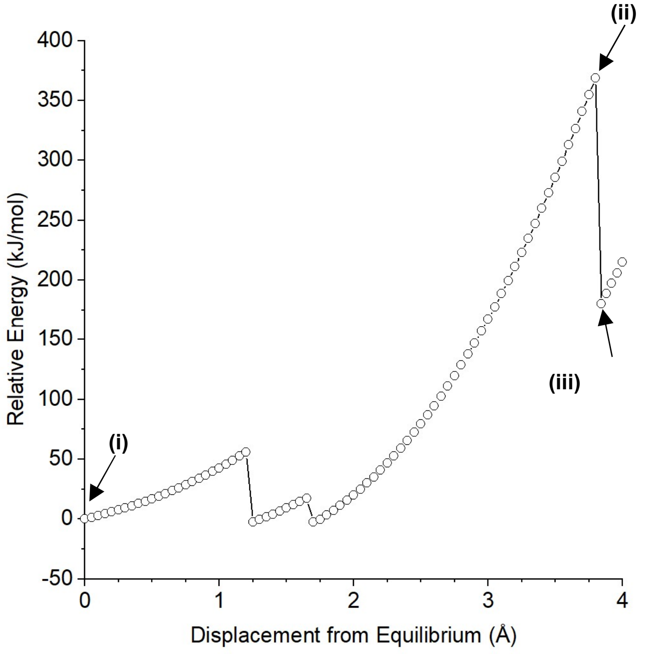

(i) Equilibrium Geometry

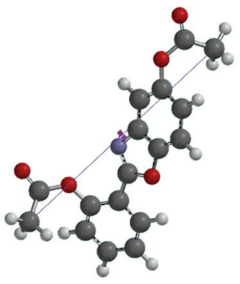

11.66 Å

(ii) Immediately Prior to Bond Cleavage

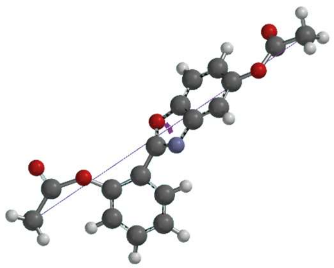

15.41 Å

(iii) Immediately After Bond Cleavage

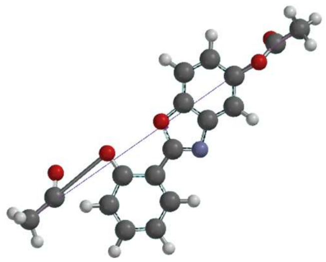

15.46 Å

Summary of CoGEF Results	
F_{max}	4.7 nN
E_{max}	369 kJ/mol
Force-Bond Angle	15°

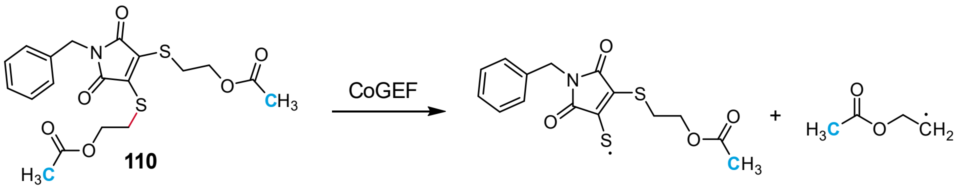

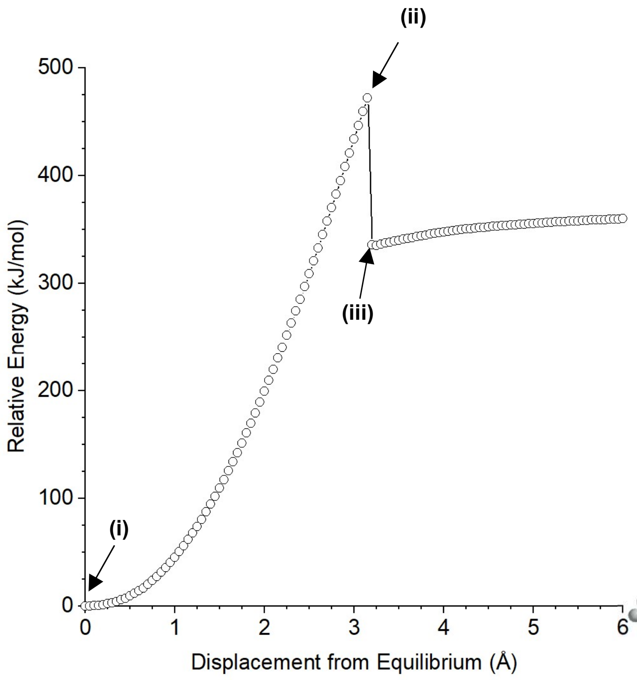

Summary of CoGEF Results	
***F*$_{max}$**	4.3 nN
***E*$_{max}$**	472 kJ/mol
Force-Bond Angle	24°

(i) Equilibrium Geometry

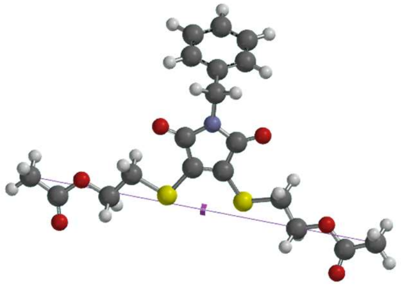

15.926 Å

(ii) Immediately Prior to Bond Cleavage

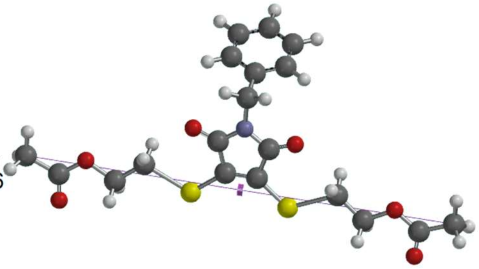

19.076 Å

(iii) Immediately After Bond Cleavage

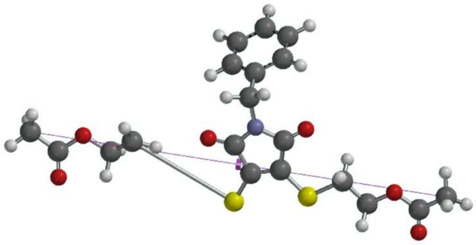

19.126 Å

111

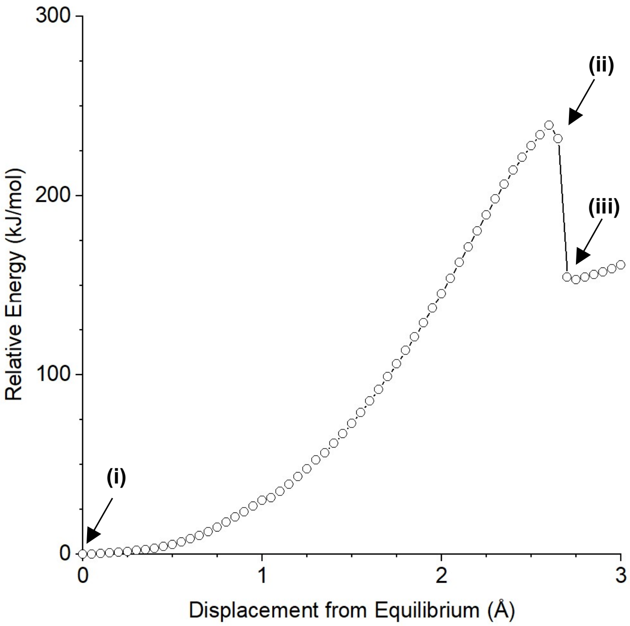

(i) Equilibrium Geometry

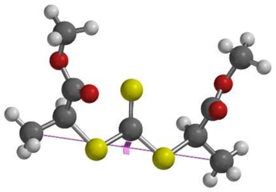

8.199 Å

(ii) Immediately Prior to Bond Cleavage

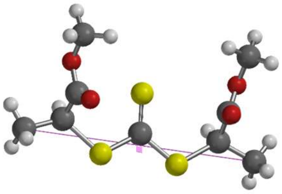

9.699 Å

(iii) Immediately After Bond Cleavage

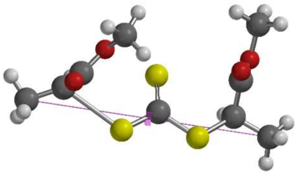

9.749 Å

Summary of CoGEF Results

F_{max}	4.3 nN
E_{max}	227 kJ/mol
Force-Bond Angle	35°

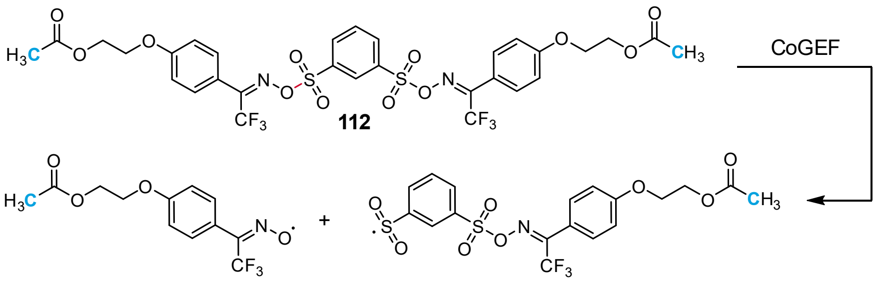

(i) Equilibrium Geometry

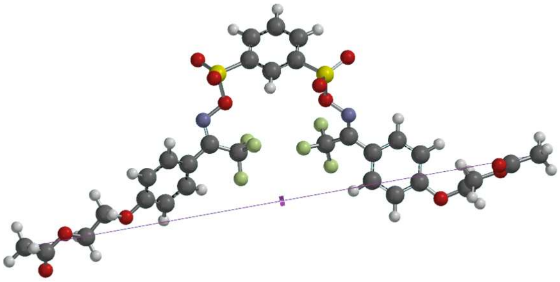

26.482 Å

(ii) Immediately Prior to Bond Cleavage

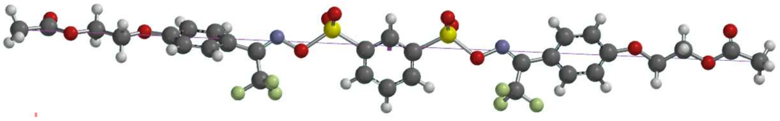

38.432 Å

(iii) Immediately After Bond Cleavage

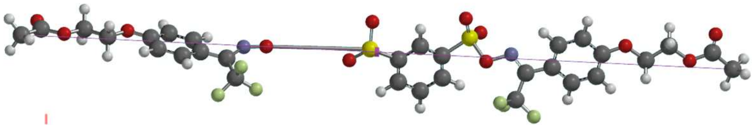

38.482 Å

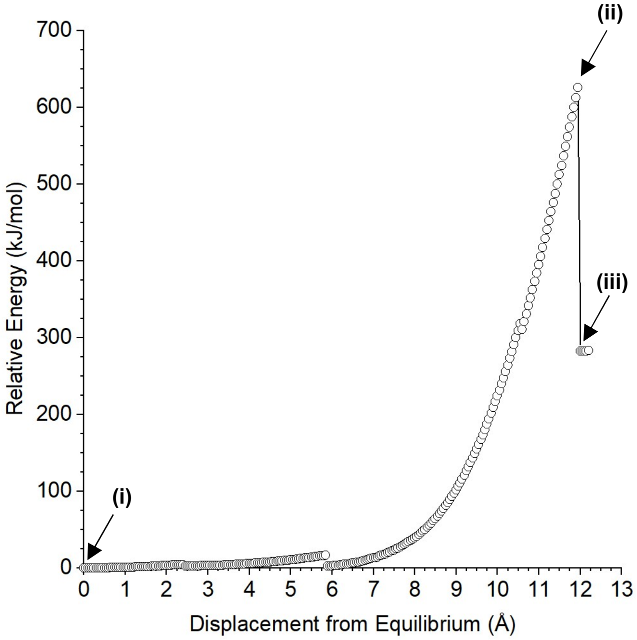

Summary of CoGEF Results	
F_{max}	4.3 nN
E_{max}	625 kJ/mol
Force-Bond Angle	28°

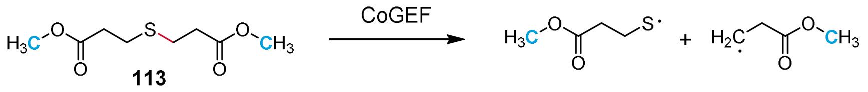

113

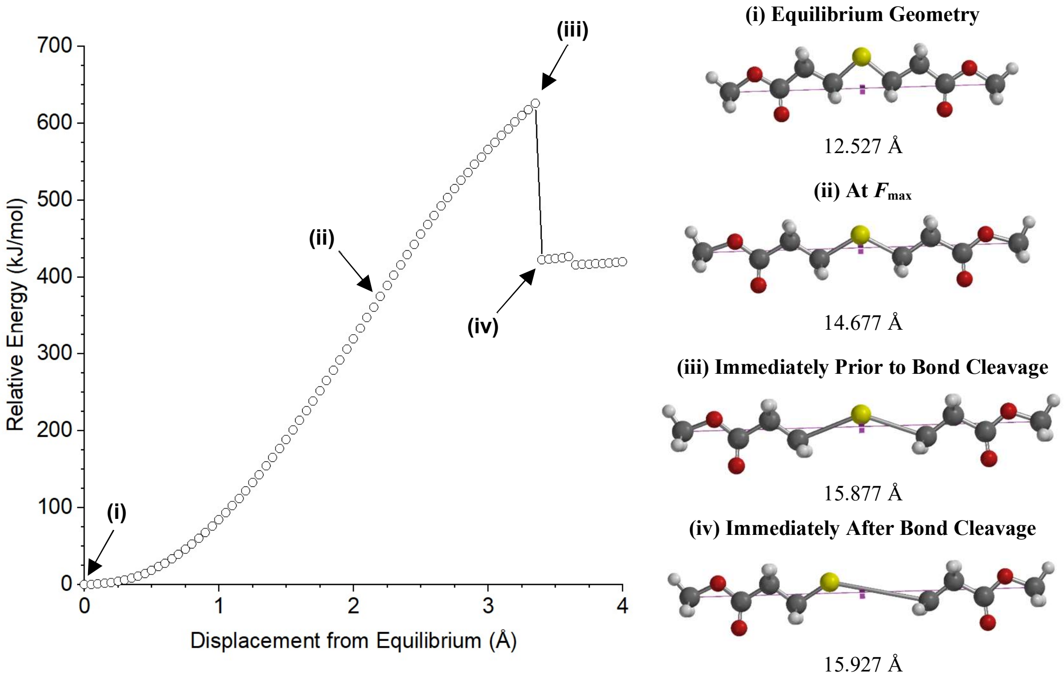

(i) Equilibrium Geometry

12.527 Å

(ii) At F_{max}

14.677 Å

(iii) Immediately Prior to Bond Cleavage

15.877 Å

(iv) Immediately After Bond Cleavage

15.927 Å

Summary of CoGEF Results	
F_{max}	4.6 nN
E_{max}	626 kJ/mol
Force-Bond Angle	20°

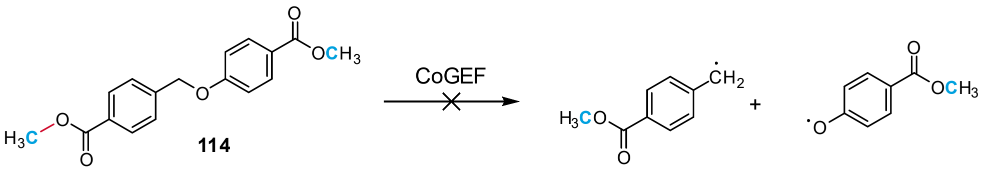

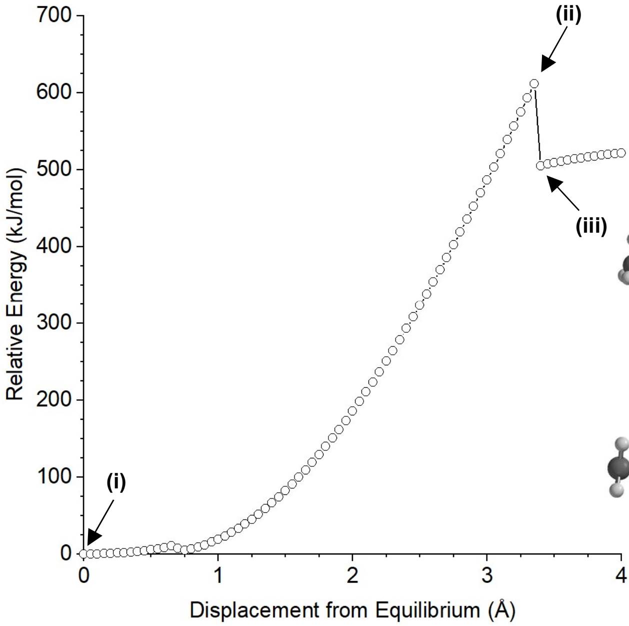

(i) Equilibrium Geometry

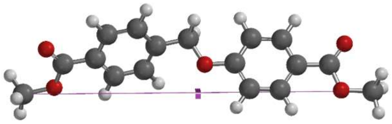

15.877 Å

(ii) Immediately Prior to Bond Cleavage

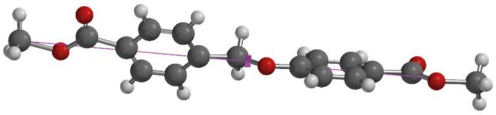

19.227 Å

(iii) Immediately After Bond Cleavage

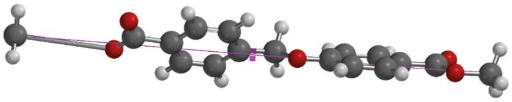

19.277 Å

Summary of CoGEF Results	
***F**$_{max}$*	6.1 nN
***E**$_{max}$*	611 kJ/mol
Force-Bond Angle	37°

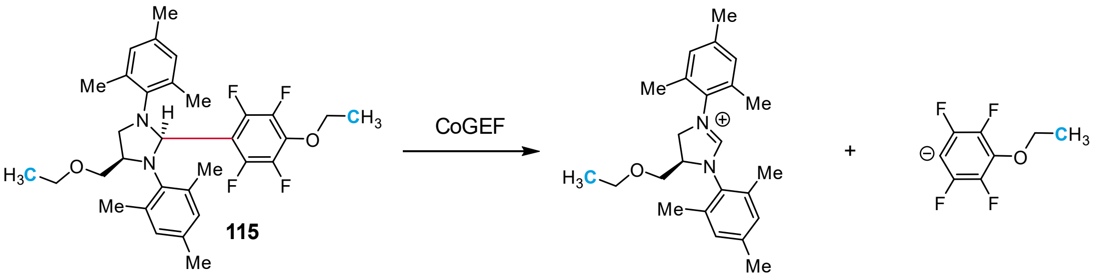

115

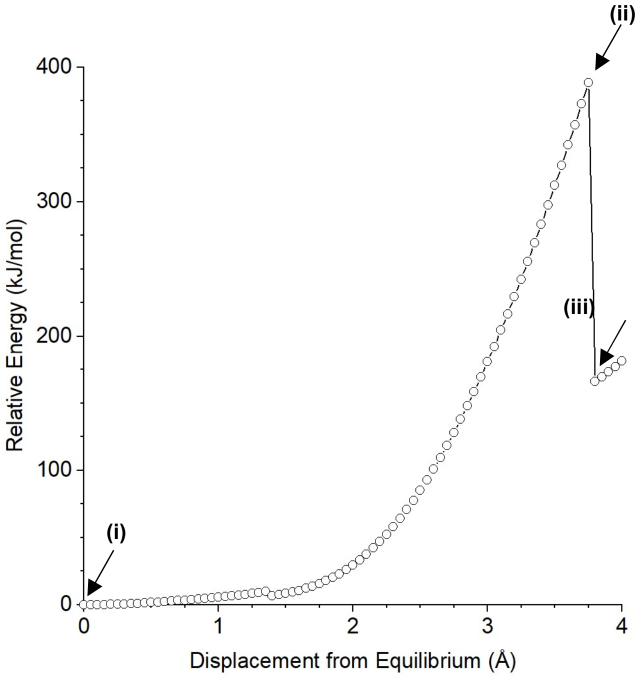

(i) Equilibrium Geometry

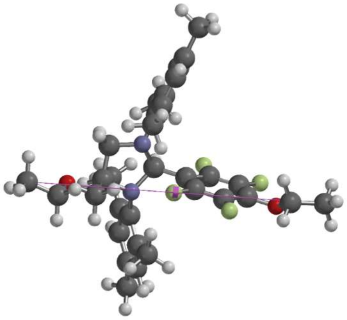

13.275 Å

(ii) Immediately Prior to Bond Cleavage

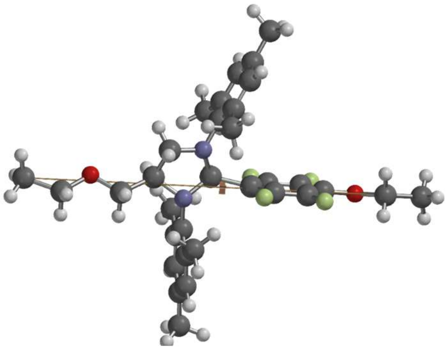

17.025 Å

Summary of CoGEF Results

***F**$_{max}$*	5.2 nN
***E**$_{max}$*	388 kJ/mol
Force-Bond Angle	13°

(iii) Immediately After Bond Cleavage

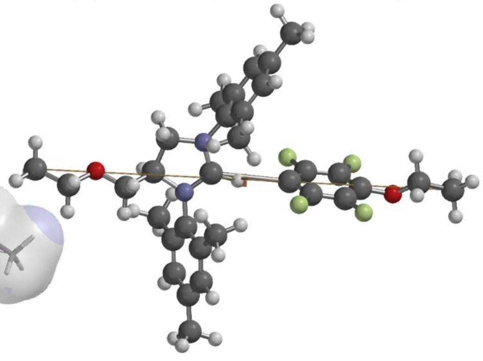

17.075 Å

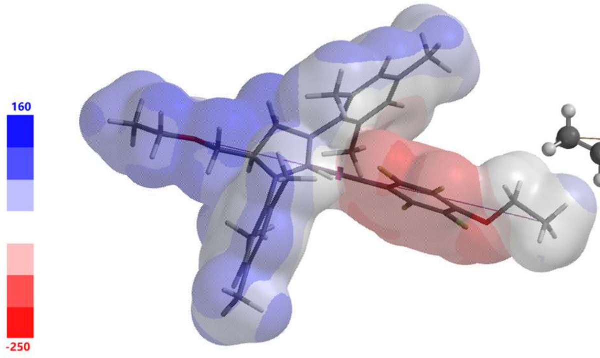

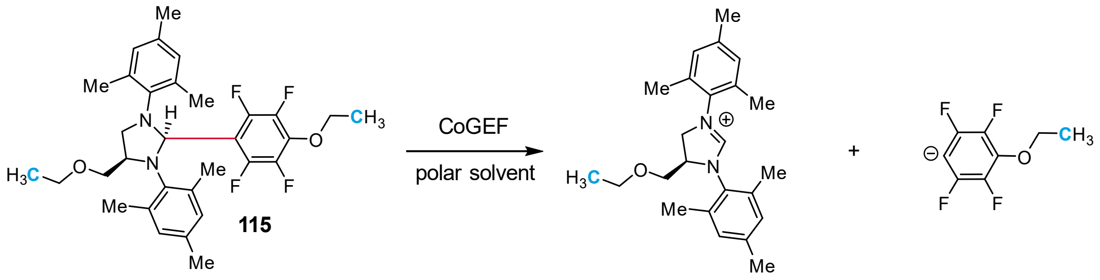

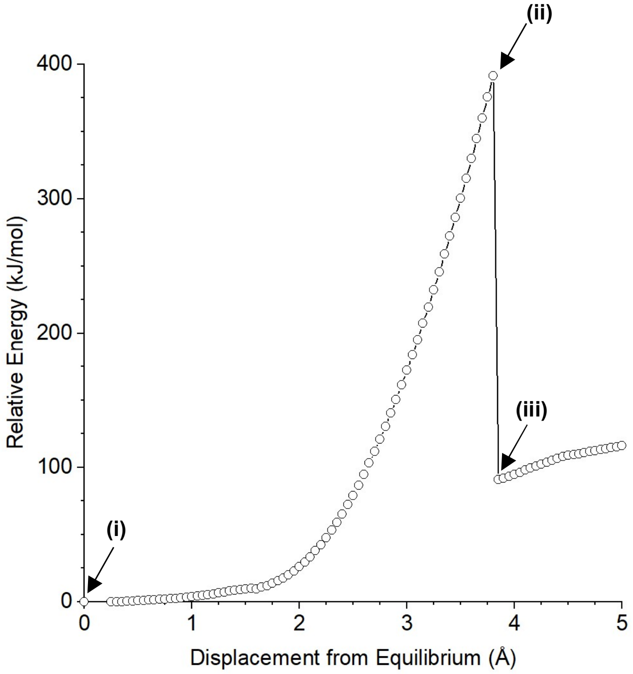

Summary of CoGEF Results

***F**$_{max}$*	5.2 nN
***E**$_{max}$*	391 kJ/mol
Force-Bond Angle	13°

(i) Equilibrium Geometry

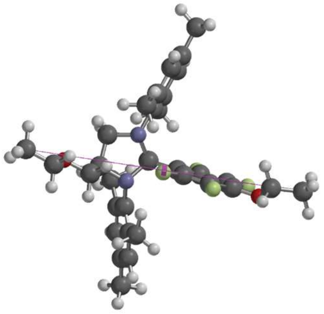

13.275 Å

(ii) Immediately Prior to Bond Cleavage

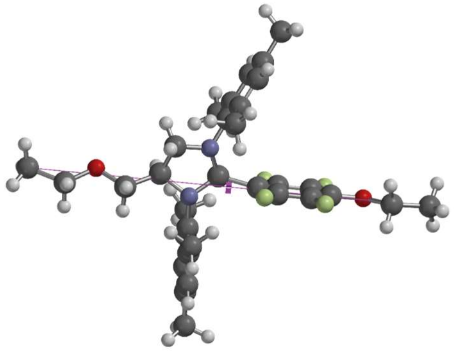

17.075 Å

(iii) Immediately After Bond Cleavage

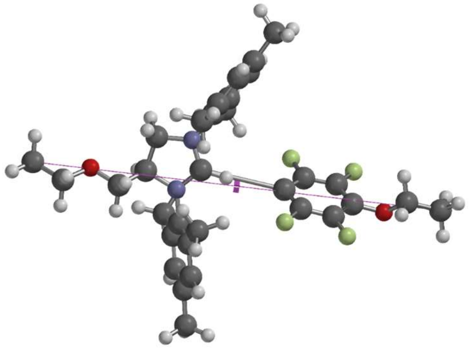

17.125 Å

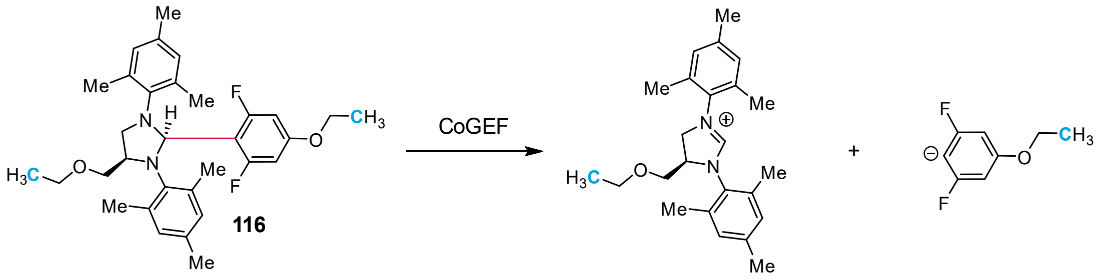

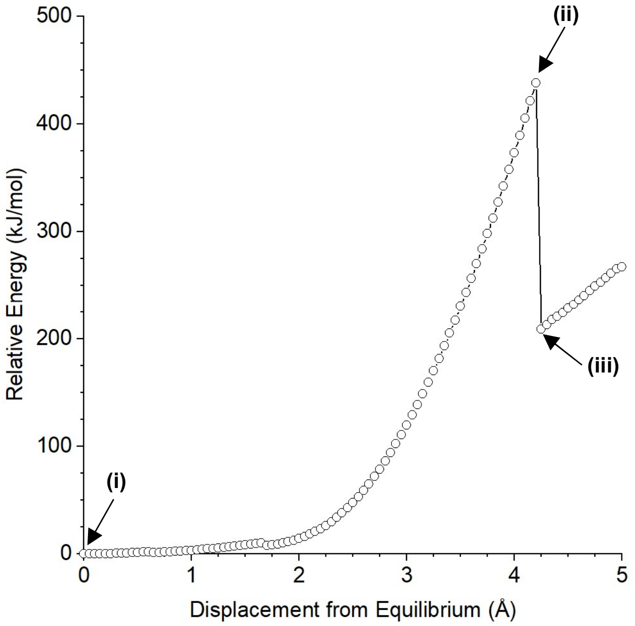

Summary of CoGEF Results	
$\boldsymbol{F_{max}}$	5.5 nN
$\boldsymbol{E_{max}}$	438 kJ/mol
Force-Bond Angle	13°

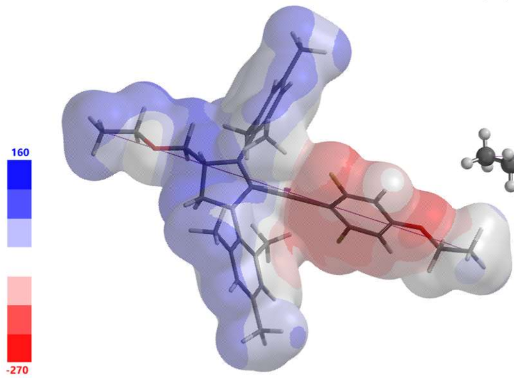

(i) Equilibrium Geometry

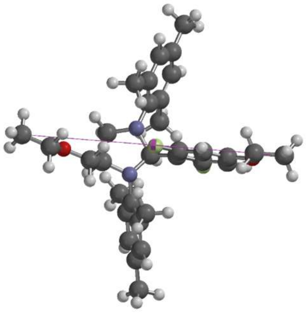

12.940 Å

(ii) Immediately Prior to Bond Cleavage

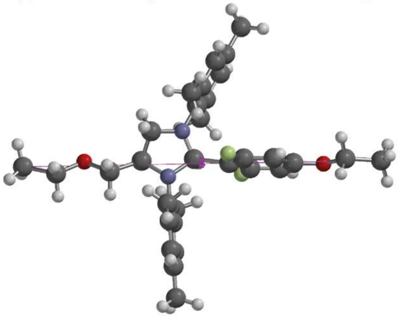

17.140 Å

(iii) Immediately After Bond Cleavage

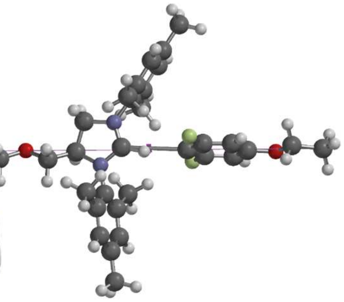

17.190 Å

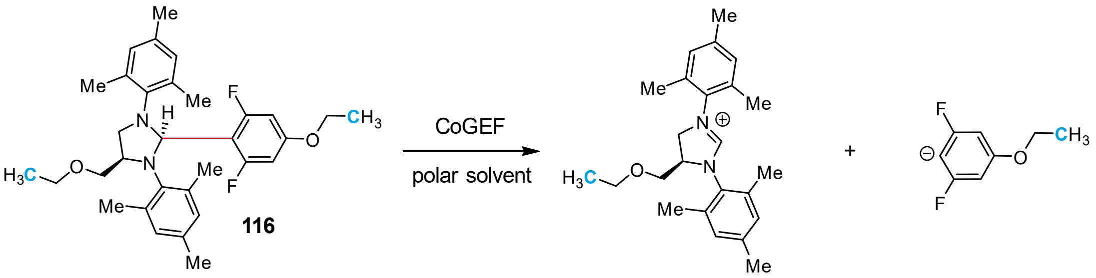

116

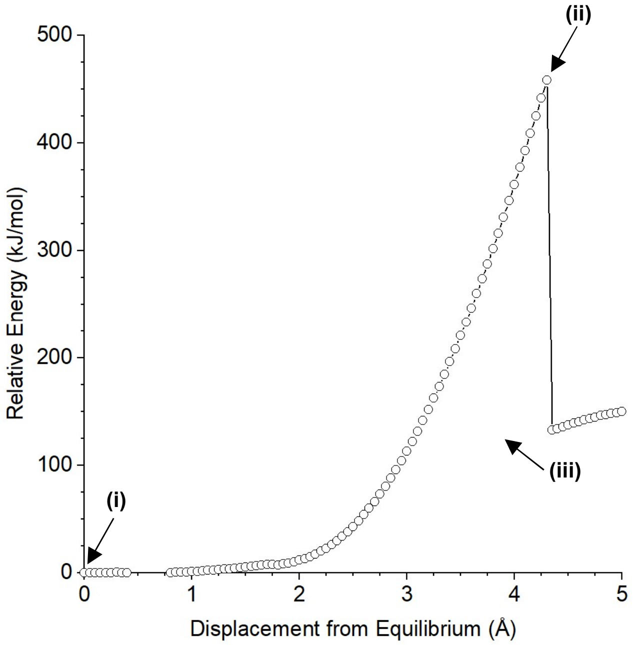

Summary of CoGEF Results

F_{max}	5.5 nN
E_{max}	458 kJ/mol
Force-Bond Angle	12°

(i) Equilibrium Geometry

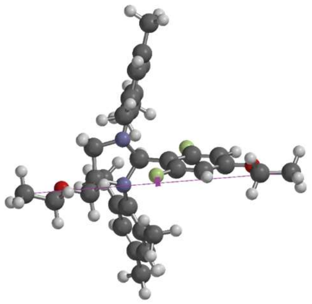

12.940 Å

(ii) Immediately Prior to Bond Cleavage

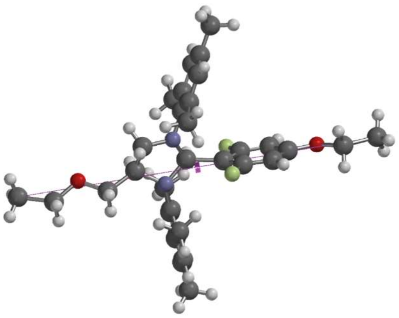

17.240 Å

(iii) Immediately After Bond Cleavage

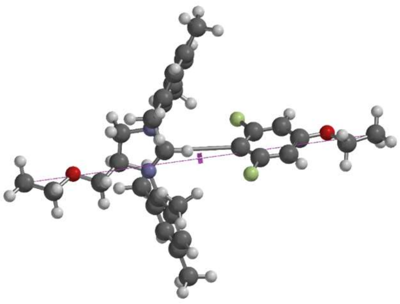

17.290 Å

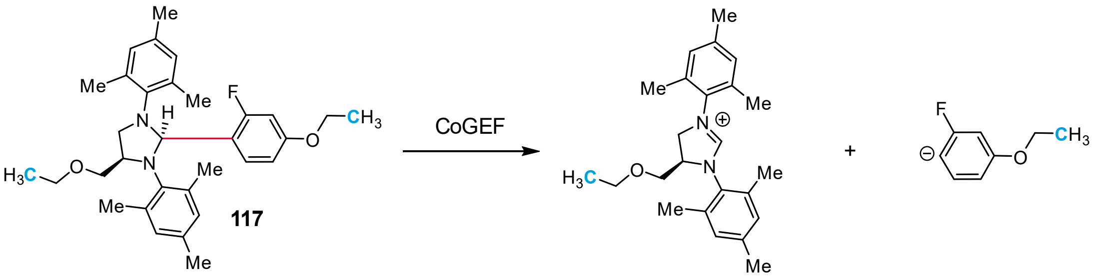

117

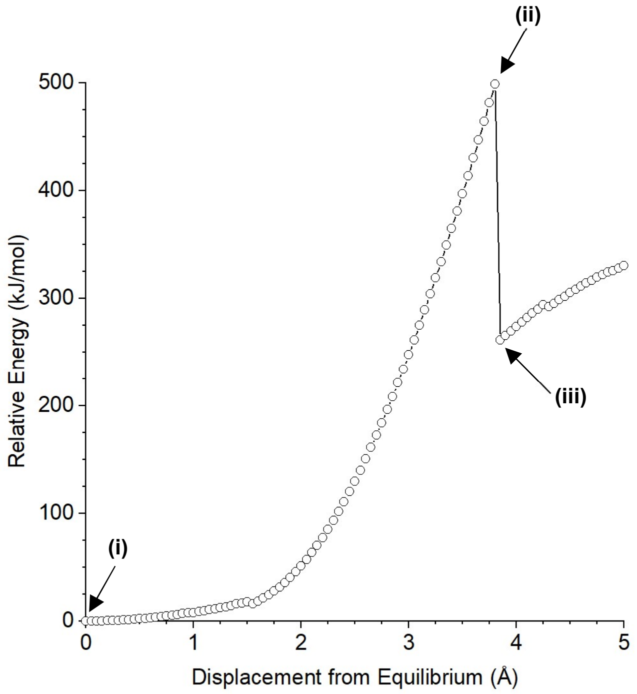

Summary of CoGEF Results	
F F_{max}	5.8 nN
E_{max}	499 kJ/mol
Force-Bond Angle	14°

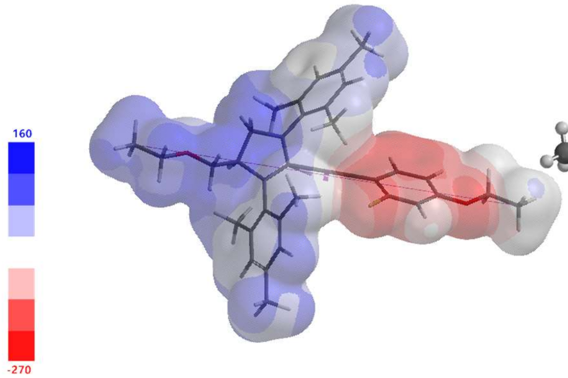

(i) Equilibrium Geometry

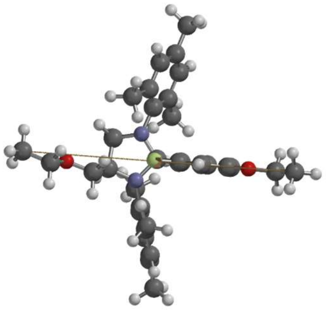

13.522 Å

(ii) Immediately Prior to Bond Cleavage

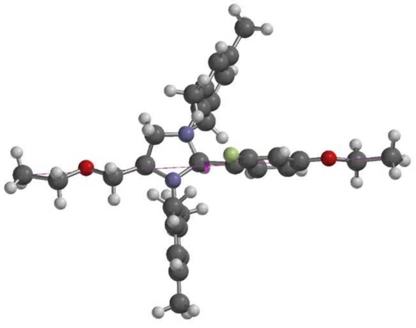

17.322 Å

(iii) Immediately After Bond Cleavage

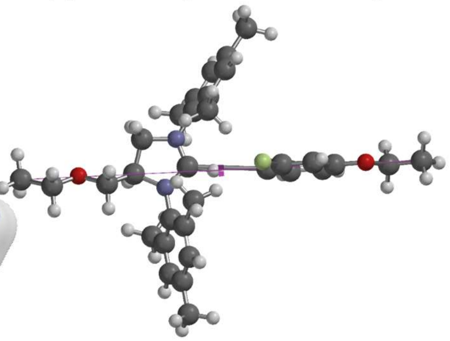

17.372 Å

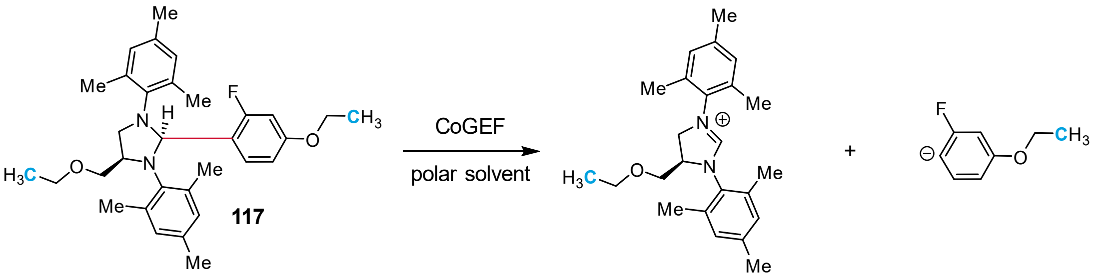

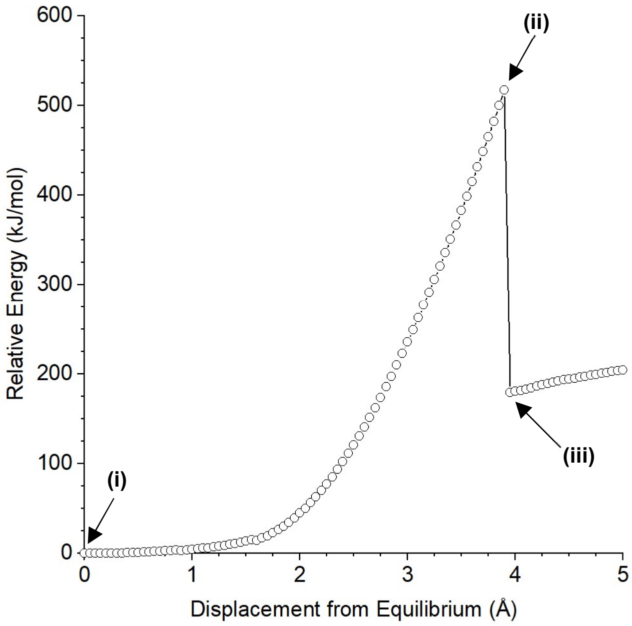

(i) Equilibrium Geometry

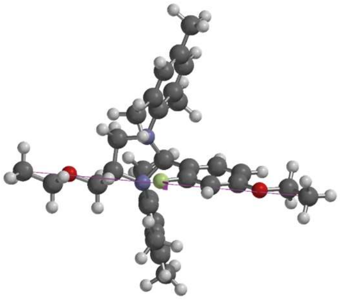

13.522 Å

(ii) Immediately Prior to Bond Cleavage

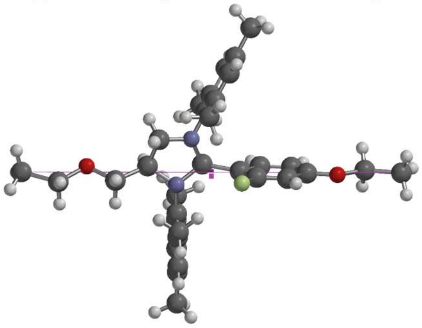

17.422 Å

(iii) Immediately After Bond Cleavage

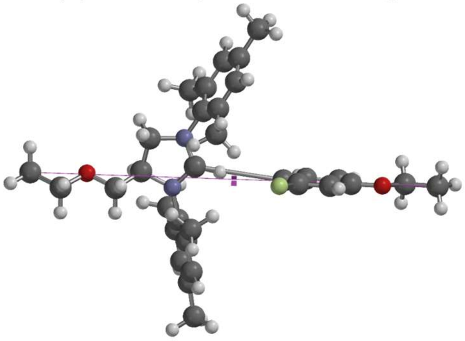

17.472 Å

Summary of CoGEF Results	
F_{max}	5.8 nN
E_{max}	517 kJ/mol
Force-Bond Angle	14°

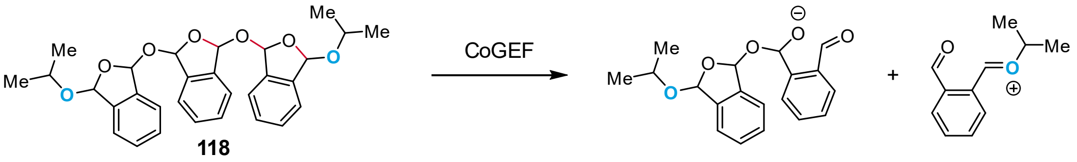

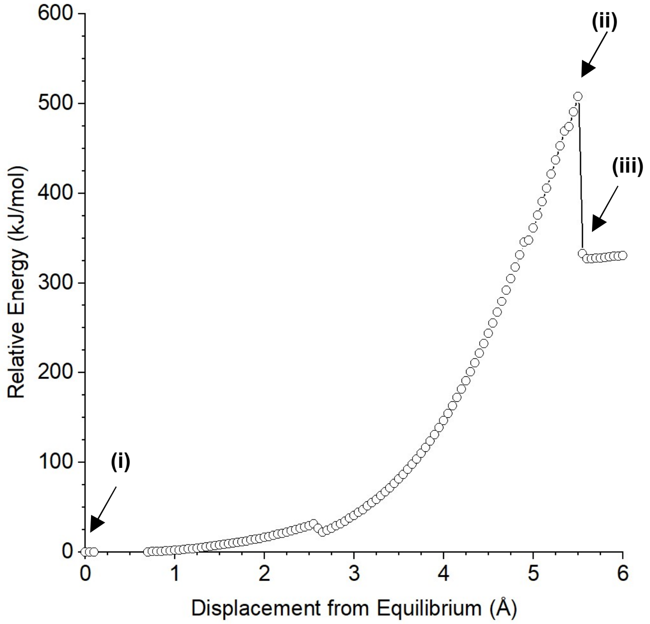

Summary of CoGEF Results

***F**$_{max}$*	5.6 nN
***E**$_{max}$*	507 kJ/mol
Force-Bond Angle	32°

(i) Equilibrium Geometry

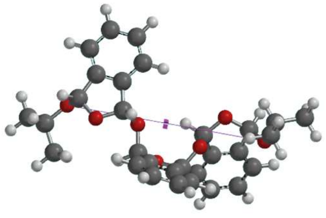

10.099 Å

(ii) Immediately Prior to Bond Cleavage

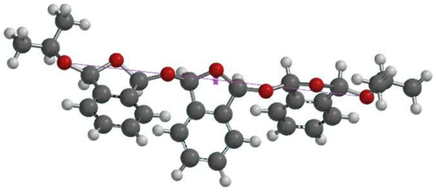

15.599 Å

(iii) Immediately After Bond Cleavage

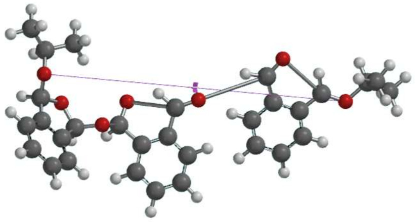

15.649 Å

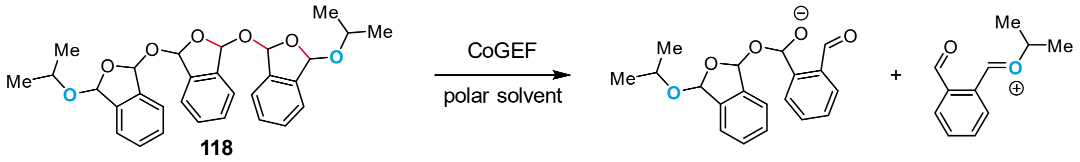

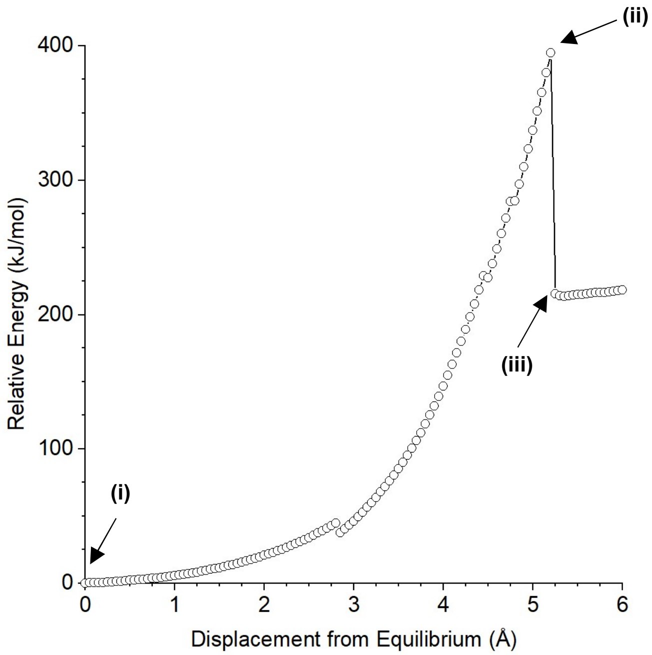

(i) Equilibrium Geometry

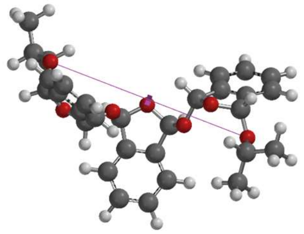

10.099 Å

(ii) Immediately Prior to Bond Cleavage

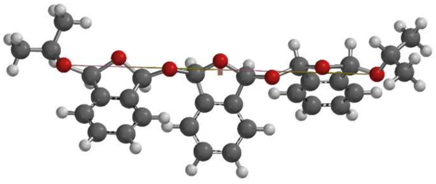

15.299 Å

(iii) Immediately After Bond Cleavage

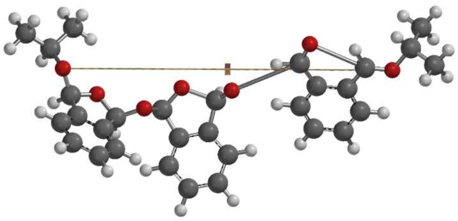

15.349 Å

Summary of CoGEF Results

***F**$_{max}$*	4.9 nN
***E**$_{max}$*	395 kJ/mol
Force-Bond Angle	33°

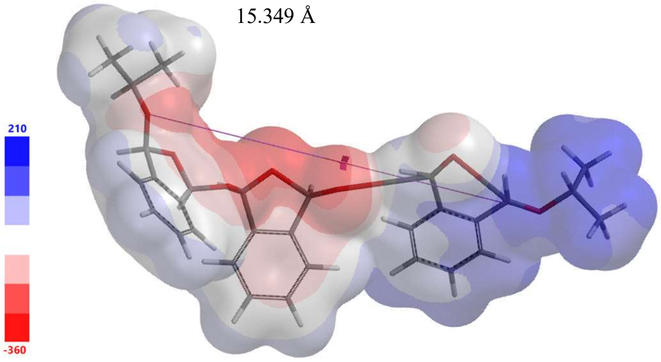

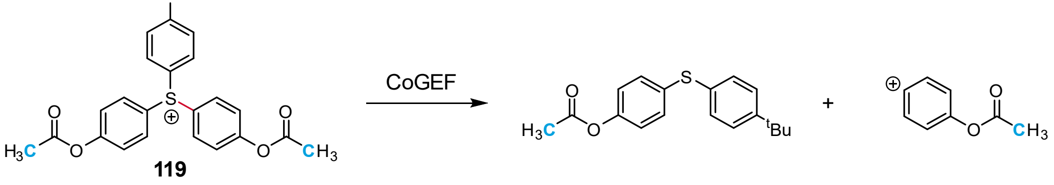

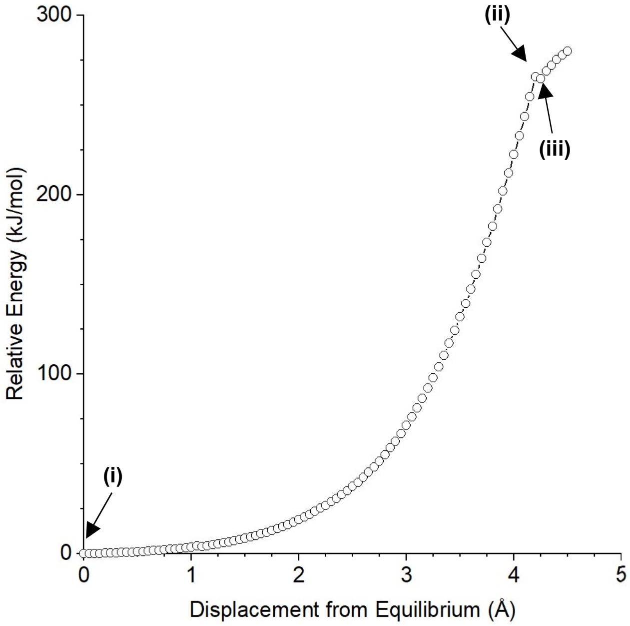

(i) Equilibrium Geometry

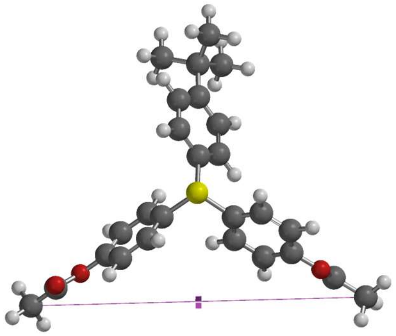

13.405 Å

(ii) Immediately Prior to Bond Cleavage

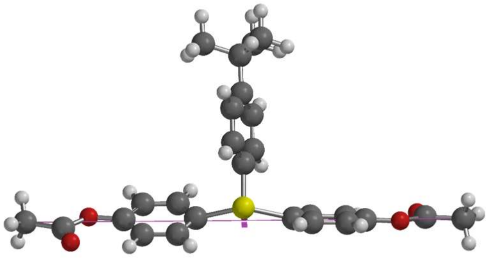

17.605 Å

(iii) Immediately After Bond Cleavage

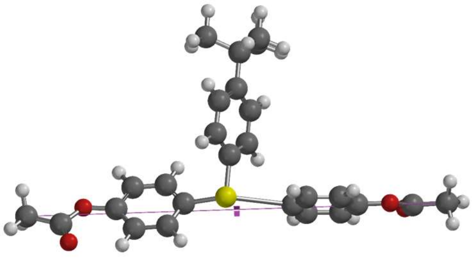

17.655 Å

Summary of CoGEF Results

***F**$_{max}$*	3.7 nN
***E**$_{max}$*	266 kJ/mol
Force-Bond Angle	17°

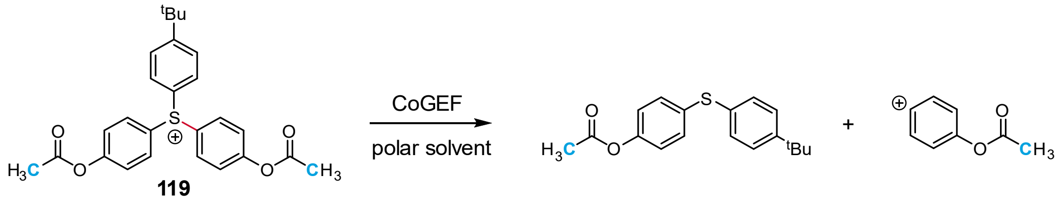

119

(ii)

(i) Equilibrium Geometry

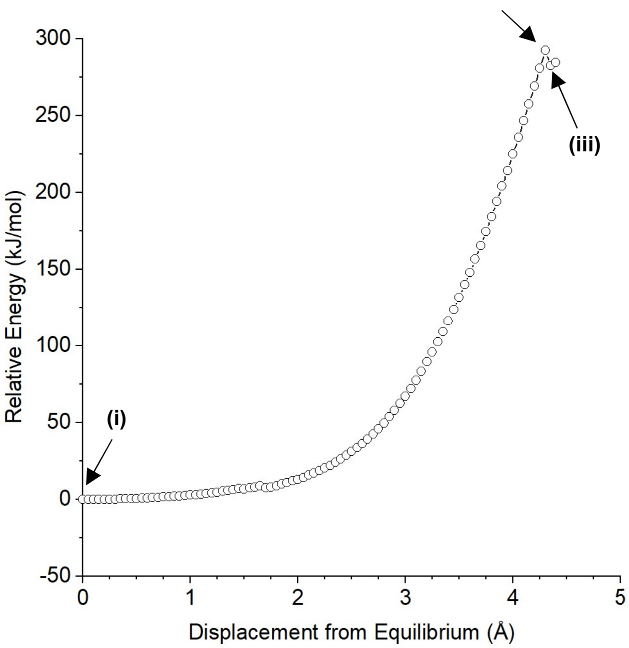

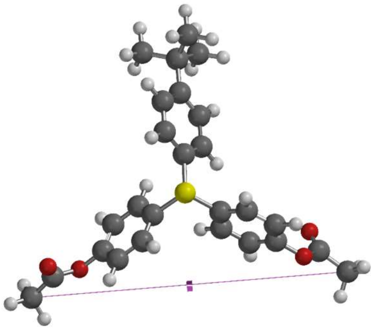

13.405 Å

(ii) Immediately Prior to Bond Cleavage

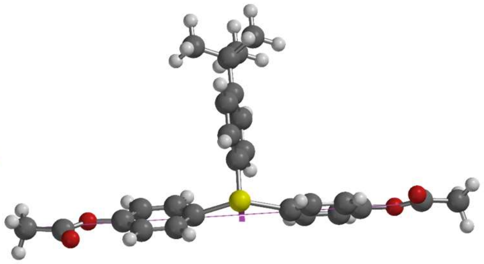

17.705 Å

Summary of CoGEF Results	
F_{max}	3.9 nN
E_{max}	292 kJ/mol
Force-Bond Angle	18°

(iii) Immediately After Bond Cleavage

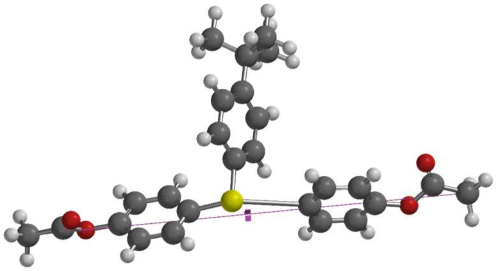

17.755 Å

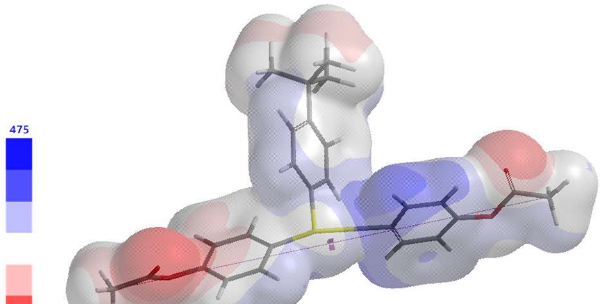

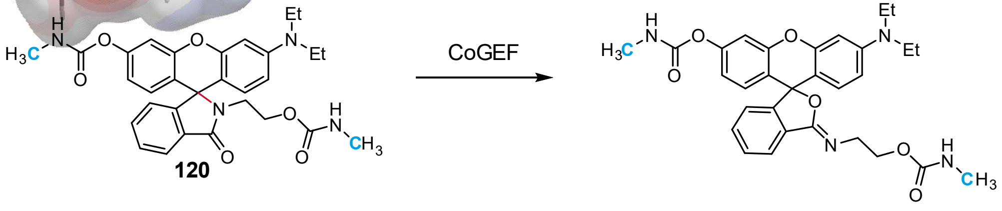

120

(ii)

(i) Equilibrium Geometry

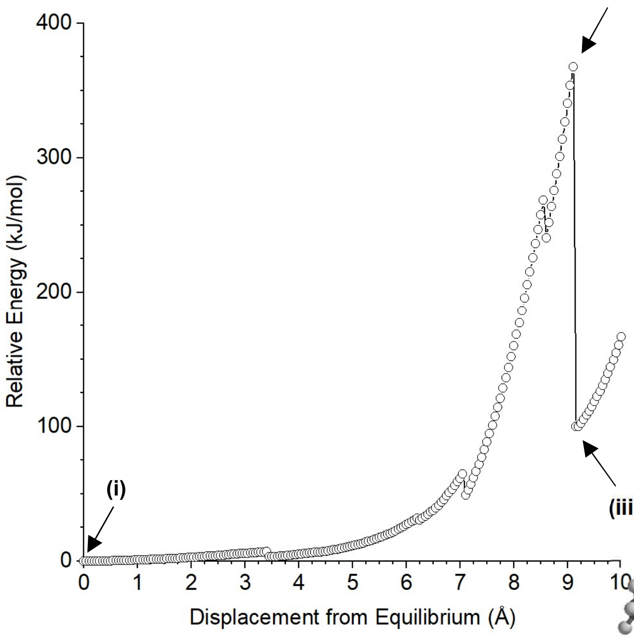

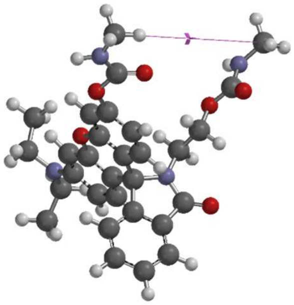

9.989 Å

(ii) Immediately Prior to Bond Cleavage

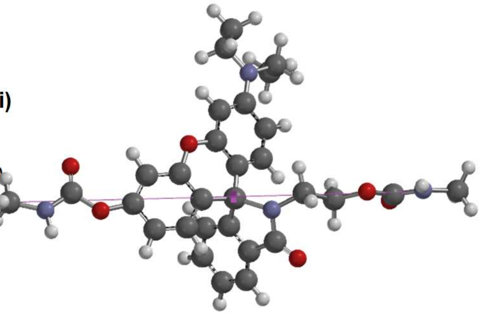

19.089 Å

(iii) Immediately After Bond Cleavage

Summary of CoGEF Results	
***F**_{max}*	4.6 nN
***E**_{max}*	368 kJ/mol
Force-Bond Angle	32°

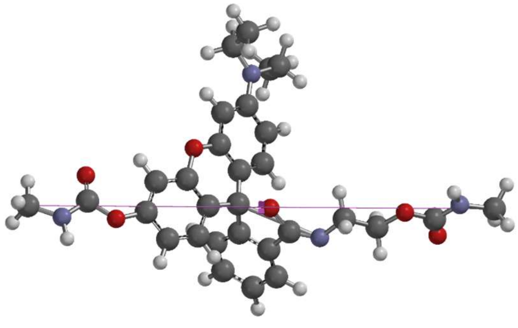

19.139 Å

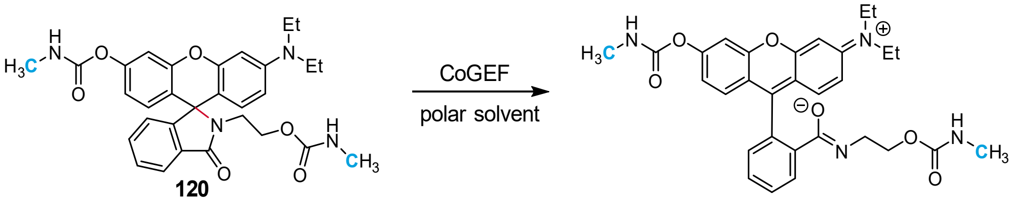

120

(ii)

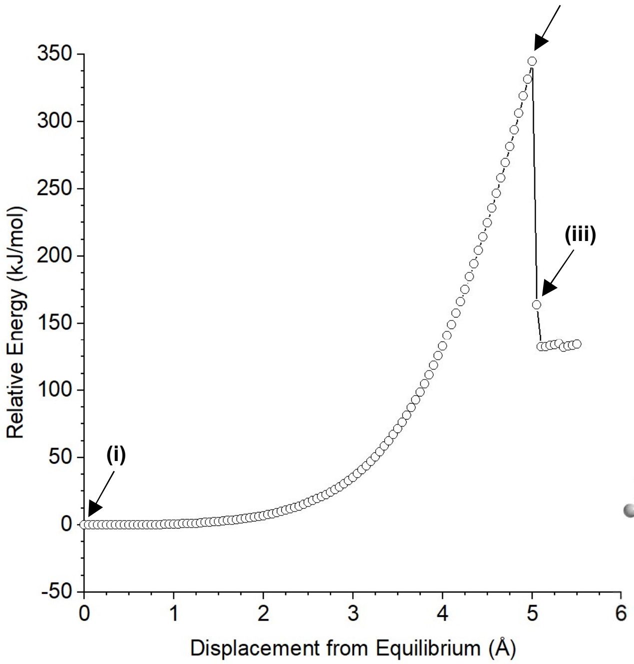

(i) Equilibrium Geometry

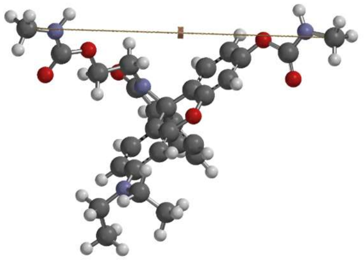

14.019 Å

(ii) Immediately Prior to Bond Cleavage

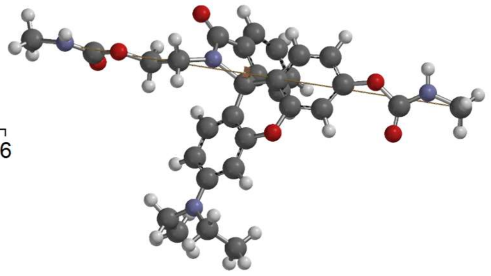

19.019 Å

Summary of CoGEF Results	
F_{max}	4.3 nN
E_{max}	345 kJ/mol
Force-Bond Angle	32°

(iii) Immediately After Bond Cleavage

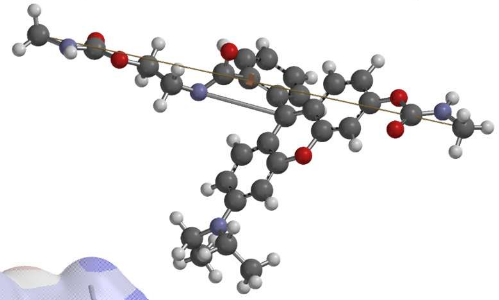

19.069 Å

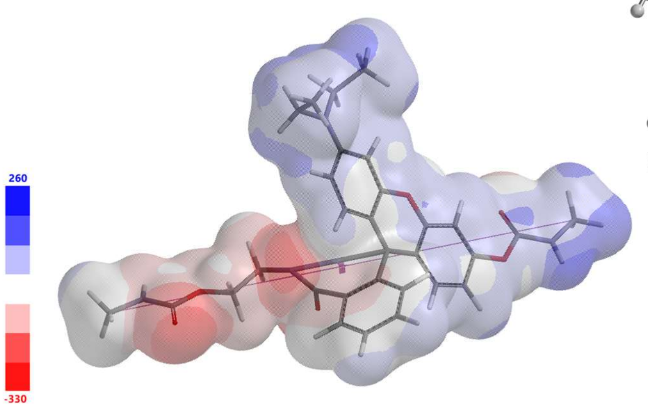

Appendix B

A GUIDE FOR IMPLEMENTING THE CONSTRAINED GEOMETRIES SIMULATE EXTERNAL FORCE (CoGEF) METHOD IN SPARTAN

This appendix will walk through the setup of a calculation using the constrained geometries simulate external force (CoGEF) method[1] to evaluate the mechanochemical reactivity of a prototypical furan–maleimide mechanophore. This method is described more fully in Chapter 1. The screen captures used for this guide are from Spartan'18 Parallel Suite software.

Setting up the calculation

Building and importing the molecule

The first step is to construct your molecule of interest in ChemDraw. You can save the structure in the MDL Molfile (*.mol) format or as ChemDraw file (*.cdx). Here, we are using an *exo* furan–maleimide adduct as an example. We have chosen methoxy pulling positions were used, but other polymer attachment motifs (e.g., acetoxy) may be more appropriate for your application.

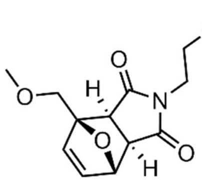

---

[1] Beyer, M. K. *J. Chem. Phys.* **2000**, *112*, 7307.

After opening the Spartan program, select File > Open. Change the file type to “All Files” and select your structure file.

If you opened a .cdx file, your structure will automatically open in the 2D editor. If you are working from a .mol file, click the 2D Edit button if you wish to use the 2D editor. This workspace is the easiest way to check that your structure was imported properly. In particular, check that the molecule depicted has retained the desired stereochemistry, as this can be scrambled upon importing. If the structure is incorrect, use the structure drawing tools in the top left-hand corner to edit the 2D structure.

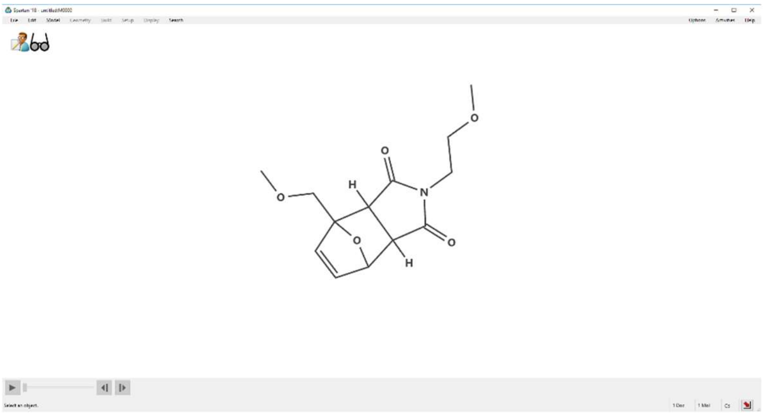

When you are satisfied with the 2D structure, click the icon to enter the 3D view.

Equilibrium conformer search and pre-stretching of the molecule

We will first run a quick Equilibrium Conformer search to obtain a coarse optimization of the molecule. Click the Calculations button . Select the following options:

Calculate: ***Equilibrium Conformer*** with ***Molecular Mechanics MMFF***.

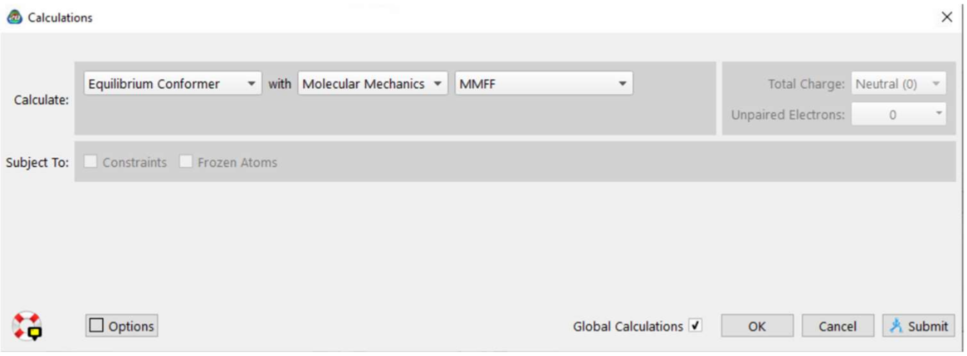

Calculations

Calculate: Equilibrium Conformer with Molecular Mechanics MMFF

Total Charge: Neutral (0)

Unpaired Electrons: 0

Subject To: ☐ Constraints ☐ Frozen Atoms

☐ Options

Global Calculations ☑

Once this calculation has finished, click the 3D Edit button .

In order obtain a smooth energy profile, we will straighten out the molecule before running the CoGEF calculation to avoid large conformational changes upon elongation. This can be accomplished by rotating bonds, especially those associated with floppy alkyl tethers. To do this, click select a bond you wish to rotate around, then Alt+left click will allow you to rotate the bond with the mouse.

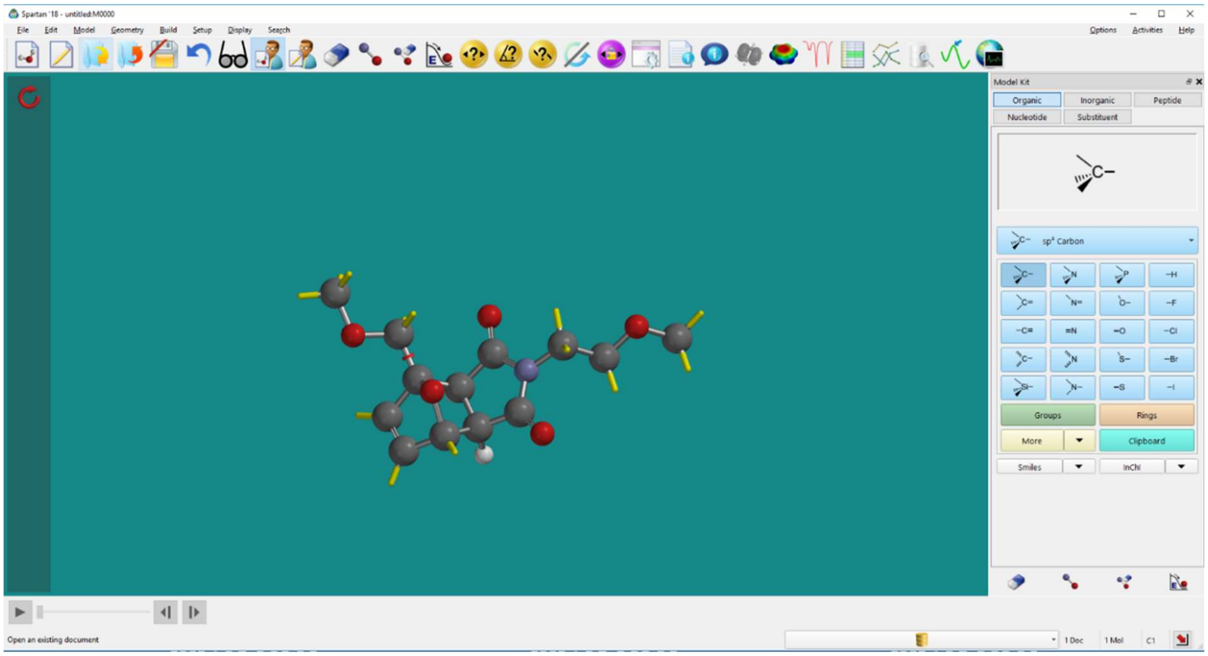

When you are done, click the icon to return to the 3D Viewer.

Equilibrium Geometry Calculation

The structure is now ready for the Equilibrium Geometry calculation. Click the Calculations button . Select the following options:

Calculate: ***Equilibrium Geometry*** at ***Ground*** state in ***Gas*** with ***Density Functional B3LYP 6-31G****

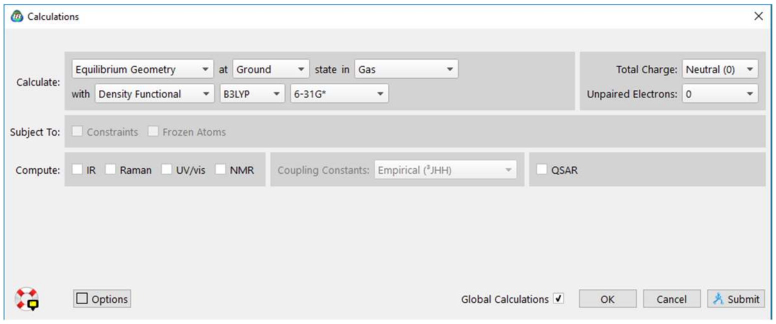

Calculations

Calculate: Equilibrium Geometry at Ground state in Gas

with Density Functional B3LYP 6-31G*

Total Charge: Neutral (0)

Unpaired Electrons: 0

Subject To: ☐ Constraints ☐ Frozen Atoms

Compute: ☐ IR ☐ Raman ☐ UV/vis ☐ NMR

Coupling Constants: Empirical (^{3}JHH)

☐ QSAR

☐ Options

Global Calculations ☑

Hit Submit. A dialogue box will confirm that the task has started.

A dialogue box will appear to inform you when the Equilibrium Geometry calculation has completed. When you accept the message, you may notice your structure changes slightly to represent the optimized geometry. Save this file.

Running the CoGEF energy profile calculation

Starting from the optimized structure found in the previous step, select the Constrain Distance icon click the two pulling position atoms on your molecule. They should become highlighted.

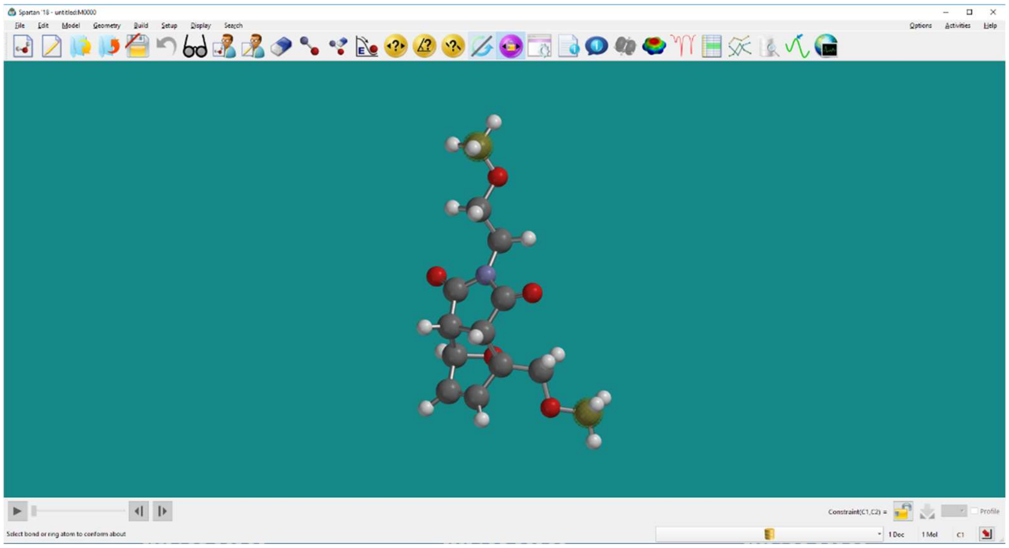

In the lower right-hand corner of the window, click the 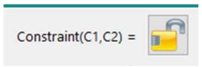 Constraint(C1,C2) = icon. A constraint line should appear between your two pulling position atoms.

Now, select the "Profile" check box. Two boxes with the same distance will appear. These should reflect the linear distance between the two pulling positions. Be sure to leave the starting bond length as it is, but adjust the second to reflect the desired final separation of the pulled atoms. We typically pull 4–7 Å using a step size of 20 steps/Å resulting in the following common values:

constraint (final) – constraint (initial)	number of steps
4 Å	81
5 Å	101
6 Å	121
7 Å	141

On the Diels-Alder example, the equilibrium distance between the two pulling atoms was 10.751 Å and a profile length of 7 Å (10.751 Å + 7 Å, 141 steps) was used for the simulation:

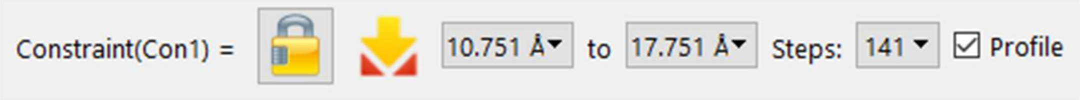

Constraint(Con1) = 10.751 Å to 17.751 Å Steps: 141 ☑ Profile

Once the constraint parameters are set, click the Calculations button. Set the parameters to:

Calculate: ***Energy Profile*** at ***Ground*** state in ***Gas*** with ***Density Functional B3LYP 6-31G****

Click Submit. A dialogue box will appear to confirm that the calculations have started. This process may take a while, depending on the size of your molecule. Do not close Spartan while this simulation is running. You can click the Status button to check the progress of the simulation. A new dialogue box will appear once the calculations are completed.

Note: if your molecule has a large number of atoms that may not affect the overall mechanochemical behavior, it may be beneficial to truncate or simplify this portion of your molecule when running an initial CoGEF simulation. Eliminating extraneous atoms will greatly reduce the run time of the simulation (DFT typically scales as $\sim N^3$ for N atoms). For example, a CoGEF calculation for **fulgide 1** took nearly 8 days, while the CoGEF calculation for **fulgide 2** was completed in about three days.

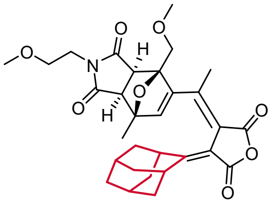

fulgide 1

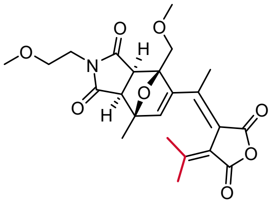

fulgide 2

Analyzing the results

Once the calculations are completed, you will be prompted to open the newly generated file, which should have the suffix "_Prof" in the filename.

Use the slider in the lower left-hand corner to see the progression of the geometry profile. Use this slider to ensure that the desired bonds are broken.

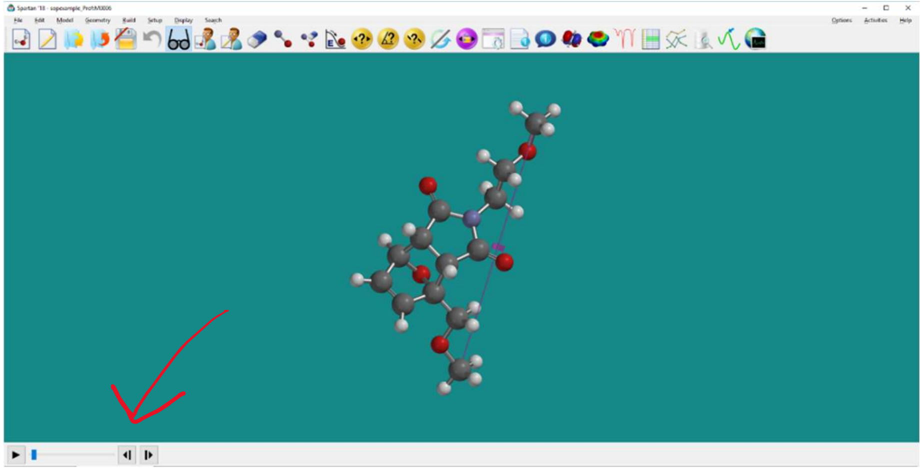

Note here that the two lengthened (broken) bonds correspond to the bonds broken during the expected retro-[4+2] reaction:

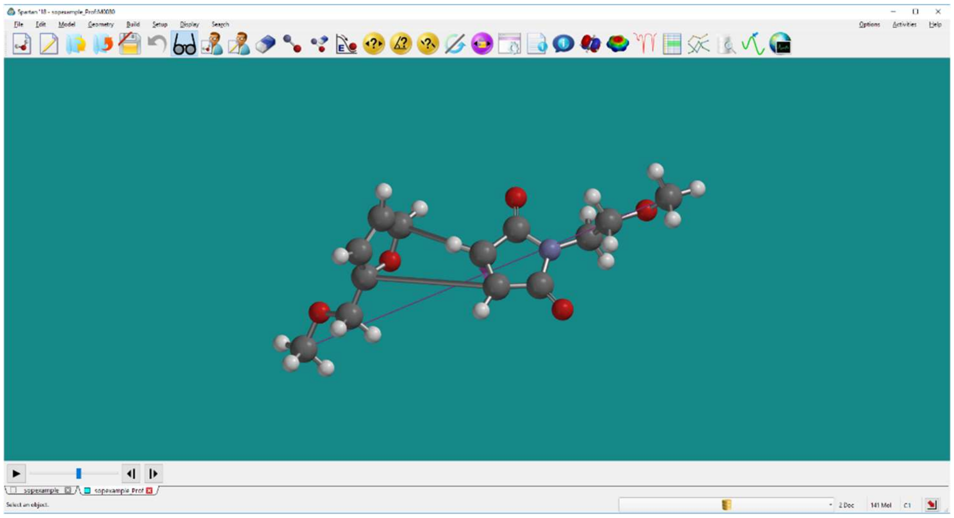

If you wish to create an image (*.png) of the 3D structure, you can do so by selecting File > Save Image As.

Be sure the slider is returned to the initial position before completing the following steps.

Open the spreadsheet window by clicking the ▦ icon.

Click “Add” and go to the “Molecule List” tab. Select “Relative Energy (kJ/mol)” from the list. You should see the relative energy values fill in the first column of the spreadsheet.

On the 3D molecule viewer, click the line between the two constrained atoms. Then, with the spreadsheet window still open, click the ⬇ icon in the lower right-hand corner. This will fill in the constraint profile values in the second column of the spreadsheet.

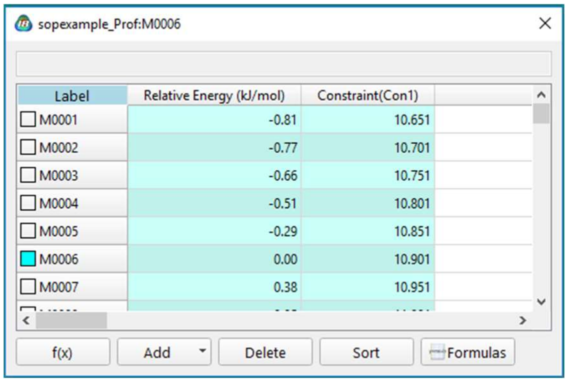

Label	Relative Energy (kJ/mol)	Constraint(Con1)
☐ M0001	-0.81	10.651
☐ M0002	-0.77	10.701
☐ M0003	-0.66	10.751
☐ M0004	-0.51	10.801
☐ M0005	-0.29	10.851
■ M0006	0.00	10.901
☐ M0007	0.38	10.951

Thes values can be used to plot the energy profile and calculate force values. The maximum force immediately prior to bond cleavage is the estimated rupture force, $F_{\max}$.

Relative energy (kJ/mol)	***Constraint (Å)***	***Displacement (Å)***	***Force (nN)***
E_n (from Spartan)	l (from Spartan)	$D = l - l_0$	$F = \frac{E_{n+1} - E_n}{D_{n+1} - D_n} \times \frac{10^{22}}{N_A}$

Extending a calculation

If the initial energy profile did not elongate the molecule enough to see a bond cleavage event, you may need to extend the calculation. In the CoGEF_Prof file, use the slider to view the final structure of the profile you previously ran. Right-click somewhere within the molecule boundaries and select “Copy.”

Click the New Build icon and paste the final structure from the previous simulation.

Select the Constrain Distance icon and click on the existing constraint line on the molecule.

Define a new profile using the Profile prompt in the lower right-hand corner. The beginning distance for this extension should reflect the final constraint distance from the first energy profile. Enter the new final bond length and the appropriate number of steps.

Click the Calculations button to set up an Energy Profile calculation as done previous.

Appending calculations

After your extended calculation is finished, make a copy of the CoGEF file that includes the first portion of the calculation and save this with a distinct name. In this copied file, go to File > Append Molecules. Select the filename of the extended profile that you wish to append. Check that the process worked properly by using the slider in the lower left-hand corner to view the full profile.

Appendix C

ATOMIC COORDINATES FOR MOLECULES DISCUSSED IN CHAPTER 2

The atomic coordinates for all numbered compounds discussed in Chapter 2 can be found below. Compounds labeled **X** are starting material geometries and those labeled **X**‡ represent the optimized transition state geometries. All final geometries were calculated at the M06-2X/6-311+G** level of theory.

1

C	-0.30396	0.00000	-3.85119
C	1.00287	0.00000	-3.50022
C	1.03423	0.00000	-2.06139
C	-0.26122	0.00000	-1.66423
O	-1.08887	0.00000	-2.73727
C	-0.93827	0.00000	-0.33776
O	0.10058	0.00000	0.64377
C	-0.31573	0.00000	1.90905
O	0.74507	0.00000	2.69882
O	-1.46640	0.00000	2.26377
C	0.46337	0.00000	4.10858
H	-0.82526	0.00000	-4.79398
H	1.84626	0.00000	-4.17224
H	1.89988	0.00000	-1.41916
H	-1.56375	0.88795	-0.21628
H	-1.56375	-0.88795	-0.21628
H	-0.09954	0.89360	4.37535
H	1.43404	0.00000	4.59531
H	-0.09954	-0.89360	4.37535

1‡

C	0.80709	-0.52524	-3.62548
C	-0.29859	-1.35165	-3.57537
C	-1.02080	-0.94134	-2.45389
C	-0.31815	0.12086	-1.88459
O	0.81391	0.34974	-2.63625
C	-0.55877	0.88069	-0.76700
O	0.53420	-0.16159	0.87916
C	0.18522	0.35641	1.98118
O	0.86314	-0.18734	3.04170
O	-0.64877	1.24110	2.17748
C	0.53760	0.32812	4.33081
H	1.63484	-0.47480	-4.31756
H	-0.53154	-2.14123	-4.27104
H	-1.94896	-1.34093	-2.07269
H	0.03819	1.75728	-0.55531
H	-1.49075	0.74927	-0.23553
H	0.74155	1.39828	4.38365
H	1.17264	-0.20646	5.03431
H	-0.51207	0.14884	4.56642

2

C	0.01933	0.00000	-3.09819
C	1.30718	0.00000	-2.67446
C	1.27156	0.00000	-1.23426
C	-0.03946	0.00000	-0.89900
O	-0.81499	0.00000	-2.01416
C	-0.78286	0.00000	0.39127
O	0.20452	0.00000	1.42536
C	-0.27583	0.00000	2.66730
O	0.74329	0.00000	3.51059
O	-1.44307	0.00000	2.96349
C	0.38977	0.00000	4.90396
C	-0.62782	0.00000	-4.43481
H	2.18076	0.00000	-3.30744
H	2.10589	0.00000	-0.55156
H	-1.41398	0.88772	0.48250
H	-1.41398	-0.88772	0.48250
H	-0.18615	0.89353	5.14165
H	1.33414	0.00000	5.43998
H	-0.18615	-0.89353	5.14165
H	0.13918	0.00000	-5.20865
H	-1.25566	-0.88468	-4.56385
H	-1.25566	0.88468	-4.56385

2‡

C	-0.08931	-0.45722	-2.97806
C	0.86422	-1.44283	-2.77539
C	1.47322	-1.14942	-1.55472
C	0.87119	0.00691	-1.06896
O	-0.09416	0.40710	-1.96784
C	1.05936	0.72182	0.09410
O	-0.32498	-0.11264	1.49807
C	-0.20519	0.48080	2.61631
O	-1.05334	-0.03701	3.55512
O	0.54810	1.40778	2.90664
C	-0.99920	0.55945	4.85045
C	-1.04241	-0.22150	-4.08335
H	1.07088	-2.25949	-3.44861
H	2.26419	-1.68907	-1.05495
H	1.89747	0.46448	0.72644
H	0.60601	1.69533	0.21833
H	-0.00809	0.44069	5.28969
H	-1.73766	0.03213	5.45065
H	-1.24797	1.62002	4.79920
H	-0.93386	-0.99799	-4.83767
H	-2.06551	-0.22438	-3.70013
H	-0.85297	0.75504	-4.53533

3

C	0.62587	0.06023	-3.07939
C	-0.63753	-0.42194	-2.98246
C	-0.95833	-0.46670	-1.57886
C	0.14103	-0.01101	-0.93428
O	1.11214	0.31405	-1.82725
C	0.48908	0.19655	0.50451
O	-0.67668	-0.23504	1.23202
C	-0.83899	0.27581	2.45048
O	-1.92921	-0.25599	2.98227
O	-0.12064	1.08538	2.97922
C	-2.25144	0.19507	4.30851
C	1.70915	-0.60163	0.93756
C	1.53488	0.34757	-4.21835
H	-1.26734	-0.71178	-3.80904
H	-1.87686	-0.79292	-1.11858
H	0.64375	1.26076	0.69898
H	-3.16002	-0.33407	4.57927
H	-2.42066	1.27095	4.30492
H	-1.44251	-0.05586	4.99331
H	1.53238	-1.66666	0.77635
H	1.92347	-0.42023	1.99132
H	2.57265	-0.29209	0.34723
H	1.03138	0.10153	-5.15262
H	1.81477	1.40344	-4.23878
H	2.44963	-0.24542	-4.14634

3‡

C	0.07360	-0.83432	-2.97931
C	-0.86957	-1.76653	-2.59637
C	-1.38512	-1.32090	-1.37052
C	-0.73728	-0.13522	-1.07160
O	0.16010	0.14380	-2.07438
C	-0.84749	0.72987	0.01510
O	0.58127	-0.09888	1.38519
C	0.27057	0.17857	2.58408
O	1.18318	-0.31683	3.47502
O	-0.70669	0.80827	2.98889
C	0.92921	-0.05023	4.85331
C	0.95318	-0.74477	-4.16591
C	-0.29578	2.10357	-0.00501
H	-1.13682	-2.65151	-3.15122
H	-2.14321	-1.78408	-0.75599
H	-1.63780	0.50201	0.72013
H	0.92006	1.02351	5.04473
H	1.74388	-0.51872	5.40137
H	-0.02392	-0.48065	5.16246
H	0.77258	-1.59384	-4.82242
H	0.75637	0.18217	-4.70937
H	2.00087	-0.74206	-3.85662
H	0.66103	2.14615	-0.52310
H	-0.21034	2.49318	1.00686
H	-1.01187	2.72743	-0.55533

4

C	0.00480	-0.49497	-4.62192
C	0.86995	-1.38937	-4.08349
C	0.91587	-1.12289	-2.66879
C	0.07700	-0.08107	-2.46255
O	-0.48493	0.31361	-3.63457
C	-0.48491	-0.23485	-5.99988
C	-0.33977	0.69221	-1.25327
C	-0.02707	2.17618	-1.36158
O	0.40326	0.10153	-0.16682
C	-0.11551	0.23532	1.04562
O	0.72952	-0.34500	1.91077
O	-1.14881	0.77556	1.32867
C	0.35040	-0.35701	3.25822
C	-0.60013	-1.26913	3.68948
C	-0.92167	-1.30533	5.04267
C	-0.29227	-0.44190	5.93744
C	0.66192	0.46260	5.47946
C	0.98999	0.51154	4.12656
H	1.41162	-2.14891	-4.62522
H	1.49257	-1.63574	-1.91622
H	-0.02625	-0.94582	-6.68615
H	-1.57049	-0.34419	-6.05578
H	-0.22796	0.77751	-6.32029
H	-1.40504	0.54033	-1.06291
H	1.04405	2.32051	-1.51370
H	-0.34335	2.69606	-0.45655
H	-0.56605	2.59650	-2.21163
H	-1.07370	-1.93415	2.97666
H	-1.66273	-2.01199	5.39654
H	-0.54457	-0.47626	6.99046
H	1.15442	1.13364	6.17290
H	1.72986	1.20547	3.74588

4‡

C	0.07164	-0.32544	-4.59647
C	-0.72442	-1.41718	-4.31407
C	-1.29174	-1.17247	-3.05546
C	-0.81966	0.05918	-2.63707
O	0.02213	0.56144	-3.59941
C	0.91964	0.00699	-5.76237
C	-1.04698	0.78331	-1.46840
C	-0.69969	2.21702	-1.33851
O	0.46646	0.03134	-0.18012
C	0.09540	0.08928	1.02483
O	1.06884	-0.43534	1.87262
O	-0.94898	0.52127	1.49604
C	0.79796	-0.43981	3.23115
C	0.28683	-1.59200	3.81402
C	0.07307	-1.62123	5.18988
C	0.36771	-0.50499	5.96919
C	0.87901	0.64428	5.36937
C	1.09668	0.68123	3.99501
H	-0.86430	-2.27293	-4.95465
H	-1.97026	-1.79829	-2.49498
H	0.88215	-0.80462	-6.48625
H	0.56651	0.92791	-6.23181
H	1.95357	0.16230	-5.44380
H	-1.79986	0.37481	-0.80445
H	0.24291	2.44986	-1.83161
H	-0.67501	2.50879	-0.29055
H	-1.49710	2.78473	-1.83550
H	0.06448	-2.45032	3.19011
H	-0.32317	-2.51817	5.65146
H	0.20154	-0.53113	7.03957
H	1.11101	1.51472	5.97191
H	1.49364	1.56548	3.51031

5

C	-0.14632	0.75383	-3.19103
C	0.14926	-0.56713	-3.11736
C	0.22382	-0.89808	-1.71705
C	-0.03889	0.25045	-1.04999
O	-0.26377	1.26392	-1.92816
C	-0.35502	1.70180	-4.31512
C	-0.12309	0.61461	0.39790
C	0.85105	1.72028	0.78017
O	0.18266	-0.59323	1.10656
C	-0.30892	-0.70176	2.36282
O	-1.03437	0.12807	2.88141
N	0.10425	-1.83601	2.94772
C	-0.31621	-2.18130	4.29464
H	0.30098	-1.22713	-3.95723
H	0.43890	-1.85623	-1.27253
H	-1.36053	2.12790	-4.28518
H	0.36376	2.52350	-4.27193
H	-0.22695	1.17521	-5.26030
H	-1.14491	0.91542	0.64260
H	1.87406	1.40511	0.56499
H	0.75582	1.95073	1.84195
H	0.62934	2.62066	0.20524
H	0.69914	-2.45925	2.42329
H	-0.01651	-1.40802	5.00309
H	0.16160	-3.11836	4.56855
H	-1.39913	-2.30502	4.34494

$5^{\ddagger}$

C	-0.03743	0.81019	-3.14227
C	-1.15630	-0.00044	-3.18806
C	-1.62172	-0.09796	-1.87131
C	-0.76999	0.66428	-1.08602
O	0.20095	1.21096	-1.89266
C	0.88456	1.28343	-4.19788
C	-0.75597	0.91142	0.27955
C	0.06975	1.97173	0.89723
O	0.45865	-0.78851	1.03894
C	0.16216	-1.02684	2.26363
O	-0.78699	-0.52134	2.89453
N	1.01319	-1.90539	2.91503
C	0.63152	-2.49840	4.18473
H	-1.56553	-0.45242	-4.07717
H	-2.47544	-0.64743	-1.50283
H	0.87473	2.37498	-4.24077
H	1.90433	0.96124	-3.97543
H	0.57923	0.88071	-5.16157
H	-1.58741	0.51085	0.84613
H	1.03144	2.07998	0.39840
H	0.19908	1.77624	1.95932
H	-0.48234	2.91434	0.78635
H	1.59822	-2.45817	2.30633
H	0.47455	-1.71836	4.92987
H	1.44213	-3.14232	4.52412
H	-0.28536	-3.09277	4.11181

6

C	0.83635	0.76372	-2.81110
C	-0.21321	-0.08037	-2.98254
C	-0.49561	-0.67042	-1.69976
C	0.41283	-0.13194	-0.84583
O	1.22599	0.74513	-1.51001
C	1.59539	1.65425	-3.72667
C	-1.57606	-1.66206	-1.39133
C	0.69258	-0.31331	0.60670
O	-0.48925	0.14402	1.32675
C	0.99691	-1.75200	0.99431
C	-0.29981	0.53624	2.58196
O	0.75857	0.58614	3.15751
O	-1.47411	0.87222	3.09898
C	-1.44017	1.33063	4.46036
H	-0.73607	-0.26265	-3.90964
H	1.18375	1.57677	-4.73236
H	1.53104	2.69494	-3.40042
H	2.65049	1.37239	-3.75689
H	-1.28962	-2.66730	-1.71153
H	-2.49450	-1.39623	-1.91804
H	-1.79369	-1.69253	-0.32338
H	1.52314	0.33935	0.87910
H	1.17476	-1.82632	2.06806
H	1.89402	-2.08129	0.46750
H	0.16934	-2.40715	0.71900
H	-1.04780	0.54738	5.10767
H	-2.47180	1.55526	4.71423
H	-0.82344	2.22515	4.53736

6‡

C	-0.88510	0.74339	-2.64474
C	0.20802	0.01199	-3.04915
C	1.04388	-0.13941	-1.92435
C	0.40453	0.52873	-0.88396
O	-0.78073	1.05877	-1.35395
C	-2.08584	1.21892	-3.36922
C	2.34746	-0.86583	-1.89083
C	0.68820	0.72912	0.46674
O	-0.41199	-0.79113	1.38911
C	2.00620	0.40940	1.07147
C	-0.77620	-0.45936	2.56205
O	-0.57485	0.60422	3.14534
O	-1.46782	-1.46264	3.17884
C	-1.92704	-1.18781	4.50201
H	0.38328	-0.36670	-4.04430
H	-2.04309	0.89385	-4.40685
H	-2.98899	0.82029	-2.90208
H	-2.13804	2.30934	-3.33406
H	3.14702	-0.21860	-1.52549
H	2.60472	-1.21333	-2.89039
H	2.28958	-1.73093	-1.22556
H	0.07222	1.46128	0.97666
H	1.94235	0.48502	2.15484
H	2.73338	1.14669	0.71088
H	2.35499	-0.58163	0.78726
H	-1.08840	-0.97695	5.16640
H	-2.44478	-2.08701	4.82862
H	-2.61296	-0.33969	4.50471

7

C	-1.65507	1.99658	-1.32755
C	-1.62190	0.74874	-1.86004
C	-0.88046	-0.04700	-0.92613
C	-0.50533	0.75997	0.09875
O	-0.98348	2.01451	-0.14531
C	-2.26153	3.27648	-1.77166
O	-0.64845	-1.39086	-1.02222
C	0.28876	0.57312	1.33849
O	-0.65814	0.63842	2.44583
C	1.04506	-0.74188	1.38754
C	-0.17194	1.03710	3.61715
O	0.96760	1.36219	3.83840
O	-1.15581	1.02304	4.50527
C	-0.79398	1.43505	5.83360
C	0.32345	-1.82258	-1.90023
C	1.18573	-0.96163	-2.57090
C	2.14872	-1.50262	-3.42260
C	2.25313	-2.87766	-3.59974
C	1.38245	-3.72479	-2.91448
C	0.41610	-3.20292	-2.06454
H	-2.06448	0.42592	-2.78936
H	-2.76252	3.12866	-2.72739
H	-2.99214	3.63065	-1.04091
H	-1.49549	4.04618	-1.88934
H	0.97141	1.41798	1.44971
H	0.35295	-1.58327	1.35468
H	1.63002	-0.78903	2.30620
H	1.72570	-0.80949	0.53637
H	-1.70721	1.36192	6.41648
H	-0.42999	2.46155	5.81943
H	-0.02928	0.77100	6.23458
H	1.11428	0.11019	-2.43365
H	2.82148	-0.83423	-3.94748
H	3.00493	-3.28754	-4.26307
H	1.45440	-4.79864	-3.04235
H	-0.26894	-3.84510	-1.52355

7‡

C	-1.27368	1.87420	-1.34475
C	-0.64710	0.76815	-1.86352
C	0.25389	0.34572	-0.86267
C	0.13698	1.22387	0.21278
O	-0.82591	2.15733	-0.12013
C	-2.31235	2.76473	-1.91005
O	1.10592	-0.68056	-0.88091
C	0.71444	1.27755	1.47657
O	-0.66549	0.31411	2.64882
C	1.90704	0.46349	1.83444
C	-0.64381	0.72577	3.85464
O	0.08337	1.58581	4.34638
O	-1.56859	0.08032	4.62208
C	-1.62051	0.46259	5.99693
C	1.06703	-1.51466	-2.00423
C	2.04658	-1.36308	-2.97145
C	2.03311	-2.21921	-4.07005
C	1.04994	-3.19865	-4.18382
C	0.07591	-3.33001	-3.19633
C	0.07916	-2.48333	-2.09177
H	-0.81972	0.33218	-2.83415
H	-2.59369	2.42076	-2.90338
H	-3.19293	2.76824	-1.26392
H	-1.93302	3.78706	-1.97435
H	0.54640	2.19066	2.03642
H	1.81037	-0.56450	1.49070
H	2.06301	0.49234	2.91077
H	2.77924	0.90923	1.34283
H	-2.40517	-0.14352	6.44451
H	-1.86419	1.52114	6.09492
H	-0.66768	0.26282	6.48895
H	2.79903	-0.59157	-2.85867
H	2.79272	-2.11756	-4.83577
H	1.04325	-3.86092	-5.04114
H	-0.68732	-4.09420	-3.28148
H	-0.66625	-2.56628	-1.30916

8

C	0.33540	-0.39409	-3.18552
C	0.23620	-1.56517	-2.50619
C	-0.45764	-1.24826	-1.29352
C	-0.73207	0.08132	-1.30961
O	-0.24994	0.60524	-2.47269
C	0.92415	-0.02343	-4.49668
O	-0.81573	-2.14637	-0.32556
C	0.07073	-2.38063	0.70503
C	-0.33455	-3.32886	1.64228
C	0.48945	-3.61439	2.72270
C	1.71279	-2.96042	2.87135
C	2.10192	-2.01677	1.92739
C	1.28567	-1.71610	0.83712
C	-1.39205	1.02654	-0.37406
O	-0.32675	1.86386	0.16531
C	-0.67781	3.07992	0.57298
O	0.39942	3.68914	1.04820
O	-1.78488	3.55398	0.51814
C	0.18932	5.02591	1.53197
C	-2.13177	0.34956	0.76480
H	0.60007	-2.53165	-2.81771
H	1.70673	0.72789	-4.36938
H	1.35691	-0.90725	-4.96348
H	0.16025	0.38830	-5.16009
H	-1.28884	-3.82525	1.51078
H	0.17357	-4.35114	3.45215
H	2.35299	-3.18492	3.71575
H	3.04974	-1.50156	2.03215
H	1.59383	-0.97644	0.10879
H	-2.06048	1.67908	-0.93943
H	-0.17344	5.66181	0.72544
H	1.16227	5.36365	1.87625
H	-0.52576	5.01641	2.35358
H	-1.43954	-0.22204	1.38516
H	-2.61872	1.10665	1.37960
H	-2.89146	-0.32453	0.36701

8‡

C	1.60947	0.91993	-2.17316
C	0.58281	1.52066	-1.48926
C	0.31277	0.66393	-0.39755
C	1.19966	-0.40086	-0.46659
O	1.98475	-0.22267	-1.58540
C	2.33625	1.31859	-3.40038
C	1.33953	-1.53123	0.33913
O	0.03661	-2.82060	-0.48551
C	-0.46033	-3.74259	0.24696
O	-0.03837	-3.69100	1.54029
O	-1.24280	-4.61099	-0.12143
C	-0.54468	-4.70382	2.40997
O	-0.61964	0.76489	0.55387
C	-1.34774	1.95793	0.60232
C	-0.73805	3.10838	1.08174
C	-1.48991	4.27735	1.15490
C	-2.82570	4.27874	0.75658
C	-3.41589	3.10931	0.28358
C	-2.67374	1.93296	0.20141
C	2.56664	-2.37079	0.27462
H	0.09726	2.44710	-1.75028
H	1.93285	2.25522	-3.78046
H	3.39916	1.44487	-3.18217
H	2.23458	0.54424	-4.16402
H	0.79623	-1.49575	1.27569
H	-0.11243	-4.49844	3.38680
H	-1.63252	-4.65576	2.46231
H	-0.23977	-5.69201	2.06433
H	0.30154	3.08197	1.38959
H	-1.03038	5.18535	1.52768
H	-3.40669	5.19133	0.81718
H	-4.45469	3.10805	-0.02560
H	-3.10731	1.00979	-0.16514
H	2.40912	-3.31726	0.78610
H	2.87479	-2.54088	-0.75589
H	3.36659	-1.82595	0.78780

9

C	-0.79964	0.75582	-2.43192
C	0.24976	-0.04492	-2.75671
C	0.95474	-0.28549	-1.52697
C	0.29072	0.38970	-0.54593
O	-0.78843	1.02592	-1.10820
C	-1.89415	1.35818	-3.23492
O	2.06367	-1.03484	-1.33845
C	2.62956	-1.59802	-2.51939
C	0.45912	0.55224	0.91499
O	-0.55478	-0.29341	1.55262
C	1.83204	0.15909	1.42752
C	-0.96412	0.07810	2.75948
O	-0.58887	1.04789	3.37113
O	-1.86576	-0.79743	3.18718
C	-2.41357	-0.53341	4.48874
H	0.48623	-0.41202	-3.74243
H	-1.78784	1.06078	-4.27734
H	-2.86832	1.02440	-2.87048
H	-1.86313	2.44847	-3.17444
H	2.91440	-0.81143	-3.22238
H	3.51329	-2.14513	-2.20059
H	1.92386	-2.28251	-2.99641
H	0.22321	1.58237	1.18841
H	2.02951	-0.89241	1.22086
H	1.88517	0.33487	2.50212
H	2.59544	0.76224	0.93375
H	-1.62096	-0.54111	5.23588
H	-3.11936	-1.33794	4.67264
H	-2.92180	0.42999	4.49123

9‡

C	-0.72096	0.86122	-2.48077
C	0.32257	0.02501	-2.78576
C	1.03599	-0.14970	-1.57459
C	0.38813	0.60570	-0.59772
O	-0.70068	1.21448	-1.19409
C	-1.80983	1.41520	-3.31818
O	2.12272	-0.86997	-1.34532
C	2.66353	-1.57742	-2.46962
C	0.58278	0.78191	0.77070
O	-0.66033	-0.56615	1.59136
C	1.84700	0.36502	1.43931
C	-1.09025	-0.20477	2.73852
O	-0.80450	0.81293	3.36324
O	-1.96164	-1.11523	3.25300
C	-2.50326	-0.80908	4.53915
H	0.53235	-0.39569	-3.75546
H	-1.71217	1.05268	-4.33967
H	-2.78004	1.11309	-2.91783
H	-1.76553	2.50658	-3.31609
H	2.94874	-0.87185	-3.25153
H	3.53925	-2.10136	-2.09846
H	1.93043	-2.29042	-2.85002
H	0.02719	1.59514	1.22441
H	2.15217	-0.63268	1.13025
H	1.72329	0.40723	2.51945
H	2.63345	1.07007	1.14892
H	-1.70914	-0.73217	5.28314
H	-3.16639	-1.63548	4.78470
H	-3.06485	0.12571	4.50899

10

C	-0.01260	-0.71797	-3.65067
C	-0.23516	-1.76005	-2.80568
C	0.36789	-1.38183	-1.56649
C	0.91942	-0.15152	-1.73336
O	0.67635	0.26187	-3.01099
C	-0.36334	-0.47148	-5.07180
O	0.41284	-2.15599	-0.44165
C	-0.08769	-1.63616	0.73873
C	0.43286	-2.17122	1.91294
C	-0.05086	-1.72530	3.13748
C	-1.04550	-0.75062	3.19061
C	-1.56017	-0.23092	2.00630
C	-1.08974	-0.67107	0.77112
C	1.63231	0.75127	-0.80947
O	0.69734	1.71347	-0.26162
C	0.74307	1.92162	1.05216
O	-0.24386	2.74594	1.37460
O	1.54526	1.45388	1.81993
C	-0.33222	3.08285	2.76842
H	-0.75353	-2.67874	-3.02983
H	-0.91895	-1.32311	-5.46196
H	-0.97904	0.42566	-5.16684
H	0.53794	-0.33235	-5.67307
H	1.20988	-2.92390	1.85101
H	0.35717	-2.13821	4.05266
H	-1.41619	-0.39977	4.14636
H	-2.33781	0.52423	2.03587
H	-1.49307	-0.26557	-0.14889
H	2.41076	1.31241	-1.32702
H	2.07431	0.17663	0.00345
H	0.57497	3.59555	3.08621
H	-1.19223	3.74080	2.85189
H	-0.48039	2.17962	3.35959

$10^{\ddagger}$

C	1.47983	0.35577	-2.57038
C	0.81681	0.97295	-1.53791
C	1.10465	0.19810	-0.39388
C	1.92782	-0.85388	-0.79218
O	2.14278	-0.72517	-2.14981
C	1.58373	0.69585	-4.00725
O	2.43909	-1.94137	-0.10449
O	1.23328	-3.51758	-0.39017
C	0.07453	-3.45419	0.15120
O	-0.07210	-2.39408	0.98589
O	-0.84258	-4.24706	-0.02874
C	-1.33403	-2.26794	1.64004
O	0.76224	0.39889	0.87731
C	-0.31866	1.23260	1.15494
O	-0.13678	2.20404	2.12674
C	-1.21684	3.01039	2.47604
O	-2.45151	2.83897	1.85569
O	-2.61160	1.85144	0.88568
C	-1.54343	1.03388	0.53093
H	0.21845	1.86650	-1.60994
H	2.62741	0.88021	-4.27172
H	1.22041	-0.13608	-4.61462
H	0.99428	1.58518	-4.22112
H	3.24470	-2.50959	-0.54934
H	2.35745	-1.93365	0.97336
H	-1.25744	-1.37443	2.25657
H	-2.13598	-2.15026	0.91025
H	-1.53244	-3.14050	2.26319
H	0.83383	2.31759	2.59420
H	-1.08863	3.77454	3.23336
H	-3.28846	3.47003	2.12928
H	-3.57317	1.70785	0.40742
H	-1.65766	0.25101	-0.21055

11

C	0.19022	2.43507	-1.73503
C	-0.90683	3.03060	-1.19952
C	-1.63723	1.99970	-0.51581
C	-0.92917	0.85707	-0.68616
O	0.18555	1.10827	-1.43024
C	1.33197	2.93250	-2.54445
C	-1.14436	-0.53902	-0.24425
O	-0.16014	-0.84466	0.76171
C	-0.17271	-2.11663	1.21629
N	0.78527	-2.32161	2.13362
O	-0.96796	-2.95781	0.83475
C	0.97128	-3.62710	2.74312
H	-1.16205	4.07533	-1.28316
H	-2.56325	2.09407	0.03007
H	2.27802	2.76700	-2.02376
H	1.21204	4.00059	-2.72210
H	1.37973	2.41913	-3.50758
H	-1.03062	-1.23859	-1.07450
H	-2.14548	-0.63976	0.17614
H	1.41244	-1.56292	2.35350
H	1.24132	-4.37464	1.99465
H	1.77284	-3.54908	3.47404
H	0.05911	-3.94754	3.24866

$11^{‡}$

C	-0.02706	2.44582	-2.01952
C	-1.01645	3.02621	-1.23772
C	-1.63549	1.98099	-0.55633
C	-1.00399	0.80321	-0.95547
O	-0.01155	1.12771	-1.85683
C	0.95107	3.03215	-2.95932
C	-1.18263	-0.50671	-0.58285
O	0.19826	-0.80548	1.12696
C	0.13252	-2.02800	1.51603
N	0.82658	-2.30614	2.68149
O	-0.50838	-2.93569	0.95551
C	1.09129	-3.67950	3.07307
H	-1.23667	4.08066	-1.19155
H	-2.45140	2.03296	0.14931
H	1.96546	2.76656	-2.65352
H	0.84572	4.11499	-2.97578
H	0.78422	2.63386	-3.96292
H	-0.67831	-1.30598	-1.10682
H	-2.02431	-0.75767	0.04676
H	1.51008	-1.61279	2.94477
H	1.69420	-4.21847	2.33396
H	1.62409	-3.67055	4.02373
H	0.15277	-4.21816	3.20702

12

C	-1.21756	2.86944	-0.44039
C	-1.24933	2.33254	0.80632
C	-1.30464	0.91361	0.60736
C	-1.30383	0.68324	-0.72782
O	-1.25861	1.88296	-1.37663
C	-1.15927	4.26519	-0.94209
C	-1.34372	-0.55612	-1.52812
O	-0.02929	-0.77610	-2.07539
C	0.09222	-1.86837	-2.86155
N	1.33756	-1.98976	-3.34687
O	-0.82737	-2.63419	-3.09231
C	1.70563	-3.11186	-4.19294
O	-1.41779	-0.05104	1.56878
C	-0.36406	-0.21228	2.44577
C	0.91534	0.27044	2.19076
C	1.92309	0.03195	3.12399
C	1.66081	-0.68067	4.28927
C	0.37302	-1.16200	4.52413
C	-0.64329	-0.92931	3.60655
H	-1.23187	2.86741	1.74302
H	-1.13412	4.95351	-0.09835
H	-2.03351	4.49145	-1.55665
H	-0.26530	4.41926	-1.55058
H	-1.62105	-1.39320	-0.88623
H	-2.06135	-0.47571	-2.34650
H	2.03144	-1.31336	-3.06694
H	1.60601	-4.05792	-3.65705
H	2.74191	-2.98163	-4.49621
H	1.07571	-3.14247	-5.08314
H	1.12634	0.81965	1.28138
H	2.92091	0.40764	2.92911
H	2.45042	-0.86042	5.00870
H	0.15605	-1.71901	5.42818
H	-1.65051	-1.29287	3.77244

12‡

C	-1.39628	2.49873	-0.22226
C	-0.82062	1.88773	0.86833
C	-0.71994	0.52812	0.51844
C	-1.25777	0.37567	-0.76376
O	-1.65619	1.62559	-1.19668
C	-1.76015	3.91177	-0.46540
C	-1.36161	-0.72863	-1.57737
O	0.40537	-0.78704	-2.68640
C	0.45766	-1.86005	-3.40390
N	1.63902	-2.02774	-4.09567
O	-0.43536	-2.71824	-3.48472
C	1.74802	-3.02899	-5.14196
O	-0.20373	-0.49425	1.19269
C	0.18139	-0.27147	2.51950
C	1.52784	-0.37410	2.82703
C	1.92103	-0.20335	4.15220
C	0.97362	0.06687	5.13601
C	-0.37530	0.16299	4.79979
C	-0.78368	-0.01076	3.48096
H	-0.51666	2.37221	1.78191
H	-1.47977	4.52004	0.39207
H	-2.83657	3.99363	-0.63309
H	-1.24807	4.27899	-1.35752
H	-1.17756	-1.70256	-1.14614
H	-1.96377	-0.68263	-2.47389
H	2.21961	-1.20610	-4.17116
H	1.55230	-4.02037	-4.73303
H	2.76419	-3.00989	-5.53371
H	1.04766	-2.85100	-5.96428
H	2.24359	-0.58423	2.04145
H	2.97002	-0.28047	4.41188
H	1.28500	0.19975	6.16511
H	-1.11463	0.36785	5.56474
H	-1.82866	0.05192	3.19883

13

C	2.61427	1.25187	-0.70164
C	2.02021	1.38659	0.51102
C	1.29308	0.16590	0.71710
C	1.49297	-0.62137	-0.36783
O	2.31263	0.03868	-1.23843
C	3.48965	2.13956	-1.50791
C	1.05110	-1.99670	-0.72151
O	0.14848	-1.95947	-1.85131
C	-1.13753	-1.62629	-1.59561
N	-1.84957	-1.52839	-2.72989
O	-1.58415	-1.45118	-0.47590
C	-3.26837	-1.21803	-2.69958
C	2.19981	-2.90148	-1.13208
O	0.59855	-0.20661	1.83306
C	-0.43785	0.59791	2.25800
C	-0.86905	0.39195	3.56633
C	-1.92835	1.14222	4.06182
C	-2.55380	2.09668	3.26037
C	-2.11291	2.28792	1.95477
C	-1.05488	1.53972	1.44100
H	2.08105	2.23824	1.17050
H	3.67054	3.06484	-0.96253
H	3.01976	2.38030	-2.46424
H	4.44773	1.65593	-1.71079
H	0.51776	-2.40503	0.13727
H	-1.38206	-1.69391	-3.60808
H	-3.44307	-0.23816	-2.24935
H	-3.63533	-1.20876	-3.72385
H	-3.81747	-1.97081	-2.12999
H	2.71029	-2.49522	-2.00675
H	2.91456	-2.97788	-0.31145
H	1.82130	-3.89646	-1.36795
H	-0.36958	-0.35266	4.17499
H	-2.26371	0.98140	5.07990
H	-3.37693	2.68296	3.65048
H	-2.59503	3.02259	1.32020
H	-0.72413	1.68317	0.41985

13‡

C	2.73567	1.17754	-0.13507
C	1.74531	1.39616	0.79086
C	0.90390	0.26563	0.70612
C	1.43130	-0.58480	-0.25944
O	2.56374	0.01354	-0.77079
C	3.91546	1.98709	-0.51481
C	0.96488	-1.79447	-0.75917
O	-0.36735	-1.20461	-2.23943
C	-1.34882	-2.03398	-2.36281
N	-2.33262	-1.63070	-3.24195
O	-1.46899	-3.10820	-1.75049
C	-3.35104	-2.56271	-3.69258
C	1.82125	-2.67820	-1.59304
O	-0.20106	-0.03174	1.39166
C	-0.70900	0.94639	2.25164
C	-0.63520	0.71688	3.61575
C	-1.18177	1.66250	4.48013
C	-1.78370	2.81124	3.97340
C	-1.84609	3.01808	2.59672
C	-1.30883	2.07927	1.72130
H	1.65268	2.25595	1.43438
H	3.93421	2.90764	0.06529
H	3.87600	2.22919	-1.57911
H	4.83151	1.42231	-0.32749
H	0.15517	-2.25100	-0.20288
H	-2.07596	-0.88015	-3.86539
H	-3.91857	-2.93825	-2.84094
H	-4.03299	-2.03406	-4.35739
H	-2.92664	-3.41811	-4.22793
H	2.40071	-2.10458	-2.31528
H	2.51940	-3.19326	-0.92294
H	1.21075	-3.42275	-2.09860
H	-0.16084	-0.18508	3.98349
H	-1.13437	1.49844	5.55004
H	-2.20690	3.54392	4.64999
H	-2.31869	3.90869	2.20009
H	-1.35252	2.21617	0.64667

14

C	-0.09327	0.67671	-2.70568
C	0.35665	-0.60123	-2.65981
C	0.37471	-0.98531	-1.27140
C	-0.06826	0.09305	-0.58323
O	-0.35580	1.11160	-1.43646
C	-0.34094	1.64336	-3.80563
C	-0.29241	0.37849	0.86688
C	0.53534	1.55315	1.36916
O	0.08560	-0.82894	1.54903
C	-0.46286	-1.05883	2.75273
O	-1.25793	-0.31137	3.26764
C	0.04232	-2.34026	3.34375
H	0.64359	-1.19986	-3.51025
H	0.67407	-1.93071	-0.84883
H	-0.09063	1.17791	-4.75847
H	-1.38990	1.94801	-3.82951
H	0.27084	2.54014	-3.68200
H	-1.35453	0.56285	1.04741
H	0.33924	1.72573	2.42777
H	0.26798	2.45236	0.81230
H	1.59745	1.34801	1.22210
H	1.12482	-2.27762	3.46662
H	-0.43502	-2.51259	4.30461
H	-0.17108	-3.16466	2.66126

14‡

C	-0.32657	0.63274	-2.61694
C	1.04954	0.54377	-2.71764
C	1.54696	0.66261	-1.41463
C	0.45128	0.82918	-0.57997
O	-0.69165	0.80251	-1.34734
C	-1.39828	0.57812	-3.63542
C	0.31859	0.96941	0.79489
C	1.47923	1.19889	1.68385
O	-0.08829	-1.13967	1.38667
C	-0.75776	-1.19736	2.47038
O	-1.18260	-0.21645	3.10192
C	-1.01026	-2.60590	2.99691
H	1.60300	0.40838	-3.63283
H	2.57882	0.63576	-1.09785
H	-0.96292	0.42525	-4.62085
H	-2.08625	-0.24002	-3.41094
H	-1.96666	1.51099	-3.63044
H	-0.66718	1.20324	1.17890
H	1.24691	0.85109	2.68843
H	1.64428	2.28245	1.73167
H	2.38727	0.72557	1.31357
H	-0.05942	-3.03665	3.32075
H	-1.70264	-2.58650	3.83754
H	-1.40540	-3.23742	2.19938

15

C	-1.54132	1.98158	-1.30994
C	-1.54872	0.67659	-1.68188
C	-0.82696	-0.01857	-0.65612
C	-0.42433	0.89738	0.26094
O	-0.86586	2.12566	-0.13822
C	-2.10847	3.21472	-1.91087
C	0.36344	0.84317	1.51857
O	-0.63491	-1.37081	-0.58354
C	0.31725	-1.93804	-1.40360
C	1.19732	-1.19375	-2.18263
C	2.13639	-1.86507	-2.96498
C	2.20075	-3.25398	-2.96740
C	1.31358	-3.98258	-2.17494
C	0.37020	-3.33026	-1.39228
C	1.09272	-0.47331	1.72400
O	-0.57632	1.06062	2.60749
C	-0.09773	1.60113	3.73764
O	1.05951	1.91558	3.88095
C	-1.17429	1.75117	4.77061
H	-2.00457	0.25402	-2.56360
H	-1.31882	3.93854	-2.12475
H	-2.61838	2.96462	-2.84025
H	-2.82412	3.68155	-1.23031
H	1.06710	1.67804	1.52675
H	1.15690	-0.11160	-2.18153
H	2.82226	-1.28782	-3.57427
H	2.93443	-3.76582	-3.57815
H	1.35483	-5.06562	-2.16635
H	-0.32735	-3.87912	-0.77062
H	1.76901	-0.65941	0.88712
H	1.67789	-0.42287	2.64226
H	0.38232	-1.29731	1.79301
H	-1.54134	0.76096	5.04715
H	-0.77352	2.25512	5.64632
H	-2.00889	2.31545	4.35341

15‡

C	-1.15262	1.84250	-1.32747
C	-0.58752	0.64001	-1.67534
C	0.24185	0.28907	-0.58875
C	0.14923	1.30336	0.36307
O	-0.73159	2.24830	-0.12772
C	-2.10479	2.72041	-2.04441
C	0.69211	1.48797	1.62889
O	1.00607	-0.79388	-0.43318
C	1.02249	-1.70805	-1.49368
C	1.94937	-1.53449	-2.50939
C	1.98405	-2.46670	-3.54289
C	1.10142	-3.54463	-3.54505
C	0.17999	-3.69625	-2.51154
C	0.13444	-2.77144	-1.47132
C	1.80790	0.64900	2.14304
O	-0.81519	0.75727	2.88547
C	-0.85164	1.35157	4.02013
O	-0.09565	2.26843	4.36531
C	-1.91122	0.82970	4.97969
H	-0.75590	0.09585	-2.59060
H	-1.65054	3.69820	-2.22002
H	-2.37605	2.27155	-2.99782
H	-3.00440	2.86613	-1.44230
H	0.56590	2.47381	2.06061
H	2.62479	-0.68717	-2.48330
H	2.70308	-2.34939	-4.34472
H	1.13293	-4.26718	-4.35171
H	-0.50598	-4.53480	-2.51217
H	-0.57203	-2.86631	-0.65503
H	2.72742	0.95803	1.63261
H	1.92875	0.81655	3.21106
H	1.64546	-0.40773	1.94042
H	-1.56975	-0.12500	5.38651
H	-2.06269	1.53117	5.79822
H	-2.84971	0.65416	4.45337

16

C	-1.87952	1.57207	-2.79122
C	-1.77944	0.21806	-2.85554
C	-1.40812	-0.20156	-1.53995
C	-1.31488	0.91015	-0.76490
O	-1.59488	2.00093	-1.53356
C	-2.22964	2.61304	-3.78981
C	-0.93022	1.10646	0.65293
O	0.46646	1.53366	0.65679
C	-1.76001	2.14898	1.37982
C	1.37481	1.05678	1.51042
S	0.79719	-0.04167	2.78682
O	2.52734	1.38641	1.40612
C	2.39865	-0.42343	3.53755
O	-1.24096	-1.50030	-1.14997
C	-0.04525	-1.87237	-0.56146
C	1.15218	-1.20464	-0.79741
C	2.31366	-1.66860	-0.18320
C	2.28308	-2.78589	0.64562
C	1.07576	-3.44856	0.86000
C	-0.09250	-2.99540	0.25880
H	-1.94950	-0.40615	-3.71832
H	-2.42080	2.14210	-4.75311
H	-1.41284	3.32931	-3.90272
H	-3.12334	3.15988	-3.48075
H	-1.00801	0.13116	1.13775
H	-2.80793	1.84545	1.38049
H	-1.41851	2.24430	2.41142
H	-1.66993	3.11463	0.88082
H	2.18417	-1.12775	4.34002
H	3.04697	-0.88565	2.79609
H	2.85057	0.48012	3.93952
H	1.17930	-0.33420	-1.44193
H	3.24745	-1.14677	-0.35930
H	3.19116	-3.13721	1.12096
H	1.03934	-4.32033	1.50303
H	-1.04181	-3.49302	0.41816

16‡

C	1.59546	2.23514	-1.11917
C	0.77239	2.15489	-0.02697
C	0.44477	0.78224	0.09158
C	1.10098	0.10600	-0.91962
O	1.79726	1.02729	-1.66647
C	2.26881	3.38762	-1.76122
C	1.10228	-1.25546	-1.26331
O	-0.40443	-1.37808	-2.47282
C	2.17719	-1.81411	-2.13205
C	-1.20045	-2.38294	-2.53163
S	-0.71290	-3.82299	-1.54003
O	-2.22162	-2.42980	-3.19563
C	-2.09474	-4.93473	-1.89900
O	-0.37599	0.16852	0.95391
C	-0.73625	0.85643	2.11242
C	-2.08795	1.04621	2.35300
C	-2.47406	1.68259	3.53036
C	-1.51458	2.11926	4.44046
C	-0.16132	1.91486	4.17773
C	0.23859	1.27493	3.00854
H	0.45109	2.97633	0.59293
H	2.01398	4.30396	-1.23225
H	1.95510	3.47336	-2.80373
H	3.35196	3.24903	-1.74121
H	0.68751	-1.89529	-0.49068
H	3.09185	-1.86807	-1.53193
H	1.92393	-2.81803	-2.46684
H	2.36336	-1.16691	-2.98825
H	-1.89745	-5.85129	-1.34426
H	-3.02886	-4.49233	-1.56308
H	-2.13870	-5.14762	-2.96398
H	-2.81455	0.69989	1.62758
H	-3.52730	1.83829	3.73204
H	-1.81981	2.61520	5.35418
H	0.58800	2.24687	4.88678
H	1.28644	1.09874	2.79263

17

C	-0.59430	2.77314	0.93351
C	-0.25298	2.39455	2.19219
C	0.39725	1.12746	2.04562
C	0.41285	0.82101	0.72494
O	-0.19370	1.82846	0.03992
C	-1.28775	3.96442	0.38396
C	0.93507	-0.33480	-0.04472
Br	1.09549	0.07501	3.43264
O	-0.22457	-1.12210	-0.43852
C	1.71783	0.07079	-1.28178
C	-0.00823	-2.41536	-0.66184
O	-1.14943	-2.97189	-1.04005
O	1.04552	-2.98703	-0.53684
C	-1.08697	-4.38089	-1.31627
H	-0.43427	2.93820	3.10539
H	-1.54881	4.63950	1.19783
H	-2.20104	3.67096	-0.13832
H	-0.64411	4.49353	-0.32216
H	1.54490	-0.94268	0.62451
H	2.58354	0.66531	-0.98542
H	1.09018	0.66507	-1.94715
H	2.06610	-0.81753	-1.80924
H	-0.38789	-4.57025	-2.12987
H	-0.77962	-4.92256	-0.42267
H	-2.09507	-4.66230	-1.60567

17‡

C	-0.32113	2.89990	1.01317
C	-0.42200	2.19190	2.19606
C	0.14701	0.94413	1.92948
C	0.57803	0.94221	0.60439
O	0.26360	2.16659	0.06568
C	-0.72911	4.27432	0.65495
C	1.16171	-0.04499	-0.16679
Br	0.28830	-0.49079	3.09788
O	-0.60082	-1.20064	-0.79766
C	1.70395	0.20638	-1.51929
C	-0.33517	-2.43785	-0.77595
O	-1.42748	-3.20699	-1.08467
O	0.74255	-2.97991	-0.52039
C	-1.22525	-4.61890	-1.07777
H	-0.85358	2.54315	3.11924
H	-1.19891	4.75511	1.51025
H	-1.43059	4.24803	-0.18203
H	0.14644	4.85096	0.34723
H	1.47828	-0.94017	0.35593
H	2.70907	0.62878	-1.38948
H	1.10067	0.92397	-2.07303
H	1.79717	-0.72886	-2.06745
H	-0.46567	-4.90701	-1.80523
H	-0.92359	-4.96187	-0.08741
H	-2.18348	-5.05746	-1.34709

18

C	-3.08129	0.40048	0.47619
C	-2.49027	0.29836	1.68702
C	-1.08033	0.11851	1.43083
C	-0.93005	0.12861	0.07474
O	-2.12821	0.29627	-0.50506
C	-4.48144	0.59004	0.02621
C	-0.06788	-0.02310	2.41733
N	0.70963	-0.12859	3.26022
C	0.24239	0.01526	-0.84591
O	1.34049	-0.34705	0.00246
C	0.03690	-1.02699	-1.93364
C	2.55638	0.03290	-0.39717
O	3.43342	-0.38993	0.49626
O	2.80328	0.65352	-1.39823
C	4.80581	-0.06272	0.21615
H	-2.97267	0.33858	2.65025
H	-4.80242	-0.24573	-0.59918
H	-4.57868	1.51054	-0.55321
H	-5.13346	0.65033	0.89651
H	0.44583	0.99408	-1.28815
H	0.92369	-1.07126	-2.56643
H	-0.81959	-0.75103	-2.54954
H	-0.14336	-2.00543	-1.48535
H	5.10806	-0.50852	-0.73053
H	5.37512	-0.48591	1.03804
H	4.92865	1.01876	0.18017

18‡

C	-2.66757	0.88437	0.38848
C	-2.99996	-0.28036	1.07167
C	-2.04229	-1.22020	0.69904
C	-1.16383	-0.59985	-0.20221
O	-1.59067	0.69249	-0.35648
C	-3.30062	2.21662	0.36313
C	-1.98123	-2.57358	1.14098
N	-1.95226	-3.66196	1.50774
C	-0.02782	-0.99291	-0.87549
O	1.64383	-0.14131	0.59063
C	0.50400	-2.36653	-0.89873
C	2.51728	0.41221	-0.12534
O	3.49390	1.04000	0.61620
O	2.58719	0.45181	-1.36034
C	4.52113	1.70028	-0.11724
H	-3.83170	-0.41234	1.74495
H	-3.63422	2.44313	-0.65257
H	-2.57334	2.97534	0.66022
H	-4.15165	2.23475	1.04011
H	0.40260	-0.26705	-1.55839
H	1.55847	-2.34448	-1.16609
H	-0.03510	-2.91005	-1.68747
H	0.35963	-2.89650	0.04093
H	5.07405	0.99268	-0.73654
H	5.18480	2.13955	0.62524
H	4.10536	2.48390	-0.75243

19

C	0.68191	-3.27926	-0.07084
C	1.11850	-3.18471	1.21041
C	0.92438	-1.81755	1.61473
C	0.37729	-1.18952	0.54728
O	0.22189	-2.06246	-0.48478
C	0.60889	-4.39027	-1.05372
C	-0.02949	0.21850	0.26759
C	1.10418	1.07666	-0.30232
O	-0.47326	0.77485	1.52386
C	-1.26299	1.83918	1.42229
O	-1.57849	2.25452	2.63431
O	-1.63547	2.34256	0.38720
C	-2.43436	3.40997	2.69209
C	1.36616	0.81369	-1.78650
C	0.14019	1.07005	-2.66428
O	-0.46356	2.33461	-2.41155
H	1.52703	-3.99152	1.79861
H	1.15543	-1.36941	2.56827
H	0.99884	-5.30061	-0.59962
H	1.19944	-4.16219	-1.94418
H	-0.42276	-4.56820	-1.36598
H	-0.88616	0.19832	-0.40941
H	0.84135	2.12936	-0.17095
H	2.00717	0.89235	0.28395
H	-2.58417	3.60220	3.75004
H	-3.38254	3.19347	2.20233
H	-1.94597	4.25686	2.21227
H	1.69655	-0.21801	-1.94416
H	2.18159	1.46710	-2.10719
H	0.43829	1.07622	-3.71350
H	-0.59893	0.27053	-2.54232
H	-0.89094	2.31272	-1.54395

19‡

C	1.11952	-3.36249	0.22621
C	-0.20211	-3.68533	0.45752
C	-0.92694	-2.49275	0.31426
C	-0.01296	-1.50473	-0.00577
O	1.24254	-2.06189	-0.05146
C	2.35508	-4.17709	0.23157
C	-0.17839	-0.13861	-0.24289
C	0.85880	0.67956	-0.93154
O	-0.06107	0.68989	1.67338
C	-0.65686	1.80899	1.71312
O	-0.67304	2.34180	2.96202
O	-1.19115	2.41634	0.77755
C	-1.31321	3.61210	3.10239
C	0.49825	0.85333	-2.42184
C	-0.80708	1.61652	-2.64103
O	-0.82377	2.86997	-1.97538
H	-0.57444	-4.66839	0.69675
H	-1.99082	-2.34048	0.42118
H	2.11346	-5.21048	0.47238
H	3.05741	-3.78720	0.97181
H	2.83613	-4.13622	-0.74827
H	-1.20993	0.19037	-0.29389
H	0.90178	1.66607	-0.47035
H	1.83735	0.21103	-0.83180
H	-1.22296	3.87252	4.15441
H	-2.36437	3.54618	2.82108
H	-0.81716	4.36224	2.48615
H	0.42961	-0.12064	-2.91554
H	1.31946	1.40246	-2.88926
H	-0.92370	1.82078	-3.70673
H	-1.66769	1.01217	-2.33162
H	-0.95174	2.71396	-1.02443

20

C	1.71579	-1.95509	-2.22055
C	2.60022	-0.94277	-2.41839
C	2.26166	0.08500	-1.47510
C	1.19562	-0.37735	-0.77647
O	0.85354	-1.62032	-1.22343
C	1.52190	-3.28277	-2.85744
C	0.38909	0.16580	0.34637
C	0.51436	1.67397	0.52061
C	-0.02767	2.48714	-0.66062
C	-1.40783	2.04627	-1.11574
O	0.87484	-0.49177	1.55532
C	0.00234	-0.63707	2.54762
O	0.61914	-1.22522	3.56381
O	-1.15473	-0.29872	2.53319
C	-0.19239	-1.45807	4.72655
O	-2.27972	2.03483	-0.00086
C	-3.55252	1.51528	-0.32769
H	3.39373	-0.93098	-3.14896
H	2.74680	1.03966	-1.34031
H	2.26290	-3.41897	-3.64427
H	1.63555	-4.08565	-2.12526
H	0.52438	-3.36079	-3.29571
H	-0.65576	-0.12628	0.22229
H	-0.03897	1.93790	1.42433
H	1.56514	1.92260	0.69394
H	0.64622	2.41656	-1.51771
H	-0.06398	3.53925	-0.36614
H	-1.79251	2.72866	-1.88450
H	-1.36911	1.04086	-1.56029
H	0.46483	-1.93961	5.44444
H	-1.02771	-2.11018	4.47463
H	-0.56070	-0.51117	5.11912
H	-4.03013	2.11320	-1.11262
H	-4.16429	1.54805	0.57296
H	-3.47003	0.47775	-0.67312

$20^{‡}$

C	1.86727	-1.98106	-2.28106
C	2.76231	-0.94991	-2.49282
C	2.34418	0.10729	-1.67400
C	1.20740	-0.32545	-1.01020
O	0.93631	-1.61753	-1.39926
C	1.77910	-3.34684	-2.84341
C	0.37391	0.27311	-0.07056
C	0.46375	1.72470	0.24164
C	-0.27901	2.55802	-0.82544
C	-1.69631	2.07431	-1.07664
O	1.17832	-0.46781	1.77934
C	0.25225	-0.67016	2.62415
O	0.74263	-1.11876	3.81982
O	-0.95945	-0.51079	2.47764
C	-0.22293	-1.38649	4.83580
O	-2.37197	1.97947	0.16191
C	-3.67074	1.44023	0.01787
H	3.60721	-0.98125	-3.16172
H	2.79940	1.08087	-1.56671
H	2.56718	-3.49469	-3.57900
H	1.88526	-4.08650	-2.04640
H	0.80614	-3.49502	-3.31674
H	-0.55209	-0.23891	0.17016
H	-0.00105	1.88858	1.21308
H	1.50674	2.04042	0.29144
H	0.26967	2.52877	-1.77023
H	-0.29720	3.59507	-0.48280
H	-2.22251	2.76954	-1.74263
H	-1.69023	1.08886	-1.56525
H	0.34550	-1.70046	5.70877
H	-0.90070	-2.18299	4.52520
H	-0.79956	-0.49073	5.06900
H	-4.29343	2.08417	-0.61388
H	-4.11081	1.37201	1.01185
H	-3.62654	0.43995	-0.42893

21

C	-0.04411	3.48625	0.42674
C	0.27772	3.04906	1.67199
C	0.42937	1.62390	1.57842
C	0.18685	1.30140	0.28438
O	-0.10598	2.42817	-0.42629
C	-0.33017	4.82691	-0.14496
C	0.19602	0.02522	-0.47743
C	0.17070	-1.21061	0.41011
O	1.42126	0.03794	-1.26914
C	1.41041	-0.68113	-2.38694
O	2.59920	-0.57534	-2.96520
O	0.48016	-1.32053	-2.81091
C	2.75236	-1.29809	-4.19764
C	-1.18281	-1.42745	1.08504
C	-1.20598	-2.69861	1.93184
C	-2.55834	-2.91962	2.60528
H	0.39064	3.66698	2.54890
H	0.67836	0.93577	2.37165
H	0.37894	5.06987	-0.93967
H	-0.24980	5.57953	0.63852
H	-1.33778	4.86327	-0.56548
H	-0.64254	0.01201	-1.17773
H	0.40100	-2.07542	-0.21870
H	0.96601	-1.13168	1.15852
H	2.60706	-2.36371	-4.02503
H	3.76875	-1.09894	-4.52385
H	2.03598	-0.93611	-4.93398
H	-1.96301	-1.48849	0.31708
H	-1.42877	-0.56847	1.71772
H	-0.96274	-3.55763	1.29755
H	-0.41935	-2.63736	2.69153
H	-2.56151	-3.83146	3.20609
H	-2.80492	-2.08138	3.26256
H	-3.35298	-3.00426	1.85904

21‡

C	-0.12394	3.61232	0.44063
C	0.32004	3.21577	1.68693
C	0.42450	1.81859	1.64078
C	0.02970	1.42983	0.37141
O	-0.29980	2.55362	-0.35065
C	-0.42463	4.94621	-0.12548
C	-0.05434	0.18884	-0.25585
C	0.05437	-1.07766	0.50926
O	1.82388	0.10664	-1.29480
C	1.73854	-0.63861	-2.31916
O	2.92945	-0.72510	-2.98722
O	0.75355	-1.24773	-2.73584
C	2.93813	-1.54372	-4.15578
C	-1.32110	-1.43666	1.10792
C	-1.28239	-2.79308	1.80961
C	-2.63222	-3.15466	2.42428
H	0.53560	3.87312	2.51385
H	0.74316	1.15326	2.42964
H	0.19955	5.13061	-1.00265
H	-0.23459	5.71456	0.62133
H	-1.47067	4.99410	-0.43644
H	-0.55058	0.15222	-1.21986
H	0.36667	-1.86734	-0.17558
H	0.79472	-0.98733	1.30682
H	2.68759	-2.57582	-3.90743
H	3.95163	-1.49107	-4.54806
H	2.23123	-1.16853	-4.89677
H	-2.07441	-1.45614	0.31303
H	-1.62237	-0.66075	1.81880
H	-0.98298	-3.56052	1.08889
H	-0.51215	-2.77183	2.58736
H	-2.59374	-4.12609	2.92122
H	-2.93392	-2.40848	3.16394
H	-3.40848	-3.19860	1.65587

22

C	-0.96136	3.35936	-0.18406
C	0.35557	3.66285	-0.44729
C	1.02498	2.43476	-0.71507
C	0.09347	1.42524	-0.60161
N	-1.10698	2.00483	-0.28279
C	0.21671	-0.05179	-0.76286
C	1.54788	-0.48462	-1.34570
O	0.06297	-0.62435	0.57429
C	-0.36624	-1.87924	0.63774
O	-0.65705	-2.58015	-0.29973
O	-0.42949	-2.23838	1.91379
C	-0.88788	-3.57826	2.15578
H	-1.79968	3.99111	0.06276
H	0.78761	4.65155	-0.45134
H	2.06695	2.30518	-0.96558
H	-1.97015	1.50107	-0.13297
H	-0.61055	-0.43308	-1.36502
H	2.36908	-0.12416	-0.72362
H	1.59334	-1.57227	-1.40346
H	1.65990	-0.07681	-2.35133
H	-0.21292	-4.29359	1.68757
H	-0.87931	-3.69528	3.23536
H	-1.89685	-3.70396	1.76512

22‡

C	-0.97391	3.42178	-0.46033
C	0.39800	3.69346	-0.51483
C	1.04555	2.48196	-0.74663
C	0.06170	1.48309	-0.84036
N	-1.15986	2.11123	-0.65296
C	0.16823	0.10286	-1.04005
C	1.43581	-0.53133	-1.47806
O	0.12860	-0.63432	0.92911
C	-0.29507	-1.83203	0.97584
O	-0.67025	-2.54076	0.04320
O	-0.30301	-2.31913	2.25317
C	-0.76656	-3.65952	2.41236
H	-1.80864	4.08725	-0.30158
H	0.84801	4.66635	-0.39780
H	2.10843	2.31979	-0.84399
H	-2.05722	1.64263	-0.65912
H	-0.74844	-0.44242	-1.23767
H	2.30764	-0.05292	-1.03395
H	1.42421	-1.59430	-1.24563
H	1.49583	-0.42193	-2.56743
H	-0.13821	-4.35405	1.85336
H	-0.70097	-3.87238	3.47739
H	-1.79986	-3.75532	2.07598

23

C	-0.15487	-0.49536	-3.39480
C	0.61572	0.64392	-3.32852
C	0.87417	0.89307	-1.95295
C	0.24283	-0.10050	-1.23375
N	-0.37992	-0.94121	-2.11987
C	-1.17576	-2.11120	-1.77382
C	0.23341	-0.37327	0.23763
O	0.20551	0.92268	0.88715
C	-0.27104	0.95165	2.12636
O	-0.18622	2.19468	2.57967
O	-0.71401	0.01199	2.73846
C	-0.67737	2.39863	3.91434
C	1.46078	-1.14386	0.70358
H	-0.56839	-1.02763	-4.23749
H	0.95250	1.22877	-4.17061
H	1.44832	1.70327	-1.52935
H	-0.58315	-2.82091	-1.19478
H	-2.05517	-1.81874	-1.19792
H	-1.49803	-2.58880	-2.69686
H	-0.67691	-0.90694	0.51709
H	-0.10597	1.79476	4.61815
H	-0.53545	3.45630	4.11554
H	-1.73350	2.13727	3.96687
H	2.36247	-0.57908	0.45845
H	1.41950	-1.32362	1.77905
H	1.50056	-2.10587	0.18836

23‡

C	-0.43600	-0.52852	-3.20899
C	0.88151	-0.17707	-3.53210
C	1.60480	-0.18701	-2.34500
C	0.72377	-0.56239	-1.31427
N	-0.52497	-0.75826	-1.89414
C	-1.73738	-1.11718	-1.16771
C	0.93908	-0.71205	0.05913
O	0.22771	1.08855	0.82497
C	-0.36483	0.93297	1.94012
O	-0.88217	2.10763	2.40622
O	-0.50527	-0.10508	2.58424
C	-1.57268	2.04000	3.65364
C	2.30292	-0.67768	0.64624
H	-1.30422	-0.62529	-3.84443
H	1.24244	0.05339	-4.52172
H	2.65319	0.03683	-2.21644
H	-1.62412	-2.10406	-0.71884
H	-1.92948	-0.37805	-0.38937
H	-2.56541	-1.13127	-1.87254
H	0.18013	-1.22631	0.63798
H	-0.90691	1.69689	4.44624
H	-1.90889	3.05337	3.86180
H	-2.42955	1.36901	3.58461
H	2.94118	0.05515	0.15439
H	2.24851	-0.47264	1.71376
H	2.74667	-1.67091	0.51221

24

C	-0.58610	0.00000	3.36365
C	-1.83361	0.00000	2.78396
C	-1.64151	0.00000	1.37268
C	-0.28152	0.00000	1.15201
N	0.35334	0.00000	2.36507
C	1.79581	0.00000	2.55855
C	0.50989	0.00000	-0.11445
O	-0.43502	0.00000	-1.19067
C	0.09436	0.00000	-2.41074
O	-0.89068	0.00000	-3.29551
O	1.27241	0.00000	-2.66318
C	-0.48127	0.00000	-4.67300
H	-0.27879	0.00000	4.39804
H	-2.77570	0.00000	3.31025
H	-2.40093	0.00000	0.60668
H	2.24073	-0.89026	2.11053
H	1.99939	0.00000	3.62741
H	2.24073	0.89026	2.11053
H	1.14684	-0.88603	-0.19453
H	1.14684	0.88603	-0.19453
H	0.10388	-0.89338	-4.88776
H	-1.40297	0.00000	-5.24722
H	0.10388	0.89338	-4.88776

24‡

C	-0.33267	-0.39923	3.31662
C	-1.52725	0.33925	3.27220
C	-1.52477	1.03179	2.07163
C	-0.32239	0.72167	1.40102
N	0.37702	-0.17125	2.20921
C	1.66738	-0.76573	1.87863
C	0.12631	1.14813	0.16008
O	-0.46743	-0.30966	-1.18117
C	-0.08412	-0.01564	-2.36133
O	-0.47787	-0.95945	-3.26445
O	0.55560	0.96701	-2.72463
C	-0.10152	-0.72532	-4.62149
H	0.03907	-1.06675	4.08058
H	-2.28347	0.34860	4.04069
H	-2.28116	1.70163	1.68972
H	1.58886	-1.30734	0.93620
H	1.93980	-1.45362	2.67553
H	2.42391	0.01434	1.79454
H	1.15892	1.01767	-0.13562
H	-0.42840	1.92769	-0.34434
H	0.98385	-0.68804	-4.71998
H	-0.49876	-1.56442	-5.18823
H	-0.53091	0.20865	-4.98541

25

C	-0.44996	3.10225	-0.69815
C	-0.42126	3.61731	0.57226
C	-0.20967	2.52740	1.46582
C	-0.11749	1.38336	0.70840
N	-0.27029	1.73858	-0.61552
C	0.23028	-0.01887	1.12165
C	1.64448	-0.41332	0.71640
O	0.12091	-0.01290	2.56437
C	-0.05268	-1.14546	3.23889
O	-0.09194	-1.15701	4.44269
O	-0.18008	-2.21061	2.45933
C	-0.37413	-3.46243	3.14057
C	-0.26388	0.86634	-1.74449
C	0.65177	1.08725	-2.77052
C	0.65865	0.24261	-3.87601
C	-0.23462	-0.82376	-3.94910
C	-1.14919	-1.03533	-2.92046
C	-1.17440	-0.18508	-1.81914
H	-0.60865	3.56847	-1.65807
H	-0.54842	4.65606	0.83523
H	-0.11774	2.57122	2.53954
H	-0.49161	-0.73268	0.72632
H	1.73712	-0.38819	-0.37111
H	1.87275	-1.42317	1.05988
H	2.35897	0.29122	1.14637
H	0.48020	-3.66938	3.78332
H	-0.45401	-4.20794	2.35525
H	-1.28882	-3.42410	3.72989
H	1.35571	1.90778	-2.69032
H	1.37036	0.41246	-4.67528
H	-0.22136	-1.48466	-4.80759
H	-1.85559	-1.85482	-2.97981
H	-1.90541	-0.32257	-1.03062

25‡

C	-0.49800	2.97156	-0.84587
C	-0.03060	3.87198	0.11366
C	0.72496	3.13971	1.02815
C	0.72981	1.80221	0.60615
N	-0.03497	1.74180	-0.55919
C	1.26570	0.65418	1.20594
C	2.15025	0.73984	2.39374
O	-0.43541	-0.13509	2.10807
C	-0.83930	-1.29055	1.75732
O	-1.93486	-1.78627	2.00827
O	0.08783	-1.99677	1.04362
C	-0.29478	-3.30767	0.63032
C	-0.37207	0.53681	-1.25669
C	0.60569	-0.12508	-1.99041
C	0.27759	-1.31333	-2.63549
C	-1.01537	-1.82272	-2.54603
C	-1.98561	-1.14780	-1.80922
C	-1.66579	0.03707	-1.15526
H	-1.12286	3.13340	-1.71227
H	-0.22665	4.93244	0.12332
H	1.23223	3.51666	1.90387
H	1.33955	-0.24169	0.60181
H	3.16042	0.97094	2.03527
H	2.18548	-0.21879	2.90808
H	1.83821	1.52389	3.08256
H	-0.44086	-3.95391	1.49688
H	0.52763	-3.67951	0.02079
H	-1.21022	-3.27301	0.03979
H	1.60614	0.28958	-2.04866
H	1.03233	-1.83796	-3.20923
H	-1.26615	-2.75064	-3.04652
H	-2.98966	-1.54861	-1.73263
H	-2.40066	0.56730	-0.56014

26

C	-0.33248	2.75232	-3.45566
C	-0.97923	3.07024	-2.21874
C	-1.05593	2.16318	-1.19663
C	-0.47554	0.87727	-1.38257
C	0.17575	0.55835	-2.62488
C	0.23674	1.52583	-3.66549
C	-0.38403	-0.25454	-0.57009
N	0.29505	-1.20816	-1.28053
C	0.64298	-0.75100	-2.50964
C	0.58911	-2.54751	-0.78249
C	-0.85882	-0.48501	0.80943
O	0.28065	-0.38719	1.71274
C	0.01535	-0.63578	2.98983
O	1.14044	-0.53567	3.68502
C	1.01767	-0.77842	5.09589
O	-1.06863	-0.90706	3.44348
H	-0.29796	3.50456	-4.23536
H	-1.41544	4.05521	-2.09680
H	-1.54783	2.41662	-0.26345
H	0.72581	1.29024	-4.60450
H	1.18588	-1.37810	-3.19928
H	1.21046	-3.05843	-1.51426
H	1.12162	-2.47918	0.16597
H	-0.33801	-3.10437	-0.64084
H	-1.59091	0.27241	1.09024
H	-1.30343	-1.47331	0.94058
H	0.33424	-0.05614	5.54040
H	2.01892	-0.65473	5.49755
H	0.65760	-1.79163	5.27005

26‡

C	-0.36423	2.77016	-3.39963
C	-1.00785	3.05249	-2.16595
C	-1.13067	2.10230	-1.17717
C	-0.59435	0.82154	-1.41788
C	0.05482	0.54199	-2.65066
C	0.16683	1.52766	-3.65366
C	-0.54966	-0.36887	-0.64042
N	0.13512	-1.31107	-1.40731
C	0.49177	-0.80239	-2.58211
C	0.42406	-2.67094	-0.96166
C	-0.97496	-0.60825	0.66366
O	0.52896	-0.20531	1.81934
C	0.29257	-0.51485	3.04201
O	1.36694	-0.25221	3.83168
C	1.21041	-0.55301	5.21983
O	-0.73688	-0.98748	3.50635
H	-0.29322	3.55163	-4.14701
H	-1.41073	4.04591	-2.00339
H	-1.62429	2.33239	-0.23952
H	0.65926	1.30638	-4.59379
H	1.02531	-1.39699	-3.30963
H	0.99812	-3.17080	-1.73816
H	1.00204	-2.63510	-0.03813
H	-0.51128	-3.20414	-0.79164
H	-1.64018	0.11935	1.11168
H	-1.08055	-1.62383	1.02400
H	0.39429	0.02855	5.64947
H	2.15311	-0.27884	5.68779
H	1.01521	-1.61626	5.36192

27

C	-0.68682	0.99220	-4.67432
C	0.00495	-0.12775	-5.13879
C	0.94731	-0.72446	-4.29528
C	1.19272	-0.22475	-3.02123
C	0.48123	0.88550	-2.59038
C	-0.45848	1.50274	-3.39854
O	0.74403	1.43350	-1.33388
C	0.28488	0.71867	-0.29411
C	-0.48050	-0.38923	-0.15259
C	-0.58215	-0.58599	1.27576
C	0.12180	0.40995	1.85388
O	0.66464	1.22410	0.89434
C	0.42253	0.80234	3.25766
O	-0.16213	-0.20712	4.08393
C	0.02287	-0.04481	5.39266
O	-0.56495	-1.04540	6.02617
O	0.62649	0.86336	5.90332
C	-0.45290	-1.01801	7.45944
C	-0.27199	-0.69490	-6.50711
H	-1.41458	1.47557	-5.31754
H	1.50326	-1.58878	-4.64312
H	1.92670	-0.68273	-2.36779
H	-0.99196	2.37238	-3.03310
H	-0.90612	-0.98620	-0.94156
H	-1.11172	-1.37082	1.79148
H	1.50061	0.84678	3.43139
H	-0.01103	1.77560	3.50198
H	0.59587	-1.05654	7.75073
H	-0.97899	-1.90231	7.80593
H	-0.91974	-0.11524	7.85092
H	0.61951	-1.16666	-6.92290
H	-0.60864	0.08390	-7.19277
H	-1.05669	-1.45489	-6.45456

*a transition state geometry for compound **27** was not identified

Appendix D

A GUIDE FOR SIMPLE TRANSITION STATE CALCULATIONS USING SPARTAN

This appendix will walk through the setup of a transition state calculation for a furfuryl carbonate using the method described in Chapter 2. This workflow is applicable to systems beyond the decomposition of furfuryl carbonates, and places where deviations from this workflow may be required are noted throughout. The screen captures used for this guide are from Spartan'20 Parallel Suite software.

Introduction

The goal of these calculations is to determine the activation energy for a chemical transformation of interest. The activation energy ($\Delta G^{\ddagger}$) is defined as the difference in energy between the starting material ($G = G_0$) and the transition state ($G = G^{\ddagger}$), so we must find optimized geometries for both species. In this example, we will find the activation energy for the decomposition of a simple furfuryl carbonate. Our proposed mechanism involves the cleavage of a C–O bond highlighted below.

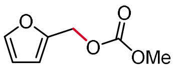

Starting material geometry calculation

We will begin by finding the optimized energy of the starting material, which will allow us to find G_0 as well as provide a starting place for the subsequent transition state search.

Begin by opening the ChemDraw file in Spartan. Ensure the structure is correct, as importing these files (especially those with stereocenters) can sometimes corrupt the structure.

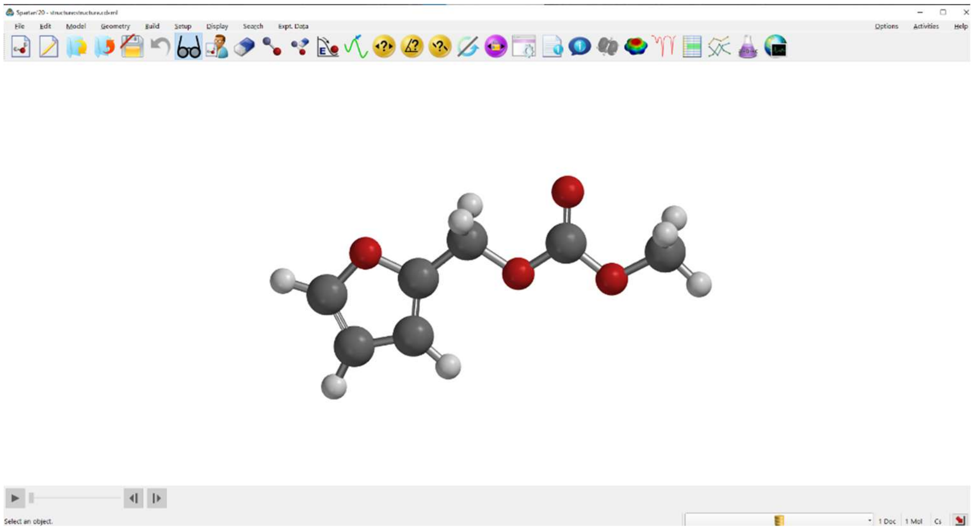

Equilibrium conformer search

The first step is to run a quick equilibrium conformer search on the molecule as a starting place to find the optimized geometry. To do this, click the Calculations icon in the top toolbar. Select "Equilibrium Conformer" with "Molecular Mechanics" and "MMFF" as the level of theory. Press "Submit" to begin the calculation. This should only take a few moments.

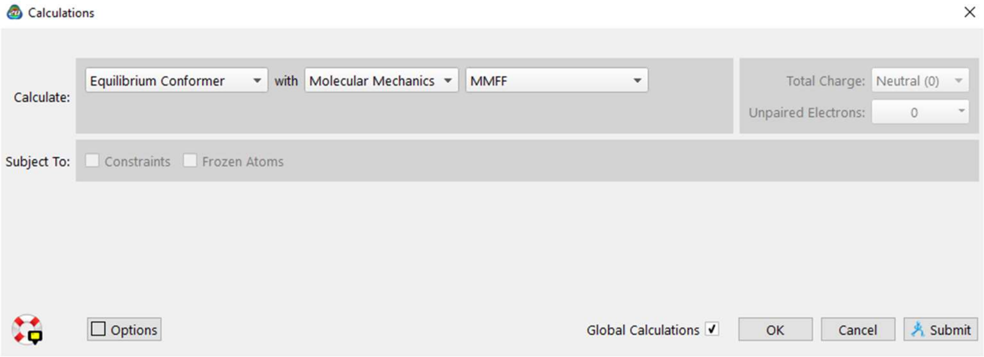

Calculations

Calculate: Equilibrium Conformer with Molecular Mechanics MMFF

Total Charge: Neutral (0)

Unpaired Electrons: 0

Subject To: ☐ Constraints ☐ Frozen Atoms

☐ Options

Global Calculations ☑

Once this initial calculation is completed, save the resulting structure as a new file to begin the equilibrium geometry calculation.

Equilibrium geometry optimization

Once again, select the Calculations button in the top toolbar. Now, we will want to run this calculation at the final level of theory desired for our transition state calculation. Ideally, this will use an appropriate functional for transition state searches, and will implement a large basis set for the most accurate results. In this example, we have chosen to use the M06-2X functional. The 6-311+G** [also represented as 6-311+G(d,p)] was chosen for its expanded orbitals and diffuse functions, since we are dealing with the formation of a carbonate anion. We have chosen to use the "Polar Solvent" option to better represent experimental conditions. We have chosen to compute "IR" to calculate thermodynamic parameters. We have selected the FINEGRID "Option" to select a large Lebedev integration grid for more precise results. The Lebedev grid is defined by (x,y) where x is the number of radial shells and y is the number of radial points. Below are the Lebedev grid options in Spartan. Note that larger grids will result in slower computation times (from: https://downloads.wavefun.com/FAQ/Energy_FAQs.html).

SG-1 and **SG-0**: small grids tuned for 6-31G* basis set
SMALL GRID: Spartan default for most DFT functionals
EMLGRID: (50,194)
BIGGRID: (70,302)
VERYBIGGRID: (100,434)
FINEGRID: (99,590)
HUGEGRID: (250,947)

We have also used the GEOMETRYCYCLE option to ensure convergence of the calculation. This option defines the maximum number of iterations Spartan will attempt before failing the calculation. This is not always necessary, especially for a simple equilibrium geometry calculation. However, including it does not hurt anything, as the calculation will finish once it converges regardless of the value entered here. Using GEOMETRYCYCLE=1000 is sufficient for most applications. Note that the "Options" are space delimited, so using FINEGRID and GEOMETRYCYCLE options should be entered as: FINEGRID GEOMETRYCYCLE=1000. Be sure the "Options" box is checked.

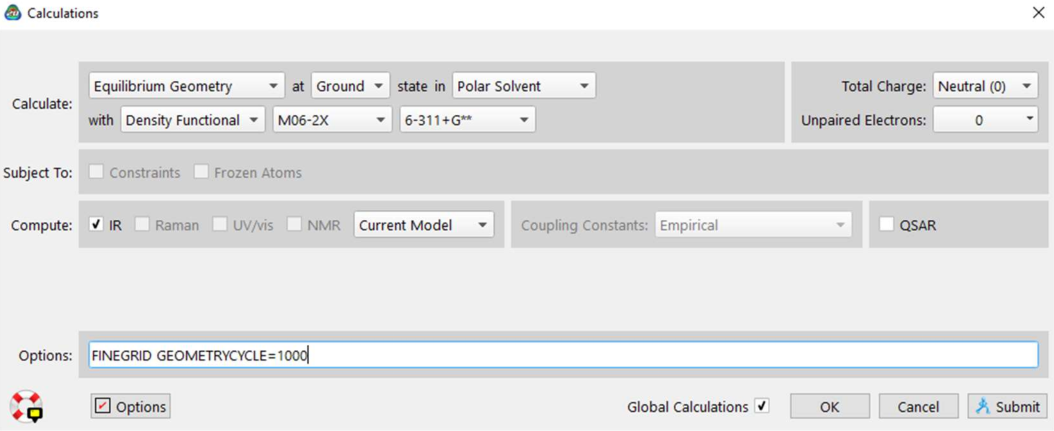

Calculations

Calculate: Equilibrium Geometry at Ground state in Polar Solvent
with Density Functional M06-2X 6-311+G**

Total Charge: Neutral (0)
Unpaired Electrons: 0

Subject To: ☐ Constraints ☐ Frozen Atoms

Compute: ☑ IR ☐ Raman ☐ UV/vis ☐ NMR Current Model
Coupling Constants: Empirical
☐ QSAR

Options: FINEGRID GEOMETRYCYCLE=1000

☑ Options
Global Calculations ☑

Once this calculation is completed, we can check the results by selecting the "Output" icon in the top toolbar. Click "IR Table" to see a list of calculated IR peaks/vibrational modes.

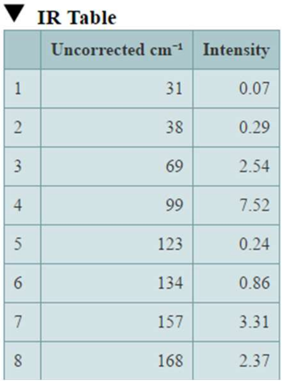

▼ IR Table

	Uncorrected cm⁻¹	Intensity
1	31	0.07
2	38	0.29
3	69	2.54
4	99	7.52
5	123	0.24
6	134	0.86
7	157	3.31
8	168	2.37

Check that the lowest value in this table is a *positive* value. If there is a negative frequency, you have not found an optimized geometry. Re-run the equilibrium conformer and equilibrium geometry calculations. Here, we see that the lowest frequency is 31 cm^{-1}, so we are good to go.

In the same window, now click on "Thermodynamic Properties at 298.15 K." The value we want is "Gibbs Energy." *DO NOT* use the "Energy" value listed in the top table.

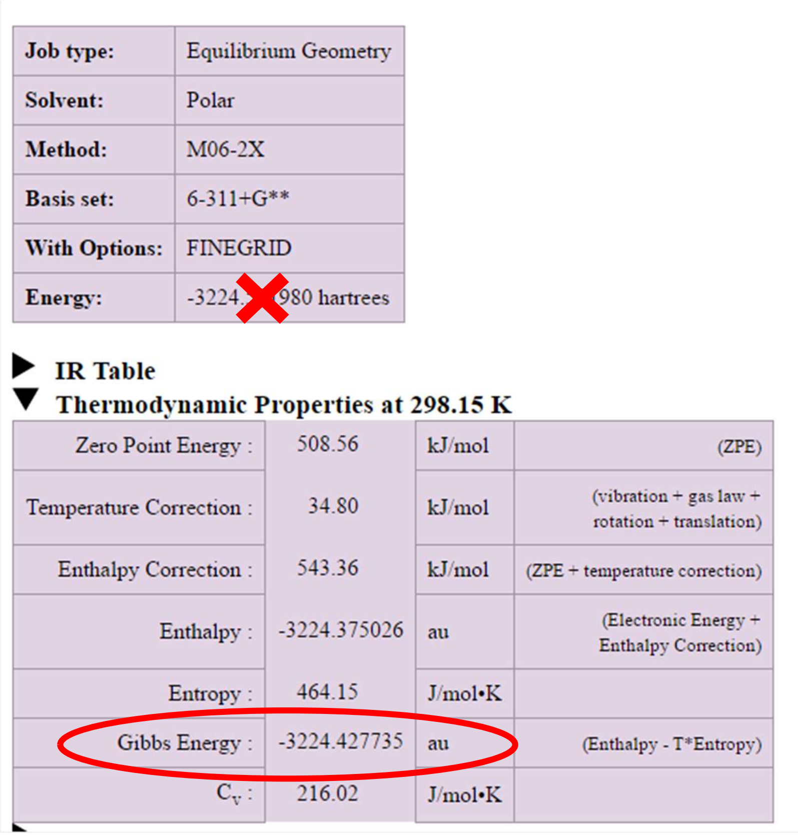

Job type:	Equilibrium Geometry
Solvent:	Polar
Method:	M06-2X
Basis set:	6-311+G**
With Options:	FINEGRID
Energy:	-3224.[illegible]980 hartrees

▶ **IR Table**

▼ **Thermodynamic Properties at 298.15 K**

Zero Point Energy :	508.56	kJ/mol	(ZPE)
Temperature Correction :	34.80	kJ/mol	(vibration + gas law + rotation + translation)
Enthalpy Correction :	543.36	kJ/mol	(ZPE + temperature correction)
Enthalpy :	-3224.375026	au	(Electronic Energy + Enthalpy Correction)
Entropy :	464.15	J/mol•K	
Gibbs Energy :	-3224.427735	au	(Enthalpy - T*Entropy)
C_V :	216.02	J/mol•K	

You have now found the value of G_0 for your molecule!

Transition state geometry search and optimization

Now that we have found G_0, we must calculate $G^{\ddagger}$, which is a more involved process.

Finding an initial transition state guess through a "relaxed scan"

Before we can use the transition state optimization algorithm built into Spartan, we must first find an initial "guess" that is close to the actual geometry of the transition state. Otherwise, our calculation will just collapse to the starting material geometry. Since we are probing a bond breaking event, we will elongate the bond of interest and equilibrate ("relax") the molecule at each step. Evaluating the energy values along this profile will allow us to find a decent guess for the transition state.

Starting from the optimized geometry of the starting material, save a new copy to use for this next step. We will begin by performing an "Energy Profile" calculation as we extend the C–O bond of interest. Begin by clicking the Constrain Distance 🔒 icon in the top toolbar. Now click the bond of interest, which should become highlighted.

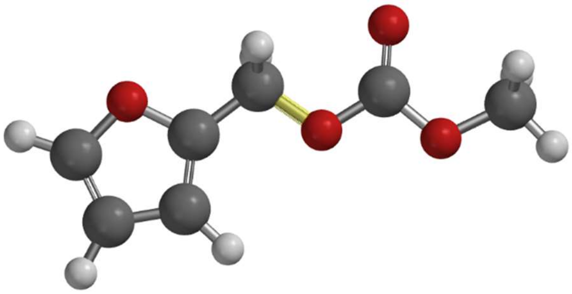

In the lower right of the window, click the open lock icon 🔓 . Select the "Profile" checkbox. We can now define the parameters for the elongation profile. Leave the starting bond length the same, but change the final bond length to an appropriate value for the transformation of interest. For furfuryl carbonate decomposition, a scan of 1.5 Å over 20 steps is sufficient. Other substrates may require more precision or more elongation. Here, we are extending the bond from 1.428 Å to 2.928 Å over 20 steps.

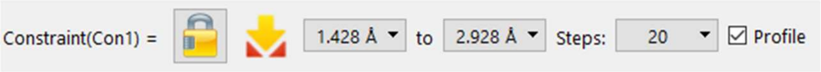

Constraint(Con1) = 1.428 Å to 2.928 Å Steps: 20 ☑ Profile

Next, click the Calculations icon . Select "Energy Profile" from the drop-down menu. Now, select the level of theory and solvent conditions to best match your system. Here, we are using the "Polar Solvent" option to best match our experimental conditions. We have selected Hartree-Fock/6-31+G* (HF/6-31+G*) as the level of theory based on testing of various HF and DFT methods. This may require some testing for different substrates, depending on the results of this relaxed scan. Ideally, this step should be performed at a low level of theory with a small basis set.

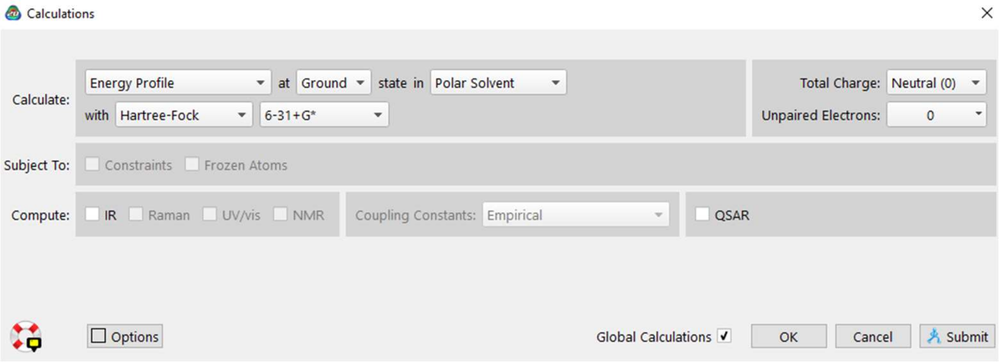

Calculations

Calculate: Energy Profile at Ground state in Polar Solvent

with Hartree-Fock 6-31+G*

Total Charge: Neutral (0)

Unpaired Electrons: 0

Subject To: ☐ Constraints ☐ Frozen Atoms

Compute: ☐ IR ☐ Raman ☐ UV/vis ☐ NMR Coupling Constants: Empirical ☐ QSAR

☐ Options Global Calculations ☑

Once the profile calculations are completed, we can view the results. First, click the constrained bond. Then, click the yellow and red button in the far bottom right of the page.

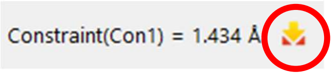

Constraint(Con1) = 1.434 Å

Click the “Spreadsheet” icon to show the spreadsheet that should already have the constraint values listed in a column labeled ‘Constraint(Con1).”

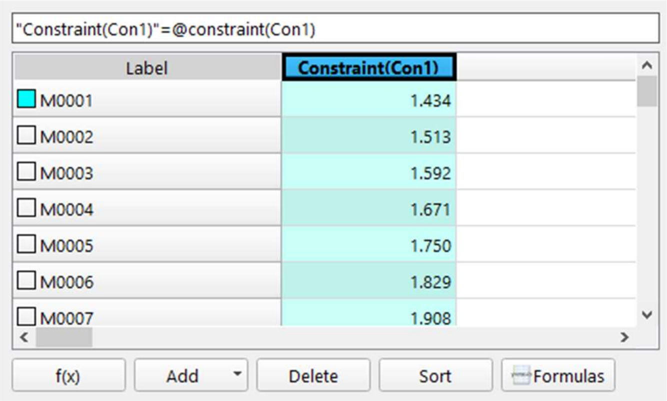

"Constraint(Con1)"=@constraint(Con1)

Label	Constraint(Con1)
☐ M0001	1.434
☐ M0002	1.513
☐ M0003	1.592
☐ M0004	1.671
☐ M0005	1.750
☐ M0006	1.829
☐ M0007	1.908

Click the empty column to the right, then press the “Add” button. Under the “Molecule List” tab, select “Δ Energy (kJ/mol).”

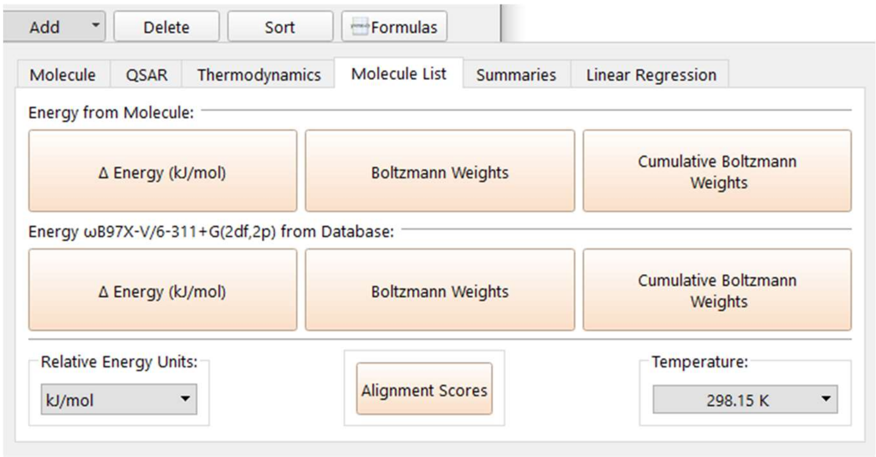

Relative Energy Units: kJ/mol

Temperature: 298.15 K

This should populate the empty column with relative energy values.

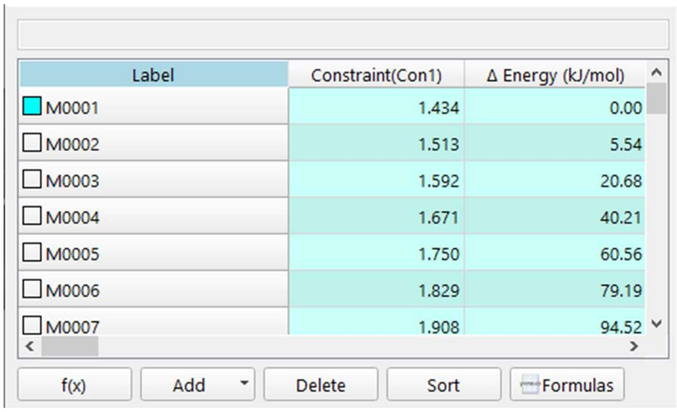

Label	Constraint(Con1)	Δ Energy (kJ/mol)
🟦 M0001	1.434	0.00
☐ M0002	1.513	5.54
☐ M0003	1.592	20.68
☐ M0004	1.671	40.21
☐ M0005	1.750	60.56
☐ M0006	1.829	79.19
☐ M0007	1.908	94.52

We can visualize this data by clicking the Plots icon in the top toolbar. In the window that appears, click the Add button . Set "X Axis" to "Constraint(Con1)" and "Y Axis" to "Δ Energy (kJ/mol)."

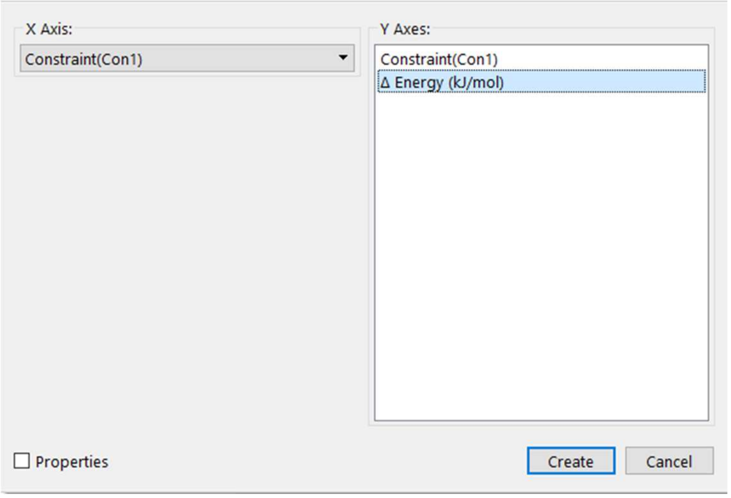

X Axis: Constraint(Con1)

Y Axes:
Constraint(Con1)
Δ Energy (kJ/mol)

☐ Properties

Click "Create" and you should now see the energy vs. constraint plot.

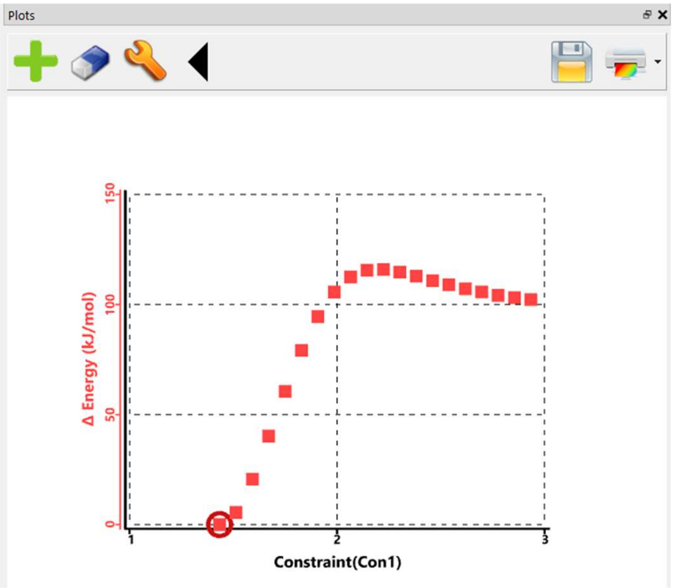

Ideally, this plot rises in energy, has a clear maximum, and then falls again. If the plot looks different from this, you may need to extend the energy profile or use a different method/basis set. The plot above shows an ideal energy profile.

Use the arrows or slider on the bottom left of the Spartan window to identify the structure associated with the highest energy in the profile.

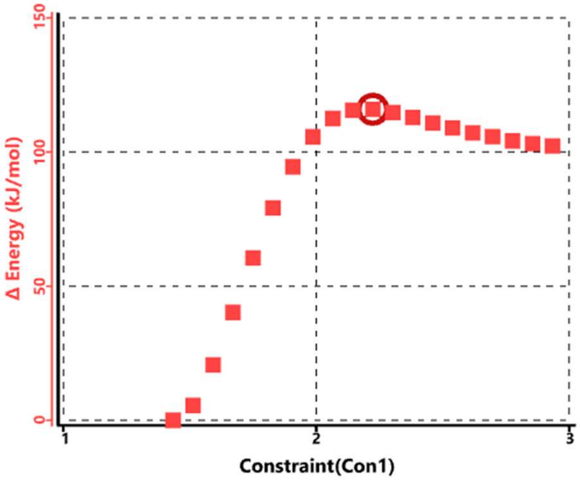

Right-click this structure and copy it to a new Spartan window. Ensure that the bond length of the elongated bond is the same as the high energy structure from the energy profile. Save this new document as we move to the transition state optimization step.

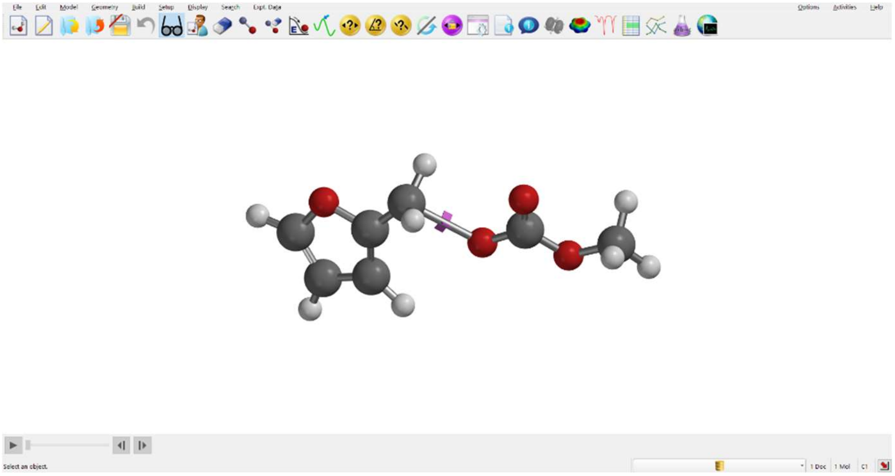

Transition state optimization

With this high energy structure as our initial guess, we can now use the Transition State Geometry method built into Spartan. Remove the bond constraint on the copied structure by clicking the constrained bond and then clicking the closed lock 🔒 button in the lower right of the window. The lock icon should switch from closed to open, and the constraint marker should disappear from the structure.

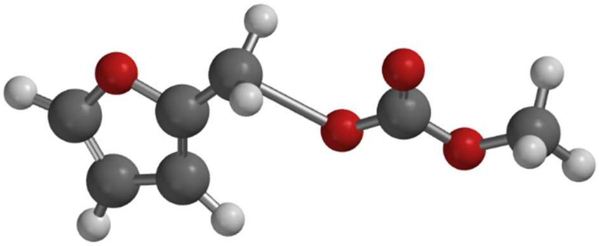

Click the Calculations button in the top toolbar to open the Calculations window. Select "Transition State Geometry" from the drop-down menu. Again, we are selecting "Polar Solvent" for our example. We are continuing with a low level of theory (HF/6-31+G*), as we found this to work well for this system. You may choose to use a higher level of theory for your calculations. Optimization of this procedure will require trial and error, and can be revisited after evaluating the final transition state geometry.

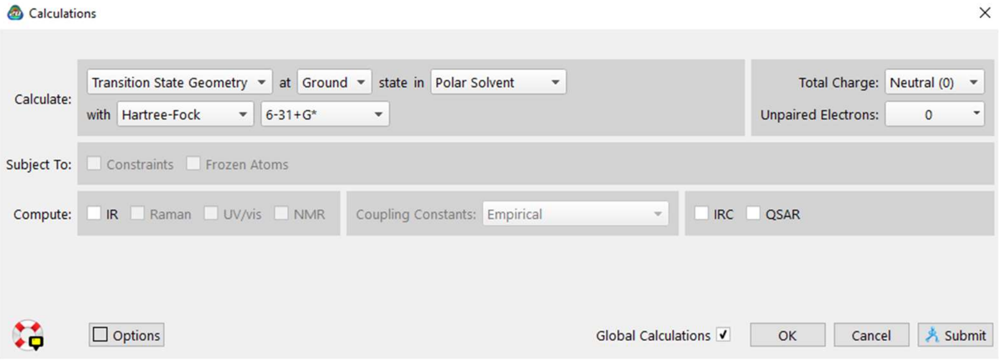

Calculations

Calculate: Transition State Geometry at Ground state in Polar Solvent

with Hartree-Fock 6-31+G*

Total Charge: Neutral (0)

Unpaired Electrons: 0

Subject To: ☐ Constraints ☐ Frozen Atoms

Compute: ☐ IR ☐ Raman ☐ UV/vis ☐ NMR Coupling Constants: Empirical ☐ IRC ☐ QSAR

☐ Options Global Calculations ☑

Once this calculation is completed, check that the bond length of the bond of interest is similar to the initial transition state guess. If the input structure is too far from a transition state, the Transition State Geometry calculation may collapse back to the equilibrium geometry. Here, we see that the C–O bond length is still much longer than expected for a typical equilibrium bond.

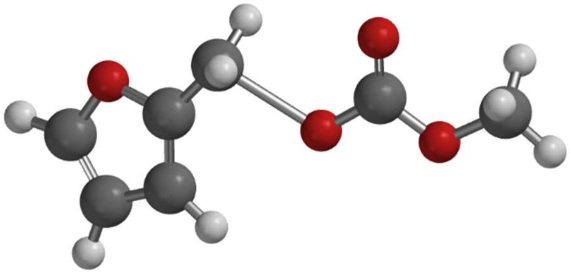

Save this structure as a new file before moving to the final step.

Constrained equilibrium geometry and transition state energy calculation

For the final step, we will transition to a higher level of theory to provide more accurate energy values for our transition state geometry. We will also use a constrained geometry equilibration to relax portions of the molecule not involved in the transition state of interest. We will begin by once again constraining the bond of interest. Click the bond of interest, then click the Constrain Distance button , and then the open lock button in the lower right of the Spartan window.

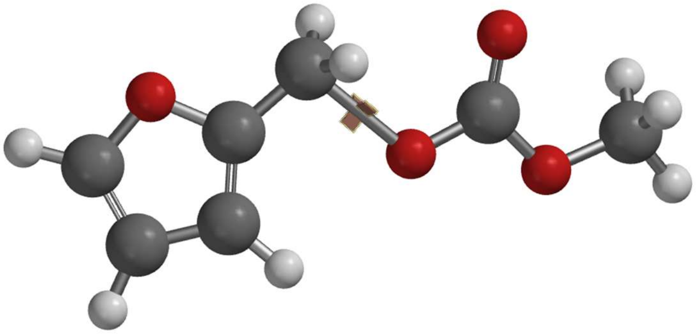

Once the bond is constrained, click the Calculations icon in the top toolbar. Select "Equilibrium Geometry" from the drop-down menu. Choose the same solvent conditions as before. We will need to select the same level of theory as for our initial Equilibrium Geometry calculation for the starting material. In our example, that was M06-2X/6-311+G**. As we did for that starting material calculation, we will select "IR" and use the FINEGRID and GEOMETRYCYCLE=1000 options. We must also select the "Subject To: Constrains" box in order to keep our molecule from equilibrating to the starting material.

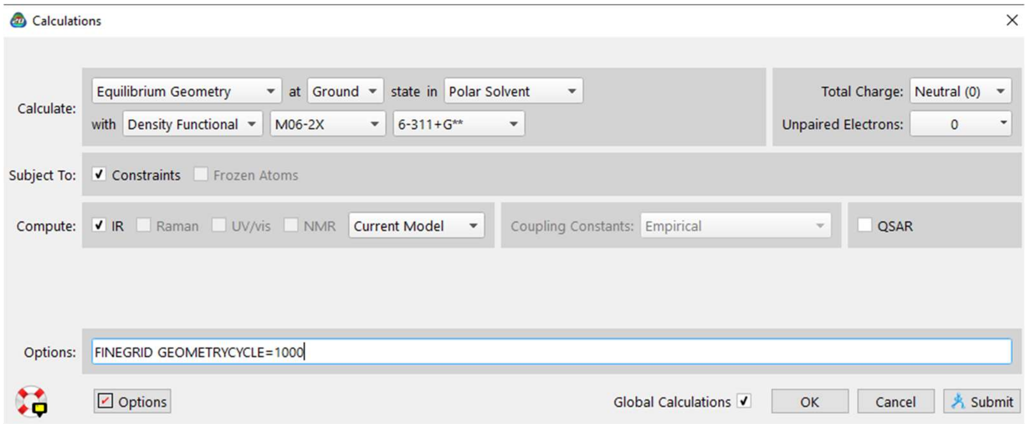

Calculations

Calculate: Equilibrium Geometry at Ground state in Polar Solvent

with Density Functional M06-2X 6-311+G**

Total Charge: Neutral (0)

Unpaired Electrons: 0

Subject To: ☑ Constraints ☐ Frozen Atoms

Compute: ☑ IR ☐ Raman ☐ UV/vis ☐ NMR Current Model

Coupling Constants: Empirical ☐ QSAR

Options: FINEGRID GEOMETRYCYCLE=1000

Run this calculation. Note that this will be the longest calculation in the workflow. For a simple furfuryl carbonate like our example, this may take 2–3 hours.

Once the calculation is complete, click the Output button in the top toolbar and open "IR Table."

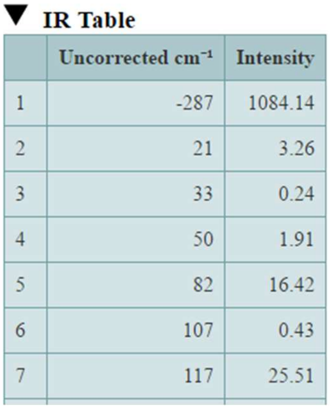

▼ IR Table

	Uncorrected cm^{-1}	Intensity
1	-287	1084.14
2	21	3.26
3	33	0.24
4	50	1.91
5	82	16.42
6	107	0.43
7	117	25.51

Here, the lowest value should be a negative frequency. Here, we see –287 cm^{-1}. If there is no negative frequency, you have not found a transition state. Check that the result of your calculation using the Transition State Geometry method did not collapse to the equilibrium geometry. If your structure collapsed during the last (constrained) Equilibrium Geometry step, you likely did not select the "Subject To: Constraints" box in the Calculations window. If you see more than one negative frequency, you have not found a first-order transition state. Often, we will see one large negative frequency accompanied by several smaller negative frequencies. This is an indication that your transition state geometry needs further optimization. If you see multiple large negative frequencies, you may be barking up the wrong tree with the predicted transition state. If you see one very small negative frequency ($0\ \text{cm}^{-1} > v \gtrsim -50\ \text{cm}^{-1}$), it likely does not correspond to the transition state of interest. For furfuryl carbonate decomposition, we typically find $v < -250\ \text{cm}^{-1}$. If you see a single large negative frequency value, congratulations! *You have found a transition state.*

To verify we have found the transition state of interest, click the Spectra icon in the top toolbar. In the window that appears, click the Add button and select “IR Calculated” from the list of spectra.

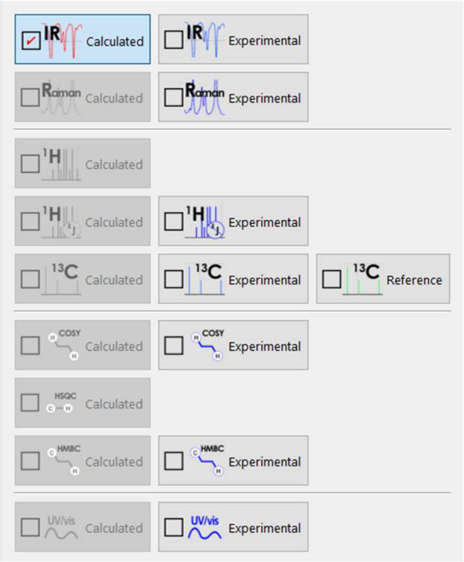

A calculated IR spectrum should appear.

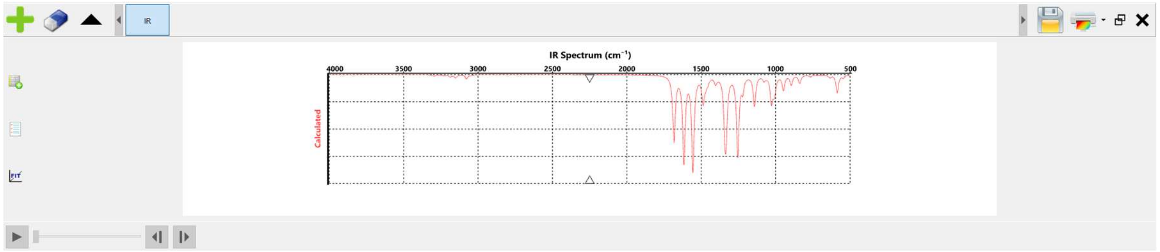

Click the Tables icon on the right side of the Spectra window. You should now see the list of calculated frequency values.

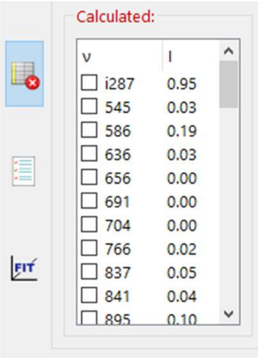
Calculated:

v	I
☐ i287	0.95
☐ 545	0.03
☐ 586	0.19
☐ 636	0.03
☐ 656	0.00
☐ 691	0.00
☐ 704	0.00
☐ 766	0.02
☐ 837	0.05
☐ 841	0.04
☐ 895	0.10

Click the negative frequency to visualize the vibrational mode on the molecular structure. You should see the Spartan structure moving! Convince yourself that the vibrational mode you see corresponds to the desired transition state. For the C–O bond cleavage event for the furfuryl carbonate we studied, we see that the single negative frequency corresponds to a stretching mode of the C–O bond of interest.

If you have undesired additional negative frequency values, this is a good way to understand where they are coming from. Small negative frequencies often arise from small perturbations in the molecule such as methyl rotors or large-scale gentle bending modes. Once you have identified these undesired vibrational modes, you can adjust those portions of the molecule and re-run the constrained equilibrium geometry calculation. For a methyl rotor, spinning the offending methyl group and re-equilibrating is often successful. For large-scale bending motions, a slight rotation around a bond at the center of the bend may solve this problem.

If you are satisfied that you have identified a valid first-order transition state, you can find the energy of this species by clicking the Output icon and extracting the Gibbs energy value from the "Thermodynamic Properties at 298.15 K" tab. This value is $G^{\ddagger}$.

Now that you have found both G_0 and $G^{\ddagger}$, you can calculate $\Delta G^{\ddagger}$:

$$\Delta G^{\ddagger} = G^{\ddagger} - G_0$$

The energy values provided by Spartan have units of hartrees, so multiple the value of $\Delta G^{\ddagger}$ by 627.5 to derive the activation energy in units of kcal/mol.

You have now successfully calculated the activation energy for your chemical transformation!

Appendix E

SPECTRA RELEVANT TO CHAPTER 3: INCORPORATION OF A TETHERED ALCOHOL ENABLES EFFICIENT MECHANICALLY TRIGGERED RELEASE IN APROTIC ENVIRONMENTS

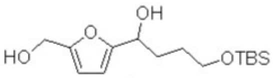

1

^{1}H (400 MHz, CD_3CN)

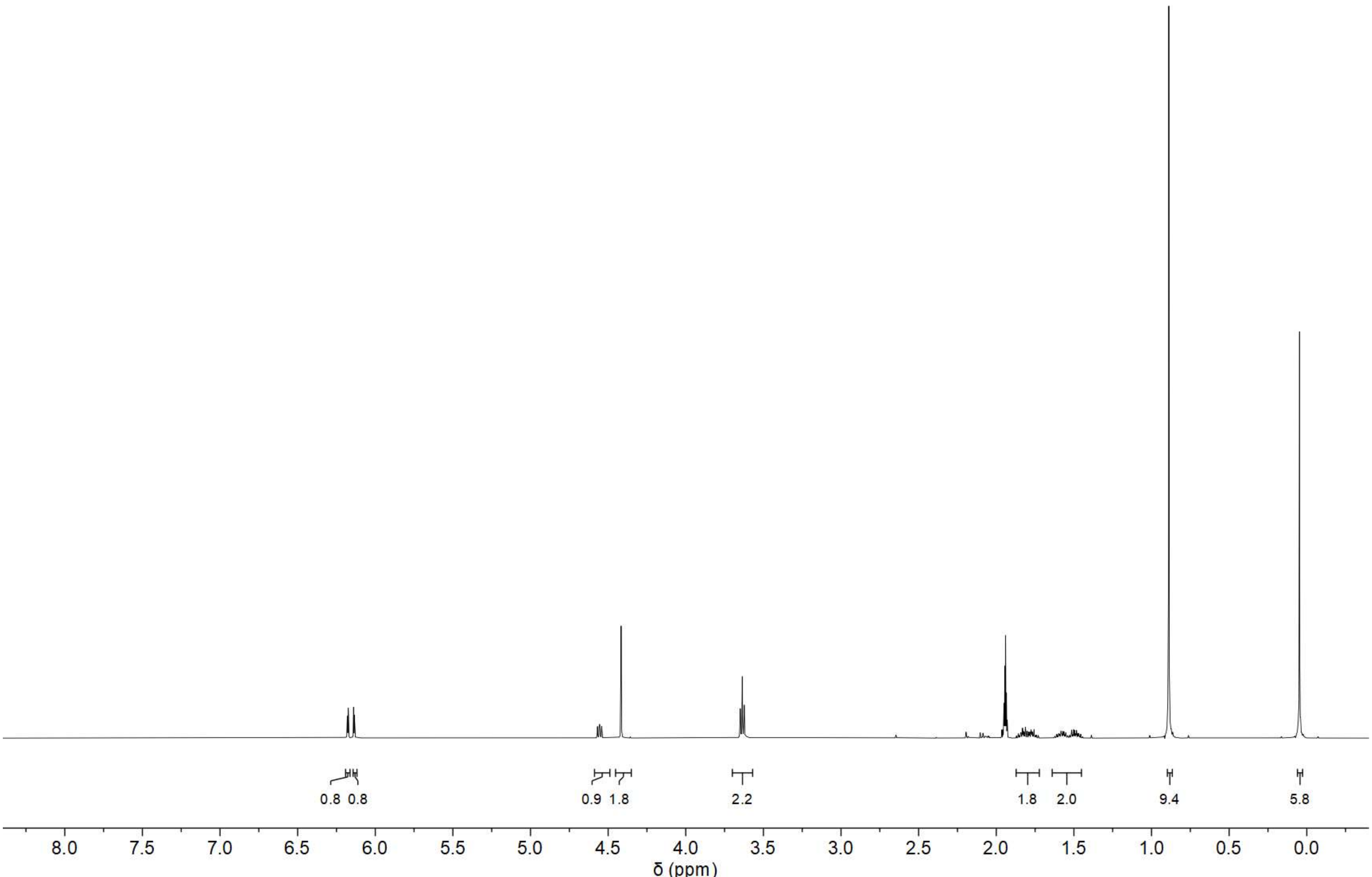

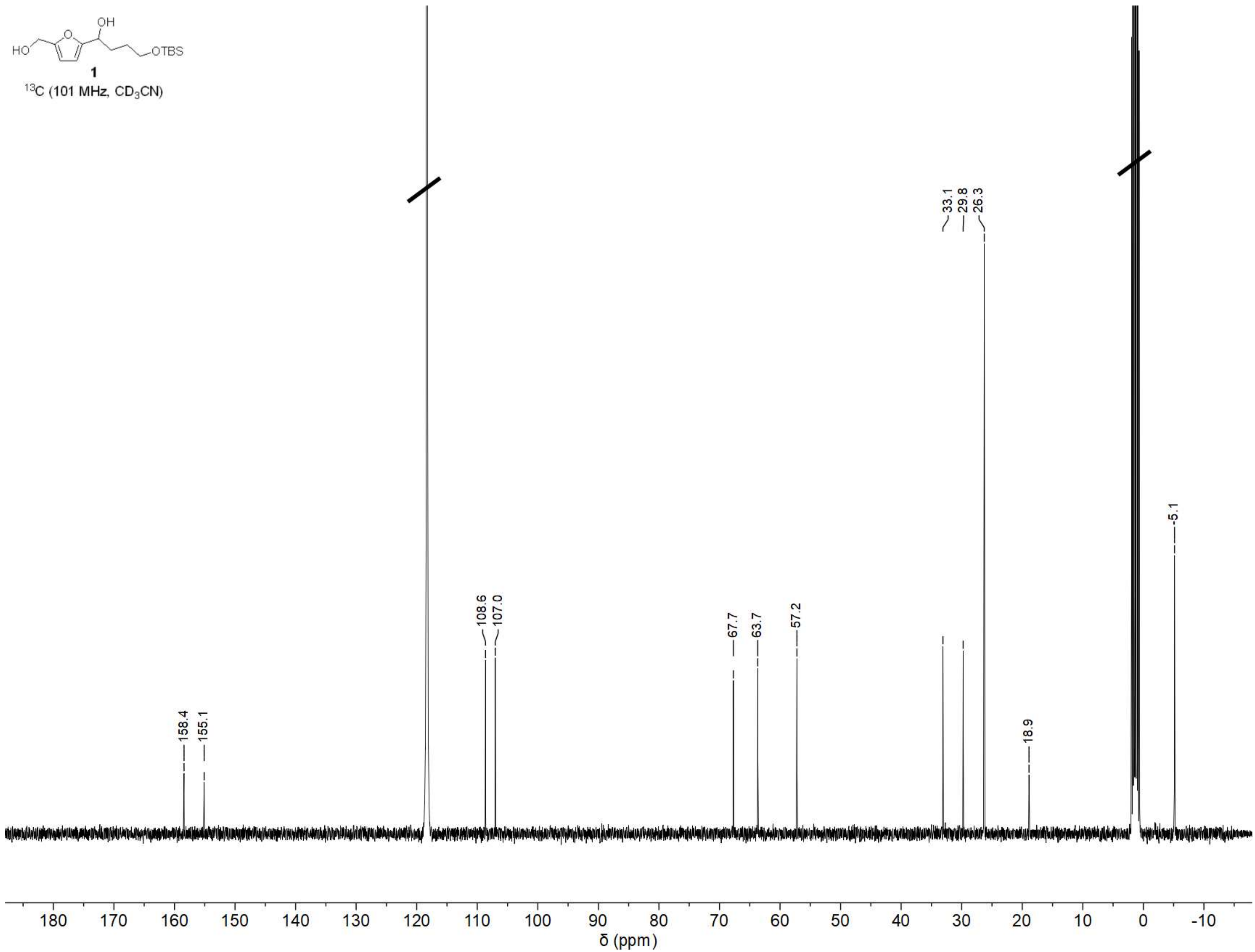

1

^{13}C (101 MHz, CD$_3$CN)

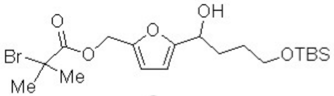

2

^{1}H (400 MHz, CDCl$_3$)

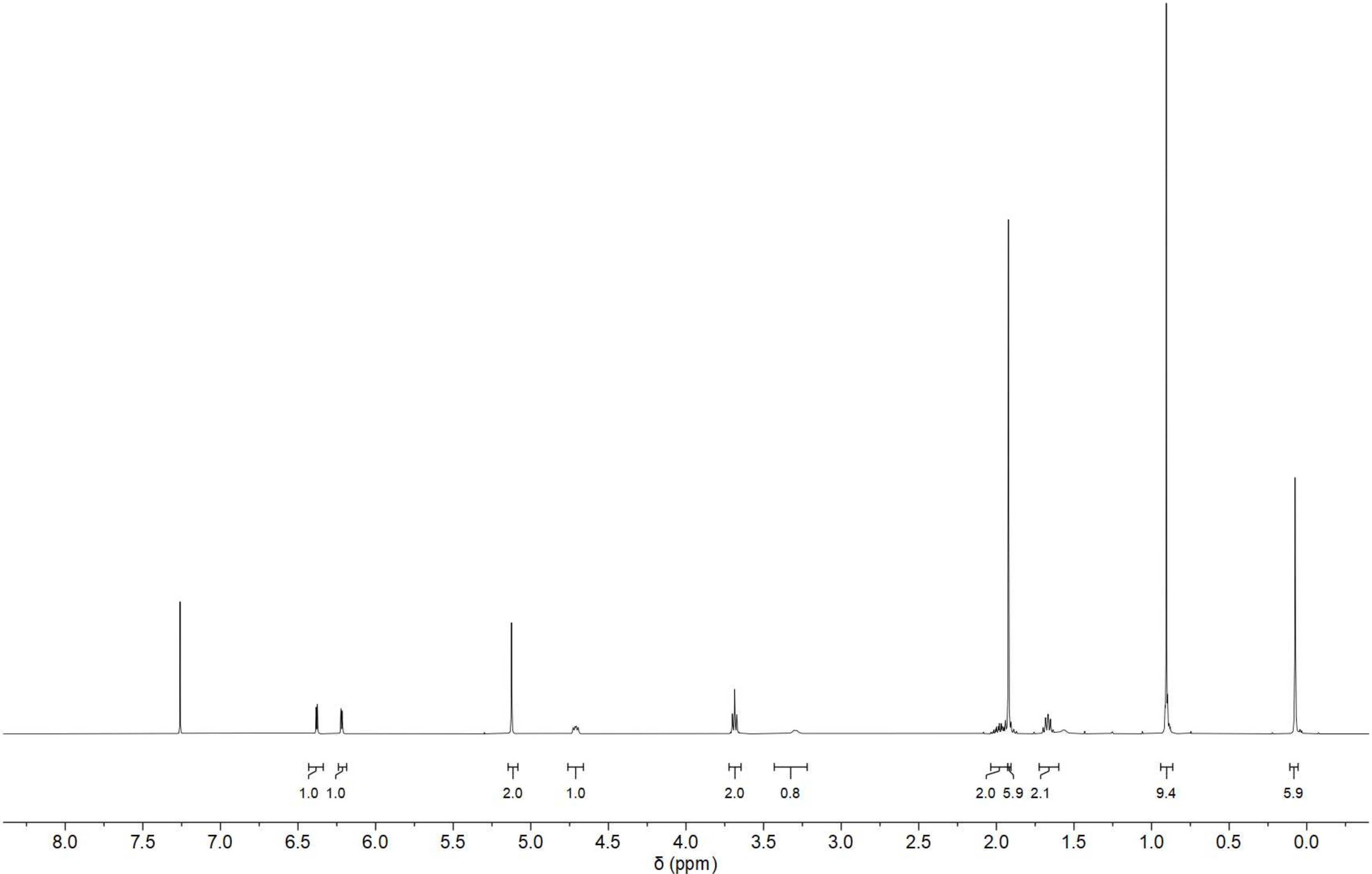

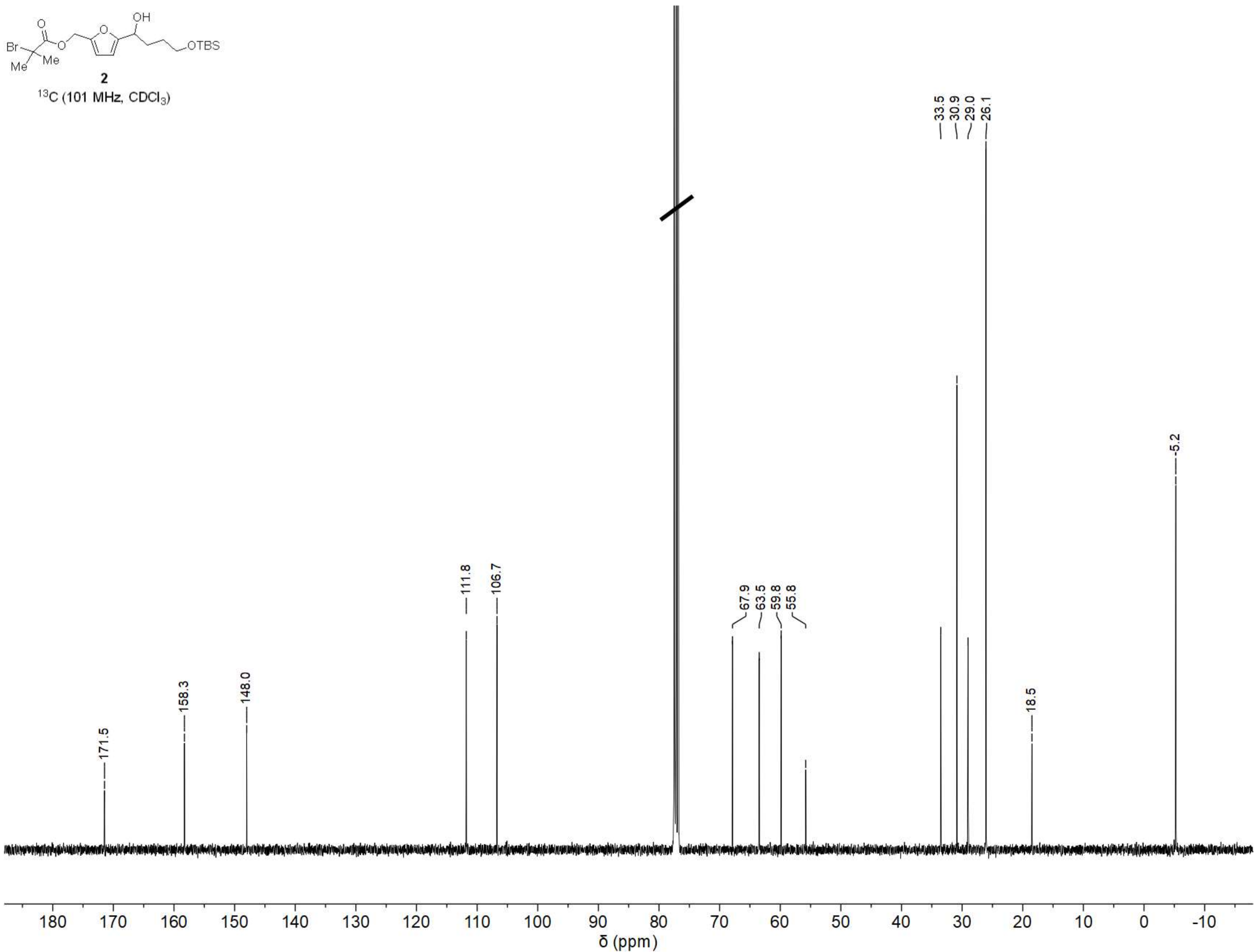

2

^{13}C (101 MHz, $CDCl_3$)

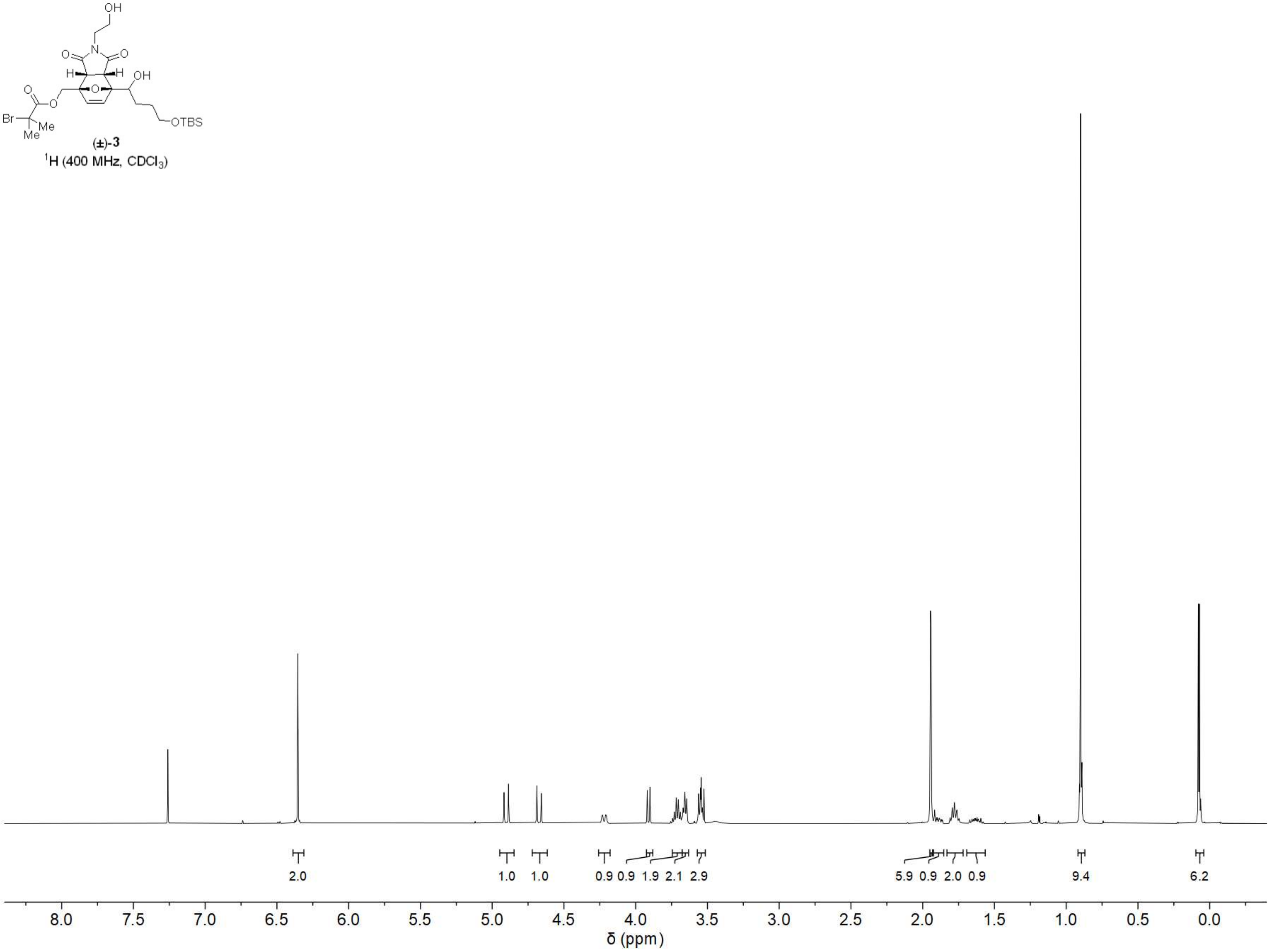

(±)-**3**

^{1}H (400 MHz, CDCl$_3$)

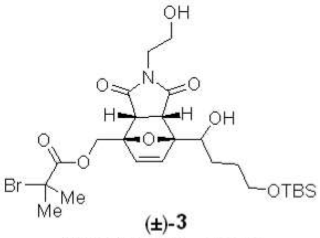

(±)-3

^{13}C (101 MHz, CDCl$_3$)

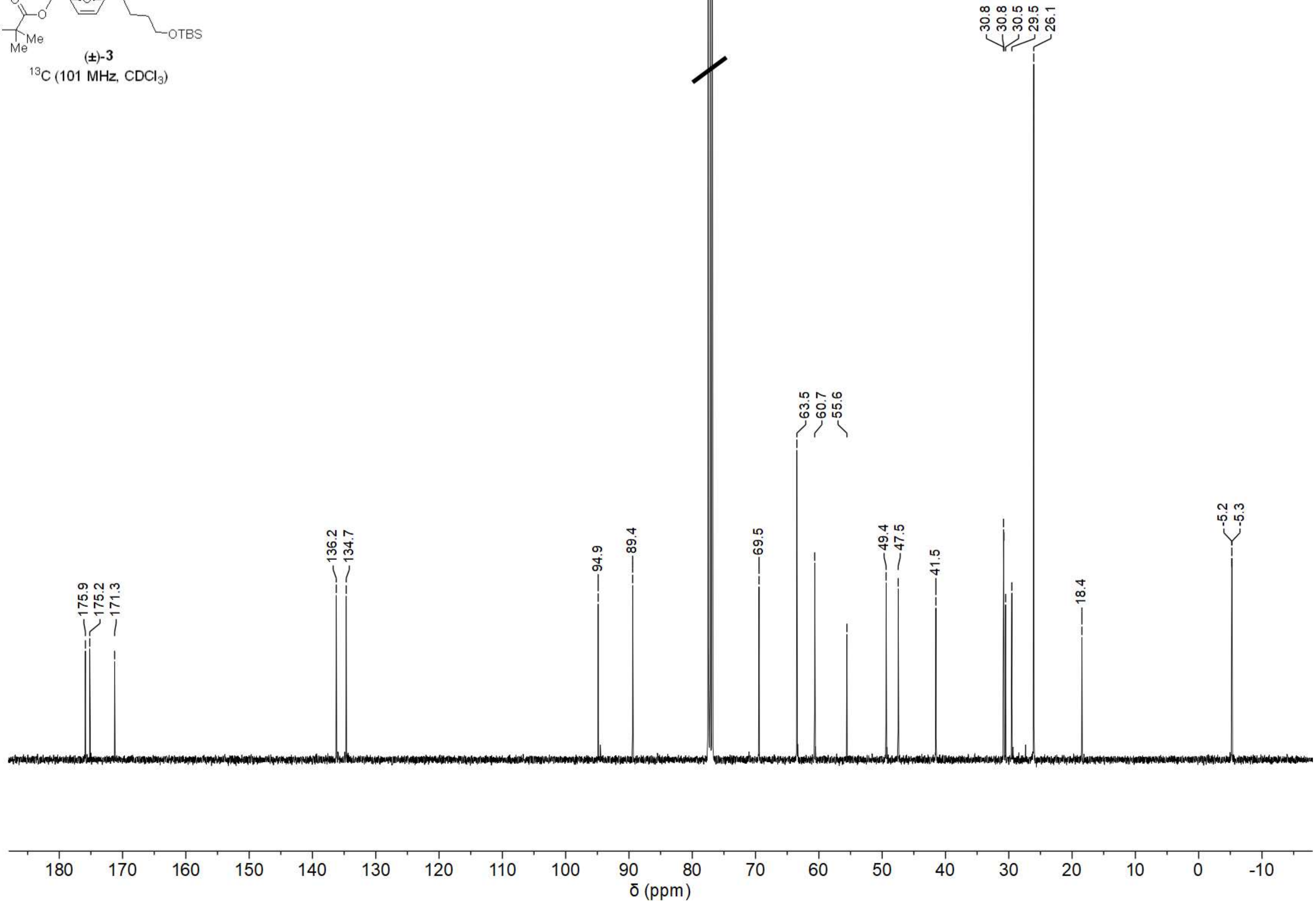

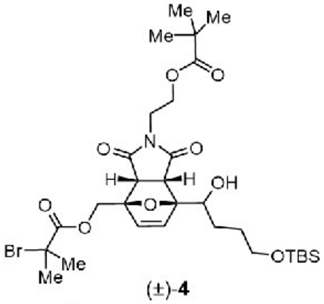

(±)-**4**

^{1}H (400 MHz, CDCl$_3$)

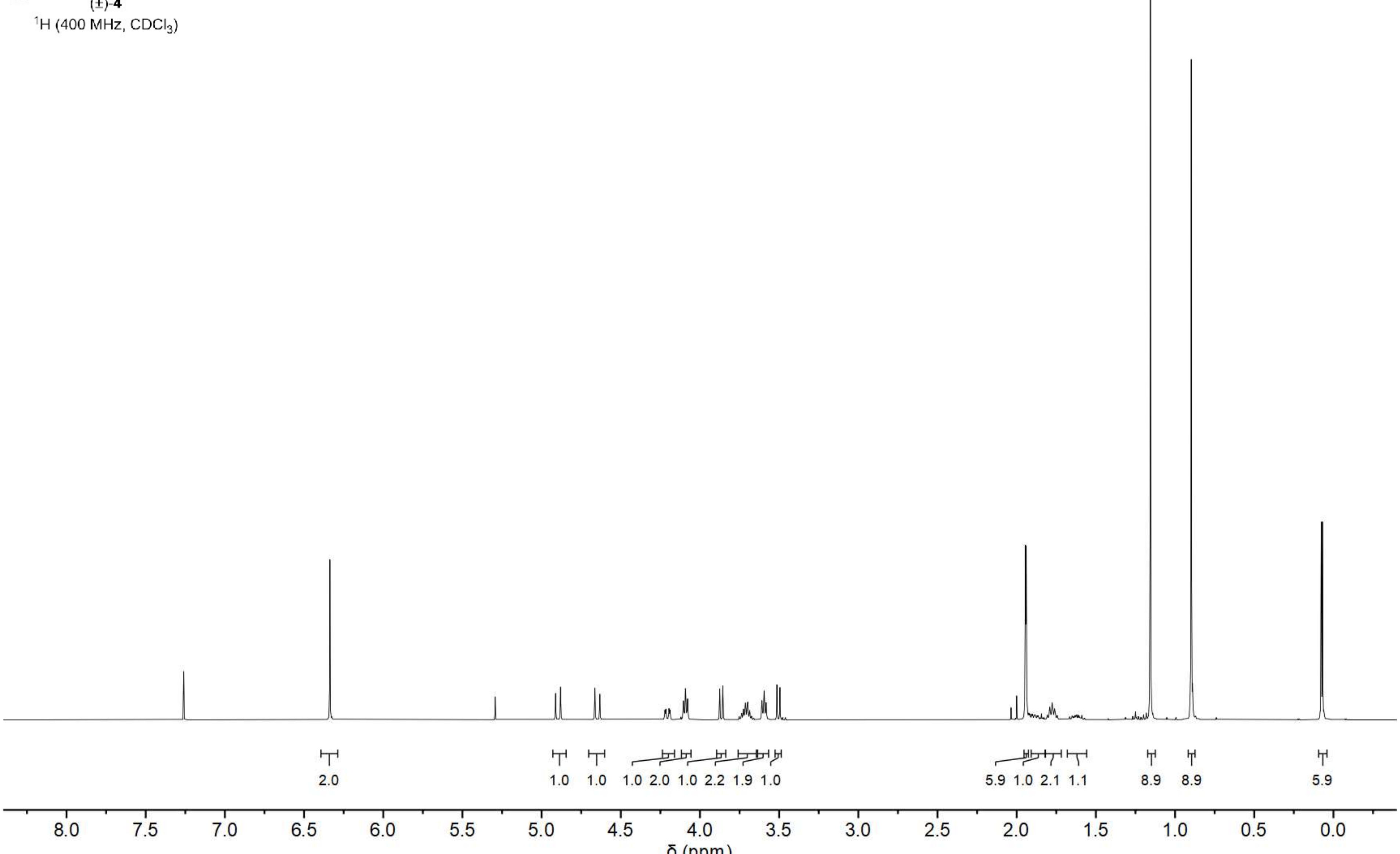

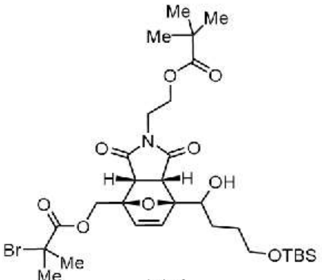

(±)-**4**

^{13}C (101 MHz, CDCl$_3$)

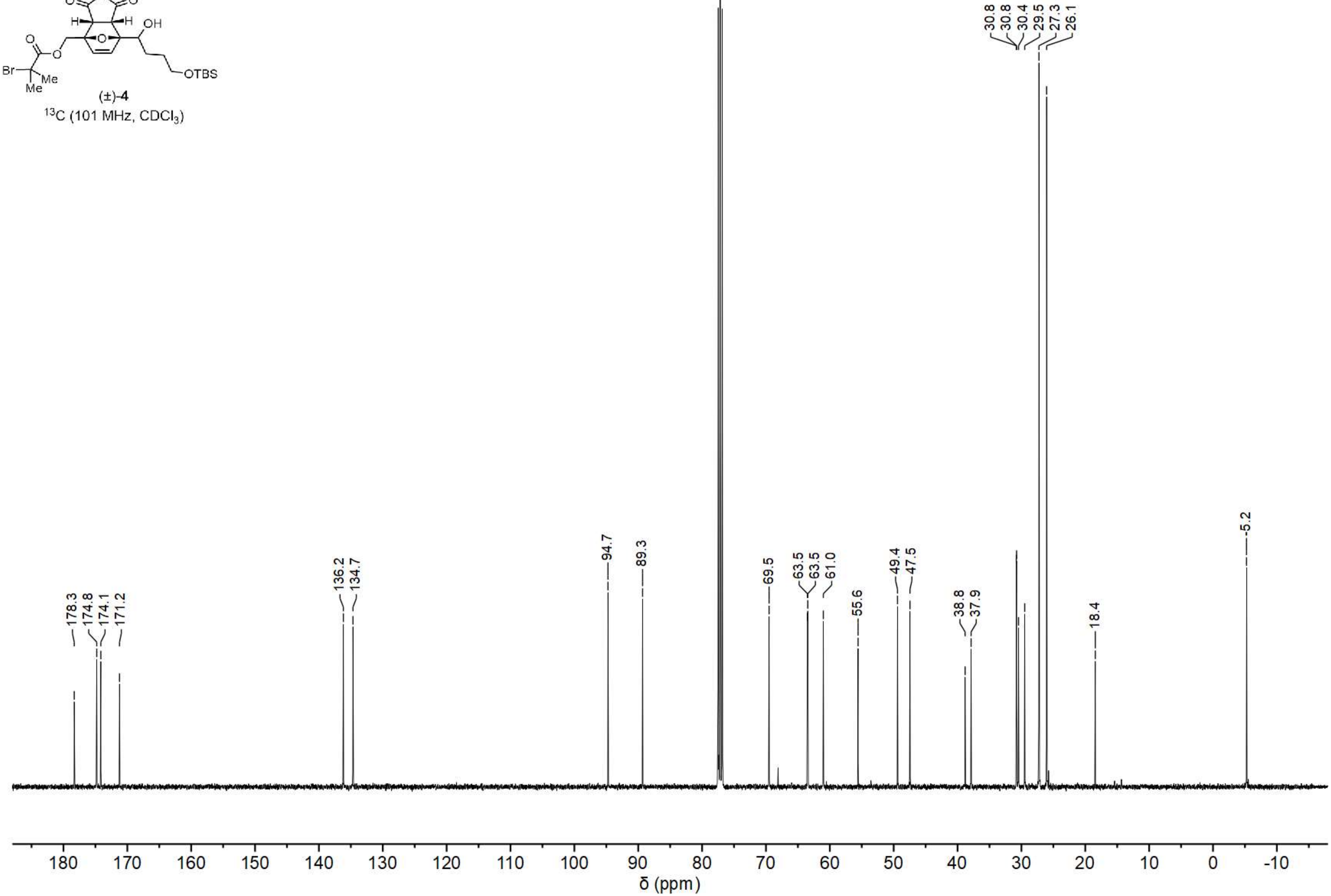

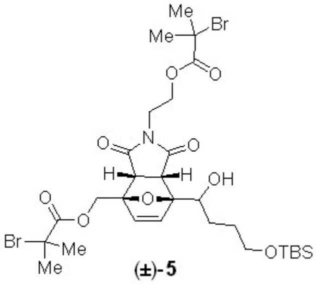

(±)-5

^{1}H (400 MHz, CD$_2$Cl$_2$)

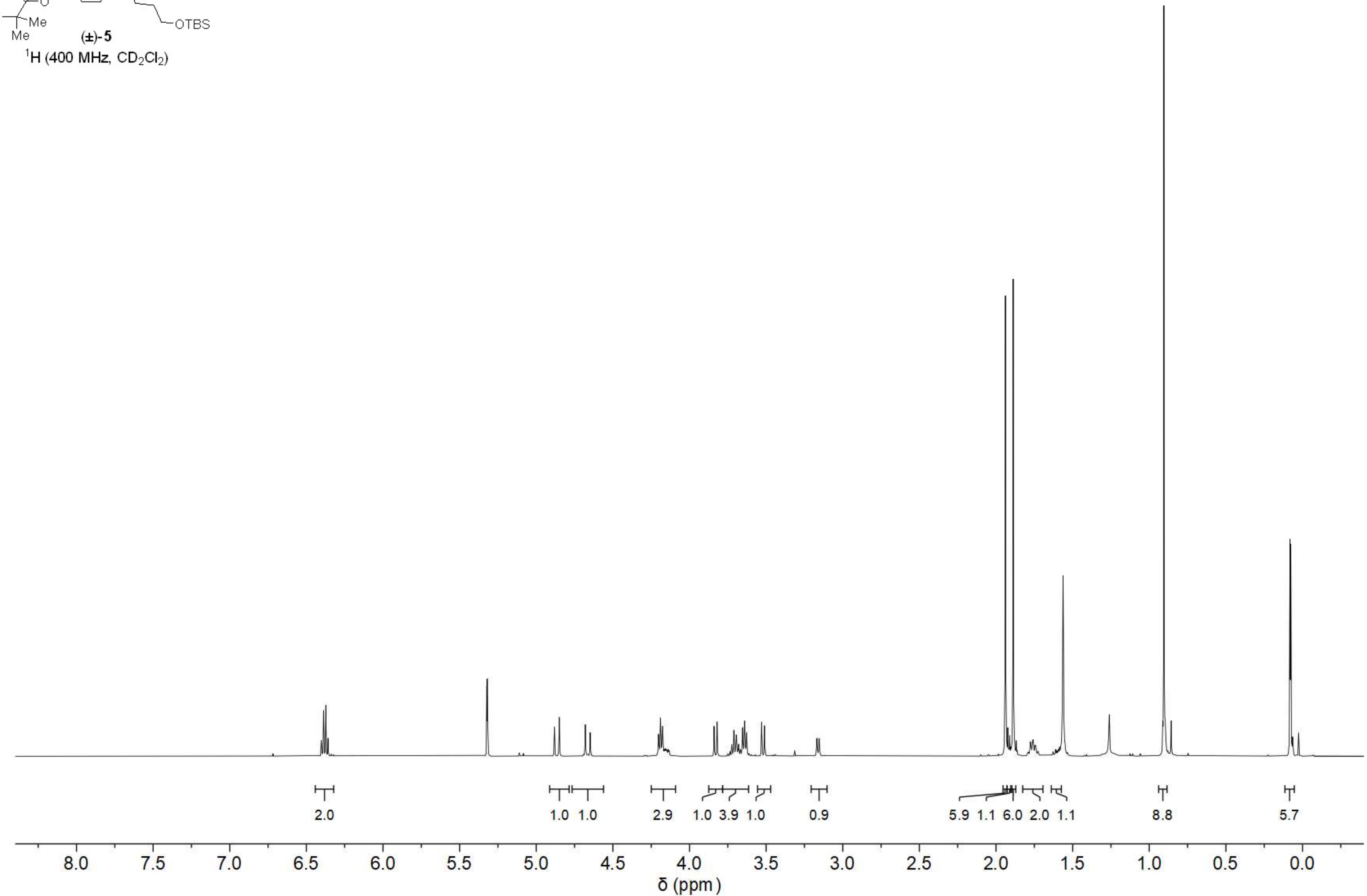

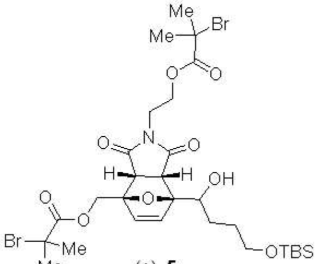

(±)-**5**

^{13}C (101 MHz, CD_2Cl_2)

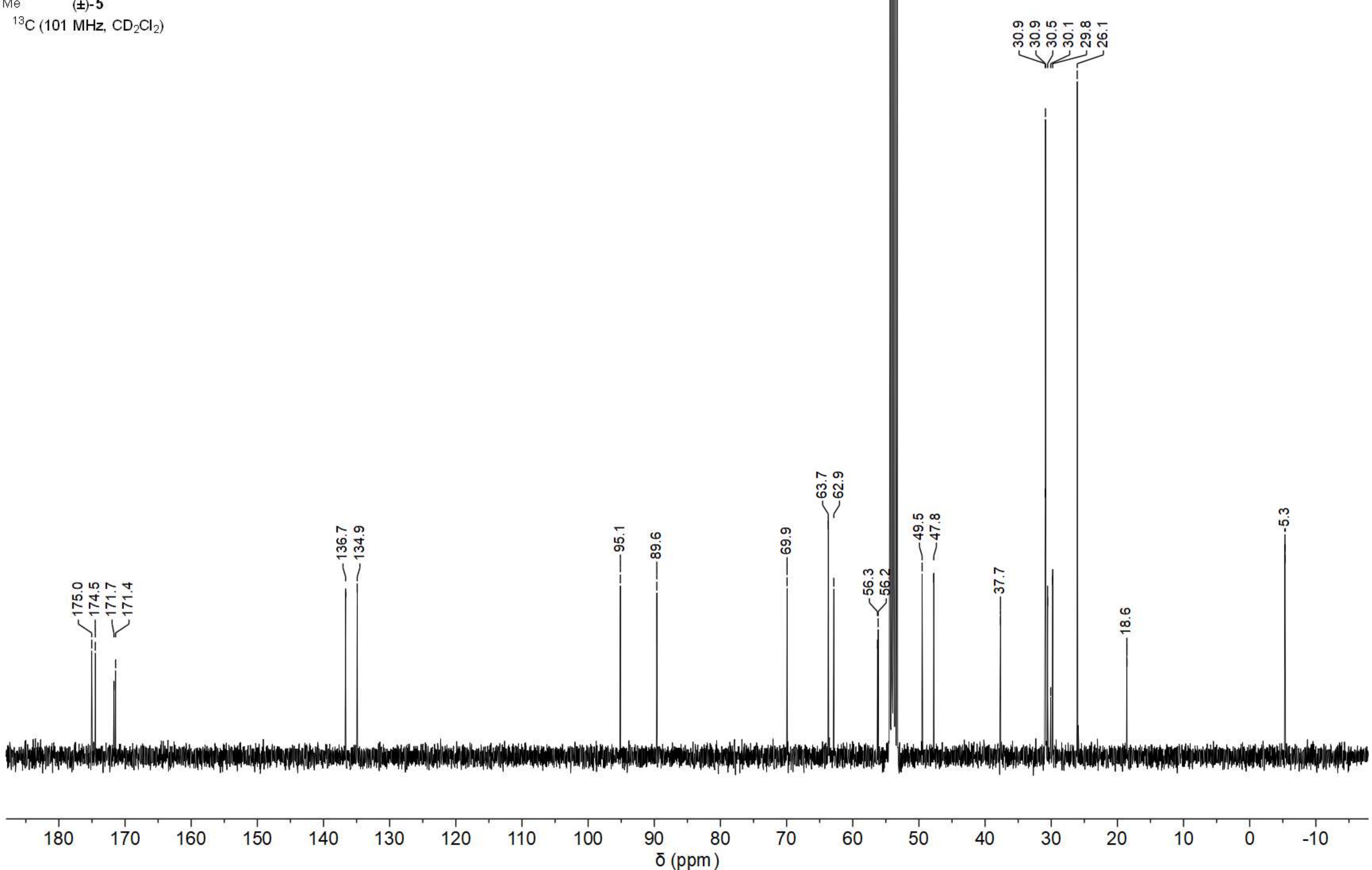

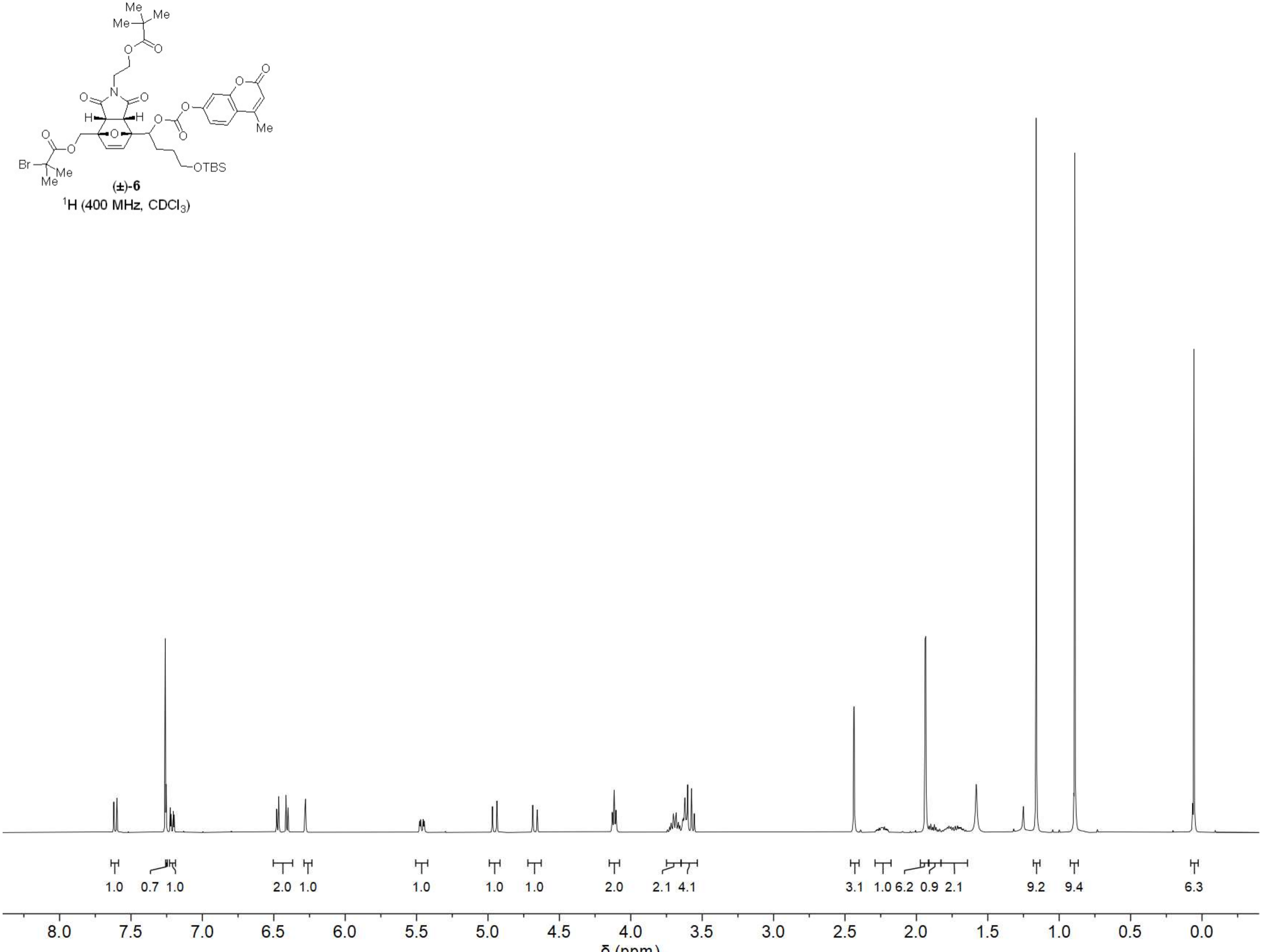

(±)-**6**

^{1}H (400 MHz, CDCl$_3$)

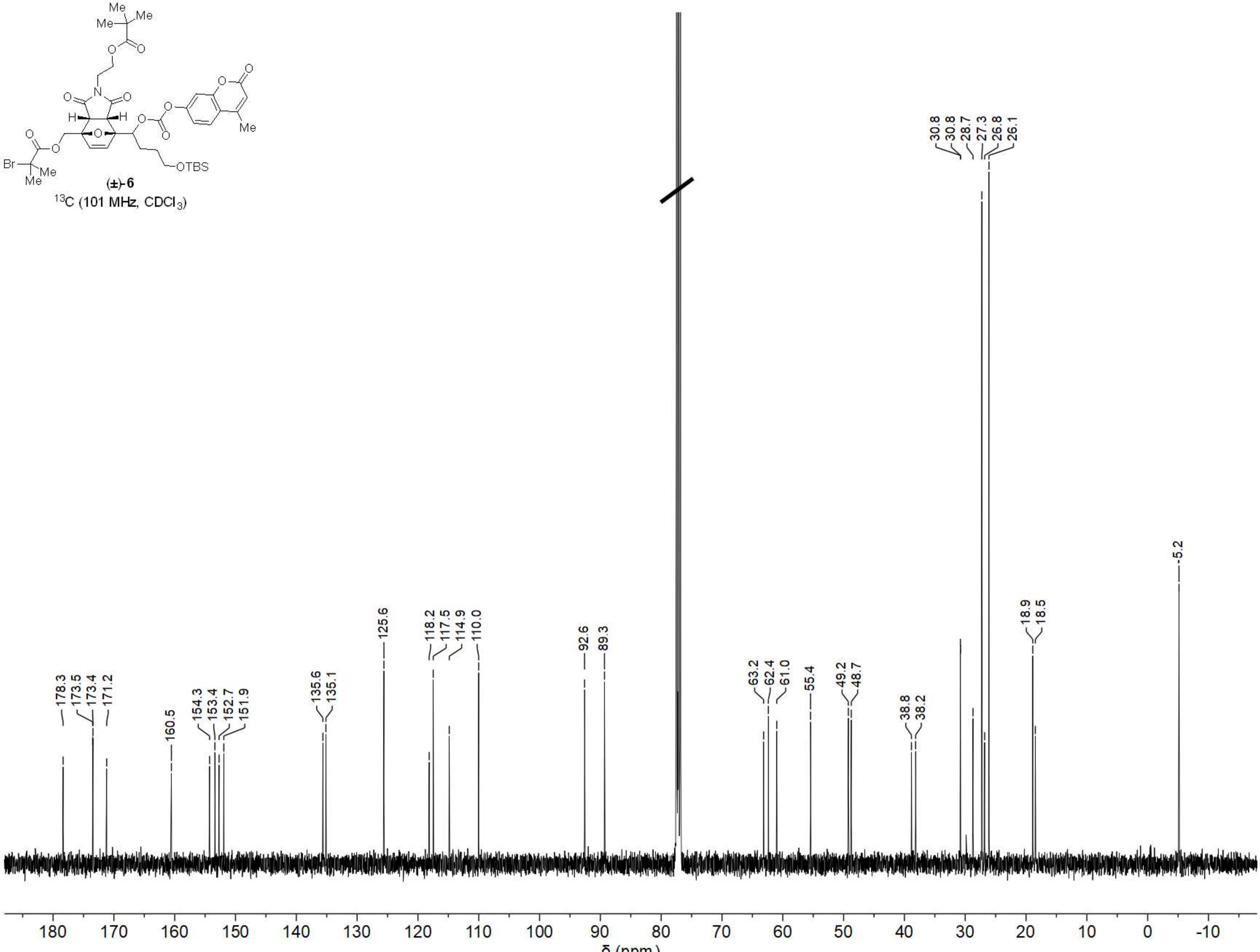
(±)-6

^{13}C (101 MHz, CDCl$_3$)

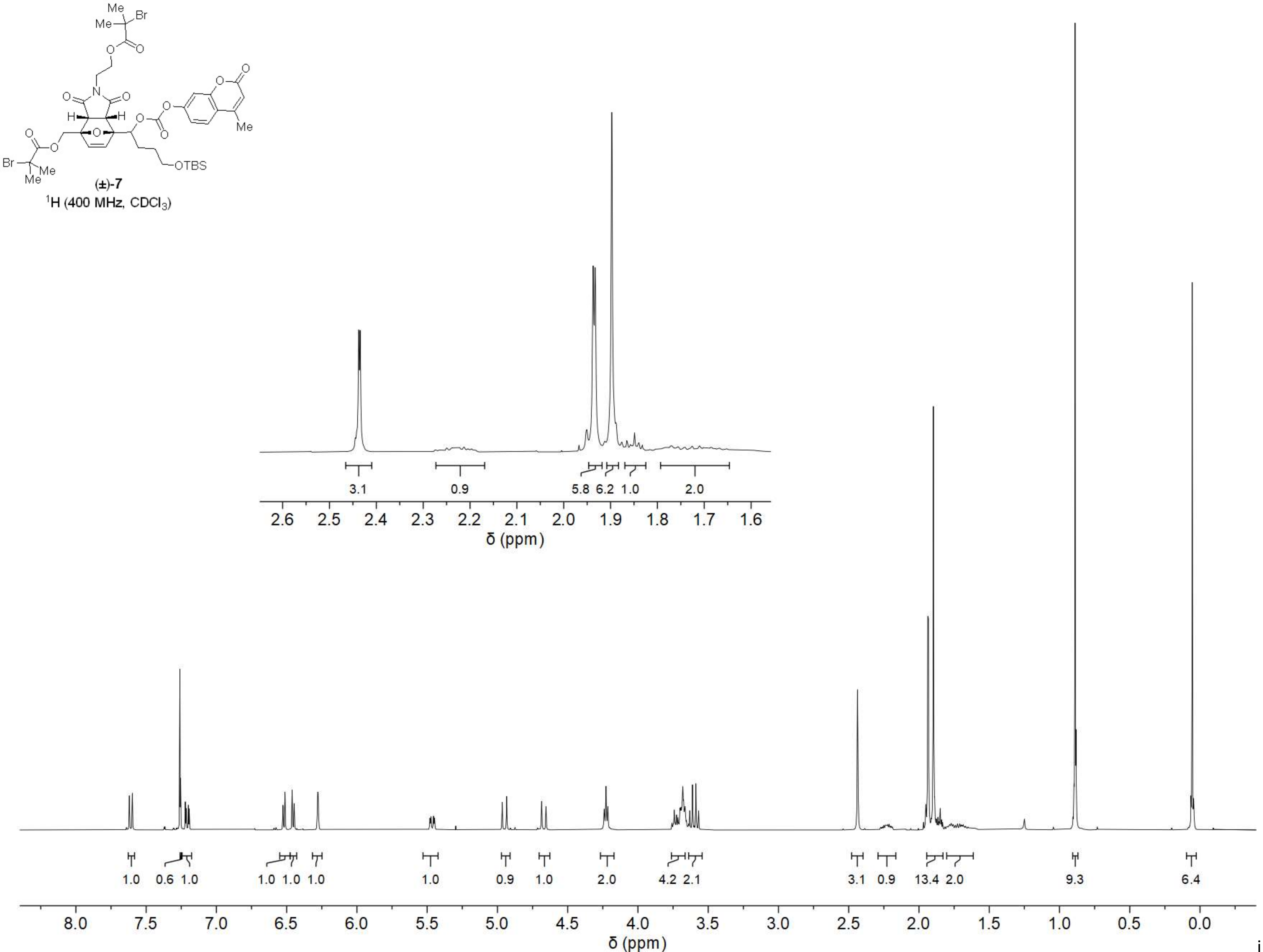

(±)-7

^{1}H (400 MHz, CDCl$_3$)

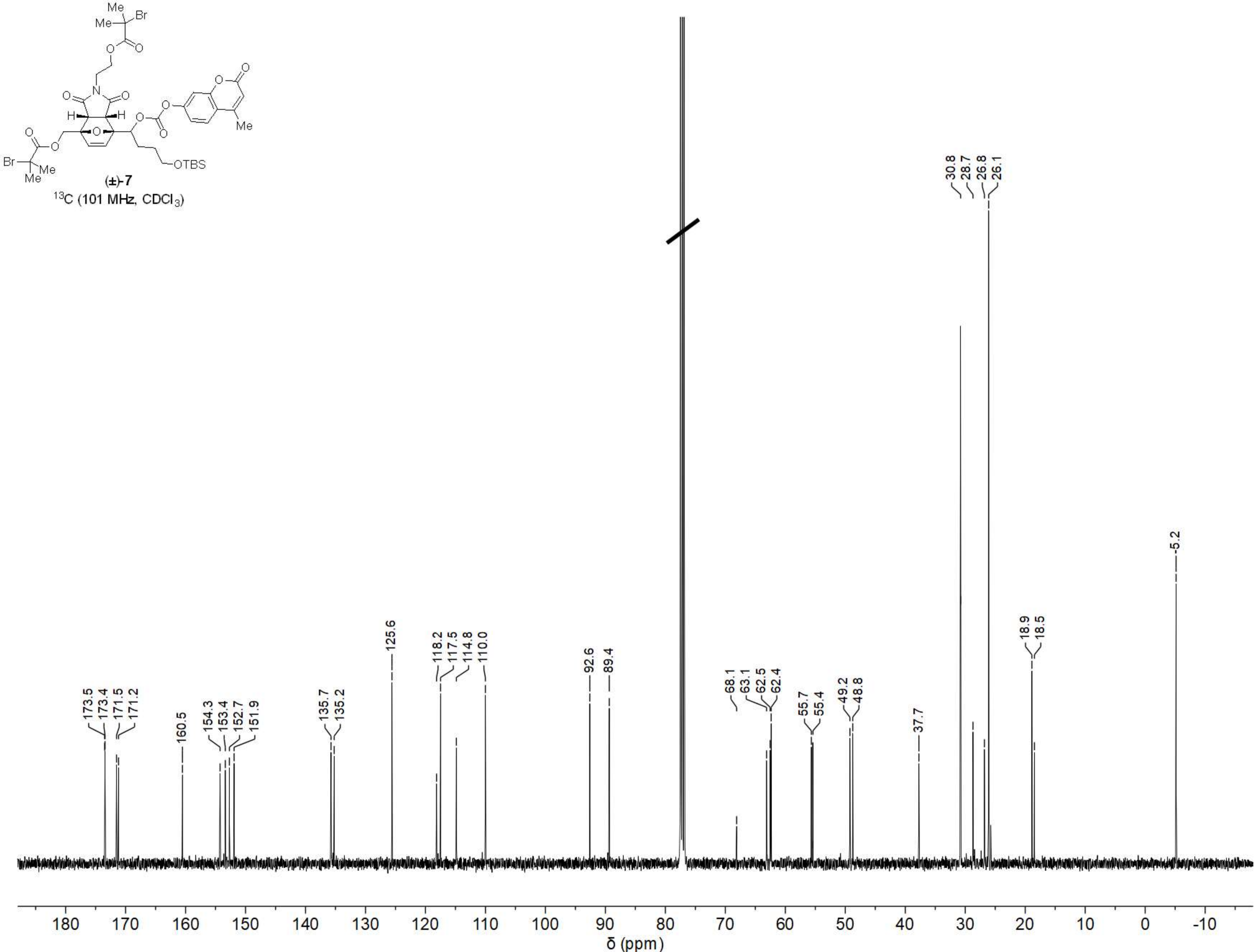

(±)-7

^{13}C (101 MHz, CDCl$_3$)

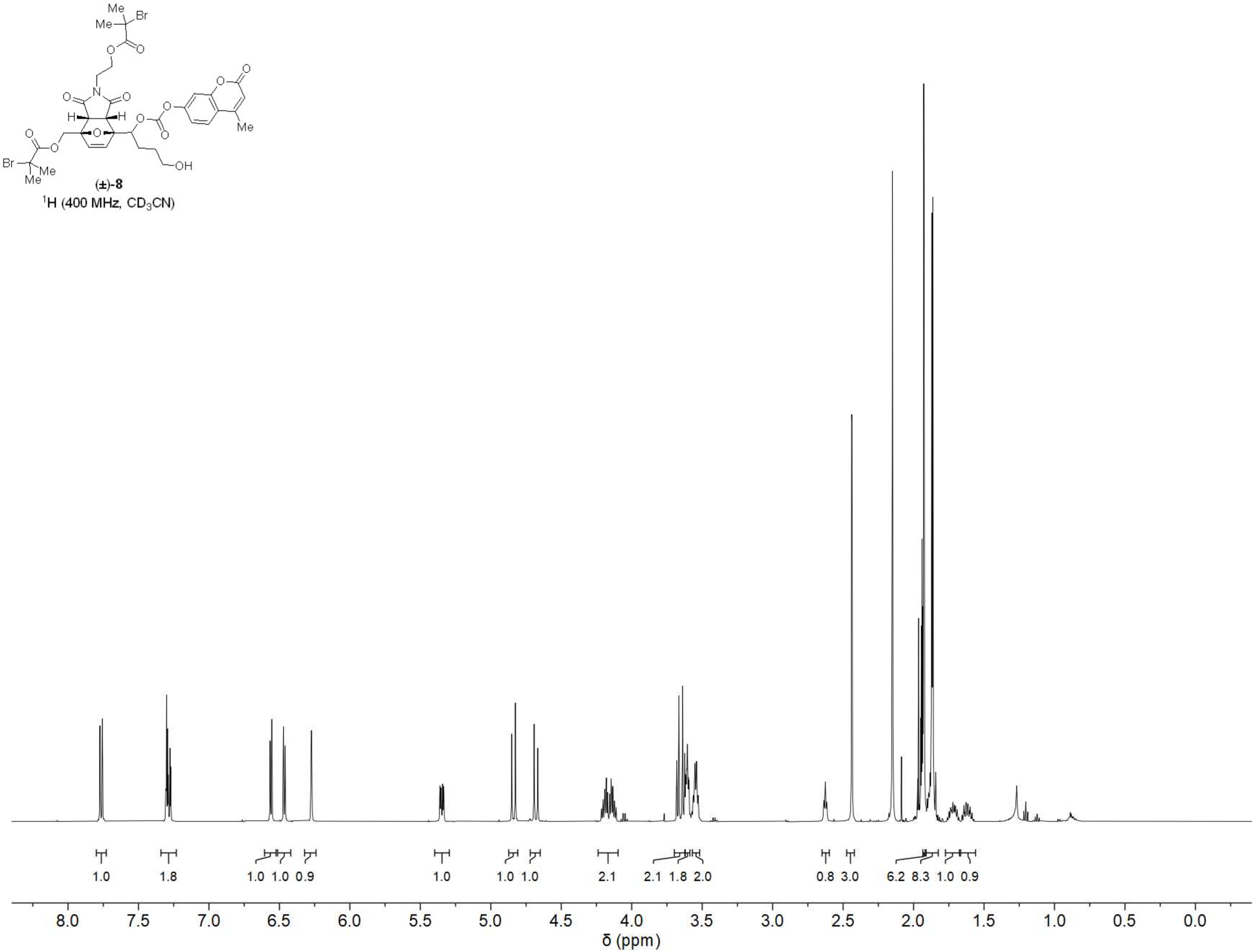
(±)-8

^{1}H (400 MHz, CD$_3$CN)

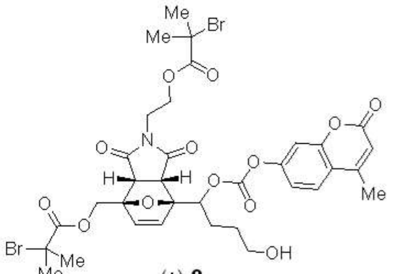

(±)-**8**

^{13}C (101 MHz, CDCl$_3$)

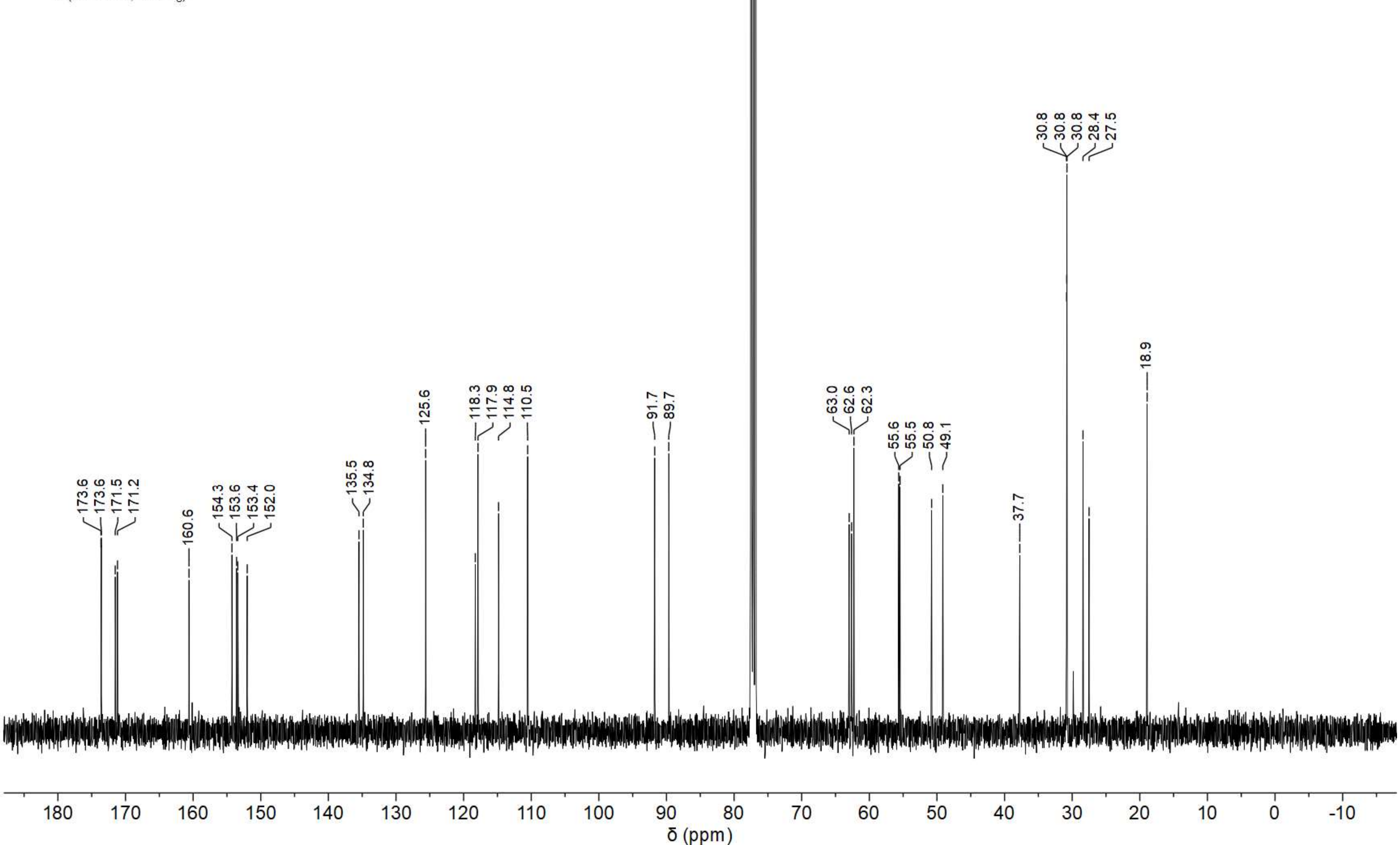

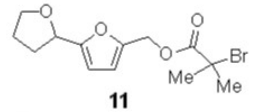

11

^{1}H (400 MHz, CDCl$_3$)

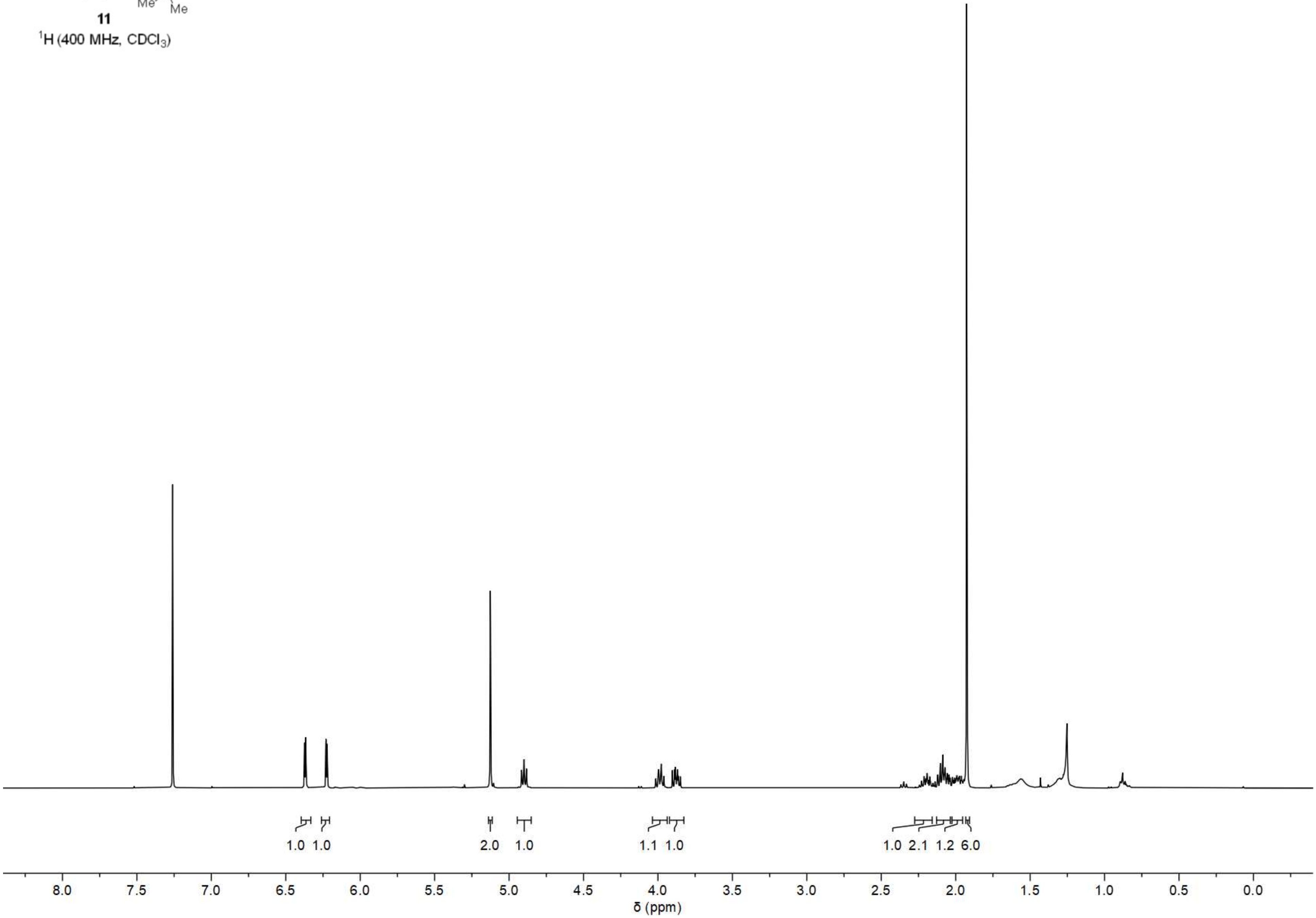

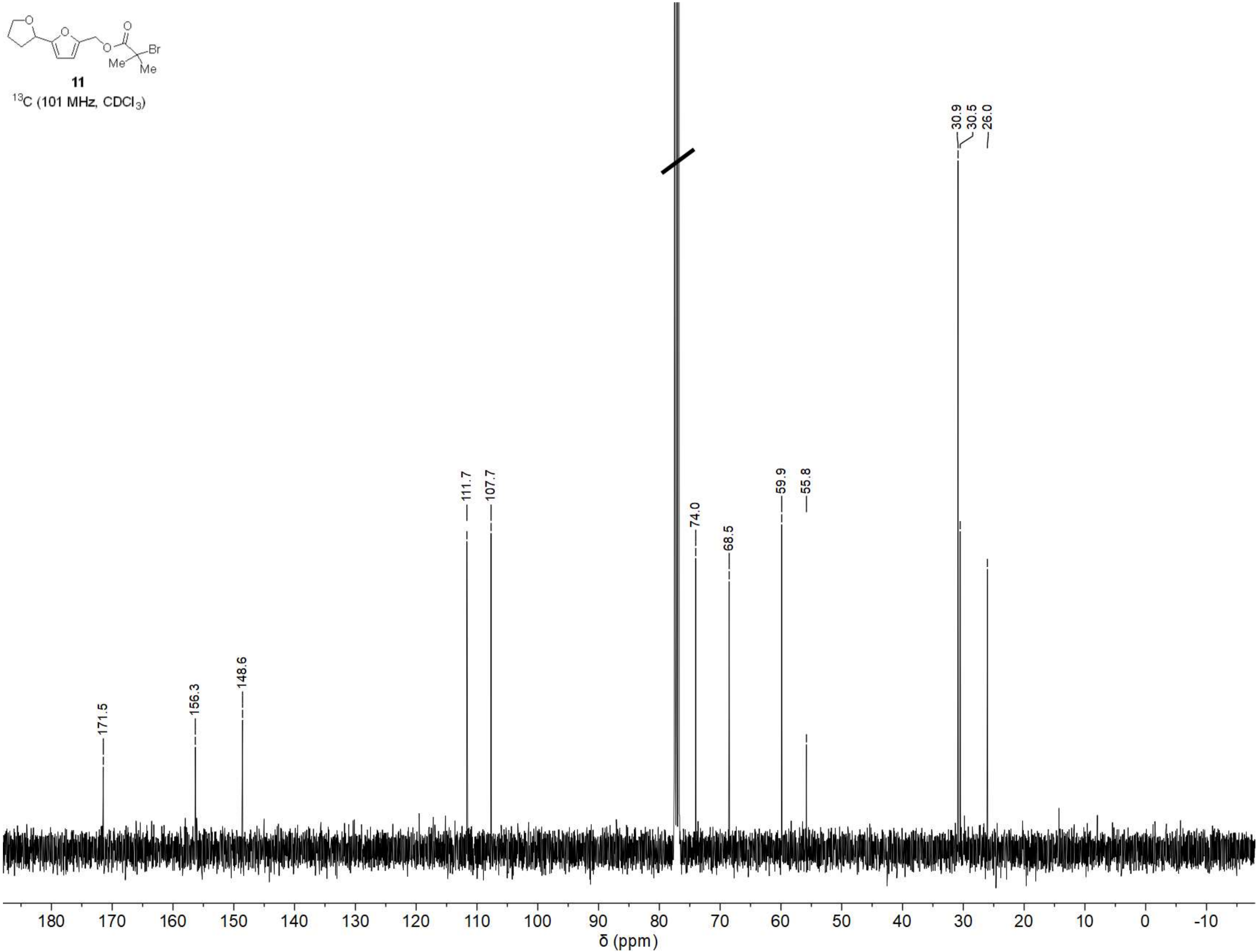

11

^{13}C (101 MHz, CDCl$_3$)

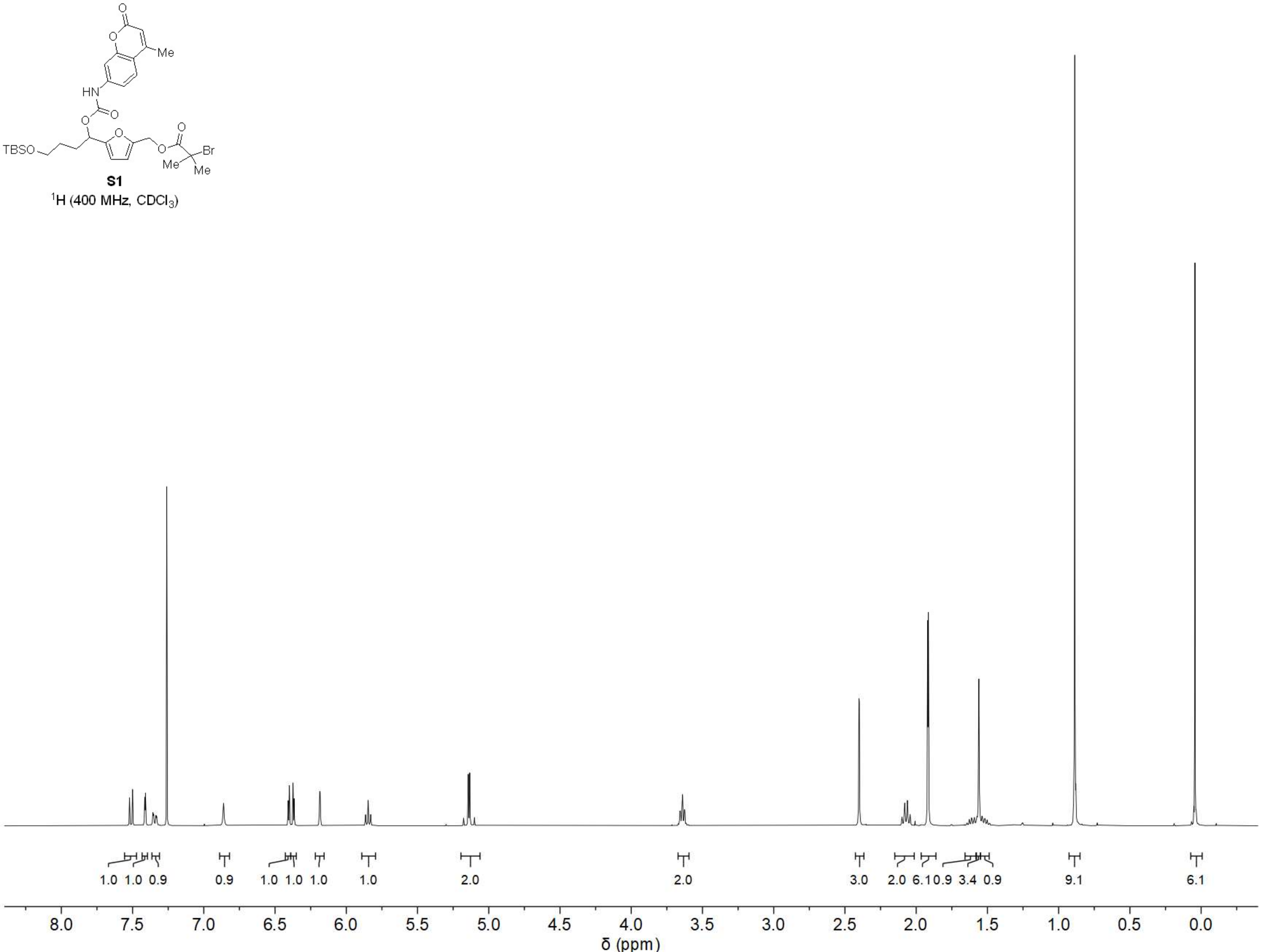

S1

^{1}H (400 MHz, CDCl$_3$)

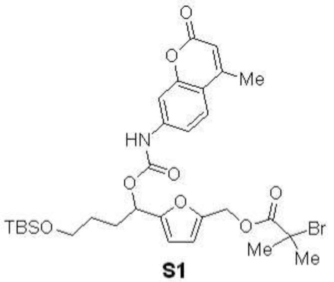

S1

^{13}C (101 MHz, $CDCl_3$)